DECEMBER 2021

AJNR

VOLUME 42 • PP 2109–2260

AJNR

AMERICAN JOURNAL OF NEURORADIOLOGY

DECEMBER 2021
VOLUME 42
NUMBER 12
WWW.AJNR.ORG

THE JOURNAL OF DIAGNOSTIC AND INTERVENTIONAL NEURORADIOLOGY

Changes in ventricular and cortical volumes following shunt placement in iNPH

7T MRI for the identification of incidental intracranial aneurysms

Pulsatile tinnitus due to stenosis of the marginal sinus

Prenatal evaluation of intracranial hemorrhage on fetal MRI

Official Journal ASNR • ASFNR • ASHNR • ASPNR • ASSR

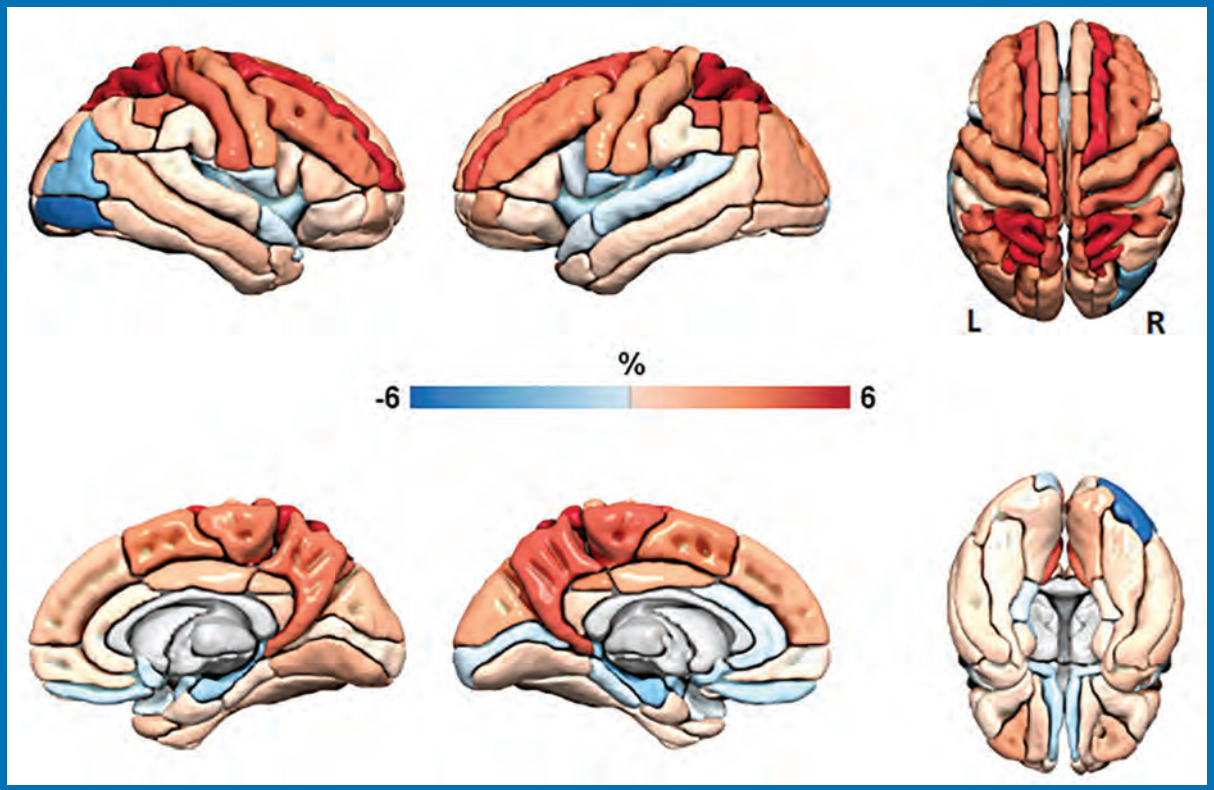

WEB™ Embolization: **Clinically Proven**

12,000 +
Patients Treated

100 +
Publications

10 Years
of Continuous Innovation

MicroVention™
TERUMO

microvention.com

WEB™ 17

Aneurysm Embolization System

LOWER PROFILE

NEW SIZES

MORE ACCESS OPTIONS

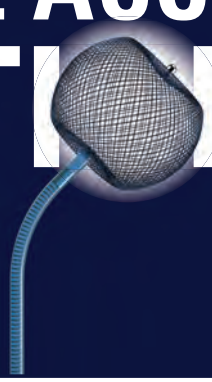

INDICATIONS FOR USE:
The WEB Aneurysm Embolization System is intended for the endovascular embolization of ruptured and unruptured intracranial aneurysms and other neurovascular abnormalities such as arteriovenous fistulae (AVF). The WEB Aneurysm Embolization System is also intended for vascular occlusion of blood vessels within the neurovascular system to permanently obstruct blood flow to an aneurysm or other vascular malformation

POTENTIAL COMPLICATIONS:
Potential complications include but are not limited to the following: hematoma at the site of entry, aneurysm rupture, emboli, vessel perforation, parent artery occlusion, hemorrhage, ischemia, vasospasm, clot formation, device migration or misplacement, premature or difficult device detachment, non-detachment, incomplete aneurysm filling, revascularization, post-embolization syndrome, and neurological deficits including stroke and death. For complete indications, potential complications, warnings, precautions, and instructions, see instructions for use (IFU provided with the device).

VIA 21, 27, 33 - The VIA Microcatheter is intended for the introduction of interventional devices (such as the WEB device/stents/flow diverters) and infusion of diagnostic agents (such as contrast media) into the neuro, peripheral, and coronary vasculature.

VIA 17,17 Preshaped - The VIA Microcatheter is intended for the introduction of interventional devices (such as the WEB device/stents/flow diverters) and infusion of diagnostic agents (such as contrast media) into the neuro, peripheral, and coronary vasculature.

The VIA Microcatheter is contraindicated for use with liquid embolic materials, such as n-butyl 2-cyanoacrylate or ethylene vinyl alcohol & DMSO (dimethyl sulfoxide).

The device should only be used by physicians who have undergone training in all aspects of the WEB Aneurysm Embolization System procedure as prescribed by the manufacturer.

RX Only: Federal law restricts this device to sale by or on the order of a physician.

For healthcare professional intended use only.

MicroVention™
TERUMO

MicroVention Worldwide Innovaton Center — PH +1.714.247.8000

35 Enterprise
Aliso Viejo, CA 92656 USA

MicroVention UK Limited — PH +44 (0) 191 258 6777
MicroVention Europe, S.A.R.L. — PH +33 (1) 39 21 77 46
MicroVention Deutschland GmbH — PH +49 211 210 798-0
Website — microvention.com

CE 0297

WEB™ and VIA™ are registered trademarks of Sequent Medical, Inc. in the United States.

©2021 MicroVention, Inc. MM1184 WW 11/2021

Explore the New ASNR Career Center

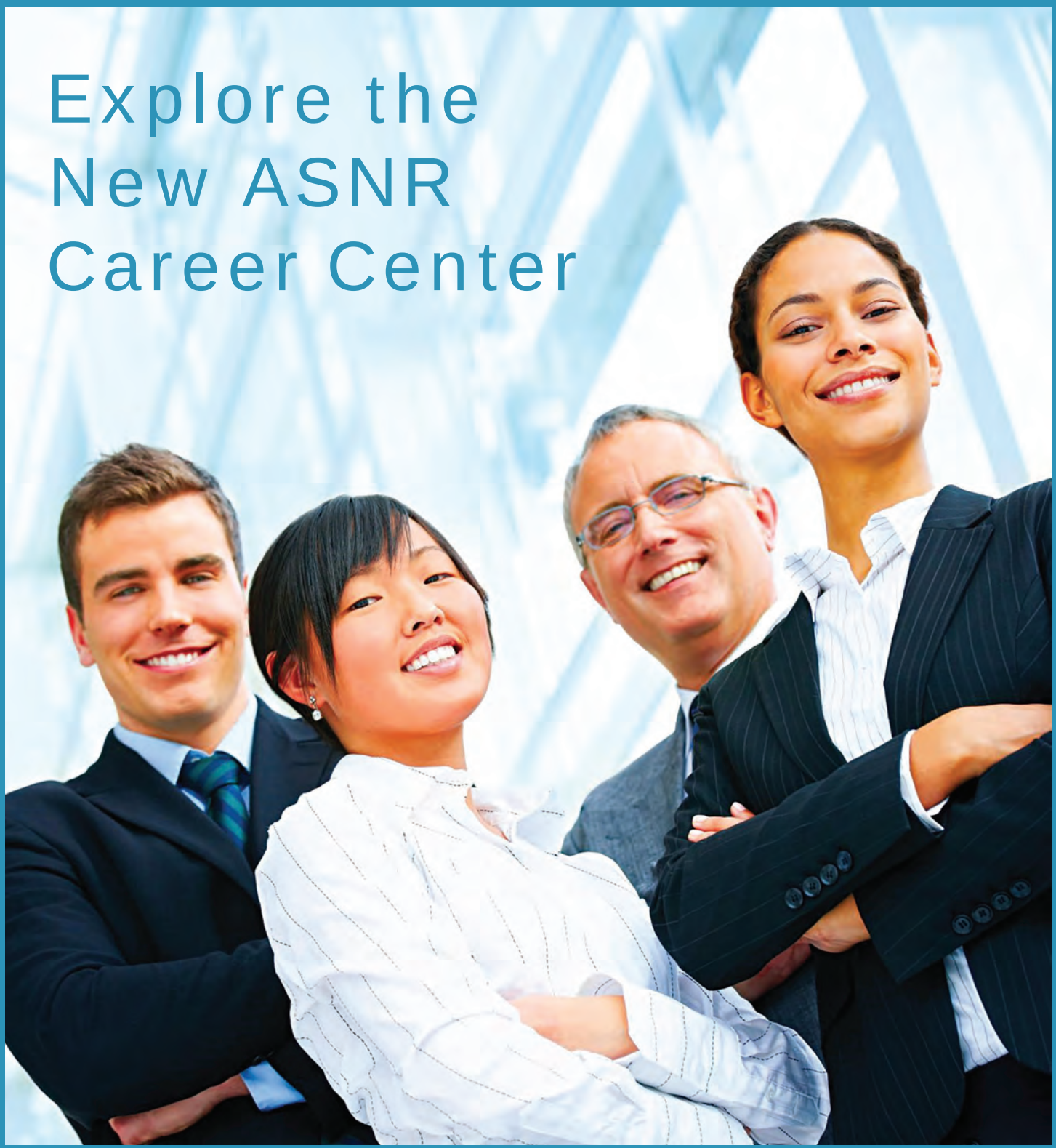

Your Premier Resource for Professional Development

- Access to jobs in the National Healthcare Career Network
- Confidential resume posting
- One-time free resume review
- Professional online profile
- Saved jobs capability

Start here: careers.asnr.org

ASNR
American Society of Neuroradiology

AJNR
AMERICAN JOURNAL OF NEURORADIOLOGY

CALL FOR AJNR EDITORIAL FELLOWSHIP CANDIDATES

2022 Candidate Information and Requirements

ASNR and AJNR are pleased once again to join efforts with other imaging-related journals that have training programs on editorial aspects of publishing for trainees or junior staff (<5 years on staff), including Radiology (Olmsted fellowship), AJR (Figley and Rogers fellowships), JACR (Bruce J. Hillman fellowship), and Radiologia.

GOALS

- Increase interest in editorial and publication-related activities in younger individuals.
- Increase understanding and participation in the AJNR review process.
- Incorporate into AJNR's Editorial Board younger individuals who have previous experience in the review and publication process.
- Fill a specific need in neuroradiology not offered by other similar fellowships.
- Increase the relationship between "new" generation of neuroradiologists and more established individuals.
- Increase visibility of AJNR among younger neuroradiologists.

ACTIVITIES OF THE FELLOWSHIP

- Serve as Editorial Fellow for one year. This individual will be listed on the masthead as such.
- Review at least one manuscript per month for 12 months. Evaluate all review articles submitted to AJNR.
- Learn how electronic manuscript review systems work.
- Be involved in the final decision of selected manuscripts together with the Editor-in-Chief.
- Participate in all monthly Senior Editor telephone conference calls.
- Participate in all meetings of the Editors during the annual meetings of ASNR and RSNA and the Radiology Editors Forum as per candidate's availability. The Foundation of the ASNR will provide $2000 funding for this activity.
- Evaluate progress and adjust program to specific needs in annual meeting or telephone conference with the Editor-in-Chief.
- Embark on an editorial scientific or bibliometric project that will lead to the submission of an article to AJNR or another appropriate journal as determined by the Editor-in-Chief. This project will be presented by the Editorial Fellow at the ASNR annual meeting.
- Recruit trainees as reviewers as determined by the Editor-in-Chief.
- Organize and host a Fellows' Journal Club podcast.
- Serve as Guest Editor for an issue of AJNR's News Digest with a timely topic.

QUALIFICATIONS

- Be a fellow in neuroradiology from North America, including Canada (this may be extended to include other countries).
- Be a junior faculty neuroradiology member (< 5 years) in either an academic or private environment.
- Be an "in-training" or member of ASNR in any other category.

APPLICATION

- Include a short letter of intent with statement of goals and desired research project. CV must be included.
- Include a letter of recommendation from the Division Chief or fellowship program director. A statement of protected time to perform the functions outlined is desirable.
- Applications will be evaluated by AJNR's Senior Editors prior to the ASNR annual meeting. The name of the selected individual will be announced at the meeting.
- Applications should be received by March 1, 2022 and sent to Ms. Karen Halm, AJNR Managing Editor, electronically at khalm@asnr.org.

AJNR

AMERICAN JOURNAL OF NEURORADIOLOGY

Publication Preview at www.ajnr.org features articles released in advance of print. Visit www.ajnrblog.org to comment on AJNR content and chat with colleagues and AJNR's News Digest at http://ajnrdigest.org to read the stories behind the latest research in neuroimaging.

DECEMBER 2021 • VOLUME 42 • NUMBER 12 • WWW.AJNR.ORG

EDITOR-IN-CHIEF

Jeffrey S. Ross, MD
Professor of Radiology, Department of Radiology, Mayo Clinic College of Medicine, Phoenix, AZ

SENIOR EDITORS

Harry J. Cloft, MD, PhD
Professor of Radiology and Neurosurgery, Department of Radiology, Mayo Clinic College of Medicine, Rochester, MN

Christopher G. Filippi, MD
Professor and Alice Ettinger-Jack R. Dreyfuss Chair of Radiology, Tufts University School of Medicine, Radiologist-in-Chief Tufts University Medical Center, Boston, MA

Thierry A.G.M. Huisman, MD
Radiologist-in-Chief, Texas Children's Hospital, Houston, TX

Yvonne W. Lui, MD
Associate Professor of Radiology, Chief of Neuroradiology, New York University School of Medicine, New York, NY

C.D. Phillips, MD, FACR
Professor of Radiology, Weill Cornell Medical College, Director of Head and Neck Imaging, New York-Presbyterian Hospital, New York, NY

Lubdha M. Shah, MD, MS
Professor of Radiology and Director of Spine Imaging, University of Utah Department of Radiology and Imaging Sciences, Salt Lake City, UT

STATISTICAL SENIOR EDITOR

Bryan A. Comstock, MS
Senior Biostatistician, Department of Biostatistics, University of Washington, Seattle, WA

ARTIFICIAL INTELLIGENCE DEPUTY EDITOR

Peter D. Chang, MD
Assistant Professor-in-Residence, Departments of Radiological Sciences, Computer Sciences, and Pathology, Director, Center for Artificial Intelligence in Diagnostic Medicine (CAIDM), University of California, Irvine, Irvine, CA

EDITORIAL BOARD

Ashley H. Aiken, *Atlanta, GA*
Lea M. Alhilali, *Phoenix, AZ*
Mohammed A. Almekhlafi, *Calgary, Alberta, Canada*
Joachim Berkefeld, *Frankfurt, Germany*
Aashim Bhatia, *Pittsburgh, PA*
Waleed Brinjikji, *Rochester, MN*
Judah Burns, *New York, NY*
Danielle Byrne, *Dublin, Ireland*
Federico Cagnazzo, *Montpellier, France*
J. Levi Chazen, *New York, NY*
James Y. Chen, *San Diego, CA*
Gloria C. Chiang, *New York, NY*
Daniel Chow, *Irvine, CA*
Kars C.J. Compagne, *Rotterdam, The Netherlands*
Arturo Consoli, *Suresnes, France*
Seena Dehkharghani, *New York, NY*
Nilesh K. Desai, *Houston, TX*
Yonghong Ding, *Rochester, MN*
Birgit Ertl-Wagner, *Toronto, Ontario, Canada*
Clifford J. Eskey, *Hanover, NH*
Massimo Filippi, *Milan, Italy*
Nils D. Forkert, *Calgary, Alberta, Canada*
Ana M. Franceschi, *New York, NY*
Frank Gaillard, *Melbourne, Australia*
Joseph J. Gemmete, *Ann Arbor, Michigan*
Wende N. Gibbs, *Phoenix, AZ*
Philipp Gölitz, *Erlangen, Germany*
Brent Griffith, *Detroit, MI*
Joseph M. Hoxworth, *Phoenix, Arizona*
Raymond Y. Huang, *Boston, MA*
Gábor Janiga, *Magdeburg, Germany*
Christof Karmonik, *Houston, TX*
Timothy J. Kaufmann, *Rochester, MN*
Hillary R. Kelly, *Boston, MA*
Toshibumi Kinoshita, *Akita, Japan*
Alexander W. Korutz, *Chicago, IL*
Stephen F. Kralik, *Houston, TX*
Alexander Lerner, *Los Angeles, CA*
Yinsheng Li, *Madison, WI*
Franklin A. Marden, *Chicago, IL*
Markus A. Möhlenbruch, *Heidelberg, Germany*
Kambiz Nael, *Los Angeles, CA*
Renato Hoffmann Nunes, *Sao Paulo, Brazil*
Sasan Partovi, *Cleveland, OH*
Johannes A.R. Pfaff, *Salzburg, Austria*
Laurent Pierot, *Reims, France*
Alireza Radmanesh, *New York, NY*
Prashant Raghavan, *Baltimore, MD*
Eytan Raz, *New York, NY*
Paul M. Ruggieri, *Cleveland, OH*
Sebastian Schafer, *Madison, WI*
Maksim Shapiro, *New York, NY*
Timothy Shepherd, *New York, NY*
James Shin, *New York, NY*
Mark S. Shiroishi, *Los Angeles, CA*
Bruno P. Soares, *Baltimore, MD*
Jason F. Talbott, *San Francisco, CA*
Ruth Thiex, *Everett, Washington*
Vincent Thijs, *Melbourne, Victoria, Australia*
Anderanik Tomasian, *Los Angeles, CA*
Fabio Triulzi, *Milan, Italy*
Anja G. van der Kolk, *Utrecht, the Netherlands*
Arastoo Vossough, *Philadelphia, PA*
Elysa Widjaja, *Toronto, Ontario, Canada*
Leonard Yeo, *Singapore*
Woong Yoon, *Gwangju, South Korea*
David M. Yousem, *Evergreen, CO*
Carlos Zamora, *Chapel Hill, NC*
Chengcheng Zhu, *Seattle, WA*

EDITORIAL FELLOW

Vivek Yedavalli, *Baltimore, MD*

SPECIAL CONSULTANTS TO THE EDITOR

AJNR Blog Editor
Neil Lall, *Denver, CO*
Case of the Month Editor
Nicholas Stence, *Aurora, CO*
Case of the Week Editors
Matylda Machnowska, *Toronto, Ontario, Canada*
Anvita Pauranik, *Calgary, Alberta, Canada*
Vinil Shah, *San Francisco, CA*
Classic Case Editor
Sandy Cheng-Yu Chen, *Taipei, Taiwan*
Health Care and Socioeconomics Editor
Pina C. Sanelli, *New York, NY*
Physics Editor
Greg Zaharchuk, *Stanford, CA*
Podcast Editor
Courtney Tomblinson, *Nashville, TN*
Deputy Podcast Editor
Kevin Hiatt, *Winston-Salem, NC*
Twitter Editor
Roger Jordan, *Houston, TX*

Official Journal:

American Society of Neuroradiology
American Society of Functional Neuroradiology
American Society of Head and Neck Radiology
American Society of Pediatric Neuroradiology
American Society of Spine Radiology

Founding Editor
Juan M. Taveras
Editors Emeriti
Mauricio Castillo, Robert I. Grossman, Michael S. Huckman, Robert M. Quencer

Managing Editor
Karen Halm
Assistant Managing Editor
Laura Wilhelm
Executive Director, ASNR
Mary Beth Hepp

AJNR

AMERICAN JOURNAL OF NEURORADIOLOGY

DECEMBER 2021
VOLUME 42
NUMBER 12
WWW.AJNR.ORG

Publication Preview at www.ajnr.org features articles released in advance of print. Visit www.ajnrblog.org to comment on AJNR content and chat with colleagues and AJNR's News Digest at http://ajnrdigest.org to read the stories behind the latest research in neuroimaging.

2109 **PERSPECTIVES** *M. Hauben*

REVIEW ARTICLES

2110 **Spinal Vascular Shunts: A Patterned Approach** *M.P. Kona, et al.* — SPINE

2119 **Safety of Oral P2Y12 Inhibitors in Interventional Neuroradiology: Current Status and Perspectives** *L.M. Camargo, et al.* — INTERVENTIONAL

EDITORIAL

2127 **The American Society of Neuroradiology: Cultivating a Diverse and Inclusive Culture to Build a Stronger Organization** *P.M. Bunch, et al.*

GENERAL CONTENTS

2130 **Deep Learning Enables 60% Accelerated Volumetric Brain MRI While Preserving Quantitative Performance: A Prospective, Multicenter, Multireader Trial** *S. Bash, et al.* — ADULT BRAIN FUNCTIONAL

2138 **Hemodynamic Analysis of Cerebral AVMs with 3D Phase-Contrast MR Imaging** *Y. Takeda, et al.* — ADULT BRAIN FUNCTIONAL

2146 **Decreased CSF Dynamics in Treatment-Naive Patients with Essential Hypertension: A Study with Phase-Contrast Cine MR Imaging** *L. Ma, et al.* — ADULT BRAIN

2152 **Identification of *BRAF p. V600E*-Mutant and Wild-Type by MR Imaging in Pleomorphic Xanthoastrocytoma and Anaplastic Pleomorphic Xanthoastrocytoma** *W. Huang, et al.* — ADULT BRAIN

2160 **Idiopathic Intracranial Hypertension is Associated with a Higher Burden of Visible Cerebral Perivascular Spaces: The Glymphatic Connection** *O. Jones, et al.* — ADULT BRAIN

2165 **Changes in Ventricular and Cortical Volumes following Shunt Placement in Patients with Idiopathic Normal Pressure Hydrocephalus** *P.M. Cogswell, et al.* — ADULT BRAIN FUNCTIONAL

2172 **Clinical Implementation of 7T MRI for the Identification of Incidental Intracranial Aneurysms versus Anatomic Variants** *P. Radojewski, et al.* — ADULT BRAIN

2175 **Disparities in the Use of Mechanical Thrombectomy Alone Compared with Adjunctive Intravenous Thrombolysis in Acute Ischemic Stroke in the United States** *W. Wahood, et al.* — INTERVENTIONAL

AJNR (Am J Neuroradiol ISSN 0195–6108) is a journal published monthly, owned and published by the American Society of Neuroradiology (ASNR), 800 Enterprise Drive, Suite 205, Oak Brook, IL 60523. Annual dues for the ASNR include approximately 21% for a journal subscription. The journal is printed by Intellicor Communications, 330 Eden Road, Lancaster, PA 17601; Periodicals postage paid at Oak Brook, IL and additional mailing offices. Printed in the U.S.A. POSTMASTER: Please send address changes to American Journal of Neuroradiology, P.O. Box 3000, Denville, NJ 07834, U.S.A. Subscription rates: nonmember $430 ($505 foreign) print and online, $320 online only; institutions $495 ($565 foreign) print and basic online, $980 ($1050 foreign) print and extended online, $380 online only (basic), $825 online only (extended); single copies are $35 each ($40 foreign). Indexed by PubMed/MEDLINE, BIOSIS Previews, Current Contents (Clinical Medicine and Life Sciences), EMBASE, Google Scholar, HighWire Press, Q-Sensei, RefSeek, Science Citation Index, SCI Expanded, ReadCube, and Semantic Scholar. Copyright © American Society of Neuroradiology.

2181 **Risks of Undersizing Stent Retriever Length Relative to Thrombus Length in Patients with Acute Ischemic Stroke** *N.F. Belachew, et al.* — INTERVENTIONAL

2188 **Perceived Limits of Endovascular Treatment for Secondary Medium-Vessel-Occlusion Stroke** *P. Cimflova, et al.* — INTERVENTIONAL

2194 **Pulsatile Tinnitus Due to Stenosis of the Marginal Sinus: Diagnosis and Endovascular Treatment** *J. Cortese, et al.* — INTERVENTIONAL

2199 **Carotid Plaque Composition Assessed by CT Predicts Subsequent Cardiovascular Events among Subjects with Carotid Stenosis** *E. Choi, et al.* — EXTRACRANIAL VASCULAR

2207 **Quantitative Analysis of the Olfactory System in COVID-19: An MR Imaging Study** *E. Altunisik, et al.* — HEAD & NECK

2215 **Retrospective Review of Midpoint Vestibular Aqueduct Size in the 45° Oblique (Pöschl) Plane and Correlation with Hearing Loss in Patients with Enlarged Vestibular Aqueduct** *K. Bouhadjer, et al.* — HEAD & NECK

2222 **Prenatal Evaluation of Intracranial Hemorrhage on Fetal MRI: A Retrospective Review** *K.N. Epstein, et al.* — PEDIATRICS

2229 *Commentary*
Intracranial Hemorrhage on Prenatal MR Imaging *M. Bekiesinska-Figatowska*

2231 **Can MRI Differentiate between Infectious and Immune-Related Acute Cerebellitis? A Retrospective Imaging Study** *G. Orman, et al.* — PEDIATRICS

2238 **Maternal Obesity during Pregnancy is Associated with Lower Cortical Thickness in the Neonate Brain** *X. Na, et al.* — PEDIATRICS

2245 **Anatomic Neuroimaging Characteristics of Posterior Fossa Type A Ependymoma Subgroups** *N.D. Sabin, et al.* — PEDIATRICS

2251 **A Closer Investigation of the Synchronous Bilateral Pattern of MRI Lesions in Acute Necrotizing Encephalopathy Type 1** *A. Horváthy-Szőcs, et al.* — PEDIATRICS

2254 **Accuracy and Clinical Utility of Reports from Outside Hospitals for CT of the Cervical Spine in Blunt Trauma** *K. Rao, et al.* — SPINE

ONLINE FEATURES

LETTERS

E79 **Vessel Wall Imaging: A Powerful Diagnostic Tool but Not a Substitute for Biopsies** *S.R. Zeiler, et al.*

E80 **Usefulness of a Radial-Specific Neurointerventional Guiding Sheath** *Y. Hanaoka, et al.*

BOOK REVIEWS *R.M. Quencer, Section Editor*

Please visit www.ajnrblog.org to read and comment on Book Reviews.

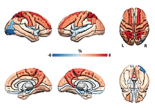

Surface-renderings of mean percentage change in cortical volume among all participants by cortical region from Cogswell et al, in this issue.

Indicates Editor's Choices selection
Indicates Fellows' Journal Club selection
Indicates open access to non-subscribers at www.ajnr.org
Indicates article with supplemental online data
Indicates article with supplemental online video
EBM 1 Evidence-Based Medicine Level 1
EBM 2 Evidence-Based Medicine Level 2

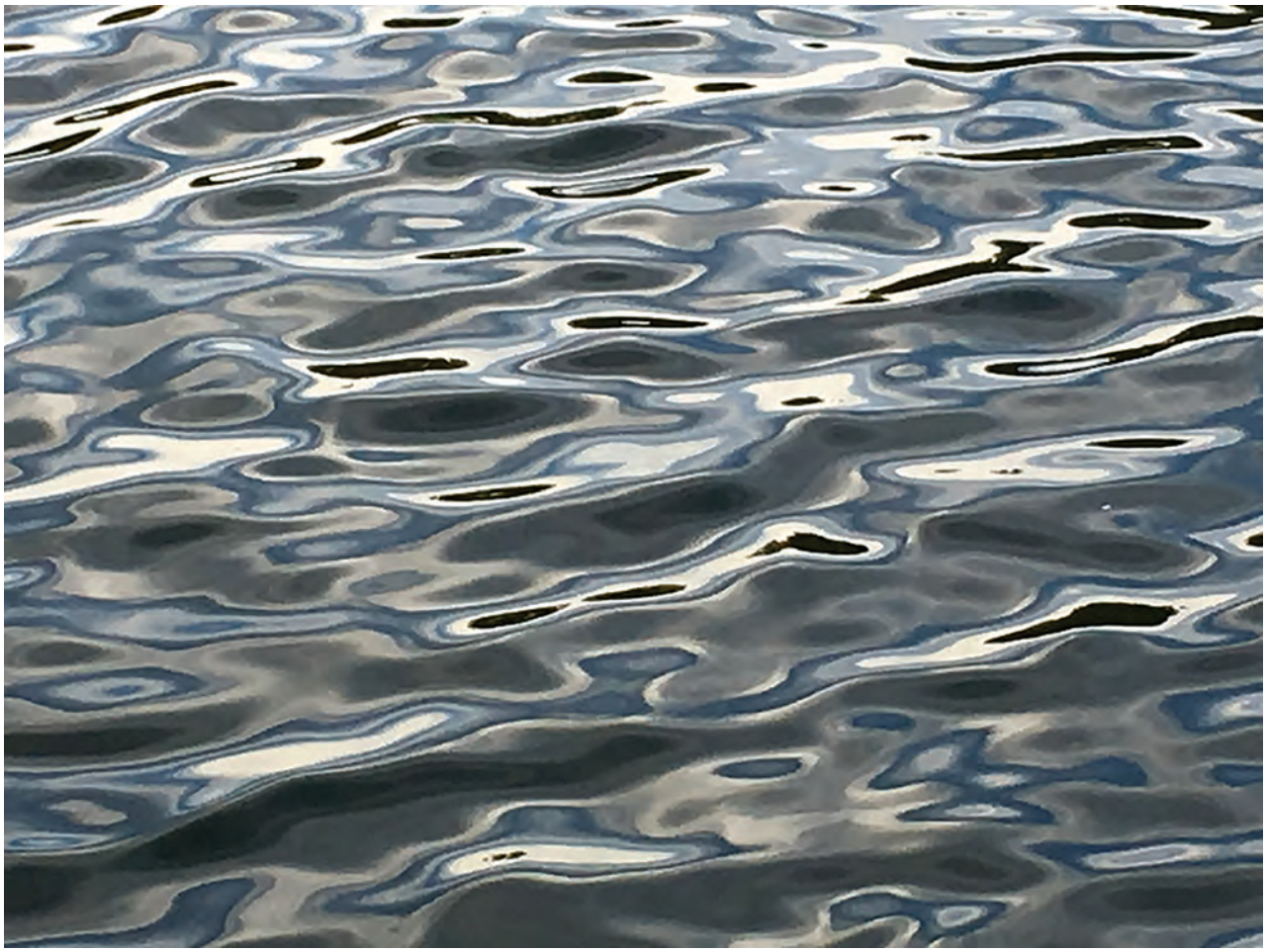

Title: East River Reflections, New York City. The glassy undulating surface of water is a nonstop, delightful, and hypnotic visual display. Ignoring hydrodynamic complexities, the mosaic of shapes and colors (blues, greens, blacks, whites, browns, and sometimes red and yellow) results from the physical/geometric optics and chemical physics of the water and surrounding environment. With the caveat that color is subjective sensation of an intrinsic property of radiation, not matter, the "color of water" perceived by a given observer at a point in space and time is determined by upwelling light from beneath the surface, reflected skylight, and the light scattered by the intervening air, collectively involving absorption, refraction, reflection, and scattering. More specifically, the resulting appearance of the water is influenced by sunlight/cloud coverage, sediment/clarity, bubbles, depth, bottom vegetation, the viewing angle, and whether the water is calm or ruffled by waves. Waves can create 2 reflecting surfaces, 1 tilting toward the observer and 1 away. Water is more reflective the more glancing the angle of observation, so the surface tilting away is more reflective than the toward-tilting surface, thus, the alternating lighter and darker regions. One of water's unique properties is that its intrinsic blueness results from atomic (ie, internuclear) vibrational transitions while most or all other blue substances owe their color to electronic transitions. In his delightful book *Clouds in a Glass of Beer*, Dr. Craig F. Bohren writes that "The world was not designed for the convenience of those who frame multiple choice questions." Undoubtedly true, unless there are numerous choices including "All of the Above."

Manfred Hauben, MD, MPH, Pfizer Inc and NYU Langone Health, New York City

Spinal Vascular Shunts: A Patterned Approach

M.P. Kona, K. Buch, J. Singh, and S. Rohatgi

ABSTRACT

SUMMARY: Spinal vascular shunts, including fistulas and malformations, are rare and complex vascular lesions for which multiple classification schemes have been proposed. The most widely adopted scheme consists of 4 types: type I, dural AVFs; type II, intramedullary glomus AVMs; type III, juvenile/metameric AVMs; and type IV, intradural perimedullary AVFs. MR imaging and angiography techniques permit detailed assessment of spinal arteriovenous shunts, though DSA is the criterion standard for delineating vascular anatomy and treatment planning. Diagnosis is almost exclusively based on imaging, and features often mimic more common pathologies. The radiologist's recognition of spinal vascular shunts may improve outcomes because patients may benefit from early intervention.

ABBREVIATIONS: ASA = anterior spinal artery; CS = classification scheme; IPAVF = intradural perimedullary arteriovenous fistula; PSA = posterior spinal artery; SDAVF = spinal dural arteriovenous fistula; SGAVM = spinal "glomus" arteriovenous malformation; SJAVM = spinal juvenile (metameric) arteriovenous malformation; SVS = spinal vascular shunt

Spinal vascular shunts (SVSs) including arteriovenous fistulas (AVFs) and malformations (AVMs) are rare lesions accounting for 3%–4% of intradural spinal lesions.[1-4] The SVS presents a challenge from both an imaging and management perspective. Since the first SVS classification scheme (CS) was proposed in 1971 by Di Chiro et al,[5] physicians from various specialties have proposed CSs on the basis of anatomy and/or management considerations typically relevant to the authors' fields of expertise.[5-10] The current, most widely referenced CS is derived from the works of multiple authors.[5-8] This article offers a review of the commonly referenced historic classification schemes, clinical symptomology, imaging findings, differential diagnoses, and management considerations.

Normal Spinal Vascular Anatomy

The cord is supplied by intramedullary sulcal branches of the anterior spinal artery (ASA) and radial perforators from the pial-based vasacorona (Fig 1).[11] The ASA and paired posterior spinal arteries (PSAs) originate from the intradural vertebral arteries and sometimes the posterior inferior cerebellar arteries. The ASA, PSA, and vasocorona receive collateral flow from approximately 7 or 8 medullary arteries, which share a common origin with the radicular and dural arteries supplying the nerve roots and dural sleeves. These radiculomedullary arteries arise from ventral spinal branches of segmental arteries. The well-known radiculomedullaris magna artery of Adamkiewicz provides collateral flow to the thoracolumbar cord, typically arising on the left between T9 and T12.[2]

Normal spinal venous anatomy grossly mirrors that of the arterial counterpart, with single anterior and dual posterior spinal veins coursing through a pial surface plexus. Medullary and radicular veins drain via transdural emissaries to intervertebral, longitudinal efferent, and other level-specific venous channels.[4]

Historical Classification Schemes

Various proposed SVS CSs have been historically based on anatomic, management, prognostic, or other considerations relevant to the authors' fields of expertise (Table 1).[5,9] Modified versions of earlier SVS CSs have also challenged the scope of included lesions and/or degrees of subclassification.[6-8,10] Although no proposal has been universally adopted, the recent emergence of a composite CS appears to seek a compromise.[3,12-19] At the time of this publication, the most widely referenced CS reflects the contributions of multiple authors, beginning with types I–III of Di

Received March 21, 2021; accepted after revision June 29.

From the Division of Neuroradiology (M.P.K.), Department of Radiology, Hunter Holmes McGuire VA Medical Center, Richmond, Virginia; Division of Neuroradiology (K.B.), Department of Radiology, Massachusetts General Hospital, Harvard Medical School, Boston, Massachusetts; and Division of Neuroradiology (J.S., S.R.), Department of Radiology, University of Massachusetts Medical School, Worcester, Massachusetts.

Paper previously presented, in part, as an educational poster in a short digital format at: Annual Meeting of the European Congress of Radiology, July 15–19, 2020; Virtual.

Please address correspondence to Matthew P. Kona, MD, Division of Neuroradiology, Department of Radiology, Hunter Homes McGuire VA Medical Center, 1201 Broad Rock Blvd, Richmond, VA 23249; e-mail: mpkona@gmail.com

Indicates open access to non-subscribers at www.ajnr.org

http://dx.doi.org/10.3174/ajnr.A7312

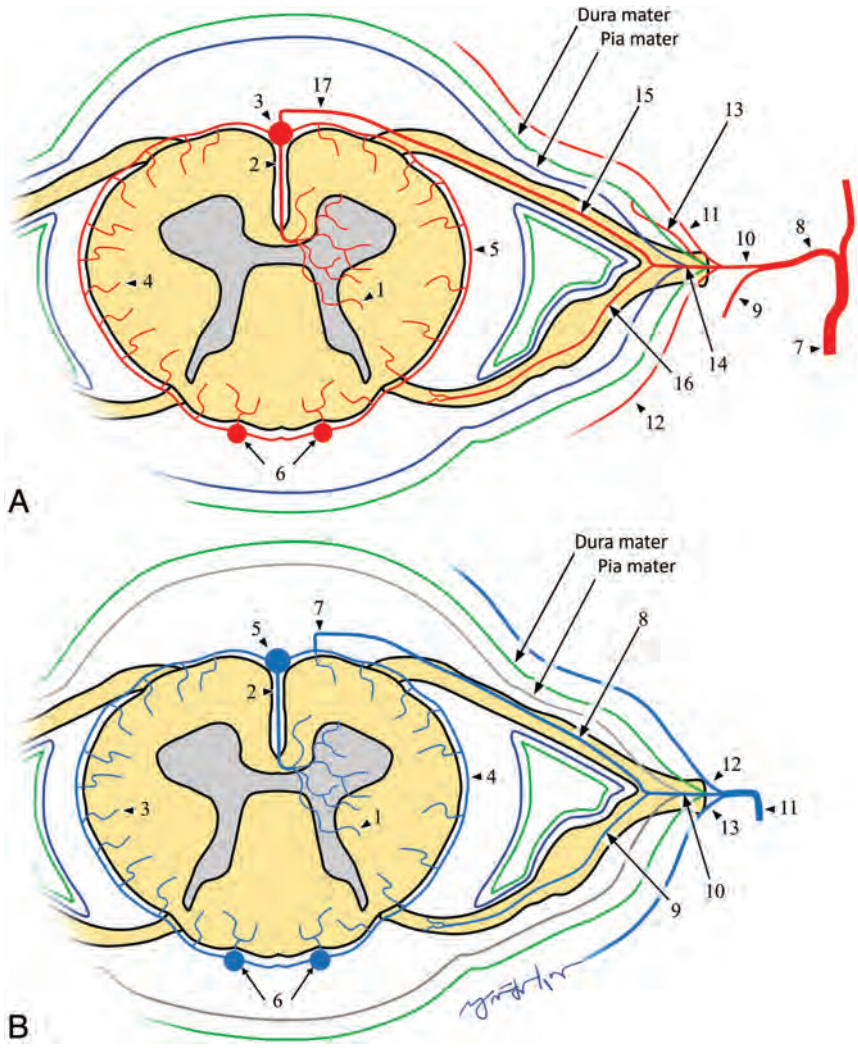

FIG 1. *A*, Normal arterial anatomy: 1, intramedullary branches; 2, sulcal artery; 3, anterior spinal artery; 4, radial perforators; 5, pial arterial plexus; 6, posterior spinal arteries; 7, segmental artery; 8, spinal artery; 9, dorsal branch of the dorsospinal artery; 10, ventral branch of dorsospinal artery; 11, ventral epidural plexus; 12, dorsal epidural plexus; 13, dural artery; 14, radicular artery; 15, ventral radicular artery; 16, dorsal radicular artery; 17, medullary artery. *B*, Normal venous anatomy: 1, Intramedullary veins; 2, sulcal vein; 3, radial veins; 4, pial venous plexus; 5, anterior spinal vein; 6, posterior spinal veins; 7, medullary vein; 8, ventral radicular vein; 9, dorsal radicular vein; 10, emissary vein; 11, intervertebral vein; 12, branches from ventral epidural venous plexus; 13, branches from dorsal epidural venous plexus.

Chiro et al[5] based on angiographic morphology (1971). The proposed type IV AVF addition of Heros et al[6] (1986); the further subclassification by Gueguen et al,[7] of type IV into 3 subtypes based on size and number of arterial feeders; and the proposed subdivision by Spetzler et al[8] of type I AVF into subtypes A (single arterial feeder) and B (multiple feeders).

Type I: Spinal Dural AVF. Spinal dural arteriovenous fistulas (SDAVFs) account for 70% of all SVSs (Fig 2*A*).[3,12] Approximately 80% of SDAVFs are found along the dorsal lower thoracic cord surface between levels T6 and L2.[6,8,13] Anatomically, an SDAVF is an anomalous intradural communication between a dural artery and radicular vein within the intervertebral foramen without an intervening capillary network. Drainage is typically retrograde via a medullary vein and the pial venous network.[13,20,21] SDAVFs are slow-flow lesions, mostly acquired, possibly related to chronic fibrosis and/or venous thrombosis.[1,18] Arterial flow is transferred to engorged venous collaterals, producing the angiographic "single coiled vessel" appearance.[5]

Type II: Spinal Glomus AVM. Type II spinal "glomus" arteriovenous malformations (SGAVMs) account for 19%–45% of all SVSs. SGAVMs are congenital, high-flow lesions that may be thoracic (51%), cervical (29%), or lumbar/conus (20%) (Fig 2*B*).[1,12,17,22] From a morphologic perspective, Di Chiro et al[5] distinguished SGAVMs from SDAVFs by the presence of a "localized vascular plexus confined to a short cord segment." This intramedullary and/or pial-based nidus of abnormal vascular channels may be supplied by ≥1 branch of the ASA, PSA, vertebral arteries, dural arteries, and/or vasocorona.[23]

Type III: Spinal Juvenile AVM. Type III spinal juvenile (metameric) arteriovenous malformations (SJAVMs) are the least common[3,12] type of SVS, with estimated frequencies between 5.4% and 9%. Most cases involve the thoracic spine, followed by the cervical spine (Fig 2*C*).[16,24]

These voluminous,[5] high-flow lesions are sometimes characterized as possessing normal cord tissue within their interstices.[2,25,26] Besides the cord, these lesions may involve the bony spine, paraspinal tissues, and skin, sharing a common metameric tissue origin.[3,27]

Type IV: Intradural Perimedullary AVF. The intradural perimedullary AVF (IPAVF) was first described by Djindjian et al,[28] in 1977, and later proposed as a type IV[6] addition to the 1971 CS of Di Chiro et al[5] (Fig 2*D*). IPAVF prevalence is approximately 8%–19% of SVSs.[14] The IPAVFs are pial-based lesions supplied by the ASA and/or PSA, sometimes with a small intervening nidus. In 1987, Gueguen et al[7] proposed IPAVF types I–III according to the size and number of arterial feeders, now frequently referenced as subtypes IVa, IVb, and IVc.

However, this morphologically based SVS CS is limited in scope because some SVSs remain outside their descriptive criteria. Recent proposals to address this limitation include a location-based CS

Table 1: Historical spinal vascular shunt classification schemes

Authors	Year	Classification Summary
Di Chiro et al[5]	1971	Type I: Single coiled vessel (AVF) Type II: Glomus type (AVM) Type III: Juvenile (AVM)
Heros et al[6]	1986	Type IV: Direct AVF (IPAVF) involving the intrinsic arterial supply of the cord
Gueguen et al[7]	1987	3 Types of classification of IPAVF (type IV) I) Single arterial feeder, small AVF II) Multiple feeders, medium AVF III) Multiple feeders, giant AVF
Spetzler et al[8]	2002	AVF types (and subtypes): Extradural Intradural (dorsal or ventral; and single (A) or multiple (B) feeders) AVM types (and subtypes): Extradural-intradural Intradural (intramedullary, intramedullary-extramedullary, or conus medullaris)
Zozulya et al[9]	2006	Type I: Intramedullary Type II: Intradural or perimedullary Type III: Dural Type IV: Epidural Type V: Intravertebral Type VI: Combined
Takai[10]	2017	Proposed the addition of Type V: Extradural AVF, with subtypes Va/Vb: with/without intradural venous drainage

consisting of 6 lesion types proposed by Zozulya et al[9] and a type V extradural AVF proposed by Takai.[10]

Clinical Symptomology

Type I: Spinal Dural AVF. The typical presentation is an older (range, 55–60 years of age) man (male/female ratio = 5:1)[13] with a history of nonspecific progressive myelopathic symptoms. The clinical picture is sometimes referred to as Foix-Alajouanine syndrome.[4,29] Symptoms are related to cord edema and ischemia resulting from arterialized intravenous pressure competing with cord drainage, though venous thrombosis has also been described.[30-32]

Type II: Spinal Glomus AVM. Patients are typically in their second-to-fourth decades of life (mean age, 28 years) without sex predilection.[11,23] Approximately 50%–75% of patients present with acute or subacute symptoms related to subarachnoid hemorrhage or, less commonly, venous thrombosis.[23,27]

Type III: Spinal Juvenile AVM. Although the low frequency of SJAVMs limits available data, the typical presentation age is younger than 15 years, with a slight male predominance (male/female ratio = 1.7:1).[12,16,26] As reported in a 2014 meta-analysis of 51 cases of SJAVM,[16] the most common presentation was a progressive neurologic deficit in 35%, followed closely by acute hemorrhage (31%) and an acute neurologic deficit without hemorrhage (22%). Twelve percent of cases were incidental discoveries. Cobb syndrome refers to the clinical manifestations of SJAVM involving all tissues of the involved metamere.[33]

Type IV: Intradural Perimedullary AVF. Although the clinical presentation of IPAVF varies with subtype, approximately 93% of patients present with neurologic deficits, among which 29% are acute, typically resulting from subarachnoid hemorrhage.[15,22] A 2013 meta-analysis[15] consisting of 213 cases found subtype IVa to be more common in males (male/female ratio = 1.4:1), with a mean age of 46.9 years. Mean ages for subtypes IVb and IVc were 34.3 and 18.7 years, both without sex predilection.

Syndromic associations with IPAVFs have been reported, including Osler-Weber-Rendu, Proteus, Klippel-Trenaunay, and Down syndromes.[3,6,15,22,34-37]

Imaging Findings

Type I: Spinal Dural Arteriovenous Fistula. T2-weighted MR imaging depicts serpiginous perimedullary flow voids, typically overlying the dorsal cord and conus, without an intramedullary nidus (Fig 3 and Table 2). Secondary congestive myelopathy is also best-depicted on routine T2-weighted TSE and STIR imaging as nonspecific, hyperintense signal within an expanded cord.[38,39] Contrast-enhanced T1 fat-suppression MR imaging or CT may show cord enhancement related to chronic venous congestion and compromise of the blood−spinal cord barrier.[40] The presence of a thin T2 hypointense rim may be more specific to SDAVFs, possibly due to the presence of deoxyhemoglobin within dilated peripheral capillaries of the distended cord.[14,39-41]

First-pass MRA may depict the involved dural artery communicating with a prominent arterial network along the dural root sleeve at the level of the fistula, with a prominent early filling radicular vein. Multiphase time-resolved MRA depicts progressive enhancement through the same vascular structures and may increase the rate of successful SDAVF localization.[42]

Selective DSA injection of the involved segmental artery shows shunted contrast advancing through the fistulous connection with retrograde reflux into a dilated radicular vein and perimedullary venous network.[38,39]

Type II: Spinal Glomus AVM. The eccentric (not centered) nidus of a SGAVM shows variable enhancement and may be partially or completely intramedullary (Fig 4 and Table 2).[14,43] Surrounding T2-hyperintensity with regional cord expansion may represent edema, gliosis, and/or ischemia.[11,26] Subarachnoid or intramedullary signal loss on gradient MR imaging may reflect hemorrhage.[26] The presence of prominent radicular venous outflow depicted as intra- and perimedullary flow voids on T2-weighted MR imaging is variable.[44]

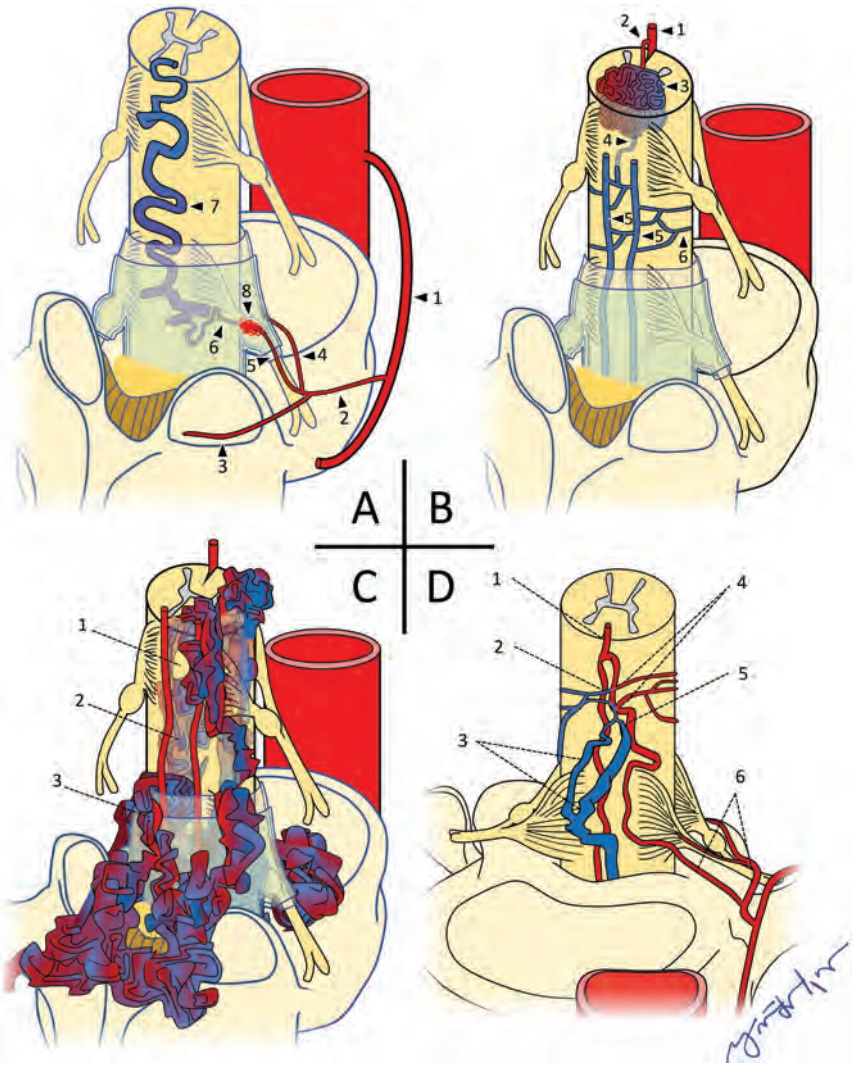

FIG 2. *A*, Type I spinal dural AVF: 1, Intercostal artery; 2, spinal artery; 3, dorsal/muscular branch; 4, radicular artery, ventral branch; 5, radicular artery, dorsal branch; 6, radicular vein; 7, engorged perimedullary vein; 8, dural AVF. *B*, Type II spinal glomus AVM: 1, anterior spinal artery; 2, feeding arterial branch; 3, intramedullary glomus/nidus; 4, draining branch to pial venous network; 5, posterior spinal veins; 6, pial venous network. *C*, Type III spinal juvenile/metameric AVM: 1, normal cord tissue within the nidal interstices; 2, intramedullary elements of AVM; 3, extramedullary elements of AVM. *D*, Type IV IPAVF: 1, anterior spinal artery; 2, fistula; 3, multiple dilated perimedullary veins; 4, multiple contributing arterial feeders; 5, medullary artery; 6, ventral and dorsal radicular arteries.

Selective DSA injections typically show ≥1 feeding branch originating from the ASA, PSA, or vertebral arteries directed toward the intramedullary nidus. Intranidal aneurysms may opacify in up to one-third of cases. Drainage is typically via veins of the coronal and epidural venous plexuses, which may or may not be engorged.[44]

Type III: Metameric Spinal AVM. T2-weighted imaging depicts extensive ectatic intramedullary flow voids with variable involvement of the subarachnoid and epidural spaces, as well as surrounding spinal elements and extraspinal tissues in a metameric distribution (Fig 5 and Table 2).[45] Parenchymal cord tissue may be visible within the interstices of the nidus.[2,25,26] Cord compression from the markedly dilated extramedullary vascular architecture is also best-depicted on MR imaging.[14]

Volume-rendered surface reconstructions from CTA source data permit further assessment of soft-tissue involvement, particularly with regard to the bony spinal elements, and are useful for surgical planning.[45]

Numerous ectactic high-flow intra- and extramedullary shunts are typically present with extremely rapid antegrade drainage via the often-dilated perimedullary and epidural venous pathways.[45]

Type IV: Intradural Perimedullary AVF. T2-weighted MR imaging demonstrates prominent perimedullary flow voids typically along the ventral cord surface, in contrast to SDAVFs, which are typically dorsal (Fig 6 and Table 2). Depending on the degree of arterial and venous ectasia, cord compression and displacement may be present. Less consistently, T2 signal hyperintensity reflecting cord edema, ischemia, and/or gliosis may be present, as well as enhancement of the pia arachnoid.[35,45]

The angioarchitectural findings of IPAVFs depicted on CTA or MRA depend on the subtype. Findings of subtype IVa lesions include enhancement of a normal-caliber ASA branch and a mildly dilated perimedullary vein along the ventral surfaces of the conus medullaris or filum terminale.[45,46]

Subtypes IVb and IVc IPAVFs both depict ≥1 arterial feeder and/or shunt, with ectatic perimedullary drainage. Subtype IVc generally has a greater number and size of involved vessels and shunts compared with subtype IVb.[46] Selective DSA injection may depict this shunt/vessel multiplicity as an abrupt transition to a larger caliber vessel, with contrast dilution from unopacified converging feeders.[47] The rate of contrast progression through the vascular elements increases with subtype order.[7]

Differential Diagnoses/Mimics

CSF Flow Artifacts. Sequences using short-TE, thinner slices, and imaging planes perpendicular to the direction of CSF flow can create signal voids mimicking the vascular flow voids related to shunting (Fig 7*A*).[39] Heavily T2-weighted sequences are most likely to distinguish vascular from CSF flow voids.[14]

Tortuous Redundant Roots. Severe thecal sac stenosis can result in tortuous cauda equina roots appearing as serpentine areas of

perimedullary low signal (Fig 7*B*).[48] The close proximity of these low-signal areas to the level of stenosis can help distinguish this finding from vascular flow voids.

Spinal Vascular Masses. Vascular masses of the cord may exhibit imaging features similar to the those of the nidus of a type II spinal AVM (Fig 8*A*).[13,26,49] For example, hemangioblastomas may be accompanied by surrounding cord edema and a dilated draining vein. Distinction is made by lesion multifocality, avid enhancement, or syndromic associations such as Von Hippel-Lindau disease.[26,50]

Mass effect sometimes imparted by cavernous malformations may result in regional venous engorgement.[40] However, a thin rim of susceptibility signal loss related to hemosiderin staining, as well as the characteristic "popcorn" signal pattern and the angiographically occult nature, may distinguish a cavernous malformation from a type II spinal AVM.[13,51]

Collateral Venous Flow. Obstructive pathologies compromising normal venous drainage with resulting collateral venous engorgement may be difficult to distinguish from the vascular prominence of SVS types lacking an intervening nidus.[52] Recognizing characteristic patterns of collateral venous engorgement and identifying a source of obstruction can help distinguish this process from an SVS.

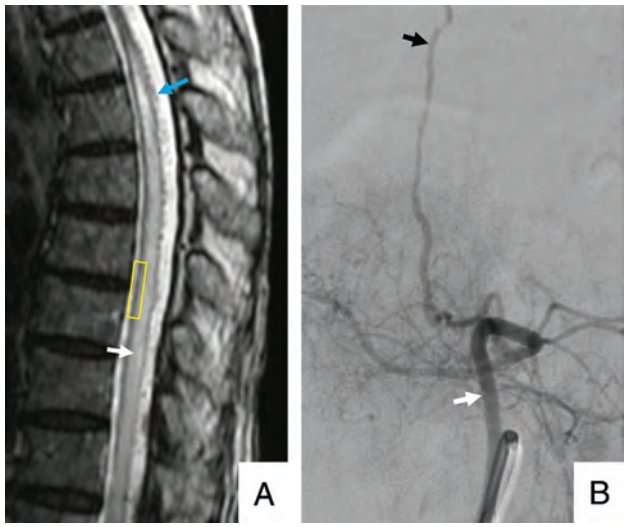

FIG 3. A 79-year-old man with a type I spinal dural AVF. *A*, Sagittal T2 MR imaging of the thoracic spine shows extensive intramedullary edema as signal hyperintensity (*white arrow*) throughout the cord. The thin peripheral hypointense rim (*yellow rectangle*) may reflect deoxyhemoglobin within dilated peripheral capillaries. Serpiginous perimedullary flow voids (*blue arrow*) are most conspicuous along the dorsal aspect of the thoracic cord. *B*, Frontal view DSA injection of the left L3 segmental artery (*white arrow*) shows early filling of an ectatic spinal vein (*black arrow*).

Management

Type I: Dural AVF. Operative management involves ligation of the fistulized vein through a laminectomy.[21] Endovascular management typically involves cannulation of the involved segmental artery followed by embolization of the fistula and draining vein.

Type II: Glomus AVM. Although the technique varies with lesion location and operator preferences, multilevel laminectomies typically afford sufficient lesion access[23,53] for microsurgical resection of extramedullary SGAVM elements. Presurgical embolization may achieve partial lesion obliteration and facilitate intraoperative localization via casting of the embolic material.[23,53]

Stereotactic radiosurgery is an emerging treatment strategy, with 2 single-center studies demonstrating rates of lesion-size reduction between 50% and 100%, with complete obliteration rates up to 19%.[17,54]

Table 2: Imaging findings of spinal vascular shunts types I–IV

Shunt Type	MRI	CTA/MRA	DSA
I (SDAVF)	T2 bright cord edema, ± thin T2 dark rim Cord expansion Prominent dorsal perimedullary flow voids	May localize the involved dural artery along dorsal dural root sleeve Prominent draining medullary vein	Definitive shunt localization Spinal arterial stasis in setting of cord edema
II (SGAVM)	Eccentric intramedullary flow voids of nidus on T2WI T2 bright cord edema Cord expansion ± Prominent perimedullary flow voids	Heterogeneous nidal enhancement May depict multiplicity of arterial feeders	Delineation of arterial feeders Aneurysms in one-third of cases ± Engorged perimedullary veins
III (SJAVM)	Extensive, ectatic flow voids may involve any tissues of a single metamere Normal cord tissue within nidal interstices ± Cord compression from large vascular structures	Variable enhancement of the extensively involved vascular structures	Numerous ectatic high-flow intra- and extramedullary shunts Rapid antegrade drainage via intra-, or extramedullary venous structures
IV (IPAVF)	Prominent ventral perimedullary flow voids on T2 MR imaging ± Cord compression from perimedullary venous ectasia ± Cord edema/expansion on T2 MR imaging	≥1 arterial feeder and draining veins of variable size based on subtype ± Pia arachnoid enhancement	Progressively increasing rates of flow with subtypes IVa–c May depict dilation of small pial surface arteries or venous aneurysms

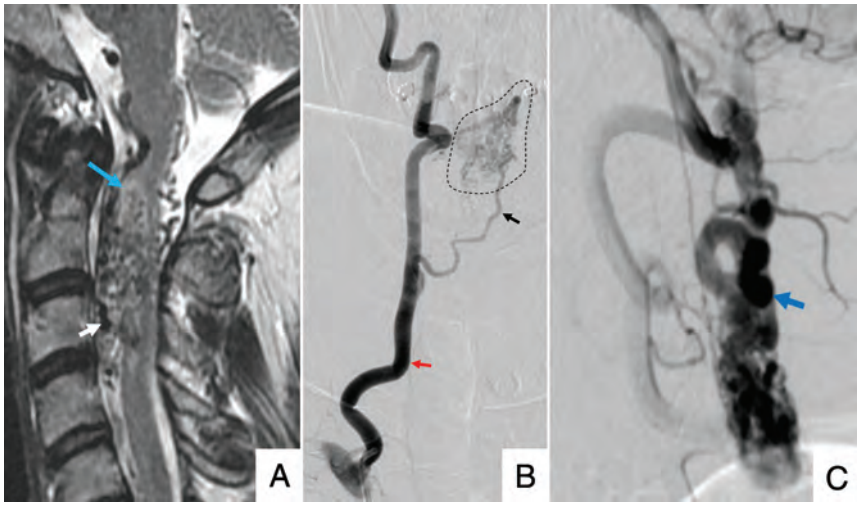

FIG 4. A 45-year-old man with a type II spinal glomus AVM. *A*, Sagittal T2 MR imaging of the cervical spine shows serpiginous intramedullary and perimedullary flow voids (*white arrow*), with adjacent cord hyperintensity (*blue arrow*). *B*, Frontal view DSA injection of the right vertebral artery (*red arrow*) shows opacification of a feeding arterial branch (*black arrow*) and nidal elements (*dashed outline*). *C*, Lateral view DSA shows early filling of ectatic perimedullary veins (*blue arrow*).

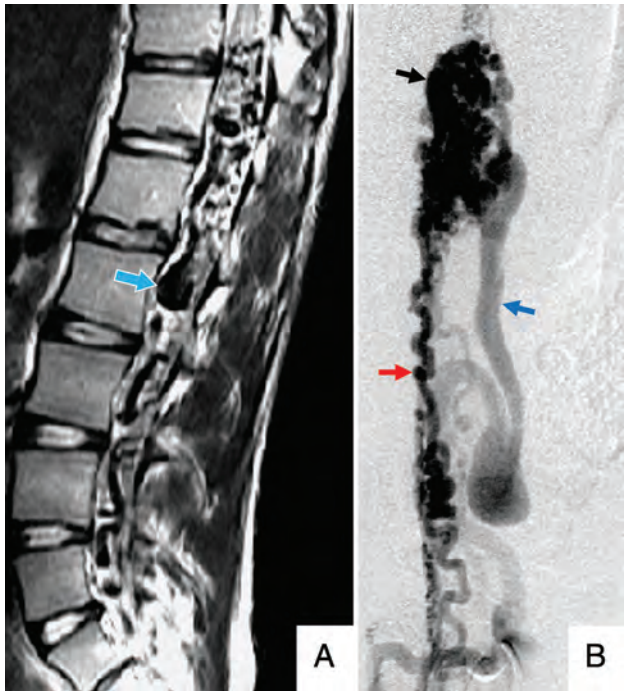

FIG 5. A 14-year-old girl with a type III spinal juvenile/metameric AVM. *A*, Sagittal T2 MR imaging of the lumbar spine shows numerous ectatic perimedullary and intramedullary flow voids (*blue/white arrow*). *B*, Frontal view DSA injection of the right L2 lumbar artery shows opacification of a prominent anterior spinal artery (*red arrow*), intramedullary and extramedullary nidal elements (*black arrow*), and early filing of an ectatic perimedullary vein (*blue arrow*).

Type III: Spinal Juvenile AVM. SJAVMs are not frequently amenable to intervention, and benefits are often brief, with high rates of additional procedures required.[1,26,34] When attempted, embolization is generally regarded as first-line therapy for SJAVMs due to high rates of intraoperative hemorrhage.

Type IV: Intradural Perimedullary AVF. The treatment approach depends on the number and size of the involved arterial feeders and thus the IPAVF subtype. Therapy generally consists of endovascular embolization, surgery, or a combination of both.

CONCLUSIONS

The relatively infrequent and anatomically complex nature of spinal vascular shunts can present diagnostic and therapeutic challenges to radiologic and surgical teams. Assessment of these lesions can be further complicated by the lack of a universally accepted classification scheme. However, a working knowledge of the 4 most frequently described types of spinal vascular shunts permits a useful initial evaluation of these lesions. Imaging is critical, and radiologists play a pivotal role in suggesting a diagnosis and planning selective treatment options. Early diagnosis improves outcomes, because patients may benefit from early intervention.

REFERENCES

1. Bao Y, Ling F. **Classification and therapeutic modalities of spinal vascular malformations in 80 patients.** *Neurosurgery* 1997;40:75–81 CrossRef Medline
2. Singh R, Lucke-Wold B, Gyure K, et al. **A review of vascular abnormalities of the spine.** *Ann Vasc Med Res*2016;3:1045 Medline
3. Endo T, Endo H, Sato K, et al. **Surgical and endovascular treatment for spinal arteriovenous malformations.** *Neurol Med Chir (Tokyo)* 2016;56:457–64 CrossRef Medline
4. Flores BC, Klinger DR, White JA, et al. **Spinal vascular malformations: treatment strategies and outcome.** *Neurosurg Rev* 2017;40:15–28 CrossRef Medline
5. Di Chiro GJ, Doppman L, Ommaya AK. Radiology of spinal cord arteriovenous malformations. In: Di Chiro GJ, Doppman L, Ommaya AK. *Progress in Neurological Surgery*. Karger Publishers; 1971;4:329–54 CrossRef
6. Heros RC, Debrun GM, Ojemann RG, et al. **Direct spinal arteriovenous fistula: a new type of spinal AVM.** *J Neurosurg* 1986;64:134–39 CrossRef Medline
7. Gueguen B, Merland JJ, Riche MC, et al. **Vascular malformations of the spinal cord: intrathecal perimedullary arteriovenous fistulas fed by medullary arteries.** *Neurology* 1987;37:969–79 CrossRef Medline
8. Spetzler RF, Detwiler PW, Riina HA, et al. **Modified classification of spinal cord vascular lesions.** *J Neurosurg* 2002;96:145–56 CrossRef Medline
9. Zozulya YP, Slin'ko EI, Al-Qashqish II. **Spinal arteriovenous malformations: new classification and surgical treatment.** *Neurosurg Focus* 2006;20: E7 CrossRef Medline
10. Takai K. **Spinal arteriovenous shunts: angioarchitecture and historical changes in classification.** *Neurol Med Chir (Tokyo)* 2017;57:356–65 CrossRef Medline

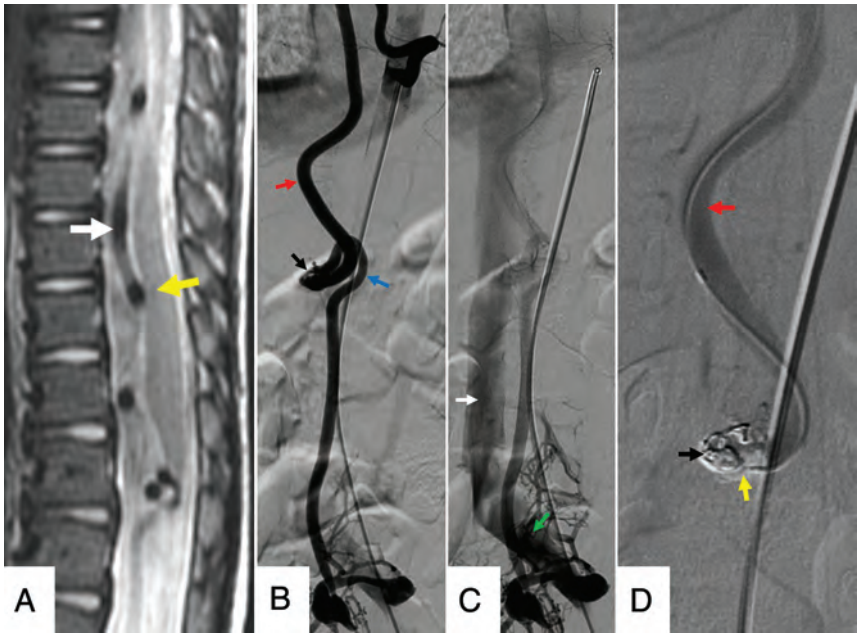

FIG 6. An 11-year-old boy with a type IV intradural-perimedullary spinal AVF. *A*, Sagittal T2 MR imaging of the thoracic spine shows enlarged, predominantly ventral, perimedullary flow voids (*white arrow*) indenting the ventral cord (*yellow arrow*). *B* and *C*, Sequential frontal view DSA images from injection of the left T9 segmental artery show contrast progression through the ASA (*red arrow*), nidus (*black arrow*), ectatic left radiculomedullary vein (*blue arrow*), left common iliac vein (*green arrow*), and inferior vena cava (*white arrow*). *D*, Frontal magnified DSA shows a catheter traversing the opacified ASA (*red arrow*) and embolization coil (*black arrow*) and Onyx (Covidien) (*yellow arrow*) material within the nidus. The draining vein no longer opacifies as a result of shunt obliteration.

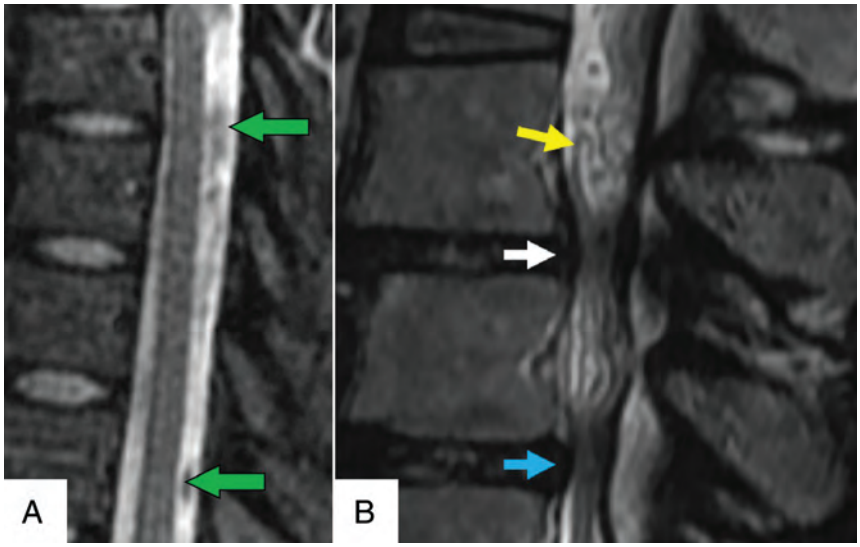

FIG 7. *A*, A 41-year-old woman with normal CSF flow-related signal voids. Sagittal T2 MR imaging of the thoracic spine shows multiple prominent CSF flow voids (*green arrows*), mimicking the perimedullary vascular flow voids characteristic of spinal vascular shunts. *B*, A 71-year-old man with spinal stenosis. Sagittal T2 MR imaging of the lumbar spine shows multiple tortuous, redundant-appearing cauda equina nerve roots (*yellow arrow*) mimicking the perimedullary flow voids of a spinal vascular shunt above the levels of thecal sac stenoses (*white and blue arrows*).

11. Krings T, Mull M, Gilsbach JM, et al. **Spinal vascular malformations.** *Eur Radiol* 2005;15:267–78 CrossRef Medline
12. Ferch RD, Morgan MK, Sears WR. **Spinal arteriovenous malformations: a review with case illustrations.** *J Clin Neurosci* 2001;8:299–304 CrossRef Medline
13. Krings T, Geibprasert S. **Spinal dural arteriovenous fistulas.** *AJNR Am J Neuroradiol* 2009;30:639–48 CrossRef Medline
14. Higano S. Magnetic resonance imaging of spinal vascular lesions. *Neurovascular Imaging.* London: Springer; 2011:487–505
15. Gross BA, Du R. **Spinal pial (type IV) arteriovenous fistulae: a systematic pooled analysis of demographics, hemorrhage risk, and treatment results.** *Neurosurgery* 2013;73:141–51 CrossRef Medline
16. Gross BA, Du R. **Spinal juvenile (type III) extradural-intradural arteriovenous malformations.** *J Neurosurg Spine* 2014;20:452–58 CrossRef Medline
17. Kalani MA, Choudhri O, Gibbs IC, et al. **Stereotactic radiosurgery for intramedullary spinal arteriovenous malformations.** *J Clin Neurosci* 2016;29:162–67 CrossRef Medline
18. Singh B, Behari S, Jaiswal AK, et al. **Spinal arteriovenous malformations: is surgery indicated?** *Asian J Neurosurg* 2016;11:134 CrossRef
19. Eddleman CS, Jeong H, Cashen TA, et al. **Advanced noninvasive imaging of spinal vascular malformations.** *Neurosurg Focus* 2009;26:E9 CrossRef Medline
20. Sorenson T, Giordan E, Cannizzaro D, et al. **Surgical ligation of spinal dural arteriovenous fistula.** *Acta Neurochir (Wien)* 2018;160:191–94 CrossRef Medline
21. Goyal A, Cesare J, Lu VM, et al. **Outcomes following surgical versus endovascular treatment of spinal dural arteriovenous fistula: a systematic review and meta-analysis.** *J Neurol Neurosurg Psychiatry* 2019;90:1139–46 CrossRef Medline
22. Mourier KL, Gobin YP, George B, et al. **Intradural perimedullary arteriovenous fistulae: results of surgical and endovascular treatment in a series of 35 cases.** *Neurosurgery* 1993;32:885–91 CrossRef Medline
23. Connolly E Jr, Zubay GP, McCormick PC, et al. **The posterior approach to a series of glomus (type II) intramedullary spinal cord arteriovenous malformations.** *Neurosurgery* 1998;42:774–84 CrossRef Medline
24. Samonenko YM, Shchehlov DV, Sviridyuk OE, et al. **Endovascular and microsurgical treatment for spinal arteriovenous malformations:**

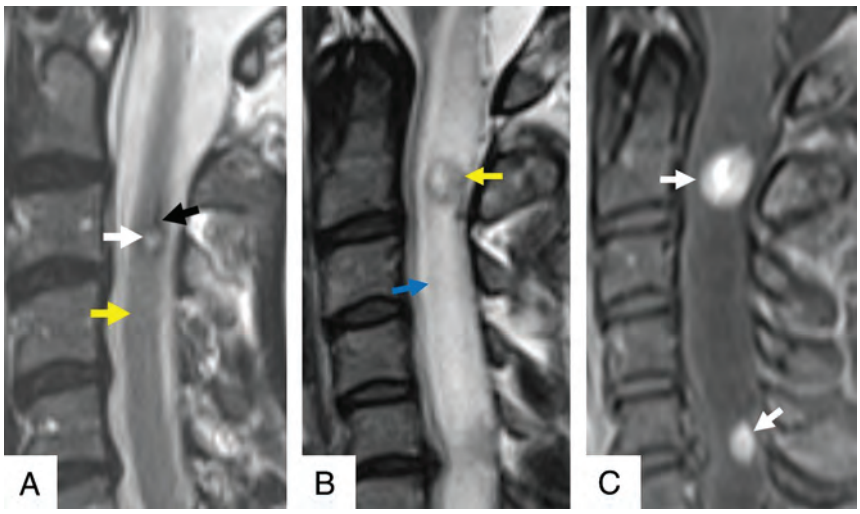

FIG 8. *A*, A 61-year-old man with a cavernous malformation of the cervical cord. Sagittal T2 MR imaging of the cervical spine shows a small intramedullary mass with central hyperintense signal (*white arrow*) and a peripheral rim of low signal (*black arrow*), indicative of blood products in various stages of degradation. There is normal signal in the adjacent cord (*yellow arrow*). *B*, A 42-year-old woman with a history of Von Hippel-Lindau disease and cervical cord hemangioblastomas. Sagittal T2 MR imaging shows a small intramedullary mass (*yellow arrow*) with heterogeneous hyperintense internal signal and surrounding cord edema with cord expansion (*blue arrow*). *C*, Sagittal contrast-enhanced T1 with fat saturation depicts intense enhancement (*white arrows*) within multiple lesions.

our experience. *Endovasc Neuroradiol* 2019;27:32–40 CrossRef

25. Rosenblum B, Oldfield EH, Doppman JL, et al. **Spinal arteriovenous malformations: a comparison of dural arteriovenous fistulas and intradural AVM's in 81 patients.** *J Neurosurg* 1987;67:795–802 CrossRef Medline
26. Do-Dai DD, Brooks MK, Goldkamp A, et al. **Magnetic resonance imaging of intramedullary spinal cord lesions: a pictorial review.** *Curr Probl Diagn Radiology* 2010;39:160–85 CrossRef Medline
27. Niimi Y, Berenstein A, Setton A, et al. **Embolization of spinal dural arteriovenous fistulae: results and follow-up.** *Neurosurgery* 1997;40:675–83 CrossRef Medline
28. Djindjian M, Djindjian R, Rey A, et al. **Intradural extramedullary spinal arterio-venous malformations fed by the anterior spinal artery.** *Surg Neurol* 1977;8:85–93 Medline
29. Wyburn-Mason R. *The Vascular Abnormalities and Tumours of the Spinal Cord and Its Membranes*. Henry Kimpton; 1943
30. Shinoyama M, Endo T, Takahash T, et al. **Long-term outcome of cervical and thoracolumbar dural arteriovenous fistulas with emphasis on sensory disturbance and neuropathic pain.** *World Neurosurg* 2010;73:401–08 CrossRef Medline
31. Sasamori T, Hida K, Yano S, et al. **Long-term outcomes after surgical and endovascular treatment of spinal dural arteriovenous fistulae.** *Eur Spine J* 2016;25:748–54 CrossRef Medline
32. Criscuolo GR, Oldfield EH, Doppman JL. **Reversible acute and subacute myelopathy in patients with dural arteriovenous fistulas: Foix-Alajouanine syndrome reconsidered.** *J Neurosurg* 1989;70:354–59 CrossRef Medline
33. Cobb S. **Haemangioma of the spinal cord: associated with skin naevi of the same metamere.** *Ann Surg* 1915;62:641–49 CrossRef Medline
34. Rubin MN, Rabinstein AR. **Vascular diseases of the spinal cord.** *Neurol Clin* 2013;31:153–81 CrossRef Medline
35. Antonietti L, Sheth SA, Halbach VV, et al. **Long-term outcome in the repair of spinal cord perimedullary arteriovenous fistulas.** *AJNR Am J Neuroradiol* 2010;31:1824–30 CrossRef Medline
36. Cullen S, Alvarez H, Rodesch G, et al. **Spinal arteriovenous shunts presenting before 2 years of age: analysis of 13 cases.** *Childs Nerv Syst* 2006;22:1103–10 CrossRef Medline
37. Rohany M, Shaibani A, Arafat O, et al. **Spinal arteriovenous malformations associated with Klippel-Trenaunay-Weber syndrome: a literature search and report of two cases.** *AJNR Am J Neuroradiol* 2007;28:584–89 Medline
38. Kular S, Tse G, Budu A, et al. **Transarterial CT angiography for surgical planning of spinal dural arteriovenous fistula.** *Br J Radiol* 2020;93:20200020 CrossRef Medline
39. Jeng Y, Chen DY, Hsu HL, et al. **Spinal dural arteriovenous fistula: imaging features and its mimics.** *Korean J Radiol* 2015;16:1119–31 CrossRef Medline
40. Krings T. **Vascular malformations of the spine and spinal cord.** *Clin Neuroradiol* 2010;20:5–24 CrossRef Medline
41. Hurst RW, Grossman RI. **Peripheral spinal cord hypointensity on T2-weighted MR images: a reliable imaging sign of venous hypertensive myelopathy.** *AJNR Am J Neuroradiol* 2000;21:781–86 Medline
42. Mathur S, Bharatha A, Huynh TJ, et al. **Comparison of time-resolved and first-pass contrast-enhanced MR angiography in pretherapeutic evaluation of spinal dural arteriovenous fistulas.** *AJNR Am J Neuroradiol* 2017;38:206–12 CrossRef Medline
43. Boo S, Hartel J, Hogg JP. **Vascular abnormalities of the spine: an imaging review.** *Curr Probl Diagn Radiol* 2010;39:110–17 CrossRef Medline
44. Lee YJ, Terbrugge KG, Saliou G, et al. **Clinical features and outcomes of spinal cord arteriovenous malformations: comparison between nidus and fistulous types.** *Stroke* 2014;45:2606–12 CrossRef Medline
45. Vuong SM, Jeong WJ, Morales H, et al. **Vascular diseases of the spinal cord: infarction, hemorrhage, and venous congestive myelopathy.** *Semin Ultrasound CT MR* 2016;37:466–81 CrossRef Medline
46. Patsalides A, Knopman J, Santillan A, et al. **Endovascular treatment of spinal arteriovenous lesions: beyond the dural fistula.** *AJNR Am J Neuroradiol* 2011;32:798–808 CrossRef Medline
47. Ricolfi F, Gobin PY, Aymard A, et al. **Giant perimedullary arteriovenous fistulas of the spine: clinical and radiologic features and endovascular treatment.** *AJNR Am J Neuroradiol* 1997;18:677–87 Medline
48. Schizas C, Theumann N, Burn A, et al. **Qualitative grading of severity of lumbar spinal stenosis based on the morphology of the dural sac on magnetic resonance images.** *Spine (Phila Pa 1976)* 2010;35:1919–24 CrossRef Medline
49. Thron A, Mull M, Reith W. **Spinal arteriovenous malformations.** *Radiologe* 2001;41:949–54 CrossRef Medline
50. Koeller KK, Rosenblum RS, Morrison AL. **Neoplasms of the spinal cord and filum terminale: radiologic-pathologic correlation.** *Radiographics* 2000;20:1721–49 CrossRef Medline

51. Hegde AN, Mohan S, Lim CC. **Cavernous haemangioma:"popcorn" in the brain and spinal cord.** *Clin Radiology* 2012;67:380–88 CrossRef Medline
52. Marini TJ, Chughtai K, Nuffer Z, et al. **Blood finds a way: pictorial review of thoracic collateral vessels.** *Insights Imaging* 2019;10:63–68 CrossRef Medline
53. Velat GJ, Chang SW, Abla AA, et al. **Microsurgical management of glomus spinal arteriovenous malformations: pial resection technique.** *J Neurosurg Spine* 2012;16:523–31 CrossRef Medline
54. Hida K, Shirato H, Isu T, et al. **Focal fractionated radiotherapy for intramedullary spinal arteriovenous malformations: 10-year experience.** *J Neurosurg* 2003;99:34–38 Medline

Safety of Oral P2Y12 Inhibitors in Interventional Neuroradiology: Current Status and Perspectives

L.M. Camargo, P.C.T.M. Lima, K. Janot, and I.L. Maldonado

ABSTRACT

SUMMARY: In the field of interventional neuroradiology, antiplatelet agents are commonly used to prepare patients before the implantation of permanent endovascular materials. Among the available drugs, clopidogrel is the most frequently used one, but resistance phenomena are considered to be relatively common. Prasugrel and ticagrelor were recently added to the pharmacologic arsenal, but the safety of these agents in patients undergoing neurointerventional procedures is still a subject of discussion. The cumulative experience with both drugs is less extensive than that with clopidogrel, and the experience with patients in the neurology field is less extensive than in the cardiology domain. In the present article, we provide a narrative review of studies that investigated safety issues of oral P2Y12 inhibitors in interventional neuroradiology and discuss potential routes for future research.

ABBREVIATION: CYP = cytochrome P450

Antiplatelet agents are commonly used to prepare patients before the implantation of permanent endovascular materials. In the field of interventional neuroradiology, oral P2Y12 inhibitors are used in combination with aspirin for dual-antiplatelet therapy. Clopidogrel is the most frequently used P2Y12 inhibitor for this kind of preparation. As a prodrug, it is transformed into its active form by the liver and acts through an irreversible blockade of the adenosine diphosphate receptor in the plasmatic membrane of platelets.[1-7] There is evidence of a prophylactic effect in subjects with a history of transient ischemic attack and ischemic stroke.[8,9] Clopidogrel use also reduces the occurrence of thromboembolic adverse events during angioplasty and stent placement.[1,4,10-12] In some individuals, however, the use of clopidogrel does not have the desired effect. Nonresponsive patients are usually classified as drug-resistant.[2-5,10,13-17] Because interventional neuroradiology procedures not infrequently include the implantation of definitive endovascular prostheses such as stents or flow diverters, resistance may lead to intrastent thrombosis with vessel occlusion or stenosis.[3,5,11,16-21] This increased risk seems to not only concern the perioperative period but extends postoperatively as well.[2,3,14]

Since the advice of the FDA on clopidogrel hyporesponsiveness in 2010,[22,23] alternative drugs have been studied at greater lengths. In the context of both preoperative preparation and postoperative antiaggregation, 2 other oral agents, prasugrel[24-37] and ticagrelor,[25,38-46] have been intensively discussed (Online Supplemental Data). Prasugrel is a third-generation thienopyridine, a group of drugs that irreversibly inhibits the P2Y12 receptor and, consequently, adenosine diphosphate–dependent activation and platelet aggregation.[7,47] Ticagrelor is a cyclopentyltriazolopyrimidine, which is directly active after administration, thereby differentiating it from thienopyridines.[48] The cumulative experience with these 2 antiplatelet agents in interventional neuroradiology is, however, less extensive than with clopidogrel. In the present article, we provide a narrative review of studies that investigated safety issues with oral P2Y12 inhibitors (clopidogrel, prasugrel, and ticagrelor) in interventional neuroradiology and discuss potential routes for future research.

Clopidogrel Resistance in Interventional Neuroradiology

Resistance to clopidogrel increases the risk of endovascular procedures, a phenomenon that was first described in the cardiology literature.[2,3,11,14,16,19,28,29,49-51] The criterion standard method to identify resistant patients is laboratory light transmission aggregometry.[5,7] To detect poor responders promptly, point-of-care tests have been developed and widely used both for their convenience and speed. Specifically, they assess the action of the drug at

Received March 15, 2021; accepted after revision July 22.

From the Faculdade de Medicina (L.M.C.), Universidade Salvador, Salvador, Brazil; Serviço de Clínica Médica (P.C.T.M.L.), Hospital Santo Antônio, Associação Obras Sociais Irmã Dulce, Salvador, Brazil; Service de Neuroradiologie (K.J.), Centre Hospitalier Régional Universitaire de Tours, Tours, France; and U1253, iBrain (I.L.M.), Université de Tours, Institut National de la Santé et de la Recherche Médicale, Tours, France.

Please address correspondence to Igor Lima Maldonado, MD, PhD, UMR 1253, iBrain, Université de Tours, Inserm, Tours, France, 10 Boulevard Tonnellé, 37032 Tours, France; e-mail: limamaldonado@univ-tours.fr

Indicates open access to non-subscribers at www.ajnr.org

Indicates article with online supplemental data.

http://dx.doi.org/10.3174/ajnr.A7303

bedside and make possible adjustments to the care of high-risk patients. One of the most widely distributed is the VerifyNow P2Y12 assay (Accumetrics), a portable device that enables measurement in a blood sample without preparation or centrifugation.[5,7] It presents the results initially in P2Y12 reactive units and allows the calculation of the percentage of inhibition.

The values (either the number of units or the percentage of inhibition) can be used to classify the patient as a responder or nonresponder by applying a threshold defined by the operator. Many authors consider >40% to be an adequate inhibition rate.[2,5,52,53] However, because an intermediate response is observed above 20%, others propose to consider only patients with <20% as resistant.[14] The manufacturer presents 208 P2Y12 reactive units as the target under which specific evidence of a pharmacodynamic effect has been observed, being also associated with the reduction of thrombosis and increase of bleeding rates. Neurointerventional studies, however, have used different cutoffs in varied contexts, varying from 208 to 295.[12,20,27-29,31,40,54] A value of <60 was reported to be associated with a higher risk of hemorrhagic complications.[28,29] In a study of 279 patients under dual antiplatelet therapy, a value of 175 was observed to discriminate patients with hemorrhagic complications from those without.[21] In another study in 47 patients, focused on the bleeding risk of the 7 patients defined as hyper-responders (≥72% of platelet inhibition), 3 patients (42.8%) had a major bleeding complication.[55]

An important clinical issue is the degree of platelet inhibition obtained after a single loading dose—ie, a higher dose of the drug that can be administered at the beginning of the treatment before dropping to a lower maintenance dose. By means of 40% as a threshold, up to 64% of patients exhibited a low response after 300 mg of clopidogrel.[2,5,11,52,53] The absence of a precise definition of low response as well as the multiplicity of diagnostic methods have contributed to the variation in the figures reported, especially in the initial series. Some studies have suggested that the drug resistance is related to genetic polymorphisms, but individual factors, such as diabetes mellitus, age older than 65 years, hypercholesterolemia, weight, adherence to treatment, and concomitant drugs also play a role.[2,3,5,6,15,56]

A typical example of genetic polymorphism is the alteration of the enzyme cytochrome (CYP)2C19, which is involved in the metabolism of clopidogrel. Altered alleles lead to high platelet reactivity despite clopidogrel administration, but great variability is noted within each genotype group.[57] Genetic alterations involving the P2Y12 receptor also occur.[1,5] Nevertheless, because resistant individuals have less exposure to the active metabolite, it is possible that the resistance is more associated with the concentration of the active metabolite than with insufficient sensitivity of the P2Y12 receptor.[58] The effectiveness of clopidogrel depends on factors that influence both the metabolite concentration and final effect. The result is a variable response.[57]

Specific genetic testing can identify patients with constitutional alterations in clopidogrel metabolism.[14] In clinical practice, these tests are generally used after the patient shows a clinical or laboratory manifestation of resistance. A particular difficulty is the time these examinations usually demand (≥5 days). It is also known that a subject can present with the normal allele and be resistant for other reasons. Conversely, a given patient who has the altered allele may have low platelet activity due to mechanisms not yet fully elucidated, limiting the predictive value of genetic testing.[57] Considering the cost and impracticality of genetic testing and the great variability of the causal factors, it has been preferable in daily practice to perform tests that evaluate the final drug effect, ie, platelet aggregation.[7]

Interest in the epigenetics of clopidogrel resistance has also increased in the past years. Most studies focus on microRNA and DNA methylation. MicroRNA molecules can bind to RNA and interfere with transcription. MiR-26, miR-28, and miR-96 are possible regulators of platelet activity through different mechanisms.[59,60] Considerable discussion exists regarding miR-223 as a potential biomarker because higher miR-223 levels were associated with better platelet inhibition after clopidogrel administration.[60,61] Hypomethylation of a number of promoters, such as abc1, abc3, and P2RY12 possibly decreases platelet reactivity, but the results have not been homogeneous.[60,62] Decreased methylation of P2RY12 was associated with clopidogrel resistance in patients with coronary artery disease.[60,63]

The FDA has recommended considering alternative dosing strategies for clopidogrel or using another antiplatelet drug in resistant patients.[22,23] Although the increase in the loading dose from 300 to 600 mg decreases the percentage of low responses in general, doubling the dose in patients with the genetic mutation did not significantly alter final aggregation rates.[3,5,57,64] Patients with increased baseline levels of platelet aggregation are also more susceptible to antiplatelet resistance; this issue is seen in those presenting with diabetes mellitus or recent thrombotic events.[5,52,56] An illustration of this issue is that low-dose aspirin does not have the same antithrombotic effects if there is concomitant arthritis, surgical stress, or diabetes mellitus.[65] In this specific situation, it is believed that the oxidative stress and elevated C-reactive protein can compensate for and overcome the inhibitory effect on cyclooxygenase 1.

Thromboembolic complications are multifactorial. Failure of therapy may also be a result of drug interactions. Among the main interactions, the use of proton pump inhibitors, particularly omeprazole, has been described as a factor that decreases the active metabolite of clopidogrel by altering the prodrug metabolism.[7,14] Ketoconazole is a potent CYP3A inhibitor and has also been reported to reduce the plasma level of the active metabolite of clopidogrel by about 50% in addition to reducing the antiplatelet effect.[66,67] The same was observed to a lesser degree with erythromycin and troleandomycin, which are CYP3A4 inhibitors.[67] Aspirin resistance, though less frequent, also increases the risk of undesirable events in patients on dual-antiplatelet therapy.[68] On the other hand, rifamycin is acknowledged to be a CYP3A4 inducer, capable of increasing the active metabolite formation and antiplatelet effect of clopidogrel.[67,69] Similar observations have been made in smokers for reasons possibly related to the CYP1A-inducing effect of polycyclic aromatic hydrocarbons.[70-72]

An inverse relationship between body mass and response to clopidogrel has also been noted.[2,6,11,15] In 2008, Lee et al[2] reported an association between high body mass and a low response in a population of patients with cerebrovascular disease. In 2014, the results of 182 VerifyNow tests in a consecutive series of

interventional neuroradiology procedures were analyzed after a 300-mg loading dose.[11] In subjects weighing >60 kg, significantly lower percentages of antiaggregation and a higher prevalence of resistance were observed, regardless of the cutoff (20% or 40%). This phenomenon may have important implications regarding the way we prepare patients for neuroendovascular treatment. Although the exact mechanism is not yet understood, it is supposedly related to the volume of distribution and pharmacokinetics of the drug, as is the case with other antithrombotic agents (eg, heparin and platelet glycoprotein IIb/IIIa inhibitors).[52] For clopidogrel, dose adjustment has not been regularly advocated in the past, and traditional preoperative preparation protocols have usually recommended a homogeneous single loading dose of 300 mg.[2,52]

Some authors have observed an association between body mass index and resistance to clopidogrel.[52,73] This association with the index, not just absolute values of body mass, favors implicating metabolic phenomena, not just a pharmacokinetic mechanism, in clopidogrel resistance. Wagner et al[6] hypothesized that less exposure to the active metabolite may be a mechanism of low response in overweight patients. It has been suggested that overweight patients may have higher baseline platelet activity compared with normal-weight patients. This difference is maintained under clopidogrel, with overweight subjects presenting suboptimal responses more frequently.[7,52]

It is important to distinguish truly resistant patients and those for whom clopidogrel inefficacy is due to pharmacokinetics. In individuals who are resistant due to pharmacodynamic factors, dose changes would have no significant effect. For the other patients, case-by-case dosage adjustment can be discussed. Consequently, the use of the term "resistance" to describe every therapeutic failure may not be appropriate because it would denote a necessarily persistent situation. In patients undergoing coronary stent angioplasty, increasing the standard dose was reported to improve platelet inhibition without increasing the risk of bleeding.[52] Nevertheless, these data should be interpreted with caution because patients with cerebrovascular disease belong to a very different population, and hemorrhagic accidents are more frequent in neuroendovascular procedures than in interventional cardiology. Interest in tailoring doses was, however, first and more frequently addressed in cardiology than in neuroradiology.[64,74-77] A loading dose of 600 mg was reported to reduce the proportion of low responders, though not all patients would benefit from such an increased dose.[12,64]

Novel Oral P2Y12 Inhibitors: Prasugrel and Ticagrelor

Prasugrel. In 1993, Japanese researchers claimed the patent for a series of hydrothienopyridine derivatives with antithrombotic activity.[78,79] Among these, prasugrel was shown to have a greater antithrombotic effect than clopidogrel. Studies in rodents showed that it had additional properties, such as a longer and more intense effect.[78] In 2009, the FDA approved prasugrel for use in patients with acute coronary syndrome undergoing percutaneous coronary intervention.[80]

Prasugrel is also a prodrug and must be metabolized to be active. After being absorbed, it is rapidly esterase-hydrolyzed to an inactive thiolactone, which, in turn, is oxidized in the liver by CYP, leading to the formation of the active metabolite R-138727.[47,78] Despite being extensive, the metabolism of prasugrel is rapid. The presence of the active metabolite in the plasma approximately 15 minutes after its administration is a consequence of this phenomenon.[81] Its half-life is around 7.4 hours, the maximum plasma concentration occurs around 30 minutes, and the antiplatelet action lasts for about 96 hours.[66,78,81] It is possible to obtain clinically meaningful levels of the active metabolite with daily maintenance doses of 5 or 10 mg, much lower than those used for clopidogrel (75 mg per day).[78] The activation, which occurs in 1 hepatic step, is different from that of clopidogrel, which requires a second oxidation stage.

Prasugrel is mainly converted by CYP3A4. Because it is converted by a number of isoenzymes of the CYP complex, some studies have observed that when a single isoenzyme involved in the formation of R-138727 is compromised, the others may fulfill the need instead, ensuring the formation of the active metabolite.[78] In this case, it is possible that prasugrel is less subject to hyporesponsiveness phenomena than clopidogrel.[47] The use of prasugrel is contraindicated in patients with severe hepatic impairment due to their metabolism by CYP, and the dose adjustment may be used in the case of mild liver disease, though there is no clear evidence on the subject.

Proton pump inhibitors, such as omeprazole and pantoprazole, are known to reduce the effect of clopidogrel due to interference with CYP2C19.[67] Interaction of these drugs with prasugrel was not observed.[78] It is believed that prasugrel does not require dosage adjustment when administered concomitantly with drugs that are metabolized by the CYP.[47] The use of the antiretroviral ritonavir has, however, been reported to inhibit the formation of the active metabolite.[67] Additionally, concomitant administration of ketoconazole (a potent CYP3A5 inhibitor) decreased the maximum active metabolite concentration of prasugrel by 46%, despite its antiplatelet effect being preserved.[66,67]

Patients with diabetes mellitus have been reported to respond favorably to prasugrel as part of dual-antiplatelet therapy.[78,82] The greater efficacy of prasugrel (a 60-mg loading dose and a 10-mg daily maintenance dose) over clopidogrel (a 300-mg loading dose and a 75-mg daily maintenance dose) in reducing the combined rate of death from cardiovascular disease, nonfatal acute myocardial infarction, and stroke after percutaneous coronary intervention in patients with acute coronary syndrome was observed in the Trial to Assess Improvement in Therapeutic Outcomes by Optimizing Platelet Inhibition with Prasugrel–Thrombolysis in Myocardial Infarction (TRITON-TIMI 38) study,[83,84] but prasugrel led to an increase in the rate of bleeding. In the secondary prevention of recurrent stroke, a lower dose (3.75 mg) was assessed in a clinical trial with 3747 Japanese patients, the comparison of PRAsugrel and clopidogrel in Japanese patients with ischemic STROke (the PRASTRO-I trial).[85] The study failed to demonstrate that this lower dose of prasugrel was noninferior to 75 mg of clopidogrel because the relative-risk confidence interval exceeded predefined margins. In the trial, the proportion of patients who experienced bleeding was similar. This was also the case in the subsequent study (PRASTRO-II), which compared 2.5 and 2.75 mg of prasugrel with 50 mg of clopidogrel.[86]

Prasugrel is similar in its structure and mechanism of action to clopidogrel, but its greater potency and the faster onset may be advantageous when a fast preoperative preparation or rescue

antiaggregation is needed.[47] Conversely, these characteristics increase the severity of bleeding if it occurs. In addition, considerable discussion exists on whether they increase the risk of intracranial hemorrhage per se.

A comparative study with 76 patients in neurology procedures ($n = 86$) found a higher risk of bleeding with dual-antiplatelet therapy when using a full dose of prasugrel (60-mg loading dose and 10-mg/day maintenance) than when using clopidogrel.[24] Hemorrhagic complications were observed in a total of 3.6% patients treated with clopidogrel and aspirin and 19.4% of those treated with prasugrel and aspirin. This observation suggests that the antiplatelet regimen could be related to an increase in the rate of bleeding. Various degrees of vascular injury may occur during endovascular procedures, ranging from clinically insignificant arterial wall damage to clear perforations with active extravasation. The platelet inhibition obtained with prasugrel and aspirin may facilitate occult bleeding progressing to a major, clinically significant hemorrhagic event.[24] For many authors, clopidogrel remains the drug of choice. In cases of resistance, other antiplatelet agents may be necessary. Patients under prasugrel in interventional neuroradiology series were mostly those who presented with resistance to clopidogrel.[24,78] Moreover, sample sizes in interventional neuroradiology have been relatively smaller.

With a 60-mg loading dose of prasugrel, approximately 50% platelet inhibition is observed at 30 minutes and approaches the maximum effect before 2 hours.[78] A daily dose of 10 mg also results in a greater platelet inhibition than that achieved with the usual 75 mg of clopidogrel.[47,78] Patients taking clopidogrel who switch to prasugrel do not lose the antiplatelet effects in the transition. Because prasugrel is an irreversible inhibitor, it takes 7–10 days for the patient to experience normal platelet function.[13,47] The high risk of hemorrhage and the increasing use of prasugrel in an at-risk population made it necessary for the FDA to issue a warning.[87] It was recommended to prefer a reduced maintenance dose (5 mg/day) in patients weighing <60 kg and to reserve this drug for patients younger than 75 years of age in the presence of a risk factor for thrombosis.

In 2013, a chart review of 16 cases of patients allergic or hyporesponsive to clopidogrel who received prasugrel and underwent neurointerventional procedures reported favorable results with no cerebral ischemia or evident intracranial hemorrhage.[36] In a French study with 2 parallel groups of 100 patients, the use of prasugrel in patients undergoing endovascular treatment of nonruptured cerebral aneurysms was not related to hemorrhagic events.[37] Prasugrel also potentially reduced, in comparison with clopidogrel, the clinical consequences of thromboembolic complications. In a retrospective study on 297 cases, a notable reduction in the frequency of procedure-related thromboembolism in subjects with unruptured cerebral aneurysms was observed.[27] The VerifyNow system showed lower values of P2Y12 reactive units and higher inhibition percentages in the prasugrel group, but the rate of hemorrhagic complications did not increase.

In a recent study, Higashiguchi et al,[31] in 2021, proposed a tailored therapy in which prasugrel replaced clopidogrel when the result of the VerifyNow assay was inferior to 240 P2Y12 reactive units. They observed a reduction in the frequency of thromboembolic complications after treatment of unruptured aneurysms (16% versus 6%, $P < .048$, $n = 217$) after a 1-month follow-up without an increase in the rate of hemorrhagic complications. It is, therefore, clear that specific prospective studies on patients in neurovascular procedures and larger samples are now necessary.[36]

Ticagrelor. Ticagrelor is rapidly absorbed, has a half-life of 7–12 hours, and reaches its maximum concentration approximately 2–3 hours after administration.[48] A classic loading dose is 180 mg, and the maintenance dose is 90 mg.[88] The drug has a reversible effect on P2Y12 receptors, making it a temporary allosteric antagonist. Thus, its effect can be assessed by VerifyNow.[89] Because ticagrelor does not require hepatic activation, it may be advantageous in patients with a genetic mutation in the enzyme CYP2C19 or when the situation calls for urgent antiaggregation.[48] The prevalence of hyporesponsiveness appears to be extremely low.[39]

Ticagrelor is known to be a substrate and a weak inhibitor of CYP3A. It is extensively metabolized by CYP3A4 and, to a lesser, extent by CYP3A5.[90] As a consequence, strong CYP3A4 inhibitors, such as ketoconazole, increase ticagrelor exposure, and combined use is not recommended.[67,91] Moderate inhibitors, however, such as diltiazem are not contraindicated. Additionally, potent inducers of CYP3A4 may reduce the efficacy of the drug. For example, rifampicin may decrease its maximum concentration. Coadministration of ticagrelor with CYP3A4 substrates with a narrow therapeutic index is also not recommended because it can increase the exposure of these drugs. Statins are metabolized by CYP3A4. Within an interaction study in healthy volunteers, an increase in the maximal concentration of simvastatin was observed when coadministered with ticagrelor.[92] Coadministration of ticagrelor with doses of simvastatin or lovastatin of >40 mg/day could result in adverse effects caused by the statins, such as gastrointestinal disorders and headache.[91]

Ticagrelor leads to platelet inhibition faster and more intensively than clopidogrel.[93] Its effects also fade more quickly. Ticagrelor coadministered with aspirin has been shown to lead to adequate P2Y12 inhibition in patients resistant to clopidogrel.[93] A randomized, double-blind trial comparing ticagrelor with clopidogrel in patients with coronary artery disease found that ticagrelor was associated with higher rates of inhibition, including in low responders to clopidogrel.[90] A multicentric trial of 18,624 patients with acute coronary syndrome showed that ticagrelor was characterized as a fast and potent antiplatelet agent, with an overall favorable safety profile in patients in cardiology studies.[48,94,95] Compared with classic treatment regimens, the drug appears to be more effective in preventing ischemic coronary events but comes with an increase in the rate of non-procedure-related bleeding.[48,95]

In an interventional neuroradiology series in 2014, eighteen subjects who did not respond to clopidogrel were treated with ticagrelor.[39] The result was favorable, in the sense that ticagrelor could effectively replace clopidogrel, but 1 event is worth noting: A patient nonresponsive to clopidogrel was forced to switch from ticagrelor to clopidogrel after a flow-diverter placement due to a shortage of the drug. This patient developed partial thrombosis after his treatment was changed. This incident further suggests the efficacy of ticagrelor but calls attention to the potentially serious consequences of stopping treatment with the drug. In this context, ticagrelor may be considered an alternative antiplatelet agent, but its indication should be evaluated on a case-by-case

basis. Chronic use of ticagrelor is associated with greater drawbacks than clopidogrel.

Elderly patients have a higher drug exposure compared with younger ones, and women have greater exposure than men.[91] Most interesting, elderly patients also have a lower platelet aggregation index, suggesting that platelets are less sensitive in this subgroup. Despite these differences, no age- or sex-related dose adjustment has been recommended. Renal insufficiency does not seem to influence dosing needs to a significant degree.[91] However, exposure is increased in patients with mild hepatic impairment. Because changes in pharmacodynamics or tolerability are not significant, dose adjustment in these groups does not seem necessary, but caution must be used because there are still no available data on patients with moderate or severe hepatic impairment.[48]

Bleeding is the main safety concern. An increased risk of minor bleeding with ticagrelor compared with clopidogrel was reported, though there were few major bleeding events.[91] Although the percentages were small, an increase in fatal intracranial bleeding with ticagrelor compared with clopidogrel (0.1% versus 0.01%) was noted in the PLATelet inhibition and patient Outcomes (PLATO) trial in patients in a cardiology study.[95] Bleeding times also increase in patients on ticagrelor compared with those on clopidogrel.[91] Dyspnea is another frequent adverse event, but the need to discontinue therapy because of it does not seem to be very common.[48,91]

Narata et al,[46] in 2019, analyzed a consecutive series of 154 patients with unruptured aneurysms undergoing stent placement or flow-diverter implantation procedures under aspirin and ticagrelor. The authors observed more neurologic complications than in previous neurointerventional reports that used aspirin with ticagrelor or clopidogrel, but all observed deaths ($n = 4$) were related to intracranial hemorrhaging. They reported that the number of neurologic complications was lower when a lower dose of heparin was used and indicated that more neurovascular studies comparing clopidogrel with ticagrelor under different heparin regimens are necessary.[46] In the same year, Soize et al[45] reported a study of 80 patients undergoing aneurysm treatment with a flow diverter/disrupter in which dual-antiplatelet therapy with aspirin and clopidogrel was compared with aspirin and ticagrelor. After 1 month, no significant difference was observed between groups regarding thromboembolic complications or hemorrhage. After 3 months, no delayed infarction or hemorrhage was observed.

In a 2020 study of 72 patients comparing rates of thromboembolism after stent-assisted coiling for unruptured aneurysms, postprocedural infarction was observed on diffusion-weighted imaging more frequently in the ticagrelor group than in the aspirin-plus-clopidogrel group.[41] After multivariable logistic regression analysis, however, the authors concluded that postprocedural infarction was more associated with aneurysm type than antiplatelet medication per se in their series.

In the Acute Stroke or Transient Ischaemic Attack Treated with Aspirin or Ticagrelor and Patient Outcomes (SOCRATES) trial, which compared ticagrelor with aspirin in 13,199 patients with acute stroke or transient ischemic attack, ticagrelor was not found to be superior to aspirin in reducing the rate of stroke, myocardial infarction, or death at 90 days, and no increase in intracranial bleeding was observed.[96] Nevertheless, increased rates of minor bleeding and dyspnea were noted. The rates of discontinuation of treatment due to dyspnea or any bleeding were 6.2% and 1.3%, respectively, in the ticagrelor group and 1.4% and 0.3%, respectively, in the aspirin group. More recently, the Acute Stroke or Transient Ischaemic Attack Treated with Ticagrelor and Aspirin for Prevention of Stroke and Death (THALES) trial compared ticagrelor and aspirin to aspirin alone for the same conditions in a total of 11,016 patients.[97] The risk of a stroke or death within 30 days was lower with dual therapy, but there was no difference in the incidence of disability. Severe bleeding was more frequent with ticagrelor ($n = 28$, 0.5% of severe bleeding, 0.4% intracranial bleeding). These rates of bleeding in the intracranial space were within the range observed with patients taking clopidogrel and aspirin in the Clopidogrel in High-Risk Patients with Acute Nondisabling Cerebrovascular Events (CHANCE) trial (0.3% with moderate and severe hemorrhage, 0.3% with hemorrhagic stroke) and the Platelet-Oriented Inhibition in New TIA and Minor Ischemic Stroke (POINT) trial (0.9% with major hemorrhage, 0.2% with intracranial bleeding).[8,9]

An important topic of discussion is the reversibility of the effect of ticagrelor. It was reported that although the antiaggregation induced by aspirin could be efficiently reversed by platelet transfusion, the same cannot be accomplished with ticagrelor. Even in high doses, platelets do not seem to be a potent antidote. Because the drug reversibly binds the P2Y12 receptor, the suggested mechanism is that circulating ticagrelor and its active metabolite inhibit the fresh platelets administered.[98] In an in vitro and ex vivo study, gel-filtered platelets from patients who had received ticagrelor were shown to suppress donor platelet function after mixing, suggesting the transfer of ticagrelor to the donor platelets without recovery of the responsiveness of the patient's platelets.[99] Antibody-based strategies are emerging as a potential pathway for achieving rapid drug reversal.[100]

CONCLUSIONS

In the domain of interventional neuroradiology, antiplatelet treatment is intended to reduce the risk of perioperative thromboembolic phenomena. For preoperative preparation, clopidogrel is used very frequently and point-of-care aggregometry tests have been developed. Nevertheless, in a considerable number of patients, significant resistance to the drug is observed in association with a risk for cerebral ischemia after implantation of intracranial endovascular material. Prasugrel and ticagrelor are proving to be promising drugs, given their effective use in patients with resistance to clopidogrel. There remains, however, a need for larger studies on patients in neurointerventional procedures, in particular regarding treatment tailoring. The same is true of reversal strategies, particularly for ticagrelor.

REFERENCES

1. Gorelick PB, Farooq MU. **Advances in our understanding of "resistance" to antiplatelet agents for prevention of ischemic stroke.** *Stroke Res Treat* 2013;2013:727842 CrossRef Medline
2. Lee DH, Arat A, Morsi H, et al. **Dual antiplatelet therapy monitoring for neurointerventional procedures using a point-of-care platelet function test: a single-center experience.** *AJNR Am J Neuroradiol* 2008;29:1389–94 CrossRef Medline

3. Muller-Schunk S, Linn J, Peters N, et al. **Monitoring of clopidogrel-related platelet inhibition: correlation of nonresponse with clinical outcome in supra-aortic stenting.** *AJNR Am J Neuroradiol* 2008;29:786–91 CrossRef Medline
4. Pandya DJ, Fitzsimmons BF, Wolfe TJ, et al. **Measurement of antiplatelet inhibition during neurointerventional procedures: the effect of antithrombotic duration and loading dose.** *J Neuroimaging* 2010;20:64–69 CrossRef Medline
5. Prabhakaran S, Wells KR, Lee VH, et al. **Prevalence and risk factors for aspirin and clopidogrel resistance in cerebrovascular stenting.** *AJNR Am J Neuroradiol* 2008;29:281–85 CrossRef Medline
6. Wagner H, Angiolillo DJ, ten Berg JM, et al. **Higher body weight patients on clopidogrel maintenance therapy have lower active metabolite concentrations, lower levels of platelet inhibition, and higher rates of poor responders than low body weight patients.** *J Thromb Thrombolysis* 2014;38:127–33 CrossRef Medline
7. Falcao FJ, Carvalho L, Chan M, et al. **P2Y12 platelet receptors: importance in percutaneous coronary intervention.** *Arq Bras Cardiol* 2013;101:277–82 CrossRef Medline
8. Wang Y, Wang Y, Zhao X, et al. **Clopidogrel with aspirin in acute minor stroke or transient ischemic attack.** *N Engl J Med* 2013;369:11–19 CrossRef Medline
9. Johnston SC, Easton JD, Farrant M, et al. Clinical Research Collaboration, Neurological Emergencies Treatment Trials Network, and the POINT Investigators. **Clopidogrel and aspirin in acute ischemic stroke and high-risk TIA.** *N Engl J Med* 2018;379:215–25 CrossRef Medline
10. Hussein HM, Emiru T, Georgiadis AL, et al. **Assessment of platelet inhibition by point-of-care testing in neuroendovascular procedures.** *AJNR Am J Neuroradiol* 2013;34:700–06 CrossRef Medline
11. Maldonado IL, Seris C, Mernes R, et al. **Clopidogrel-related platelet inhibition: correlation with perioperative adverse events in neurointerventional procedures.** *The eJournal of the European Society of Minimally Invasive Neurological Therapy*. 2014. http://ejmint.org/sites/default/files/pdf/original_article_1437000160.pdf. Accessed March 14, 2021
12. Tan LA, Keigher KM, Munich SA, et al. **Thromboembolic complications with Pipeline Embolization Device placement: impact of procedure time, number of stents and pre-procedure P2Y12 reaction unit (PRU) value.** *J NeuroIntervent Surg* 2015;7:217–21 CrossRef Medline
13. Gandhi CD, Bulsara KR, Fifi J, et al; SNIS Standards and Guidelines Committee. **Platelet function inhibitors and platelet function testing in neurointerventional procedures.** *J Neurointerv Surg* 2014;6:567–77 CrossRef Medline
14. Nordeen JD, Patel AV, Darracott RM, et al. **Clopidogrel resistance by P2Y12 platelet function testing in patients undergoing neuroendovascular procedures: incidence of ischemic and hemorrhagic complications.** *J Vasc Interv Neurol* 2013;6:26–34 Medline
15. Drazin D, Choulakian A, Nuno M, et al. **Body weight: a risk factor for subtherapeutic antithrombotic therapy in neurovascular stenting.** *J Neurointerv Surg* 2011;3:177–81 CrossRef Medline
16. Fifi JT, Brockington C, Narang J, et al. **Clopidogrel resistance is associated with thromboembolic complications in patients undergoing neurovascular stenting.** *AJNR Am J Neuroradiol* 2013;34:716–20 CrossRef Medline
17. Flechtenmacher N, Kämmerer F, Dittmer R, et al. **Clopidogrel resistance in neurovascular stenting: correlations between light transmission aggregometry, VerifyNow, and the Multiplate.** *AJNR Am J Neuroradiol* 2015;36:1953–58 CrossRef Medline
18. de Souza R, Pena MI, de Vasconcelos AV, et al. **Carotid and vertebral artery stenting: REMAT data (Madre Teresa Registry).** *Revista Brasileira de Cardiologia Invasiva* 2013;21:152–58 CrossRef
19. Asai T, Miyachi S, Izumi T, et al. **Relationship between low response to clopidogrel and periprocedural ischemic events with coil embolization for intracranial aneurysms.** *J Neurointerv Surg* 2016;8:752–55 CrossRef Medline
20. Daou B, Starke RM, Chalouhi N, et al. **P2Y12 reaction units: effect on hemorrhagic and thromboembolic complications in patients with cerebral aneurysms treated with the Pipeline Embolization Device.** *Neurosurgery* 2016;78:27–33 CrossRef Medline
21. Nishi H, Nakahara I, Matsumoto S, et al. **Platelet reactivity and hemorrhage risk in neurointerventional procedures under dual antiplatelet therapy.** *J Neurointerv Surg* 2016;8:949–53 CrossRef Medline
22. Holmes DR Jr, Dehmer GJ, Kaul S, et al. Society for Cardiovascular Angiography Interventions, Society of Thoracic Surgeons, Writing Committee Members, **ACCF/AHA Clopidogrel clinical alert: approaches to the FDA "boxed warning": a report of the American College of Cardiology Foundation Task Force on Clinical Expert Consensus Documents and the American Heart Association.** *Circulation* 2010;122:537–57 CrossRef Medline
23. United States Food & Drug Administration. FDA Drug Safety Communication: Reduced effectiveness of Plavix (clopidogrel) in patients who are poor metabolizers of the drug. https://www.fda.gov/drugs/postmarket-drug-safety-information-patients-and-providers/fda-drug-safety-communication-reduced-effectiveness-plavix-clopidogrel-patients-who-are-poor. Accessed July 8, 2021
24. Akbari SH, Reynolds MR, Kadkhodayan Y, et al. **Hemorrhagic complications after prasugrel (Effient) therapy for vascular neurointerventional procedures.** *J Neurointerv Surg* 2013;5:337–43 CrossRef Medline
25. Atallah E, Saad H, Bekelis K, et al. **The use of alternatives to clopidogrel in flow-diversion treatment with the Pipeline Embolization Device.** *J Neurosurg* 2018;129:1130–35 CrossRef Medline
26. Choi HH, Cho YD, Han MH, et al. **Antiplatelet premedication-free stent-assisted coil embolization in acutely ruptured aneurysms.** *World Neurosurg* 2018;114:e1152–60 CrossRef Medline
27. Choi HH, Lee JJ, Cho YD, et al. **Antiplatelet premedication for stent-assisted coil embolization of intracranial aneurysms: low-dose prasugrel vs clopidogrel.** *Neurosurgery* 2018;83:981–88 CrossRef Medline
28. Delgado Almandoz JE, Crandall BM, Scholz JM, et al. **Pre-procedure P2Y12 reaction units value predicts perioperative thromboembolic and hemorrhagic complications in patients with cerebral aneurysms treated with the Pipeline Embolization Device.** *J Neurointerv Surg* 2013;5:iii3–10 CrossRef Medline
29. Delgado Almandoz JE, Crandall BM, Scholz JM, et al. **Last-recorded P2Y12 reaction units value is strongly associated with thromboembolic and hemorrhagic complications occurring up to 6 months after treatment in patients with cerebral aneurysms treated with the Pipeline Embolization Device.** *AJNR Am J Neuroradiol* 2014;35:128–35 CrossRef Medline
30. Ha EJ, Cho WS, Kim JE, et al. **Prophylactic antiplatelet medication in endovascular treatment of intracranial aneurysms: low-dose prasugrel versus clopidogrel.** *AJNR Am J Neuroradiol* 2016;37:2060–65 CrossRef Medline
31. Higashiguchi S, Sadato A, Nakahara I, et al. **Reduction of thromboembolic complications during the endovascular treatment of unruptured aneurysms by employing a tailored dual antiplatelet regimen using aspirin and prasugrel.** *J Neurointerv Surg* 2021 Feb 25. [Epub ahead of print] CrossRef Medline
32. Kurniawan RG, Song Y, Kwon B, et al. **Tailored antiplatelet agent medication in clopidogrel hyporesponsive patients before stent-assisted coiling: single-center experience.** *Neuroradiology* 2020;62:1709–15 CrossRef Medline
33. Lee D, Song Y, Han M, et al. **Low-dose prasugrel in patients with resistance to clopidogrel for the treatment of cerebral aneurysms.** *Neurointervention* 2018;13:124–27 CrossRef Medline
34. Oran I, Cinar C, Gok M, et al. **Aggregometry response to half-dose prasugrel in flow-diverting stent implantation.** *Clin Neuroradiol* 2020;30:463–69 CrossRef Medline
35. Parthasarathy R, Gupta V, Gupta A. **Safety of prasugrel loading in ruptured blister like aneurysm treated with a Pipeline Device.** *Br J Radiol* 2018;91:20170476 CrossRef Medline

36. Stetler WR, Chaudhary N, Thompson BG, et al. **Prasugrel is effective and safe for neurointerventional procedures.** *J Neurointerv Surg* 2013;5:332–36 CrossRef Medline
37. Sedat J, Chau Y, Gaudart J, et al. **Prasugrel versus clopidogrel in stent-assisted coil embolization of unruptured intracranial aneurysms.** *Interv Neuroradiol* 2017;23:52–59 CrossRef Medline
38. DeGrote JR, Olafson EM, Drofa A, et al. **Ticagrelor and acetylsalicylic acid after placement of Pipeline Embolization Device for cerebral aneurysm: a case series.** *Can J Hosp Pharm* 2019;71:349–55
39. Hanel RA, Taussky P, Dixon T, et al. **Safety and efficacy of ticagrelor for neuroendovascular procedures: a single-center initial experience.** *J Neuronterv Surg* 2014;6:320–22 CrossRef
40. Kang HS, Kwon BJ, Kim JE, et al. **Preinterventional clopidogrel response variability for coil embolization of intracranial aneurysms: clinical implications.** *AJNR Am J Neuroradiol* 2010;31:1206–10 CrossRef Medline
41. Kim SH, Lee H, Kim SB, et al. **Differences in thromboembolism after stent-assisted coiling for unruptured aneurysms between aspirin plus clopidogrel and ticagrelor.** *J Clin Neurosci* 2020;82:128–33 CrossRef Medline
42. Mohammaden MH, English SW, Stapleton CJ, et al. **Safety and efficacy of ticagrelor as single antiplatelet therapy in prevention of thromboembolic complications associated with the Pipeline Embolization Device (PED): multicenter experience.** *J Neurointerv Surg* 2020;12:1113–16 CrossRef Medline
43. Moore JM, Adeeb N, Shallwani H, et al. **A multicenter cohort comparison study of the safety, efficacy, and cost of ticagrelor compared to clopidogrel in aneurysm flow diverter procedures.** *Neurosurgery* 2017;81:665–71 CrossRef Medline
44. Park KY, Ozaki T, Kostynskyy A, et al. **Ticagrelor versus clopidogrel in the dual antiplatelet regimen for intracranial stenting or flow-diverter treatment for unruptured cerebral aneurysms: a single-center cohort study.** *AJNR Am J Neuroradiol* 2021;42:1638–44 CrossRef Medline
45. Soize S, Foussier C, Manceau PF, et al. **Comparison of two preventive dual antiplatelet regimens for unruptured intracranial aneurysm embolization with flow diverter/disrupter: a matched-cohort study comparing clopidogrel with ticagrelor.** *J Neuroradiol* 2019;46:378–83 CrossRef Medline
46. Narata AP, Amelot A, Bibi R, et al. **Dual antiplatelet therapy combining aspirin and ticagrelor for intracranial stenting procedures: a retrospective single center study of 154 consecutive patients with unruptured aneurysms.** *Neurosurgery* 2019;84:77–83 CrossRef Medline
47. Scott DM, Norwood RM, Parra D. **P2Y12 inhibitors in cardiovascular disease: focus on prasugrel.** *Ann Pharmacother* 2009;43:64–76 CrossRef Medline
48. Capodanno D, Dharmashankar K, Angiolillo DJ. **Mechanism of action and clinical development of ticagrelor, a novel platelet ADP P2Y12 receptor antagonist.** *Expert Rev Cardiovasc Ther* 2010;8:151–18 CrossRef Medline
49. Maldonado IL, Machi P, Costalat V, et al. **Neuroform stent-assisted coiling of unruptured intracranial aneurysms: short- and mid-term results from a single-center experience with 68 patients.** *AJNR Am J Neuroradiol* 2011;32:131–36 CrossRef Medline
50. Gurbel PA, Bliden KP, Hiatt BL, et al. **Clopidogrel for coronary stenting: response variability, drug resistance, and the effect of pretreatment platelet reactivity.** *Circulation* 2003;107:2908–13 CrossRef Medline
51. Koerner H, Derveaux C, Alexandrou M, et al. **Do clopidogrel non-responders have an increased risk of adverse events during supra-aortal angioplasty and stenting?** *Stroke Res Treat* 2012;2012:904534 CrossRef Medline
52. Angiolillo DJ, Fernandez-Ortiz A, Bernardo E, et al. **Identification of low responders to a 300-mg clopidogrel loading dose in patients undergoing coronary stenting.** *Thromb Res* 2005;115:101–08 CrossRef Medline
53. Karan V, Vyas D, Bohra V, et al. **Ticagrelor use in Indian patients undergoing neuroendovascular procedures: a single center experience.** *Neurointervention* 2019;14:125–30 CrossRef Medline
54. Yi HJ, Hwang G, Lee BH. **Variability of platelet reactivity on antiplatelet therapy in neurointervention procedure.** *J Korean Neurosurg Soc* 2019;62:3–9 CrossRef Medline
55. Goh C, Churilov L, Mitchell P, et al. **Clopidogrel hyper-response and bleeding risk in neurointerventional procedures.** *AJNR Am J Neuroradiol* 2013;34:721–26 CrossRef Medline
56. Nakagawa I, Park HS, Yokoyama S, et al. **Influence of diabetes mellitus and cigarette smoking on variability of the clopidogrel-induced antiplatelet effect and efficacy of active management of the target P2Y12 reaction unit range in patients undergoing neurointerventional procedures.** *J J Stroke Cerebrovasc Dis.*2016;25:163–71 CrossRef Medline
57. Anderson CD, Biffi A, Greenberg SM, et al. **Personalized approaches to clopidogrel therapy: are we there yet?** *Stroke* 2010;41:2997–3002 CrossRef Medline
58. Wallentin L. **P2Y(12) inhibitors: differences in properties and mechanisms of action and potential consequences for clinical use.** *Eur Heart J* 2009;30:1964–77 CrossRef Medline
59. Sunderland N, Skroblin P, Barwari T, et al. **MicroRNA biomarkers and platelet reactivity: the clot thickens.** *Circ Res* 2017;120:418–35 CrossRef Medline
60. Zhang YJ, Li MP, Tang J, et al. **Pharmacokinetic and pharmacodynamic responses to clopidogrel: evidences and perspectives.** *Int J Environ Res Public Health* 2017;14:301 CrossRef Medline
61. Willeit P, Zampetaki A, Dudek K, et al. **Circulating microRNAs as novel biomarkers for platelet activation.** *Circ Res* 2013;112:595–600 CrossRef Medline
62. Luchessi AD, Silbiger VN, Cerda A, et al. **Increased clopidogrel response is associated with ABCC3 expression: a pilot study.** *Clin Chim Acta* 2012;413:417– 21 CrossRef Medline
63. Su J, Li X, Yu Q, et al. **Association of P2Y12 gene promoter DNA methylation with the risk of clopidogrel resistance in coronary artery disease patients.** *Biomed Res Int* 2014;2014:1–8 CrossRef Medline
64. Neubauer H, Kaiser AF, Endres HG, et al. **Tailored antiplatelet therapy can overcome clopidogrel and aspirin resistance: the BOchum CLopidogrel and Aspirin Plan (BOCLA-Plan) to improve antiplatelet therapy.** *BMC Med* 2011;9:3 CrossRef Medline
65. Gasparyan AY. **Aspirin and clopidogrel resistance: methodological challenges and opportunities.** *Vasc Health Risk Manag* 2010;6:109–12 CrossRef Medline
66. Farid NA, Payne CD, Small DS, et al. **Cytochrome P450 3A inhibition by ketoconazole affects prasugrel and clopidogrel pharmacokinetics and pharmacodynamics differently.** *Clin Pharmacol Ther* 2007;81:735–41 CrossRef Medline
67. Siller-Matula JM, Trenk D, Krähenbühl S, et al. **Clinical implications of drug-drug interactions with P2Y12 receptor inhibitors.** *J Thromb Haemost* 2014;12:2–13 CrossRef Medline
68. Gabriel SA, Beteli CB, Tanighuchi RS, et al. **Aspirin resistance and atherothrombosis.** *Rev Bras Cir Cardiovasc* 2007;22:96–103 CrossRef Medline
69. Judge HM, Patil SB, Buckland RJ, et al. **Potentiation of clopidogrel active metabolite formation by rifampicin leads to greater P2Y12 receptor blockade and inhibition of platelet aggregation after clopidogrel: P2Y12 receptor blockade.** *J Thromb Haemost* 2010;8:1820–27 CrossRef Medline
70. Bliden KP, DiChiara J, Lawal L, et al. **The association of cigarette smoking with enhanced platelet inhibition by clopidogrel.** *J Am Coll Cardiol* 2008;52:531–33 CrossRef Medline
71. Elsherbiny ME, Brocks DR. **The ability of polycyclic aromatic hydrocarbons to alter physiological factors underlying drug disposition.** *Drug Metab Rev* 2011;43:457–75 CrossRef Medline
72. Desai NR, Mega JL, Jiang S, et al. **Interaction between cigarette smoking and clinical benefit of clopidogrel.** *J Am Coll Cardiol* 2009;53:1273–78 CrossRef Medline

73. Sibbing D, von Beckerath O, Schömig A, et al. **Impact of body mass index on platelet aggregation after administration of a high loading dose of 600 mg of clopidogrel before percutaneous coronary intervention.** *Am Jo Cardiol* 2007;100:203–05 CrossRef Medline
74. Wong P, Tesoro E, Aletich V, et al. **Accumetrics-based clopidogrel dosing in endovascular neurosurgery.** *Neurol Res* 2015;37:998–1005 CrossRef Medline
75. Ari H, Ozkan H, Karacinar A, et al. **The EFFect of hIgh-dose ClopIdogrel treatmENT in patients with clopidogrel resistance (the EFFICIENT trial).** *Int J Cardiol* 2012;157:374–80 CrossRef Medline
76. Collet JP, Hulot JS, Anzaha G, et al. **High doses of clopidogrel to overcome genetic resistance: the randomized crossover CLOVIS-2 (Clopidogrel and Response Variability Investigation Study 2).** *JACC Cardiovasc Interv* 2011;4:392–402 CrossRef Medline
77. Zhuo X, Zhuo B, Ouyang S, et al. **Adverse clinical outcomes associated with double dose clopidogrel compared to the other antiplatelet regimens in patients with coronary artery disease: a systematic review and meta-analysis.** *BMC Pharmacol Toxicol* 2018;19:54 CrossRef Medline
78. Shan J, Sun H. **The discovery and development of prasugrel.** *Expert Opin Drug Discov* 2013;8:897–905 CrossRef Medline
79. Koike H, Asai F, Sugidachi A, et al. **Hydropyridine derivatives having antithrombotic activity.** *CA2077695* 1993
80. Center for Drug Evaluation and Research. EFFIENT™ Approval letter. (NDA 22-307). https://www.accessdata.fda.gov/drugsatfda_docs/appletter/2009/022307s000_ltr.pdf. Accessed July 8, 2021
81. Norgard NB, Dinicolantonio JJ. **Clopidogrel, prasugrel, or ticagrelor? A practical guide to use of antiplatelet agents in patients with acute coronary syndromes.** *Postgrad Med* 2013;125:91–102 CrossRef Medline
82. Wiviott SD, Braunwald E, Angiolillo DJ, et al. **Greater clinical benefit of more intensive oral antiplatelet therapy with prasugrel in patients with diabetes mellitus in the trial to assess improvement in therapeutic outcomes by optimizing platelet inhibition with prasugrel-Thrombolysis in Myocardial Infarction 38.** *Circulation* 2008;118:1626–36 CrossRef Medline
83. Montalescot G, Wiviott SD, Braunwald E, et al; TRITON-TIMI 38 Investigators. **Prasugrel compared with clopidogrel in patients undergoing percutaneous coronary intervention for ST-elevation myocardial infarction (TRITON-TIMI 38): double-blind, randomised controlled trial.** *Lancet* 2009;373:723–31 CrossRef Medline
84. Wiviott SD, Braunwald E, McCabe CH, et al. **Prasugrel versus clopidogrel in patients with acute coronary syndromes.** *N Engl J Med* 2007;357:2001–15 CrossRef Medline
85. Ogawa A, Toyoda K, Kitagawa K, et al; PRASTRO-I Study Group. **Comparison of prasugrel and clopidogrel in patients with non-cardioembolic ischaemic stroke: a phase 3, randomised, non-inferiority trial (PRASTRO-I).** *Lancet Neurol* 2019;18:238–47 CrossRef Medline
86. Kitagawa K, Toyoda K, Kitazono T, et al. **Safety and efficacy of prasugrel in elderly/low body weight Japanese patients with ischemic stroke: randomized PRASTRO-II.** *Cerebrovasc Dis* 2020;49:152–59 CrossRef Medline
87. United States Food & Drug Administration. Highlights of prescribing information. https://www.accessdata.fda.gov/drugsatfda_docs/label/2020/022307s018lbl.pdf. Accessed July 8, 2021
88. Byrne JV. *Tutorials in Endovascular Neurosurgery and Interventional Neuroradiology*. Springer International Publishing; 2017
89. Jeong YH, Bliden KP, Antonino MJ, et al. **Usefulness of the VerifyNow P2Y12 assay to evaluate the antiplatelet effects of ticagrelor and clopidogrel therapies.** *Am Heart J* 2012;164:35–42 CrossRef Medline
90. Gurbel PA, Bliden KP, Butler K, et al. **Response to ticagrelor in clopidogrel nonresponders and responders and effect of switching therapies: the RESPOND study.** *Circulation* 2010;121:1188–99 CrossRef Medline
91. Dobesh PP, Oestreich JH. **Ticagrelor: pharmacokinetics, pharmacodynamics, clinical efficacy, and safety.** *Pharmacotherapy* 2014;34:1077–90 CrossRef Medline
92. Teng R, Mitchell PD, Butler KA. **Pharmacokinetic interaction studies of co-administration of ticagrelor and atorvastatin or simvastatin in healthy volunteers.** *Eur J Clin Pharmacol* 2013;69:477–87 CrossRef Medline
93. Gurbel PA, Bliden KP, Butler K, et al. **Randomized double-blind assessment of the ONSET and OFFSET of the antiplatelet effects of ticagrelor versus clopidogrel in patients with stable coronary artery disease: the ONSET/OFFSET Study.** *Circulation* 2009;120:2577–85 CrossRef Medline
94. James SK, Roe MT, Cannon CP, et al; PLATO Study Group. **Ticagrelor versus clopidogrel in patients with acute coronary syndromes intended for non-invasive management: substudy from prospective randomised PLATelet inhibition and patient Outcomes (PLATO) trial.** *BMJ* 2011;342:d3527 CrossRef Medline
95. Wallentin L, Becker RC, Budaj A, et al. **Ticagrelor versus clopidogrel in patients with acute coronary syndromes.** *N Engl J Med* 2009;361:1045–57 CrossRef Medline
96. Johnston SC, Amarenco P, Albers GW, et al; SOCRATES Steering Committee and Investigators. **Ticagrelor versus aspirin in acute stroke or transient ischemic attack.** *N Engl J Med* 2016;375:35–43 CrossRef Medline
97. Johnston SC, Amarenco P, Denison H, et al; THALES Investigators. **Ticagrelor and aspirin or aspirin alone in acute ischemic stroke or TIA.** *N Engl J Med* 2020;383:207–17 CrossRef Medline
98. Godier A, Taylor G, Gaussem P. **Inefficacy of platelet transfusion to reverse ticagrelor.** *N Engl J Med* 2015;372:196–97 CrossRef Medline
99. Bertling A, Fender AC, Schungel L, et al. **Reversibility of platelet P2Y12 inhibition by platelet supplementation: ex vivo and in vitro comparisons of prasugrel, clopidogrel and ticagrelor.** *J Thromb Haemost* 2018;16:1089–98 CrossRef Medline
100. Bhatt DL, Pollack CV, Weitz JI, et al. **Antibody-based ticagrelor reversal agent in healthy volunteers.** *N Engl J Med* 2019;380:1825–33 CrossRef Medline

The American Society of Neuroradiology: Cultivating a Diverse and Inclusive Culture to Build a Stronger Organization

P.M. Bunch, L.A. Loevner, R. Bhala, M.B. Hepp, J.A. Hirsch, M.H. Johnson, K.L. Lyp, E.P. Quigley, N. Salamon, J.E. Jordan, and E.S. Schwartz

As an organization, the American Society of Neuroradiology (ASNR) is committed to a welcoming environment for all and encourages a culture of bystander allyship, positive mentorship, and professional modeling.[1] Central to achieving this welcoming environment is the need to acknowledge, respect, and celebrate diversity in our organization and to actively include and elevate the underrepresented. We believe embracing diversity and inclusion is in the best interest of our patients, our specialty, our Society, and ourselves, and we also expect that embracing diversity and inclusion will enhance our collective ability to achieve quality and excellence.

As physicians and scientists in neuroradiology, our foremost responsibility is the care of our patients. We are deeply concerned by the well-documented disparities in health care access and outcomes attributable to race and ethnicity,[2] sexual orientation,[3] gender identity,[4] religion,[5] poverty,[6] aging,[7] and other factors. Neuroradiology is not exempt from these issues. There are documented racial and ethnic differences in diagnostic imaging use during US emergency department visits.[8] Disparities have also been shown in a number of disease processes in which neuroradiologists directly or indirectly provide clinical care, including stroke,[9,10] dementia,[11] pain management including osteoporotic compression fracture,[12,13] and head and neck cancer.[14] Furthermore, pre-existing disparities have been further exacerbated by the coronavirus disease 2019 (COVID-19) pandemic,[15-18] particularly in impoverished communities and communities of color. Although the root causes of health disparities are complex, they can be grouped into health system, patient, and provider factors.[2]

Our committee has attempted to mitigate contributing provider factors through a series of educational webinars that do the following: 1) highlight the existence of health care disparities in the context of COVID-19 (Neuroradiology Updates & COVID-19, August 5, 2020), artificial intelligence (Artificial Intelligence: What the Neuroradiologist Needs to Know, October 7, 2020), and back pain (Oh My Aching Back!: What the Neuroradiologist Needs to Know about Back Pain in 2020, November 4, 2020); 2) educate neuroradiologists about respectfully and compassionately caring for vulnerable populations (Diversity & Inclusion Matters, July 8, 2020; Understanding the Terminology and Making a Difference, September 2, 2020; Imaging of the Transgender and Gender Diverse Patient, March 31, 2021); and 3) define allyship as well as provide strategies for being an effective ally and speaking up against microaggressions encountered in the professional radiology setting (Understanding the Terminology and Making a Difference, September 2, 2020). We are also committed to combating "ableism," which is defined as discrimination and social prejudice against individuals with disabilities.[19]

Diversity and inclusion are also critical to the long-term health of our specialty. A diverse neuroradiology workforce not only improves our ability to address health disparities by mitigating the negative effects of language barriers, mistrust, and cultural misunderstandings[20] but also positions us to benefit from enriched collaborations, innovation, and growth.[21] For example, an age-inclusive workforce facilitates intergenerational learning and has been linked to higher productivity, lower turnover, and higher rates of creativity and innovation.[22]

Historically, neuroradiology has been a male-dominated field.[23,24] Although more work is needed in neuroradiology to achieve gender parity with the medical school graduate and graduate medical education trainee pools, we are encouraged by recent progress in gender equity within the ASNR leadership ranks. More specifically, 5 of the 10 ASNR Presidents from 2010 to 2019 were women, and 3 of the 4 Presidents from 2020 to 2023 will be women, as opposed to just 2 female Presidents from 1962 to 2009.[25] Furthermore, there is strong female leadership among ASNR staff, with 8 of the 10 departments at headquarters led by women as well as a female Managing Editor of the *American Journal of Neuroradiology*. We celebrate the progress embodied by our Society's record of recent female leaders and the positive example the ASNR has set for other major medical societies in this regard;[26] however, we are also committed to confronting other existing gender imbalances within the organization, including only 2 women having received the ASNR Gold Medal and no female Editors-in-Chief of the *American Journal of Neuroradiology*.

When thinking about the long-term health of our specialty within the United States, societal demographics and demographic trends are relevant. In 2016, minority groups, including African Americans, Hispanics and Latinos, Asians, American Indians, Alaskan Natives, Native Hawaiians, and Pacific Islanders accounted for >38% of the United States population.[27] By 2045, white Americans are projected to no longer be in the majority.[27] However, underrepresented minority groups in medicine (African Americans, Hispanics, Native Americans, Alaskan Natives, Native Hawaiians, and Pacific Islanders) comprise only 6.5% of practicing radiologists and only 8.3% of radiology residents, compared with 15.3% of medical school graduates.[28] Shared race or ethnicity between patients and physicians has been shown to positively affect communication, patient satisfaction, compliance, and overall health outcomes.[29-32] Furthermore, lack of diversity within radiology may impair the ability of our field to address the underlying causes of the previously described health care disparities related to radiology. For these reasons, our committee supports existing radiology pipeline initiatives intended to expose and attract talented individuals from backgrounds underrepresented in medicine to our specialty, including the American College of Radiology's Pipeline Initiative

http://dx.doi.org/10.3174/ajnr.A7310

for the Enrichment of Radiology internship directed toward rising second-year medical students. Additionally, we are actively exploring the potential for similar pipeline programs specific to neuroradiology and the ASNR.

Just as diversity strengthens our specialty, it also strengthens our organization and should, therefore, be viewed as a strategic imperative. It is well-documented that corporations that value and prioritize diversity perform better.[33] For example, organizations in the top quartile with respect to racial and ethnic diversity are 35% more likely to have above-median financial performance, and organizations in the top quartile for gender diversity are 15% more likely to have above-median financial performance.[34] Organizational diversity improves employee engagement, analytical thinking, and innovation.[35] In problem-solving, groups composed of individuals with a wide range of backgrounds, perspectives, and abilities outperform groups of like-minded experts, particularly when problems are unique or difficult.[36]

The ASNR annual meeting program is one of the most highly visible products of our organization, where the presence or absence of diversity is readily apparent. Thus, our committee prioritized the creation of an annual meeting programming diversity checklist, encouraging diverse and inclusive representation in the following areas: 1) geographic, including international; 2) institutional; 3) gender and gender identification; 4) age and career level; 5) race, ethnicity, culture, and nationality; 6) neuroradiologic subspecialty; 7) practice environment; 8) training institution; and 9) accommodations for all levels of abilities. Additional initiatives intended to strengthen the ASNR as a diverse and inclusive organization include the Committee Chair Orientation Toolkit and invitations to ASNR Committee Chairs to join Diversity and Inclusion Committee calls and partner on aligning strategic initiatives.

Cultural competence is not innate. Rather, this is a skill set developed through interest and intentional effort facilitated by education, travel, and experience. We are fortunate to inhabit a fascinating world teeming with biologic diversity. A certain awe for and desire to understand these diverse biologic processes and leverage them for the benefit of humankind likely motivated many of us to pursue a career in medicine. We suggest approaching human diversity with this same sense of wonder, appreciation, and desire to understand, recognizing the tremendous creativity and vitality that these differences may catalyze.

Finally, the committee views health equity for the patients we serve as an extremely important endeavor for medicine in general, as well as neuroradiology in particular. We must remain vigilant regarding the social, environmental, economic, political, and cultural frameworks that affect individual and population health. It is becoming increasingly clear that radiology can play a pivotal role in addressing these issues. For example, the American College of Radiology recently convened the Radiology Health Equity Coalition to advance awareness of health disparities and equity in the delivery of health care in the United States.[37] As the pandemic has highlighted substantial inequities in health status and health care, the American College of Radiology became convinced that patient-centered care achieved through health equity is good for patients and providers alike. At the request of the American College of Radiology Commission on Neuroradiology, the committee recently recommended that the ASNR become a member organization of the Coalition, and the ASNR Board of Directors unanimously voted to join.

Although we hope that our shared responsibility to do what is best for our patients would serve as sufficient motivation to enthusiastically support the diversity and inclusion efforts of the ASNR, we believe there are also very good reasons to participate from the standpoints of our specialty, our society, and ourselves. Please, come join us in this important work! There is not only much to do but also much reason for excitement and optimism about a better and stronger future together.

All Diversity and Inclusion webinars mentioned in this article are available for on-demand viewing at ASNR Education Connection (https://www.asnr.org/education/education-connection/).

REFERENCES

1. ASNR Welcoming Environment Policy. https://www.asnr.org/asnr/about-us/about-asnr/. Accessed August 1, 2021
2. Smedley BD, Stith AY, Nelson AR, eds; Committee on Understanding and Eliminating Racial and Ethnic Disparities in Health Care. *Unequal Treatment: Confronting Racial and Ethnic Disparities in Health Care*. National Academies Press; 2003
3. Fredriksen-Goldsen KI, Kim H-J, Shui C, et al. **Chronic health conditions and key health indicators among lesbian, gay, and bisexual older US adults, 2013-2014.** *Am J Public Health* 2017;107:1332–88 CrossRef Medline
4. James SE, Herman JL, Rankin S, et al. **The Report of the 2015 U.S. Transgender Survey.** National Center for Transgender Equality; 2016
5. Samari G, Alcalá HE, Sharif MZ. **Islamophobia, health, and public health: a systematic literature review.** *Am J Public Health* 2018;108:e1–e9
6. Price JH, Khubchandani J, Webb FJ. **Poverty and health disparities: what can public health professionals do?** *Health Promot Pract* 2018;19:170–74 CrossRef Medline
7. Hill CV, Pérez-Stable EJ, Anderson NA, et al. **The National Institute on Aging Health disparities research framework.** *Ethn Dis* 2015;25:245–54 CrossRef Medline
8. Schrager JD, Patzer RE, Kim JJ, et al. **Racial and ethnic differences in diagnostic imaging utilization during adult emergency department visits in the United States, 2005 to 2014.** *J Am Coll Radiology* 2019;16:1036–45 CrossRef Medline
9. Brinjikji W, Rabinstein AA, McDonald JS, et al. **Socioeconomic disparities in the utilization of mechanical thrombectomy for acute ischemic stroke in US hospitals.** *AJNR Am J Neuroradiol* 2014;35:553–56 CrossRef Medline
10. Sacco RL. **Stroke Disparities: From Observations to Actions—Inaugural Edward J. Kenton Lecture 2020.** *Stroke* 2020;51:3392–405 CrossRef Medline
11. Mayeda ER, Glymour MM, Quesenberry CP, et al. **Inequalities in dementia incidence between six racial and ethnic groups over 14 years.** *Alzheimers Dement* 2016;12:216–24 CrossRef Medline
12. Gu CN, Brinjikji W, El-Sayed AM, et al. **Racial and health insurance disparities of inpatient spine augmentation for osteoporotic vertebral fractures from 2005 to 2010.** *AJNR Am J Neuroradiol* 2014;35:2397–402 CrossRef Medline
13. Orhurhu V, Agudile E, Chu R, et al. **Socioeconomic disparities in the utilization of spine augmentation for patients with osteoporotic fractures: an analysis of National Inpatient Sample from 2011 to 2015.** *Spine J* 2020;20:547–55 CrossRef Medline
14. Vyfhuis MA, Suzuki I, Bentzen SM, et al. **Adherence to guideline-concordant care and its effect on survival in Black patients with head and neck cancers: a SEER-Medicare Analysis.** *Oncologist* 2021;26:579–87 CrossRef Medline

15. Anyane-Yeboa A, Sato T, Sakuraba A. **Racial disparities in COVID-19 deaths reveal harsh truths about structural inequality in America.** *J Intern Med* 2020;288:479–80 CrossRef Medline
16. Aboul Nour H, Affan M, Mohamed G, et al. **Impact of the COVID-19 pandemic on acute stroke care, time metrics, outcomes, and racial disparities in a Southeast Michigan health system.** *J Stroke Cerebrovasc Dis* 2021;30:105746 CrossRef Medline
17. Al Kasab S, Almallouhi E, Alawieh A, et al; STAR collaborators. **Alarming downtrend in mechanical thrombectomy rates in African American patients during the COVID-19 pandemic: insights from STAR.** *J NeuroInterv Surg* 2021;13:304–07 CrossRef Medline
18. Heslin KC, Hall JE. **Sexual orientation disparities in risk factors for adverse COVID-19-related outcomes, by race/ethnicity: behavioral risk factor surveillance system, United States, 2017-2019.** *MMWR Morb Mortal Wkly Rep* 2021;70:149–54 CrossRef Medline
19. Meeks LM, Poullos P, Swenor BK. **Creative approaches to the inclusion of medical students with disabilities.** *AEM Educ Train* 2020;4:292–97 CrossRef Medline
20. Betancourt JR, Tan-McGrory A, Flores E, et al. **Racial and ethnic disparities in radiology: a call to action.** *J Am Coll Radiol* 2019;16:547–53 CrossRef Medline
21. Lightfoote JB, Fielding JR, Deville C, et al. **Improving diversity, inclusion, and representation in radiology and radiation oncology, Part 1: why these matter.** *J Am Coll Radiol* 2014;11:673–80 CrossRef Medline
22. Accius J, Suh JY; AARP Thought Leadership. **The economic impact of age discrimination: how discriminating against older workers could cost the U.S. economy $850 billion.** 2020. https://doi.org/10.26419/int.00042.003. Accessed August 1, 2021
23. Lewis RS, Bhargavan M, Sunshine JH. **Women radiologists in the United States: results from the American College of Radiology's 2003 Survey.** *Radiology* 2007;242:802–10 CrossRef Medline
24. Ahmadi M, Khurshid K, Sanelli PC, et al. **Influences for gender disparity in academic neuroradiology.** *AJNR Am J Neuroradiol* 2018;39:18–23 CrossRef Medline
25. Meltzer CC, Sanelli PC, Hepp MB, et al. **Women rising to the top: the tipping point for the ASNR.** *AJNR Am J Neuroradiol* 2019;40:2–4 CrossRef Medline
26. Silver JK, Ghalib R, Poorman JA, et al. **Analysis of gender equity in leadership of physician-focused medical specialty societies, 2008-2017.** *JAMA Intern Med* 2019;179:433–35 CrossRef Medline
27. **2017 National Tables; Main Series: Main Projections for the United States**, 2017-2060. U.S. Census Bureau, Population Division 2018. https://www.census.gov/data/tables/2017/demo/popproj/2017-summary-tables.html. Accessed August 1, 2021
28. Chapman CH, Hwang WT, Both S, et al. **Current status of diversity by race, Hispanic ethnicity, and sex in diagnostic radiology.** *Radiology* 2014;270:232–40 CrossRef Medline
29. Cooper-Patrick L, Gallo JJ, Gonzales JJ, et al. **Race, gender, and partnership in the patient-physician relationship.** *JAMA* 1999;282:583–89 CrossRef Medline
30. Saha S, Komaromy M, Koepsell TD, et al. **Patient-physician racial concordance and the perceived quality and use of health care.** *Arch Intern Med* 1999;159:997–1004 CrossRef Medline
31. Saha S, Arbelaez JJ, Cooper LA. **Patient-physician relationships and racial disparities in the quality of health care.** *Am J Public Health* 2003;93:1713–19 CrossRef Medline
32. Kumar D, Schlundt DG, Wallston KA. **Patient-physician race concordance and its relationship to perceived health outcomes.** *Ethn Dis* 2009;19:345–51 Medline
33. Norbash A, Kadom N. **The business case for diversity and inclusion.** *J Am Coll Radiol* 2020;17:676–78 CrossRef Medline
34. Hunt V, Layton D, Prince S. **Why Diversity Matters.** https://www.mckinsey.com/business-functions/organization/our-insights/why-diversity-matters. Accessed August 1, 2021
35. Kubik-Huch RA, Vilgrain V, Krestin GP, et al. **Women in radiology: gender diversity is not a metric—it is a tool for excellence.** *Eur Radiol* 2020;30:1644–52 CrossRef Medline
36. Page SE. *The Difference: How the Power* of *Diversity Creates Better Groups, Firms, Schools,* and *Societies.* Princeton University Press; 2007
37. Fleishon HB. **Radiology's Health Equity Coalition.** *J Am Coll Radiology* 2021;18:631–32 CrossRef Medline

Deep Learning Enables 60% Accelerated Volumetric Brain MRI While Preserving Quantitative Performance: A Prospective, Multicenter, Multireader Trial

S. Bash, L. Wang, C. Airriess, G. Zaharchuk, E. Gong, A. Shankaranarayanan, and L.N. Tanenbaum

ABSTRACT

BACKGROUND AND PURPOSE: In this prospective, multicenter, multireader study, we evaluated the impact on both image quality and quantitative image-analysis consistency of 60% accelerated volumetric MR imaging sequences processed with a commercially available, vendor-agnostic, DICOM-based, deep learning tool (SubtleMR) compared with that of standard of care.

MATERIALS AND METHODS: Forty subjects underwent brain MR imaging examinations on 6 scanners from 5 institutions. Standard of care and accelerated datasets were acquired for each subject, and the accelerated scans were enhanced with deep learning processing. Standard of care, accelerated scans, and accelerated–deep learning were subjected to NeuroQuant quantitative analysis and classified by a neuroradiologist into clinical disease categories. Concordance of standard of care and accelerated–deep learning biomarker measurements were assessed. Randomized, side-by-side, multiplanar datasets (360 series) were presented blinded to 2 neuroradiologists and rated for apparent SNR, image sharpness, artifacts, anatomic/lesion conspicuity, image contrast, and gray-white differentiation to evaluate image quality.

RESULTS: Accelerated–deep learning was statistically superior to standard of care for perceived quality across imaging features despite a 60% sequence scan-time reduction. Both accelerated–deep learning and standard of care were superior to accelerated scans for all features. There was no difference in quantitative volumetric biomarkers or clinical classification for standard of care and accelerated–deep learning datasets.

CONCLUSIONS: Deep learning reconstruction allows 60% sequence scan-time reduction while maintaining high volumetric quantification accuracy, consistent clinical classification, and what radiologists perceive as superior image quality compared with standard of care. This trial supports the reliability, efficiency, and utility of deep learning–based enhancement for quantitative imaging. Shorter scan times may heighten the use of volumetric quantitative MR imaging in routine clinical settings.

ABBREVIATIONS: DL = deep learning; FAST = accelerated scan; HOC = hippocampal occupancy score; HV = hippocampal volumes; ILV = inferior lateral ventricles; MCI = mild cognitive impairment; SLV = superior lateral ventricles; SOC = standard of care

Deep learning (DL) is a subset of machine learning that uses convolutional neural networks to process large volumes of data.[1-6] While traditional reconstruction techniques can be limited by long scan times, SNR constraints, and motion artifacts, the recent application of DL to image reconstruction can enable faster image acquisitions with equal or enhanced image quality.[2,3] While DL can boost SNR among other advantages over conventional methods,[2-6] concerns exist over whether postprocessing can mask or alter pathology and whether the quantitative values derived are consistent with those obtained from routine standard of care (SOC) scans over the gamut of scanner vendors and across field strengths.

MR imaging depicts brain anatomy with high spatial and contrast resolution, qualities crucial when applying anatomic segmentation and quantitative volumetric analysis. Quantitative volumetric analysis requires 3D radiofrequency spoiled gradient-echo T1-weighted scans, and *k*-space acceleration opportunities have limits. Reduced excitations and undersampling techniques like compressed sensing accelerate scans at a cost of increased image noise (reduced SNR). Acceleration via decreases in the imaging matrix can improve both SNR and contrast resolution

Received October 25, 2020; accepted after revision August 17, 2021.

From RadNet Inc (S.B., L.N.T.), Los Angeles, California; Subtle Medical (L.W., E.G., A.S.), Menlo Park, California; Cortechs.ai. (C.A.), San Diego, California; Stanford University Medical Center (G.Z.), Stanford, California; and Lenox Hill Radiology (L.N.T.), New York, New York.;

Paper previously presented at: Annual Meetings and Exhibitions of the International Society for Magnetic Resonance in Medicine and the Society for Magnetic Resonance Technologists, August 8–14, 2020; Virtual; and May 14–20, 2021, Virtual; Annual Meetings of the American Society of Neuroradiology, May 30 to June 4, 2020; Virtual; and May 15–20, 2021; Virtual; and Annual Meeting of the European Congress of Radiology, May 3–7, 2021, Porto Alegre, Brazil.

Please address correspondence to Suzie Bash, MD, RadNet, 1510 Cotner Ave, Los Angeles, CA 90025; e-mail: suzie.bash@radnet.com; @suzie_bash

Indicates open access to non-subscribers at www.ajnr.org

http://dx.doi.org/10.3174/ajnr.A7358

but reduce image sharpness. For this study, both undersampling and reduced imaging matrices were used for the accelerated scans (FAST), which were then processed with a commercially available DL tool (SubtleMR; Subtle Medical) that provides both denoising and sharpness enhancement (FAST-DL). Our goal was to match or exceed SOC image SNR and spatial resolution while maintaining clinical and quantitative integrity.[7]

In this prospective, multireader, multicenter study, we explored the impact of DL-based enhancement of 60% accelerated 3D T1-weighted brain MR image acquisitions. We found that the DL-processed images demonstrated high volumetric quantification accuracy and matched clinical disease status predictability and provided what readers perceived as superior image quality compared with the longer SOC examinations, suggesting good generalizability, accuracy, and potential utility of DL enhancement in routine clinical settings.

MATERIALS AND METHODS

Participants

With Western Institutional Review Board approval and patient consent, 40 consecutive subjects (mean age, 69 [SD, 17] years; 21 men, 19 women) undergoing clinically indicated brain MR imaging examinations for subjective memory loss were prospectively recruited during an 8-month period.

Image Acquisition

Imaging was obtained on 6 scanners (3T Skyra, Siemens; 3T Discovery 750 and 3T Discovery 750w, 3T Signa Premier, and 1.5T HDxt, GE Healthcare; 3T Verio, Siemens) at 3T ($n = 32$) and 1.5T ($n = 8$) from 5 different institutions in New York ($n = 8$) and California ($n = 32$).

The image acquisitions consisted of paired 3D T1-weighted sagittally acquired datasets: 1 SOC image set (mean scan time, 6 minutes, 56 seconds for 3T and 4 minutes for 1.5T), and 1 FAST image set (mean scan time, 2 minutes, 44 seconds for 3T and 2 minutes, 40 seconds for 1.5T). Native sagittal images were acquired and quantitatively postprocessed at 1-mm section thickness (for 3T) and 1.2-mm section thickness (for 1.5T). The spatial-resolution matrix was 256 × 256 for SOC and 128 × 256 for FAST. Acquisition parameters included MPRAGE (flip angle = 9°, TI = 1100 ms, section thickness = 1.0–1.2 mm); fast-spoiled gradient recalled (flip angle = 8°, TI = 900 ms, section thickness = 1.0–1.2 mm); and BRAVO (GE Healthcare; flip angle = 12°, TI = 450 ms, section thickness = 1.0–1.2 mm). The average pooled (3T + 1.5T) 3D T1WI scan times for all 40 patients ($n = 32$/3T and $n = 8$/1.5T) were 6 minutes, 1 second for SOC (range, 4–7 minutes) and 2 minutes, 43 seconds for the FAST dataset (range, 2–2 minutes, 50 seconds), representing a 60% sequence scan-time reduction for the FAST acquisition.

Image Processing

FAST-DL was performed off-line using an FDA-cleared, vendor-agnostic, DICOM-based, convolutional neural networks–dependent deep learning artificial intelligence image-enhancement software product, SubtleMR (Version 1.2). The training set included hundreds of thousands of MR imaging datasets from a variety of vendors (GE Healthcare, Philips Healthcare, Siemens, Hitachi, and so forth), scanner models, field strengths, and clinical sites, as well as a variety of disease states/clinical indications, thus experiencing a range of tissue contrasts, acquisition parameters, patient anatomies, and variable image quality.

The DL network was trained on paired low-/high-resolution images to impart structure-preserving noise reduction and sharpness enhancement to newly acquired images.[7] Processing does not use proprietary raw *k*-space input (DICOM-based) and is, thus, vendor-agnostic. For the study, DL processing required <1 minute per series on a scanner-connected GPU server and finished before the next sequence acquisition was completed, thus not impacting overall examination time. Images were gathered from different sites and presented to the reviewers on a commercial DICOM viewer.

The SOC, FAST, and FAST-DL image sets were processed with a machine learning–based FDA-cleared quantitative volumetric software product, NeuroQuant (Cortechs.ai). The hippocampal occupancy score (HOC), a biomarker to predict the progression of neurodegenerative diseases, as well as the volumes of the hippocampi (HV), superior lateral ventricles (SLV), and inferior lateral ventricles (ILV) were analyzed for this study.

Radiologic Assessment

For the image-quality assessment, 2 experienced board-certified neuroradiologists (>17 years' experience each) were presented with 40 paired side-by-side multiplanar 3D T1-weighted series datasets (360 series). The blinded datasets (SOC versus FAST, SOC versus FAST-DL, FAST-DL versus FAST) were randomized in disease classification, image plane, and left-right display order. The readers evaluated 2 images side-by-side and provided a single Likert scale ranking between 1 and 5 that described whether the left or right image was superior (3 = both images were preferred equally; 2 or 4 = right/left mildly preferred; 1 or 5 = right/left strongly preferred) for the following: 1) perceived SNR; 2) perceived spatial resolution (sharpness); 3) imaging artifacts; 4) anatomic/lesion conspicuity; 5) image contrast; and 6) gray-white matter differentiation. Anatomic conspicuity of brain structures such as the deep gray nuclei was used in cases in which a lesion was not conspicuous on the 3D T1-weighted images. Sample lesions in our datasets included infarcts and prominent white matter ischemic disease.

To assess clinical classification performance, we categorized the quantitative biomarkers obtained from 80 datasets (40 SOC and 40 FAST-DL) in a blinded, randomized fashion. Each dataset was rated using a binary predictive classification system (healthy/mild cognitive impairment [MCI] versus dementia) with ground truth established according to the statistical significance of 3 biomarkers falling >2 SDs from the mean: HOC (<5%), HV (<5%), and ILV (>95%) based on an ($n > 4000$) age- and sex-matched normative data base, with 0/3 and 1/3 statistically significant biomarkers categorized as healthy/MCI; and 2/3 and 3/3 categorized as likely dementia.

Following qualitative feature ranking and quantitative analysis, both readers were presented the SOC and FAST-DL datasets in a side-by-side fashion, randomized in right-left orientation to qualitatively assess the overall diagnostic quality of the 3D T1-weighted images before postprocessing with NeuroQuant and

Table 1: Wilcoxon rank sum test results—both readers combined[a]

Feature	SOC vs FAST		FAST-DL vs SOC		FAST-DL vs FAST	
	Mean	*P* Value	Mean	*P* Value	Mean	*P* Value
Perceived SNR	4.1 (SD, 0.8)	<.001	3.5 (SD, 1.3)	<.001	4.3 (SD, 1.0)	<.001
Sharpness	4.5 (SD, 0.7)	<.001	3.5 (SD, 1.5)	.005	4.7 (SD, 0.9)	<.001
Artifacts	3.9 (SD, 0.8)	<.001	3.5 (SD, 1.1)	<.001	4.1 (SD, 0.9)	<.001
Anatomic/lesion conspicuity	4.2 (SD, 0.7)	<.001	3.3 (SD, 1.1)	.006	4.3 (SD, 0.7)	<.001
Image contrast	4.0 (SD, 0.7)	<.001	3.4 (SD, 1.1)	.004	4.1 (SD, 0.8)	<.001
GM/WM differentiation	4.3 (SD, 0.7)	<.001	3.4 (SD, 1.2)	.009	4.5 (SD, 0.8)	<.001

[a] SOC is superior to FAST for all criteria (*P* values <.001). Numbers higher than 3 represent preference for the first of the 2 sequences listed in the upper row. FAST-DL is superior to SOC for all criteria (*P* values < .008), except for GM/WM differentiation. While this metric trended to be superior for FAST-DL versus SOC, it did not reach statistical significance after Bonferroni correction (*P* = .009). FAST-DL is superior to FAST for all criteria (*P* values <.001).

Table 2: Paired *t* test for SOC versus FAST-DL[a]

	SOC	FAST-DL	Paired *t* Test
HOC (mean)	0.68 (SD, 0.16)	0.68 (SD, 0.16)	0.58
HV (mean) (cm^3)	6.45 (SD, 1.70)	6.47 (SD, 1.69)	0.77
SLV volume (mean) (cm^3)	44.30 (SD, 20.60)	43.63 (SD, 20.35)	<0.05
ILV volume (mean) (cm^3)	3.07 (SD, 1.78)	3.04 (SD, 1.69)	0.27

[a] There is excellent agreement between SOC and FAST-DL for quantitative assessment of HOC, HV, SLV volume, and ILV volume.

Table 3: Paired *t* test for SOC versus FAST[a]

	SOC	FAST	Paired *t* Test
HOC (mean)	0.68 (SD, 0.16)	0.68 (SD, 0.17)	0.63
HV (mean) (cm^3)	6.45 (SD, 1.70)	6.56 (SD, 1.88)	0.60
SLV volume (mean) (cm^3)	44.30 (SD, 20.60)	43.44 (SD, 20.01)	<0.05
ILV volume (mean) (cm^3)	3.07 (SD, 1.78)	3.17 (SD, 1.85)	0.93

[a] There is less optimal agreement between SOC versus FAST (compared with SOC versus FAST-DL) for quantitative assessment of HOC, HV, SLV volume, and ILV volume.

again after postprocessing with NeuroQuant, with the goal of visually assessing the quality of matched color-coded segmentation of the latter. The FAST scans were excluded from this analysis because they would not be typically used as input to quantitative segmentation software given their lower spatial resolution.

Statistical Analysis

Wilcoxon rank sum tests were performed to assess the equivalence or superiority of the image quality for each feature (Table 1). Statistically significant superiority for a feature was determined by a *P* value < .05.

Adjustment for significance tests for multiple comparisons was made using the Bonferroni correction, which adjusts the significance level to $P < .05/.06$ (0.00833).

Paired *t* test analysis was performed to test the equivalence of quantitative data on both the SOC versus FAST-DL images (Table 2) and SOC versus FAST images (Table 3). Linear regression graphs (Figs 1 and 2) and Bland-Altman analysis (Figs 3 and 4) were performed to assess quantitative volumetric biomarker equivalence of the datasets. The Spearman rank correlation test was applied to assess interreader agreement between the 2 neuroradiologists on image-quality ratings. Additionally, interrater reliability analysis was performed using an equal-spacing weighted Cohen κ statistic to measure the consistency of the 2 readers' evaluation of image quality.

RESULTS

Qualitative and Quantitative Performance

FAST-DL was statistically superior to SOC in subjective image quality for perceived SNR, sharpness, artifact reduction, anatomic/lesion conspicuity, and image contrast (all *P* values < .008), despite a 60% reduction in sequence scan time. Both FAST-DL and SOC were statistically superior to FAST for all analyzed features (all *P* values < .001). Wilcoxon rank sum statistical results are collectively summarized in Table 1.

Paired *t* test analysis demonstrated excellent agreement of quantitative data on both the SOC and FAST-DL images (Table 2). As expected, there was less agreement between the SOC and FAST datasets (Table 3) due to the lower spatial resolution of the FAST images. There was no statistically significant difference between mean HOC values in the SOC (0.68 [SD, 0.16]) and the mean FAST-DL (0.68 [SD, 0.16]) datasets. The difference of the HV, SLV volumes, and ILV volumes was also negligible (<2%) for the SOC and FAST-DL datasets. The linear regression graphs (Fig 1) and Bland-Altman plot graph analysis (Fig 3) further demonstrated strong agreement between quantitative values in each dataset across the range of conditions (normal, MCI, Alzheimer disease) with the HOC ranging from 0.32 to 0.95 mL. There was 100% agreement in clinical disease classification of both the SOC and FAST-DL datasets ($n = 29$ healthy/MCI and $n = 11$ dementia). The cross-correlation factor and degree of scatter was consistently worse for the SOC and FAST images compared with the SOC and FAST-DL images as demonstrated on the linear regression graphs (Fig 2) and Bland Altman plot graph analysis (Fig 4).

There was excellent interreader agreement between the 2 neuroradiologists on the Spearman rank correlation test applied to the Likert image quality ratings, with a Spearman ρ value of 0.725 ($P < .01$). The κ value of 0.62 ($P < .001$) also confirms substantial interrater agreement on the Likert scale rankings.

Overall Diagnostic Quality

All SOC and FAST-DL datasets were rated of diagnostic quality by both interpreting neuroradiologists. Both readers determined that there was similar quality of segmentation for both the SOC and FAST-DL datasets. Representative imaging examples for image-

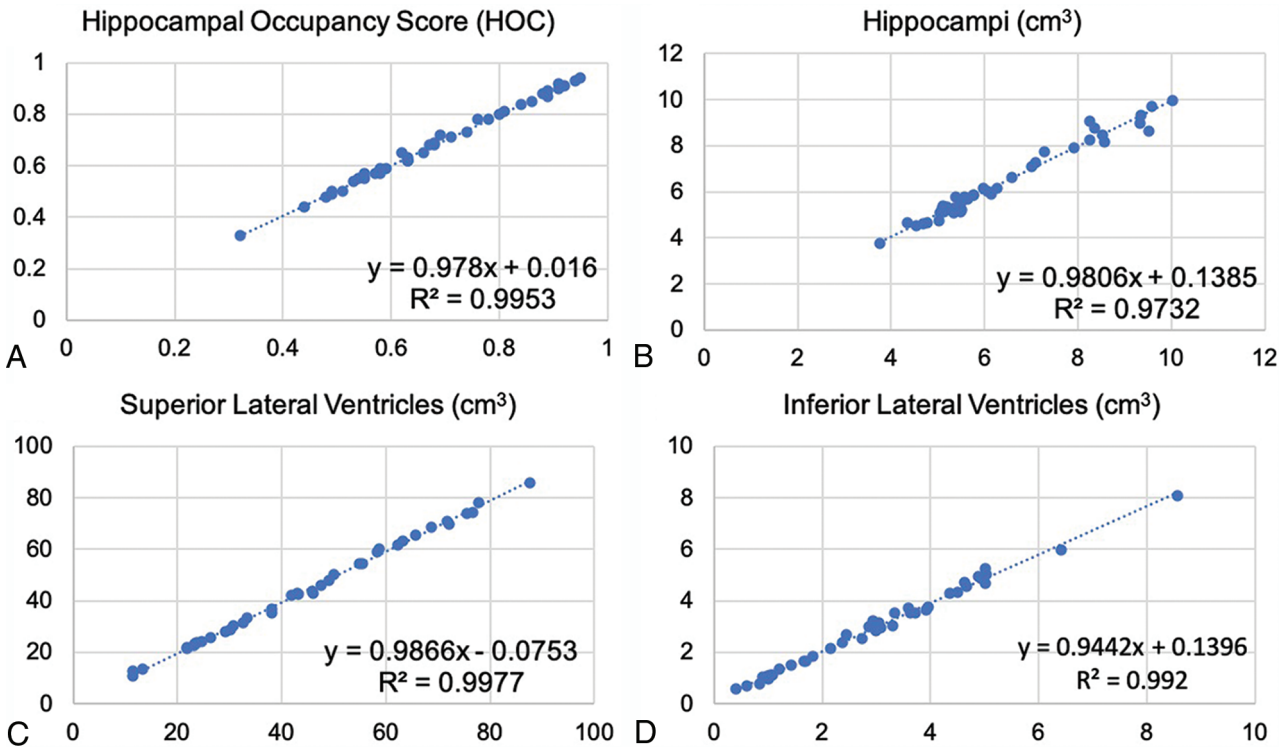

FIG 1. Linear regression results for SOC versus FAST-DL. The plot graphs demonstrate linear distribution without scatter, indicating consistent concordance between SOC (x-axis) and FAST-DL (y-axis) in quantitative assessment of HOC (*A*), HV (*B*), SLV volume (*C*), and ILV volume (*A*).

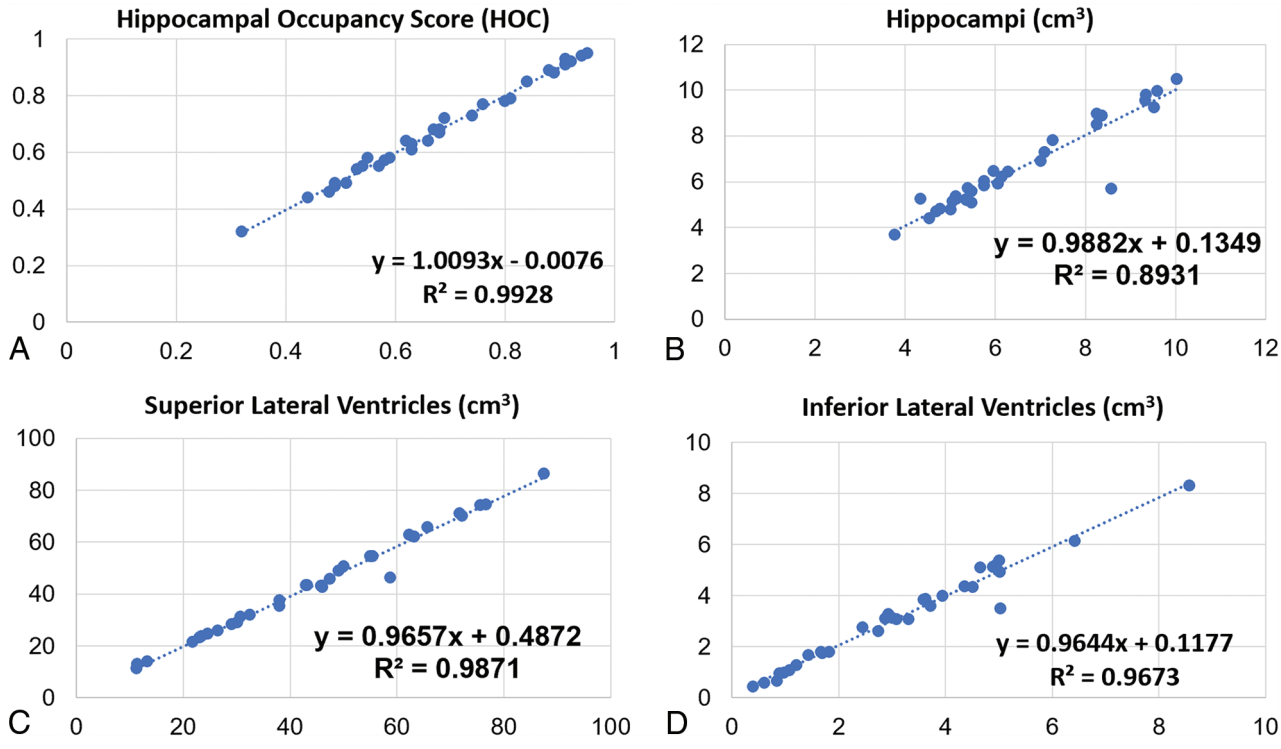

FIG 2. Linear regression results for SOC versus FAST. The plot graphs demonstrate a modestly linear distribution though some scatter is present, indicating less optimal concordance of the cross-correlation factor between SOC (x-axis) and FAST (y-axis) (compared with SOC versus FAST-DL) in a quantitative assessment of HOC (*A*), HV (*B*), SLV volume (*C*), and ILV volume (*A*).

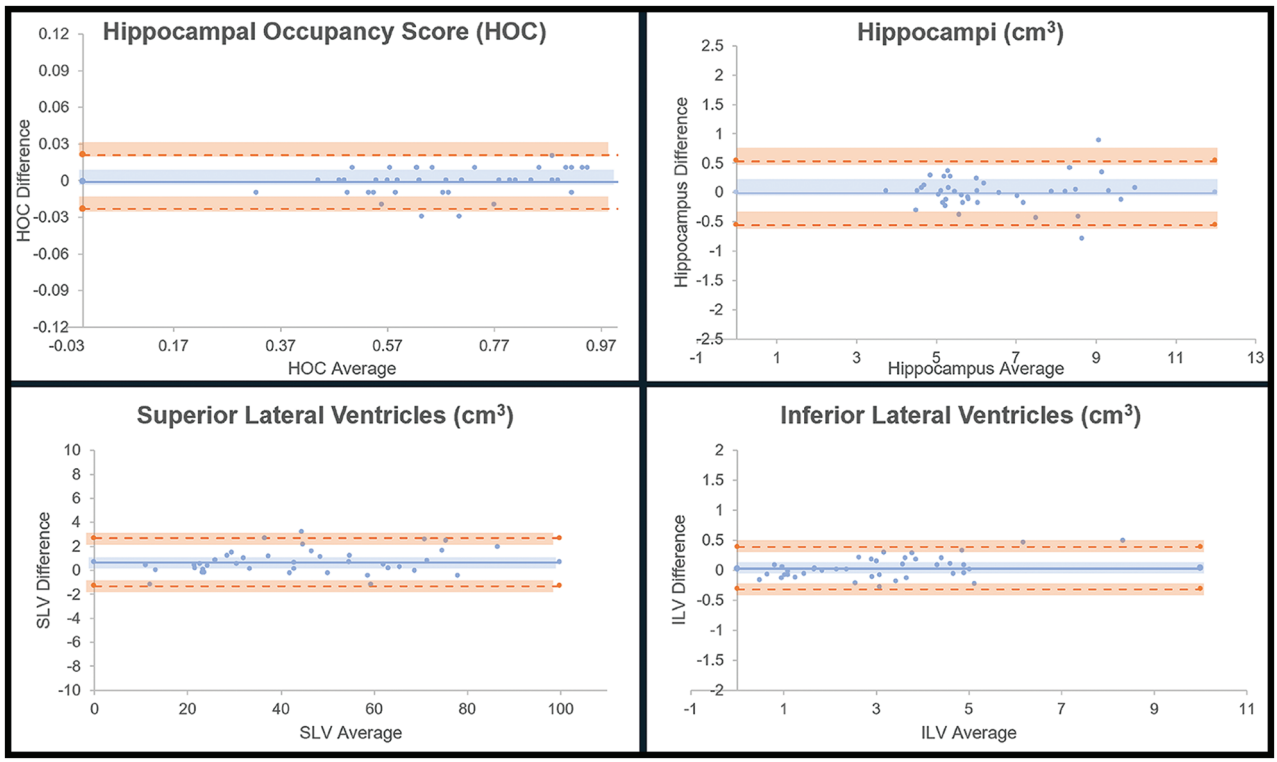

FIG 3. Bland-Altman results for SOC versus FAST-DL. The plot graphs demonstrate a linear distribution without significant scatter, indicating consistent concordance between SOC and FAST-DL in the quantitative assessment of HOC, HV, SLV volume, and ILV volume.

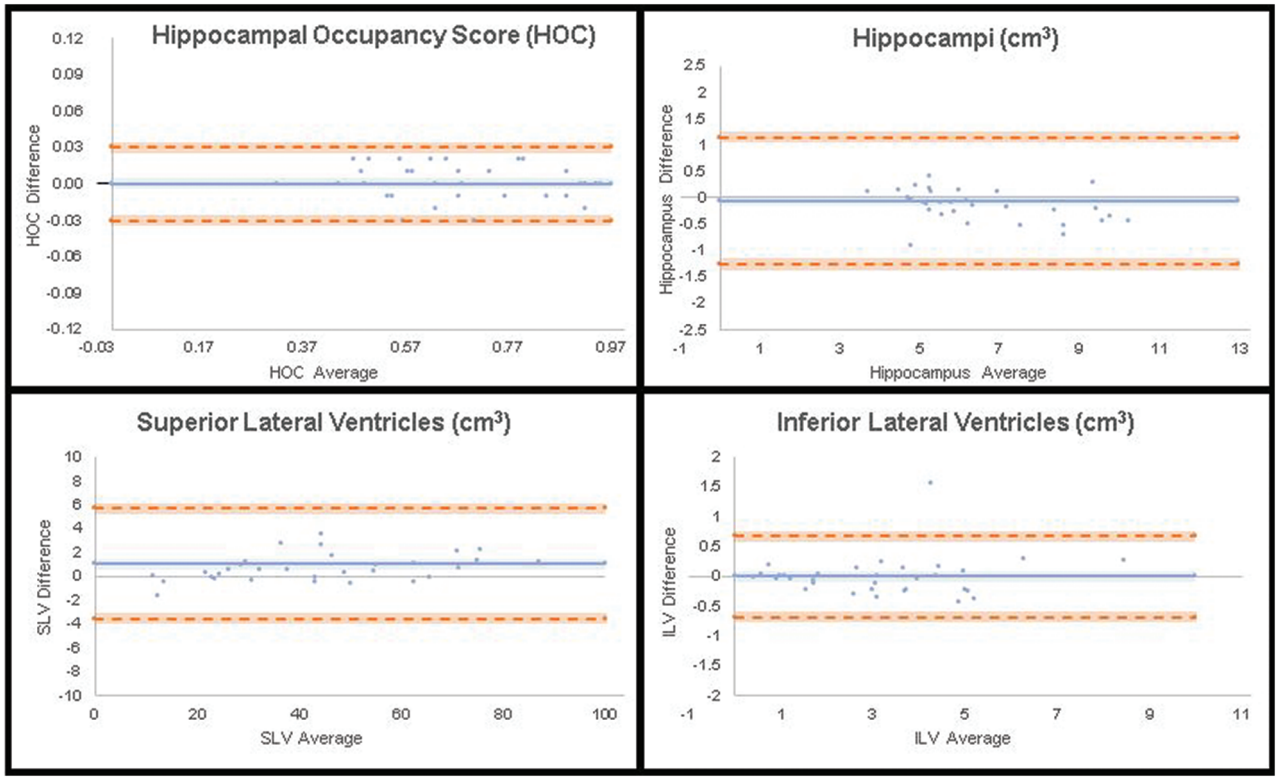

FIG 4. Bland-Altman results for SOC versus FAST. The plot graphs demonstrate a modestly linear distribution though some scatter is present, indicating less optimal concordance of the cross-correlation factor between SOC versus FAST (compared with SOC versus FAST-DL) in the quantitative assessment of HOC, HV, SLV volume, and ILV volume.

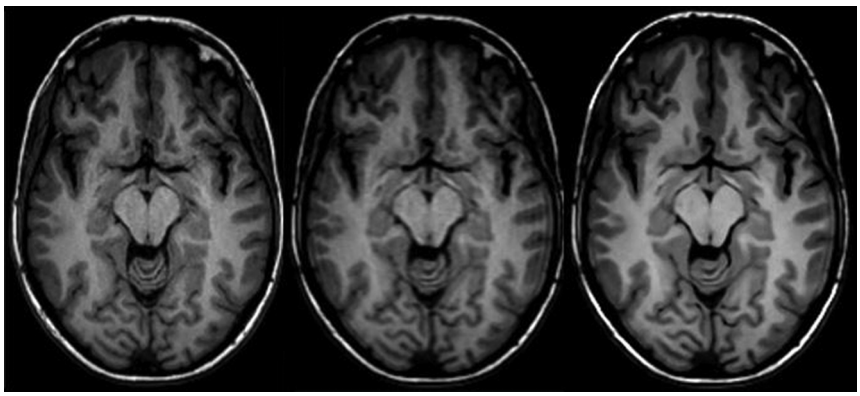

FIG 5. Representative axial 3D T1-weighted images on a 3T scanner. *Left to right*, SOC (scan time, 4 minutes, 55 seconds), FAST (scan time, 2 minutes, 10 seconds), FAST-DL (scan time, 2 minutes, 10 seconds).

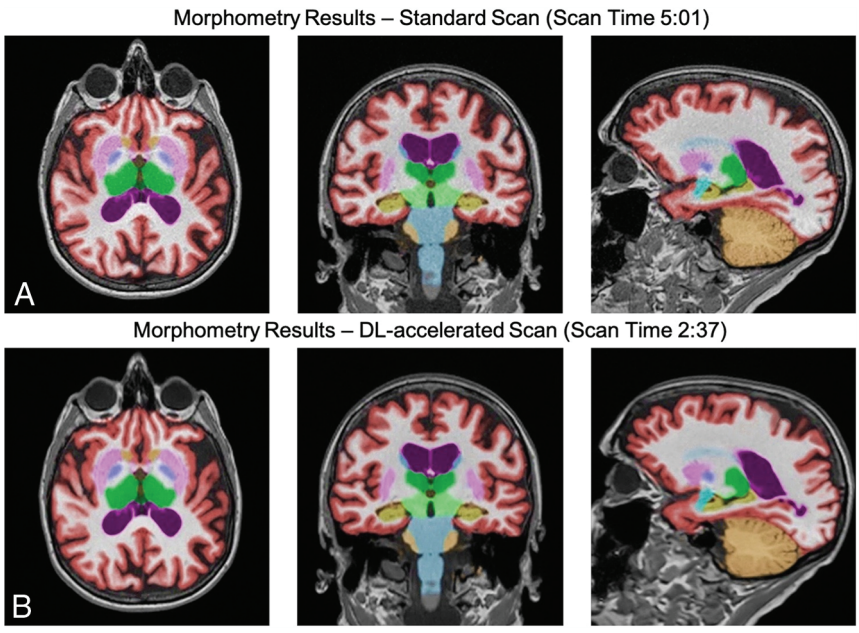

FIG 6. Representative 3D T1-weighted multiplanar images with volumetric segmentation on a 3T scanner. *Left to right*, Axial, coronal, sagittal T1-weighted images with SOC (scan time, 5 minutes, 01 second) on the upper row (*A*) and FAST-DL (scan time, 2 minutes, 37 seconds) on lower row (*B*).

quality analysis for SOC, FAST, and FAST-DL are shown in Fig 5. Sample volumetric segmentation of the SOC and FAST-DL images are shown in Fig 6.

DISCUSSION

DL enhancement of MR images is known to provide multiple benefits, including increased SNR,[2,3] but questions remain about reliability in general clinical use.[8] The approach used in our multicenter, multivendor study explored the impact on the image quality and consistency of quantitative volumetric analysis results obtained with FAST-DL compared with that obtained with SOC scans.

Quantitative volumetric MR imaging analytical tools are in widespread clinical use for the evaluation of patients with dementia, seizures, multiple sclerosis, traumatic brain injury, and pediatric brain disorders. The software segments, labels, and calculates the volumes of substructures (including lesions) in the brain. The derived quantitative values are compared with a large normative age and sex-matched data base, aiding in the diagnosis and longitudinal follow-up of clinical conditions such as Alzheimer's disease. Quantitative assessment reduces reader subjectivity.[9-12]

MR imaging provides excellent anatomic detail and superb contrast resolution but involves trade-offs in SNR, spatial resolution, and scan duration.[7] While DL-based augmentation is a recognized solution for accelerated MR imaging, it is important to validate the reliability and generalizability of its enhancement capabilities with quantitative biomarker accuracy.[7]

The MR imaging experience is uncomfortable and associated with frank anxiety reactions in up to 30% of patients.[13,14] Faster MR image acquisition can thus increase patient satisfaction and may reduce motion artifacts. Motion is a significant challenge in MR imaging, occurring in 29% of inpatient/emergency department examinations and 7% of outpatient studies and can lead to repeat portions of or even complete examinations.[15] Andre et al[16] found that 19.8% of all MR imaging sequences need to be repeated due to motion artifacts, a $592 revenue loss per hour and $115,000 loss annually per scanner due to motion artifacts. DL-based reconstruction solutions promise to enable shorter examinations with decreased patient motion and improved patient comfort.[14]

In our study, we achieved a scan-time reduction of 60% while exceeding perceived routine 3D T1-weighted image quality. If DL-enhanced fast protocols were used on all pulse sequences across every study, one could anticipate a proportional increase in examination-based workflow efficiency for an imaging facility. One recent trial explored DL enhancement across all pulse sequences in clinical spine MR imaging, with preservation of quantitative features using a structural similarity index measure as well as gains in perceived SNR and artifact reduction, despite a 40% scan-time reduction.[2] Future research could explore whether scan-time reduction of this scale results in a true-positive impact on workflow, eg, the ability to scan more patients per day.

In this trial, the SOC images serve as the standard for image preference. Our randomized blinded assessment of the imaging features is meant to reflect human subjective perception

of comparative image quality. A radiologist's qualitative assessment of noninferiority is critical before a DL-enhanced alternative would be considered acceptable for clinical use. On the other hand, processed images should satisfy both qualitative and quantitative measures to ensure that diagnostically relevant features are not altered and the integrity of the processed image information is maintained.

Concerns exist about DL postprocessing introducing instabilities in an image, in which tiny perturbations in the sampling domain have been shown to be capable of translating into noticeable artifacts on the reconstructed image.[8] This issue has been shown for highly-contrived noise additions to *k*-space data, but it is unclear whether such effects occur under normal operating conditions. The current method starts from image-based DICOM data rather than within the *k*-space and is likely less susceptible to this effect.

To our knowledge, this is the first prospective, randomized, multicenter study of DL reconstruction capabilities assessing the impact on the integrity of quantitative volumetric analysis of clinical brain MR imaging examinations. The DL tool applied in this study shifts the usual MR imaging trade-off equation by imprinting a boost in spatial resolution on the target FAST series, which, due to inherently larger native voxel sizes, can have a higher SNR and contrast-to-noise ratio than even the basis SOC series.[7] Along with sharpness enhancement, DL offers structure-preserving denoising, contributing to statistically significant gains in perceived SNR compared with SOC.

Blinded subjective assessment by the neuroradiologists found that the 60% accelerated, DL-enhanced 3D T1-weighted brain MR images delivered consistent clinical classification and were superior to standard of care MR imaging across essentially all analyzed quality features (perceived SNR, perceived spatial resolution, artifact reduction, anatomic/lesion conspicuity, and image contrast). These findings offer confidence that DL processing can add value and efficiency to clinical MR imaging brain examinations.

The quantitative biomarkers of HV, HOC, SLV volume, and ILV volume were statistically equivalent for the FAST-DL sequences and the SOC, supporting the absence of corruption by DL processing and demonstrating the robustness of the DL tool in maintaining quantitative integrity and enhancing image quality despite significant scan-time acceleration. Not unexpectedly, the cross-correlation factor was inferior for the SOC versus the lower resolution FAST dataset.

The strengths of this study include the use of a prospective, randomized, multicenter, multireader study design with images obtained on magnets from multiple vendors and of variable ages and field strengths, with preserved accuracy of quantitative volumetric measures and clinical predictive categories. The results of this trial support the use of DL enhancement to shorten clinical MR imaging brain examinations, even when additional quantitative tools such as volumetric analysis are applied.

Weaknesses include the small number of imaging subjects and the use of only a single DL and quantitative brain-analysis tool. The DL-enhancement tool used in this study is a vendor-agnostic, DICOM-based, commercially available solution. It is possible that alternative vendor-specific, *k*-space-based, commercially available DL enhancement tools may perform differently, though preliminary data suggest observed gains in acceleration and perceived quality with other DL-enhancement tools as well.[17,18] However, this is the first study that the authors are aware of that specifically confirms the quantitative volumetric accuracy and consistent clinical disease categorization of the DL-enhanced dataset.

Future investigations might explore different methods and tools. Another area of future research might include a similar methodology applied to different clinical scenarios that demand accurate segmentation but where scan time acceleration would be desirable, such as in patients with multiple sclerosis, intracranial metastases, epilepsy, and traumatic brain injury. Follow-up studies could also assess whether the difference between the FAST and FAST-DL datasets was significant enough to impact the correct clinical diagnosis or alter the reader's ability to detect a lesion.

CONCLUSIONS

DL can enable 60% faster brain MR image acquisitions with matched clinical disease status predictability and statistically superior perceived image quality, while maintaining high quantitative accuracy compared with the longer SOC examinations. This trial supports the reliability, efficiency, and utility of DL-based enhancement for quantitative imaging. Shorter scan times may boost the use of volumetric quantitative MR imaging in routine clinical settings.

Disclosures: Suzie Bash—*UNRELATED*: *Consultancy*: Cortechs.ai, icometrix, Subtle Medical, Guerbet, GE Pharmaceuticals, *Comments*: 1) honoraria in the past for consultancy work for each entity listed, and 2) Medical Advisory Board member for Cortechs.ai (stipend and stock options) and icometrix (stipend only); *Payment for Lectures Including Service on Speakers Bureaus*: icometrix, Subtle Medical, Guerbet, *Comments*: Honoraria for webinars/talks for the entities listed; *Stock/Stock Options*: Cortechs.ai, *Comments*: stock options as member of MAB; *Travel/Accommodations/Meeting Expenses Unrelated To Activities Listed*: Cortechs.ai, GE Pharmaceuticals, *Comments*: travel/accommodations for consultancy work. Greg Zaharchuk—*UNRELATED*: *Board Membership*: Subtle Medical*; *Grants/Grants Pending*: various National Institutes of Health projects, GE Healthcare, Bayer Healthcare*; *Patents (Planned, Pending or Issued)*: assorted patents on deep learning; *Royalties*: Cambridge University Press; *Stock/Stock Options*: equity in Subtle Medical. Ajit Shankaranarayanan—*UNRELATED*: *Employment*: Subtle Medical; *Stock/Stock Options*: Subtle Medical, *Comments*: equity in the company. Lawrence Tanenbaum—*UNRELATED*: *Consultancy*: Subtle Medical, GE Healthcare, Philips Healthcare, Hitachi, Siemens, Fuji Healthcare, Bracco Diagnostics; *Payment for Lectures Including Service on Speakers Bureaus*: GE Healthcare, Fuji, Subtle Medical, Guerbet, Bracco, Philips Healthcare, Money paid to the individual; *Stock Options*: Subtle Medical; *Other*: Aidoc, Enlitic, Agamon, iMedis, *Comments*: consultant. Long Wang—*UNRELATED*: *Employment*: Subtle Medical. Enhao Gong—*UNRELATED*: *Board Membership*: Subtle Medical; *Employment*: Subtle Medical; *Stock/Stock Options*: Subtle Medical. *Money paid to the institution.

REFERENCES

1. Radlak K, Malinski L, Smolka B. **Deep learning-based switching filter for impulsive noise removal in color images.** *Sensors* 2020;20:2782 CrossRef
2. Tanenbaum LN, Bash S, Johnson B, et al. **Deep learning reconstructed, 40% faster spine MR examinations match or exceed the quality of standard of care exams..** In: *Proceedings of the Annual Meeting of the Radiological Society of North America*; November 29 to December 5, 2020; Virtual
3. Tanenbaum LN, Bash S, Gibbs W, et al. **CNN based deep learning enhances brain 3D FLAIR perceived quality, SNR and resolution at ~30% less scan time.** In: *Proceedings of the Annual Meeting of the American Society of Neuroradiology*, May 30 to June 4, 2020; Virtual

4. Tian C, Xu Y, Li Z, et al. **Attention-guided CNN for image denoising.** *Neural Netw* 2020;124:117–29 CrossRef Medline
5. Zhang K, Zuo W, Chen Y, et al. **Beyond a Gaussian denoiser: residual learning of deep CNN for image denoising.** *IEEE Trans Image Process* 2017;26:3142–55 CrossRef Medline
6. Lunderwold AS, Lunderwold A. **An overview of deep learning in medical imaging focusing on MRI.** *Z Med Phys* 2019;29:102–27 CrossRef Medline
7. Chaudhari A, Zhongnan F, Lee J, et al. **Deep learning super-resolution enables rapid simultaneous morphological and quantitative magnetic resonance imaging.** In: *Proceeding of Machine Learning for Medical Image Reconstruction Workshop at MICCA,* Granada, Spain; September 16, 2018
8. Antun V, Renna F, Poon C, et al. **On instabilities of deep learning in image reconstruction and the potential costs of AI.** *Proc Natl Acad Sci U S A* 2020;117:30088–95 CrossRef Medline
9. Bash S. **Eye on AI: enhancing neuroimaging with artificial intelligence.** *Appl Radiol* 2020;49:20–21
10. Bryant M. **Eye on AI: the potential and reality of AI in clinical application.** *Appl Radiol* 2020;49:10–11
11. Tanenbaum LN, Bash S, Davis M. **Appl Radiol (AR Connect Expert Discussions); AI: clinical applications.** In: *Proceedings of the Annual Meeting of the Radiological Society of North America,* Chicago, Illinois; December 1–6, 2019
12. Bryant M. **Bringing AI and genetics together to support clinical decisions.** *Appl Radiol* July 1, 2020. https://appliedradiology.com/communities/Artificial-Intelligence/bringing-ai-and-genetics-together-to-support-clinical-decisions. Accessed July 1, 2020
13. Melendez JC, McCrank E. **Anxiety-related reactions associated with magnetic resonance imaging examinations.** *JAMA* 1993;270:745–47 CrossRef Medline
14. Tanenbaum L. **Quality, efficiency and survival with patient centric imaging.** In: *Proceedings of the 7th Snowmass 2019: Hot Topics in Radiology: Advanced Applications and Artificial Intelligence*, Snowmass, Colorado; February 10–15, 2019
15. Zaitsev M, Maclaren J, Herbst M. **Motion artifacts in MRI: a complex problem with many partial solutions.** *J Magn Reson Imaging* 2015;42:887–901 CrossRef Medline
16. Andre J, Bresnahan B, Mossa-Basha M, et al. **Toward quantifying the prevalence, severity, and cost associated with patient motion during clinical MR examinations.** *J Am Coll Radiol* 2015;12:689–95 CrossRef Medline
17. Bash S, Thomas M, Fung M, et al. **K-space based deep learning reconstruction empowers 60-70% acceleration of MR imaging of the spine.** In: *Proceedings of the Annual Meeting of the Radiological Society of North America,* Chicago, Illinois; December 1–6, 2019
18. Tanenbaum LN, Bash S, Thomas M, et al. ***K*-space based deep learning reconstruction empowers 50% acceleration of MR spine imaging: a prospective, multicenter, multireader trial.** In: *Proceedings of the European Congress of Radiology,* February 26 to March 1, 2020; Virtual

Hemodynamic Analysis of Cerebral AVMs with 3D Phase-Contrast MR Imaging

Y. Takeda, T. Kin, T. Sekine, H. Hasegawa, Y. Suzuki, H. Uchikawa, T. Koike, S. Kiyofuji, Y. Shinya, M. Kawashima, and N. Saito

ABSTRACT

BACKGROUND AND PURPOSE: The hemodynamics associated with cerebral AVMs have a significant impact on their clinical presentation. This study aimed to evaluate the hemodynamic features of AVMs using 3D phase-contrast MR imaging with dual velocity-encodings.

MATERIALS AND METHODS: Thirty-two patients with supratentorial AVMs who had not received any previous treatment and had undergone 3D phase-contrast MR imaging were included in this study. The nidus diameter and volume were measured for classification of AVMs (small, medium, or large). Flow parameters measured included apparent AVM inflow, AVM inflow index, apparent AVM outflow, AVM outflow index, and the apparent AVM inflow-to-outflow ratio. Correlation coefficients between the nidus volume and each flow were calculated. The flow parameters between small and other AVMs as well as between nonhemorrhagic and hemorrhagic AVMs were compared.

RESULTS: Patients were divided into hemorrhagic ($n = 8$) and nonhemorrhagic ($n = 24$) groups. The correlation coefficient between the nidus volume and the apparent AVM inflow and outflow was .83. The apparent AVM inflow and outflow in small AVMs were significantly smaller than in medium AVMs ($P < .001$ for both groups). The apparent AVM inflow-to-outflow ratio was significantly larger in the hemorrhagic AVMs than in the nonhemorrhagic AVMs ($P = .02$).

CONCLUSIONS: The apparent AVM inflow-to-outflow ratio was the only significant parameter that differed between nonhemorrhagic and hemorrhagic AVMs, suggesting that a poor drainage system may increase AVM pressure, potentially causing cerebral hemorrhage.

ABBREVIATIONS: FDNG = flow distribution network graph; PCMR = phase-contrast MR imaging; VENC = velocity-encoding

Patients with cerebral AVMs are at an increased risk of cerebral hemorrhage, with the incidence of hemorrhage in these patients being approximately 2%–4% annually, depending on several clinical and angioarchitectural features.[1,2] Moreover, the hemodynamic changes associated with AVMs are also thought to contribute to their pathophysiology and clinical presentations.[3] So far, various modalities such as direct blood pressure measurement,[4-6] transcranial Doppler,[5,7] DSA,[8-11] and hemodynamic MR imaging[12-17] have been used to investigate the hemodynamic features of AVMs. In particular, several studies have suggested that an inadequate development of the drainage system or hemodynamic imbalance in the AVMs might lead to high blood pressure in the nidus, potentially causing cerebral hemorrhage.[4-6,8,9,11,16,17] Therefore, measuring the total AVM inflow and outflow may be important to estimate how much pressure exists in the AVMs and to evaluate the risk of cerebral hemorrhage, but evidence is scarce.

Phase-contrast MR imaging (PCMR) is a type of hemodynamic MR imaging that uses a bipolar gradient to create a phase shift of blood flow proportional to its velocity. PCMR allows the noninvasive measurement of flow parameters, such as flow velocity and flow rate, even in highly complex vessels such as AVMs.[18] Currently, electrocardiogram-gated 4D-flow MR imaging is the most commonly used MR imaging technique for hemodynamic analysis of intracranial vascular diseases. However, 4D-flow MR imaging requires a relatively long scan time, which impedes the implementation of this scan in routine clinical practice. Furthermore, 4D-flow MR imaging with both high spatial resolution and dual velocity-

Received April 20, 2021; accepted after revision July 28.

From the Departments of Neurosurgery (Y.T., T.K., H.H., H.U., T.K., S.K., Y.Shinya, M.K., N.S.) and Radiology (Y. Suzuki), The University of Tokyo, Tokyo, Japan; and Department of Radiology (T.S.), Nippon Medical School Musashi-Kosugi Hospital, Kanagawa, Japan.

Dr Kin received grant support from the Japan Society for the Promotion of Science KAKENHI (grant No. JP18K08938) and the Japan Science and Technology Agency CREST (JPMJCR17A1).

Please address correspondence to Taichi Kin, MD, Department of Neurosurgery, University of Tokyo, 7-3-1 Hongo, Bunkyo-ku, Tokyo 113-8655, Japan; e-mail: tashiryuku@gmail.com

Indicates open access to non-subscribers at www.ajnr.org

http://dx.doi.org/10.3174/ajnr.A7314

encodings (VENCs), which are desirable for intracranial vessel flow study,[19-21] is impractical in the clinical setting because these parameters further increase scan time. Therefore, non-electrocardiogram-gated 3D PCMR, which requires less scan time than 4D-flow MR imaging, could be an alternative tool for analysis.

The aim of this retrospective study was to try to quantify the AVM inflow and outflow using 3D PCMR with dual VENC and to elucidate whether the hemodynamic imbalance between the AVM inflow and outflow was associated with cerebral hemorrhage in patients with AVMs.

MATERIALS AND METHODS

Patient Population

This retrospective study was approved by the Ethical Review Committee of the University of Tokyo (IRB No. 12057). At the time of initial treatment, written informed consent was obtained from all patients for future use of their clinical data for research purposes.

Between March 2016 and November 2020, sixty-seven patients with supratentorial AVMs who had previously received no treatment underwent 3D PCMR at our institution. Most patients in this cohort were referred to our hospital for gamma knife surgery, except for a few cases of direct surgery. During this period, 35 patients were excluded because of insufficient MR imaging data because the circle of Willis was not covered ($n = 23$). In addition, patients with a faint nidus with extremely low-flow draining veins that could not be evaluated ($n = 4$) and those with involvement of perforating feeder vessels from A1, M1, and P1 segments ($n = 3$); occlusion of the MCA ($n = 2$); feeding arteries arising from bilateral sides ($n = 2$); and multiple nidi ($n = 1$) were also excluded because of the difficulty in maintaining an apparent AVM inflow.

For analysis, 32 patients were included in the study and were divided into 2 groups: nonhemorrhagic ($n = 24$) and hemorrhagic ($n = 8$). The nidus diameter and volume in each AVM were measured using the gamma knife planning software, Leksell GammaPlan (Elekta), for classification into small (<30 mm), medium (30–60 mm), or large (>60 mm) AVMs, depending on the diameter.[22] The mean duration between the gamma knife surgery and the onset of hemorrhage was 62 days (median, 68 days; range, 24–91 days). All patients had undergone DSA before gamma knife treatment. The patients in the hemorrhagic group, with the exception of 3 patients, had also undergone DSA during the acute phase of cerebral hemorrhage (<3 weeks). The interval time from the onset to the imaging in the hemorrhage group was 43 days (range, 6–87 days; median, 36 days), except in 2 patients for whom the interval was unknown. These 2 patients had obvious findings of old hemorrhage on MR imaging in accordance with the location of the nidus. Their estimated interval time from onset to imaging was at least 6 months, because the duration between the date when the patients were found to have AVMs and the imaging date was longer than 6 months.

MR Imaging Protocol and Definition of Flow Parameters

3D PCMR was performed with a 3T scanner (Magnetom Skyra; Siemens) without a contrast agent, using a 20-channel head array coil. The imaging parameters for the 3D PCMR were TR/TE, 37.7/5.46 ms; number of excitations, 2 (until July 2019) and 1 (since August 2019); flip angle, 10°; generalized autocalibrating partially parallel acquisition factor, 3; FOV, 199 × 220 mm; matrix, 348 × 384; voxel size, 0.57 × 0.57 × 1 mm; slices, 64 (until July 2019) and 128 (since August 2019); and bandwidth, 365 Hz/pixel. The scan matrix was 174 × 194, and zero-filling and low-pass filter were applied for the reconstruction of the matrix. The purpose of the reconstruction was to keep the signal-to-noise ratio as high as possible at a high resolution. The image data were corrected for Maxwell terms in online reconstruction. We set 2 different VENCs, 50 and 100 cm/s, in 3 directions (anterior-posterior, right-left, and superior-inferior) in all cases. The total scan time was approximately 15 min.

We measured the apparent AVM inflow, AVM inflow index, apparent AVM outflow, AVM outflow index, and the apparent AVM inflow-to-outflow ratio as an indicator of divergence between apparent AVM inflow and outflow. The apparent AVM inflow was calculated using the following formula:[14,16,17]

(Ipsilateral A2 Segment + M1 Segment + P2 Segment),

(Contralateral A2 Segment + M1 Segment + P2 Segment).

If feeding perforators from the ICA existed, these flow rates were re-added. The apparent AVM outflow was defined as the total flow rate of each draining vein in the nidus. The AVM inflow and outflow indices were calculated by the following formula:[16]

AVM Inflow Index = Apparent AVM Inflow (mL/min) /Nidus Volume (mL),

AVM Outflow Index = Apparent AVM Outflow (mL/min)/ Nidus Volume (mL).

Image Processing and Flow Analysis

First, all phase and magnitude data from the 3D PCMR were transferred to commercially available image-processing software, Amira (Thermo Fisher Scientific). A 3D surface-rendering using the magnitude images was created with the software to visualize the general vasculature of the AVM and identify every draining vein (Fig 1). We also referred to DSA to confirm the number and approximate location of the draining veins, which allowed easy identification of the draining veins in the PCMR. If there was velocity aliasing on the phase images from the 100 -cm/s VENC, a correction for velocity aliasing was performed as follows:

If V_a is the velocity at a voxel that shows the velocity aliasing and V_c is the corrected velocity at the voxel, the velocity aliasing was corrected as follows:[23]

$V_c = 2 \times \text{VENC} - |V_a|$.

All procedures were performed by the first author, who is a board-certified neurosurgeon with 10 years of experience.

Second, the processed data were transferred to flow-analysis software, IV-FLOW (Maxnet). IV-FLOW automatically displays the centerline of the vessel and allows users to measure the vessel flow rate at any point by setting the perpendicular plane on this line. The segmentation and flow measurement of A2, M1, and P2 were conducted by the 100-cm/s VENC data. Meanwhile, the segmentation of draining veins was conducted by the 50-cm/s VENC data. The flow measurement of draining veins was conducted by the 100 cm/s VENC data simultaneously with the flow measurement of A2, M1, and P2. The measurement points of draining veins were adjacent to the nidus (Fig 1).

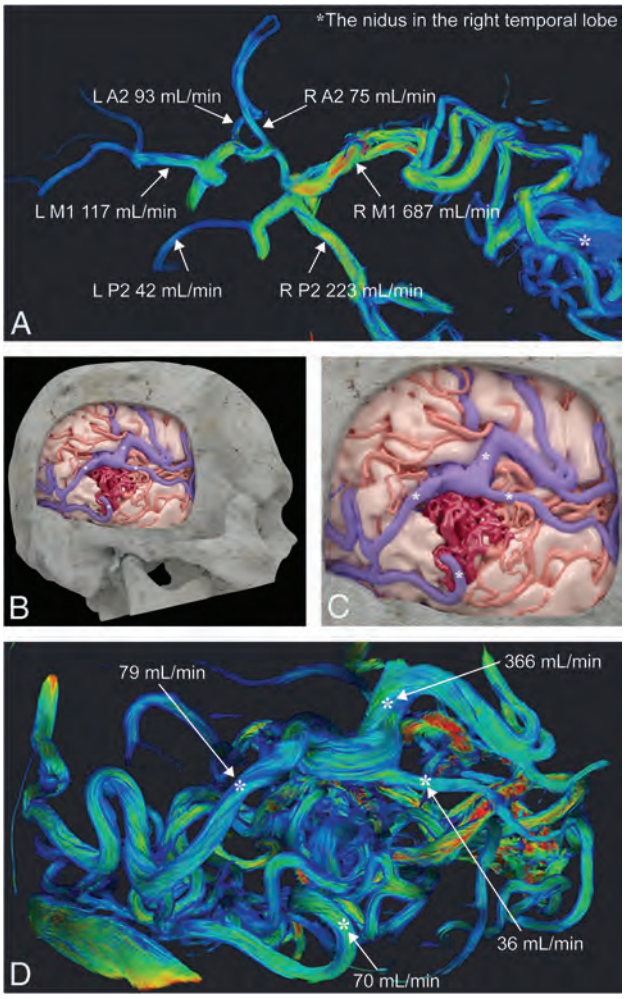

FIG 1. A representative case (No. 22) from the hemorrhagic group. *A*, 3D PCMR with streamline visualization using Amira shows vessel flow rates at A2, M1, P2 and the nidus in the right temporal lobe. *B* and *C*, A 3D surface-rendering model with texture processing shows the cortical artery including feeding arteries (red), the draining veins (blue), and the nidus (dark red). The 4 *asterisks* on the draining veins indicate the measurement points of cerebral AVM outflow in this case. *D*, 3D PCMR with streamline visualization from the same angle as in *B* and C shows vessel flow rates at the draining veins. The *asterisks* in *D* correspond to those in *B* and *C*.

Statistical Analysis

All statistical analyses were conducted using JMP15 (SAS Institute Inc). To verify the credibility of the apparent AVM inflow and outflow, we calculated the Pearson correlation coefficient scores between the nidus volume and each flow rate in the whole cohort. Next, the 5 flow parameters, including 2 flow rates, 2 flow indices, and the apparent AVM inflow-to-outflow ratio were compared between the small and medium AVMs and between the nonhemorrhagic and hemorrhagic AVMs using the Wilcoxon rank sum test. Moreover, a multivariate regression model was used to determine whether hemodynamics had an independent effect on the presentation of hemorrhage. The model included the risk factors for cerebral hemorrhage, associated arterial aneurysms, exclusively deep venous drainage, nidus volume, and apparent AVM inflow-to-outflow ratio. The Pearson correlation coefficient scores between the nidus volume and the apparent AVM inflow-to-outflow ratio was also calculated. A P value $< .05$ was considered significant.

RESULTS

There were 17 cases (71%) of small AVMs in the nonhemorrhage group and 6 cases (75%) in the hemorrhage group, whereas there were no cases of large AVMs in the entire cohort. Spetzler-Martin grades were I–IV in each cohort.[22] There were no significant differences in patient demographics and AVM characteristics, except for the associated arterial aneurysm (Table 1).

The correlation coefficient between the nidus volume and the apparent AVM inflow as well as outflow was 0.83 (Fig 2). The apparent AVM inflow and outflow were significantly smaller in the small AVMs compared with the medium AVMs ($P < .001$, respectively) (Fig 3). The details of the flow according to AVM size are summarized in Table 2. The apparent AVM inflow and outflow between nonhemorrhagic and hemorrhagic AVMs were not significantly different ($P = .95$ and .40, respectively) (Fig 4). The AVM inflow index was higher and the AVM outflow index was lower in the hemorrhagic than in the nonhemorrhagic AVMs, but the difference was not significant ($P = .09$ and .47, respectively) (Fig 4). The apparent AVM inflow-to-outflow ratio was significantly larger in the hemorrhagic AVMs than in the nonhemorrhage AVMs ($P = .02$) (Fig 4). A comparison of the above-mentioned flow parameters is summarized in Table 3. The multivariate regression

Table 1: Comparison of patient demographics and angioarchitectural features between nonhemorrhage and hemorrhage groups

Characteristic	Nonhemorrhage ($n = 24$)	Hemorrhage ($n = 8$)	P Value
Age (mean) (range) (yr)[a]	36 (8–72)	38 (15–62)	.76
Sex, female[a]	10 (50%)	3 (38%)	.69
Spetzler-Martin grade[b]	.89		
I	3	1	
II	12	5	
III	8	2	
IV–V	1	0	
Mean AVM volume (median) (range) (mL)[a]	5.6, 4.2 (0.6–19.3)	4.5, 2.9 (0.2–15.6)	.31
Small size (<30 mm)[b]	17 (71%)	6 (75%)	1.00
Eloquent location[b]	14 (58%)	4 (50%)	.70
Venous drainage[b]			
Exclusively deep	3 (13%)	2 (25%)	.58
Any deep	11 (46%)	5 (63%)	.69
Associated arterial aneurysm[b]	1 (4%)	3 (38%)	.04

[a] Calculated by Wilcoxon rank sum test.
[b] Calculated by the Fisher exact test.

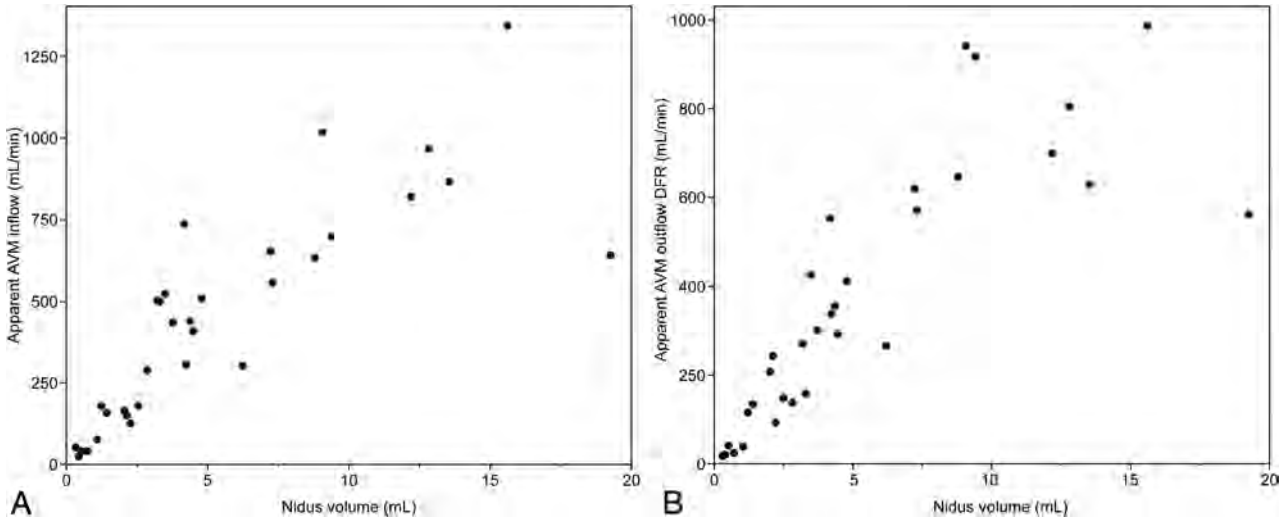

FIG 2. Correlations between nidus volume and each flow rate, apparent cerebral arteriovenous malformation inflow, and outflow. The scatterplot between the nidus volume and each flow, apparent AVM inflow (*A*), and outflow (*B*) shows high correlation (correlation coefficient scores = 0.83 for both flows).

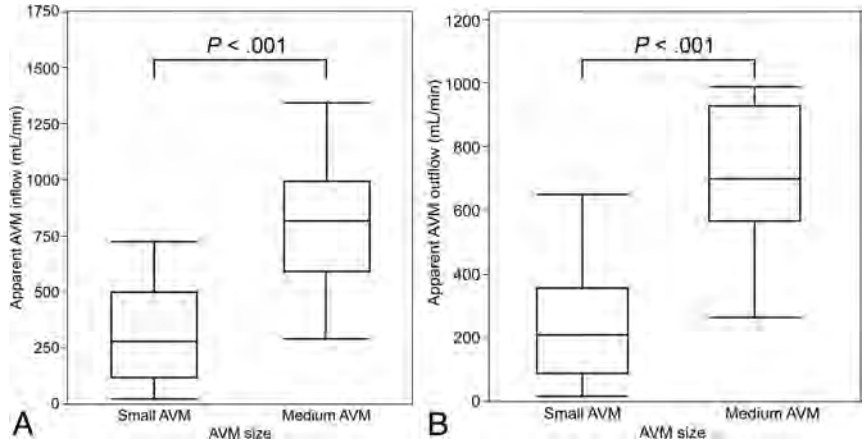

FIG 3. Boxplots comparing cerebral AVM inflow and outflow between small and medium AVMs. The apparent AVM inflow (*A*) and outflow (*B*) in small AVMs are significantly smaller between nonhemorrhagic and hemorrhagic AVMs compared with medium AVMs using the Wilcoxon rank sum test ($P < .001$, for both groups).

Table 2: Comparison of flow parameters between small and medium AVMs

Parameters[a]	Small AVMs ($n = 23$)	Medium AVMs ($n = 9$)	*P* Value
Median apparent AVM inflow (range) (mL/min)	280 (18–732)	817 (296–1347)	<.001
Median apparent AVM outflow (range) (mL/min)	203 (11–646)	698 (263–990)	<.001

[a] Data are calculated by the Wilcoxon rank sum test.

model demonstrated that the associated arterial aneurysm and the apparent AVM inflow-to-outflow ratio were significant factors ($P = .02$ for both), while the exclusively deep venous drainage and the nidus volume were not significant ($P = .51$ and 0.72, respectively). The Pearson correlation coefficient score between the nidus volume and the apparent AVM inflow-to-outflow ratio was −0.26.

Other Hemodynamic Parameters

In the hemorrhage group, rupture of the associated arterial aneurysm was the cause of hemorrhage in 3 patients, and the mean apparent AVM inflow-to-outflow ratio of these patients was 1.26. It was <2.44 in the remaining 5 patients with rupture of the nidus. The apparent AVM inflow-to-outflow ratio was significantly larger in the 5 patients with rupture of the nidus than in the nonhemorrhage group ($P = .005$). The mean apparent AVM inflow and nidus volume in the whole cohort were 441 mL/min and 5.4 mL, respectively. The mean blood flow rate of the MCA on the opposite side of the AVM in patients older than 20 years of age was 158 mL/min. The mean cerebral blood flow rate (A2 segment + M1 segment + P2 segment) on the opposite side of the AVM in the whole cohort was 317 mL/min, and 291 mL/min in patients older than 20 years of age (Table 4).

DISCUSSION

Several hemodynamic studies have been conducted to elucidate the pathophysiology of AVMs. One of the strengths of our study is the elucidation of the association between the hemodynamic status of AVMs and hemorrhagic presentation based on the AVM size. As expected, larger AVMs had a higher apparent inflow and outflow. In contrast, the apparent AVM inflow and outflow showed no significant difference between the nonhemorrhagic and hemorrhagic groups in our cohort without size bias. Incidentally, whether

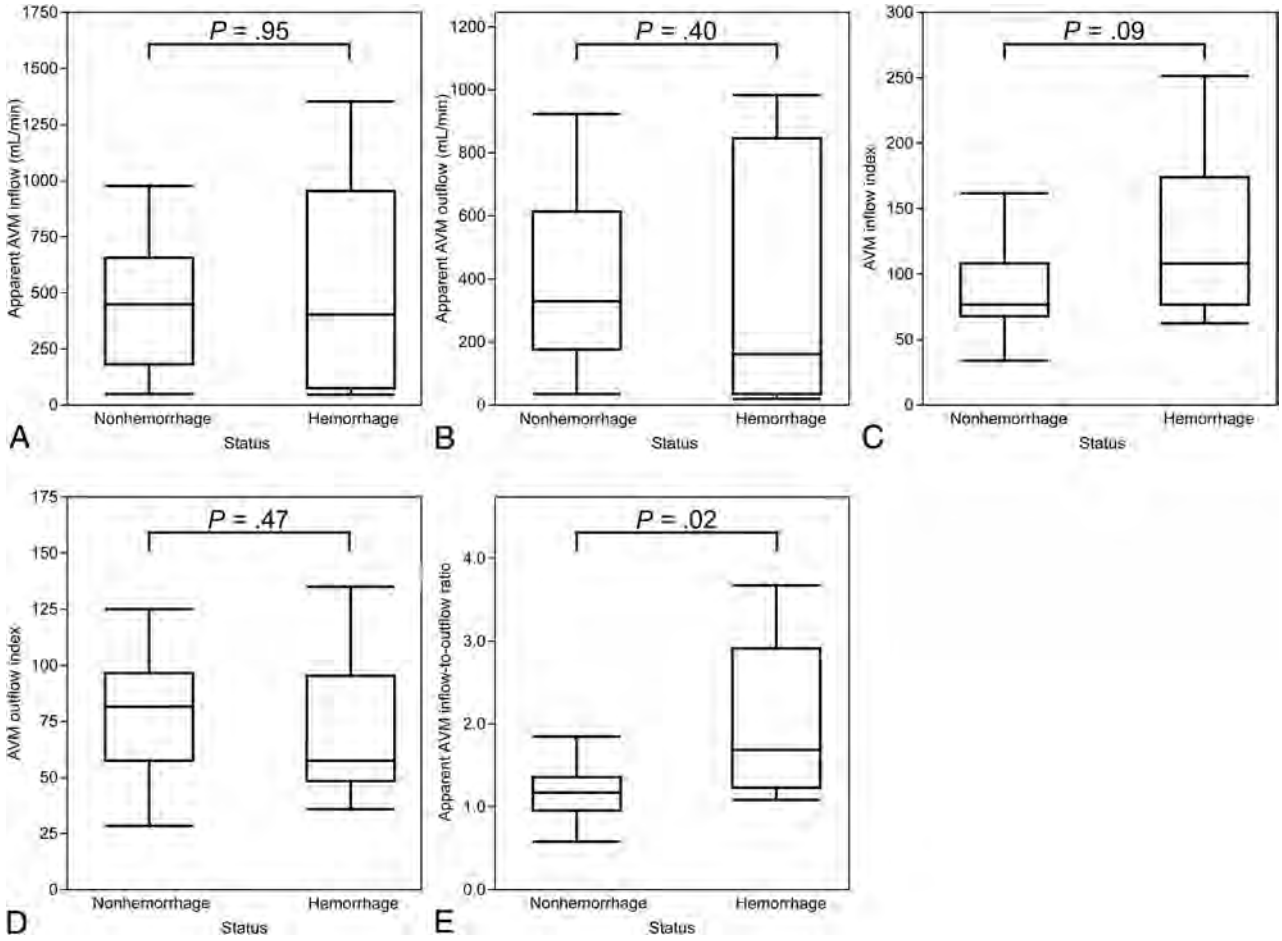

FIG 4. Boxplots comparing apparent cerebral AVM inflow and outflow (*A* and B), AVM inflow and outflow indices (*C* and *D*), and the cerebral AVM inflow-to-outflow ratio (*E*) between nonhemorrhagic and hemorrhagic AVMs. *E*, The apparent AVM inflow-to-outflow ratio is significantly larger in hemorrhagic AVMs than in nonhemorrhagic AVMs (*P* = . 02), according to the Wilcoxon rank sum test.

Table 3: Comparison of flow parameters between nonhemorrhage and hemorrhage groups

Parameters[a]	Nonhemorrhage (*n* = 24)	Hemorrhage (*n* = 8)	*P* Value
Mean apparent AVM inflow (median) (range) (mL/min)	422, 431 (30–965)	499, 386 (18–1347)	.95
Mean apparent AVM outflow (median) (range) (mL/min)	377, 317 (19–918)	354, 144 (11–990)	.40
Mean AVM inflow index (median) (range)	87, 76 (33–161)	128, 108 (62–251)	.09
Mean AVM outflow index (median) (range)	77, 82 (29–126)	70, 58 (36–135)	.47
Mean apparent AVM inflow-to-outflow ratio (median) (range)	1.17, 1.17 (0.57–1.86)	2.00, 1.69 (1.08–3.68)	.02

[a] Data are calculated by the Wilcoxon rank sum test.

Table 4: Mean blood flow of the middle cerebral artery and cerebral blood flow

	Whole Cohort (*n* = 32)	Older Than 20 Years of Age (*n* = 25)
Mean blood flow of the middle cerebral artery (median) (range) (mL/min)	170, 160 (60–323)	158, 147 (60–323)
Mean cerebral blood flow (median) (range) (mL/min)	317, 289 (169–557)	291, 270 (169–557)

hemorrhagic AVMs have an increased or decreased inflow compared with nonhemorrhagic AVMs is a controversial topic.[4-6,9-11,13,16,17,24-26] One of the reasons for this disagreement is likely derived from size bias, because several previous hemodynamic studies comprised hemorrhage cohorts with mostly small AVMs, while their nonhemorrhage cohorts mostly comprised medium or large AVMs.[4-6,16,25] These results do not correlate with ours.

The AVM inflow index in the hemorrhagic group was larger than that in the nonhemorrhagic group, though the difference was not statistically significant. The AVM outflow index showed no significant difference between the 2 groups. These results imply that the AVM inflow in hemorrhagic AVMs might increase to a greater extent than expected for its size, but the AVM outflow might increase proportional to its size. Moreover, the

apparent AVM inflow-to-outflow ratio was significantly larger in the hemorrhagic group compared with the nonhemorrhagic group. The apparent AVM inflow-to-outflow ratio is a newly defined indicator and signifies that the higher the apparent AVM inflow-to-outflow ratio is, the larger the hemodynamic imbalance in the AVM will be. Our results of the apparent AVM inflow-to-outflow ratio are comparable with those in previous hemodynamic studies using other modalities such as DSA. Todaka et al[9] reported that the mean transit time ratio of draining vein to feeding artery on DSA was significantly larger in hemorrhagic-versus-nonhemorrhagic AVMs. Likewise, Lin et al[26] demonstrated that a higher stasis index of the most dominant drainage vein was associated with hemorrhage of AVMs. They commonly inferred that the imbalanced hemodynamics in AVMs caused venous congestion, resulting in rupture of the AVMs. Our results support their conclusion, and we also infer that quantitative analysis of both the AVM inflow and outflow may be required for risk measurement of AVM rupture.

Confounding factors for cerebral hemorrhage may exist in the current study. There were concerns that the nidus volume could be a confounding factor because the apparent AVM inflow and outflow showed a very high correlation with the nidus volume. Therefore, the multivariate regression model was used to determine whether hemodynamics had an independent effect on the presentation of hemorrhage. As a result, the multivariate regression model demonstrated that the associated arterial aneurysm and the apparent AVM inflow-to-outflow ratio were significant risk factors for cerebral hemorrhage. The correlation between nidus volume and the apparent AVM inflow-to-outflow ratio was weak. However, consideration should be given to the small cohort used for multivariate regression modeling, which may result in an unstable model.

To the best of our knowledge, this is the first study to focus on the measurement of the total AVM inflow and outflow using a non-electrocardiogram-gated 3D PCMR with dual VENC. Electrocardiogram-gated 2D PCMR and electrocardiogram-gated 4D-flow MR imaging have been the mainstream modalities for the hemodynamic study of AVMs. However, 2D PCMR is not suitable for the identification of draining veins because of the lack of 3D volume data. 4D-flow MR imaging can be used for the identification of draining veins, but drawbacks include relatively low spatial resolution and long scan times. Meanwhile, 3D PCMR can offer 3D volume data with high spatial resolution and a reasonable scan time. Recently, Rijnberg et al[27] reported on hemodynamic evaluation of the Fontan pathway using 2D-, 3D-, and 4D-flow MR imaging and demonstrated that 3D PCMR could obtain time-averaged flow rates with good-to-excellent agreement with 2D and 4D-flow, but with a 10-fold reduction in scan time. 3D PCMR also significantly improved image quality compared with 4D-flow MR imaging. In the current study, we used 3D PCMR with a high spatial resolution ($0.57 \times 0.57 \times 1$ mm) for hemodynamic evaluation of AVMs, and the apparent AVM inflow and outflow had a very high correlation with the nidus volume. This result seems to be reasonable from a clinical perspective and suggests that 3D PCMR with high spatial resolution may be a good application for cerebral vascular hemodynamic studies involving small vessels for improving the image quality.

Our work also benefited from the low VENC data regarding the segmentation of the draining veins. Schnell et al[28] demonstrated that the low VENC and dual VENC data showed less noise, fewer artifacts, and a superior vessel depiction than the high VENC data with not much difference in vessel depiction of the venous system between the low and dual VENC data. Therefore, we used the low VENC data instead of the high VENC data in the segmentation of the draining veins. On the other hand, Schnell et al also demonstrated that the Bland-Altman analysis of high-versus-dual VENC confirmed the underestimation of the net flow of the high VENC acquisition. However, the error was not large in absolute value. In our preliminary survey, the differences in flow values of the draining veins between the 50- and 100-cm/s VENC data were also trivial. Therefore, the high VENC data were adopted for flow quantification of draining veins instead of the low VENC data to improve the efficiency of the workflow.

However, the MR imaging protocols in the current study were not state-of-the-art. 3D PCMR was acquired with the generalized autocalibrating partially parallel acquisition acceleration factor of 3,[29] and 2 VENCs were acquired with 2 back-to-back scans. In contrast, there have been emerging research sequences for decreasing the scan time without major drawbacks. For example, 4D-flow MR imaging with non-Cartesian sampling, such as radial acquisitions, can be acquired with an isotropic spatial resolution of 0.7 mm in about 7 minutes covering the whole head.[30] Additionally, using a total of 7 encodings instead of 8 for dual-VENC acquisitions allows a reduction in scan time in a elegant way with no apparent drawbacks.[28,31]

Furthermore, there are still more interesting methods with a 4D-flow MR imaging. Aristova et al[19] showed the feasibility of flow distribution network graph (FDNG) analysis by quantifying and comparing flow, peak velocity, and the pulsatility index between healthy controls and patients with AVMs. In performing the flow analysis of complex neurovascular lesions, FDNG could be a more robust approach than conventional approaches such as ours because FDNG can reconstruct the flow distribution by simply using graph theory. In addition, the flow-conservation rule can be used as a metric of internal validation in the absence of ground truth with FDNG. When we considered these remarkable developments in AVM evaluation with 4D-flow MR imaging, if the aim of the flow analysis is to focus on the quantification of time-averaged parameters such as time-averaged flow rate, the combination of time-averaged 3D PCMR with the accelerated techniques and FDNG would provide dependable results.

There should be no difference between the "true" AVM inflow and outflow. However, in this study, a difference was observed between the "apparent" AVM inflow and outflow. Furthermore, the apparent AVM inflow-to-outflow ratio was significantly larger in the hemorrhagic AVMs than in the nonhemorrhagic AVMs. The method of measuring apparent AVM inflow and outflow in the current study has the possibility of overestimating AVM inflow and underestimating AVM outflow. Ideally, AVM inflow is calculated by totaling the flow rate of every single feeding pedicle to the AVM nidus, instead of calculating the difference between the ipsilateral and contralateral cerebral blood flow rates. However, this method is unfeasible because of the difficulty

in identifying every feeding pedicle in 3D PCMR and it being a time-consuming procedure. Concerning AVM outflow, although 3D PCMR with the lower VENC allowed us to measure the draining veins with low flow rates, there is still the possibility of underestimation because not all sources of venous drainage may have been identified. Even if these limitations are taken into consideration, our results of the apparent AVM inflow-to-outflow ratio being larger in the hemorrhagic AVMs than in the nonhemorrhagic AVMs are of interest. There is a possibility that the underestimation of AVM outflow in the hemorrhagic group may be increased because of the increase in the flow rate in small draining veins adjacent to the AVM nidus. Sato et al[32] demonstrated in their pathologic study that a perinidal dilated capillary network was connected not only to the nidus, feeding arteries, and draining veins via arterioles and venules but also to normal capillaries, arterioles, and venules. The perinidal dilated capillary network plays an important role in a compensatory mechanism for increased pressure in ruptured AVMs. However, this could not be well-captured in PCMR and might contribute to the underestimation of AVM outflow because the network drains blood from the AVM nidus directly before the measurement points of draining veins. Therefore, the apparent AVM inflow-to-outflow ratio may be an indicator of how much pressure exists in AVMs.

Notably, the apparent AVM inflow in the current study was higher than that in previous studies.[16,17] The mean apparent AVM inflow (441 mL/min) in the whole cohort was higher than (316 mL/min) in the previous study by Shakur et al,[16] and the mean nidus volume (5.4 mL) in the current study was equal to that (5.4 mL) of the same previous study. Our exclusion criteria for AVMs fed by the perforating artery might be related to this inconsistency regarding apparent AVM inflow. The perforating feeding artery arising from the A1, M1, and P1 segments disturbs the accuracy of apparent AVM inflow, contributing to the smaller apparent AVM inflow. On the other hand, the mean cerebral and middle cerebral artery blood flow rates on the opposite side of the AVM in patients older than 20 years of age were 291 and 158 mL/min, respectively. These flow rates were equivalent to those reported in previous surveys of cerebral blood flow in healthy adults using a 2D PCMR.[33,34]

Limitations

There were several limitations to this study. First, there was a relatively large selection bias among the patients in the study. Although we started to perform 3D PCMR on patients with AVMs in our institution, the FOV of MR imaging was confined to only 64 mm along the Z-axis with the intention of focusing on the nidus alone. Therefore, we had to exclude 23 patients at an early stage due to insufficient MR imaging data due to the circle of Willis not being covered because the flow rates at A2, M1, and P2 were needed for calculating AVM inflow. Second, we could not determine whether the difference in the apparent AVM inflow-to-outflow ratio between the nonhemorrhagic and hemorrhagic AVMs is the cause or the result of cerebral hemorrhage due to the retrospective design of our study. A prospective hemodynamic study would provide the answer to this question, but it may lack feasibility because of the low prevalence of AVMs and the low incidence of cerebral hemorrhage in patients with AVMs.

Third, the optimal approach for quantifying AVM inflow volume is to sum up the flow volumes of all the feeding pedicles to the AVM nidus. At first, we tried to quantify the AVM inflow volume using this method. However, it was practically unfeasible for multiple technical reasons. One reason was that the feeding pedicles were winding in most patients, making reproducible flow measurements difficult due to a slight difference in the measurement points in the winding vessels, which led to a large difference in the flow volume. The other reasons were that false recognition of the feeding pedicles could occur because AVMs have very complex structures and the number of feeding pedicles to the AVMs often exceeded 10, which can result in flow analysis taking several hours in each case.

Fourth, 3 patients with associated arterial aneurysms in the hemorrhage group showed a lower apparent AVM inflow-to-outflow ratio than the remaining 5 patients with rupture of the nidus. These results might be because the etiology of the rupture was different between the rupture of the associated arterial aneurysm and the AVM nidus. However, our study had a relatively small sample size, which did not allow us to draw strong conclusions. Fifth, we reported hemodynamic evaluation of AVMs using a non-electrocardiogram-gated 3D PCMR, which is less commonly used than the 2D- or 4D-flow MR imaging. The high correlation between the nidus volume and the apparent AVM inflow and outflow in the current study seems to be reasonable from a clinical perspective. Also, the mean cerebral and middle cerebral blood flow rates on the opposite side of the AVM in patients older than 20 years of age in the current study were compatible with those in previous studies.[33,34] Therefore, we believe that the 3D PCMR could be an alternative option for blood flow analysis of AVMs. However, comparative investigation of 3D and other phase-contrast MR imaging is warranted.

Finally, correction of *P* values for multiple comparisons might have been ideal because 5 parameters were tested in the current study. However, it remains controversial whether the strict correction of the *P* value is necessary in exploratory studies such as the present study.[35,36] The strict correction of *P* values for multiple comparisons was not performed in this study to prevent false-negative results. Our results, particularly the significance of the apparent AVM inflow-to-outflow ratio, need further validation.

CONCLUSIONS

The apparent AVM inflow and outflow seem irrelevant to the presentation of cerebral hemorrhage in patients with AVM. The apparent AVM inflow-to-outflow ratio is the only significantly differing parameter between nonhemorrhagic and hemorrhagic AVMs, suggesting that a poorly developed drainage system may increase AVM pressure, potentially causing cerebral hemorrhage.

REFERENCES

1. Gross BA, Du R. **Natural history of cerebral arteriovenous malformations: a meta-analysis.** *J Neurosurg* 2013;118:437–43 CrossRef Medline
2. Kim H, Al-Shahi Salman R, McCulloch CE, et al; MARS Coinvestigators. **Untreated brain arteriovenous malformation:**

patient-level meta-analysis of hemorrhage predictors. *Neurology* 2014;83:590–97 CrossRef Medline
3. Fennell VS, Martirosyan NL, Atwal GS, et al. **Hemodynamics associated with intracerebral arteriovenous malformations: the effects of treatment modalities.** *Neurosurgery* 2018;83:611–21 CrossRef Medline
4. Spetzler RF, Hargraves RW, McCormick PW, et al. **Relationship of perfusion pressure and size to risk of hemorrhage from arteriovenous malformations.** *J Neurosurg* 1992;76:918–23 CrossRef Medline
5. Kader A, Young WL, Pile-Spellman J, et al. **The influence of hemodynamic and anatomic factors on hemorrhage from cerebral arteriovenous malformations.** *Neurosurgery* 1994;34:807–08; discussion 807–08 CrossRef Medline
6. Miyasaka Y, Kurata A, Irikura K, et al. **The influence of vascular pressure and angiographic characteristics on haemorrhage from arteriovenous malformations.** *Acta Neurochir (Wien)* 2000;142:39–43 CrossRef Medline
7. Mast H, Mohr JP, Thompson JL, et al. **Transcranial Doppler ultrasonography in cerebral arteriovenous malformations: diagnostic sensitivity and association of flow velocity with spontaneous hemorrhage and focal neurological deficit.** *Stroke* 1995;26:1024–27 CrossRef Medline
8. Norris JS, Valiante TA, Wallace MC, et al. **A simple relationship between radiological arteriovenous malformation hemodynamics and clinical presentation: a prospective, blinded analysis of 31 cases.** *J Neurosurg* 1999;90:673–79 CrossRef Medline
9. Todaka T, Hamada J, Kai Y, et al. **Analysis of mean transit time of contrast medium in ruptured and unruptured arteriovenous malformations: a digital subtraction angiographic study.** *Stroke* 2003;34:2410–14 CrossRef Medline
10. Chen X, Cooke DL, Saloner D, et al. **Higher flow is present in unruptured arteriovenous malformations with silent intralesional microhemorrhages.** *Stroke* 2017;48:2881–84 CrossRef Medline
11. Burkhardt JK, Chen X, Winkler EA, et al. **Delayed venous drainage in ruptured arteriovenous malformations based on quantitative color-coded digital subtraction angiography.** *World Neurosurg* 2017;104:619–27 CrossRef Medline
12. Ansari SA, Schnell S, Carroll T, et al. **Intracranial 4D-flow MRI: toward individualized assessment of arteriovenous malformation hemodynamics and treatment-induced changes.** *AJNR Am J Neuroradiol* 2013;34:1922–28 CrossRef Medline
13. Raoult H, Bannier E, Maurel P, et al. **Hemodynamic quantification in brain arteriovenous malformations with time-resolved spin-labeled magnetic resonance angiography.** *Stroke* 2014;45:2461–64 CrossRef Medline
14. Alaraj A, Amin-Hanjani S, Shakur SF, et al. **Quantitative assessment of changes in cerebral arteriovenous malformation hemodynamics after embolization.** *Stroke* 2015;46:942–47 CrossRef Medline
15. Wu C, Ansari SA, Honarmand AR, et al. **Evaluation of 4D vascular flow and tissue perfusion in cerebral arteriovenous malformations: influence of Spetzler-Martin grade, clinical presentation, and AVM risk factors.** *AJNR Am J Neuroradiol* 2015;36:1142–49 CrossRef Medline
16. Shakur SF, Liesse K, Amin-Hanjani S, et al. **Relationship of cerebral arteriovenous malformation hemodynamics to clinical presentation, angioarchitectural features, and hemorrhage.** *Neurosurgery* 2016;63(Suppl 1):136–40 CrossRef Medline
17. Brunozzi D, Hussein AE, Shakur SF, et al. **Contrast time-density time on digital subtraction angiography correlates with cerebral arteriovenous malformation flow measured by quantitative magnetic resonance angiography, angioarchitecture, and hemorrhage.** *Neurosurgery* 2018;83:210–16 CrossRef Medline
18. Conway SA, Bowling SM, Geyer JD, et al. **Quantitative magnetic resonance angiography of the cerebrovasculature in physiologic and pathologic states.** *J Neuroimaging* 2008;18:34–37 CrossRef Medline
19. Aristova M, Vali A, Ansari SA, et al. **Standardized evaluation of cerebral arteriovenous malformations using flow distribution network graphs and dual-VENC 4D-flow MRI.** *J Magn Reson Imaging* 2019;50:1718–30 CrossRef Medline
20. Orita E, Murai Y, Sekine T, et al. **Four-dimensional flow MRI analysis of cerebral blood flow before and after high-flow extracranial-intracranial bypass surgery with internal carotid artery ligation.** *Neurosurgery* 2019;85:58–64 CrossRef Medline
21. Wu C, Schnell S, Vakil P, et al. **In vivo assessment of the impact of regional intracranial atherosclerotic lesions on brain arterial 3D hemodynamics.** *AJNR Am J Neuroradiol* 2017;38:515–22 CrossRef Medline
22. Spetzler RF, Martin NA. **A proposed grading system for arteriovenous malformations.** *J Neurosurg* 1986;65:476–83 CrossRef Medline
23. Lotz J, Meier C, Leppert A, et al. **Cardiovascular flow measurement with phase-contrast MR imaging: basic facts and implementation.** *Radiographics* 2002;22:651–71 CrossRef Medline
24. Illies T, Forkert ND, Saering D, et al. **Persistent hemodynamic changes in ruptured brain arteriovenous malformations.** *Stroke* 2012;43:2910–15 CrossRef Medline
25. Kubalek R, Moghtaderi A, Klisch J, et al. **Cerebral arteriovenous malformations: influence of angioarchitecture on bleeding risk.** *Acta Neurochir (Wien)* 2003;145:1045–52; discussion 1052 CrossRef Medline
26. Lin TM, Yang HC, Lee CC, et al. **Stasis index from hemodynamic analysis using quantitative DSA correlates with hemorrhage of supratentorial arteriovenous malformation: a cross-sectional study.** *J Neurosurg* 2020;132:1574–82 CrossRef Medline
27. Rijnberg FM, van Assen HC, Juffermans JF, et al. **Reduced scan time and superior image quality with 3D flow MRI compared to 4D-flow MRI for hemodynamic evaluation of the Fontan pathway.** *Sci Rep* 2021;11:6507 CrossRef Medline
28. Schnell S, Ansari SA, Wu C, et al. **Accelerated dual-VENC 4D-flow MRI for neurovascular applications.** *J Magn Reson Imaging* 2017;46:102–14 CrossRef Medline
29. Bammer R, Hope TA, Aksoy M, et al. **Time-resolved 3D quantitative flow MRI of the major intracranial vessels: initial experience and comparative evaluation at 1.5T and 3.0T in combination with parallel imaging.** *Magn Reson Med* 2007;57:127–40 CrossRef Medline
30. Rivera-Rivera LA, Turski P, Johnson KM, et al. **4D-flow MRI for intracranial hemodynamics assessment in Alzheimer's disease.** *J Cereb Blood Flow Metab* 2016;36:1718–30 CrossRef Medline
31. Nett EJ, Johnson KM, Frydrychowicz A, et al. **Four-dimensional phase contrast MRI with accelerated dual velocity encoding.** *J Magn Reson Imaging* 2012;35:1462–71 CrossRef Medline
32. Sato S, Kodama N, Sasaki T, et al. **Perinidal dilated capillary networks in cerebral arteriovenous malformations.** *Neurosurgery* 2004;54:163–70 CrossRef Medline
33. Zarrinkoob L, Ambarki K, Wåhlin A, et al. **Blood flow distribution in cerebral arteries.** *J Cereb Blood Flow Metab* 2015;35:648–54 CrossRef Medline
34. Amin-Hanjani S, Du X, Pandey DK, et al. **Effect of age and vascular anatomy on blood flow in major cerebral vessels.** *J Cereb Blood Flow Metab* 2015;35:312–18 CrossRef Medline
35. Althouse AD. **Adjust for multiple comparisons? It's not that simple.** *Ann Thorac Surg* 2016;101:1644–45 CrossRef Medline
36. Rothman KJ. **No adjustments are needed for multiple comparisons.** *Epidemiology* 1990;1:43–46 CrossRef Medline

Decreased CSF Dynamics in Treatment-Naive Patients with Essential Hypertension: A Study with Phase-Contrast Cine MR Imaging

L. Ma, W. He, X. Li, X. Liu, H. Cao, L. Guo, X. Xiao, Y. Xu, and Y. Wu

ABSTRACT

BACKGROUND AND PURPOSE: Arterial sclerosis resulting from hypertension slows CSF transportation in the perivascular spaces, showing the intrinsic relationship between the CSF and the blood vasculature. However, the exact effect of hypertension on human CSF flow dynamics remains unclear. The present study aimed to evaluate CSF flow dynamics in treatment-naive patients with essential hypertension using phase-contrast cine MR imaging.

MATERIALS AND METHODS: The study included 60 never-treated patients with essential hypertension and 60 subjects without symptomatic atherosclerosis. CSF flow parameters, such as forward flow volume, forward peak velocity, reverse flow volume, reverse peak velocity, average flow, and net flow volume, were measured with phase-contrast cine MR imaging. Differences between the 2 groups were assessed to determine the independent determinants of these CSF flow parameters.

RESULTS: Forward flow volume, forward peak velocity, reverse flow volume, reverse peak velocity, and average flow in the patients with hypertension significantly decreased (all, $P < .05$). Increasing systolic blood pressure was significantly associated with lower forward flow volume ($\beta = -0.44$ mL/mL/mm Hg; 95% CI, −0.83 to −0.06 mL/mL/mm Hg), forward peak velocity ($\beta = -0.50$ cm/s/mm Hg; 95% CI, −0.88 to −0.12 cm/s/mm Hg), reverse flow volume ($\beta = -0.61$ mL/mL/mm Hg; 95% CI, −0.97 to −0.26 mL/mL/mm Hg), reverse peak velocity ($\beta = -0.55$ cm/s/mm Hg; 95% CI, −0.91–0.18 cm/s/mm Hg), and average flow ($\beta = -0.50$ mL/min/mm Hg; 95% CI, −0.93 to −0.08 mL/min/mm Hg).

CONCLUSIONS: The CSF flow dynamics in patients with hypertension are decreased, and increasing systolic blood pressure is strongly associated with lower CSF flow dynamics.

ABBREVIATIONS: AF = average flow; DBP = diastolic blood pressure; FFV = forward flow volume; FPV = forward peak velocity; RFV = reverse flow volume; NFV = net flow volume; PCC-MRI = phase-contrast cine MR imaging; PP = pulse pressure; RPV = reverse peak velocity; SBP = systolic blood pressure

The brain consists of 4 fluid compartments: CSF, interstitial fluid, intracellular fluid, and blood. In mammals, CSF comprises 10% of the total fluid volume within the cranial cavity.[1] CSF formed in the choroid plexi flows through the cerebral ventricles and the subarachnoid space to its ultimate sites of reabsorption into the bloodstream via arachnoid villi of the dural sinuses, along cranial nerve sheaths and the spinal nerve root or through the nasal lymphatics.[2,3] This conventional view, however, has been challenged by the new findings in a recent study: Subarachnoid CSF rapidly enters the brain parenchyma along with arterial perivascular spaces, and this flow plays a vital role in driving the clearance of metabolic waste from the interstitial fluid at more downstream locations.[1,2] Furthermore, a study in mice demonstrated that arterial sclerosis resulting from hypertension disrupts this pump of CSF transportation in the perivascular spaces and sharply slows interstitial fluid waste removal.[4] These studies have shown that an intrinsic relationship lies between the 2 brain fluid compartments, CSF and blood vasculature. At present, however, the exact effect of hypertension on human CSF dynamics is unclear. Accurate assessment of CSF dynamics characteristics in patients with hypertension may have both potential clinical value and scientific significance.

Received January 8, 2021; accepted after revision August 5.

From the Department of Medical Imaging (L.M., X. Li, X. Liu, H.C., L.G., X.X., Y.X., Y.W.), Nanfang Hospital, Southern Medical University, Guangzhou, China; and Department of Radiology (W.H.), Guangdong 999 Brain Hospital, Guangzhou, China.

Lichao Ma and Wenle He contributed equally to data postprocessing and writing of this study and were considered co-first authors.

This study has received funding from the Natural Science Foundation of Guangdong Province, China (grant No. S201301005689), the Science and Technology Program of Guangzhou, China (grant No. 201707010003), and the Special Foundation of President of Nanfang Hospital, Southern Medical University (grant No. 2016B026).

Please address correspondence to Yuankui Wu, MD, Department of Medical Imaging, Nanfang Hospital, Southern Medical University, Guangzhou, China; e-mail: ripleyor@126.com

Indicates open access to non-subscribers at www.ajnr.org

http://dx.doi.org/10.3174/ajnr.A7284

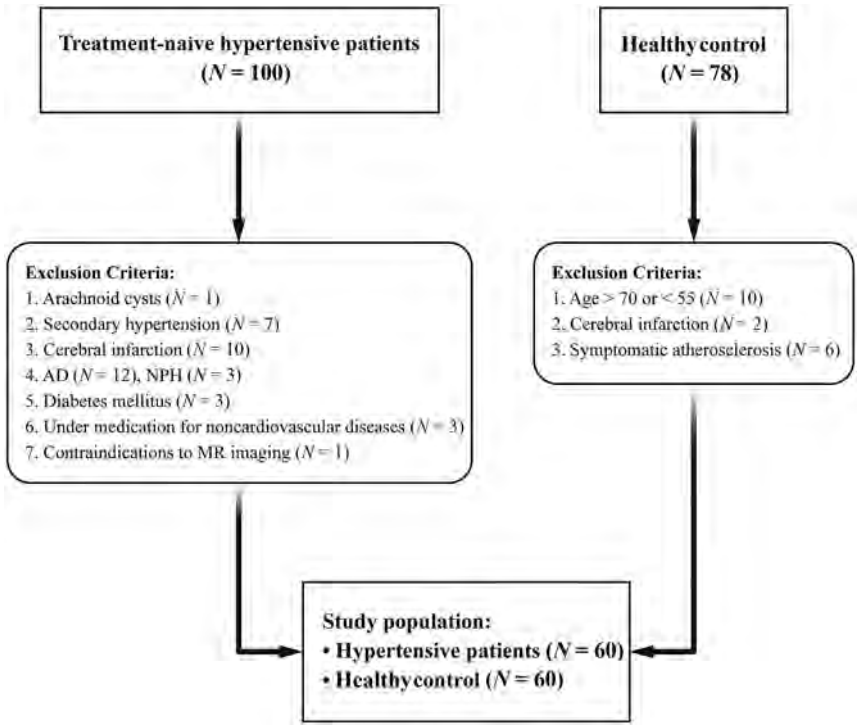

FIG 1. Flow chart of the study population.

The relative inaccessibility of the subarachnoid space impedes the pace of investigations in this area. To date, invasive techniques, such as spinal puncture with the introduction of contrast medium, have been the mainstay of the investigation of CSF flow dynamics.[5] Phase-contrast cine MR imaging (PCC-MRI) is extremely sensitive even to very slow flow. Studies have shown that PCC-MRI can give quantitative and qualitative information noninvasively and within a short analysis time on CSF flow physiology without the need for injection of contrast agent and x-ray exposure.[6-9] PCC-MRI has played an important role in the diagnosis of communication hydrocephalus, obstructive hydrocephalus, spontaneous intracranial hypotension/hypertension, and many other diseases.[6,10-14]

To the best of our knowledge, however, there are no studies in the literature concerning the impact on CSF flow dynamics on established hypertension. Therefore, we hypothesized that PCC-MRI can assess the effect of hypertension on human CSF dynamics. In this study, PCC-MRI was used to evaluate the CSF flow dynamics in patients with hypertension.

MATERIALS AND METHODS

Study Participants

This prospective study received ethics approval from the local Medical Ethics Committee and informed consent was obtained for all patients. We studied 100 patients with hypertension visiting the outpatient clinic of our hospital (Nanfang Hospital Southern Medical University), and eventually, 60 patients were enrolled (Fig 1) (31 men; 55–70 years of age; mean age, 61.24 years [SD, 8.93] years; disease duration [from the onset of hypertension to the date of brain MR imaging] 4.92 [SD, 2.72] years) with never-treated essential hypertension. Patients reported that their blood pressure was found elevated either by medical personnel during a routine annual checkup or by themselves accidentally. Patients with arachnoid cysts ($n = 1$), secondary hypertension ($n = 7$), cerebral infarction ($n = 10$), specific types of brain atrophy (Alzheimer disease, $n = 12$, and normal-pressure hydrocephalus, $n = 3$), diabetes mellitus ($n = 3$), as well as those patients under medication for noncardiovascular diseases ($n = 3$) were excluded from the study. Patients with contraindications to MR imaging (ie, pacemaker and claustrophobia) were also excluded ($n = 1$).

We studied 78 patients visiting the outpatient clinic of our hospital, and eventually, 60 control subjects were enrolled (Fig 1) (33 men; 55–70 years of age; mean age, 60.38 [SD, 7.54] years) without symptomatic atherosclerosis or abnormalities on MR imaging and MRA of the brain who were matched for age and sex with the patients. Patients older than 70 years of age or younger than 55 years of age ($n = 10$) and those with cerebral infarction ($n = 2$) and symptomatic atherosclerosis ($n = 6$) were excluded from the study.

All patients with hypertension and controls were subject to 3 office blood pressure measurements.

Office Blood Pressure Measurement

Morning office blood pressure was measured with the patient in the supine position by the wrist electronic blood pressure monitor (EW3005, Panasonic) in the operating room 30 minutes before the MR imaging examination, approximately at the same morning hour of the day, by the same cardiologist with a mercury sphygmomanometer (first and fifth phases of Korotkoff sounds taken as systolic blood pressure [SBP] and diastolic blood pressure [DBP], respectively) after the subjects had rested for 5–10 minutes in a sitting position. Three measurements were taken at 1- minute intervals, and the average was used to define clinical SBP and DBP. Office pulse pressure (PP) was calculated as SBP–DBP.[15] Hypertension was diagnosed with the patient having SBP >140 mm Hg or DBP >90 mm Hg according to the Seventh Report of the Joint National Committee on Prevention, Detection, Evaluation and Treatment of High Blood Pressure guidelines.[16] Subjects were required to avoid smoking or drinking coffee at least for 2 hours before the examination.

MR Imaging Acquisition

MR imaging was performed with a clinical 3T imaging unit equipped with an 8-channel head coil (Achieva; Philips Healthcare). Each subject underwent both conventional MR

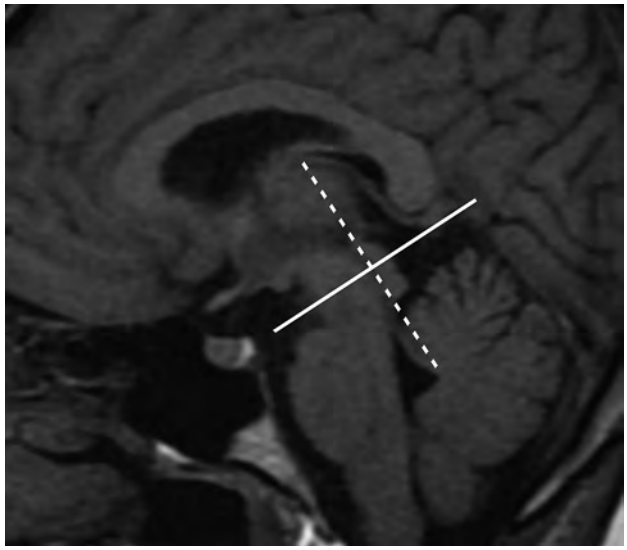

FIG 2. Illustration of the location of phase-contrast MR imaging planes. The midline sagittal T1WI MR image shows the phase-contrast MR imaging planes (*solid line*) located at the ampulla level of the cerebral aqueduct and perpendicular to its long axis (*dotted line*).

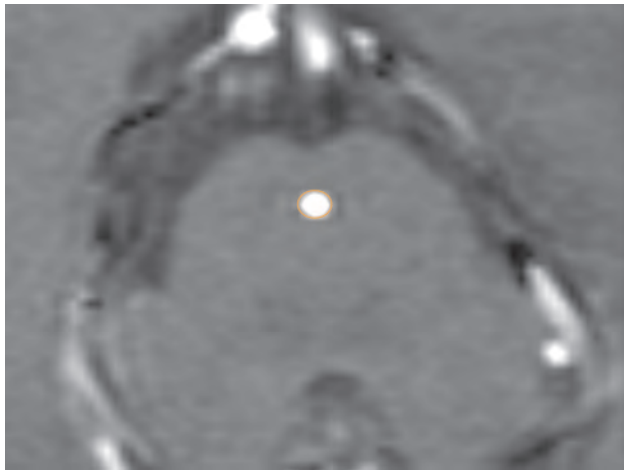

FIG 3. Placement of ROI to contain the whole aqueduct.

imaging and PCC-MRI; the controls underwent MRA in the same session.

Conventional MR images included axial FLAIR (TR/TI/TE = 11,000/2200/125 ms, voxel size = 0.7 × 0.7 × 6 mm^3, 20 slices), axial T2WI (TR/TE = 3000/80 ms, voxel size = 0.5 × 0.7 × 6 mm^3, 20 slices), axial T1WI (TR/TE = 2000/20 ms, voxel size = 0.5 × 0.9 × 6 mm^3, 20 slices), and sagittal T1WI (TR/TE = 2000/20 ms, voxel size = 0.7 × 0.9 × 6 mm^3, 20 slices). Each healthy subject also underwent MRA. Parameters for the MRA pulse sequence were TR/TE = 23/3.5 ms, voxel size = 0.45 × 0.68 × 1.2 mm^3, 140 slices.

Parameters for the PCC-MRI pulse sequence were the following: velocity encoding = 10 cm/s, FOV = 150 × 150 mm, section thickness = 4 mm, matrix = 256 × 178, TR = 24 ms, TE = 14 ms, flip angle = 15°, and 16 frames per cardiac cycle with peripheral retrospective pulse gating. The scans were obtained on sagittal T1-weighted imaging perpendicular to the CSF flow direction at the ampulla of the aqueduct (Fig 2). The "craniocaudal flow direction" was defined as positive, and the "caudocranial flow direction" was defined as negative. The scanning time for each patient was approximately 5 minutes.

Imaging Analysis

All the MR imaging analyses were performed in a blinded manner. Two neuroradiologists (L. M. and Y. W., with 7 and 20 years of experience, respectively) reviewed the MR images. No obvious abnormalities were found on conventional MR imaging and MRA in the controls and conventional MR imaging in patients with hypertension. Quantitative measurements of CSF flow at the ampulla of the aqueduct were processed using the Philips Q-flow software on the EWS MR imaging workstation. CSF flow quantification was performed on phase images showing maximum velocity, flow values, and velocity-time curves, which can change during the cardiac cycle using ROI measurements. The ROI measurement was performed by one of the authors on the independent console (Fig 3). Any type of dispute was resolved through consensus. The 16 axial sections, crossing the ampulla of the aqueduct and obtained in a cardiac cycle, were opened with Q-flow software. The ROI placement on the ampulla of the aqueduct was performed manually for each of 16 axial sections to obtain a quantitative measurement, separately. During the cardiac cycle, the software automatically calculated the forward flow volume (CSF flow volume toward the fourth ventricle) (FFV), reverse flow volume (CSF flow volume toward the third ventricle) (RFV), net flow volume flowing through the cerebral aqueduct in each cardiac cycle (NFV) (in milliliters), forward peak velocity (maximum velocity toward the fourth ventricle) (FPV), and the reverse peak velocity (maximum velocity toward the third ventricle, centimeters/second) (RPV) in each cardiac cycle. Additionally, the software automatically calculated the average flow (average of the absolute values of the bidirectional flow) (AF) through the cerebral aqueduct per minute (milliliter/minute).

Statistical Analysis

All descriptive and statistical analyses were performed using SPSS (Version 20.0; IBM). All the CSF flow parameters (FFV, FPV, RFV, RPV, AF, and NFV) between patients and control subjects were compared using the Student unpaired *t* test. In the hypertension group, univariate linear regression was performed for determinants of these parameters. To ascertain independent determinants of these parameters, we performed multiple linear regression analysis after evaluating whether the continuous variables were normally distributed. For each factor, we calculated the adjusted regression coefficients (β), which yielded the slope of the regression that was fitted by the model and indicated the increase (positive value) or decrease (negative value) in these parameters. For the test results, 95% confidence intervals are given.[17] A 95% CI that did not include the value of 0 had a P value $< .05$.

RESULTS

Characteristics of the study population are summarized in Table 1. There were no significant differences in age ($P = .84$) or sex ($P = .71$) between the 2 groups.

CSF flow parameters between the patients with hypertension and the control group are given in Table 2. FFV, FPV, RFV, RPV

Table 1: Clinical characteristics of patients with essential hypertension and healthy subjects

Characteristics	Patients	Controls	*P* Value
No.	60	60	
Age (mean) (yr)	61.24 (SD, 8.9)	60.38 (SD, 7.54)	.84
Male	31	33	.71
PP (mean) (mm Hg)	53.78 (SD, 14.86)	42.43 (SD, 4.36)	<.001
SBP (mean) (mm Hg)	148.54 (SD, 13.55)	123.40 (SD, 6.06)	.001
DBP (mean) (mm Hg)	94.76 (SD, 7.72)	80.97 (SD, 2.42)	<.001
Disease duration (mean) (yr)	4.92 (SD, 2.72)	0	<.001

Table 2: Comparison of mean CSF flow parameters in the hypertension and control groups

Group	FFV (mL)	FPV (cm/s)	RFV (mL)	RPV (cm/s)	AF (mL/min)	NFV (mL)
Patients	0.054 (SD, 0.021)	5.338 (SD, 2.024)	0.042 (SD, 0.019)	4.837 (SD, 2.196)	7.480 (SD, 3.221)	0.012 (SD, 0.005)
Controls	0.080 (SD, 0.040)	6.197 (SD, 2.394)	0.070 (SD, 0.042)	5.823 (SD, 2.821)	9.824 (SD, 5.435)	0.010 (SD, 0.011)
P value	<.001	.04	.005	.04	.006	.12

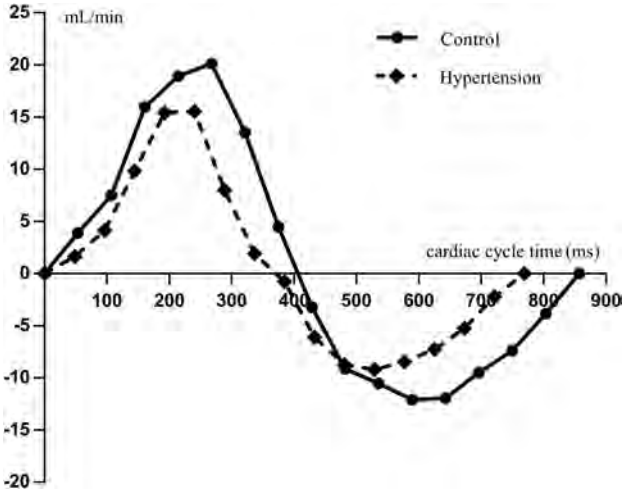

FIG 4. Flow curves of the essential hypertension and control groups. Flows are plotted during the successive phases of a cardiac cycle time (millisecond) and expressed in milliliter/minute. Each flow curve for both groups represents average flow values. Positive deflections represent craniocaudal flow (CSF systole), and negative deflections represent caudocranial flow (CSF diastole).

and AF in patients with hypertension were significantly lower than in the control subjects (all, $P < .05$). On the other hand, the NFV for the patients with hypertension and control subjects was not significantly different ($P = .12$). Figure 4 plots the AF curves in a cardiac cycle of the 2 groups, demonstrating a global decrease in AF values in the patients with hypertension compared with the control group.

In the hypertension group, univariate linear regression showed that increasing disease duration, PP, and SBP were associated with lower FFV, FPV, RFV, RPV, and AF (all, $P < .05$). However, no significant associations between these CSF flow parameters and DBP, age, or sex were found (all, $P > .05$) (Table 3). Multiple linear regression analysis showed a negative correlation between SBP and CSF flow dynamics (all, $P < .05$) (Table 4).

DISCUSSION

Our study used PCC-MRI to evaluate CSF dynamics in subjects with hypertension. We found that the FFV, FPV, RFV, RPV, and AF of CSF in patients with hypertension were obviously decreased; that disease duration, SBP, and PP significantly negatively correlated with these CSF dynamic parameters; and that SBP was more strongly negatively associated with CSF dynamics compared with disease duration or PP.

The brain is contained within a rigid skull and composed of the brain, CSF, and blood. According to the Monro-Kellie doctrine, any volume change in one intracranial component requires a compensatory change in another. During the systole, there is arterial inflow into the cranium, which initiates a cascade of craniocaudal CSF flush through the cerebral aqueduct (then to the fourth ventricle, subarachnoid space, and arachnoid villi, and finally to the venous sinus) to maintain homeostatic pressure in the cranium, while during the diastole, CSF flows through the aqueduct caudocranially.[18-21] Therefore, blood circulation is closely related to CSF circulation. Hypertension can lead to atherosclerosis, which reduces the elasticity of cerebral vessels and restricts blood flow to the brain during the systole.[15,22-26] To the best of our knowledge, however, there has been no study on CSF dynamics in patients with hypertension. In our present study, a significant decrease of FFV and FPV of CSF during the systole; RFV and RPV of CSF during the diastole; and AF throughout the whole cardiac cycle was observed in patients with hypertension, respectively. This finding indicates that the CSF flow dynamics of patients with hypertension is generally in a state of decline.[1,2]

In recent years, a so-called glymphatic system was found in the brain, ie, a paravascular pathway facilitating CSF flow through the brain parenchyma and the clearance of interstitial solutes.[1,2] In 2018, Mestre et al[4] pointed out that arteriosclerosis in hypertensive mice disrupts the above glymphatic flow and sharply slows CSF transportation in the perivascular spaces. This finding might suggest that arteriosclerosis may affect the circulation of CSF and cause changes in the CSF dynamics of the aqueduct in humans. Our study preliminarily investigated the changes of CSF dynamics in patients with hypertension but not the changes of CSF and the insulin sensitivity factor in the perivascular spaces. Therefore, the relationship between them remains unclear and needs further study.

In this study, SBP, PP, and disease duration were negatively correlated with CSF flow dynamics. SBP was more significantly correlated with CSF dynamics than PP. Our results highlight a major limitation of PP, which is "floating" and has no relation to an absolute blood pressure level. For example, a PP of 60 mm Hg

Table 3: Univariate linear regression coefficients for relationships between hypertension parameters and CSF flow parameters[a]

Variables	FFV (mL)[b]	FPV (cm/s)[b]	RFV (mL)[b]	RPV (cm/s)[b]	AF (mL/min)[b]
Duration	−0.81 (−0.98 to −0.64)[c]	−0.83 (−0.99 to −0.67)[c]	−0.84 (−0.99 to −0.68)[c]	−0.83 (−0.99 to −0.67)[c]	−0.77 (−0.95 to −0.58)[c]
PP	−0.76 (−0.95 to −0.57)[c]	−0.73 (−1.01 to −0.71)[c]	−0.74 (−0.94 to −0.55)[c]	−0.25 (−1.01−0.03)[c]	−0.74 (−0.94 to −0.54)[c]
SBP	−0.86 (−1.01 to −0.71)[c]	−0.86 (−0.97 to −0.62)[c]	−0.88 (−1.02 to −0.75)[c]	−0.87 (−0.75 to −0.72)[c]	−0.83 (−0.99 to −0.67)[c]
DBP	0.05 (−0.33−0.25)	−0.10 (−0.39−0.19)	−0.12 (−0.41−0.17)	−0.11 (−0.40−0.18)	0.04 (−0.33−0.25)
Age	−0.13 (−0.42−0.16)	−0.05 (−0.34−0.24)	−0.11 (−0.40−0.18)	−0.09 (−0.38−0.20)	−0.07 (−0.36−0.22)
Sex	−0.09 (−0.38−0.20)	−0.10 (−0.38−0.19)	−0.12 (−0.41−0.17)	−0.11 (−0.40−0.18)	−0.14 (−0.43−0.15)

[a] Numbers in parentheses are 95% CI.
[b] Crude regression coefficients indicative of increase (positive value) or decrease (negative value) in CSF flow parameters.
[c] $P < .05$.

Table 4: Multiple linear regression coefficients for relationships between hypertension parameters and CSF flow parameters[a]

Variables	FFV (mL)[b]	FPV (cm/s)[b]	RFV (mL)[b]	RPV (cm/s)[b]	AF (mL/min)[b]
Duration	−0.34 (−0.61 to −0.07)[c]	−0.37 (−0.64 to −0.10)[c]	−0.31 (−0.56 to −0.07)[c]	−0.35 (−0.61 to −0.09)[c]	−0.25 (−0.55−0.05)[c]
SBP	−0.44 (−0.83 to −0.06)[c]	−0.50 (−0.88 to −0.12)[c]	−0.61 (−0.97 to −0.26)[c]	−0.55 (−0.91 to −0.18)[c]	−0.50 (−0.93 to −0.08)[c]
PP	−0.25 (−0.43−0.13)[c]	−0.16 (−0.33−0.22)[c]	−0.11 (−0.26−0.25)[c]	−0.23 (−0.30−0.24)[c]	−0.34 (−0.45−0.17)[c]

[a] Numbers in parentheses are 95% CI.
[b] β, adjusted regression coefficients indicative of an increase (positive value) or decrease (negative value) in CSF flow parameters.
[c] $P < .05$.

could be associated with a blood pressure of 180/120 mm Hg or 120/60 mm Hg. Of note, in addition, SBP is more strongly associated with arteriosclerosis.[27]

In this study, CSF dynamics parameters in the control group were slightly different from those in the previous literature.[6,10,14,20,28-30] This finding may be related to the scan level of the aqueduct and velocity encoding. Anatomically, the cerebral aqueduct is divided into 3 parts, namely, the pars anterior, ampulla, and pars posterior. The pars posterior has the narrowest lumen of the cerebral aqueduct, while the ampulla has the widest lumen.[5] Because the cerebral aqueduct is very small, partial volume errors can result in falsely lower peak velocities and falsely higher mean flows. Positioning perpendicular to the imaging plane and adjusting the ROI size of the cerebral aqueduct help to minimize this potential source of error. Therefore, in our study, we measured CSF dynamics at the site of ampulla of the aqueduct, the largest part of the lumen. Previous studies measured CSF flow dynamics at a variety of different locations other than the cerebral aqueduct; their results were different from ours.[29] Also, velocity encoding is an important parameter determining the sensitivity of flow velocity in the examined area. The CSF flow velocity should be the same as or slightly lower than the selected velocity encoding to obtain the optimal signal,[31] CSF flow velocities greater than velocity encoding can produce aliasing artifacts, whereas velocities much smaller than velocity encoding can result in a weak signal. In a previous study with a 3T Achieva scanner (Philips Healthcare), velocity encoding was set at 10 cm/s.[20] In our study, we set velocity encoding to 10 cm/s because the maximum velocity was about 7 and 9 cm/s in the hypertensive and control groups, respectively.

Our study has several limitations. First, the sample size was relatively small. Therefore, a larger cohort study is needed to validate these results. Second, we did not measure cerebral arterial and venous blood flow. Third, only untreated patients were included in this study. It was reported that cerebral blood flow will recover after blood pressure is controlled in patients with hypertension.[23] In further studies, we will continue to focus on the changes in CSF flow after treatment in patients with hypertension. Also, patients with SBP ≥ 180 mm Hg were not included in the study because they usually take medicine early due to related symptoms, which did not meet an inclusion criterion of our present study. Last, we did not quantify small white matter lesions on T2WI.[32] We will study the potential role of these lesions in CSF dynamics in the future.

CONCLUSIONS

Our study used PCC-MRI to evaluate CSF flow dynamics in treatment-naive patients with essential hypertension. We found that FFV, FPV, RFV, RPV, and AF of CSF in patients with hypertension were significantly decreased. SBP is more strongly negatively associated with these parameters compared with disease duration and PP.

REFERENCES

1. Jessen NA, Munk AS, Lundgaard I, et al. **The glymphatic system: a beginner's guide.** *Neurochem Res* 2015;40:2583–99 CrossRef Medline
2. Iliff JJ, Wang M, Liao Y, et al. **A paravascular pathway facilitates CSF flow through the brain parenchyma and the clearance of interstitial solutes, including amyloid.** *Sci Transl Med* 2012;4:147ra111 CrossRef Medline
3. Proulx ST. **Cerebrospinal fluid outflow: a review of the historical and contemporary evidence for arachnoid villi, perineural routes, and dural lymphatics.** *Cell Mol Life Sci* 2021;78:2429–57 CrossRef Medline
4. Mestre H, Tithof J, Du T, et al. **Flow of cerebrospinal fluid is driven by arterial pulsations and is reduced in hypertension.** *Nat Commun* 2018;9:4878 CrossRef Medline
5. Edelman RR, Wedeen VJ, Davis KR, et al. **Multiphasic MR imaging: a new method for direct imaging of pulsatile CSF flow.** *Radiology* 1986;161:779–83 CrossRef Medline
6. Akay R, Kamisli O, Kahraman A, et al. **Evaluation of aqueductal CSF flow dynamics with phase contrast cine MR imaging in idiopathic intracranial hypertension patients: preliminary results.** *Eur Rev Med Pharmacol Sci* 2015;19:3475–79 Medline
7. Battal B, Kocaoglu M, Bulakbasi N, et al. **Cerebrospinal fluid flow imaging by using phase-contrast MR technique.** *Br J Radiol* 2011;84:758–65 CrossRef Medline

8. Kelly EJ, Yamada S. **Cerebrospinal fluid flow studies and recent advancements.** *Semin Ultrasound CT MR* 2016;37:92–99 CrossRef Medline
9. Lee JH, Lee HK, Kim JK, et al. **CSF flow quantification of the cerebral aqueduct in normal volunteers using phase contrast cine MR imaging.** *Korean J Radiol* 2004;5:81–86 CrossRef Medline
10. Hasiloglu ZI, Albayram S, Gorucu Y, et al. **Assessment of CSF flow dynamics using PC-MRI in spontaneous intracranial hypotension.** *Headache* 2012;52:808–19 CrossRef Medline
11. Qvarlander S, Ambarki K, Wåhlin A, et al. **Cerebrospinal fluid and blood flow patterns in idiopathic normal pressure hydrocephalus.** *Acta Neurol Scand* 2017;135:576–84 CrossRef Medline
12. Hoxworth JM. **Measuring CSF flow dynamics in spontaneous intracranial hypotension with phase-contrast magnetic resonance imaging: potential implications for diagnosis and treatment.** *Cephalalgia* 2014;34:565–67 CrossRef Medline
13. Lindstrøm EK, Ringstad G, Mardal K, et al. **Cerebrospinal fluid volumetric net flow rate and direction in idiopathic normal pressure hydrocephalus.** *Neuroimage Clin* 2018;20:731–41 CrossRef Medline
14. Yılmaz TF, Aralasmak A, Toprak H, et al. **Evaluation of CSF flow metrics in patients with communicating hydrocephalus and idiopathic intracranial hypertension.** *Radiol Med* 2019;124:382–91 CrossRef Medline
15. Feihl F, Liaudet L, Waeber B. **The macrocirculation and microcirculation of hypertension.** *Curr Hypertens Rep* 2009;11:182–89 CrossRef Medline
16. Muntner P, Carey RM, Gidding S, et al. **Potential U.S. population impact of the 2017 ACC/AHA high blood pressure guideline.** *J Am Coll Cardiol* 2018;71:109–18 CrossRef Medline
17. Gardner MJ, Altman DG. **Confidence intervals rather than P values: estimation rather than hypothesis testing.** *BMJ (Clin Res Ed)* 1986;292:746–50 CrossRef Medline
18. Sakhare AR, Barisano G, Pa J. **Assessing test–retest reliability of phase contrast MRI for measuring cerebrospinal fluid and cerebral blood flow dynamics.** *Magn Reson Med* 2019;82:658–70 CrossRef Medline
19. Kim D, Czosnyka Z, Kasprowicz M, et al. **Continuous monitoring of the Monro-Kellie doctrine: is it possible?** *J Neurotraum* 2012;29:1354–63 CrossRef Medline
20. ElSankari S, Balédent O, van Pesch V, et al. **Concomitant analysis of arterial, venous, and CSF flows using phase-contrast MRI: a quantitative comparison between MS patients and healthy controls.** *J Cereb Blood Flow Metab* 2013;33:1314–21 CrossRef Medline
21. Bhadelia RA, Bogdan AR, Kaplan RF, et al. **Cerebrospinal fluid pulsation amplitude and its quantitative relationship to cerebral blood flow pulsations: a phase-contrast MR flow imaging study.** *Neuroradiology* 1997;39:258–64 CrossRef Medline
22. Pires PW, Dams Ramos CM, Matin N, et al. **The effects of hypertension on the cerebral circulation.** *Am J Physiol Heart Circ Physiol* 2013;304:H1598–614 CrossRef Medline
23. Meyer JS, Rogers RL, Mortel KF. **Prospective analysis of long term control of mild hypertension on cerebral blood flow.** *Stroke* 1985;16:985–90 CrossRef Medline
24. Li Y, Shen Q, Huang S, et al. **Cerebral angiography, blood flow and vascular reactivity in progressive hypertension.** *Neuroimage* 2015;111:329–37 CrossRef Medline
25. Domanski M, Norman J, Wolz M, et al. **Cardiovascular risk assessment using pulse pressure in the first national health and nutrition examination survey (NHANES I).** *Hypertension* 2001;38:793–97 CrossRef Medline
26. Safar ME. **Pulse pressure, arterial stiffness, and cardiovascular risk.** *Curr Opin Cardiol* 2000;15:258–63 CrossRef Medline
27. Mosley WJ, Greenland P, Garside DB, et al. **Predictive utility of pulse pressure and other blood pressure measures for cardiovascular outcomes.** *Hypertension* 2007;49:1256–64 CrossRef Medline
28. Stoquart-ElSankari S, Balédent O, Gondry-Jouet C, et al. **Aging effects on cerebral blood and cerebrospinal fluid flows.** *J Cereb Blood Flow Metab* 2007;27:1563–72 CrossRef Medline
29. Luetmer PH, Huston J, Friedman JA, et al. **Measurement of cerebrospinal fluid flow at the cerebral aqueduct by use of phase-contrast magnetic resonance imaging: technique validation and utility in diagnosing idiopathic normal pressure hydrocephalus.** *Neurosurgery* 2002;50:534–43 CrossRef Medline
30. Oner Z, Kahraman AS, Kose E, et al. **Quantitative evaluation of normal aqueductal cerebrospinal fluid flow using phase-contrast cine MRI according to age and sex.** *Anat Rec (Hoboken)* 2017;300:549–55 CrossRef Medline
31. Bapuraj JR, Londy FJ, Delavari N, et al. **Cerebrospinal fluid velocity amplitudes within the cerebral aqueduct in healthy children and patients with Chiari I malformation.** *J Magn Reson Imaging* 2016;44:463–70 CrossRef Medline
32. Yu X, Wang G, Zhan J, et al. **Risk factors of pure leukoaraiosis and the association with preclinical carotid atherosclerosis.** *Atherosclerosis* 2018;275:328–32 CrossRef Medline

Identification of *BRAF p. V600E*-Mutant and Wild-Type by MR Imaging in Pleomorphic Xanthoastrocytoma and Anaplastic Pleomorphic Xanthoastrocytoma

W. Huang, J. Cai, N. Lin, Y. Xu, H. Wang, Z. Wu, and D. Kang

ABSTRACT

BACKGROUND AND PURPOSE: Compared with *BRAF p. V600E* wild-type pleomorphic xanthoastrocytoma, *BRAF p. V600E*-mutant pleomorphic xanthoastrocytoma showed a higher survival rate. In this study, we focused on finding preoperative MR imaging differences between *BRAF p. V600E* mutant and wild-type in pleomorphic xanthoastrocytoma and anaplastic pleomorphic xanthoastrocytoma.

MATERIALS AND METHODS: Twenty-three patients with pathologically confirmed pleomorphic xanthoastrocytoma or anaplastic pleomorphic xanthoastrocytoma in our hospital were retrospectively analyzed from January 2015 to December 2020. They were divided into a *BRAF p. V600E*-mutant group (including 6 pleomorphic xanthoastrocytomas and 5 anaplastic pleomorphic xanthoastrocytomas) and a wild-type group (including 8 pleomorphic xanthoastrocytomas and 4 anaplastic pleomorphic xanthoastrocytomas). The preoperative MR imaging characteristics of these groups were statistically compared.

RESULTS: The wild-type pleomorphic xanthoastrocytoma group presented with more aggressive conventional and advanced MR imaging features than the mutant pleomorphic xanthoastrocytoma group, including greater mean maximum tumor diameter (3.1 [SD, 0.9] cm versus 1.7 [SD, 0.4] cm, $P < .05$), more frequent heterogeneous contrast enhancement of solid portions (100% versus 0%, $P < .001$), more obvious peritumoral edema (mean, [2.1 SD, 0.7] cm versus 0.6 [SD, 0.2] cm, $P < .01$), and lower mean minimum relative ADC (896 [SD, 86] versus 988 [SD, 73], $P < .05$) and mean relative ADC (1060 [SD, 159] versus 1248 [SD, 116], $P < .05$) on DWI. However, there was no significant difference in either conventional or advanced MR imaging features between the wild-type anaplastic pleomorphic xanthoastrocytoma group and the mutant anaplastic pleomorphic xanthoastrocytoma group.

CONCLUSIONS: Neurosurgeons should carefully interpret MR images before an operation and select appropriate surgical strategies according to genotype prediction.

ABBREVIATIONS: ADCmean = mean relative ADC; ADCmin = minimum relative ADC; APXA = anaplastic pleomorphic xanthoastrocytoma; PXA = pleomorphic xanthoastrocytoma; WHO = World Health Organization

Pleomorphic xanthoastrocytoma (PXA) is an infrequent glioma affecting 1% of patients with brain tumors, thought to originate from subpial astrocytes or their precursors and usually occurring in children and adolescents.[1] PXA was first described by Kepes et al,[2] in 1979. In 1993, it was officially included in the World Health Organization (WHO) Classification System for Tumors of the Central Nervous System as a grade II tumor.[3] Although PXA is classified as a WHO grade II tumor, "PXA with anaplastic features" comprise 15%–50% of these lesions.[4-7] According to the 2016 WHO classification system, PXA is divided into 2 distinct entities based on histopathologic characteristics: WHO grade II PXA and WHO grade III anaplastic PXA (APXA).[8,9] APXA is defined as the presence of 5 mitoses per 10 high-power fields. Patients with PXA can undergo only total resection, while patients with APXA require total resection and adjuvant therapy.[5,10] In addition, APXA has been reported to have a worse prognosis than PXA, with a 5-year overall survival rate of 57.1%.[5,11,12]

The most frequently found mutant gene in PXA is *BRAF p. V600E*, which encodes an intracellular component of the MAPK pathway.[13-16] *BRAF p. V600E*-mutants were found in 70% of typical PXAs but appeared less commonly in APXA (17%–

Received May 19, 2021; accepted after revision August 10.

From the Department of Neurosurgery (W.H., J.C., Y.X., H.W., Z.W., D.K.), The First Affiliated Hospital of Fujian Medical University, Fuzhou, Fujian, China; The First Clinical Medical College of Fujian Medical University (W.H., J.C., Y.X., H.W., Z.W., D.K.), Fuzhou, Fujian, China; and The School of Medical Technology and Engineering (N.L.), Fujian Medical University, Fuzhou, Fujian, China.

Wei Huang, Jiawei Cai, and Ni Lin contributed equally to this study.

This work was supported by the Natural Science Foundation of Fujian Province, 2018J01851 and the Science and Technology Projects of Fujian Province, 2020GGA054.

Please address correspondence to Zanyi Wu, MD, Department of Neurosurgery, The First Affiliated Hospital of Fujian Medical University, 88 Jiaotong Rd, Fuzhou, Fujian 350005, China; e-mail: kirby98@126.com

Indicates open access to non-subscribers at www.ajnr.org

http://dx.doi.org/10.3174/ajnr.A7324

65%).[5,13,17,18] *BRAF p. V600E*-mutant may divide these tumors into 2 clinically relevant subsets, both associated with natural history and response to treatment.[19] Compared with the wild-type, *BRAF p. V600E*-mutant PXA showed a higher survival rate.[5,20,21] *BRAF p. V600E*-mutant PXA has also shown a response to *BRAF*-targeted therapy,[22] though no prospective comparative trials have been conducted in this patient population.

APXA can present with more aggressive conventional and advanced MR imaging features, mimicking high-grade astrocytoma at initial diagnosis, than PXA.[23] However, there have been few reports on the MR imaging characteristics of PXA with *BRAF p. V600E*-mutant, especially its differentiation from *BRAF p. V600E* wild-type PXA. Therefore, the purpose of this study was to investigate the MR imaging characteristics of *BRAF p. V600E*-mutant PXA and *BRAF p. V600E* wild-type PXAs to determine whether there are differences in the imaging characteristics of these 2 entities to aid in planning a treatment strategy and predicting prognosis.

MATERIALS AND METHODS

Case Selection

The study was approved by the Branch for Medical Research and Clinical Technology Application, Ethics Committee of the First Affiliated Hospital of Fujian Medical University and informed consent was signed. Of 317 astrocytic tumor cases from January 2015 to December 2020, twenty-eight (0.89%) with diagnoses containing the term "pleomorphic xanthoastrocytoma" or " anaplastic pleomorphic xanthoastrocytoma" on first surgical resection were extracted. Three (of 28) cases lacked MR imaging data before the first operation and were excluded. Twenty-five adult patients with PXA were included in this study, and a review of all their clinical and radiologic records was performed. The analyzed clinical information included sex, age, and symptoms (seizures, increased intracranial pressure, and neurologic deficits). These data were obtained from the electronic medical record system.

Histopathologic and Molecular Sequencing

Paraffin-embedded tumor tissue was cut into 4-mm sections and stained with H&E, and 10-mm sections were used for molecular sequencing. All histologic specimens were reviewed by our institutional neuropathologist (with 15 years of experience in neuropathology), who reclassified PXA (WHO grade II) and APXA (WHO grade III) according to the 2016 WHO classification of central nervous system tumors and the Consortium to Inform Molecular and Practical Approaches to CNS Tumor Taxonomy (cIMPACT-NOW) update 6.[24] The diagnostic criteria included tumors demonstrating a relatively solid growth pattern composed of spindle-shaped, pleomorphic, and multinucleated cells associated with both pale and bright eosinophilic granular bodies to be diagnosed as PXA. Anaplastic features, which included a mitotic index of 5 of 10 high-power fields with or without necrosis and endothelial proliferation, were diagnosed as APXA. Twenty-five patients were studied. Of these, 10 PXA and 13 APXA specimens were confirmed. We excluded 2 cases: One was reclassified as "diffuse astrocytoma, *IDH* wild-type with pleomorphic/PXA-like features," and the other was previously diagnosed as "pleomorphic xanthoastrocytoma with anaplastic features" and reclassified as "giant cell glioblastoma." All 23 cases were available for molecular sequencing. Molecular analyses were performed to test the presence of the *BRAF p. V600E*-mutant, which was confirmed by sequencing. Of these, 11 *BRAF p. V600E*-mutant PXAs (including 6 cases of PXA and 5 cases of APXA) and 12 *BRAF p. V600E* wild-type PXAs (including 4 cases of PXA and 8 cases of APXA) were confirmed.

Preoperative MR Imaging Techniques

All patients underwent MR imaging on 3T scanners (Magnetom Verio or Magnetom Skyra; Siemens) or a 1.5T scanner (Signa TwinSpeed; GE Healthcare). The retrospective nature of this study resulted in variability in MR images and imaging protocols. Conventional MR imaging protocols included an axial T2-weighted sequence, nonenhanced axial and sagittal T1-weighted sequences, and 3 orthogonal plane contrast-enhanced T1-weighted sequences. An FOV of 22 cm^2, imaging matrix of 256 × 256, and section thickness of 5 mm were uniformly applied in all sequences.

DWI was performed in 10 patients with PXA and 13 patients with APXA using an axial echo-planar sequence according to the following technique parameters: TR/TE = 8200/102 ms, FOV = 22 × 22 cm, section thickness/gap = 5/1 mm, diffusion gradient encoding = b = 0, 1000 s/mm^2. The diffusion gradient was used in 3 orthogonal directions. ADC maps were automatically calculated using a monoexponential model.

MR Imaging Analysis

All images were reviewed in consensus by 2 radiologists (readers 1 and 2 with 20 and 8 years of experience in neuroimaging, respectively) to make a factual comparison and minimize the confounding effects. The readers were blinded to tumor histology and recorded the following tumor characteristics: 1) tumor location (frontal, occipital, temporal, or parietal; superficial or deep); 2) tumor size (largest diameter, in centimeters); 3) the presence of cystic degeneration; 4) enhancement characteristics of the solid component (heterogeneous or homogeneous); 5) the presence and degree of peritumoral edema (largest diameter, in centimeters); 6) leptomeningeal contact; and 7) the presence of restricted diffusion, defined as high signal on DWI and corresponding low signal on ADC maps compared with contralateral normal brain parenchyma.

Tumor size was defined by the maximum diameter as measured on contrast-enhanced T1WI. The extent of peritumoral edema was defined by a region of very bright signal intensity on T2 surrounding the enhanced tumor on contrast-enhanced T1WI. The tumor location was defined as main lobe involvement when >1 lobe was involved.

For quantitative ADC evaluation, MR images were postprocessed as follows: 1) identification of the axial DWI and corresponding ADC image section displaying the lowest ADC values within solid tumor tissue components; 2) definition of a circular ROI of 6-mm diameter, manually drawn within the perceived lowest ADC solid tumor component, recording the minimum relative ADC (ADCmin) and mean relative ADC (ADCmean) values of this tumoral ROI (the ROI was systematically moved within the solid tumoral area, as depicted by conventional MR imaging, to measure regions with the lowest ADC values); 3)

Table 1: Demographic data and conventional MR imaging characteristics of PXA and APXA

	PXA	APXA	*P* Value
Clinical data			
Male sex (No.) (%)	3 (30%)	6 (46.1%)	.363
Mean age (yr)	34 (SD, 10)	41 (SD, 10)	.232
Presenting symptoms (No.)			.899
Seizures	6	9	
Headache or increased ICP	2	2	
Neurologic deficit	2	2	
BRAF p. V600E-mutant	6 (60%)	5 (38.5%)	.273
Location (No.)			.526
Frontal lobe	0	3	
Temporal lobe	5	5	
Occipital lobe	1	1	
Parietal lobe	2	3	
Insula	2	1	
Superficial location (No.) (%)	8 (80%)	11 (84.6%)	.596
Conventional MR imaging			
Mean size (cm)	2.2 (SD, 0.9)	3.2 (SD, 0.6)	<.01
Presence of cystic degeneration (No.) (%)	6 (60%)	9 (69.2%)	.490
Peritumoral edema (mean) (cm)	1.2 (SD, 0.8)	2.1 (SD, 0.9)	.021
Heterogeneous enhancement (No.) (%)	4 (40%)	11 (84.6%)	<.001
Leptomeningeal contact (No.) (%)	8 (80%)	11 (84.6%)	.596

Note:—ICP indicates intracranial pressure.

definition and assessment of the reference region minimum and mean ADC values, by placing a similar ROI on the normal-appearing thalamus (because it is a readily identifiable structure on ADC maps and is considered generally resistant to changes related to hydrocephalus);[25] and 4) finally, the mean and minimum ADC values of the tumoral ROIs with the lowest ADC value were normalized with their corresponding reference region, obtaining ADCmean and ADCmin. This computation was performed because ADC values of normal brain vary with age,[26] and the contrast achieved between tumor and surrounding tissue depends on this ratio; at the same time, this computation allowed data comparison of brain MR imaging performed with different scanners.

Statistical Analysis

The normality of all continuous parameters was initially assessed using the Kolmogorov-Smirnov test. Characteristics of the patients were summarized with means or medians and SDs or ranges for continuous data (as appropriate) and with frequencies and percentages for categoric data. The Fisher exact test was used to assess the differences in the categoric variables (age, sex, location, cystic degeneration, enhancement characteristics, and leptomeningeal contact) between the different groups. The Mann–Whitney *U* test was used to assess the differences in continuous variables (edema, tumor size, and ADC values) between the different groups because they did not conform to the normal distribution.

The MR imaging differences between the *BRAF p. V600E*-mutant PXA group and the *BRAF p. V600E* wild-type PXA group and the *BRAF p. V600E*-mutant APXA group and the *BRAF p. V600E* wild-type APXA group were statistically analyzed. Statistical analysis was performed with the Statistical Package for the Social Sciences (SPSS 24.0 Version for Windows; IBM). All reported *P* values were double-tailed, and *P* values less $< .05$ were regarded as statistically significant.

RESULTS

Clinical Data and Conventional MR Imaging

According to molecular analysis, 10 cases of PXA were divided into a *BRAF p. V600E*-mutant PXA group ($n = 6$) and a wild-type PXA group ($n = 4$); 13 cases of APXA were divided into a *BRAF p. V600E*-mutant APXA group ($n = 5$) and a wild-type APXA group ($n = 8$). Clinical data, molecular analysis, location, and conventional imaging features of PXA and APXA are summarized in Table 1. All 23 tumors were in the supratentorial region. Eight PXAs (8/10, 80%) and 11 APXAs (11/13, 84.6%) were superficial (on the surface of the brain parenchyma). There was no significant difference in tumor location between the PXA and APXA groups. The presence of heterogeneous enhancement of solid portions was observed less frequently in patients with PXA than in patients with APXA (4/10 versus 11/13, $P < .001$). Leptomeningeal contact was seen in 8 PXA cases and 11 APXA cases. In preoperative images, the lesion was significantly larger in patients with APXA than in patients with PXA (mean, 3.2 [SD, 0.6] cm versus 2.2 [SD, 0.9] cm, $P < .01$). The average maximum diameter of peritumoral edema in the APXA group was larger than the average maximum diameter of peritumoral edema in the PXA group (2.1 [SD, 0.9] cm versus 1.2 [SD, 0.8] cm, $P = .021$) (Fig 1).

Table 2 and Table 3 summarize the clinical data, localization, and conventional imaging features of *BRAF p. V600E* subtypes of PXAs and APXAs, respectively. There was no significant difference in location between the *BRAF V600E* mutant and wild-type groups for either PXAs or APXAs. In preoperative images, the presence of heterogeneous enhancement of solid portions was observed less frequently in patients with *BRAF p. V600E*-mutant PXA than in patients with wild-type PXA (0/6 versus 4/4, $P < .001$). However, there was no significant difference in the presence of heterogeneous enhancement of the location of solid portions between the 2 groups in APXAs (5/5 versus 6/8, $P = .359$). The mean tumor size (the maximum diameter represents the size of the tumor) was significantly larger in patients with *BRAF p. V600E* wild-type PXA than in patients in the group with mutant PXA (3.1 [SD, 0.9] cm versus 1.7 [SD, 0.4] cm, $P = .038$). The maximum diameter of peritumoral edema in the *BRAF p. V600E* wild-type PXA group was significantly larger than the mutant PXA group (mean, 2.1 [SD, 0.7] cm versus 0.6 [SD, 0.2] cm, $P < .01$). However, there was no significant difference in either mean tumor size (3.3 [SD, 0.7] cm versus 3.2 [SD, 0.5] cm, $P = .943$) or the mean maximum diameter of peritumoral edema (2.4 [SD, 0.9] cm versus 1.8 [SD, 0.4] cm, $P = .3$) between the *BRAF p. V600E*-mutant type APXA group and the wild-type APXA group (Fig 2).

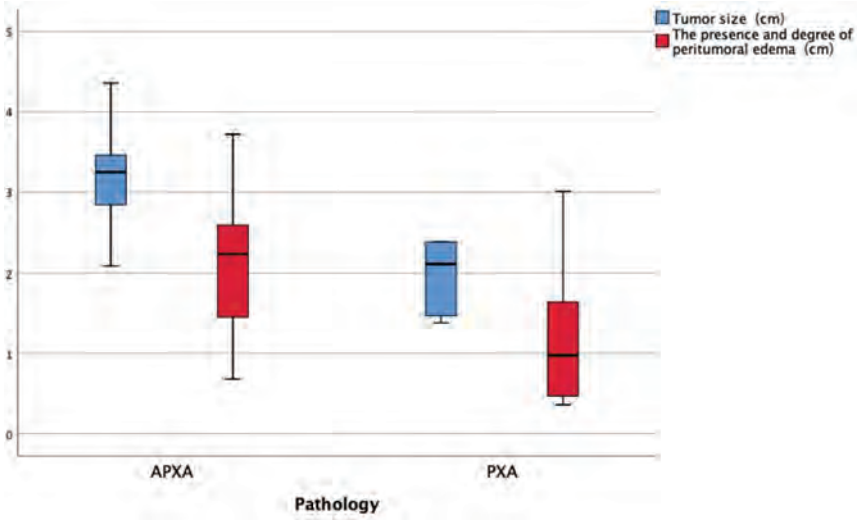

FIG 1. Boxplots representing tumor size and the presence and degree of peritumoral edema of PXA and APXA. A significant difference ($P < .05$) between PXA and APXA is demonstrated with both tumor size and the presence and degree of peritumoral edema.

Table 2: Demographic data and conventional MR imaging characteristics of *BRAF p. V600E*-mutant and *BRAF p. V600E* wild-type PXA

	BRAF p. V600E-Mutant PXA	*BRAF p. V600E* Wild-Type PXA	*P* Value
Clinical data			
Male sex (No.) (%)	2 (33.3%)	1 (25%)	.667
Mean age (yr)	32 (SD, 8.6)	37(SD, 13)	.762
Presenting symptoms (No.)			.870
Seizures	4	2	
Headache or increased ICP	1	1	
Neurologic deficit	1	1	
Location (No.)			.405
Frontal lobe	0	0	
Temporal lobe	3	2	
Occipital lobe	0	1	
Parietal lobe	2	0	
Insula	1	1	
Superficial location (No.) (%)	4 (66.6%)	4 (100%)	.333
Conventional MR imaging			
Mean size (cm)	1.7 (SD, 0.4)	3.1 (SD, 0.9)	.038
Presence of cystic degeneration (No.) (%)	2 (33.3%)	4 (100%)	.071
Peritumoral edema (mean) (cm)	0.6 ± 0.2	2.1 ± 0.7	<.01
Heterogeneous enhancement (No.) (%)	0 (0%)	4 (100%)	<.001
Leptomeningeal contact (No.) (%)	6 (100%)	2 (50%)	.03

Note:— ICP indicates intracranial pressure.

Advanced MR Imaging Findings

Table 4 and Figure 3 summarize the features of PXAs and APXAs with DWI. Both mean ADCmin values (755 [SD, 77] versus 951 [SD, 88]; $P < .001$) and ADCmean values (956 [SD, 106] versus 1173 [SD, 159], $P < .001$) were significantly lower in the whole APXA group than in the PXA group. Both mean ADCmin values (896 [SD, 86] versus 988 [SD, 73], $P < .05$) and ADCmean values (1060 [SD, 159] versus 1248 [SD, 116], $P < .05$) were significantly lower in the whole group of *BRAF p. V600E* wild-type PXA than in mutant-PXA group. However, there was no significant difference in mean ADCmin (750 [SD, 73] versus 762 [SD, 92], $P = 1$) and ADCmean (974 [SD, 92] versus 925 [SD, 131], $P = .724$) values between the 2 groups in APXAs (Fig 4, Tables 5 and 6). Representative cases are shown in Figure 5.

DISCUSSION

To the best of our knowledge, few studies have evaluated and compared the imaging features of *BRAF p. V600E* wild-type PXA and *BRAF p. V600E*-mutant PXA. Our results show that PXAs with *BRAF p. V600E* wild-type show more aggressive MR imaging features than those with the *BRAF p. V600E*-mutant according to MR imaging features, namely, larger tumor size, more heterogeneous contrast enhancement, obvious peritumoral edema, lower ADCmin, and lower ADCmean ratio on DWI.

PXA is histologically classified as a grade II astrocytoma according to the 2016 WHO classification of the central nervous system.[8] The outcomes in cases of PXAs are relatively favorable, with 5- and 10-year overall survival rates of 75%–81% and 67%–70%, respectively, after total resection.[7,27] APXA is more likely to be derived from a previous PXA with the development of anaplastic histologic features.[28] In the present study, APXA accounted for 56.5% of PXAs and showed anaplastic features. Findings comparable with the results reported by Hirose et al[6] were that approximately 50% of PXAs showed anaplastic features.

The *BRAF p. V600E*-mutant is a distinctive genomic alteration of PXA and APXA.[17,29,30] Previous studies demonstrated that *BRAF p. V600E*-mutant status is an independent prognostic factor

after adjusting for anaplasia, age, sex, and initial symptoms.[12] In the present study, approximately 60% of PXAs and 38.4% of APXAs showed a *BRAF p. V600E*-mutant, findings comparable with the results reported by Dias-Santagata et al[13] that *BRAF p. V600E*-mutants are found in 70% of typical PXAs but appear less commonly in APXAs.

Most large case series have reported no sex predilection. However, the proportion of women in our series was much higher than the proportion of men. PXA most frequently occurred in young adults in our study, consistent with previous studies.[1,5,27] APXA was reported to be more common in older adults with a median age of 40–65 years.[31-33] In our series, 9 of 13 patients with APXA were middle-aged adults with a mean age of 44.67 years at their first presentation, which is consistent with findings in previous studies.[27]

The most common tumor location of PXA was the temporal lobe (50.0%), which is in accordance with findings in previous studies.[34,35] Our results show that the principal initial manifestation was seizures, which were observed in 60% and 69.2% of patients with PXA and APXA, respectively. These results correspond to findings that seizures were obviously related to tumor involvement of the temporal lobe in PXA.[12] Almost all PXA and APXA tumors in our series showed a superficial location in the cerebral hemispheres with leptomeningeal contact. Both PXA and APXA are believed to develop from subpial astrocytes, which partly explains why these 2 tumors preferably arise from superficial cortical sites.[2]

In our study, we found that APXA shows more aggressive MR imaging features than PXA, namely, larger tumor size, more heterogeneous contrast enhancement, and obvious peritumoral edema, consistent with previously reported findings.[23] *BRAF p. V600E*-mutant PXAs have been reported to show histologic heterogeneity and display pleomorphic giant cells, xanthomatous changes, and fascicular and storiform growth patterns.[13] Purkait et al[36] also proposed the possibility of a morphologic spectrum of *BRAF p. V600E*-mutant tumors with astroblastoma at one end and PXA at the other. We found that *BRAF p. V600E* wild-type PXA showed significantly different imaging characteristics from mutant PXA, including larger tumor size, more heterogeneous contrast enhancement, and obvious peritumoral edema, which suggests that

Table 3: Demographic data and conventional MR imaging characteristics of *BRAF p. V600E*-mutant and *BRAF p. V600E* wild-type APXA

	BRAF p. V600E-Mutant APXA	*BRAF p. V600E* Wild-Type APXA	*P* Value
Clinical data			
Male sex (No.) (%)	3 (60%)	3 (37.5%)	.413
Mean age (yr)	33 (SD, 13)	43 (SD, 6)	.284
Presenting symptoms (No.)			.850
Seizures	3	6	
Headache or increased ICP	1	1	
Neurologic deficit	1	1	
Location (No.)			.276
Frontal lobe	0	3	
Temporal lobe	2	3	
Occipital lobe	1	0	
Parietal lobe	2	1	
Insula	0	1	
Superficial location (No.) (%)	4 (80.0%)	7 (87.5%)	.641
Conventional MR imaging			
Mean size (cm)	3.2 (SD, 0.5)	3.3 (SD, 0.7)	.943
Presence of cystic degeneration (No.) (%)	3 (60%)	6 (75%)	.343
Peritumoral edema (mean) (cm)	1.8 (SD, 0.4)	2.4 (SD, 0.9)	.354
Heterogeneous enhancement (No.) (%)	5 (100%)	6 (75%)	.359
Leptomeningeal contact (No.) (%)	4 (80%)	7 (87.5%)	.641

Note:— ICP indicates intracranial pressure.

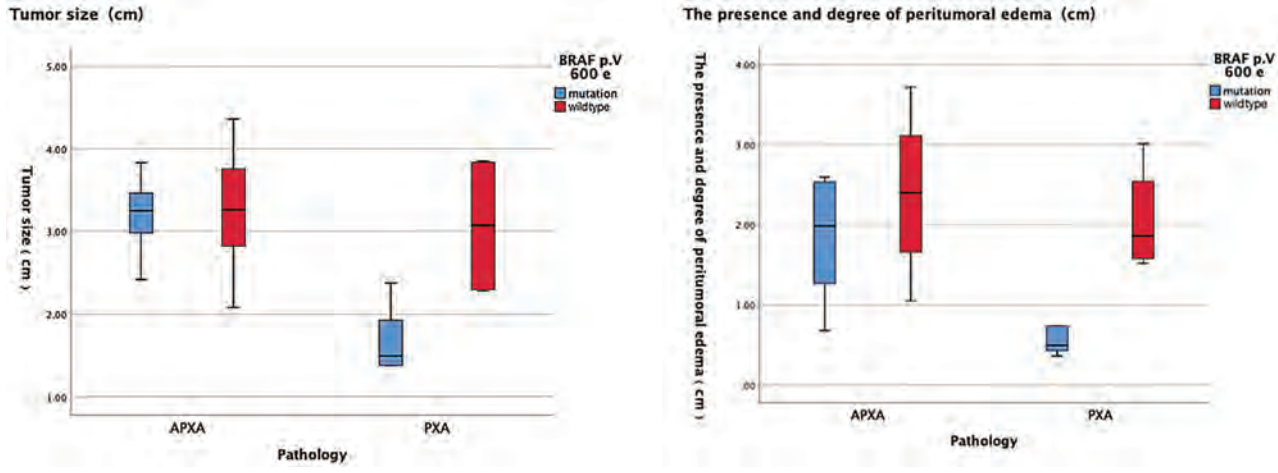

FIG 2. A significant difference ($P < .05$) between the *BRAF p. V600E*-mutant type PXA group and the *BRAF p. V600E* wild-type PXA group is demonstrated with both tumor size and the presence and degree of peritumoral edema. However, there was no significant difference in both tumor size and the maximum diameter of peritumoral edema between the *BRAF p. V600E*-mutant type APXA group and *BRAF p. V600E* wild-type APXA group.

BRAF p. V600E wild-type PXA may be more similar to high-grade gliomas in morphology. This conclusion may provide clinicians with strategies for tumor resection: For tumors identified by preoperative MR imaging such as *BRAF p. V600E* wild-type, more aggressive and expanded resection may be performed. For *BRAF p. V600E*-mutant tumors judged by preoperative MR imaging, a relatively conservative treatment strategy should be adopted, especially if the tumors are located in functional areas.

Table 4: Advanced MR imaging characteristics of the PXA and APXA groups

	PXA	APXA	*P* Value
ADCmin ($\times 10^{-6}$ mm^2/s)	951 (SD, 88)	755 (SD, 77)	<.001
ADCmean ($\times 10^{-6}$ mm^2/s)	1173 (SD, 159)	956 (SD, 106)	<.001

In the present study, we demonstrate that the rate of water diffusion of APXA, as reflected by the ADC ratio, was significantly lower than the rate of water diffusion of PXA, consistent with previous studies. Compared with *BRAF p. V600E*-mutant PXA, the ADC value of wild-type PXA was significantly lower. These results might be due to markedly high cellularity and a high nuclear/cytoplasmic ratio. Therefore, our findings reveal that ADC could be a useful imaging parameter for assessing the differences between *BRAF p. V600E*-mutant PXA and wild-type PXA. Only a few prior studies in the literature evaluated PXA using DWI.[37] The results of this study underline the usefulness of this simple imaging biomarker for radiogenomic correlation. However, future investigations are needed to better define the relationship between DWI features of *BRAF p. V600E*-mutant PXA and tumoral microarchitecture.

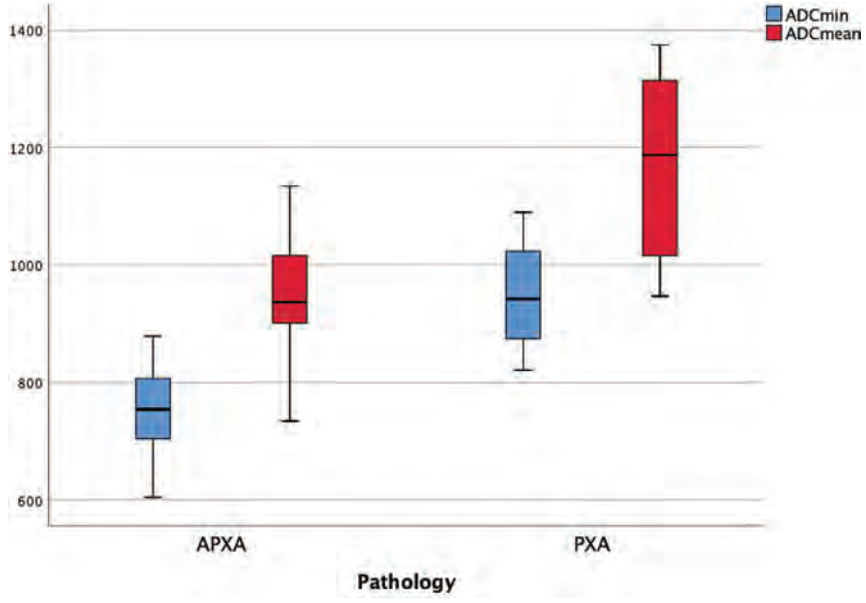

FIG 3. Boxplots representing ADCmin and ADCmean of PXA and APXA. A significant difference ($P < .05$) between PXA and APXA is demonstrated with both ADCmin and ADCmean.

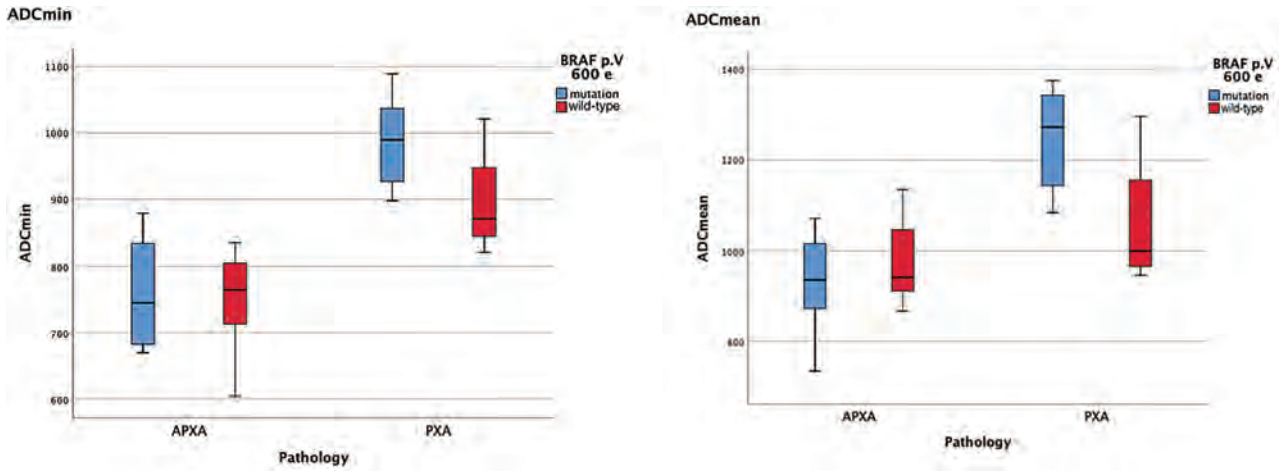

FIG 4. A significant difference ($P < .05$) between the *BRAF p. V600E*-mutant type PXA group and the *BRAF p. V600E* wild-type PXA group is demonstrated with both ADCmin and ADCmean. However, there was no significant difference in both ADCmin and ADCmean between the *BRAF p. V600E*-mutant type APXA group and *BRAF p. V600E* wild-type APXA group.

Table 5: Advanced MR imaging characteristics of the *BRAF p. V600E*-mutant PXA and *BRAF p. V600E* wild-type PXA groups

	BRAF p. V600E-Mutant PXA	*BRAF p. V600E* Wild-Type PXA	*P* Value
ADCmin ($\times 10^{-6}$ mm^2/s)	988 (SD, 73)	896 (SD, 86)	.047
ADCmean ($\times 10^{-6}$ mm^2/s)	1248 (SD, 116)	1060 (SD, 159)	.049

Table 6: Advanced MR imaging characteristics of the *BRAF p. V600E*-mutant APXA and *BRAF p. V600E* wild-type APXA groups

	BRAF p. V600E-Mutant APXA	*BRAF p. V600E* Wild-Type APXA	*P* Value
ADCmin ($\times 10^{-6}$ mm^2/s)	762 (SD, 92)	750 (SD, 73)	1
ADCmean ($\times 10^{-6}$ mm^2/s)	925 (SD, 131)	974 (SD, 92)	.724

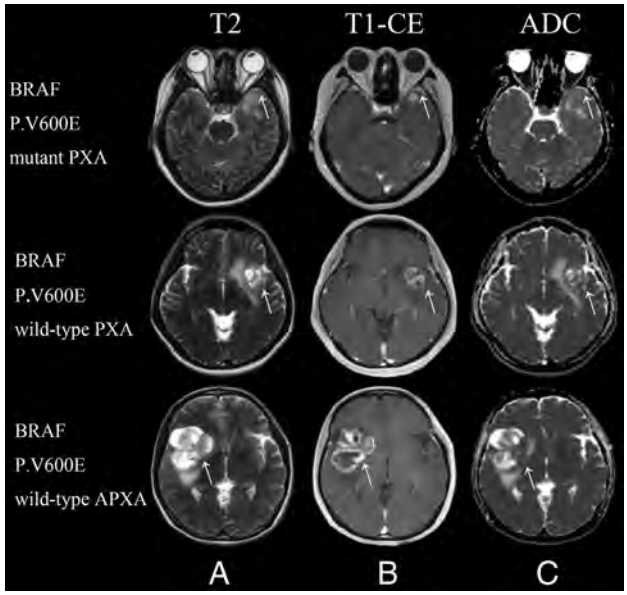

FIG 5. Conventional and advanced MR images of *BRAF p. V600E*-mutant and wild-type PXA. *Upper row*: A 27-year-old female patient with a *BRAF p. V600E*-mutant pleomorphic astrocytoma. T2WI (*A*) and contrast-enhanced T1WI (*B*) show a homogeneous contrast-enhancing solid tumor with mild perilesional edema located in the temporal lobe. *C*, A correlative ADC map shows the tumor with an elevated ADC value (ADCmin = 1089). *Second row:* A 53-year-old male patient with a *BRAF p. V600E* wild-type pleomorphic astrocytoma. T2WI (*A*) and contrast-enhanced T1WI (*B*) show a heterogeneous contrast-enhancing tumor with cystic degeneration and marked perilesional edema located in the insula. *C*, A correlative ADC map shows the lesion with a decreased ADC value (ADCmin = 875). *Third row*: A 46-year-old female patient with a *BRAF p. V600E* wild-type anaplastic pleomorphic astrocytoma. T2WI (*A*) and contrast-enhanced T1WI (*B*) show a heterogeneous contrast-enhancing tumor with cystic degeneration and marked perilesional edema located in the insula. *C*, A correlative ADC map shows the lesion with diffusion restriction (ADCmin = 704). CE indicates contrast-enhanced.

We did not find any MR imaging differences between the *BRAF p. V600E*-mutant APXA and the wild-type, whether using conventional or advanced imaging, possibly because the imaging features of APXA itself, similar to the imaging features of high-grade astrocytomas, mask the differences caused by *BRAF p. V600E*-mutant. Vuong et al[20] previously proposed that *BRAF p. V600E* only showed a significant improvement in patient survival in low-grade tumors. These results illustrate the limitations of the *BRAF p. V600E*-mutant on MR imaging morphologic and clinical outcomes of APXA.

Several potential limitations of this study should be mentioned. First, our research is a single-center observational retrospective study. The influence caused by the deviation of the retrospective study cannot be excluded. Second, although the sample size included in this study is relatively large among the reports on PXA thus far, the number of patients in our study remained limited, whether it was PXA or APXA, *BRAF p. V600E*-mutant or wild-type. Therefore, the conclusions should be interpreted with caution. Third, because ADC values were not used to guide the biopsy in this retrospective study, it was not possible to evaluate the correlations between regions of lower ADC in PXA and hypercellularity point to point. These correlations should be performed in our future study. Larger multicenter prospective studies are necessary to perform an accurate analysis of the relationship between imaging features and genomic characteristics of this rare tumor.

CONCLUSIONS

BRAF p. V600E wild-type PXA can present with more aggressive conventional and advanced MR imaging features, mimicking high-grade astrocytomas at initial diagnosis, than *BRAF p. V600E*-mutant PXA. Greater maximum tumor diameter, heterogeneous contrast enhancement, obvious peritumoral edema, and lower ADCmin and ADCmean are more common features in *BRAF p. V600E* wild-type PXA compared with *BRAF p. V600E*-mutant PXA. Neurosurgeons should carefully interpret MR images before an operation in cases that may be considered PXA and select an appropriate surgical strategy according to the prediction of *BRAF p. V600E* genotype.

Disclosure forms provided by the authors are available with the full text and PDF of this article at www.ajnr.org.

REFERENCES

1. Rao AA, Laack NN, Giannini C, et al. **Pleomorphic xanthoastrocytoma in children and adolescents.** *Pediatr Blood Cancer* 2010;55:290–94 CrossRef Medline
2. Kepes JJ, Rubinstein LJ, Eng LF. **Pleomorphic xanthoastrocytoma: a distinctive meningocerebral glioma of young subjects with relatively favorable prognosis—a study of 12 cases.** *Cancer* 1979;44:1839–52
3. Kleihues P, Burger PC, Scheithauer BW. **The new WHO classification of brain tumors.** *Brain Pathol* 1993;3:255–68 CrossRef Medline
4. Louis DN, Ohgaki H, Wiestler OD, et al. **The 2007 WHO classification of tumors of the central nervous system.** *Acta Neuropathol* 2007;114:97–109 CrossRef Medline
5. Ida CM, Rodriguez FJ, Burger PC, et al. **Pleomorphic xanthoastrocytoma: natural history and long-term follow-up.** *Brain Pathol* 2015;25:575–86 CrossRef Medline
6. Hirose T, Ishizawa K, Sugiyama K, et al. **Pleomorphic xanthoastrocytoma: a comparative pathological study between conventional and anaplastic types.** *Histopathology* 2008;52:183–93 CrossRef Medline
7. Giannini C, Scheithauer BW, Burger PC, et al. **Pleomorphic xanthoastrocytoma: what do we really know about it?** *Cancer* 1999;85:2033–45

8. Louis DN, Perry A, Reifenberger G, et al. **The 2016 World Health Organization Classification of Tumors of the Central Nervous System: a summary.** *Acta Neuropathol* 2016;131:803–20 CrossRef Medline
9. Wesseling P, Capper D. **WHO 2016 classification of gliomas.** *Neuropathol Appl Neurobiol* 2018;44:139–50 CrossRef Medline
10. Marton E, Feletti A, Orvieto E, et al. **Malignant progression inpleomorphic xanthoastrocytoma: personal experience and review of the literature.** *J Neurol Sci* 2007;252:144–53 CrossRef Medline
11. Rutkowski MJ, Oh T, Niflioglu GG, et al. **Pleomorphic xanthoastrocytoma with anaplastic features: retrospective case series.** *World Neurosurg* 2016;95:368–74 CrossRef Medline
12. Ma C, Feng R, Chen H, et al. **BRAF V600E, TERT, and IDH2 mutations in pleomorphic xanthoastrocytoma: observations from a large case-series study.** *World Neurosurg* 2018;120:e1225–33 CrossRef Medline
13. Dias-Santagata D, Lam Q, Vernovsky K, et al. **BRAF V600E mutations are common in pleomorphic xanthoastrocytoma: diagnostic and therapeutic implications.** *PLoS One* 2011;6:e17948 CrossRef Medline
14. Tatevossian RG, Lawson AR, Forshew T, et al. **MAPK pathway activation and the origins of pediatric low-grade astrocytomas.** *J Cell Physiol* 2010;222:509–14 CrossRef Medline
15. Jacob K, Quang-Khuong DA, Jones DT, et al. **Genetic aberrations leading to MAPK pathway activation mediate oncogene-induced senescence in sporadic pilocytic astrocytomas.** *Clin Cancer Res* 2011;17:4650–60 CrossRef Medline
16. Maurer G, Tarkowski B, Baccarini M. **Raf kinases in cancer: roles and therapeutic opportunities.** *Oncogene* 2011;30:3477–88 CrossRef Medline
17. Schindler G, Capper D, Meyer J, et al. **Analysis of BRAF V600E mutation in 1,320 nervous system tumors reveals high mutation frequencies in pleomorphic xanthoastrocytoma, ganglioglioma and extra-cerebellar pilocytic astrocytoma.** *Acta Neuropathol* 2011;121:397–405 CrossRef Medline
18. Chamberlain MC. **Salvage therapy with BRAF inhibitors for recurrent pleomorphic xanthoastrocytoma: a retrospective case series.** *J Neurooncol* 2013;114:237– 40 CrossRef Medline
19. Tabouret E, Bequet C, Denicolaï E, et al. **BRAF mutation and anaplasia may be predictive factors of progression-free survival in adult pleomorphic xanthoastrocytoma.** *Eur J Surg Oncol* 2015;41:1685–90 CrossRef Medline
20. Vuong HG, Altibi AM, Duong UN, et al. **BRAF mutation is associated with an improved survival in glioma-a systematic review and meta-analysis.** *Mol Neurobiol* 2018;55:3718–24 CrossRef Medline
21. Tonse R, Gupta T, Epari S, et al. **Impact of WHO 2016 update of brain tumor classification, molecular markers and clinical outcomes in pleomorphic xanthoastrocytoma.** *J Neurooncol* 2018;136:343–50 CrossRef Medline
22. Brown NF, Carter T, Kitchen N, et al. **Dabrafenib and trametinib in BRAFV600E mutated glioma.** *CNS Oncol* 2017;6:291–96 CrossRef Medline
23. She D, Liu J, Xing Z, et al. **MR imaging features of anaplastic pleomorphic xanthoastrocytoma mimicking high-grade astrocytoma.** *AJNR Am J Neuroradiol* 2018;39:1446–52 CrossRef Medline
24. Louis DN, Wesseling P, Aldape K, et al. **cIMPACT-NOW update 6: new entity and diagnostic principle recommendations of the cIMPACT-Utrecht meeting on future CNS tumor classification and grading.** *Brain Pathol* 2020;30:844–56 CrossRef Medline
25. Gimi B, Cederberg K, Derinkuyu B, et al. **Utility of apparent diffusion coefficient ratios in distinguishing common pediatric cerebellar tumors.** *Acad Radiol* 2012;19:794–800 CrossRef Medline
26. Mukherjee P, Miller JH, Shimony JS, et al. **Normal brain maturation during childhood: developmental trends characterized with diffusion-tensor MR imaging.** *Radiology* 2001;221:349–58 CrossRef Medline
27. Perkins SM, Mitra N, Fei W, et al. **Patterns of care and outcomes of patients with pleomorphic xanthoastrocytoma: a SEER analysis.** *J Neurooncol* 2012;110:99–104 CrossRef Medline
28. Yan J, Cheng J, Liu F, et al. **Pleomorphic xanthoastrocytomas of adults: MRI features, molecular markers, and clinical outcomes.** *Sci Rep* 2018;8:14275 CrossRef Medline
29. Yang RR, Aibaidula A, Wang WW, et al. **Pediatric low-grade gliomas can be molecularly stratified for risk.** *Acta Neuropathol* 2018;136:641–55 CrossRef Medline
30. Lindsay AJ, Rush SZ, Fenton LZ. **Pediatric posterior fossa gangliomglioma: unique MRI features and correlation with BRAF V600E mutation status.** *J Neurooncol* 2014;118:395–404 CrossRef Medline
31. Ostrom QT, Gittleman H, Liao P, et al. **CBTRUS Statistical Report: Primary brain and other central nervous system tumors diagnosed in the United States in 2010-2014.** *Neuro Oncol* 2017;19:v1–88 CrossRef Medline
32. Thakkar JP, Dolecek TA, Horbinski C, et al. **Epidemiologic and molecular prognostic review of glioblastoma.** *Cancer Epidemiol Biomarkers Prev* 2014;23:1985–96 CrossRef Medline
33. Rasmussen BK, Hansen S, Laursen RJ, et al. **Epidemiology of glioma: clinical characteristics, symptoms, and predictors of glioma patients grade I-IV in the Danish Neuro-Oncology Registry.** *J Neurooncol* 2017;135:571–79 CrossRef Medline
34. Yu S, He L, Zhuang X, et al. **Pleomorphic xanthoastrocytoma: MR imaging findings in 19 patients.** *Acta Radiol* 2011;52:223–28 CrossRef Medline
35. Crespo-Rodriguez AM, Smirniotopoulos JG, Rushing EJ. **MR and CT imaging of 24 pleomorphic xanthoastrocytomas (PXA) and a review of the literature.** *Neuroradiology* 2007;49:307–15 CrossRef Medline
36. Purkait S, Bansal S, Malgulwar PB. **BRAF V600E-mutated central nervous system tumor with divergent morphological feature: anaplastic pleomorphic xanthoastrocytoma-like and astroblastoma-like.** *Neuropathology* 2019;39:64–67 CrossRef Medline
37. Moore W, Mathis D, Gargan L, et al. **Pleomorphic xanthoastrocytoma of childhood: MR imaging and diffusion MR imaging features.** *AJNR Am J Neuroradiol* 2014;35:2192–96 CrossRef Medline

Idiopathic Intracranial Hypertension is Associated with a Higher Burden of Visible Cerebral Perivascular Spaces: The Glymphatic Connection

O. Jones, J. Cutsforth-Gregory, J. Chen, M.T. Bhatti, J. Huston, and W. Brinjikji

ABSTRACT

BACKGROUND AND PURPOSE: Research suggests a connection between idiopathic intracranial hypertension and the cerebral glymphatic system. We hypothesized that visible dilated perivascular spaces, possible glymphatic pathways, would be more prevalent in patients with idiopathic intracranial hypertension. This prevalence could provide a biomarker and add evidence to the glymphatic connection in the pathogenesis of idiopathic intracranial hypertension.

MATERIALS AND METHODS: We evaluated 36 adult (older than 21 years of age) patients with idiopathic intracranial hypertension and 19 controls, 21–69 years of age, who underwent a standardized MR imaging protocol that included high-resolution precontrast T2- and T1-weighted images. All patients had complete neuro-ophthalmic examinations for papilledema. The number of visible perivascular spaces was evaluated using a comprehensive 4-point qualitative rating scale, which graded the number of visible perivascular spaces in the centrum semiovale and basal ganglia; a 2-point scale was used for the midbrain. Readers were blinded to patient diagnoses. Continuous variables were compared using a Student *t* test.

RESULTS: The mean number of visible perivascular spaces overall was greater in the idiopathic intracranial hypertension group than in controls (4.5 [SD, 1.9] versus 2.9 [SD, 1.9], respectively; $P = .004$). This finding was significant for centrum semiovale idiopathic intracranial hypertension (2.3 [SD, 1.4] versus controls, 1.3 [SD, 1.1], $P = .003$) and basal ganglia idiopathic intracranial hypertension (1.7 [SD, 0.6] versus controls, 1.2 [SD, 0.7], $P = .009$). There was no significant difference in midbrain idiopathic intracranial hypertension (0.5 [SD, 0.5] versus controls, 0.4 [SD, 0.5], $P = .47$).

CONCLUSIONS: Idiopathic intracranial hypertension is associated with an increased number of visible intracranial perivascular spaces. This finding provides insight into the pathophysiology of idiopathic intracranial hypertension, suggesting a possible relationship between idiopathic intracranial hypertension and glymphatic dysfunction and providing another useful biomarker for the disease.

ABBREVIATIONS: IIH = idiopathic intracranial hypertension; PVS = perivascular spaces

Idiopathic intracranial hypertension (IIH), formerly known as pseudotumor cerebri and benign intracranial hypertension, is a disease of increased intracranial pressure without an identifiable cause.[1,2] Recently, a number of groups have postulated that the primary insult resulting in IIH could be dysfunction in CSF clearance via glymphatic pathways in the brain parenchyma.[3-8]

Briefly, the glymphatic system is a pseudolymphatic network in the brain performing a waste-clearance function via movement of CSF and interstitial fluid. Much of the glymphatic clearance is dependent on perivascular spaces (PVS). CSF is produced by the choroid plexus and exits the ventricular system via the foramina of Magendie and Luschka to the subarachnoid space. From the subarachnoid space, it enters the periarterial spaces (ie, PVS), traveling from the cortex toward the deep white matter along the courses of pial and perforator arteries in a centripetal distribution.[9] From the periarterial spaces, CSF is driven into the brain interstitium via aquaporin channels, mostly formed by the footplates of astrocytes.[10] CSF influx drives existing interstitial fluid back into the perivenous spaces surrounding large-caliber draining veins (Fig 1).[9] How CSF is reabsorbed at the large-caliber veins remains unclear, but a dural lymphatic pathway and a venous outflow pathway have been proposed, using dural lymphatic channels and arachnoid granulations, respectively.[4]

It has been hypothesized that in IIH, there is congestion of the lymphatic CSF outflow pathway of the glymphatic system.[3,4]

Received March 29, 2021; accepted after revision August 22.

From the Departments of Radiology (O.J., J.H., W.B.), Neurology (J.C.-G., J.C., M.T.B.), and Ophthalmology (J.C., M.T.B.), Mayo Clinic, Rochester, Minnesota.

Please address correspondence to Waleed Brinjikji, MD, Department of Radiology, Mayo Clinic, 200 First St SW, Rochester MN 55905; e-mail: brinjikji.waleed@mayo.edu; @wbrinjikji

http://dx.doi.org/10.3174/ajnr.A7326

In other words, there may be impaired transport of interstitial fluid from the glymphatic system to the venous blood of the dural venous sinuses, triggering a cascade of events resulting in IIH.

A multitude of brain and orbital MR imaging findings have been associated with IIH.[11] The most sensitive MR imaging correlate is transverse sinus stenosis.[12] Other findings include the appearance of an empty sella (>50% CSF filling of the sella with pituitary displacement), flattening of the posterior globes, protrusion of the optic nerve discs, and CSF enlarged/tortuous optic nerve sheaths.[11,13]

One imaging finding that has not been studied in association with IIH is the presence of dilated PVS, which have been proposed to be a component of the glymphatic pathway and can be dilated in a number of disease states associated with glymphatic disease, including small-vessel disease, dementia, multiple sclerosis, and other autoimmune diseases.[14-23] As discussed by others, we hypothesize that there is an element of glymphatic dysfunction in IIH. Because PVS have been shown to be a part of the glymphatic clearance pathway, we hypothesize that dilated PVS visible on T2-weighted MR imaging sequences are associated with IIH. Demonstrating this connection could provide valuable evidence toward glymphatic dysfunction contributing to the pathophysiology of IIH. This may serve as a both a useful imaging biomarker for the disease as well as a potential therapeutic target.

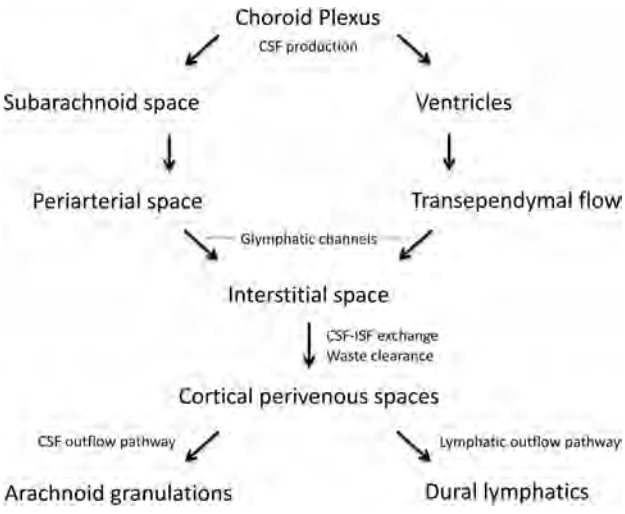

FIG 1. CSF-glymphatic flow chart. CSF is produced in the choroid plexus and takes a periarterial and/or a transependymal course into the interstitial space, displacing pre-existing interstitial fluid into cortical perivenous spaces where it is absorbed by arachnoid granulations and/or dural lymphatics. ISF indicates interstitial fluid.

MATERIALS AND METHODS

Patient Population

Adult patients with IIH were included if they met the diagnostic criteria put forth by Friedman et al[13] and had ophthalmologic evidence of papilledema.

Age-matched patients (SD, 2 years) in the control group were enrolled in accordance with the following criteria: a completed MR imaging examination without a diagnosis of intracranial hypertension as established by the above-mentioned criteria and without abnormalities on MR imaging. Patients with incomplete or poor-quality MRIs were excluded.

Imaging Protocol

The MR imaging protocol included high-resolution T2 and T1 MPRAGE precontrast images on various (GE Healthcare) 3T scanners with an 8-channel head coil. Some but not all patients underwent FLAIR imaging. Patients were scanned without sedation. The parameters for fast spin-echo T2-weighted imaging were the following: TR = 5234 ms; TE = 95.744 ms; section thickness = 4 mm without a gap; FOV = 220 mm; and matrix size = 320 × 320. All patients also underwent a 2D-TOF MR venography with TR = 29, TE = 3.3, number of excitations = 1, and matrix size = 256 × 256.

Imaging Evaluation

Two radiologists, a neuroradiology fellow and a staff radiologist, quantified the number of PVS using a comprehensive qualitative rating scale that has been shown to have good observer agreement and was validated by Potter et al.[24] The radiologists rated the following sites: basal ganglia, centrum semiovale, and midbrain PVS. Basal ganglia and centrum semiovale PVS were rated 0 (none), 1 (1–10), 2 (11–20), 3 (21–40), and 4 (>40), and midbrain PVS were rated 0 (nonvisible) or 1 (visible). T2-weighted images were used to quantify the PVS. T1-weighted images and FLAIR images (if available) were used to differentiate between PVS and other lesions.

Statistical Analysis

We calculated κ statistics for rating, assessed the consistency in the use of categories of PVS (Bhapkar test), and reviewed sources of discrepancy.

RESULTS

The visible number of overall PVS was higher in patients with IIH than in the control group (IIH mean total, 4.5 [SD, 1.9] versus controls, 2.9 [SD, 1.9]; $P = .004$). Findings are summarized in Table 1. This was true for all sites quantified except the midbrain: IIH centrum semiovale (2.3 [SD, 1.4] versus control centrum semiovale, 1.3 [SD, 1.1], $P = .003$); IIH basal ganglia (1.7 [SD, 0.6] versus control basal ganglia, 1.2 [SD, 0.7], $P = .009$); and IIH midbrain (0.5

Table 1: Quantification of perivascular spaces by site in patients with IIH versus controls

Location	IIH Mean No. of Dilated PVS (SD)	Control Mean No. of Dilated PVS (SD)	*P* Value	*k* Value (mean) (range)
Centrum semiovale	2.3 (1.4)	1.3 (1.1)	.003	0.58 (0.51–0.67)
Basal ganglia	1.7 (0.6)	1.2 (0.7)	.009	0.85 (0.81–0.89)
Midbrain	0.5 (0.5)	0.4 (0.5)	.47	0.47 (0.40–0.54)
Total	4.5 (1.9)	2.9 (1.9)	.004	0.71 (0.65–0.76)

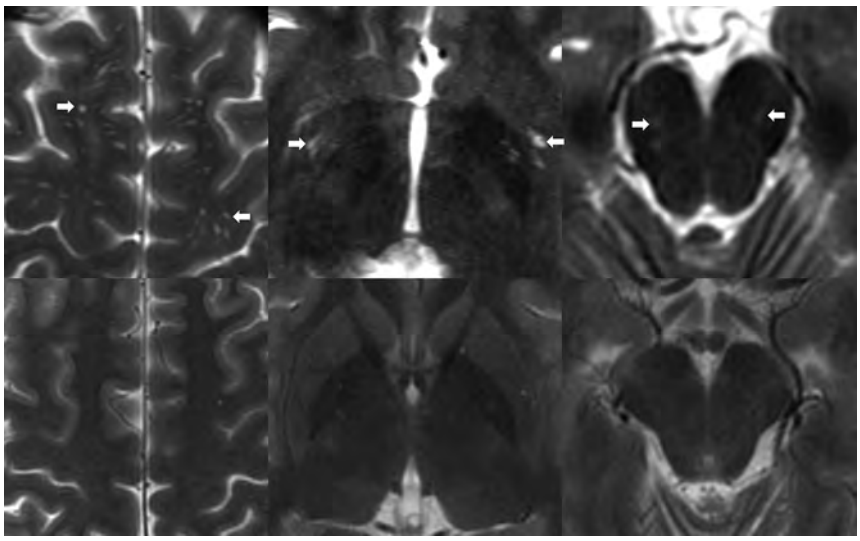

FIG 2. Fast spin-echo T2-weighted high-resolution images showing dilated PVS in the midbrain in a patient with IIH (*upper row*) and a healthy control (*lower row*). Elongated CSF-filled structures (*arrows*) are seen in the expected locations: centrum semiovale supratentorial white matter (*left*), basal ganglia (*middle*), and midbrain (*right*).

Table 2: Baseline characteristics[a]

	IIH	Control	*P* Value
No.	32	21	
Age (yr)	34.8 (9.2)	37.8 (13.5)	.38
No. (%) female sex	30 (93.8)	15 (71.4)	.03
Papilledema	32 (100.0)	0 (0.0)	<.0001
Headaches	31 (96.9)	7 (33.3)	<.0001
Pulsatile tinnitus	25 (75.0)	3 (14.3)	<.0001
Highest opening pressure	360 (133.5)	185 (35.3)	.01

[a] The average age between patients with IIH and healthy controls was similar. Most patients with IIH were women. More patients with IIH had papilledema, headaches, and pulsatile tinnitus. CSF opening pressure was lower in patients with IIH.

[SD, 0.5] versus control midbrain, 0.4 [SD, 0.5], $P = .47$). Interobserver agreement for the measurement of PVS was good ($\kappa = 0.71$ overall). By region, the κ statistic for the centrum semiovale was 0.58, for the basal ganglia, it was 0.85, and midbrain, 0.47. An example of dilated PVS in a patient with IIH and a healthy control is shown in Fig 2.

Baseline characteristics between the IIH group and healthy controls are in given Table 2. Average age was similar between the IIH group and healthy controls (IIH, 34.8 versus controls, 37.8 years; $P = .38$). There were more women in the IIH group (IIH, 30, versus controls, 15; $P = .03$). Papilledema, headaches, and pulsatile tinnitus were present in most of the IIH group and in a few healthy controls ($P < .0001$). Average highest opening pressure was 360 cm of water in the IIH group and 185 in the control group ($P < .01$). Four of 21 patients in the control group had evidence of venous sinus stenosis compared with 31 of 32 patients with IIH ($P < .0001$).

DISCUSSION

We found an increased number of dilated PVS in patients with IIH compared with controls. This correlation suggests a pathophysiologic role of the glymphatic system in IIH. Such a connection has been hypothesized in prior work on the roles of the glymphatic system in CSF accumulation and regulation.[4,9,10]

The presence of dilated PVS has been correlated with other disease states and is hypothesized to represent glymphatic disease. Glymphatic function is mediated by perivascular channels lined with aquaporin-4, cerebrovascular pulsatility, and metabolic waste clearance. Mestre et al[25] hypothesized that impairment of these components may have implications for the pathophysiology of small-vessel diseases. Perivascular spaces and their aquaporin-4 components must be structurally and functionally sound for proper glymphatic function, as confirmed by Iliff et al,[26] who used in vivo 2-photon imaging of small fluorescent tracers showing impaired glymphatic flow and function in animals lacking aquaporin-4. Impaired clearance of fluorescent-tagged amyloid β was also found, which may be significant for understanding Alzheimer disease. Iliff et al hypothesize that bulk perivascular CSF flow is impaired by glymphatic dysfunction due to vascular remodeling, enlarged perivascular spaces, aggregation of amyloid β in Alzheimer disease, and aggregation of granular osmophilic material in CADASIL. Of note, the largest observed CSF influxes, as demonstrated by fluorescent glymphatic flow imaging, are along the ventral perforating arteries of the basal ganglia, a common site for enlarged perivascular space formation.[26,27] Enlarged PVS are ubiquitous in almost all small-vessel diseases[28-30] and are independently associated with risk factors for small-vessel diseases, including hypertension and advanced age.[31-33]

Lenck et al[4] hypothesized that IIH appears to be related to glymphatic system overload. They hypothesized that overflow of the lymphatic CSF outflow pathway results in venous CSF outflow pathway restriction. In other words, if one pathway fails, the other must compensate. We speculate that impairment of interstitial fluid transport from the glymphatic system to dural venous sinus blood may trigger the hydrodynamic cascade of IIH. The degree of raised intracranial pressure may depend on the efficiency of the glymphatic system to compensate with augmented CSF reabsorption. Consequently, MR imaging signs of CSF hypertension such as transverse sinus stenosis and CSF dilated optic nerve sheaths may be a direct consequence of the overloaded glymphatic system and impaired CSF reabsorption.

Bezerra et al,[3] similarly, hypothesized that glymphatic dysfunction is a major contributor to the development of IIH. They hypothesized that diffuse interstitial fluid retention is a result of impaired glymphatic function from either augmented arterial perivascular space overflow into the interstitial fluid, impaired outflow of the interstitial fluid into the PVS, or both. In other words, the problem may be one of excessive inflow and/or

deficient outflow within the glymphatic pathway schematized in Fig 1. This hypothesis is supported by the fact that IIH-related vision loss is related to excessive fluid in the optic nerve sheaths, likely owing to impaired dural pathway glymphatic outflow along the glymphatics of the cranial nerves. Most interesting, patients with obesity, who have higher rates of IIH in general, are known to have a higher burden of perivascular and lymphatic dysfunction; this finding could lend further support to the glymphatic dysfunction hypothesis of IIH.

Patients with IIH have a substantially increased volume of extraventricular CSF and interstitial fluid,[34] including the PVS.[4] If glymphatic congestion increases interstitial and perivascular space fluid volume, this increase should contribute to increased intracranial pressure by the Monro-Kellie hypothesis. CSF-filled, dilated PVS may serve as a potential marker for the disease.

Our study has several limitations. First, ours is a hypothesis-generating study. Given the connection between an increased number of dilated PVS and glymphatic dysfunction demonstrated with other diseases and the growing number of groups hypothesizing that IIH is, in some respect, a glymphatic disorder, we sought to identify a biomarker that could allow testing of this hypothesis and lead to further study. Additional limitations include the small number of patients included, possible confounding in matching healthy controls for sex and body mass index, lack of automation in quantifying PVS, and a possible slight variance in imaging quality between studies due to patient and technical factors. Future studies with patients will be needed to confirm the association between an increased number of dilated PVS, glymphatic dysfunction, and IIH. An automated segmentation for quantifying dilated PVS such as that used by Potter et al[24] may be useful in eliminating interobserver variability. However, 2 observers were involved in this study with good interobserver variability. All patients received the same imaging protocol as it relates to quantifying the number of PVS, so variability related to technical factors was limited.

CONCLUSIONS

IIH is associated with dilated intracranial PVS, which may be detected with high-resolution T2-weighted MR imaging. These findings could provide valuable insight into the pathophysiology of IIH as it relates to glymphatic dysfunction. Future studies are needed to clarify whether the number of perivascular spaces is a biomarker in IIH disease.

ACKNOWLEDGMENTS

The authors thank Sonia Watson, PhD, for assistance in preparation of the manuscript.

Disclosures: Jeremy Cutsforth-Gregory—*UNRELATED*: *Royalties*: Oxford University Press, *Comments*: *Mayo Clinical Medical Neurosciences* (textbook). M. Tariq Bhatti—*UNRELATED*: *Consultancy*: Receptos.

REFERENCES

1. Markey KA, Mollan SP, Jensen RH, et al. **Understanding idiopathic intracranial hypertension: mechanisms, management, and future directions.** *Lancet Neurol* 2016;15:78–91 CrossRef Medline
2. Wall M. **Idiopathic intracranial hypertension.** *Neurol Clin* 2010;28:593–617 CrossRef Medline
3. Bezerra MLS, Ferreira A, de Oliveira-Souza R. **Pseudotumor cerebri and glymphatic dysfunction.** *Front Neurol* 2017;8:734 CrossRef Medline
4. Lenck S, Radovanovic I, Nicholson P, et al. **Idiopathic intracranial hypertension: the veno glymphatic connections.** *Neurology* 2018;91:515–22 CrossRef Medline
5. Mangalore S, Rakshith S, Srinivasa R. **Solving the riddle of "idiopathic" in idiopathic intracranial hypertension and normal pressure hydrocephalus: an imaging study of the possible mechanisms—Monro-Kellie 3.0.** *Asian J Neurosurg* 2019;14:440–52 CrossRef Medline
6. Mollan SP, Ali F, Hassan-Smith G, et al. **Evolving evidence in adult idiopathic intracranial hypertension: pathophysiology and management.** *J Neurol Neurosurg Psychiatry* 2016;87:982–92 CrossRef Medline
7. Mondejar V, Patsalides A. **The role of arachnoid granulations and the glymphatic system in the pathophysiology of idiopathic intracranial hypertension.** *Curr Neurol Neurosci Rep* 2020;20:20 CrossRef Medline
8. Nicholson P, Kedra A, Shotar E, et al. **Idiopathic intracranial hypertension: glymphedema of the brain.** *J Neuroophthalmol* 2021;41:93–97 CrossRef Medline
9. Benveniste H, Lee H, Volkow ND. **The glymphatic pathway: waste removal from the CNS via cerebrospinal fluid transport.** *Neuroscientist* 2017;23:454–65 CrossRef Medline
10. Jessen NA, Munk AS, Lundgaard I, et al. **The glymphatic system: a beginner's guide.** *Neurochem Res* 2015;40:2583–99 CrossRef Medline
11. Rehder D. **Idiopathic intracranial hypertension: review of clinical syndrome, imaging findings, and treatment.** *Curr Probl Diagn Radiology* 2020;49:205–14 CrossRef Medline
12. Morris PP, Black DF, Port J, et al. **Transverse sinus stenosis is the most sensitive MR imaging correlate of idiopathic intracranial hypertension.** *AJNR Am J Neuroradiol* 2017;38:471–77 CrossRef Medline
13. Friedman DI, Liu GT, Digre KB. **Revised diagnostic criteria for the pseudotumor cerebri syndrome in adults and children.** *Neurology* 2013;81:1159–65 CrossRef Medline
14. Boespflug EL, Simon MJ, Leonard E, et al. **Targeted assessment of enlargement of the perivascular space in Alzheimer's disease and vascular dementia subtypes implicates astroglial involvement specific to Alzheimer's disease.** *J Alzheimers Dis* 2018;66:1587–97 CrossRef Medline
15. Chabriat H, Joutel A, Dichgans M, et al. **CADASIL.** *Lancet Neurol* 2009;8:643–53 CrossRef Medline
16. Cordonnier C, Al-Shahi Salman R, Wardlaw J. **Spontaneous brain microbleeds: systematic review, subgroup analyses and standards for study design and reporting.** *Brain* 2007;130:1988–2003 CrossRef Medline
17. Doubal FN, MacLullich AM, Ferguson KJ, et al. **Enlarged perivascular spaces on MRI are a feature of cerebral small vessel disease.** *Stroke* 2010;41:450–54 CrossRef Medline
18. Granberg T, Moridi T, Brand JS, et al. **Enlarged perivascular spaces in multiple sclerosis on magnetic resonance imaging: a systematic review and meta-analysis.** *J Neurol* 2020;267:3199–3212 CrossRef Medline
19. Joutel A, Faraci FM. **Cerebral small vessel disease: insights and opportunities from mouse models of collagen IV-related small-vessel disease and cerebral autosomal dominant arteriopathy with subcortical infarcts and leukoencephalopathy.** *Stroke* 2014;45:1215–21 CrossRef Medline
20. Li Y, Zhu Z, Chen J, et al. **Dilated perivascular space in the midbrain may reflect dopamine neuronal degeneration in Parkinson's disease.** *Front Aging Neurosci* 2020;12:161 CrossRef Medline
21. Louveau A, Da Mesquita S, Kipnis J. **Lymphatics in neurological disorders: a neuro-lympho-vascular component of multiple sclerosis and Alzheimer's disease?** *Neuron* 2016;91:957–73 CrossRef Medline

22. Miyata M, Kakeda S, Iwata S, et al. **Enlarged perivascular spaces are associated with the disease activity in systemic lupus erythematosus.** *Sci Rep* 2017;7:12566 CrossRef Medline
23. Wardlaw JM, Smith C, Dichgans M. **Mechanisms of sporadic cerebral small vessel disease: insights from neuroimaging.** *Lancet Neurol* 2013;12:483–97 CrossRef Medline
24. Potter GM, Chappell FM, Morris Z, et al. **Cerebral perivascular spaces visible on magnetic resonance imaging: development of a qualitative rating scale and its observer reliability.** *Cerebrovasc Dis* 2015;39:224–31 CrossRef Medline
25. Mestre H, Kostrikov S, Mehta RI, et al. **Perivascular spaces, glymphatic dysfunction, and small vessel disease.** *Clin Sci (Lond)* 2017;131:2257–74 CrossRef Medline
26. Iliff JJ, Wang M, Liao Y, et al. **A paravascular pathway facilitates CSF flow through the brain parenchyma and the clearance of interstitial solutes, including amyloid beta.** *Sci Transl Med* 2012;4:147ra111 CrossRef Medline
27. Yang L, Kress BT, Weber HJ, et al. **Evaluating glymphatic pathway function utilizing clinically relevant intrathecal infusion of CSF tracer.** *J Transl Med* 2013;11:107 CrossRef Medline
28. Federico A, Di Donato I, Bianchi S, et al. **Hereditary cerebral small vessel diseases: a review.** *J Neurol Sci* 2012;322:25–30 CrossRef Medline
29. Yamamoto Y, Ihara M, Tham C, et al. **Neuropathological correlates of temporal pole white matter hyperintensities in CADASIL.** *Stroke* 2009;40:2004–11 CrossRef Medline
30. Yao M, Herve D, Jouvent E, et al. **Dilated perivascular spaces in small-vessel disease: a study in CADASIL.** *Cerebrovasc Dis* 2014;37:155–63 CrossRef Medline
31. Loos CM, Klarenbeek P, van Oostenbrugge RJ, et al. **Association between perivascular spaces and progression of white matter hyperintensities in lacunar stroke patients.** *PLoS One* 2015;10:e0137323 CrossRef Medline
32. Zhu YC, Tzourio C, Soumare A, et al. **Severity of dilated Virchow-Robin spaces is associated with age, blood pressure, and MRI markers of small vessel disease: a population-based study.** *Stroke* 2010;41:2483–90 CrossRef Medline
33. Potter GM, Doubal FN, Jackson CA, et al. **Enlarged perivascular spaces and cerebral small vessel disease.** *Int J Stroke* 2015;10:376–81 CrossRef Medline
34. Sorensen PS, Thomsen C, Gjerris F, et al. **Increased brain water content in pseudotumour cerebri measured by magnetic resonance imaging of brain water self-diffusion.** *Neurol Res* 1989;11:160–64 CrossRef Medline

Changes in Ventricular and Cortical Volumes following Shunt Placement in Patients with Idiopathic Normal Pressure Hydrocephalus

P.M. Cogswell, M.C. Murphy, M.L. Senjem, H. Botha, J.L. Gunter, B.D. Elder, J. Graff-Radford, D.T. Jones, J.K. Cutsforth-Gregory, C.G. Schwarz, F.B. Meyer, J. Huston III, and C.R. Jack Jr

ABSTRACT

BACKGROUND AND PURPOSE: While changes in ventricular and extraventricular CSF spaces have been studied following shunt placement in patients with idiopathic normal pressure hydrocephalus, regional changes in cortical volumes have not. These changes are important to better inform disease pathophysiology and evaluation for copathology. The purpose of this work is to investigate changes in ventricular and cortical volumes in patients with idiopathic normal pressure hydrocephalus following ventriculoperitoneal shunt placement.

MATERIALS AND METHODS: This is a retrospective cohort study of patients with idiopathic normal pressure hydrocephalus who underwent 3D T1-weighted MR imaging before and after ventriculoperitoneal shunt placement. Images were analyzed using tensor-based morphometry with symmetric normalization to determine the percentage change in ventricular and regional cortical volumes. Ventricular volume changes were assessed using the Wilcoxon signed rank test, and cortical volume changes, using a linear mixed-effects model ($P < .05$).

RESULTS: The study included 22 patients (5 women/17 men; mean age, 73 [SD, 6] years). Ventricular volume decreased after shunt placement with a mean change of −15.4% ($P < .001$). Measured cortical volume across all participants and cortical ROIs showed a mean percentage increase of 1.4% ($P < .001$). ROIs near the vertex showed the greatest percentage increase in volume after shunt placement, with smaller decreases in volume in the medial temporal lobes.

CONCLUSIONS: Overall, cortical volumes mildly increased after shunt placement in patients with idiopathic normal pressure hydrocephalus with the greatest increases in regions near the vertex, indicating postshunt decompression of the cortex and sulci. Ventricular volumes showed an expected decrease after shunt placement.

ABBREVIATIONS: DESH = disproportionately enlarged subarachnoid space hydrocephalus; HCTS = high-convexity or midline tight sulci; iNPH = idiopathic normal pressure hydrocephalus

Idiopathic normal pressure hydrocephalus (iNPH) is a clinicoradiologic syndrome of gait dysfunction, cognitive decline, and urinary incontinence, with a poorly understood etiology.[1] In recent years, a subtype of iNPH has been described, disproportionately enlarged subarachnoid space hydrocephalus (DESH), characterized by the imaging findings of ventriculomegaly, tight high-convexity sulci, and enlarged Sylvian fissures.[2–5] DESH is thought to represent morphologic changes related to disordered CSF dynamics and is part of the Japanese criteria for the diagnosis of iNPH.[6]

The symptoms of iNPH, particularly gait impairment, may be treated with CSF diversion, most commonly ventriculoperitoneal shunt placement.[7] Some of the morphologic features of iNPH and, in particular DESH, have also been shown to change after shunt placement. As expected, the ventricles decrease in size following shunt placement.[8,9] Additionally, the supra-Sylvian CSF spaces that are narrowed in patients with DESH increase in size with shunt placement, while the total brain parenchyma has been shown to undergo no change or slight expansion.[9,10]

Although changes in total brain parenchymal volume have been studied after shunt placement,[9] specific changes in cortical volume and how changes vary in different brain regions have not. Knowledge of changes in cortical volume is of interest to provide

Received May 22, 2021; accepted after revision August 18.

From the Departments of Radiology (P.M.C., M.C.M., J.L.G., C.G.S., J.H., C.R.J.), Information Technology (M.L.S.), Neurology (H.B., J.G.-R., D.T.J., J.K.C.-G.), Neurosurgery (B.D.E., F.B.M.), and Biomedical Engineering (B.D.E.), Mayo Clinic, Rochester, Minnesota.

This work was supported by the Theodore W. Batterman Family Foundation.

Paper previously presented, in part, at: Annual Meeting of the American Society of Neuradiology, May 20 to June 4, 2020; Virtual.

Please address correspondence to Petrice M. Cogswell, MD, PhD, Mayo Clinic, 200 First St SW, Rochester, MN 55902; e-mail: Cogswell.petrice@mayo.edu

Indicates article with online supplemental data.

http://dx.doi.org/10.3174/ajnr.A7323

further insight into morphometric disease-related changes and to better inform evaluation of cortical volumes in iNPH. We hypothesized that with decreases in ventricular volume after shunt placement, cortical volumes would increase secondary to decreased mass effect or crowding of the sulci at the vertex. We sought to investigate changes in ventricular volumes and regional changes in cortical volume in patients with iNPH following shunt placement.

MATERIALS AND METHODS

Patients

Patients with a diagnosis of iNPH and MR imaging with 3D T1WI performed before and after ventriculoperitoneal shunt placement from July 2015 through January 2021 were identified retrospectively. Patients were excluded if the 3D T1WI was not performed on a machine from the same MR imaging vendor, with the same field strength before and after shunt placement. Patients with suspected secondary hydrocephalus (eg, congenital outflow obstruction or prior intracranial intervention) based on imaging findings and review of the medical history were excluded. The study was performed under institutional review board approval.

MR Imaging

Imaging was performed on a 1.5T or 3T scanner (GE Healthcare) with a standard 8-channel head coil; by design, the field strength remained constant for each patient. Both 1.5T and 3T data were included because these field strengths have been shown to provide similar and reliable results for the morphometric analyses described below, as long as the field strength is constant within each individual. The 3D T1WI was performed with an MPRAGE sequence with the following 3T acquisition parameters: TR/TE = 6.3/2.6 ms, TI = 900 ms, FOV = 260 × 260 mm^2, matrix = 256 × 256, section thickness = 1.2 mm, sensitivity encoding Ry = 2. Acquisition parameters for 1.5T MPRAGE were TR/TE = 10.0/4.1 ms, TI = 1000 ms, FOV = 240 × 240 mm^2, matrix = 192 × 192, section thickness = 1.2 mm. If multiple imaging examinations were available, the MR imaging examination performed before and nearest to the date of shunt placement was chosen as the preshunt MR imaging examination. All eligible postshunt MR imaging examinations were included.

Qualitative Assessment for HCTS

Because we hypothesized that cortical volume would increase after shunt placement secondary to the resolution of mass effect from high-convexity or midline tight sulci (HCTS), a feature of DESH, the presence of HCTS was qualitatively determined. Two readers (P.M.C., J.G.R.) individually reviewed the preshunt MR imaging examinations for each patient to determine whether HCTS was present. Disagreement was settled by consensus review.

Measurement of Ventricular and Cortical Volume Changes

Tensor-based morphometry with symmetric normalization[11] was used to determine the percentage change in ventricular and regional cortical volumes between MR imaging examinations for each patient. In this technique, all possible pairs of MR imaging examinations for a patient are coregistered and warped to each other to reduce measurement variability, improve accuracy in longitudinal measurements, and allow improved power to detect more subtle changes compared with an analysis of independently calculated volume measurements for each time point.[11–13] Before analysis, quality control was performed to exclude examinations with motion or failed segmentation.

For the tensor-based morphometry with symmetric normalization analysis, first, each T1WI was run through the statistical parametric mapping (SPM12; http://www.fil.ion.ucl.ac.uk/spm/software/spm12) unified segmentation[14] pipeline to obtain tissue (gray matter, white matter, and CSF) segmentations as well as bias-corrected gray-scale images. For each patient, all included T1WI was rigidly coregistered to that patient's common mean using SPM12 and run through an in-house-developed differential bias-correction algorithm. The differential bias-correction algorithm–processed images were once again registered to their mean and resampled to 1-mm isotropic resolution. For each pair of MR imaging dates, the "MR imaging late" image was warped to the "MR imaging early" image, and the "MR imaging early" to "MR imaging late" image using Advanced Normalization Tools (ANTs) software (http://picsl.upenn.edu/software/ants/)[15] to derive a symmetric nonlinear deformation, which defines a mapping between the 2 images. These deformations were applied in each direction, and the resulting warped images were averaged with their original counterparts to create a "synthetic early" and a "synthetic late" image. An image of the log-transformed Jacobian determinants or voxelwise measure of local expansion or contraction of volume was formed for the deformation in each direction, and the synthetic early and synthetic late images were each run through SPM12 unified segmentation to get revised tissue probability maps in both the early and late image domains. The log-transformation (natural logarithm) of the Jacobian determinants was used for display purposes because it centers change about zero with values that approximately correspond to the percentage change.

The ventricles and cortical regions were segmented on the basis of the MCALT ADIR122 atlas (https://www.nitrc.org/projects/mcalt/),[16] by warping the MCALT template to the space of each early and late image. The ventricle atlas included the lateral and third ventricles. The cortex was parcellated into 43 regions (Online Supplemental Data) in each cerebral hemisphere for a total of 86 regions. Including only gray matter and CSF voxels for cortical and ventricle regions, respectively, the log-Jacobian images were parcellated into individual ROIs, and the mean log-Jacobian was computed within each ROI. For each ROI, the mean log-Jacobian value from the "late to early" deformation was averaged with the inverse of the log-Jacobian value in the "early to late" direction to estimate regional percentage change in volume. For primary analyses, the comparison of change between the preshunt MR imaging and the last available postshunt MR imaging was used. Surf Ice (https://www.nitrc.org/projects/surfice/) was used to visualize regional cortical volume changes.

Change in Ventricular and Cortical Volumes with Time

To evaluate the temporal profile of ventricular and cortical volume changes, we plotted the percentage change versus time. For

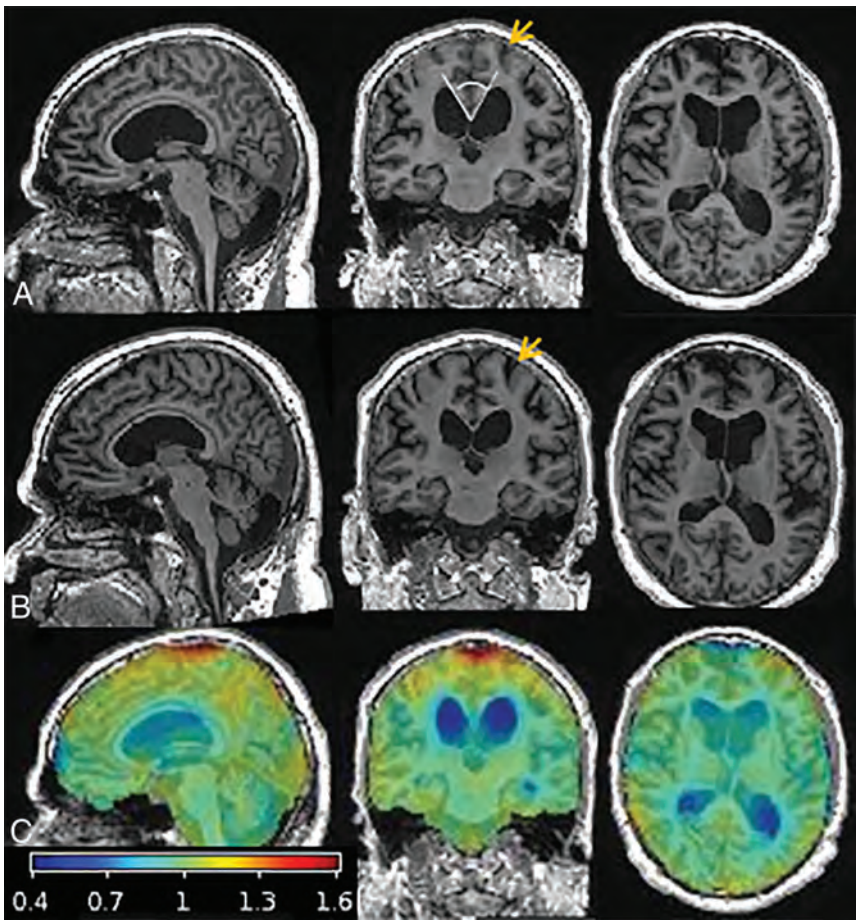

FIG 1. T1-weighted MR imaging and overlaid Jacobian maps of estimated changes between pre- and postshunt imaging for a representative patient, a 66-year-old man with iNPH. Sagittal, coronal, and axial slices of pre- (*A*) and postshunt (*B*) T1WI after registration to the patient's common mean and differential bias correction. *C*, Map of voxelwise Jacobian determinants overlaid on the preshunt T1WI to demonstrate changes that occurred after shunt placement by warping the late-to-early image: The ventricles contracted (blue) and CSF spaces at the vertex and surrounding parenchyma expanded (red and orange). Although changes in parenchymal volume are not visibly apparent on the T1WI, the coronal images demonstrate decreased crowding of the sulci at the vertex after shunt placement (*orange arrows*), corresponding to regions that showed an increase in cortical volume after shunt placement. The callosal angle measurement is demonstrated in the coronal image in row *A* (*white lines*).

these analyses, the date of the shunt placement was considered to be time zero because it is assumed that the volume changes being assessed are primarily the effect of shunt placement and that no discernible changes occurred in the patient's ventricle size or cortical volume from the date of the preshunt MR imaging to the date of shunt placement. The time (months) for each postshunt MR imaging was calculated as the time between shunt placement and the MR imaging examination. For this analysis, the calculated percentage change between each sequential set of MR imaging examinations was used.

To evaluate the degree of change that occurs in ventricular and gray matter volume in the first few months after shunt placement versus those that occur later, we computed the change in volume that occurred between the preshunt MR imaging and postshunt MR1 and the change between postshunt MR1 and MR2 in patients with 2 postshunt MR imaging examinations.

Posterior Callosal Angle

As a secondary analysis, the posterior callosal angle was evaluated because it is a more widely accessible and studied measure than ventricular volume, with an angle $<90°$ considered suggestive of iNPH.[17] The posterior corpus callosal angle was measured on the T1WI using a multiplanar reformatting tool (Visage, Version 7.1.14; Visage Imaging) as previously described[8,17] and is demonstrated in Fig 1*A*. The pre- and postshunt T1WI were coregistered. The anterior/posterior commissure plane was identified in the sagittal plane, and the callosal angle was measured on the coronal image perpendicular to the anterior/posterior commissure plane line at the posterior commissure for each of the pre- and postshunt images.

Statistical Analyses

Analyses were performed in Matlab (Version R2018a; MathWorks). A linear mixed-effects model was used to test for a significant change in cortical volume in the set of ROIs spanning the cerebral cortex. A 1-sided Wilcoxon signed rank test was used to evaluate a decrease in ventricular volume and an increase in the posterior callosal angle between the preshunt and latest MR imaging examination. For patients with 2 postshunt MR imaging examinations, the difference in volume changes between the preshunt and postshunt MR1 and the postshunt MR1 to postshunt MR2 was assessed using the Wilcoxon matched pairs signed rank test. Percentage change in ventricular and cortical volumes was summarized for patients with-versus-without HCTS, but statistical analysis was not performed due to low number of patients in the "without HCTS" group.

Pair-wise comparisons of associations in imaging metrics were assessed using the Spearman correlation. We evaluated the following associations: percent change in ventricular volume versus mean percent change in cortical volume, percent change in ventricular volume versus change in callosal angle, and change in callosal angle versus mean percent change in cortical volume.

Additional analyses were performed to assess the effect of shunt valve type and location on volume measurements. The Wilcoxon rank sum test was used to assess differences in ventricular volume and mean cortical volume change between patients with Codman Certas Plus (Integra LifeSciences) and Delta (Medtronic) valves and to compare cortical volume changes in the right-versus-left cerebral hemisphere for each cortical region,

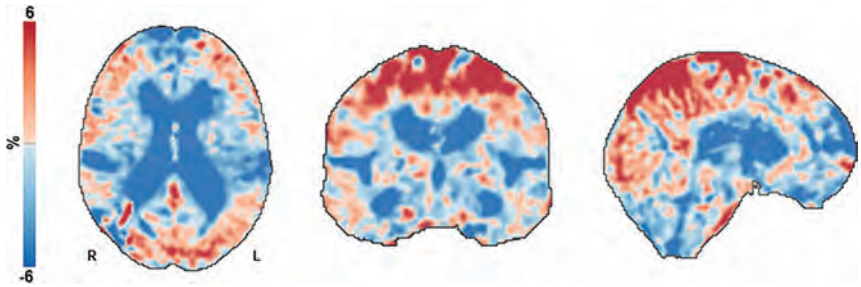

FIG 2. Voxelwise maps of estimated mean percentage change in volume from pre- to postshunt MR imaging across all patients. Axial, coronal, and sagittal slices of the mean estimated percentage change in volume (log-Jacobian, which is centered at zero) for all voxels within the total intracranial volume mask. In this display, the tissue class (CSF, gray matter, white matter) is not considered. After shunt placement, there was an expansion or increase in CSF and parenchymal volumes primarily near midline at the vertex (red). Contraction or decrease in volume occurred in the ventricles, extraventricular CSF spaces such as the Sylvian fissures, and anterior-inferior frontal and temporal convexities (blue).

because all patients had a right-sided shunt placement. For all statistical tests, $P < .05$ was considered significant.

RESULTS

Patients

We identified 26 patients with eligible pre- and postshunt MR imaging examinations. Two patients were excluded due to suspected secondary hydrocephalus in the setting of prior craniotomy for tumor resection. Two patients with iNPH were excluded, one due to image motion and one due to failed tissue-class assignment on the preshunt MR imaging examination. The study, thus, included 22 patients (5 women/17 men; mean age, 73 [SD, 6] years; range, 61–84 years). Preshunt MR imaging was performed, on average, 2.0 (SD, 2.4) months before shunt placement. There were 17 patients with 1 postshunt MR imaging examination, and the other 5 had 2 postshunt MR imaging examinations. With the date of shunt placement as time zero, the latest postshunt imaging was performed, on average, 7.0 (SD, 7.0) months (range, 1–25 months) after shunt placement. Although robust clinical metrics suitable for research purposes were not consistently available in this cohort, 20/22 patients reported sustained improvement in at least one of the clinical domains of gait, cognition, and incontinence during imaging follow-up.

Global Volume Changes

Pre- and postshunt T1WI with overlaid Jacobian determinant maps are shown for a representative patient in Fig 1. The estimated mean voxelwise percentage change in volume (log-Jacobian) from pre- to postshunt MR imaging among all patients is shown in Fig 2; the scale is compressed relative to the Jacobian maps in Fig 1, to better show regional parenchymal changes. The voxelwise maps demonstrated the global changes that occurred after shunt placement throughout the brain parenchyma, ventricles, and CSF spaces, including regions not specifically evaluated in regional analyses. The CSF spaces and parenchyma near the midline vertex expanded after shunt placement. The ventricles and Sylvian fissures contracted after shunt placement, and there were regions of parenchymal contraction at the anterior-inferior frontal and temporal lobes.

Percentage Change in Ventricular Volume

The mean percentage change in ventricular volumes across all patients was −15.4% (SD, 9.4%) ($P < .001$), while the degree of ventricular volume change varied among patients with a range of 1.1%−41.5% (Fig 3). For those patients with 2 postshunt follow-up MR imaging examinations ($n = 5$), there was a continued decrease in ventricular volume during the 2 examinations. On average, the mean percentage change in ventricular volume was similar between the preshunt MR imaging and the first postshunt examination (−9.4% [SD, 1.3%] at a mean of 2.1 [SD, 0.9] months), and in the first-to-second postshunt examinations (−10.5% [SD, 6.4%] from, on average, 3 months to 8.9 [SD, 3.4] months postshunt; $P = .81$).

Percentage Change in Cortical Volume

Measured cortical volume across all participants and cortical ROIs showed a statistically significant mean percentage increase of 1.4% (SD, 1.3%) ($P < .001$), with a range in mean cortical volume change among patients of −2.3%−3.7% (Fig 3). Consistent regional variations in percentage change in gray matter volume were seen in patients (Fig 4 and Online Supplemental Data). ROIs near the vertex showed the greatest increase in volume after shunt placement (eg, 4.1%–7.4% at the parietal superior, frontal superior, precuneus, parietal inferior, and paracentral lobule regions). Regions around the CSF spaces in the inferior brain showed, on average, small decreases in cortical volume after shunt placement (eg, −1.1% to −2.6% in the insula, amygdala, and hippocampal regions).

In the 5 patients with >1 postshunt MR imaging, the mean percentage change in cortical volume showed greater change from time zero (shunt placement) to the first postshunt examination than from the first-to-second postshunt examination, though the differences did not reach statistical significance (1.2% [SD, 1.3%] versus −0.01% [SD, 1.1%], $P = .19$). One of these patients showed a small average decrease in cortical volume from pre- to postshunt MR imaging. The other 4 patients showed an overall increase in cortical volume from the preshunt to the first postshunt MR imaging, with smaller, variable degrees of positive and negative changes from the first-to-second postshunt MR imaging. Of the 2 patients with initial increases in cortical volume followed by small decreases in cortical volume, one had a continued decrease in ventricular size from the first-to-second postshunt MRI and one had a relatively stable ventricular size between those time points.

Shunt Valve

Of the 22 patients, the first 9 had right-frontal-approach Delta 1.0 valve ventriculoperitoneal shunts, and the last 13 had right-parietal-approach Codman Certas Plus programmable valves. Differences in approach and types of shunts were due to the evolving

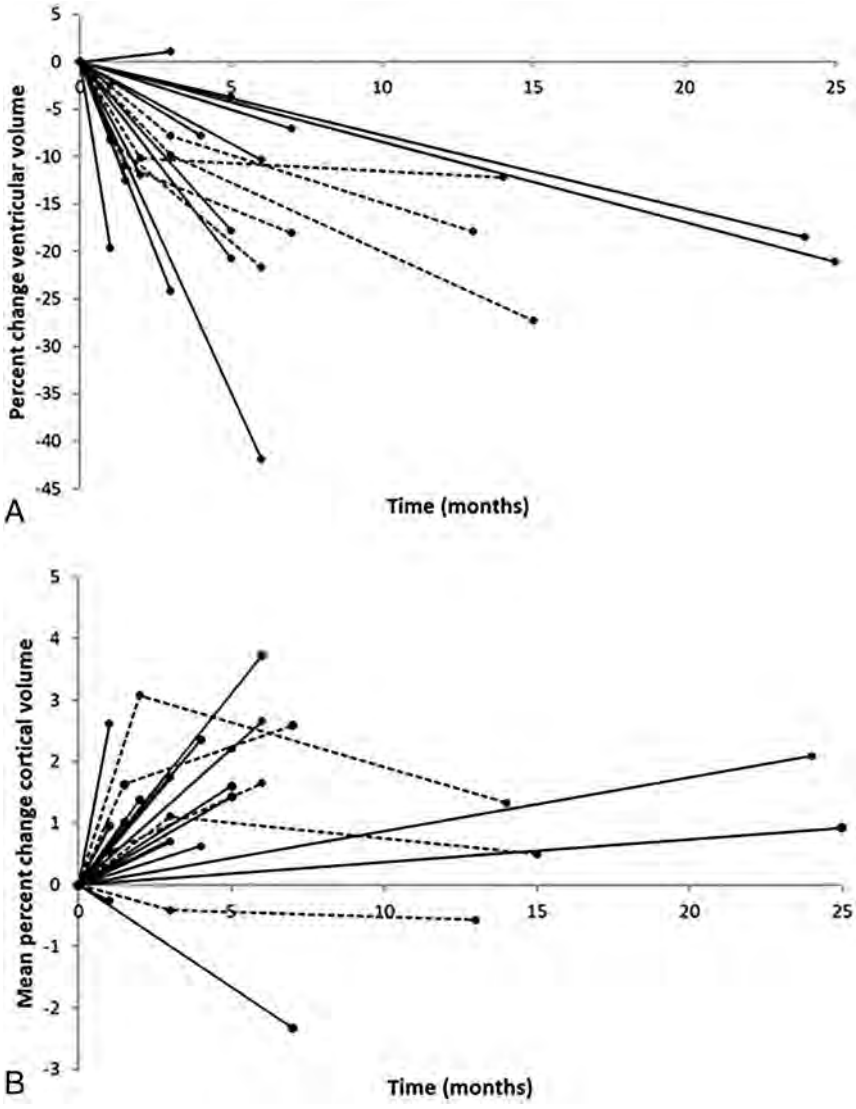

FIG 3. Percentage volume change by patient after shunt placement. Percent change in ventricular (*A*) and mean cortical (*B*) volume across all ROIs versus time. Each patient is represented by a *separate line*; patients with 1 postshunt MR imaging are represented by a *solid line*, and patients with 2 postshunt MRIs are represented by a *dotted line*. Time zero is the date of shunt placement. In general, ventricular volumes decreased and mean cortical volume increased after shunt placement. In the patients with 2 postshunt MRIs, there was a continued decrease in ventricular volume from postshunt MR1 to MR2 and a small variable change in cortical volume during that interval.

neurosurgical practice and surgeon preference. For all patients with the programmable valve, the initial shunt setting was 6, which was chosen as a conservative starting point to avoid overdrainage,[18] and the shunt setting was reduced to 5 within the first several months of follow-up.

The Delta valve did not produce any susceptibility artifacts or obscure adjacent parenchyma. The Codman Certas Plus valve caused susceptibility artifacts that occurred primarily in a portion of the image that was not classified as gray matter, with the exception of the right-inferior and mid-occipital and cerebellar regions, which are not of primary focus in the results of this study. There were no cases of failed processing secondary to shunt-related artifacts.

After excluding the right-inferior and midoccipital regions, which were obscured by artifacts in patients with the Codman Certas Plus valve, there was no statistically significant difference between the right and left sides for any of the cortical regions. Patients with a Codman Certas valve and a Delta valve showed similar changes in mean ventricular (−15.0% [SD, 10.3%] and −15.9% [SD, 8.6%], respectively, $P = .64$) and cortical volumes (1.2% [SD, 1.0%] and −1.5% [SD, 1.5%], respectively, $P = .50$).

Qualitative Assessment of HCTS

The readers agreed on the presence or absence of HCTS and judged HCTS to be present on the preshunt MR imaging examination in 20/22 (91%) patients. The 2 participants on which readers disagreed had ventriculomegaly with midline and convexity sulci that were relatively narrowed though not effaced. Although statistical comparison was not performed between patients with-versus-without HCTS due to the low number, on average, those without HCTS showed less change in ventricular and cortical volumes than those with HCTS (mean ventricular volume, −9.8% [SD, 3.0%] versus −15.9% [SD, 9.7%] and mean cortical volume change, 1.0% [SD, 0.5%] versus 1.4% [SD, 1.4%]).

Change in Callosal Angle

The callosal angle, on average, increased by a mean of 16.4° (SD, 11.8°) ($P < .001$) after shunt placement (69.0° [SD,19.7°] preshunt to 85.4° [SD, 20.6°] postshunt).

Association between Changes in Imaging Metrics

The mean cortical volume increased with decreases in ventricular volume ($\rho = -0.44$, $P = .04$). The change in callosal angle was not as strongly associated with the mean percentage change in cortical volume ($\rho = 0.21$, $P = .34$). The callosal angle increased (or normalized) with a decrease in ventricular volume, though the association of these metrics did not reach statistical significance ($\rho = -0.40$, $P = .06$). These associations are shown in the Online Supplemental Data.

DISCUSSION

We investigated changes in ventricular and regional cortical volumes after ventriculoperitoneal shunt placement in patients with iNPH. Along with decreases in ventricular volumes after shunt placement, there were changes in cortical volumes, with the

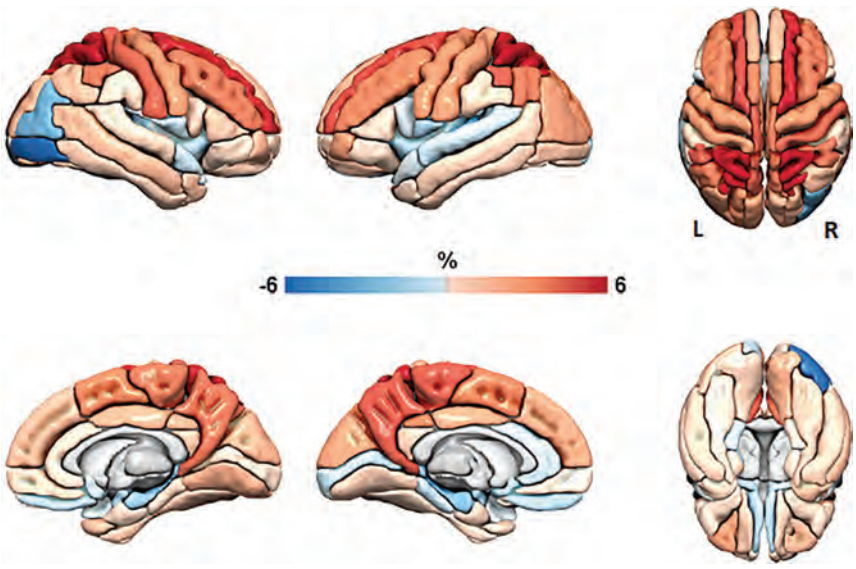

FIG 4. Regional cortical mean percentage volume change. Surface-renderings of mean percentage change in cortical volume among all participants by cortical region in the ADIR122 atlas. These data are a subset of the data shown in Fig 2, considering only voxels determined to be cortical gray matter and demonstrating ROI-wise results, the main analytic method used in this work. Red indicates an increase in volume or expansion from pre- to postshunt MR imaging examinations and is primarily present at the midline vertex regions. Blue indicates a decrease in volume or contraction and is seen adjacent to the temporal horns and Sylvian fissures as well as related to Codman Certas Plus valve artifacts (right occipital). The *first column* shows right-hemisphere lateral and medial views. *The second column* shows left-hemisphere lateral and medial views. The *third column* shows top and bottom views.

greatest increases in cortical volume at regions near the midline vertex.

The ventricles showed an anticipated decrease in size after shunt placement. The mean percentage decrease in ventricular volume of 15% in this study was similar to approximately 14% at 3–8 months after shunt placement in the study by Virhammar et al.[8] Ventricular volume changes occurred within the first few months after shunt placement, and in the subgroup of patients with multiple MR imaging examinations, there was a continued decrease in ventricular volume on subsequent imaging performed several months later. This time course of ventricular volume changes is similar to that described by Yamada et al.[9]

The posterior callosal angle showed a significant increase after shunt placement, as seen in prior studies.[8,9] The association of the change in callosal angle with the percentage change in cortical volume was not as strong as the association of the percentage change in ventricular volume with the percentage change in cortical volume. These findings support volumetric rather than linear measures of anatomy as more robust indicators of disease and treatment-related changes.[9,19]

The mean cortical volume across the cerebral cortex increased after shunt placement, though changes were topographically variable. The greatest increase in cortical volume occurred near the midline vertex, where although not quantified in this study, there was also expansion of the CSF spaces. These are the regions of sulcal effacement in patients presenting with iNPH, and, in particular, patients with DESH. Narrowing of the sulci in the midline vertex regions is associated with compression of the adjacent cortex. After shunt placement, the ventricles decrease in size, vertex CSF spaces expand, mass effect on the parenchyma lessens, and cortical volumes increase. The enlarged intra- and extraventricular CSF spaces and compression of the cortex in patients with iNPH and DESH may be misinterpreted as atrophy and has been termed "pseudoatrophy."[20] In this study, we showed that these findings are, at least in part, reversed after CSF diversion. Of note, neither DESH nor HCTS was required for inclusion in this study, nor is it required for a diagnosis of iNPH and shunt placement, but HCTS was present in all except 2 patients. These 2 patients without HCTS had lower-than-average postshunt changes in ventricular and cortical volumes. The number of patients in this study did not allow subgroup analyses comparing patients with-versus-without HCTS, other features of DESH, or the degree of DESH-like features, though such analyses would be of interest in future work.

While there was an increase in regional cortical volume near the vertex, regional cortical volume in the inferior aspect of the cerebral hemispheres, adjacent to contracted CSF spaces, showed a decrease in cortical volume after shunt placement. The etiology of these changes is likely multifactorial. Volume decreases may be due, in part, to partial volume effects from the adjacent contracting CSF spaces, given the relatively small size of the affected ROIs. Although iNPH and shunt placement are the primary drivers of morphologic changes for these patients in the study time period, a small and likely negligible degree of regional age-related cortical volume loss (which would affect temporal-limbic areas more than the cortex at the vertex) is possible.[21] Additionally, small changes (ie, on the order of $<1\%$) could be due to variability in longitudinal measurements, as has been seen in prior work.[11,13]

As in prior work evaluating total brain parenchymal volumes, in the subgroup of patients with 2 postshunt MR imaging examinations, cortical volume changes occurred predominantly in the first few months after shunt placement.[9] This observation is likely due to resolution of mass effect on the parenchyma with decreasing ventricular volume and enlarging vertex CSF spaces. After the vertex CSF spaces have decompressed, further decrease in ventricular size or change in CSF spaces would not be anticipated to have associated cortical volume changes. Small observed cortical volumes for long-term follow-up may be related to variations in CSF dynamics as well as variability in measurement.

Overall, the global CSF space and cortical volume changes observed after shunt placement correspond with improvement in the morphologic features of iNPH and DESH. As these entities have become more widely recognized in community populations[22,23] and

volumetric measurement is more widely applied in the clinical evaluation of cognitive decline, awareness of cortical volume changes associated with CSF dynamics disorders is important, to avoid misinterpretation of mass effect on the cortex or relatively low cortical volume as atrophy secondary to neurodegeneration, which may confound disease categorization and evaluation for copathology in the clinical or research setting.

There are limitations to this study. The spatial resolution varied from 1.0– to 1.2 mm, though we have found volumetric calculations at these resolutions comparable. Due to the retrospective nature and strict requirements that the 3D T1WI acquisitions be performed with the same imaging platform, the number of included patients is moderate. The time of postshunt follow-up imaging varied among patients. Despite these limitations, consistent, statistically significant changes were observed. In the future, standardized follow-up intervals and more patients with multiple postshunt MRIs would be beneficial to better delineate the timeline of morphologic changes that occur. Although it would be interesting to assess associations between imaging and clinical metrics, these patients did not undergo similar rigorous quantitative assessment of relevant clinical indices before and after shunt placement to allow such analyses.

CONCLUSIONS

We found a decrease in ventricular volume and an overall increase in cortical volume, greatest at the midline vertex, following shunt placement in patients with iNPH. Changes in cortical volume appeared to occur predominantly in the first few months after shunt placement, while ventricular volumes continued to decrease on subsequent follow-up. These changes correspond with improvement in the morphologic features of iNPH, and, specifically, DESH after CSF diversion. Awareness of the artificial reduction of cortical volumes in the setting of disordered CSF dynamics is important in the assessment for neurodegenerative disease, which may present with similar symptoms to iNPH or as copathology.

Disclosure forms provided by the authors are available with the full text and PDF of this article at www.ajnr.org.

REFERENCES

1. Adams RD, Fisher CM, Hakim S, et al. **Symptomatic occult hydrocephalus with normal cerebrospinal-fluid pressure.** *N Engl J Med* 1965;273:117–26 CrossRef Medline
2. Ishikawa M, Yamada S, Yamamoto K. **Early and delayed assessments of quantitative gait measures to improve the tap test as a predictor of shunt effectiveness in idiopathic normal pressure hydrocephalus.** *Fluids Barriers CNS* 2016;13:20 CrossRef Medline
3. Kitagaki H, Mori E, Ishii K, et al. **CSF spaces in idiopathic normal pressure hydrocephalus: morphology and volumetry.** *AJNR Am J Neuroradiol* 1998;19:1277–84 Medline
4. Yamashita F, Sasaki M, Takahashi S, et al. **Detection of changes in cerebrospinal fluid space in idiopathic normal pressure hydrocephalus using voxel-based morphometry.** *Neuroradiology* 2010;52:381–86 CrossRef Medline
5. Hashimoto M, Ishikawa M, Mori E, et al; Study of INPH on neurological improvement (SINPHONI), **Diagnosis of idiopathic normal pressure hydrocephalus is supported by MRI-based scheme: a prospective cohort study.** *Cerebrospinal Fluid Res* 2010;7:18 CrossRef Medline
6. Mori E, Ishikawa M, Kato T, et al; Japanese Society of Normal Pressure Hydrocephalus. **Guidelines for management of idiopathic normal pressure hydrocephalus: second edition.** *Neurol Med Chir (Tokyo)* 2012;52:775–809 CrossRef Medline
7. Toma AK, Papadopoulos MC, Stapleton S, et al. **Systematic review of the outcome of shunt surgery in idiopathic normal-pressure hydrocephalus.** *Acta Neurochir (Wien)* 2013;155:1977–80 CrossRef Medline
8. Virhammar J, Laurell K, Cesarini KG, et al. **Increase in callosal angle and decrease in ventricular volume after shunt surgery in patients with idiopathic normal pressure hydrocephalus.** *J Neurosurg* 2018;130:130–35 CrossRef Medline
9. Yamada S, Ishikawa M, Yamaguchi M, et al. **Longitudinal morphological changes during recovery from brain deformation due to idiopathic normal pressure hydrocephalus after ventriculoperitoneal shunt surgery.** *Sci Rep* 2019;9:17318 CrossRef Medline
10. Hiraoka K, Yamasaki H, Takagi M, et al. **Changes in the volumes of the brain and cerebrospinal fluid spaces after shunt surgery in idiopathic normal-pressure hydrocephalus.** *J Neurol Sci* 2010;296:7–12 CrossRef Medline
11. Vemuri P, Senjem ML, Gunter JL, et al; Alzheimer's Disease Neuroimaging Initiative. **Accelerated vs. unaccelerated serial MRI based TBM-SyN measurements for clinical trials in Alzheimer's disease.** *Neuroimage* 2015;113:61–69 CrossRef Medline
12. Ashburner J, Ridgway GR. **Symmetric diffeomorphic modeling of longitudinal structural MRI.** *Front Neurosci* 2012;6:197 CrossRef Medline
13. Cash DM, Frost C, Iheme LO, et al. **Assessing atrophy measurement techniques in dementia: results from the MIRIAD atrophy challenge.** *Neuroimage* 2015;123:149–64 CrossRef Medline
14. Ashburner J, Friston KJ. **Unified segmentation.** *Neuroimage* 2005;26:839–51 CrossRef Medline
15. Avants BB, Epstein CL, Grossman M, et al. **Symmetric diffeomorphic image registration with cross-correlation: evaluating automated labeling of elderly and neurodegenerative brain.** *Med Image Anal* 2008;12:26–41 CrossRef Medline
16. Schwarz CG, Gunter JL, Ward CP, et al. **The Mayo Clinic adult lifespan template: better quantification across the life span.** *Alzheimers Dement* 2017;13:P792 CrossRef
17. Ishii K, Kanda T, Harada A, et al. **Clinical impact of the callosal angle in the diagnosis of idiopathic normal pressure hydrocephalus.** *Eur Radiol* 2008;18:2678–83 CrossRef Medline
18. Khan QUA, Wharen RE, Grewal SS, et al. **Overdrainage shunt complications in idiopathic normal-pressure hydrocephalus and lumbar puncture opening pressure.** *J Neurosurg* 2013;119:1498–502 CrossRef Medline
19. Crook JE, Gunter JL, Ball CT, et al. **Linear vs volume measures of ventricle size: relation to present and future gait and cognition.** *Neurology* 2020;94:e549–56 CrossRef Medline
20. McCarty AM, Jones DT, Dickson DW, et al. **Disproportionately enlarged subarachnoid-space hydrocephalus (DESH) in normal pressure hydrocephalus misinterpreted as atrophy: autopsy and radiological evidence.** *Neurocase* 2019;25:151–55 CrossRef Medline
21. Jack CR, Petersen RC, Xu Y, et al. **The rate of medial temporal lobe atrophy in typical aging and Alzheimer's disease.** *Neurology* 1998;51:993–99 CrossRef Medline
22. Andersson J, Rosell M, Kockum K, et al. **Prevalence of idiopathic normal pressure hydrocephalus: a prospective, population-based study.** *PLoS One* 2019;14:e0217705 CrossRef Medline
23. Graff-Radford J, Gunter JL, Jones DT, et al. **Cerebrospinal fluid dynamics disorders: relationship to Alzheimer biomarkers and cognition.** *Neurology* 2019;93:e2237–46 CrossRef Medline

Clinical Implementation of 7T MRI for the Identification of Incidental Intracranial Aneurysms versus Anatomic Variants

P. Radojewski, J. Slotboom, A. Joseph, R. Wiest, and P. Mordasini

ABSTRACT

SUMMARY: Most unruptured intracranial aneurysms can be adequately characterized using 1.5T and 3T MR imaging. Findings in a subgroup of patients can remain unclear due to difficulties in distinguishing aneurysms from vascular anatomic variants. We retrospectively analyzed clinical data from 30 patients with suspected incidental aneurysms on 3T MR imaging who underwent 7T MR imaging. In all 30 cases, the differentiation of an aneurysm versus a vascular variant could be achieved. In 20 cases (66%), the initial suspected diagnosis was revised. Our findings suggest that 7T MR imaging provides a clarification tool for the group of patients with suspected unruptured intracranial aneurysms and diagnostic ambiguity after standard 3T MR imaging.

ABBREVIATION: UIA = unruptured intracranial aneurysm

The prevalence of unruptured intracranial aneurysms (UIAs) in the general population is estimated to be about 3%–5%.[1] Most UIAs can be sufficiently characterized and followed up using conventional 1.5T and 3T MR imaging. However, findings in a relevant subgroup of patients can remain ambiguous when using 1.5T and 3T MR imaging due to difficulties in distinguishing aneurysms from vascular anatomic variants such as vessel infundibula or loops. Especially, small findings (<5 mm) may remain ambiguous: Up to 18% of findings on 3T 3D-TOF may be unclear, and in the remaining 82%, they may be regarded as clear. False-positive and -negative rates of up to 6% and 2% can be observed.[2-4] Diagnostic uncertainty may lead to potentially unnecessary follow-up examinations or even invasive diagnostic procedures (DSA). The consequence is patient anxiety, risk of co-morbidities, and considerable additional costs.

MR imaging at 7T may provide a definitive noninvasive diagnosis in this subgroup of patients because the higher magnetic field strength enables image acquisition with a higher signal-to-noise ratio, higher spatial resolution, and higher vessel contrast. MR imaging at 7T has recently received the CE mark and FDA clearance and can be implemented beyond research settings. Previous studies have suggested the superiority of 7T MR imaging over 1.5T or 3T MR imaging in the depiction and characterization of aneurysms.[5] A strong correlation between 7T and DSA has also been shown previously, with some studies reporting sensitivity rates comparable with those of DSA.[6] However, most of the existing evidence is derived from an experimental setting. We report our single-institution experience of integration of 7T MR imaging in a clinical routine work-up for the management of patients with ambiguous neurovascular findings on 3T MR imaging suspicious for small UIAs. We hypothesize that 7T MR imaging provides definitive, noninvasive discrimination of intracranial aneurysms versus normal vascular variants.

MATERIALS AND METHODS

Patients

We identified 30 patients with suspected incidental UIAs after routine 3T MR imaging who underwent additional 7T MR imaging. The interdisciplinary neurovascular board at Bern University Hospital screened and selected the patients during the clinical-management process. Approximately 800 patients with confirmed or suspected intracranial aneurysms are presented for evaluation annually to this board, representing all cases referred to our institution as a tertiary referral center. Patients with small, incidental ambiguous findings, ie, suspected UIAs, on recent routine 3T MR imaging were additionally examined with 7T MR imaging on the basis of the recommendation of the board. The findings were reviewed by the board, and a management recommendation was

Received June 2, 2021; accepted after revision August 30.

From the Institute of Diagnostic and Interventional Neuroradiology (P.R., J.S., R.W., P.M.), Bern University Hospital, Inselspital, University of Bern, Bern, Switzerland; Advanced Clinical Imaging Technology (A.J.), Siemens Healthcare AG, Bern, Switzerland; Translational Imaging Center (A.J.), Sitem-Insel, Bern, Switzerland; and Departments of Radiology and Biomedical Research (A.J.), University of Bern, Bern, Switzerland.

Please address correspondence to P. Radojewski, MD, Universitätsinstitut für Diagnostische und Interventionelle Neuroradiologie, Freiburgstr 18, 3010 Bern, Switzerland; e-mail: piotr.radojewski@insel.ch

Indicates open access to non-subscribers at www.ajnr.org

Indicates article with online supplemental data.

http://dx.doi.org/10.3174/ajnr.A7331

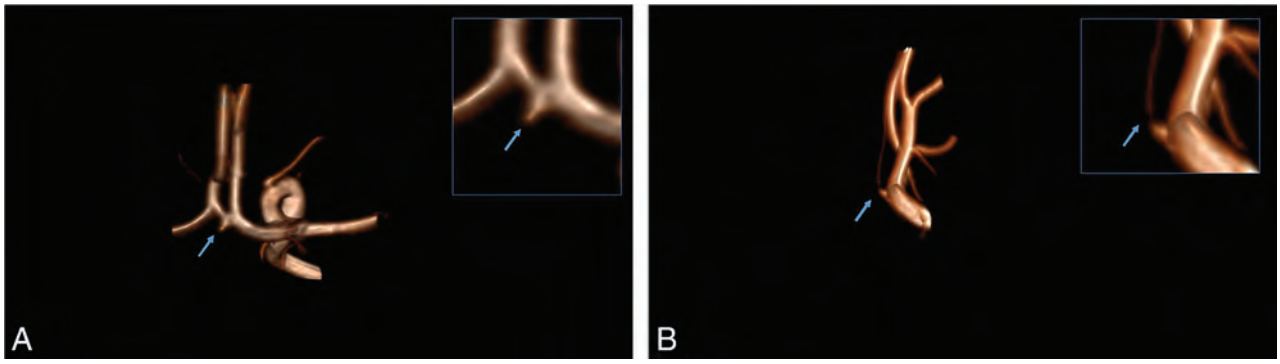

FIG 1. *A*, A UIA was reported on the basis of 3T MR imaging (MIP reconstruction of the 3D-TOF angiography, zoom in the *right upper corner*). *B*, MIP reconstruction of the TOF acquired at 7T MR imaging depicts an infundibulum emerging from the anterior communicating artery (zoom in the *right upper corner*). The *blue arrow* is indicating the finding of interest.

made. All patients were examined between October 2019 and March 2021. All patients signed the informed consent form, and the analysis was approved by the local ethics committee.

Imaging Protocol

All patients were scanned on a clinically approved 7T whole-body MR imaging scanner (Magnetom Terra, clinical mode; Siemens) equipped with a 1-channel transmit and 32-channel receive head coil (Nova Medical, Wilmington, MA, USA) and on a 3T Magnetom Prisma scanner (Siemens) equipped with a 32-channel head coil (Nova Medical, Wilmington, MA, USA).

The 7T imaging comprised the following sequences: sagittal T1 MPRAGE, $0.6 \times 0.6 \times 0.6$ mm^3; axial T2 spin-echo, $0.3 \times 0.3 \times 1.5$ mm^3; axial SWI, $0.2 \times 0.2 \times 1.2$ mm^3; axial arterial TOF angiography, $0.14 \times 0.14 \times 0.25$ mm^3 (interpolated, acquired: $0.36 \times 0.28 \times 0.50$ mm^3), and sagittal T1 sampling perfection with application optimized contrast by using different flip angle evolution (SPACE; Siemens), $0.5 \times 0.5 \times 0.5$ mm^3 (Online Supplemental Data). No intravenous contrast agent was administered. The 3T imaging was a standardized contrast-enhanced protocol (including arterial TOF angiography and contrast-enhanced angiography) (Online Supplemental Data).

Analysis

In clinical routine, all images were reviewed by 2 readers and subsequently presented to the referring board. We analyzed the following: 1) board decisions and recommendations before 7T MR imaging, 2) reports from 3T MR imaging and subsequent 7T MR imaging, and 3) board decisions and recommendations after 7T MR imaging to capture changes in diagnosis and management. We used a simple binomial test considering ambiguous-versus-nonambiguous diagnoses. *P* values $< .05$ were considered statistically significant.

RESULTS

Thirty patients with suspected incidental UIAs after routine 3T MR imaging were included (19 women and 11 men; median age, 56 years; mean age, 51 years; range, 16–71 [SD, 15.5] years) (Online Supplemental Data). All MR imaging examinations were performed without interruption or adverse effects. All images fulfilled the criteria of diagnostic quality within routine image reading. In all 30 cases, no ambiguous findings remained after 7T MR imaging, and a definitive diagnosis was made according to the analyzed reports ($P < .001$).

In 20 cases (66%), the initial suspected diagnosis was revised. In 18 of the 20 cases (60%), the initial diagnosis of suspected UIA was revised in favor of a normal vessel (infundibulum, Fig 1, or perforating artery, Fig 2, and Online Supplemental Data). As a result, because UIA was ruled out, no further follow-up was recommended by the interdisciplinary neurovascular board. In the 2 remaining cases (6.7%) (prominent tip of the basilar artery and vessel loop, but UIA could not be ruled out), the initial suspected diagnosis was revised in favor of a true aneurysm. In 1 of these 2 cases, a standard follow-up was recommended; in the remaining case, DSA was recommended due to a high-risk profile.

In 10 cases (33%), the initial diagnosis was confirmed. Therefore, in 8 cases (26.7%), a definitive diagnosis of an UIA was confirmed, and as a consequence, the interdisciplinary board recommended annual MR imaging follow-up according to the institutional guidelines for small UIAs. In 2 cases (6.7%), 7T MR imaging confirmed the presence of an infundibulum and ruled out the presence of a UIA; therefore, no further follow-up was recommended.

DISCUSSION

Our findings suggest that 7T MR imaging provides a clarification tool for the group of patients with suspected UIAs and diagnostic ambiguity after standard 3T MR imaging. DSA as the criterion standard is not available for this cohort, a potential limitation; however, performing an invasive procedure would not necessarily be justifiable. The higher diagnostic confidence[7] may enable avoiding unnecessary follow-up examinations or invasive DSA. Similarly, revision of an UIA diagnosis toward a normal vascular variant reduces the number of unnecessary follow-up imaging procedures, which would be otherwise performed according to our institutional and national standards.

Most important, socioeconomic factors of suspected, incidental aneurysms and ambiguous vascular findings on 1.5T and 3T MR imaging should be taken into consideration. In this context, resolving diagnostic ambiguities can be especially impactful for young patients with long life expectancies. In our cohort, 26% of patients were younger than 40 years of age. Several studies evaluated the psychological aspects of the UIA diagnosis, suggesting a

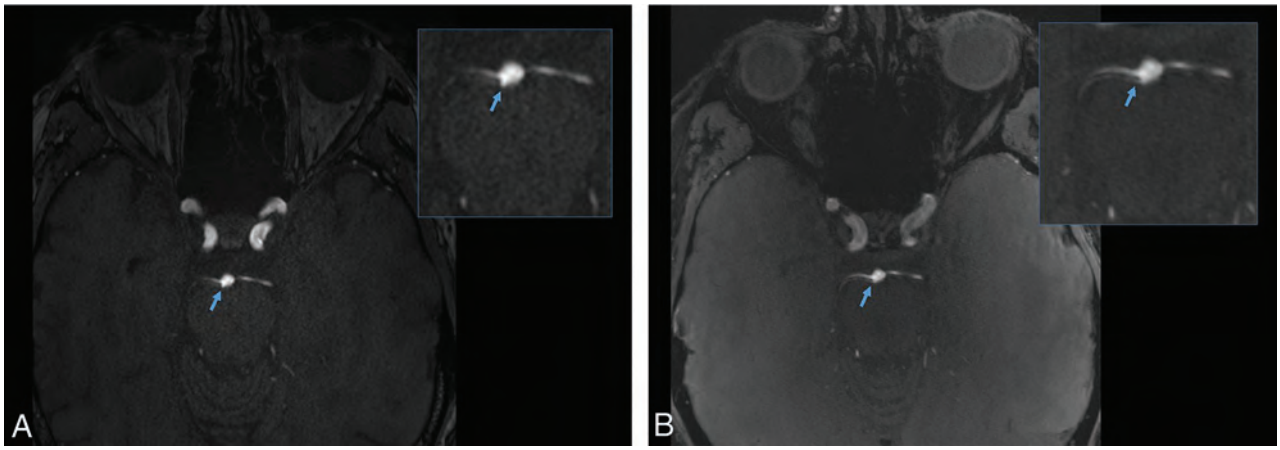

FIG 2. *A*, A UIA was suspected on the basis of 3T MR imaging (axial 3D-TOF angiography, zoom in the *right upper corner*). *B*, MR imaging at 7T depicts a perforator artery parallel to the right superior cerebellar artery (axial 3D-TOF angiography, zoom in the *right upper corner*). The *blue arrow* is indicating the finding of interest.

relevant decrease in quality of life, depression, and anxiety.[8,9] The impact of ambiguous findings is less explored[10,11] and depends largely on the case-specific communication; however, a similar effect could be expected. Increased diagnostic accuracy, diagnostic confidence, and, as a consequence, reduction of ambiguity due to 7T imaging could potentially improve the quality of life and reduce a patient's anxiety.

Financial savings due to avoided unnecessary noninvasive or even invasive diagnostic procedures and outpatient consultations in ambiguous findings are expected; however, this expectation is specific to each national reimbursement system. Thus, a dedicated analysis is not within the scope of this study.

We hypothesized that 7T MR imaging allowed us to resolve the ambiguity, first, due to improvement of the signal-to-noise ratio, resulting in better contrast between the vessel and the surrounding tissue and, second, due to the improved spatial resolution resulting in precise assessment of the shape of the vessels. Finally, the maximum-intensity-projection reconstruction of TOF acquired at 7T allows superior visual 3D analysis. As expected, we observed pulsation artifacts and field inhomogeneity in all patients under investigation. However, these artifacts did not influence the diagnostic confidence within the routine use of 7T MR imaging using dedicated vascular imaging sequences.

CONCLUSIONS

Clinical implementation of 7T MR imaging in patients with suspected small incidental UIAs has the potential to reduce the number of ambiguous vascular findings and to secure a definitive diagnosis and has, therefore, an impact on patient management as well as quality of life and cost of health services.

Disclosure forms provided by the authors are available with the full text and PDF of this article at www.ajnr.org.

REFERENCES

1. Seibert B, Tummala RP, Chow R, et al. **Intracranial aneurysms: review of current treatment options and outcomes.** *Front Neurol* 2011;2:45 CrossRef Medline
2. Li MH, Li YD, Gu BX, et al. **Accurate diagnosis of small cerebral aneurysms ≤5 mm in diameter with 3.0-T MR angiography**. *Radiology* 2014;271:553–60 CrossRef Medline
3. White PM, Teasdale EM, Wardlaw JM, et al. **Intracranial aneurysms: CT angiography and MR angiography for detection prospective blinded comparison in a large patient cohort.** *Radiology* 2001;219:739–49 CrossRef Medline
4. Okahara M, Kiyosue H, Yamashita M, et al. **Diagnostic accuracy of magnetic resonance angiography for cerebral aneurysms in correlation with 3D-digital subtraction angiographic images: a study of 133 aneurysms.** *Stroke* 2002;33:1803–08 CrossRef Medline
5. Wrede KH, Dammann P, Monninghoff C, et al. **Non-enhanced MR imaging of cerebral aneurysms: 7 Tesla versus 1.5 Tesla.** *PLoS One* 2014;9:e84562 CrossRef Medline
6. Wrede KH, Matsushige T, Goericke SL, et al. **Non-enhanced magnetic resonance imaging of unruptured intracranial aneurysms at 7 Tesla: comparison with digital subtraction angiography.** *Eur Radiol* 2017;27:354–64 CrossRef Medline
7. Springer E, Dymerska B, Cardoso PL, et al. **Comparison of routine brain imaging at 3 T and 7T.** *Invest Radiol* 2016;51:469–82 CrossRef Medline
8. Su SH, Xu W, Hai J, et al. **Cognitive function, depression, anxiety and quality of life in Chinese patients with untreated unruptured intracranial aneurysms.** *J Clin Neurosci* 2014;21:1734–39 CrossRef Medline
9. Towgood K, Ogden JA, Mee E. **Psychosocial effects of harboring an untreated unruptured intracranial aneurysm.** *Neurosurgery* 2005;57:858–60; discussion 858–60 CrossRef Medline
10. Kumbhar SS, Baheti AD, Itani M, et al. **Ambiguous findings on radiographs.** *Curr Probl Diagn Radiol* 2021;50:4–10 CrossRef Medline
11. Domen RE. **The ethics of ambiguity: rethinking the role and importance of uncertainty in medical education and practice.** *Acad Pathol* 2016;3:2374289516654712 CrossRef Medline

Disparities in the Use of Mechanical Thrombectomy Alone Compared with Adjunctive Intravenous Thrombolysis in Acute Ischemic Stroke in the United States

W. Wahood, A.A. Rizvi, Y. Alexander, M.A. Alvi, K.R. Rajjoub, H. Cloft, A.A. Rabinstein, and W. Brinjikji

ABSTRACT

BACKGROUND AND PURPOSE: For patients with large-vessel occlusion, mechanical thrombectomy (MT) without IV-tPA is a proved strategy. The relative benefit of direct MT versus MT+IV-tPA for patients with indications for IV-tPA is being actively investigated. We used a national inpatient database to assess trends in use and patient profiles after MT+IV-tPA versus mechanical thrombectomy alone.

MATERIALS AND METHODS: The National Inpatient Sample was queried between 2013 and 2018 for patients undergoing mechanical thrombectomy for acute ischemic stroke. Patients who received mechanical thrombectomy alone were compared with those who underwent MT+IV-tPA. The Cochran-Armitage test was conducted to assess the linear trend of use of mechanical thrombectomy alone among the entire cohort and between admissions involving non-White and White patients. All estimates were nationalized using discharge weights.

RESULTS: A total of 89,645 weighted admissions were identified pertaining to mechanical thrombectomy for acute ischemic stroke from 2013 to 2018. Of these, 59,935 (66.9%) admissions involved mechanical thrombectomy alone. There was an increase in the trend toward the use of mechanical thrombectomy alone (trend: 3.26%; $P < .001$) per year. Multivariable regression analysis regarding patient profiles indicated that patients who identified as Black (OR = 0.83, $P = .001$) or Hispanic (OR = 0.79; $P < .001$) were more likely to undergo mechanical thrombectomy alone compared with those who identified as White. There was no statistically significant difference in the slope between non-White and White populations receiving mechanical thrombectomy alone (trend: +0.93% in favor of non-White; $P = .096$).

CONCLUSIONS: Our results indicated that mechanical thrombectomy alone was used more frequently than MT+IV-tPA among patients with acute ischemic stroke. The disparity between those who identify as White and non-White persisted across the years, though it is closing.

ABBREVIATIONS: ADSS = Administrative Data Stroke Scale; AIS = acute ischemic stroke; ASOV = Administrative Stroke Outcome Variable; ICD = International Classification of Diseases; MT = mechanical thrombectomy; NIS = Nationwide Inpatient Sample

Guidelines for acute ischemic stroke (AIS) are rapidly changing with the advent of 5 randomized trials in 2015 that supported the use of mechanical thrombectomy (MT) over alteplase alone for large-vessel occlusion.[1] The Highly Effective Reperfusion evaluated in Multiple Endovascular Stroke (HERMES) trial meta-analysis showed the superiority of the tPA along with MT over tPA alone and lowered rates of disability at the 3-month mark.[1]

In 2018, American Heart Association/American Stroke Association released guidelines regarding early management of stroke, which recommended the use of MT within 16–24 hours of stroke onset. It also stressed that IV-tPA treatment should not be delayed.[2] In 2020 and 2021, three clinical trials, Direct Endovascular Thrombectomy vs Combined IVT and Endovascular Thrombectomy for Patients With Acute Large Vessel Occlusion in the Anterior Circulation (DEVT); Direct Intra-arterial Thrombectomy in Order to Revascularize AIS Patients with Large Vessel Occlusion Efficiently in Chinese Tertiary Hospitals: A Multicenter Randomized Clinical Trial (DIRECT-MT); and Direct Mechanical Thrombectomy in Acute LVO Stroke (SKIP), all investigated the efficacy of various combinations of endovascular and medical treatments for AIS. Two of the 3 trials (DEVT and DIRECT-MT) demonstrated noninferiority of MT alone compared with MT+IV-tPA.[3-5]

While the trends in AIS are changing due to new research into treatment and management, other studies have found disparities

Received July 14, 2021; accepted after revision September 2.

From the Dr. Kiran C. Patel College of Allopathic Medicine (W.W., A.A.R.), Nova Southeastern University, Davie, Florida; Neuro-informatics Laboratory (Y.A., M.A.A.), and Departments of Neurological Surgery (Y.A., M.A.A., H.C., W.B.), Radiology (H.C., W.B.), and Neurology (A.A.R.), Mayo Clinic, Rochester, Minnesota; and Department of Neurosurgery (K.R.R.), Jacobs School of Medicine and Biomedical Sciences, University at Buffalo, Buffalo, New York.

Please address correspondence to Waseem Wahood, MS, Dr. Kiran C. Patel College of Allopathic Medicine, Nova Southeastern University, 3200 University Dr, Davie, FL 33328; e-mail: ww412@mynsu.nova.edu

Indicates article with online supplemental data.

http://dx.doi.org/10.3174/ajnr.A7332

in the use of MT for patients with AIS associated with race and ethnicity.[6] To investigate whether the gap in the use of the aforementioned techniques between races is closing, we studied the trends in outcomes, use, and patient profiles of MT alone compared with MT+IV-tPA in the United States using a national inpatient database.

MATERIALS AND METHODS

Data Source

The Nationwide Inpatient Sample (NIS) database was queried from January 1, 2013, to December 31, 2018. The NIS is created by the Healthcare Cost and Utilization Project. It samples ~7 million hospitalized patients per year, representing 20% of all discharges annually. This database is the largest public national all-payer database, sponsored by the Agency for Healthcare Research and Quality.[7] Furthermore, the NIS contains discharge weights that aid investigators in extrapolating discharges using the variable discharge weight (for data after 2012) and trend weight (for data before 2012). In turn, the cases in the NIS are converted to national estimates.

Cohort Selection

The 9th and 10th editions of the International Classification of Diseases (ICD-9 and -10) were used to identify patients with AIS who underwent MT from 2013 to 2018. These years were selected to include only the modern era of MT devices, mostly involving stent retrievers, because the first 2 stent retrievers received FDA approval in 2012.[8,9] Patients with a primary diagnosis of subarachnoid hemorrhage or intracerebral hemorrhage or any diagnosis of head trauma were excluded. Diagnosis codes regarding postoperative hemorrhage were also selected. All included ICD-9 and ICD-10 codes are available in the Online Supplemental Data.

Outcomes and Variables of Interest

We recorded the following demographic variables: age, sex, race, insurance type, and Elixhauser Comorbidity Indices. Elixhauser Comorbidity Indices are based on 31 predefined comorbidities that use ICD-9 and -10 codes, which identify risks of poor outcomes.[10] These comorbidities are listed in the Online Supplemental Data. We collected the following hospital data: bed size, location (rural/urban), teaching status, and region (Northeast, Midwest, South, West).

The Administrative Data Stroke Scale (ADSS) and Administrative Stroke Outcome Variable (ASOV) were both calculated in this study, both based on Patel et al.[11] The ADSS is a validated scale with a moderate correlation with the admission NIHSS with a Spearman correlation of 0.39 and a strong correlation with NIHSS >15 ($P < .001$) at discharge. The ADSS consists of the following variables: mechanical ventilation, coma, aphasia, stupor, cerebral edema, cerebral herniation, nasogastric tube placement, parenteral nutrition, dysphagia, and neglect. The ADSS is derived using the sum of the odds ratio of each variable in a multivariable regression model. The ASOV represents poor functional outcome if any of the following were present: in-hospital mortality, discharge to hospice care, discharge to long-term acute care facility, or discharge to skilled nursing facility. This has substantial agreement with a 90-day mRS > 3 cutoff (κ statistic = 0.69). Poor functional outcome is a surrogate for mRS > 3 at 90-day follow-up. More information can be seen in the study published by Patel et al.[11]

Statistical Analysis

The cohort was divided into 2 groups: admissions involving MT alone and those involving MT+IV-tPA. The Cochran-Armitage test was conducted to assess linear trends in the proportions of use of MT alone compared with MT+IV-tPA among all admissions involving MT for AIS. The numerator of this proportion was MT alone, and the denominator was patients who underwent MT alone in addition to those who underwent MT+IV-tPA. This analysis was also conducted to assess trends in the use of MT alone between admissions involving non-White and White patients. For each group, the numerator was the number of those who received MT alone, and the denominator was those who received either treatment. Trend lines were compared between the 2 groups using the ANOVA test, which produces a mean difference in trend with its corresponding 95% CI. Linear trends in the proportion of admissions with poor functional outcome among the 2 groups were also assessed by the Cochran-Armitage test.[12] The Cuzick nonparametric test was used to assess linear trends in mean ADSS scores in the 2 groups.[13] Results from this analysis are represented as a change in the slope of proportion per year with its 95% confidence interval. Multivariable stepwise logistic regression analysis, stratified by hospital region and year, was conducted to assess patient profiles for MT alone versus MT+IV-tPA. The Wald test was performed to investigate the evidence of whether the outcome of MT alone varied across the different groups for each categoric variable within the regression. A $P < .05$ for this test indicates that there is no difference between the groups regarding the outcome.

Regression results are represented as ORs and their respective 95% CIs. χ^2 tests were used to compare the proportion of each categoric variable between the 2 groups. A Student *t* test was used to compare the means of each continuous variable between the 2 groups. Statistical analysis was performed using STATA 16 (StataCorp).[14] *P* values < .05 were considered statistically significant. All estimates were nationalized using discharge weights provided by the Healthcare Cost and Utilization Project.

RESULTS

Patient Characteristics

A total of 89,645 admissions were identified from 2013 to 2018, including 59,935 undergoing MT alone and 29,710 undergoing MT+IV-tPA. The mean age was 68.3 (standard error: ±0.15) years for MT alone and 68.4 (±0.18) years for MT+IV-tPA. There were 29,915 (49.9%) women in the cohort of MT alone and 15,070 (50.7%) in the cohort with MT+IV-tPA. The mean ADSS score was 4.46 (SE, 0.09) for MT alone and 4.63 (SE, 0.12) for MT+IV-tPA. There were 40,465 admissions (71.56%) involving patients who identified as White in the MT alone group and 19,100 (67.43%) in the MT+IV-tPA group ($P < .001$). Additional patient characteristics can be seen in the Online Supplemental Data.

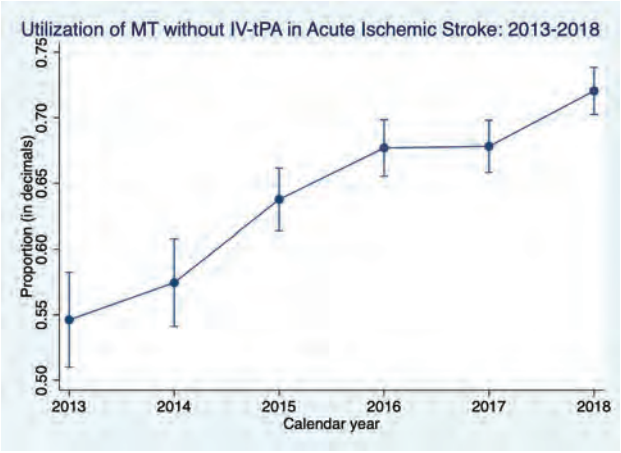

FIG 1. Use of MT alone among those with AIS undergoing MT.

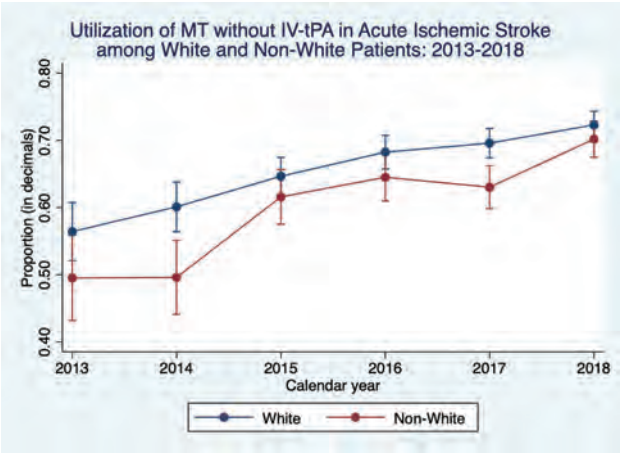

FIG 2. Use of MT alone among those who identify as White versus non-White among those with AIS.

Trend Analysis

The use of MT alone ranged from 3315 in 2013 (54.6% of all MT cases that year) to 20,230 (72.0%) in 2018. There was an increase in the trend toward the use of MT without IV-tPA among patients with AIS by an average of 3.26% per year (95% CI, 2.64%–3.87%; $P < .001$). This is also depicted as a line graph in Fig 1.

The prevalence of the use of MT alone among those who identified as White increased from 2259 (56.43% of all admissions involving those who identify as White) in 2013 to 13,535 (72.30%) in 2018. There was an average increase in the proportion of MT alone by 2.96% per year (95% CI, 2.25%–to 3.66%). The prevalence of the use of MT alone among those who identified as non-White ranged from 795 (49.53%) in 2013 to 5764 (70.18%) in 2018. There was an average increase in the proportion of MT alone by 3.89% per year (95% CI, 2.89%–4.89%). There was no statistically significant difference in slope between the 2 groups (difference in slope: +0.93% in favor of non-White; 95% CI: −0.17%–2.03%; $P = .096$). This analysis is also depicted as a line graph in Fig 2.

The proportion of poor functional outcome among admissions involving MT alone decreased from 83.1% ($n = 2755$) in 2013 to 78.1% ($n = 15{,}790$) in 2018. There was an average decrease in the proportion of poor functional outcomes by −0.67% per year (95% CI, −1.22 to −0.12). On the other hand, the proportion of poor functional outcomes among admissions involving MT+IV-tPA decreased from 2245 (81.5%) in 2013 to 5800 (73.9%) in 2018. There was an average decrease in the proportion of poor functional outcomes by −0.98% per year (95% CI, −1.69 to −0.27). There was no statistically significant difference in slope between the 2 groups (difference in slope: +0.31% in favor of MT alone; 95% CI, −0.54%−1.16%; $P = .47$). This analysis is also depicted as a line graph in Fig 3.

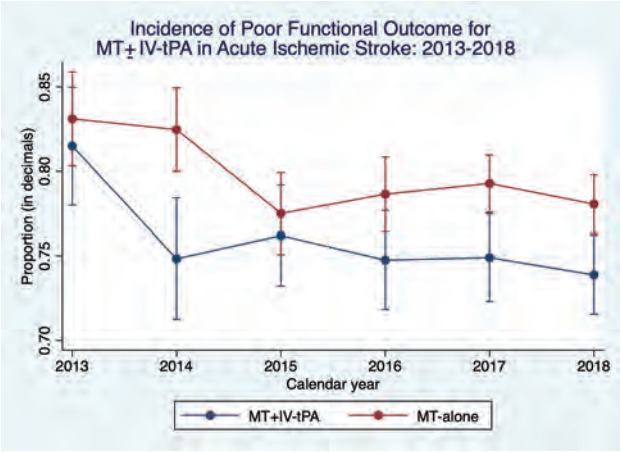

FIG 3. The incidence of poor functional outcome for MT versus MT+IV-tPA.

The mean ADSS among admissions involving MT alone decreased by an average of −0.41 per year (95% CI, −0.56 to −0.27). Meanwhile those involving MT+IV-tPA decreased from 2013 to 2018 (trend: −0.37; 95% CI, −0.51% to −0.22%). There was no significant statistical difference between the 2 slopes (difference in slope: MT alone lower by 0.046; 95% CI, −0.24−0.15; $P = .65$). This analysis is also depicted as a line graph in the Online Supplemental Data.

Multivariable Regression

Multivariable regression assessing the association between patient profiles and the type of therapy received (MT alone versus MT+IV-tPA) was conducted. Patients who identified as Black had lower odds of receiving MT alone compared with those who identified as White (OR = 0.83; 95% CI, 0.75−0.92; $P = .001$). Those who identified as Hispanic also had lower odds of receiving MT alone compared with those who identified as White (OR = 0.79; 95% CI, 0.70−0.89; $P < .001$). Those who identified as any of the other races had similar odds of receiving MT alone compared with those who identified as White (OR = 0.90; 95% CI, 0.79−1.02; $P = .10$). Admissions in urban teaching hospitals had higher odds of receiving MT alone compared with those in urban nonteaching hospitals (OR = 1.44; 95% CI, 1.29−1.61; $P < .001$). Admissions in rural hospitals had similar odds of patients undergoing MT alone compared with those in urban nonteaching hospitals (OR = 0.80; 95% CI, 0.37−1.72; $P = .57$). Additional results can be seen in the Table.

DISCUSSION

Based on our analysis, there was an increasing trend in the use of MT alone over MT+IV-tPA. Our multivariable regression

Multivariable regression on patient profiles of MT alone (versus MT+IV-tPA)

Outcome: MT Alone (vs MT+IV-tPA)	Odds Ratio	*P* Value	95% CI	
Race		<.001[a]		
White	1.000	–	–	–
Black	0.830	.001	0.747	0.922
Hispanic	0.788	<.001	0.698	0.890
Other	0.899	.102	0.792	1.021
Region of hospital		<.001[a]		
Northeast	1.000	–	–	–
Midwest	0.979	.783	0.845	1.135
South	0.886	.064	0.779	1.007
West	0.826	.008	0.716	0.952
Median household income national quartile for patient ZIP code		.032[a]		
0–25th Percentile	1.000	–	–	–
26th–50th Percentile	1.078	.111	0.983	1.183
51st–75th Percentile	1.022	.666	0.926	1.127
>75th Percentile	0.934	.221	0.838	1.042
Location/teaching status of hospital		<.001[a]		
Urban nonteaching	1.000			
Urban teaching	1.442	<.001	1.286	1.616
Rural	0.802	.571	0.374	1.721
ADSS score	0.998	.267	0.994	1.002
Elixhauser Comorbidity Index score	1.017	.050	1.000	1.034

Note:—-indicates not available (reference group).
[a] *P* value for Wald test.

indicated that those who identified as Black or Hispanic were more likely to receive MT+IV-tPA over MT alone compared with those who identified as White. The Midwest and South had similar odds of using MT alone compared with the Northeast, while those in the West had higher odds of receiving MT alone. Our analysis also revealed that the trends in the use of MT alone were increasing at a similar rate for both White and non-White populations with AIS receiving MT. The overall rate of the use of MT alone was still higher in Whites than in Hispanics, Blacks, and other races/ethnicities, showing a possible presence of disparities.

Brinjikji et al[6] found that among the patients with a primary diagnosis of AIS, the use of MT among Black patients was less than among White patients. This finding was similar to ours, though they used the NIS from 2006 to 2010. Our analysis showed no difference in the use of MT among differing insurance statuses, which contradicted their findings. Brinjikji et al indicated a significant reduction in the use of MT in uninsured patients compared with those with private insurance.[6] Golnari et al[15] investigated thrombectomy rates, outcomes, and readmission across the United States between 2016 and 2017 using the NIS and National Readmission Database (NRD) and compared the results with those of the HERMES collaboration meta-analysis.[16] Golnari et al also found a similar rate of nonroutine discharge to our cohort of NIS from 2013–2018 (78.2% versus 78.0% for all thrombectomies, respectively). They indicated that a racial disparity existed for thrombectomy; those who identified as Black were less likely to receive MT than those who identified as White (OR = 0.88; $P < .001$). Our study also shows a racial disparity in the differences between MT alone and MT+IV-tPA; those who identified as a minority were less likely to receive MT alone (versus MT+IV-tPA) compared with those who identified as White. Moreover, this finding was contradictory to the findings of Rinaldo et al.[17]Among those who underwent MT, there was no difference in the odds of tPA administration among those who identified as Black or Hispanic compared with those who identified as White.[17] This difference may be due to the fewer number of years in a different database that Rinaldo et al analyzed. Last, our results show that MT alone has a lower rate of postoperative hemorrhage than MT+IV-tPA, which was similar to the findings of Rinaldo et al.

Nagaraja et al[18] also analyzed racial disparities among those who underwent MT, MT+IV-tPA, and tPA alone in the NIS in 2016. They reported that there was no disparity in use, but there were differences in outcomes.[1] Non-White patients were less likely to be discharged to home compared with White patients if they underwent tPA alone or MT alone.[18] On the contrary, we identified disparities in use. This difference may be due to the inclusion of a single year in the study of Nagaraja et al.[18] This can be seen in Fig 2 of our study, which shows that the proportion of the use of MT alone in 2016 was similar among White and Non-White patients.

Additionally, our analysis shown in Fig 2 indicates that the gap in racial disparities for use of MT alone and MT+IV-tPA is closing across the years. This finding is supported by Otite et al,[19] who analyzed the 10-year trend in racial disparity in tPA and MT use in the NIS. Although they analyzed tPA and MT use separately, the conclusion was similar to ours. They concluded that the use of both stroke treatments was lower among non-White patients compared with White patients, but the gap is closing.

Future Implications

The HERMES collaboration helped shed light on the efficacy of thrombectomy for AIS, while the 3 recent clinical trials (DIRECT-MT, DEVT, and SKIP) contributed to the literature by investigating the efficacy of MT alone compared with

MT+IV-tPA.[4,5,15,20] Moreover, 3 additional clinical trials are ongoing with more countries being involved (A Randomized Controlled Trial of DIRECT Endovascular Clot Retrieval Versus Standard Bridging Thrombolysis With Endovascular Clot Retrieval [DIRECT-SAFE], NCT03494920; Bridging Thrombolysis Versus Direct Mechanical Thrombectomy in Acute Ischemic Stroke [SWIFT-DIRECT], NCT03192332; and Intravenous Treatment followed by Endovascular Treatment versus Direct Endovascular Treatment for Acute Ischemic Stroke Caused by a Proximal Intracranial Occlusion Trial [MR CLEAN NO-IV], ISRCTN80619088).[21-23] These results may further increase the use of MT alone during the next several years. We hope that future studies will evaluate trends and disparities of use as more data from randomized controlled trials become available. We intend to conduct further subanalysis regarding relevant comorbidities with our current data for this study.

Strengths and Limitations

Our study has strengths that are worth highlighting. The NIS is a validated national database that contains all-payer information and is widely used for studies on inpatient trends and analyses.[7] It is not limited by selection bias, and it is representative of all types of hospitals in the United States. However, our study also has limitations that need to be considered. Administrative databases depend on the quality of data entry, which may be variable.[6,11,16,24-26] We based our selection of ICD codes for this study on previously published studies and clinicians' expertise.[6,11,16,25,26] Additionally, ICD codes cannot differentiate between the different MT devices, which have shown heterogeneity.[27] The modern era of mechanical thrombectomies mostly involves stent retrievers. Two of these devices received FDA approval in 2012, Trevor Pro (Stryker) and Solitaire (Covidien).[11] Thus, the cohort of our study begins in 2013. The NIS is also limited in terms of identifying the timing of tPA delivery. Therefore, the increased use of MT alone could be partially due to the longer time window for its use.

The choice of treatment is confounded by the onset of stroke presentation, which is not captured in the NIS. It is also confounded by the lack of information on the incidence of large-vessel occlusions, which reflects the prevalence of patients eligible for these treatments. The MT and MT+IV-tPA cohorts in our analysis may represent, at least in part, 2 different types of patients (with patients with MT alone having later presentation); consequently, the comparison of outcomes with the 2 strategies must be interpreted with caution. However, this limitation does not affect our results regarding trends in use and racial/ethnic disparities. Although we used novel stroke scales for the administrative databases, ADSS and ASOV have shown strong concordance with the NIHSS score and 90-day mRS >3 in the authors' institutional cohort, respectively.[11] We did not use mRS > 2 as a cutoff because it showed a low-to-moderate correlation with ASOV in the aforementioned study.

CONCLUSIONS

Our results indicated that MT alone was used more frequently than MT+IV-tPA among patients with AIS. The disparities between those who identify as White and non-White persisted across the years, though the gap is closing. Regression analysis indicated that MT alone was less likely to be received by Blacks and Hispanics compared with Whites. MT alone was also less common in urban nonteaching hospitals compared with urban teaching hospitals.

Disclosure forms provided by the authors are available with the full text and PDF of this article at www.ajnr.org.

REFERENCES

1. Saver JL, Goyal M, van der Lugt A, et al; HERMES Collaborators, **Time to treatment with endovascular thrombectomy and outcomes from ischemic stroke: a meta-analysis.** *JAMA* 2016;316:1279–89 CrossRef Medline
2. Powers WJ, Rabinstein AA, Ackerson T, et al; American Heart Association Stroke Council. **Guidelines for the early management of patients with acute ischemic stroke: a guideline for healthcare professionals from the American Heart Association/American Stroke Association.** *Stroke* 2018;49:e46–110 CrossRef Medline
3. Yang P, Treurniet KM, Zhang L, et al; DIRECT-MT investigators. **Direct Intra-arterial thrombectomy in order to Revascularize AIS patients with large vessel occlusion Efficiently in Chinese Tertiary hospitals: a multicenter randomized clinical trial (DIRECT-MT)—Protocol.** *Int J Stroke* 2020;15:689–98 CrossRef Medline
4. Suzuki K, Matsumaru Y, Takeuchi M, et al; SKIP Study Investigators. **Effect of mechanical thrombectomy without vs with intravenous thrombolysis on functional outcome among patients with acute ischemic stroke: the SKIP randomized clinical trial.** *JAMA* 2021;325:244–53 CrossRef Medline
5. Zi W, Qiu Z, Li F, et al; DEVT Trial Investigators. **Effect of endovascular treatment alone vs intravenous alteplase plus endovascular treatment on functional independence in patients with acute ischemic stroke: the DEVT randomized clinical trial.** *JAMA* 2021;325:234–43 CrossRef Medline
6. Brinjikji W, Rabinstein AA, Cloft HJ. **Socioeconomic disparities in the use of mechanical thrombectomy for acute ischemic stroke.** *J Stroke Cerebrovasc Dis* 2014;23:979–84 CrossRef Medline
7. Healthcare Cost and Utilization Project US NIS Overview. https://www.hcup-us.ahrq.gov/nisoverview.jsp. Accessed June 1, 2021
8. Nogueira RG, Jadhav AP, Haussen DC, et al. **Thrombectomy 6 to 24 hours after stroke with a mismatch between deficit and infarct.** *N Engl J Med* 2018;378:11–21 CrossRef Medline
9. Dávalos A, Pereira VM, Chapot R, et al. **Retrospective multicenter study of Solitaire FR for revascularization in the treatment of acute ischemic stroke.** *Stroke* 2012;43:2699–705 CrossRef Medline
10. Moore BJ, White S, Washington R, et al. **Identifying increased risk of readmission and in-hospital mortality using hospital administrative data: the AHRQ Elixhauser Comorbidity Index.** *Med Care* 2017;55:698–705 CrossRef Medline
11. Patel PD, Salwi S, Liles C, et al. **Creation and validation of a stroke scale to increase utility of national inpatient sample administrative data for clinical stroke research.** *J Stroke Cerebrovasc Dis* 2021;30:105658 CrossRef Medline
12. Mehta CR, Patel NR, Senchaudhuri P. **Exact power and sample-size computations for the Cochran-Armitage Trend Test.** *Biometrics* 1998;54:1615–21 CrossRef
13. Cuzick J. **A Wilcoxon-type test for trend.** *Stat Med* 1985;4:87–90 CrossRef Medline
14. **STATA Statistical Software: Release 16.** StataCorp; 2019 https://www.scirp.org/reference/referencespapers.aspx?referenceid=2757660. Accessed June 1, 2021
15. Golnari P, Nazari P, Ansari SA, et al. **Endovascular thrombectomy after large-vessel ischemic stroke: use, outcomes, and readmissions across the United States.** *Radiology* 2021;299:179–89 CrossRef Medline
16. Goyal M, Menon BK, van Zwam WH, et al. **Endovascular thrombectomy after large-vessel ischaemic stroke: a meta-analysis of**

individual patient data from five randomised trials. *Lancet* 2016;387:1723–31 CrossRef Medline
17. Rinaldo L, Rabinstein AA, Cloft H, et al. **Racial and ethnic disparities in the use of thrombectomy for acute stroke.** *Stroke* 2019;50:2428–32 CrossRef Medline
18. Nagaraja N, Olasoji EB, Patel UK. **Sex and racial disparity in use and outcomes of t-PA and thrombectomy in acute ischemic stroke.** *J Stroke Cerebrovasc Dis* 2020;29:104954 CrossRef Medline
19. Otite FO, Saini V, Sur NB, et al. **Ten-year trend in age, sex, and racial disparity in tPA (alteplase) and thrombectomy use following stroke in the United States.** *Stroke* 2021;53;2562–70 CrossRef Medline
20. Yang P, Zhang Y, Zhang L, et al; DIRECT-MT Investigators. **Endovascular thrombectomy with or without intravenous alteplase in acute stroke.** *N Engl J Med* 2020;382:1981–93 CrossRef Medline
21. **DIRECT-SAFE. A Randomized Controlled Trial of DIRECT Endovascular Clot Retrieval Versus Standard Bridging Thrombolysis With Endovascular Clot Retrieval,** https://clinicaltrials.gov/ct2/show/NCT03494920. Accessed June 1, 2021
22. **Bridging Thrombolysis Versus Direct Mechanical Thrombectomy in Acute Ischemic Stroke (SWIFT DIRECT).** https://clinicaltrials.gov/ct2/show/NCT03192332, Accessed June 1, 2021
23. Roos Y, Majoie C. **Is intravenous alteplase still of added benefit in patients with acute ischaemic stroke who undergo intra-arterial treatment?** https://www.isrctn.com/ISRCTN80619088. Accessed June 1, 2021 CrossRef
24. Rabinstein AA. **Administrative medical databases for clinical research: the good, the bad, and the ugly.** *Neurocrit Care* 2018;29:323–25 CrossRef Medline
25. Sussman ES, Jin M, Pendharkar AV, et al. **Dual antiplatelet therapy after carotid artery stenting: trends and outcomes in a large national database.** *J Neurointerv Surg* 2021;13:8–13 CrossRef Medline
26. Kuybu O, Javalkar V, Amireh A, et al. **Implications of the use of mechanical thrombectomy on outcome in large vessel occlusion following the 2015 landmark trials.** *J Neurointerv Surg* 2021;13:4–7 CrossRef Medline
27. Munich SA, Vakharia K, Levy EI. **Overview of mechanical thrombectomy techniques.** *Neurosurgery* 2019;85:S60–67 CrossRef Medline

Risks of Undersizing Stent Retriever Length Relative to Thrombus Length in Patients with Acute Ischemic Stroke

N.F. Belachew, T. Dobrocky, T.R. Meinel, A. Hakim, J. Vynckier, M. Arnold, D.J. Seiffge, R. Wiest, E.I. Piechowiak, U. Fischer, J. Gralla, P. Mordasini, and J. Kaesmacher

ABSTRACT

BACKGROUND AND PURPOSE: Results regarding the association of thrombus length, stent retriever length, and recanalization success in patients with acute ischemic stroke are inconsistent. We hypothesized that the ratio of thrombus length to stent retriever length may be of particular relevance.

MATERIALS AND METHODS: Patients with acute ischemic stroke undergoing stent retriever thrombectomy at our institution between January 2010 and December 2018 were reviewed retrospectively. Thrombus length was assessed by measuring the susceptibility vessel sign on SWI using a 1.5T or 3T MR imaging scanner. Multivariable logistic regression models were used to determine the association between thrombus length, stent retriever length, and thrombus length/stent retriever length ratio with first-pass recanalization, overall recanalization, and embolization in new territories. Results are shown as adjusted ORs with 95% CIs. Additional mediation analyses were performed to test for indirect effects on first-pass recanalization and overall recanalization success.

RESULTS: The main analysis included 418 patients (mean age, 74.9 years). Increasing stent retriever length was associated with first-pass recanalization. Decreasing thrombus length and lower thrombus length/stent retriever length ratios were associated with first-pass recanalization and overall recanalization. Thrombus length and stent retriever length showed no association with first-pass recanalization or overall recanalization once thrombus length/stent retriever length ratio was factored in, while thrombus length/stent retriever length ratio remained a significant factor in both models (adjusted OR, 0.316 [95% CI, 0.112–0.892]; $P = .030$ and adjusted OR, = 0.366 [95% CI, 0.194–0.689]; $P = .002$). Mediation analyses showed that decreasing thrombus length and increasing stent retriever length had a significant indirect effect on first-pass recanalization mediated through thrombus length/stent retriever length ratio. The only parameter associated with embolization in new territories was an increasing thrombus length/stent retriever length ratio (adjusted OR, 5.079 [95% CI, 1.332–19.362]; $P = .017$).

CONCLUSIONS: Information about thrombus and stent length is more valuable when combined. High thrombus length/stent retriever length ratios, which may raise the risk of unsuccessful recanalization and embolization in new territories, should be avoided by adapting stent retriever selection to thrombus length whenever possible.

ABBREVIATIONS: aOR = adjusted OR; ENT = embolization into unaffected (new) territories; eTICI = expanded TICI; FP = first-pass; FPR = first-pass recanalization; SL = stent retriever length; SVS = susceptibility vessel sign; TL = thrombus length

Increasing thrombus size has a negative impact on the efficacy of intravenous thrombolysis in patients with acute ischemic stroke.[1] It is uncertain whether this also holds true for recanalization after mechanical thrombectomy. Whereas some studies have found no association,[2-4] others suggest that the likelihood of successful recanalization after mechanical thrombectomy also decreases with increasing thrombus size.[5-8] Opinions are also divided on whether stent retriever size plays a role in this context.[9-11] We hypothesized that recanalization success is predominantly influenced by the thrombus-to-stent retriever length ratio (TL/SL), which ultimately affects clinical outcome. Therefore, our goal was to evaluate the direct and indirect influence of thrombus length (TL), stent retriever length (SL), and TL/SL on first-pass recanalization (FPR),

Received April 14, 2021; accepted after revision July 30.

From the Departments of Diagnostic and Interventional Neuroradiology (N.F.B., T.D., A.H., R.W., E.I.P., J.G., P.M., J.K.), Neurology (T.R.M., J.V., M.A., D.J.S., U.F.), and Diagnostic, Interventional and Pediatric Radiology (J.K.), Inselspital, Bern University Hospital, and University of Bern, Bern, Switzerland.

P. Mordasini and J. Kaesmacher contributed equally to this work.

The work of J. Kaesmacher was supported by the Swiss Stroke Society, the Bangerter-Rhyner-Foundation, and grants provided by the Clinical Trial Unit Bern.

Please address correspondence to Nebiyat Filate Belachew, MD, Department of Diagnostic and Interventional Neuroradiology, Inselspital, Freiburgstr 18, CH-3010, Switzerland; e-mail: nebiyatfilate.belachew@insel.ch; @NFBelachew

Indicates open access to non-subscribers at www.ajnr.org

Indicates article with online supplemental data.

http://dx.doi.org/10.3174/ajnr.A7313

overall recanalization, and the risk of embolization in previously unaffected (new) territories (ENT).

MATERIALS AND METHODS

Inclusion Criteria

We conducted a retrospective post hoc analysis of patients with acute ischemic stroke who presented to Bern University Hospital for mechanical thrombectomy. The clinical and radiologic data presented in this study were gathered by manual review of patients with acute ischemic stroke who underwent mechanical thrombectomy at our hospital between January 2010 and December 2018. The inclusion criteria were as follows: 1) a final clinical diagnosis of acute ischemic stroke; 2) admission MR imaging with SWI available; 3) susceptibility vessel sign (SVS) apparent on SWI; 4) occlusion of at least one intracranial artery on angiography; and 5) the patient having undergone stent retriever thrombectomy. SWI quality was classified as "poor" if the SVS was not assessable due to major artifacts. If the thrombus was masked because of its proximity to the skull base or overlaid by other pathologies (eg, hemorrhage), SVS was considered "technically undeterminable." Patients with poor-quality SWI or technically undeterminable SVS status were excluded.

Most patients with stroke admitted to our institution are primarily scanned using MR imaging. However, the final decision on whether to perform MR imaging or CT is made by the neuroradiologists and neurologists in charge on a case-by-case basis depending on clinical aspects and contraindications. This study was approved by the local ethics committee (Bernese/Swiss Stroke Registry: Kantonale Ethikkommission für die Forschung Bern, Bern, Switzerland, amendment access number: 231/2014 and BEYOND-SWIFT registry, access number: 2018–00766). Patients gave written or oral consent for the use of their data for research. Before January 1, 2015, the need for consent was waived in accordance with regulations of the Swiss law and the local ethics committee.

Data Collection

We collected information on demographics, baseline characteristics, and clinical data, such as age, sex, history of stroke, medication before acute ischemic stroke (antiplatelet therapy, anticoagulants, statins), and documented cardiovascular risk factors such as hypertension, diabetes mellitus, dyslipidemia, and smoking habits. Furthermore, we recorded the following admission data: systolic and diastolic blood pressure, glucose levels, NIHSS score, and stroke subtypes according to Trial of Org 10172 in acute stroke treatment (TOAST) classification. Moreover, IV thrombolysis before imaging (transfer patients) and before mechanical thrombectomy as well as time from symptom onset/last seen well to admission and to mechanical thrombectomy and time from groin puncture to recanalization were documented.

Technical Information: MR Imaging

Imaging was performed on a 1.5T or 3T MR imaging unit (1.5T: Magnetom Avanto or Magnetom Aera; 3T: Magnetom Verio; Siemens). SWI using the 1.5T scanners was performed with the following parameters: TR, 49 ms; TE, 40 ms; flip angle, 15.0°; section thickness, 1.6, 1.8, or 2.0 mm; and intersection gap, 0 mm. 3T SWI was performed with the following parameters: TR, 27 ms; TE, 20 ms; flip angle, 15.0°; section thickness, 2.0 mm; and intersection gap, 0 mm.

Imaging Analysis

Naggara et al[12] have shown excellent correlation between TL as measured on T2* gradient-echo sequences and those determined by DSA. However, SWI has proved to be superior to T2* gradient-echo sequences for evaluating the SVS.[13] The presence and length of the SVS were evaluated retrospectively by 1 independent neuroradiologist (N.F.B.) with 5 years of experience who was blinded to all outcome parameters and had no role in patient treatment. SWI was classified as SVS+ if a distinct signal loss corresponding to an acutely occluded, symptomatic intracranial artery could be identified regardless of how its diameter compared with that of the contralateral artery. TL was measured in a multiplanar SWI reconstruction along the axis of the occluded vessel and recorded in millimeters (Figs 1 and 2). If the SVS was discontinuous (ie, a fractured or heterogeneous clot), the visible sections of the thrombus demonstrating a circumscribed signal loss on SWI were measured and the total was calculated. MR imaging field strength and time from symptom onset to imaging were documented for each case. Additionally, the DWI-ASPECTS was evaluated.

DSA and Stent Retriever Thrombectomy

The primary site of occlusion was determined on the basis of conventional angiography findings. Tandem occlusions were also documented. Stent retriever thrombectomy was performed by experienced interventional neuroradiologists according to the current clinical practice guidelines and institutional protocols. The ex vivo length of the first-line stent retriever device as provided by the manufacturer as well as the total number of passes performed during mechanical thrombectomy were recorded. The expanded TICI (eTICI) score[14] was documented after the first pass and at the end of mechanical thrombectomy. Successful FPR and overall recanalization were defined as an eTICI of 2b or better. DSA was screened for ENT and for peri-interventional complications (vasospasm, dissection, and perforation) by a research fellow with 3 years of experience (J.K.). SL was used to calculate the TL/SL. In addition, all patients were categorized binarily as TL>SL if TL was longer than SL and TL≤SL if TL was not longer than SL. The first-line endovascular treatment technique was categorized as follows: 1) stent retriever alone, 2) stent retriever with a balloon-guided catheter, 3) stent retriever with contact aspiration, or 4) stent retriever with both contact aspiration and a balloon-guided catheter.

Outcome

The NIHSS was evaluated by a neuroradiologist 24 hours after treatment. Mortality and favorable outcome 90 days after treatment were assessed according to the mRS during clinical follow-up by a neurologist or a study nurse. Patients were considered functionally independent if the mRS was ≤2 90 days after treatment. Symptomatic intracranial hemorrhage within 48 hours after stent retriever thrombectomy was assessed according to the European Cooperative Acute Stroke Study (ECASS II).[15]

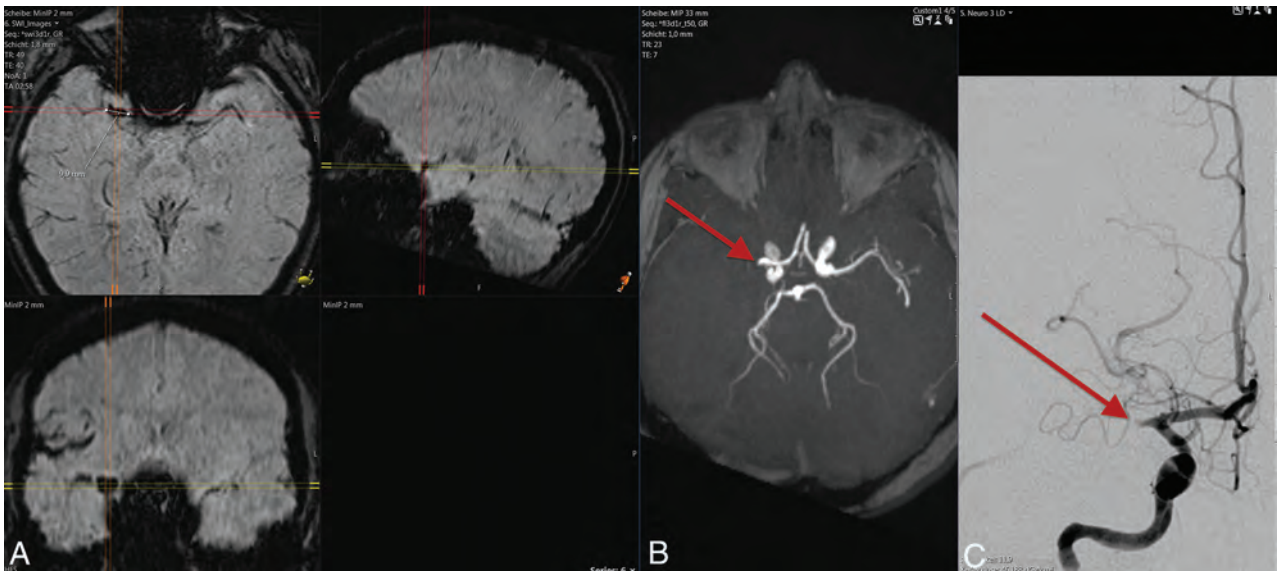

FIG 1. A male patient with acute ischemic stroke after occlusion of the right MCA main trunk (M1-segment). The occlusive thrombus can be seen on SWI (*A*) as a circumscribed loss of signal along the main trunk of the MCA. Corresponding images of the arterial TOF sequence (*B*) and DSA (*C*) show the same vessel occlusion. Thrombus measurement was performed on multiplanar SWI reconstruction along the longitudinal axis of the occluded vessel (*C*). The *red arrow* points to the proximal end of the vessel occlusion on arterial TOF and DSA.

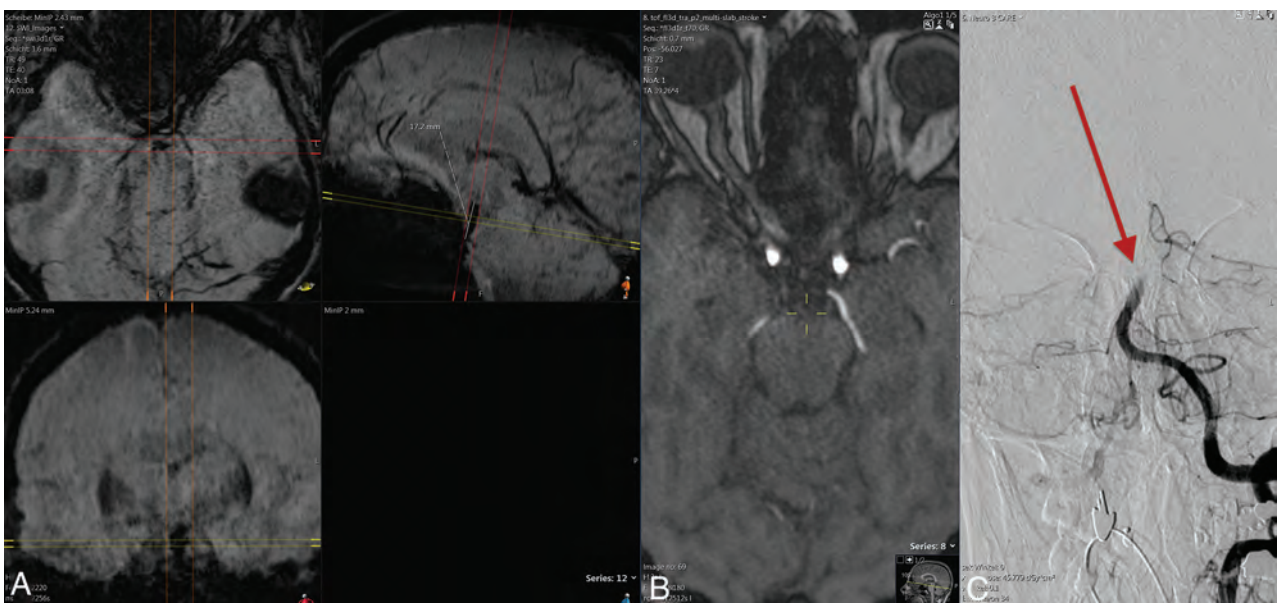

FIG 2. A patient with acute ischemic stroke after occlusion of the basilar artery. The occlusive thrombus can be seen on SWI (*A*) as a circumscribed loss of signal along the basilar artery. Corresponding images of the arterial TOF sequence (*B*) and DSA (*C*) show the same vessel occlusion. The *yellow crosshairs* are centered on the middle portion of the vessel occlusion on arterial TOF (*B*). Thrombus measurement was performed on multiplanar SWI reconstruction along the longitudinal axis of the occluded vessel (*C*). The *red arrow* points to the proximal end of the vessel occlusion on digital subtraction angiography.

Statistical Analysis

Data were analyzed using SPSS Statistics software (Version 25.0; IBM). Continuous variables were compared using the Mann-Whitney *U* test; and categoric variables, with the χ^2 test. Multivariable binary logistic regression analyses were performed to determine the association between TL, SL, and TL/SL with FPR, overall recanalization, and ENT. Adjustment was made for all cofactors with $P < .150$ as well as additional cofactors that are known or suspected to influence the variables of interest (ie, age, sex, bridging therapy, stroke subtype, symptomatic intracerebral hemorrhage). Mediation analyses were performed to test the indirect effects of TL and SL on FPR and overall recanalization after adjusting for age, sex, previous stroke, primary site of occlusion, stroke subtype, tandem occlusion, bridging thrombolysis, and first-line endovascular treatment technique. Results with 2-tailed *P* values $< .05$ were considered statistically significant and are

shown as median (interquartile range, 25%–75%), median comparisons with respective *P* values, or adjusted OR (aOR) with 95% CIs.

RESULTS

Between January 2010 and December 2018, at Bern University Hospital, 1317 patients underwent endovascular treatment for acute ischemic stroke; 676 underwent MR imaging on admission. SWI was performed in 624 of those cases. A further 168 patients were excluded due either to poor-quality SWI, technically undeterminable SVS status, or absence of SVS. A stent retriever device was used 422 times alone or in combination with another device or devices among the remaining cases as part of the first-line retrieval technique; stent size was documented in 418 of them. The Online Supplemental Data outline the patient-selection process. On average, TL was 14 mm (10–20 mm), while SL was 20 mm (20–30 mm). In 11 patients, TL was >40 mm and hence exceeded the longest stents available. Online Supplemental Tables 1 and 2 show all the results for first-pass (FP) recanalizers versus non-FP recanalizers. The Online Supplemental Data list all stent retriever devices used in this study.

Association between Thrombus-to-Stent Size Ratio and First-Pass Recanalization

TL was significantly longer for non-FP recanalizers than for FP recanalizers (15 versus 13 mm, $P = .013$), whereas SL was significantly shorter for non-FP recanalizers than for FP recanalizers (20 versus 20 mm, $P = .003$). TL exceeded the length of the chosen stent more frequently in non-FP recanalizers than in FP recanalizers (TL>SL: 20.2% [$n = 33/163$] versus 12.0% [$n = 31/259$], $P = .018$). TL/SL was greater for non-FP recanalizers than for FP recanalizers (0.71 versus 0.55, $P = .000$). A subgroup analysis showed a first-pass recanalization rate of 36.4% ($n = 4/11$) when TL exceeded the longest stents available (>40 mm), which was significantly lower than the overall FPR rate of 61.4% ($n = 259/422$). In 3 separate multivariate binary regression models, decreasing TL and TL/SL (TL: aOR, 0.955 [95% CI, 0.930–0.981]; $P = .001$; TL/SL: aOR, 0.296 [95% CI, 0.162–0.543]; $P = .000$), as well as increasing SL (aOR, 1.046 [95% CI, 1.016–1.077]; $P = .002$) were associated with FPR after adjusting for all cofactors with $P < .15$ (Online Supplemental Table 1) as well as for age, sex, previous stroke, stroke subtype, bridging therapy, primary site of occlusion, tandem occlusion, and first-line endovascular treatment technique. TL and SL showed no significant association with FPR once the TL/SL was factored in (TL: aOR, 0.996 [95% CI, 0.950–1.045], $P = .885$; SL: aOR, 1.029 [95% CI, 0.998–1.061], $P = .070$), whereas decreasing TL/SL remained significantly associated with FPR (TL/SL after including TL: aOR, 0.316 [95% CI, 0.112–0.892], $P = .030$; TL/SL after including SL: aOR, 0.366 [95% CI, 0.194–0.689]; $P = .002$). The distribution of first-pass eTICI according to TL/SL quartiles is visualized in Fig 3.

The Online Supplemental Data illustrate the adjusted probabilities of achieving FPR depending on the TL/SL. A sensitivity analysis with FPR defined as TICI 3 on first pass did not change this observation (Online Supplemental Data). A subgroup analysis exclusively examining mechanical thrombectomies performed with Solitaire (Medtronic) stents of 4-mm diameter (Online Supplemental Data) confirmed that these findings were independent of stent diameter or stent design.

On mediation analysis, decreasing TL showed no direct effect on FPR (aOR, −0.006 [95% CI, −0.046 to 0.035]; $P = .784$), but a significant and positive indirect effect on FPR mediated through TL/SL was observed (effect, 0.046 [95% bootstrap CI, 0.011–0.096]; $P < .05$). In another mediation analysis, increasing SL showed no direct effect on FPR (aOR, 0.026 [95% CI, −0.002 to 0.083]; $P = .073$), but it had a significant and positive indirect effect on FPR mediated through SL/TL (effect, 0.018 [95% bootstrap CI, 0.004–0.037]; $P < .05$). Further subgroup analyses examining the impact of favorable-versus-unfavorable TL/SL on FPR can be found in the Online Supplemental Data. TL and SL are not significantly different between FP recanalizers and non-FP recanalizers if categorized by the TL/SL quartile (Online Supplemental Data). As illustrated by the Online Supplemental Data, there are no significant differences between TL quartile distribution in FP recanalizers and non-FP recanalizers if categorized according to TL/SL quartiles.

Association between Thrombus-to-Stent Size Ratio and Overall Recanalization

TL was also longer for overall nonrecanalizers than for overall recanalizers (16 versus 13 mm, $P = .025$). SL was significantly shorter for nonrecanalizers than for recanalizers (20 versus 20 mm, $P = .007$). TL exceeded the length of the chosen stent more frequently in overall nonrecanalizers than in overall recanalizers (29.0% [$n = 20/69$] versus 12.8% [$n = 49/382$], $P = .001$). TL/SL was significantly greater for overall nonrecanalizers than for overall recanalizers (0.75 versus 0.6, $P = .000$). After adjusting for the effects of all parameters with $P < .15$ when comparing overall recanalizers with overall nonrecanalizers (Online Supplemental Table 1) as well as age, sex, stroke subtype, previous stroke, and tandem occlusion, SL showed no significant association with overall recanalization (aOR, 1.029 [95% CI, 0.989–1.071]; $P = .157$). In 2 separate multivariable regression models using the same covariates, decreasing TL and TL/SL were associated with overall recanalization (TL: aOR, 0.950 [95% CI, 0.919–0.982], $P = .003$; TL/SL: aOR, 0.272 [95% CI, 0.130–0.570], $P = .001$). In another multivariate regression model using the same covariates and including both TL and TL/SL, TL showed no association with overall recanalization (aOR, 1.016 [95% CI, 0.944–1.093]; $P = .670$), whereas a decreasing TL/SL remained significantly associated with overall recanalization (aOR, 0.206 [95% CI, 0.047–0.907]; $P = .037$). On mediation analysis, a decreasing TL showed no direct effect on overall recanalization (aOR, −0.053 [95% CI, −0.119 to 0.014]; $P = .119$) but proved to have a significant and positive indirect effect on overall recanalization mediated through the TL/SL (effect, 0.101 [95% bootstrap CI, 0.046–0.212]; $P < .05$).

Association between Thrombus-to-Stent Size Ratio and ENT

TL and SL were not significantly different between patients who showed ENT on angiography and those who did not (TL: 21 versus 14, $P = .120$; SL: 20 versus 20, $P = .245$). TL exceeded the

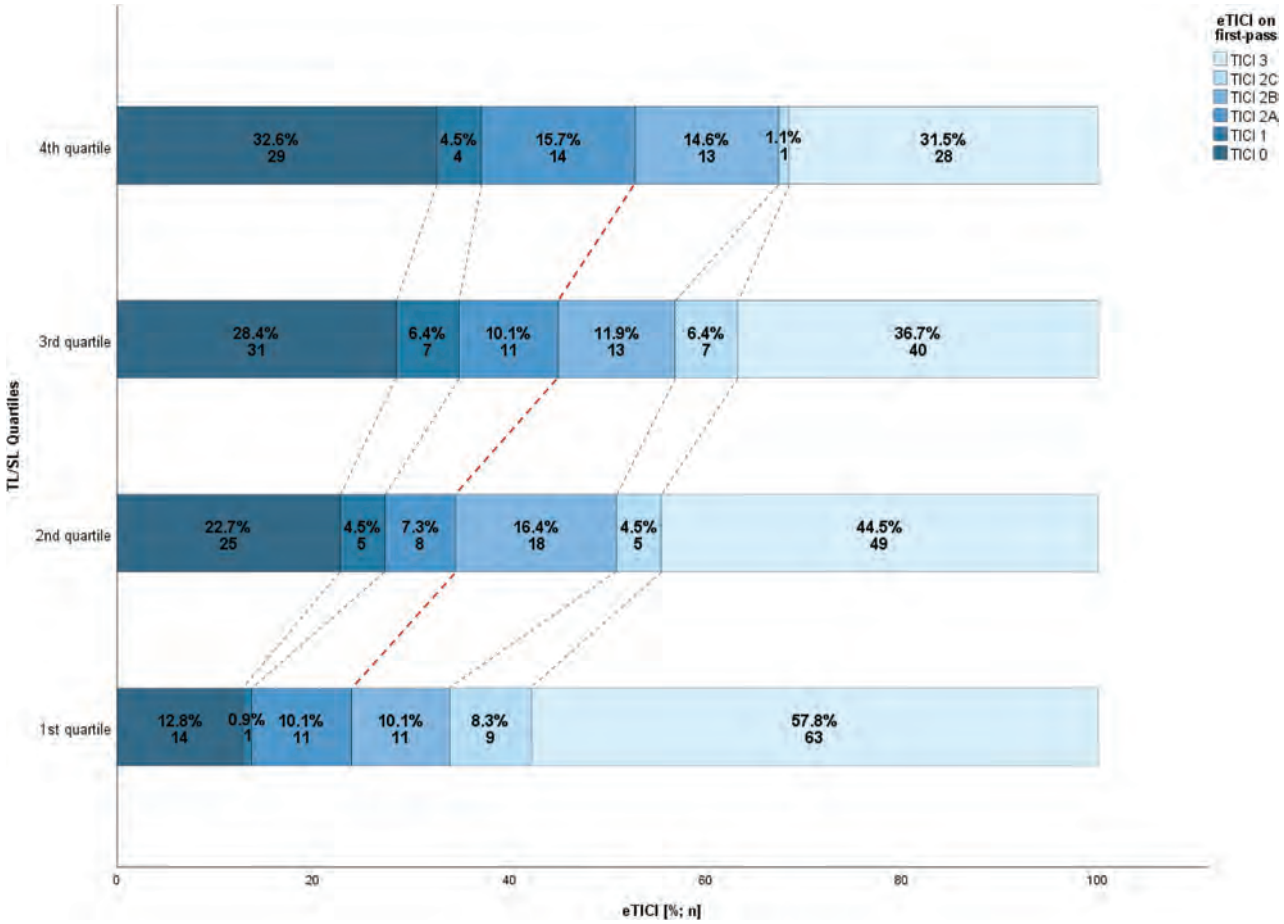

FIG 3. First-pass eTICI distribution according to TL/SL quartiles ($P = .004$). The quartile limits are as follows: 0.25-quartile = 0.425; 0.5-quartile = 0.600; 0.75-quartile = 0.900. The *black and red dotted lines* mark the eTICI margins. The *red dotted line* also marks the threshold for successful recanalization defined as eTICI ≥ 2B.

length of the chosen stent more frequently in patients in whom ENT was observed later (36.8% [$n = 7/19$] versus 14.4% [$n = 62/431$], $P = .005$). The TL/SL ratio was significantly higher for patients who showed ENT (0.79 versus 0.60, $P = .037$). After adjusting for all cofactors with $P < .15$ when comparing patients with and without ENT (Online Supplemental Data) as well as age, sex, previous stroke, stroke subtype, and first-line endovascular treatment technique, an increasing TL/SL ratio was associated with ENT (aOR, 5.079 [95% CI, 1.332–19.362]; $P = .017$).

DISCUSSION

The main findings of this study are as follows: Increasing SL was associated with FPR. Decreasing TL and TL/SL were associated with FPR and overall recanalization. TL and SL alone showed no association with FPR or overall recanalization once TL/SL was factored in, whereas TL/SL remained a significant factor in both models. Mediation analyses showed that a decreasing TL had a significant and positive indirect effect on FPR and overall recanalization mediated through TL/SL, whereas SL had a significant and positive indirect effect on FPR success mediated through SL/TL. Increasing TL/SL was the only parameter associated with ENT.

Previous studies have come to different conclusions about the influence of thrombus and stent size on recanalization success.[2-11] Multiple explanations for these discrepancies are possible: 1) Different parameters have been used to evaluate thrombus size (thrombus length,[5,8] thrombus volume,[6] clot burden score[7]). 2) Sensitivity may differ depending on the imaging tool or technique used (MR imaging [2,5,7] versus CT [6] versus DSA;[2] T2* gradient recalled-echo[5,7] versus SWI;[2] and field strength and manufacturer of the MR imaging scanner). 3) If thrombus size is evaluated by measuring the SVS, differences in the SVS definition may influence patient selection and thrombus-size measurement.[2,4] 4) Fractured clots may hinder uniform and reproducible thrombus measurement. 5) Comparability of studies that examine TL is often limited owing to differing inclusion criteria (ie, M1 or anterior acute ischemic stroke only[2,7,9-11] versus other occlusion patterns[5]). 6) Because many institutions have a preferred set of retrieval devices, stent size comparison is usually limited to 1–3 size categories.[9-11] 7) Stent retriever thrombectomy may be performed in combination with a balloon-guided catheter[16] and/or contact aspiration.[17] The first-line endovascular treatment technique that may influence recanalization success has not always been documented.[10] 8) High-volume centers may achieve recanalization more often and with fewer attempts in difficult cases than low- or medium-volume centers, thus limiting the comparability of results from different centers. 9) Thrombus and stent size as individual parameters may not affect

recanalization success directly but rather have an indirect influence, which is mediated by their relation to each other.

Our results support the assumption that the last of these explanations is likely to account for most of the discrepancies so far. Because the physical interaction between retriever device and clot is at the center of successful stent retriever thrombectomy, we hypothesized that looking at thrombus size in relation to stent size may provide more specific information than is gained by considering them separately. This hypothesis is based on the supposition that the chances of clot-to-device interaction are not necessarily higher for longer stents if the occlusive clot is small enough. On the other hand, we expected that large thrombi would not inevitably lead to an increased risk of fragmentation or distal migration if the size of the stent retrieval device selected is adequate. Our analyses show that TL and SL are both associated with recanalization success but suggest that the TL/SL ratio serves as a more informative variable. Using mediation analyses, we were able to demonstrate that decreasing TL and increasing SL had a significant and positive indirect influence on successful FPR mediated through TL/SL or SL/TL, respectively, whereas decreasing TL also had a positive indirect influence on overall recanalization mediated through TL/SL.

Our results also show that FPR, which was more often achieved by avoiding a high TL/SL, led to more favorable clinical outcomes 90 days after treatment in first-pass recanalizers.

Data regarding the influence of thrombus or stent size on the risk of embolization in previously unaffected territories are scarce. Seker et al[3] found no association between TL and ENT, which was supported by our results. However, the TL/SL was associated with ENT, confirming the additional value of this parameter. To improve comparability, we adjusted all our statistical analyses for the primary site of occlusion, which may affect interventional and clinical outcome parameters.[18] The use of balloon-guided catheters has been found to increase recanalization success[16] and reduce the risk of ENT.[19] Therefore, we also took the first-line endovascular treatment technique into account in our calculations.

Our results suggest that avoiding a high TL/SL by adjusting stent retriever selection according to the presumed TL on admission imaging may be beneficial. If such an assessment is not feasible, the neurointerventionalist should reduce the probability and risks of a high TL/SL by selecting the longest stent retriever device with which she or he is comfortable from those that are otherwise adequate. Although stent retrievers with shorter diameters are believed to pose less risk for vascular injury,[20] some studies have shown that longer stents might be just as safe.[11,21] Future studies may examine whether this assumption would remain true for new stent retriever devices, which could be even longer than the ones currently available. Nonetheless, we can assume that the application of unnecessarily long stents carries the risk of periinterventional complications, especially if the diameter of the occluded vessel is small and the neurointerventionalist is unaccustomed to the specific stent retriever device used. Devices designed to have an adequate length but little radial force might be an option, particularly when operating in distal vessel segments.[22] The preinterventional assessment of TL could lower this risk by allowing a more nuanced stent retriever selection. In this context, possible shortening of the stent retriever device depending on the deployment technique should be considered beforehand. Regardless of the stent size and brand, extra caution is necessary when working with new or unaccustomed devices.

Limitations

This was a retrospective single-center study, which may limit generalizability. Patients who were ineligible for MR imaging or showed complete recanalization on DSA before stent retriever thrombectomy were excluded, possibly leading to selection bias. A previous study has shown that baseline criteria and reperfusion outcome of patients with stroke may differ depending on the initial imaging technique.[23] TL was measured assuming that all thrombus margins are delineated by the SVS. Although some studies have shown that the SVS allows accurate TL measurement,[2,12] TL assessment was not double-checked via DSA in this study, possibly leading to some over- or underestimation of TL due to blooming artifacts and/or fibrin-rich segments in heterogeneous thrombi. TL may have been underestimated in intracranial ICA occlusions that extended extracranially through the skull base. In a small number of patients, TL may have changed between admission MR imaging and mechanical thrombectomy due to thrombosis, thrombolysis, or fragmentation.

Clot density, which may impact recanalization success, could not be assessed on MR imaging. Clot composition, which may also influence recanalization success, was not evaluated in detail. Stent selection was at the discretion of the neurointerventionalist, allowing possible selection bias. Because some thrombi exceeded the longest stents available, it is uncertain whether longer stents would have been equally safe and efficient in those cases.

Ex vivo SL as provided by the manufacturer was considered for analysis. Although stent retriever devices are not designed to change in length after deployment, in vivo SL might differ slightly depending on deployment technique and vascular anatomy. Finally, data on first-pass eTICI may not always reflect the true success of the intervention in patients with multiple vessel occlusions within the same territory.

CONCLUSIONS

Thrombus length and stent length provide more useful information when considered in relation to one another. A high TL/SL ratio, which may raise the risk of unsuccessful recanalization and ENT, should be avoided whenever possible. The preinterventional assessment of TL allows a more nuanced stent retriever selection and may, thereby, help to avoid unnecessarily long stents, which would increase the risk of peri-interventional complications.

ACKNOWLEDGMENT

We thank Susan Kaplan for editorial assistance.

Disclosures: Marcel Arnold—*RELATED: Consulting fee or honorarium:* Honoraria for lectures from AstraZeneca, Bayer, Covidien, and Medtronic, and honoraria for scientific advisory boards of Amgen, Bayer, Bristol Myers Squibb, Daichi Sankyo, Medtronic, Novartis, and Sanofi; *UNRELATED: Grants/grants pending*: Research Grants from Swiss National Science Foundation and Swiss Heart Foundation.* Roland Wiest—*UNRELATED: Consultancy*: Biogen SA*; *Grants/grants pending*: Swiss National Foundation. Urs Fischer—*UNRELATED:*

Consultancy: Medtronic, Stryker, CSL Behring*; *Grants/grants pending*: Medtronic, Swiss Heart Foundation, Swiss National Science Foundation, *Comments*: SWIFT DIRECT, BEYOND SWIFT, SWITCH, ELAN*; *Payment for lectures including service on speakers bureaus*: Boehringer Ingelheim.* Jan Gralla—*RELATED: Grant*: Medtronic, *Comments*: Global Principal Investigator of STAR and Swift Direct (Medtronic), Consultancy*; *UNRELATED: Grants/grants pending*: Swiss National Foundation SNF, *Comments*: MRI in stroke.* Johannes Kaesmacher–*RELATED: Grant*: SAMW/Bangerter, Swiss Stroke Society, Clinical Trial Unit Bern*; *Consulting fee or honorarium*: Stryker, *Comments*: Webinar. *Money paid to institution.

REFERENCES

1. Riedel CH, Zimmermann P, Jensen-Kondering U, et al. **The importance of size: successful recanalization by intravenous thrombolysis in acute anterior stroke depends on thrombus length.** *Stroke* 2011;42:1775–77 CrossRef Medline
2. Weisstanner C, Gratz PP, Schroth G, et al. **Thrombus imaging in acute stroke: correlation of thrombus length on susceptibility-weighted imaging with endovascular reperfusion success.** *Eur Radiol* 2014;24:1735–41 CrossRef Medline
3. Seker F, Pfaff J, Wolf M, et al. **Impact of thrombus length on recanalization and clinical outcome following mechanical thrombectomy in acute ischemic stroke.** *J Neurointerv Surg* 2017;9:937–39 CrossRef Medline
4. Kang DW, Jeong HG, Kim DY, et al. **Prediction of stroke subtype and recanalization using susceptibility vessel sign on susceptibility-weighted magnetic resonance imaging.** *Stroke* 2017;48:1554–59 CrossRef Medline
5. Soize S, Batista AL, Rodriguez Regent C, et al. **Susceptibility vessel sign on T2* magnetic resonance imaging and recanalization results of mechanical thrombectomy with stent retrievers: a multicentre cohort study.** *Eur J Neurol* 2015;22:967–72 CrossRef Medline
6. Baek JH, Yoo J, Song D, et al. **Predictive value of thrombus volume for recanalization in stent retriever thrombectomy.** *Sci Rep* 2017;7:15938 CrossRef Medline
7. Derraz I, Bourcier R, Soudant M, et al; THRACE Investigators. **Does clot burden score on baseline T2*-MRI impact clinical outcome in acute ischemic stroke treated with mechanical thrombectomy?** *J Stroke* 2019;21:91–100 CrossRef Medline
8. Gralla J, Burkhardt M, Schroth G, et al. **Occlusion length is a crucial determinant of efficiency and complication rate in thrombectomy for acute ischemic stroke.** *AJNR Am J Neuroradiol* 2008;29:247–52 CrossRef Medline
9. Haussen DC, Al-Bayati AR, Grossberg JA, et al. **Longer stent retrievers enhance thrombectomy performance in acute stroke.** *J Neurointerv Surg* 2019;11:6–8 CrossRef Medline
10. Zaidat OO, Haussen DC, Hassan AE, et al. **Impact of stent retriever size on clinical and angiographic outcomes in the STRATIS stroke thrombectomy registry.** *Stroke* 2019;50:441–47 CrossRef Medline
11. Yang D, Hao Y, Zi W, et al. **Effect of retrievable stent size on endovascular treatment of acute ischemic stroke: a multicenter study.** *AJNR Am J Neuroradiol* 2017;38:1586–93 CrossRef Medline
12. Naggara O, Raymond J, Domingo Ayllon M, et al. **T2* "susceptibility vessel sign" demonstrates clot location and length in acute ischemic stroke.** *PLoS One* 2013;8:e76727 CrossRef
13. Allibert R, Billon Grand C, Vuillier F, et al. **Advantages of susceptibility-weighted magnetic resonance sequences in the visualization of intravascular thrombi in acute ischemic stroke.** *Int J Stroke* 2014;9:980–84 CrossRef Medline
14. Liebeskind DS, Bracard S, Guillemin F, et al; HERMES Collaborators. **ETICI reperfusion: defining success in endovascular stroke therapy.** *J Neurointerv Surg* 2019;11:433–38 CrossRef Medline
15. Hacke W, Kaste M, Fieschi C, et al. **Randomised double-blind placebo-controlled trial of thrombolytic therapy with intravenous alteplase in acute ischaemic stroke (ECASS II).** *Lancet* 1998;352:1245–51 CrossRef Medline
16. Velasco A, Buerke B, Stracke CP, et al. **Comparison of a balloon guide catheter and a non-balloon guide catheter for mechanical thrombectomy.** *Radiology* 2016;280:169–76 CrossRef Medline
17. Texakalidis P, Giannopoulos S, Karasavvidis T, et al. **Mechanical thrombectomy in acute ischemic stroke: a meta-analysis of stent retrievers vs direct aspiration vs a combined approach.** *Neurosurgery* 2020;86:464–77 CrossRef Medline
18. Demchuk AM, Goyal M, Yeatts SD, et al; For the IMS III Investigators. **Recanalization and clinical outcome of occlusion sites at baseline CT angiography in the Interventional Management of Stroke II trial.** *Radiology* 2014;273:202–10 CrossRef Medline
19. Chueh JY, Kühn AL, Puri AS, et al. **Reduction in distal emboli with proximal flow control during mechanical thrombectomy: a quantitative in vitro study.** *Stroke* 2013;44:1396–401 CrossRef Medline
20. Haussen DC, Lima A, Nogueira RG. **The Trevo XP 320 mm retriever ('Trevo') for the treatment of distal intracranial occlusions.** *J Neurointerv Surg* 2016;8:295–99 CrossRef Medline
21. Girdhar G, Epstein E, Nguyen K, et al. **Longer 6-mm diameter stent retrievers are effective for achieving higher first pass success with fibrin-rich clots.** *Interv Neurol* 2019;8:187–95 CrossRef Medline
22. Kurre W, Aguilar-Pérez M, Martinez-Moreno R, et al. **Stent retriever thrombectomy of small caliber intracranial vessels using pREset LITE: safety and efficacy.** *Clin Neuroradiol* 2017;27:351–60 CrossRef Medline
23. Meinel TR, Kaesmacher J, Mosimann PJ, et al. **Association of initial imaging modality and futile recanalization after thrombectomy.** *Neurology* 2020;95:e2331–42 CrossRef Medline

Perceived Limits of Endovascular Treatment for Secondary Medium-Vessel-Occlusion Stroke

P. Cimflova, R. McDonough, M. Kappelhof, N. Singh, N. Kashani, J.M. Ospel, A.M. Demchuk, B.K. Menon, M. Chen, N. Sakai, J. Fiehler, and M. Goyal

ABSTRACT

BACKGROUND AND PURPOSE: Thrombus embolization during mechanical thrombectomy occurs in up to 9% of cases, making secondary medium vessel occlusions of particular interest to neurointerventionalists. We sought to gain insight into the current endovascular treatment approaches for secondary medium vessel occlusion stroke in an international case-based survey because there are currently no clear recommendations for endovascular treatment in these patients.

MATERIALS AND METHODS: Survey participants were presented with 3 cases involving secondary medium vessel occlusions, each consisting of 3 case vignettes with changes in the patient's neurologic status (improvement, no change, unable to assess). Multivariable logistic regression analyses clustered by the respondent's identity were used to assess factors influencing the decision to treat.

RESULTS: In total, 366 physicians (56 women, 308 men, 2 undisclosed) from 44 countries provided 3294 responses to 9 scenarios. Most (54.1%, 1782/3294) were in favor of endovascular treatment. Participants were more likely to treat occlusions in the anterior M2/3 (74.3%; risk ratio = 2.62; 95% CI, 2.27–3.03) or A3 (59.7%; risk ratio = 2.11; 95% CI, 1.83–2.42) segment compared with the M3/4 segment (28.3%; reference). Physicians were less likely to pursue endovascular treatment in patients who showed neurologic improvement than in patients with an unchanged neurologic deficit (49.9% versus 57.0% responses in favor of endovascular treatment, respectively; risk ratio = 0.88, 95% CI, 0.83–0.92). Interventionalists and more experienced physicians were more likely to treat secondary medium vessel occlusions.

CONCLUSIONS: Physicians' willingness to treat secondary medium vessel occlusions endovascularly is limited and varies per occlusion location and change in neurologic status. More evidence on the safety and efficacy of endovascular treatment for secondary medium vessel occlusion stroke is needed.

ABBREVIATIONS: EVT = endovascular treatment; LVO = large-vessel occlusion; MeVO = medium vessel occlusion; RR = risk ratio

Medium vessel occlusions (MeVOs) (ie, occlusions of the M2, M3, A2, A3, P2, or P3 vessel segment) account for 25%–40% of all acute ischemic stroke cases.[1,2] They can be classified as primary and those that occur de novo (similar to large-vessel occlusion, [LVO]) or secondary and those that occur due to breakdown of LVO and migrate into more distal vessel segments.

Secondary MeVOs have been shown to occur in up to 14% of patients with LVO without treatment or intervention due to spontaneous thrombus migration and fragmentation.[3] Iatrogenic secondary MeVOs can be induced either by thrombolytic treatment or endovascular treatment (EVT).[4,5] With periprocedural embolization occurring in up to 9% of all EVT cases,[4] secondary MeVOs are of particular interest to neurointerventionalists.

The clinical course of MeVO strokes can be poor if left untreated. In the case of secondary MeVO, one would expect even worse outcomes because the affected area will be larger (ie, from the initial LVO) than in primary MeVOs.[1] In the setting of rapid material and technique developments enabling improved EVT efficacy and safety, EVT indications could likely be expanded to more

Received June 2, 2021; accepted after revision August 18.

From the Departments of Clinical Neurosciences (P.C., N.S., A.M.D., B.K.M., M.G.) and Diagnostic Imaging (R.M., M.K., N.K., M.G.), Foothills Medical Centre, University of Calgary, Calgary, Alberta, Canada; Department of Medical Imaging (P.C.), St. Anne's University Hospital Brno and Faculty of Medicine, Masaryk University, Brno, Czech Republic; Department of Diagnostic and Interventional Neuroradiology (R.M., J.F.), University Hospital Hamburg-Eppendorf, Hamburg, Germany; Department of Radiology and Nuclear Medicine (M.K.), University of Amsterdam, Amsterdam, the Netherlands; Division of Neuroradiology (J.M.O.), Clinic of Radiology and Nuclear Medicine, University Hospital Basel, University of Basel, Basel, Switzerland; Hotchkiss Brain Institute (A.M.D.), Cumming School of Medicine, University of Calgary, Calgary, Alberta, Canada; Department of Neurological Sciences (M.C.), Rush University Medical Center, Chicago, Illinois; and Department of Neurosurgery (N.S.), Kobe City Medical Centre General Hospital, Kobe, Japan.

P. Cimflova and R. McDonough contributed equally to the manuscript.

Please address correspondence to Mayank Goyal, MD, PhD, Department of Clinical Neurosciences, Foothills Medical Centre, 1403 29th St. NW, Calgary, AB, T2N2T9, Canada; e-mail: mgoyal@ucalgary.ca; @PCimflova; @rosevmcd; @manonkappelhof; @nishita_singh3; @NimaKashani; @johanna_ospel; @Fie0815; @mayank_GO

Indicates article with online supplemental data.

http://dx.doi.org/10.3174/ajnr.A7327

distal vessel occlusions. Due to a lack of data from randomized trials, however, there is currently neither reliable evidence nor expert consensus on whether EVT is safe and effective for MeVO strokes. Moreover, secondary MeVOs occurring before or during EVT are often only discovered on the first or control DSA runs. In such cases, the procedure has already begun, so the question remains whether to continue with EVT and not whether it is indicated. We sought to gain insight into the current management approaches regarding EVT in acute ischemic stroke cases caused by secondary MeVOs using a Web-based survey with prespecified case scenarios.

MATERIALS AND METHODS

Survey Design

To better understand current treatment practices and endovascular decision-making in cases of acute ischemic stroke caused by MeVO, we conducted an international online, cross-sectional, anonymous, invitation-only survey (MeVO-Finding Rationales and Objectifying New Targets for IntervEntional Revascularization in Stroke; MeVO-FRONTIERS) using Qualtrics (www.qualtrics.com) among stroke physicians. The survey took approximately 30 minutes to complete. Response data were obtained from November 12, 2020, to December 31, 2020. Approval by Conjoint Health Research Ethics Board of the University of Calgary was obtained. Data used in the current study are available from the author on reasonable request.

Survey Participants

Approximately 1400 stroke physicians (neurologists, interventional neurologists, interventional neuroradiologists, interventional radiologists, neurosurgeons, and other physicians directly involved in acute stroke care) were invited to participate in this survey through personal and professional networks of the study authors. No restrictions with regard to case volume or experience level were applied, and participants were from both academic and nonacademic backgrounds. Before accessing the case scenarios, the physicians provided basic personal data (age range, sex, years of experience in stroke treatment, annual personal stroke treatment volume, annual center stroke treatment volume, geographic region, subspecialty, and teaching-versus-nonteaching hospital).

Clinical Case Scenarios

The survey consisted of 7 MeVO narrative cases with illustrative images (4 primary MeVOs and 3 secondary MeVOs) with 3–6 fictional clinical case vignettes each. For the secondary cases of MeVO, presented images were single-image CT (1 section), single-image 3D MRA reconstruction, or angiography snapshots. Clinical data included the fictional patient's age, stroke severity, relevant medical history, and imaging details (ASPECTS, occlusion location).

One case described an initial carotid-T occlusion, with a secondary embolus in the A3 segment of the anterior cerebral artery after the first thrombectomy attempt. The second case showed an M1 occlusion with a secondary M3/4 occlusion after the first stent-retriever pass. In the third case, CTA showed an M1 occlusion, but only an M2/3 occlusion was present on the first DSA run. The neurologic status of the described patient (improvement, no change, unable to assess due to general anesthesia) varied in each clinical scenario.

For each vignette, the participants were asked if the described patient should be treated endovascularly. Respondents could reply, "Yes, proceed with EVT," "No, there is no need to treat this occlusion," or '"Wait 10 minutes, repeat DSA, and proceed with EVT if MeVO persists." If the procedure was initiated with the patient under general anesthesia, there was an additional option to choose, "Wake up the patient and if the symptoms [related to the occlusion territory in question] are present, treat the patient." The survey flow is shown in the Online Supplemental Data.

Statistical Analysis

Only responses from the cases of secondary MeVO (3 cases with 3 scenarios each) were analyzed in this study. Participants' baseline characteristics and response data were analyzed using descriptive statistics, and differences between groups were assessed using a χ^2 test (binary categoric variables) and a Kruskal-Wallis test (categoric variables with >2 groups).

Univariate logistic regression clustered by respondent identity was used to provide adjusted measures of effect size for baseline characteristics of prespecified scenarios (occlusion site, baseline neurologic deficit) and participant baseline characteristics (participant age and sex, specialty, years of experience in neurointervention, region of practice, personal and center stroke treatment volume per year and hospital setting) on the likelihood of pursuing EVT. Multivariable logistic regression models clustered by respondent identity were additionally performed, including all the aforementioned scenarios and baseline characteristics of the participants. The baseline ASPECTS and patient age were excluded from the multivariable logistic regression model due to the survey-design-related collinearity of these variables.

We reported risk ratios (RRs) derived from binary logistic regression and incidence-rate ratios derived from multivariable Poisson logistic regression. Response options of "No EVT treatment," "Wait 10 minutes and repeat DSA," and "Wake up the patient and reassess" were merged into 1 category of "No Immediate EVT," to determine physician characteristics that were associated with the decision to perform EVT with no delay in procedure continuation. Additionally, we performed an analysis on dichotomized data for "EVT Yes" (merging categories "Proceed with EVT," "Wait 10 minutes and repeat DSA," and "Wake up the patient and reassess") and "EVT No" categories to evaluate participant characteristics associated with a decision in favor of EVT. P values $< .05$ were considered statistically significant. Changes in decisions between scenarios of varying occlusion sites and neurologic statuses were visualized with Sankey diagrams. Data analysis was performed in STATA 16.1 (StataCorp). Figures were created with Power BI desktop 2016 (Microsoft).

RESULTS

In total, 366 physicians (56 women, 308 men, 2 of undisclosed sex) of different specialties (170 interventional neuroradiologists, 36 interventional neurologists, 18 interventional radiologists, 97 neurologists, 39 neurosurgeons, and 6 other specialists involved in acute stroke care) from 44 countries (49.5% from Europe, 26.2% from the United States and Canada, and 24.3% from the other parts of the world) completed the survey for a total of 3294

Endovascular decision-making based on patient neurologic status, stratified by site of occlusion

	Physicians' Responses to the Question Regarding EVT in Presented MeVO Cases				
	EVT Yes	Wait for 10 Min and Repeat DSA	Wake Up the Patient for Reassessment	EVT No	RR (95%CI)[a]
Decision to treat based on occlusion site					
Occlusion site (No.) (%)					
Posterior M3/4 MCA	311 (28.3)	189 (17.2)	22 (2.0)	576 (52.5)	Ref.
Anterior M2/3 MCA	816 (74.3)	157 (14.3)	16 (1.5)	109 (9.9)	2.62 (2.27–3.03)[b]
A3 ACA	655 (59.7)	190 (17.3)	15 (1.4)	238 (21.7)	2.11 (1.83–2.42)[b]
Decision to treat based on occlusion site and neurologic status					
Anterior M2/3 MCA (No.) (%)					
No improvement	299 (81.7)	42 (11.2)	NA	25 (6.8)	Ref.
Patient improved	245 (66.9)	70 (19.1)	NA	51 (13.9)	0.82 (0.77–0.87)[b]
Unknown (GA)	272 (74.3)	45 (12.3)	16 (4.4)	33 (9.0)	0.91 (0.87–0.95)[b]
Posterior M3/4 MCA (No.) (%)					
No improvement	111 (30.3)	69 (18.9)	NA	186 (50.8)	Ref.
Patient improved	89 (24.3)	66 (18.0)	NA	211 (57.7)	0.80 (0.70–0.92)[b]
Unknown (GA)	111 (30.3)	54 (14.8)	22 (6.0)	179 (48.9)	1.00 (0.90–1.11)
A3 ACA (No.) (%)					
No improvement	216 (59.0)	67 (18.3)	NA	83 (22.7)	Ref.
Patient improved	214 (58.5)	67 (18.3)	NA	85 (23.2)	0.99 (0.92–1.07)
Unknown (GA)	225 (61.5)	56 (15.3)	15 (4.1)	70 (19.1)	1.04 (0.99–1.10)

Note:—GA indicates general anesthesia; NA, not applicable; Ref., reference; ACA, anterior cerebral artery; Min, minutes.

[a]Responses to "Wait for 10 minutes and repeat DSA to look for persistent occlusion" and "Wake up the patient for reassessment" (if applicable) were included in the "No EVT" category to calculate risk ratios. Data in columns 2–5 represent the responses of physicians to a survey question "Should the presented MeVO be treated endovascularly?"

[b] P value $< .05$.

responses. Detailed respondent characteristics are listed in the Online Supplemental Data.

EVT in Secondary MeVOs

Most physicians (54.1%, 1782/3294 responses) were in favor of continuing with EVT, while 17.9% (589/3294 responses) would wait and repeat the DSA or wake up the patient for neurologic reassessment if the procedure was performed with the patient under general anesthesia. Twenty-eight percent (923/3294 responses) would not have continued with EVT. Participants were more likely to treat patients if the occlusion site was in the anterior M2/3 (74.3%; RR = 2.62; 95% CI, 2.27–3.03) and A3 (59.7%; RR = 2.11; 95% CI, 1.83–2.42) segments, compared with those in the M3/4 segments (28.3%; reference) (Table and Figure). An improvement in neurologic status led to a significant decrease in the likelihood of pursuing EVT compared with statuses of patients whose neurologic deficits remained unchanged (49.9% versus 57.0% responses in favor of EVT, respectively; RR = 0.88; 95% CI, 0.83–0.92). This finding remained statistically significant in cases with M2/3 (RR = 0.82; 95% CI, 0.77–0.87) and M3/4 (RR = 0.80; 95% CI, 0.70–0.92) occlusions, but not for A3 segment occlusions (RR = 0.99; 95% CI, 0.92–1.07) (Table and Figure).

Physician Characteristics and Decision-Making for Immediate EVT

In the univariable analyses, female physicians were less likely to proceed with immediate EVT in comparison with their male counterparts (45.6% versus 55.6%; RR = 0.82; 95% CI, 0.68–0.99). There was a significant difference in treatment decision rates among interventionalists (either interventional neuroradiologists, interventional radiologists, interventional neurologists, or neurosurgeons) compared with noninterventionalists (neurologists and other physicians) (59.7% versus 39.7%, respectively; RR = 1.50; 95% CI, 1.29–1.76).

Physicians working in nonteaching hospitals were more likely to proceed immediately with EVT in contrast to physicians working in teaching hospitals (65.5% versus 53.1%, respectively; RR = 1.23; 95% CI, 1.04–1.46). Those practicing in Europe were less restrictive in their decision to treat patients with MeVO stroke endovascularly (59.3% of responses in favor of EVT; RR = 1.18; 95% CI, 1.01–1.37) in comparison with physicians practicing in the United States and Canada (50.3%) or in other parts of the world (48.0%).

Willingness to immediately proceed with EVT was associated with the physician's experience in neurointervention (55.4%–59.8% with >5 years' experience versus 52.1% with 0–5 years' experience) and their career stage (53.6%–57.8% of board-certified physicians favored immediate EVT versus 37.0% of physicians in training). There was no statistically significant difference in EVT decision-making based on physicians' ages.

We examined the effect of annual stroke treatment volume, both at the center level and at the personal level, on decision-making in the univariable analysis and found that physicians from centers with >200 mechanical thrombectomies per year (63.2%; RR = 1.42; 95% CI, 1.13–1.79) and physicians performing >50 mechanical thrombectomies annually were more likely to treat patients with MeVO immediately (63.1%; RR = 1.58; 95% CI, 1.01–2.48).

In the multivariable analysis, the physician factors significantly associated with the decision to immediately continue with EVT were specialty (interventionists), region of practice, hospital type, and annual stroke treatment volume of >200 thrombectomies at the center level (Online Supplemental Data).

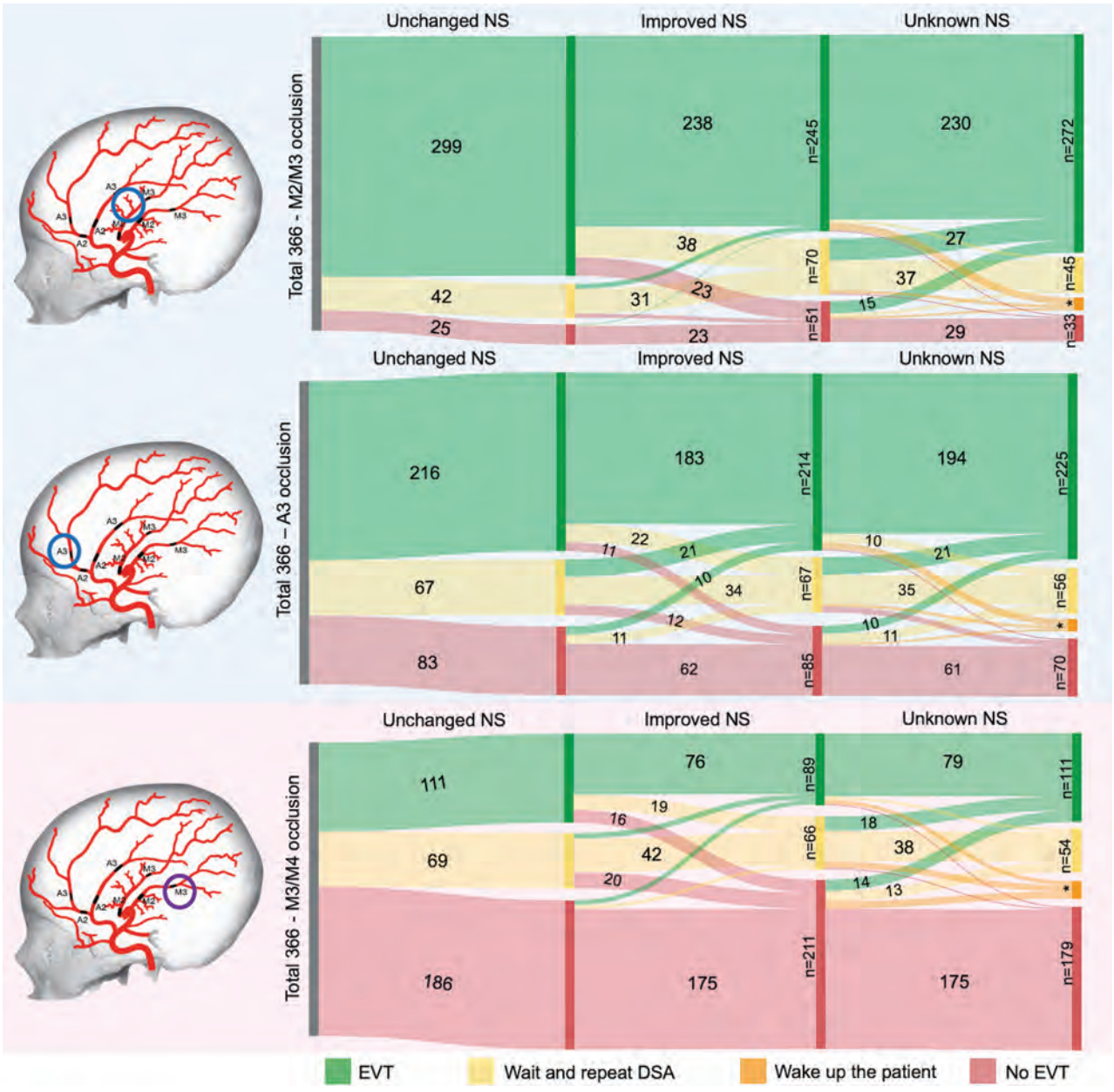

FIGURE. The effect of occlusion site and patient neurologic status (NS) on EVT decision-making for secondary MeVOs. The frequency of physicians' responses for treatment options in given scenarios with changing neurological status are listed on vertical axis in the diagram. The evolution in physicians' decision for endovascular treatment based on the changed neurological status is listed in horizontal fashion. Number of responses for category "Wake up the patient": M2/M3=16; A3=15; M3/4=22. No values are provided for response frequency of <10.

Physician Characteristics and Decision-Making for EVT (Immediately or after Reassessment)

Most physicians' baseline characteristics were associated with a preference for proceeding with EVT; rates in favor of EVT ranged from 60% to 77.8%.

In the univariable analyses, interventionalists, those practicing in Europe, and female physicians were more likely to proceed with EVT, either immediately or after reassessment (Online Supplemental Data). In the multivariable analysis, the physician factors significantly associated with the decision to continue with EVT were specialty (interventionists) and region of practice (Europe) (Online Supplemental Data).

Reasons for No EVT

Of 923 no EVT responses (28.0%), most physicians (39.0%, 360 responses) reasoned that the treatment benefit was too small for EVT. The second most frequent reason for no EVT was a too-distal location of the occlusion (31.3%, 289 responses), followed by insufficient evidence that EVT is effective (23.5%, 217 responses). Other reasons such as administration of intra-

arterial tPA, good collateral flow, low NIHSS, or high-risk/low-benefit ratio were mentioned by 4.7% of physicians, and insufficient resources to treat MeVOs was chosen by 1.5%.

DISCUSSION

Our findings suggest that a physician's willingness to treat secondary MeVOs endovascularly is limited and varies per occlusion location. Most participants were in favor of treatment of M2/3 (74.3%) and A3 (59.7%) occlusions, while less than one-third opted to proceed with EVT for the more distally located M3/4 occlusions (28.3%). These data suggest that there is a certain limit to what is perceived as safely achievable and accessible for EVT. Cases that were used to create illustrative scenarios in the survey were successfully achieved and treated endovascularly. Therefore, this finding of the limit based on occlusion location more likely reflects subjective operator experience. Indeed, a too-distal location of the thrombus was the second most frequent reason given by the survey participants for no EVT.

Physicians were less likely to pursue secondary MeVOs if the patient's clinical status improved in the scenarios in which distal embolization occurred in the initially affected territory (M2/3, M3/4). This scenario is suggestive of a hesitation of physicians to pursue EVT in secondary MeVOs in cases of early neurologic improvement. Furthermore, studies suggest that achieving TICI 2b with fewer passes is associated with better outcome compared with TICI 2c/3 reperfusion achieved with more passes.[6] The neurologic status had no impact on the participants' decisions to treat the presented case of A3 MeVO. This might be due to the initially unaffected anterior cerebral artery territory being supplied by the contralateral ICA. Thus, this MeVO can be considered embolization into a new territory, which may have affected the physician's willingness to treat.

Physician's characteristics related to an increased likelihood of immediate EVT in secondary MeVOs were interventional specialty, more experience in neurointervention, and higher annual case volumes. These are likely because interventionalists encounter such cases on a more frequent basis because LVOs migrate distally and become secondary MeVOs.[5] In contrast, an average stroke neurologist likely has a limited knowledge of interventional techniques and, therefore, is unable to decide whether a distally located occlusion is accessible for EVT and can be successfully retrieved. Nevertheless, even noninterventionalists and less experienced neurointerventionalists would consider EVT based on either persistent occlusion on repeat DSA or after neurologic reassessment (Online Supplemental Data).

The eloquence of the affected territory plays an important role in EVT decision-making in patients with MeVO stroke. Despite MeVO's relatively smaller vascular territory in comparison with LVO, the impact of ischemia can be severely disabling,[7] for example, the loss of language skills due to a left anterior M2/M3 occlusion. In secondary MeVO strokes, evaluation of a patient's neurologic status can be challenging because the neurologic deficit might be influenced by the initial LVO stroke.[4] In the presented cases of secondary MeVOs in our survey, the most frequent reason for no EVT was that the benefits are too small: The affected areas were not considered responsible for the patients' neurologic deficits, or the potential risks of the procedure were perceived to be greater than the benefits of the treatment. For example, due to the perceived fragility of the more distal, smaller-caliber vessels, there may be a potential risk of higher complication rates in MeVOs (eg, perforation, intracranial dissection).

Another aspect of a physician's decision-making is the presence/absence of collateral flow in the affected area. If collateralization behind the occlusion is insufficient, the willingness to pursue distally located occlusions will be higher than in the case of rapid retrograde filling of the vascular bed. As a part of each case presentation, we included an image demonstrating a parenchymal phase on DSA (Online Supplemental Data) to account for this factor; however, a single image cannot replace a complete DSA run, and participants may have thought that they did not have enough information to make a decision.

The accessibility of more distally located occlusions is highly dependent on the available material. In our survey, we did not imply what EVT technique should be used, and it was left to the physician's own judgment and experience to decide whether the presented occlusion was accessible. The potential challenges of MeVO EVT lie in the progressively changing and generally smaller caliber of the vessels, as well as thinner vessel walls in comparison with the more proximal vessel segments.[8] Based on a recent systemic review by Ospel and Goyal,[4] the most commonly reported complication in MeVO EVT was symptomatic intracranial hemorrhage. The prevalence of symptomatic intracranial hemorrhage ranges from 0% to 11%, with most studies reporting symptomatic intracranial hemorrhage rates of $<8\%$,[4] ie, slightly higher than that reported in the major LVO studies.[9] One of the hypothesized mechanisms of periprocedural complications is endothelial injury during stent-retriever expansion and thrombus retrieval.[10,11] This could possibly apply even more to fragile, smaller distal vessels, while it has been shown that the radial force of stent retrievers gradually rises as the vessel diameter decreases.[10] Smaller and softer devices that can be delivered through smaller microcatheters with an optimized vector of force to avoid pulling the whole vessel along with it are, therefore, warranted.

The optimization of the vector of force can be accomplished using an appropriately sized distal access catheter in conjunction with a stent retriever; such an approach can also decrease the risk of embolization into new territories. With the recent development of longer microcatheters[12] that enable delivery of stent retrievers to desired target locations, the option of coaxial delivery of a distal-access catheter over the microcatheters, and recent progress in the development of smaller stent retrievers showing promising results in achieving successful recanalization in MeVOs,[13] the perception of the thrombus accessibility is likely to be shifted beyond the M3 or A3 vessel segments, particularly as experience with the novel material further increases.

Our study has limitations. First, the included participants were contacted through personal and professional networks of the study authors, and most (92.1%) were working in teaching hospitals. Therefore, responses may not be representative of the entire stroke community, and ascertainment bias may have occurred while

more experienced and skillful interventionalists from high-volume teaching centers were predominantly represented in the survey dataset. However, replies from all over the world were collected, and we particularly assessed differences between regions to support correct local interpretation of the results. Moreover, we believe that the clinical practice in rich countries and teaching institutions serves as exemplary care that is usually followed by the rest of the medical society. Second, survey data do not always reflect real-world clinical practice. Physicians' choices may be different in practice when facing diverse practical obstacles. Third, participants may have expected that a certain answer to the question was desired from them, probably in favor of EVT, given that the survey is conducted and spread in a research network partly dedicated to improving EVT results. We tried to minimize this effect by making all responses fully anonymous. Fourth, we did not collect information regarding institutional standard stroke imaging protocols and, therefore, did not assess the impact of various imaging protocols on participant decision-making. Because the EVT decision-making was based on the findings of DSA images, the baseline imaging (either CT or MR) played only an illustrative role in the presentation of the secondary MeVO cases. Finally, physicians could have been biased by the vascular anatomy provided for a particular case; our results regarding the occlusion sites are, therefore, not generalizable.

Due to lack of high-level evidence, a decision toward continuing with EVT in secondary MeVOs is mainly made on an individual basis and involves thrombus accessibility, eloquence of the affected territory, a patient's current condition, and potential risks of the procedure. Therefore, it is clear that physicians vary in their treatment preferences with respect to secondary MeVOs and that experience with such cases is likely to play a role. Despite increasing effort to conduct a randomized controlled trial of EVT in patients with MeVO stroke, it is unlikely that patients with secondary MeVO will be randomized because it is not feasible to randomize patients during an ongoing EVT procedure. However, more evidence on the safety and efficacy of EVT for MeVO stroke is needed, for which observational or survey data could be of great use.

CONCLUSIONS

This study provides valuable information on current practice and EVT decision-making for the challenging-yet-common scenario of secondary MeVO. In the presented scenarios, physicians' willingness to treat secondary MeVOs endovascularly varied per occlusion location and was influenced by the change in neurologic status.

ACKNOWLEDGMENTS

We would like to acknowledge all survey participants for their time and effort invested in filling out the survey, and we thank Moiz Hafeez for his contribution to data entry of the survey scenarios.

Disclosure forms provided by the authors are available with the full text and PDF of this article at www.ajnr.org.

REFERENCES

1. Goyal M, Ospel JM, Menon BK, et al. **MeVO: the next frontier.** *J Neurointerv Surg* 2020;12:545–47 CrossRef Medline
2. Saver JL, Chapot R, Agid R, et al. **Thrombectomy for distal, medium vessel occlusions: a consensus statement on present knowledge and promising directions.** *Stroke* 2020;51:2872–84 CrossRef Medline
3. Alves HC, Treurniet KM, Jansen IG, et al. **Thrombus migration paradox in patients with acute ischemic stroke.** *Stroke* 2019;50:3156–63 CrossRef Medline
4. Ospel JM, Goyal M. **A review of endovascular treatment for medium vessel occlusion stroke.** *J Neurointerv Surg* 2021;13:623–30 CrossRef Medline
5. Goyal M, Kappelhof M, McDonough R, et al. **Secondary medium vessel occlusions: when clots move north.** *Stroke* 2021;52:1147–53 CrossRef Medline
6. Flottmann F, Brekenfeld C, Broocks G, et al; GSR Investigators. **Good clinical outcome decreases with number of retrieval attempts in stroke thrombectomy: beyond the first-pass effect.** *Stroke* 2021;52:482–90 CrossRef Medline
7. Ospel JM, Menon BK, Demchuk AM, et al. **Clinical course of acute ischemic stroke due to medium vessel occlusion with and without intravenous alteplase treatment.** *Stroke* 2020;51:3232–40 CrossRef Medline
8. Grossberg JA, Rebello LC, Haussen DC, et al. **Beyond large vessel occlusion strokes: distal occlusion thrombectomy.** *Stroke* 2018;49:1662–68 CrossRef Medline
9. Goyal M, Menon BK, Van Zwam WH, et al. **Endovascular thrombectomy after large-vessel ischaemic stroke: a meta-analysis of individual patient data from five randomised trials.** *Lancet* 2016;387:1723–31 CrossRef Medline
10. Katz JM, Hakoun AM, Dehdashti AR, et al. **Understanding the radial force of stroke thrombectomy devices to minimize vessel wall injury: mechanical bench testing of the radial force generated by a novel braided thrombectomy assist device compared to laser-cut stent retrievers in simulated MCA vessel diameters.** *Interv Neurol* 2019;8:206–14 CrossRef Medline
11. Perren F, Kargiotis O, Pignat JM, et al. **Hemodynamic changes may indicate vessel wall injury after stent retrieval thrombectomy for acute stroke.** *J Neuroimaging* 2018;28:412–15 CrossRef Medline
12. Pérez-García C, Rosati S, Gómez-Escalonilla C, et al. **MeVO SAVE technique: initial experience with the 167 cm long NeuroSlider 17 for a combined approach in medium vessel occlusions (MeVOs).** *J Neurointerv Surg* 2021;13:768 CrossRefMedline
13. Rikhtegar R, Mosimann PJ, Weber R, et al. **Effectiveness of very low profile thrombectomy device in primary distal medium vessel occlusion, as rescue therapy after incomplete proximal recanalization or following iatrogenic thromboembolic events.** *J Neurointerv Surg* 2021 Jan 19. [Epub ahead of print] CrossRef Medline

Pulsatile Tinnitus Due to Stenosis of the Marginal Sinus: Diagnosis and Endovascular Treatment

J. Cortese, M. Eliezer, A. Guédon, and E. Houdart

ABSTRACT

BACKGROUND AND PURPOSE: Venous pulsatile tinnitus is a disabling condition mainly caused by a stenosis of the lateral sinus. Here, we aimed to report a novel cause of venous pulsatile tinnitus, stenosis of the marginal sinus.

MATERIALS AND METHODS: We retrospectively analyzed patients with isolated venous pulsatile tinnitus for which the suspected cause was a stenosis of the marginal sinus, treated or not, between January 2017 and December 2020. Patient charts and imaging were systematically reviewed. All patients underwent noncontrast temporal bone CT and MR imaging.

RESULTS: Eight patients (7 women; median age, 36 years) were included. Six patients (75%) were overweight, and 1 patient had idiopathic intracranial hypertension. All patients presented with a typical venous pulsatile tinnitus. The stenosis of the marginal sinus was detected using oblique reconstructions on postcontrast 3D MR imaging. There was no other pathologic finding except ipsilateral stenosis of the lateral sinus in 3 patients. Four patients underwent endovascular therapy with placement of a stent in the marginal sinus, leading to complete resolution of the pulsatile tinnitus for all of them. No complication occurred. Of note, the symptoms of intracranial hypertension also regressed after stent placement in that patient.

CONCLUSIONS: Marginal sinus stenosis is a novel cause of venous pulsatile tinnitus, which can be easily detected on MR imaging. Marginal sinus stent placement is safe and efficient. We hypothesized that the marginal sinus stenosis pathophysiology is similar to that of lateral sinus stenosis, which is a common and well-known cause of venous pulsatile tinnitus, explaining the similar clinical presentation and endovascular management.

ABBREVIATIONS: IIH = idiopathic intracranial hypertension; LS = lateral sinus; MS = marginal sinus; OS = occipital sinus; PT = pulsatile tinnitus; SSS = superior sagittal sinus; VAS = visual analog scale

Pulsatile tinnitus (PT) is an uncommon-but-disabling symptom, which has numerous causes, both vascular and nonvascular.[1] Venous etiologies of PT are suspected when the tinnitus disappears by compressing the ipsilateral internal jugular vein. Venous etiologies of PT are increasingly reported and are related to venous abnormalities like lateral sinus (LS) stenosis,[2] sigmoid sinus diverticulum,[3,4] dehiscence,[5] or a mastoid emissary vein.[6] It is paramount to recognize such anomalies because they are often manageable by endovascular treatment.[2,3,6]

Here, we report the clinical and radiographic features as well as the therapeutic management of patients with PT caused by a stenosis of the marginal sinus (MS).

Received June 2, 2021; accepted after revision August 18.

From the Department of Interventional and Diagnostic Neuroradiology, Lariboisière University Hospital, University de Paris, Paris, France.

Please address correspondence to Jonathan Cortese, MD, Department of Interventional and Diagnostic Neuroradiology, Lariboisière University Hospital, 2 Rue Ambroise Paré, 75010 Paris, France; e-mail: Jonathan.cortese@aphp.fr

http://dx.doi.org/10.3174/ajnr.A7325

MATERIALS AND METHODS

Study Design

This is a single-center retrospective study. Consecutive patients between January 2017 and December 2020 with diagnosed PT caused by a stenosis of the MS were included. The medical charts of included patients were analyzed to evaluate patient backgrounds, clinical symptoms, treatment modalities, and clinical outcomes.

Tinnitus was defined as pulsatile when the patient described a sound synchronous with the heart rate. All patients underwent a complete clinical examination by our senior author (E.H.), including auscultation of the heart, neck, and the head, and vascular compression maneuvers at the neck. Disability was evaluated on a visual analog scale (VAS) from 0 (no disability) to 10 (unbearable and extreme disability).

On the basis of the clinical examination, PT was classified as venous if the sound disappeared or decreased during compression of the ipsilateral internal jugular vein and as arterial if the sound disappeared or decreased during compression of the

ipsilateral carotid artery. If the vascular compression maneuvers had no effect on the intensity of the PT, it was classified as neutral.[6,7]

Imaging Protocol and Analysis

All patients underwent MR imaging examinations (3T, Magnetom Skyra; Siemens), which included the following sequences: 3D-TOF from the vertex to the foramen magnum (TR = 1470 ms, TE = 310 ms, 384 × 345, flip angle = 120°, number of excitations = 2, generalized autocalibrating partially parallel acquisition = 2, scan time = 5 minutes 6 seconds); a postcontrast (gadobutrol, Gadovist; Bayer Schering Pharma; 0.1 mL/kg) 3D T1 gradient-echo sequence (MPRAGE; TR = 1470 ms, TE = 310 ms, 384 × 345, flip angle = 120°, number of excitations = 2, generalized autocalibrating partially parallel acquisition = 2, scan time = 5 minutes 6 seconds); and high-resolution temporal bone CT (section thickness = 0.6 mm, 350 mAs, 140 kV(peak) per section) (Somatom Sensation; Siemens).

Imaging was reviewed by 2 experienced neuroradiologists. High-resolution temporal bone and MR images were analyzed to identify potential causes for PT. The MS and the occipital sinus (OS) are not usually visible on postcontrast MR imaging, except if they are enlarged.[8] When the MS was enlarged on the side of the PT, oblique reconstructions from the postcontrast 3D T1 gradient-echo sequence aligning the superior sagittal sinus (SSS) with the OS and the MS were used to detect a stenosis. The ipsilateral LS was also evaluated as normal or hypoplastic and with or without stenosis if normal.[9]

Endovascular Procedure and Follow-up

If the patient's symptom was >5/10 on the VAS, a treatment was proposed, and informed written consent was obtained before treatment. All procedures were performed with the patients under general anesthesia and heparinization (50-IU/kg intravenous bolus followed by 500 IU/h). Briefly, biplanar angiography (Artis zee Q; Siemens) was performed through femoral arterial access with a 4F catheter (Cordis). Jugular puncture was performed under roadmap guidance, and an 8F sheath was placed. Distal access was obtained using Neuron MAX 088 (Penumbra) and Sofia 6F 125-cm catheters (MicroVention). The MS was then catheterized to the jugular bulb via the LS and the OS using a Traxcess-14 microwire (MicroVention) to navigate a 21-inch Prowler Select Plus microcatheter (Codman & Shurtleff).

Then, a 0.014-inch Doppler velocity ComboWire in combination with ComboMap matching hardware (Volcano) was used to measure Doppler velocity at the level of the stenosis in the MS (velocity signals were recorded at 200 Hz).[10] The results were expressed in centimeters per second. The acceleration of the blood velocity at the level of the stenosis was expressed as a velocity ratio (blood velocity at the stenosis/blood velocity in the OS). In our center, the velocity measurements are systematically performed before stent placement in case of PT because we believe that there is a correlation between blood flow velocity and the patient's symptoms.[10,11]

If the blood acceleration was confirmed (velocity ratio > 2), a 5× 30 mm Carotid Wallstent (Boston Scientific) was deployed covering the stenosis and the MS. Because it was a new entity, a 7 × 50 mm Carotid Wallstent was used in the LS if a stenosis was noted. Heparinization was discontinued, and patients were allowed to recover for 24 hours before discharge if no complication was observed. Before stent placement, patients were given aspirin, 75 mg, and clopidogrel, 75 mg, daily for a week. Patients were tested for clopidogrel resistance, and if the patient was resistant, clopidogrel was switched to prasugrel (10 mg). Oral medication was continued for 3 months after the stent placement, followed by aspirin alone for 9 additional months.

Patients were clinically examined at 3 months and 1 year, and a venous contrast-enhanced CT was systematically performed to confirm the absence of stent thrombosis.

RESULTS

Patient Characteristics

A total of 8 patients were included (7 women and 1 man; median age, 36 years; range, 14–60 years). The median body mass index was 29.5 (range, 18–44), with 6 patients overweight (body mass index > 25), including 4 patients who were obese (body mass index = 30). No other significant comorbidities were found.

The PT was located more frequently on the right side (5 patients, 63%) and was systematically classified as a typical venous PT (100%). PT was responsible for a major disability (VAS > 5) in 5 patients (63%). Of note, 1 patient had associated headache and papilledema due to idiopathic intracranial hypertension (IIH).

Imaging Data

All 8 patients presented with a dilated MS ipsilateral to the PT associated with an extrinsic stenosis on the segment preceding the junction with the jugular bulb. The enlarged MS was unilateral or bilateral but was always preceded by an enlarged OS. The oblique reconstruction on the postcontrast MR imaging clearly depicted the stenosis in each patient (Figs 1–3). We noted different configurations of the LS: normal caliber with a stenosis in 3 patients, normal caliber without stenosis in 2 patients, and hypoplastic in the remaining 3 patients. All other causes of PT (including dural arteriovenous fistula and sigmoid sinus diverticulum) were eliminated after initial MR imaging and CT explorations.

Endovascular Treatment

Of the 5 patients with a significant disability, 4 patients accepted the treatment (Table). In all 4 patients, stenting the MS permitted the complete resolution of the PT (VAS = 0). Patients 3 and 4 underwent stenting of both the MS and LS during the same procedure (in 1 case, LS stent placement followed the MS stent placement, whereas it was in the opposite order for the other case) (Fig 2). For patient 1, only the LS was stented during the first procedure (at the time, MS stenosis was not a suspected cause for PT), resulting in no modification of the PT immediately after the operation and at the 3-month follow-up. The second analysis of the MR imaging and an angiogram led to a proposal of a second intervention with stenting of the MS, which the patient accepted. This time the PT completely resolved after the procedure and remained healed at the 3-month and 1-year follow-ups (Fig 1).

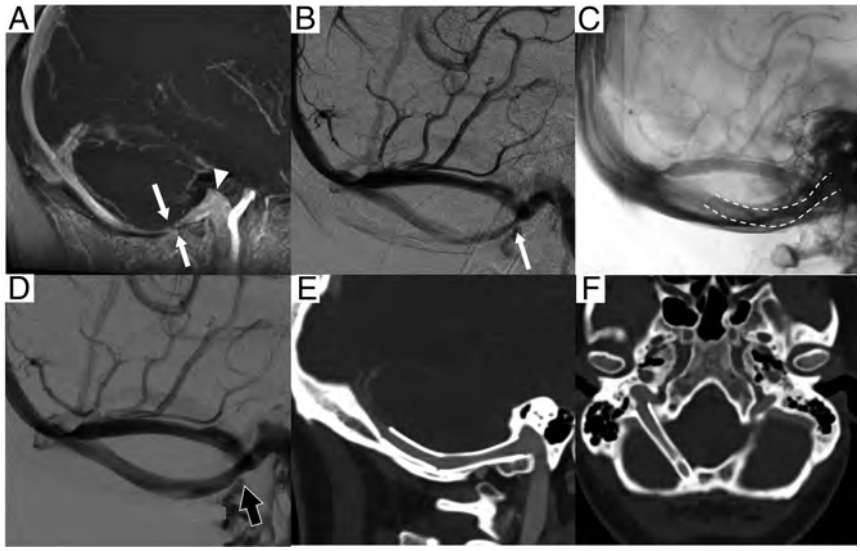

FIG 1. A patient presented with a right-sided venous PT. The patient initially underwent stenting of the lateral sinus, which was unsuccessful because the tinnitus was not modified. *A*, An oblique 3D contrast-enhanced TI sequence depicts a stenosis (*white arrows*) of the right MS before joining the jugular bulb (*white arrowhead*). *B*, A lateral angiogram confirms the stenosis (*white arrow*). *C* and *D*, Two 5 ×30 mm Carotid Wallstents were placed in the MS (*dashed white line*), lifting the stenosis and restoring a normal laminar flow (*black arrow*). The patient's tinnitus was completely cured after the procedure. *E* and *F*, In the control venous CTA at 3 months, oblique and axial reconstructions, no thrombosis is depicted. Note that the stent is in the jugular bulb, close to the temporal bone and the jugular foramen.

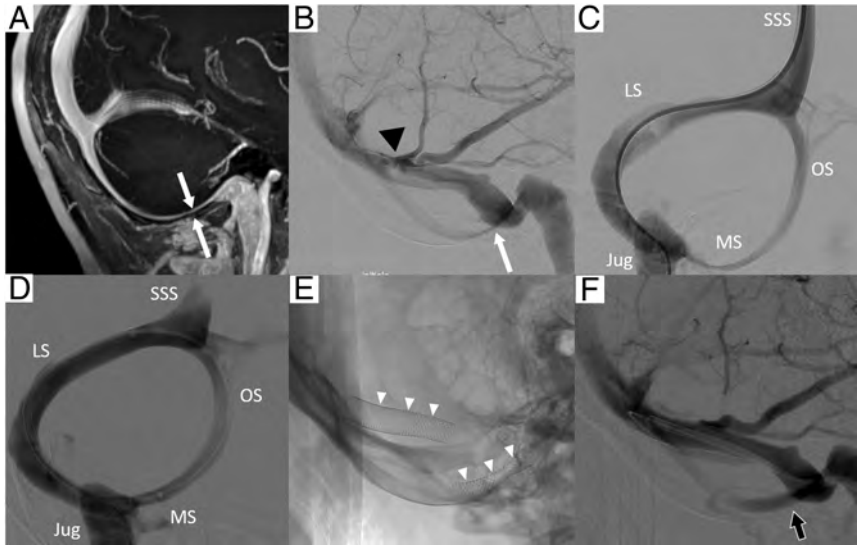

FIG 2. The patient presented with a right-sided venous PT. *A*, An oblique 3D contrast-enhanced TI sequence depicts a stenosis (*white arrows*) of the right MS (*white arrow*). Lateral angiogram (*B*) and oblique phlebography (*C*) confirm the extrinsic stenosis of the MS (*white arrow*); an intrinsic stenosis of the LS was also depicted (*black arrowhead*). Doppler measurement of the venous flow using a ComboWire confirmed the accelerated blood flow at the level of the MS stenosis. *D*, Oblique phlebography shows the deployment of the 5 ×30 mm Carotid Wallstent in the MS after placement of a first stent in the LS. *E* and *F*, Stents were placed in the MS and LS (*white arrowheads*), lifting the stenosis and restoring a normal laminar flow (*black arrow*). The patient's tinnitus was completely cured after the procedure. Jug indicates jugular vein.

There was no technical limitation. The 5-mm-caliber stent was chosen because it corresponded to the caliber of the normal MS in all 4 patients. The stent was deployed starting at the junction between the MS and the jugular bulb, then over the stenosis in the MS. In 2 cases, a second 5 × 30 mm stent was used because of an acute angle formed between the distal part of the stent and the MS at the vertical junction with the OS segment. In these cases, the stent would extend to the OS (Fig 3).

Blood velocities were obtained for 3 patients (all except patient 1); the velocity ratio was an average of 4 (range, 3–5) with mean blood velocities of 10 cm/s (range, 9–11 cm/s) at the level of the OS and at 38 cm/s at the level of the stenosis. For patients with LS stent placement during the same procedure, the velocity ratio in the LS was inferior in one case (2 versus 5 in the MS) and superior in the other case (5 versus 3 in the MS).

Follow-up

All patients treated remained free of PT (VAS = 0) at follow-up, and no complication was detected on physical or imaging evaluation. Furthermore, the patient with IIH was also improved after the stent placement, and papilledema resolved at the 1-year control.

DISCUSSION

In this study, we described 8 patients with venous PT, in whom the suspected cause was an MS stenosis. Four patients underwent stenting of the MS. The procedure was effective for all of them. To the best of our knowledge, this is the largest case series that highlights specifically the stenosis of the MS as a cause of PT. Preceding reports have described MS stenosis as a cause for venous PT[12] or IIH.[13,14] However, Li et al[12] referred to it as a stenosis of the vein of the hypoglossal canal. We believe it is an inaccurate name because the sinus is reaching the jugular bulb without crossing the hypoglossal canal.

The MS is a dural venous sinus that connects the OS posteriorly and the basilar venous plexus and the distal part of the sigmoid sinus at the junction with the internal jugular bulb anteriorly. Generally, in human adults, the LS represents the main venous outflow, and the occipital-marginal sinus system, an alternative pathway. The dominance of LS over the occipital-marginal sinus system is believed to be an epigenetic adaptation acquired with bipedalism

in early human species.[15] During fetal growth, the OS and the MS develop simultaneously from a large plexiform configuration, and by full term, both tend to have regressed to a small accessory sinus.[16] However, the occipital-marginal sinus system can be found enlarged or even dominant over the LS in approximately 4%–5% of the population.[17]

Here, we show that the MS is another potential location for dural venous sinus stenosis. MS stenosis clinical and imaging presentations were very similar to those of LS stenosis: Patients were predominantly overweight women with typical venous PT, and the stenosis could be identified on MR images. In our center, MR imaging with a postcontrast 3D T1 gradient-echo sequence is part of the initial exploration of PT. MS stenosis can be suspected when an enlarged OS (usually as large as the SSS) followed by an enlarged MS (ipsilateral to the PT) is present. Oblique 3D reconstructions aligning the SSS with the OS, the MS, and the jugular bulb were useful for easily detecting the stenosis.

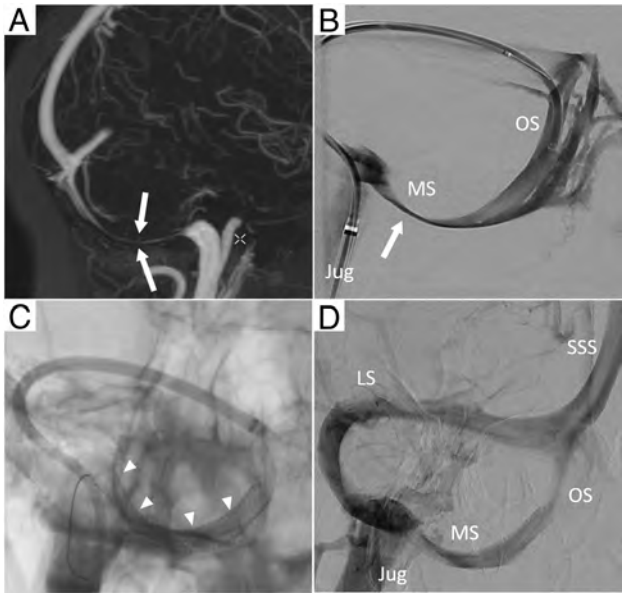

FIG 3. A patient presented with a right-sided venous PT associated with symptoms of IIH. *A*, An oblique 3D contrast-enhanced T1 sequence depicts a stenosis (*white arrows*) of the right MS; no MS was noted on the left side. *B*, Oblique phlebography confirms the extrinsic stenosis of the MS (*white arrow*); the LS was normal on the right side and absent (hypoplastic) on the left side. *C*, Two 5 × 30 mm Carotid Wallstents are deployed in the right occipital-marginal sinus (*white arrowheads*) (*D*), lifting the stenosis and restoring a normal MS caliber. Both the tinnitus and the symptoms of IIH disappeared. Jug indicates jugular vein.

The perception of a venous PT is linked to the turbulence of the blood flow following the venous stenosis, as described with the LS.[10,11,18] Because the MS has a close relationship with the temporal bone, we hypothesized that the same pathophysiology is responsible for the PT in MS stenosis. Therefore, relieving the stenosis with a stent permitted the return of a laminar blood flow in the MS, and, thus, PT disappearance.[2,19]

In 1 patient, an MS stenosis was also responsible for IIH (Fig 3). Most interesting, the ipsilateral LS was present with a normal caliber (the contralateral LS was hypoplastic). All symptoms improved after the stenting of the MS, meaning that the right lateral sinus was not sufficient for a normal cerebral blood circulation and the patient was dependent on the MS as well. LS stenosis is often associated with IIH, and stenting of the LS is safe and effective.[9,20] Two recent case reports of MS stenosis associated with IIH described clinical improvement after stenting of the sinus, supporting LS and MS stenosis being similar pathologies.[13,14]

Finally, 2 patients were treated for LS and MS stenoses during the same procedure, interpreted as a limitation of our results (because the responsibility of the MS stenosis is uncertain). However, performing 2 different interventions to test which stenosis was responsible for the PT was, in our opinion, not feasible outside a prospective clinical trial. In addition, the acceleration of the venous flow at the MS stenosis was confirmed by measurement of blood velocity before stent placement. We observed an acceleration ratio similar to the one reported for the LS (median velocity ratio of the SSS/LS stenosis, 3 [range, 2–7]).[10] It is also common to find multiple causes of venous PT, like LS stenosis and sigmoid sinus ectasia.[19,21] Moreover, in patient 1, we postponed the MS stent placement, limiting the treatment of the LS. The patient's PT remained unchanged after the first procedure but was completely cured after the second procedure (stenting of the MS), emphasizing the role of the MS. Also, 4 patients were not treated, meaning that the responsibility of the MS stenosis remains untested for them as well. Nevertheless, all 4 patients had typical venous PT, and no other pathologic findings were detected on CT or MR imaging (including LS stenosis).

This study has several diagnostic and therapeutic implications. First, an MS stenosis should be looked for on a MRI done for the exploration of a venous PT (using the 3D oblique reconstruction if the OS is enlarged); and even if a stenosis of the LS is present as both (the MS and the LS) could contribute to the

Patients with MS stenosis

No.	Type of PT	Side	Disability[a]	Ipsilateral LS	Sinus Stented	Treatment Efficiency
1	Venous	Right	8	Stenosis	LS then MS	Yes (after the MS stent placement)
2	Venous	Right	9[b]	Normal	MS	Yes
3	Venous	Left	9	Stenosis	LS+MS	Yes
4	Venous	Right	8	Stenosis	LS+MS	Yes
5	Venous	Left	3	Normal	None	
6	Venous	Right	4	Hypoplastic	None	
7	Venous	Left	5	Hypoplastic	None	
8	Venous	Right	9	Hypoplastic	None	

[a]Disability was evaluated on a VAS from 0 (no tinnitus) to 10 (unbearable and extreme tinnitus).
[b]Patient 2 also had IIH, which also resolved after the stent placement.

tinnitus. Second, treatment of the MS stenosis via stent placement is feasible and safe, as the large experience with LS stent placement could predict.

This study also has limitations. It is a retrospective study performed at a single academic center. The usual pressure measurements were not systematically performed or available and, therefore, are not reported here, though possibly being valuable information. Instead, we reported venous blood flow velocities, which limit the comparison with other studies. Finally, when both stenoses are present (MS and LS), it remains to determine which one is more "symptomatic" and whether they should be treated together.

CONCLUSIONS

In this study, we presented MS stenosis as a novel cause of venous PT. The clinical presentation of MS stenosis is similar to that of LS stenosis, which is a common and well-known cause of venous PT. MS stenosis can be easily detected on postcontrast 3D MR imaging using oblique reconstructions and could be safely and efficiently treated with a stent.

Disclosure forms provided by the authors are available with the full text and PDF of this article at www.ajnr.org.

REFERENCES

1. Liyanage SH, Singh A, Savundra P, et al. **Pulsatile tinnitus.** *J Laryngol Otol* 2006;120:93–97 CrossRef Medline
2. Lenck S, Labeyrie MA, Vallee F, et al. **Stent placement for disabling pulsatile tinnitus caused by a lateral sinus stenosis: a retrospective study.** *Oper Neurosurg (Hagerstown)* 2017;13:560–65 CrossRef Medline
3. Houdart E, Chapot R, Merland JJ. **Aneurysm of a dural sigmoid sinus: a novel vascular cause of pulsatile tinnitus.** *Ann Neurol* 2000;48:669–71
4. Amans MR, Haraldsson H, Kao E, et al. **MR venous flow in sigmoid sinus diverticulum.** *AJNR Am J Neuroradiol* 2018;39:2108–13 CrossRef Medline
5. Eisenman DJ, Raghavan P, Hertzano R, et al. **Evaluation and treatment of pulsatile tinnitus associated with sigmoid sinus wall anomalies.** *Laryngoscope* 2018;128(Suppl 2):S1–13 CrossRef Medline
6. Eliezer M, Freitas RK, Fantoni M, et al. **Selective embolization of the mastoid emissary vein for pulsatile tinnitus treatment: when is it indicated?** *J Neurointerv Surg* 2020;12:999–1001 CrossRef Medline
7. Sismanis A. **Pulsatile tinnitus: a 15-year experience.** *Am J Otol* 1998;19:472–77 Medline
8. Kobayashi K, Suzuki M, Ueda F, et al. **Anatomical study of the occipital sinus using contrast-enhanced magnetic resonance venography.** *Neuroradiology* 2006;48:373–79 CrossRef Medline
9. Lenck S, Vallée F, Labeyrie M-A, et al. **Stenting of the lateral sinus in idiopathic intracranial hypertension according to the type of stenosis.** *Neurosurgery* 2017;80:393–400 CrossRef Medline
10. Lenck S, Vallée F, Civelli V, et al. **Assessment of blood flow velocities and venous pressures using a dual-sensor guidewire in symptomatic dural sinus stenoses.** *J Neurosurg* 2018 May 1 [Epub ahead of print] CrossRef Medline
11. Haraldsson H, Leach JR, Kao EI, et al. **Reduced jet velocity in venous flow after CSF drainage: assessing hemodynamic causes of pulsatile tinnitus.** *AJNR Am J Neuroradiol* 2019;40:849–54 CrossRef Medline
12. Li B, Lv X, Wu Z, et al. **Occult pulsatile tinnitus in association with a prominent vein of hypoglossal canal: two case reports.** *Turk Neurosurg* 2016;26:953–56 CrossRef Medline
13. Alvarado AM, Nalluri P, Alvarado AM, et al. **Unique variant of idiopathic intracranial hypertension dural sinus stenting.** *Int J Neurosci* 2021;131:196–98 CrossRef Medline
14. Al Balushi A, Oliveira C, Patsalides A. **Idiopathic intracranial hypertension with stenosis of a solitary occipital venous sinus treated with stenting.** *Interv Neuroradiol* 2020;26:664–67 CrossRef Medline
15. Falk D. **Evolution of cranial blood drainage in hominids: enlarged occipital/marginal sinuses and emissary foramina.** *Am J Phys Anthropol* 1986;70:311–24 CrossRef Medline
16. Kimbel WH. **Variation in the pattern of cranial venous sinuses and hominid phylogeny.** *Am J Phys Anthropol* 1984;63:243–63 CrossRef Medline
17. Dora F, Zileli T. **Common variations of the lateral and occipital sinuses at the confluens sinuum.** *Neuroradiology* 1980;20:23–27 CrossRef Medline
18. Pereira VM, Cancelliere NM, Najafi M, et al. **Torrents of torment: turbulence as a mechanism of pulsatile tinnitus secondary to venous stenosis revealed by high-fidelity computational fluid dynamics.** *J Neurointerv Surg* 2021;13:732–37 CrossRef Medline
19. Patsalides A, Santillan A, Sundararajan SH, et al. **Venous sinus stenting for the treatment of isolated pulsatile tinnitus: results of a prospective trial.** *Interv Neuroradiol* 2021;27:266–74 CrossRef Medline
20. Koovor JM, Lopez GV, Riley K, et al. **Transverse venous sinus stenting for idiopathic intracranial hypertension: safety and feasibility.** *Neuroradiol J* 2018;31:513–17 CrossRef Medline
21. Hewes D, Morales R, Raghavan P, et al. **Pattern and severity of transverse sinus stenosis in patients with pulsatile tinnitus associated with sigmoid sinus wall anomalies.** *Laryngoscope* 2020;130:1028–33 CrossRef Medline

Carotid Plaque Composition Assessed by CT Predicts Subsequent Cardiovascular Events among Subjects with Carotid Stenosis

E. Choi, E. Byun, S.U. Kwon, N. Kim, C.H. Suh, H. Kwon, Y. Han, T.-W. Kwon, and Y.-P. Cho

ABSTRACT

BACKGROUND AND PURPOSE: Currently, the characteristics of carotid plaques are considered important factors for identifying subjects at high risk of stroke. This study aimed to test the hypothesis that carotid plaque composition assessed by CTA is associated with an increased risk of future major adverse cardiovascular events among asymptomatic subjects with moderate-to-severe carotid artery stenosis.

MATERIALS AND METHODS: This single-center, retrospective cohort study included 194 carotid plaques from 176 asymptomatic subjects with moderate-to-severe carotid artery stenosis. The association of CTA-determined plaque composition with the risk of subsequent adverse cardiovascular events was analyzed.

RESULTS: During a median follow-up of 41 months, the adverse cardiovascular event incidence among 194 carotid plaques was 19.6%. There were significant differences in plaque Hounsfield units ($P < .001$) and spotty calcium presence ($P < .001$) between carotid plaques from subjects with and without subsequent adverse cardiovascular events. Multivariable analysis revealed carotid plaque Hounsfield unit density ($P < .001$) and spotty calcium ($P < .001$) as independent predictors of subsequent adverse cardiovascular events. In association with moderate carotid artery stenosis, the plaque Hounsfield unit values were significantly lower among carotid plaques from subjects who experienced subsequent adverse cardiovascular events ($P = .002$), strokes ($P = .01$), and cardiovascular deaths ($P = .04$); the presence of spotty calcium was significantly associated with the occurrence of adverse cardiovascular events ($P = .001$), acute coronary syndrome ($P = .01$), and cardiovascular death ($P = .04$).

CONCLUSIONS: Carotid plaque Hounsfield unit density and spotty calcium were independent predictors of a greater risk of adverse cardiovascular event occurrence.

ABBREVIATIONS: ACS = acute coronary syndrome; CAS = carotid artery stenosis; DUS = Doppler ultrasound; HR = hazard ratio; IQR = interquartile range; MACE = major adverse cardiovascular event

Cardiovascular disease results in considerable morbidity and mortality worldwide; therefore, the identification of subclinical disease during the asymptomatic phase is an important public health goal.[1] Carotid atherosclerosis has been assessed by Doppler sonography (DUS)-determined intima-media thickness or plaque features for predicting cardiovascular disease, particularly cerebrovascular disease.[2] Therefore, carotid DUS screening could be a valuable tool for assisting with cardiovascular risk stratification to inform preventive strategies for asymptomatic subjects with few conventional risk factors.[3] However, DUS can be limited by operator-dependent variability, low image resolution, and acoustic shadowing;[4] therefore, the use of medical imaging to predict future cardiovascular or cerebrovascular events has been extensively investigated.[5]

Currently, a widely accepted concept is that carotid plaques go through a remodeling process, and sometimes atherosclerosis with even low-grade carotid artery stenosis (CAS) may result in cerebrovascular events.[6] Thus, plaque characteristics other than the degree of stenosis alone may be important for identifying subjects at high risk of stroke.[7] CTA provides simultaneous information about the degree of stenosis and a more detailed analysis of plaque composition.[7] Coronary plaque characterization by CTA is a well-described method for predicting major adverse cardiovascular events (MACEs) in different subpopulations,[8] whereas relatively little experience has been gained with CTA for identifying and quantifying carotid plaque composition associated with MACE

Received November 8, 2020; accepted after revision July 28, 2021.

From the Departments of Surgery (E.C., E.B., H.K., Y.H., T.-W.K., Y.-P.C.), Neurology (S.U.K.), Clinical Epidemiology and Biostatistics (N.K.), and Radiology and Research Institute of Radiology (C.H.S.), University of Ulsan College of Medicine, Asan Medical Center, Seoul, Korea.; and

Please address correspondence to Yong-Pil Cho, MD, Department of Surgery, University of Ulsan College of Medicine and Asan Medical Center, 88 Olympic-ro 43-gil, Songpa-gu, Seoul 05505, Korea; e-mail: ypcho@amc.seoul.kr

Indicates article with online supplemental data.

http://dx.doi.org/10.3174/ajnr.A7338

risk.[7] Therefore, this study aimed to test the hypothesis that carotid plaque composition detected by CTA can be used as a surrogate marker for predicting a higher risk of MACEs.

MATERIALS AND METHODS

Study Design and Study Sample

In this single-center, retrospective cohort study, we analyzed data extracted from the medical records of the subjects older than 50 years of age who underwent CTA for health screening or regular follow-up at our hospital. An electronic search was conducted using the hospital's database to identify terms, including "carotid" and "stenosis," on CTA reports.

Between January 2010 and December 2017, eight hundred seventy-six stenotic carotid arteries (876/4294, 20.4%) from 2147 consecutive CTAs were included in this analysis. The degree of CAS was measured according to the NASCET CTA criteria[9] by an expert neuroradiologist. The exclusion criteria were as follows: 1) mild stenosis (<50% diameter reduction) or total occlusion ($n = 422$); 2) CAS with totally calcified plaque formation ($n = 172$); 3) diffuse stenosis, thin plaque, or artifacts precluding interpretation ($n = 15$); 4) previous ipsilateral carotid endarterectomy or stent placement ($n = 12$); and 5) recent cardiovascular events within 6 months ($n = 61$). Subtotal occlusions ($n = 4$) were included in this study. A total of 194 carotid plaques from 176 asymptomatic subjects without cardiovascular events within 6 months, with reported CAS in the range of 50% to 99% on baseline CTA and additional DUS, were included in the final analysis (Online Supplemental Data): moderate CAS (50%–69% diameter reduction, $n = 101$, 52.1%) and severe CAS (70%–99% diameter reduction, $n = 93$, 47.9%). Clinical indications for CTA were imaging surveillance for known cerebrovascular disease (including intracranial aneurysm or stenosis) and CAS (82%), and neurologic symptoms (including headache and change of mental status) (18%).

The demographics, risk factors of interest, clinical characteristics, and outcomes for all consecutive subjects were recorded in an Excel (Microsoft) database and analyzed retrospectively. Risk factor variables were defined as previously described.[3] CTA reports were recorded by dedicated, board-certified neuroradiologists, and CTA images were independently re-evaluated for carotid plaque characterization, including the degree of CAS, plaque Hounsfield unit density, and the presence of ulceration, spotty calcium, napkin-ring sign, and calcium score by 2 specialized vascular surgeons and 1 neuroradiologist. All medication adjustments were made by the subjects' health care providers at our hospital according to each individual's atherosclerosis risk factors, determined using the American College of Cardiology Foundation/American Heart Association guidelines.[9] Eligible carotid plaques from included subjects were followed from the date that they underwent CTA and were stratified into 2 groups according to the occurrence of MACEs during follow-up: carotid plaques with MACEs and carotid plaques without MACEs. Then, we performed a subgroup analysis of carotid plaques with moderate CAS.

Study Protocol Approvals, Registrations, and Patient Consent

Approval for data collection and publication was obtained from the institutional review board at our hospital (IRB No. 2019–0663), which waived the requirements for written informed consent because of the study's retrospective design. All methods were performed in accordance with the relevant guidelines and regulations.

CTA Protocol

CTA was performed using a standard protocol (Online Supplemental Data) with the following parameters: 120 kV, automated tube current modulation using a 300-mA reference value, and a 1.0-mm reconstructed section thickness (Somatom Definition AS+ and Edge; Siemens). The scans were conducted from the aortic root to 3 cm above the skull before and after contrast injection. All CTA images were reconstructed in axial, coronal, and sagittal orientations.

Carotid Plaque Characterization

Each plaque was categorized according to the CTA findings as follows: calcified plaque composed predominantly of calcified tissue (>130 HU) (excluded from our analysis), mixed plaque composed of both calcified and noncalcified tissue, and soft plaque composed predominantly of noncalcified tissue. Carotid plaque ulceration was defined as the presence of an obvious, large excavation (>2 mm in depth) on the surface of the plaque.[10] For Hounsfield unit measurements, an ROI of 2 mm^2 was preselected on the visually least attenuated area of the plaque at the most stenotic level using a width of 850 HU and a level of 300 HU as the window-level settings on contrast-enhanced axial images to distinguish plaque from the vascular lumen. The plaque Hounsfield unit density was measured 5 times from the noncontrast axial images using prepositioned ROIs on the plaque to exclude blooming artifacts (Fig 1). The lowest measured Hounsfield unit value in each plaque was recorded. Calcium score, along with the presence of spotty calcium and the napkin-ring sign—suggested as high-risk plaque features for predicting acute coronary syndrome (ACS)—were also evaluated.[11,12] Spotty calcium was defined as the presence of calcium in the plaque with a diameter of <3 mm in any direction on curved multiplanar reformation images, occupying only 1 side and a maximum arc below 90° on cross-sectional images.[11,13] The napkin-ring sign was defined as the presence of low-attenuation plaque surrounded by a ring of high attenuation that was not >130 HU (Fig 2).[12] The calcium score was measured using semiautomated software (Syngo CaScoring; Siemens) and the method described by Agatston et al.[14]

Clinical Outcomes

The study outcomes included the occurrence of MACEs, defined as fatal or nonfatal, ipsilateral or contralateral stroke or TIA, ACS, or cardiovascular death. Data on all MACEs were centrally reviewed and blindly adjudicated by an experienced independent neurologist or cardiologist. Events were categorized as "Event," "Limited data," or "No Event" on the basis of chart review. Once an event was not confirmed due to Limited data, more information was collected by face-to-face or direct telephone interviews with the subjects or their families. For quality control, second reviews were conducted by other physicians blinded to the original adjudicated results. In the analysis, we included only ischemic strokes, as previously defined.[3] ACS was defined as acute myocardial infarction or unstable angina pectoris, according to the American College of Cardiology/

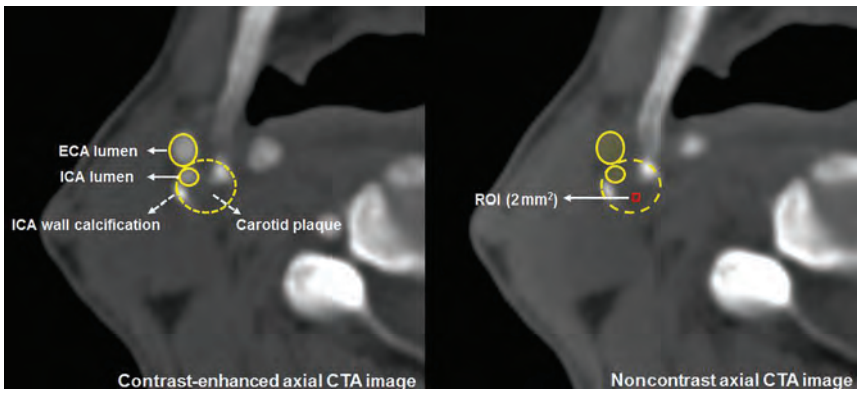

FIG 1. Representative figure of plaque Hounsfield unit value measurement. The plaque Hounsfield unit values were measured from noncontrast axial CTA images. An ROI of 2 mm^2 was preselected on the visually least attenuated area of the plaque at the most stenotic level of contrast-enhanced axial images. Measurements were performed 5 times from the noncontrast axial images using prepositioned ROIs on the plaque. The lowest Hounsfield unit value in each plaque was recorded. ECA indicates external carotid artery.

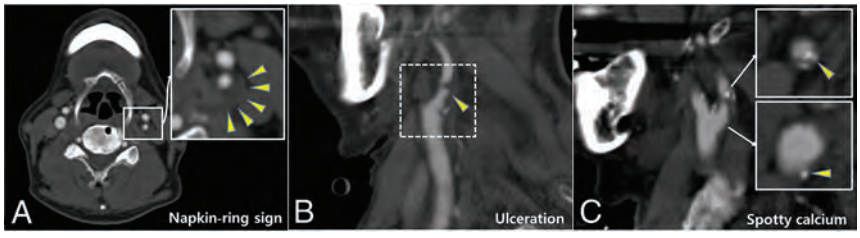

FIG 2. Representative figures of high-risk features of carotid plaque (*arrowheads*) on CTA. Napkin-ring sign (*A*), carotid plaque ulceration (*B*), and spotty calcium (*C*).

American Heart Association guidelines.[15] Only the first event of each outcome was included in the MACE analysis, whereas each MACE was analyzed individually.

Statistical Analysis

Statistical analysis was performed using PASW Statistics for Windows, Version 18 (https://www.malavida.com/en/soft/pasw/); R, Version 3.6.3 (http://www.r-project.org); and SAS version 9.4 (SAS Institute). We separately summarized the characteristics of 176 subjects and 194 carotid plaques. Categoric variables are reported as frequencies or percentages, and continuous variables, as means (SDs) or medians and interquartile ranges (IQRs), as appropriate. Cox proportional hazard models, with robust standard errors that accounted for the clustering of subjects' effects, were fitted to identify MACE predictors. The Mann-Whitney rank test was used for comparisons of non-normally distributed continuous variables. Demographic and clinical characteristics that were considered to be associated with MACEs and features of carotid plaques on CTA were included in this analysis. Variables yielding P values $< .1$ from univariable analysis were subjected to multivariable analysis, and hazard ratios (HRs) with 95% CIs were calculated. In the Kaplan-Meier survival analysis, Hounsfield unit values were dichotomized at the median value of the study cohort, and the log-rank test was used to compare the occurrence of MACEs and the individual MACE components. We performed subgroup analyses limited to carotid plaques from subjects with moderate CAS, wherein we evaluated the association between plaque composition and future MACE occurrences overall as well as the individual MACE components. The interobserver reproducibility of plaque characterization was analyzed through interclass correlation coefficient calculations. Possible interclass correlation coefficients ranged from 0 to 1.00, and measurement reliability was classified as excellent (interclass correlation coefficient > 0.9), good (0.75–0.9), moderate (interclass correlation coefficient = 0.5–0.75), or poor (interclass correlation coefficient < 0.5).[16] P values $< .05$ were considered statistically significant.

RESULTS

After all exclusions based on the predetermined criteria, a total of 194 consecutive carotid plaques from 176 subjects were analyzed. All subjects were diagnosed with moderate-to-severe CAS using CTA and additional DUS. Eligible carotid plaques were stratified into 2 groups according to the occurrence of MACEs as follows: non-MACE group (156 plaques from 142 subjects, 80.4%) and MACE group (38 plaques from 34 subjects, 19.6%). Tables 1 and 2 show the subjects' baseline, clinical, and plaque characteristics. The 2 groups did not differ significantly in terms of demographic characteristics, risk factors, or clinical characteristics, except that subjects in the MACE group were more likely to have atrial fibrillation. There were significant differences in plaque Hounsfield unit values (39.2 [SD, 15.2] versus 27.6 [SD, 12.7], $P < .001$) and spotty calcium presence (14.7% versus 44.7%, $P < .001$) between the 2 groups. The mean calcium score was higher in the MACE group than in the non-MACE group with a nonsignificant trend ($P = .06$), and the degree of CAS was not significantly different between the 2 groups (Online Supplemental Data).

Variables Associated with MACE Occurrence

During follow-up, the MACE incidence among the 194 carotid plaques was 19.6% (38/194). There were 19 strokes (9.8%), 16 ACS diagnoses (8.2%), and 12 cardiovascular deaths (6.2%). According to the per-subject analysis ($n = 176$), there were 16 strokes (9.1%), 14 ACS diagnoses (8.0%), and 12 cardiovascular deaths (6.8%). Table 3 shows the results of the regression analysis in terms of MACE occurrences on a per-carotid plaque basis. In the adjusted models, plaque Hounsfield unit density (HR = 0.96; 95% CI, 0.94–0.98; $P < .001$) and spotty calcium presence (HR =

Table 1: Baseline and clinical characteristics of the study sample, stratified by the occurrence of MACEs[a]

Subjects	Total ($n = 176$)	Non-MACE Group ($n = 142$)	MACE Group ($n = 34$)	*P* Value
Age (yr)	69.3 (SD, 7.6)	69.3 (SD, 7.7)	69.2 (SD, 6.8)	.49
Median (IQR) (yr)	70 (64–75)	69 (64–75)	71 (66–75)	
Male sex	156 (88.6)	126 (88.7)	30 (88.2)	.998
Body mass index (kg/m^2)	24.5 (SD, 3.1)	24.5 (SD, 3.0)	24.4 (SD, 3.4)	.96
Risk factors				
Diabetes mellitus	76 (43.2)	66 (46.5)	10 (29.4)	.096
Hypertension	126 (71.6)	101 (71.1)	25 (73.5)	.80
Dyslipidemia	96 (54.6)	77 (54.2)	19 (55.9)	.60
Current smoking	43 (24.4)	32 (22.5)	11 (32.4)	.42
Past smoking	68 (38.6)	56 (39.4)	12 (35.3)	.91
Atrial fibrillation	9 (5.1)	5 (3.5)	4 (11.8)	.001
Medical history				
History of stroke[b]	56 (31.8)	44 (31.0)	12 (35.3)	.66
History of ACS[b]	30 (17.1)	21 (14.8)	9 (26.5)	.30
Antiplatelet	154 (87.5)	124 (87.3)	30 (88.2)	.72
Statins	142 (80.7)	115 (81.0)	27 (79.4)	.47

[a]Any stroke, ACS, or cardiovascular mortality. Continuous data are presented as means (SD) or median (IQR); categoric data are given as (No.) (%).
[b]Subjects with any stroke or ACS who had been diagnosed >6 months previously and successfully treated.

Table 2: Plaque characteristics, stratified by the occurrence of MACEs[a]

Plaques	Total ($n = 194$)	Non-MACE Group ($n = 156$)	MACE Group ($n = 38$)	*P* Value
Stenosis (%)	68.6 (SD, 10.8)	67.9 (SD, 10.0)	71.3 (SD, 13.4)	.49
Median (IQR)	68 (60–75)	68 (60–75)	71 (62–80)	
Mixed plaque	129 (66.5)	102 (65.4)	27 (71.1)	.18
Plaque ulceration	15 (7.7)	13 (8.3)	2 (5.3)	.53
Hounsfield unit	36.9 (SD, 15.4)	39.2 (SD, 15.2)	27.6 (SD, 12.7)	<.001
Median (IQR)	36 (28–45)	40 (30–47)	28 (19–36)	
Spotty calcium	40 (20.6)	23 (14.7)	17 (44.7)	<.001
Napkin-ring sign	56 (28.9)	40 (25.6)	16 (42.1)	.09
Calcium score	443.5 (SD, 443.8)	416.3 (SD, 428.0)	551.2 (SD, 493.0)	.06
Median (IQR)	306 (101–639)	294 (74–564)	367 (165–1018)	
Follow-up (mo) (median) (IQR)	41 (29–60)	41 (30–59)	47 (22–71)	.76

[a] Any stroke, ACS, or cardiovascular mortality. Continuous data are presented as means (SD) or median (IQR); categoric data are given as (No.) (%).

3.97; 95% CI, 2.08–7.60; $P < .001$) were independent predictors of future MACEs.

Analysis of MACEs and Individual MACE Components Based on the Values Reflecting Plaque Hounsfield Unit Density and Spotty Calcium Presence

Cox proportional hazards modeling indicated a lower Hounsfield unit density among carotid plaques from subjects who experienced MACEs (HR = 0.96; 95% CI, 0.95–0.98; $P < .001$), whereas plaque Hounsfield unit density was not associated with all-cause mortality ($P = .14$) (Table 4). The prevalence of spotty calcium observed on CTA was higher among carotid plaques from subjects who experienced any MACE (HR = 4.08; 95% CI, 2.13–7.83; $P < .001$) when the composite outcome was analyzed as a single entity. When the individual MACE manifestations were analyzed separately, ipsilateral stroke ($P = .09$) and cardiovascular mortality ($P = .06$) were not associated with a higher prevalence of spotty calcium (Table 5).

On Kaplan-Meier survival analyses of the cumulative event-free rates based on the dichotomization of Hounsfield units at the median value of the cohort (36 HU), a lower plaque density (<36 HU) was associated with decreased MACE-free ($P = .002$), stroke-free ($P = .038$), and cardiovascular mortality-free ($P = .001$) survival rates, compared with a higher plaque density (≥36 HU) (Fig 3). Although lower plaque density trended toward an association with a decreased ACS-free survival rate ($P = .055$), this was not statistically significant.

Subgroup Analysis of the MACE Composite Outcome and the Individual MACE Components among Carotid Plaques from Subjects with Moderate CAS Based on the Plaque Hounsfield Unit Density and Spotty Calcium Presence

The plaque Hounsfield unit values were lower among carotid plaques from subjects who experienced any MACE (HR = 0.95; 95% CI, 0.92–0.98; $P = .002$) and stroke ($P = .01$) and those who died from a cardiovascular cause ($P = .04$). However, ACS ($P = .14$) and all-cause death ($P = .31$) were not associated with plaque Hounsfield unit density (Online Supplemental Data). The prevalence of spotty calcium on CTA was higher among carotid plaques from subjects who experienced any MACE (HR = 5.20; 95% CI, 1.94–13.92; $P = .001$), ACS ($P = .01$), and cardiovascular death ($P = .04$). However, stroke ($P = .07$) was not associated with the presence of spotty calcium on CTA when analyzed individually (Online Supplemental Data). The low number of MACEs ($n = 18$) limited our ability to include additional variables in the multivariable models.

Interobserver Reliability

Good agreement between observers (2 vascular surgeons) was found in terms of the quantification of carotid plaque density (Hounsfield unit measurement) (interclass correlation coefficient = 0.831; 95% CI, 0.781–0.870) and spotty calcium presence (interclass correlation coefficient = 0.800; 95% CI, 0.734–0.849). There was also strong interobserver reliability between the vascular surgeon and the neuroradiologist for both Hounsfield units (interclass correlation coefficient = 0.862; 95% CI, 0.764–0.913) and spotty calcium (interclass correlation coefficient = 0.830; 95% CI, 0.731–0.931).

Table 3: Cox proportional hazards model for variables associated with MACE[a] occurrence

	Model 1[b]		Model 2[c]	
	HR (95% CI)	*P* Value	HR (95% CI)	*P* Value
Diabetes mellitus	0.60 (0.28–1.24)	.17	NA	NA
Atrial fibrillation	1.07 (0.33–3.48)	.91	NA	NA
Hounsfield unit	0.96 (0.94–0.98)	<.001	0.96 (0.94–0.98)	<.001
Spotty calcium	4.00 (2.00–8.00)	<.001	3.97 (2.08–7.60)	<.001
Napkin-ring sign	0.75 (0.36–1.55)	.45	NA	NA
Calcium score	1.00 (1.00–1.001)	.25	NA	NA

Note:—NA indicates not applicable.
[a]Any stroke, ACS, or cardiovascular mortality.
[b]Model 1 is multivariable analysis including all variables with $P < .1$ in univariable analysis.
[c]Model 2 is multivariable analysis with backward elimination of variables with $P < .1$ in univariable analysis.

Table 4: Cox proportional hazards model for the association of the plaque Hounsfield unit values with the occurrence of the MACE composite outcome and the individual MACE components ($n = 194$)[a]

	MACE (–)	MACE (+)	HR (95% CI)	*P* Value
MACE[b] ($n = 38$)	39.2 (SD, 15.2)	27.6 (SD, 12.7)	0.96 (0.95–0.98)	<.001
Any stroke ($n = 19$)	37.9 (SD, 15.4)	27.8 (SD, 12.0)	0.97 (0.94–0.99)	.01
Ipsilateral stroke ($n = 14$)	37.6 (SD, 15.4)	27.4 (SD, 12.4)	0.96 (0.93–0.99)	.02
ACS ($n = 16$)	37.8 (SD, 15.2)	26.6 (SD, 14.0)	0.96 (0.93–0.99)	.01
Cardiovascular mortality ($n = 12$)	37.7 (SD, 15.4)	24.9 (SD, 8.8)	0.95 (0.92–0.99)	.01
All-cause mortality ($n = 32$)	37.7 (SD, 15.6)	32.8 (SD, 13.9)	0.98 (0.96–1.01)	.14

[a]Data are presented as mean (SD) and 95% CI of plaque Hounsfield values.
[b]Any stroke, ACS, or cardiovascular mortality.

Table 5: Cox proportional hazards model for the association of the presence of spotty calcium on CTA with the occurrence of the MACE composite outcome and the individual MACE components ($n = 194$)[a]

	MACE (–)	MACE (+)	HR (95% CI)	*P* Value
MACE[b] ($n = 38$)	23 (14.7)	17 (44.7)	4.08 (2.13–7.83)	<.001
Any stroke ($n = 19$)	32 (18.3)	8 (42.1)	3.25 (1.30–8.11)	.01
Ipsilateral stroke ($n = 14$)	35 (19.4)	5 (35.7)	2.61 (0.87–7.82)	.09
ACS ($n = 16$)	31 (17.4)	9 (56.3)	6.39 (2.34–17.45)	<.001
Cardiovascular mortality ($n = 12$)	35 (19.2)	5 (41.7)	3.01 (0.95–9.48)	.06
All-cause mortality ($n = 32$)	28 (17.3)	12 (37.5)	2.57 (1.25–5.26)	.01

[a]Data are presented as (No.) (%) and 95% CI of carotid plaques with spotty calcium detected on CTA.
[b]Any stroke, ACS, or cardiovascular mortality.

DISCUSSION

Carotid atherosclerosis is assessed by DUS-determined intima-media thickness or the degree of CAS for predicting cardiovascular disease, particularly cerebrovascular disease.[2] However, in recent years, it has been shown that both carotid plaque composition and morphology could be important additional features in the risk assessment of patients with carotid artery atherosclerosis.[10] In recent prospective clinical studies for imaging stroke biomarkers, high-risk carotid plaque features appeared to be associated with stroke in patients with moderate CAS.[17,18] Atherosclerosis is a systemic disease, and the presence of atherosclerosis in a particular vascular bed is frequently associated with disease in other vascular territories. On the basis of prior studies,[19,20] the correlation between carotid and coronary atherosclerosis is well-established. Lombardo et al[20] found that patients with unstable plaques in the coronary arteries also tended to have unstable plaques in the carotid arteries; they posited that inflammation throughout the vasculature accounted for this finding. Recently, Brunner et al[21] found that the detection of lipid cores on carotid MR imaging is associated with cardiovascular events. Furthermore, unstable carotid plaques seem to affect not only ipsilateral but also contralateral cerebral symptoms. Therefore, carotid plaques could be a surrogate marker acknowledging the systematic nature of the atherosclerotic processes affecting different vascular beds.[22]

Recent studies support the concept that carotid plaques go through remodeling;[6] some plaques regress and stabilize to be less likely to result in clinical events, whereas some plaques progress to high-risk, unstable plaques with large lipid necrotic cores and thin fibrous caps, which can rupture and cause clinical events.[23-26] The stability of atherosclerotic plaques largely depends on the composition and morphology of the plaques. Thus, plaque characteristics other than the degree of stenosis alone are important for identifying subjects at higher risk of clinical events, not only for decisions about medical therapy but also for decisions about aggressive interventions.[5-7] In this regard, the use of noninvasive imaging modalities to detect high-risk plaques and predict their natural evolution has been extensively investigated,[7,27] and several different imaging modalities, such as CTA, MR imaging, DUS, and PET have been used to assess plaque stability. The advantage of DUS lies in the detection of initial wall alterations, whereas MR imaging can characterize various plaque components. CTA has basically been used to quantify plaque subcomponents, including fatty, mixed, or calcified constituents. Although CTA is known to be less effective than MR imaging for detecting intraplaque hemorrhage or fibrous cap status, Ajduk et al[24] found multidetector row CTA to be highly sensitive and moderately specific for detecting intraplaque hemorrhage.[24,28]

CTA provides simultaneous information about the degree of luminal stenosis, a more detailed analysis of plaque composition,[7] and high-resolution 3D plaque imaging in a relatively short time. These features make this method particularly suitable for its use in clinical practice.[27] Coronary plaque characterization by CTA is well-established for predicting MACEs in different subpopulations, with higher reproducibility than other imaging modalities.[8] Although many studies have been performed to differentiate carotid plaque compositions and to compare unstable with stable plaques using histologic analysis through Hounsfield unit measurements on

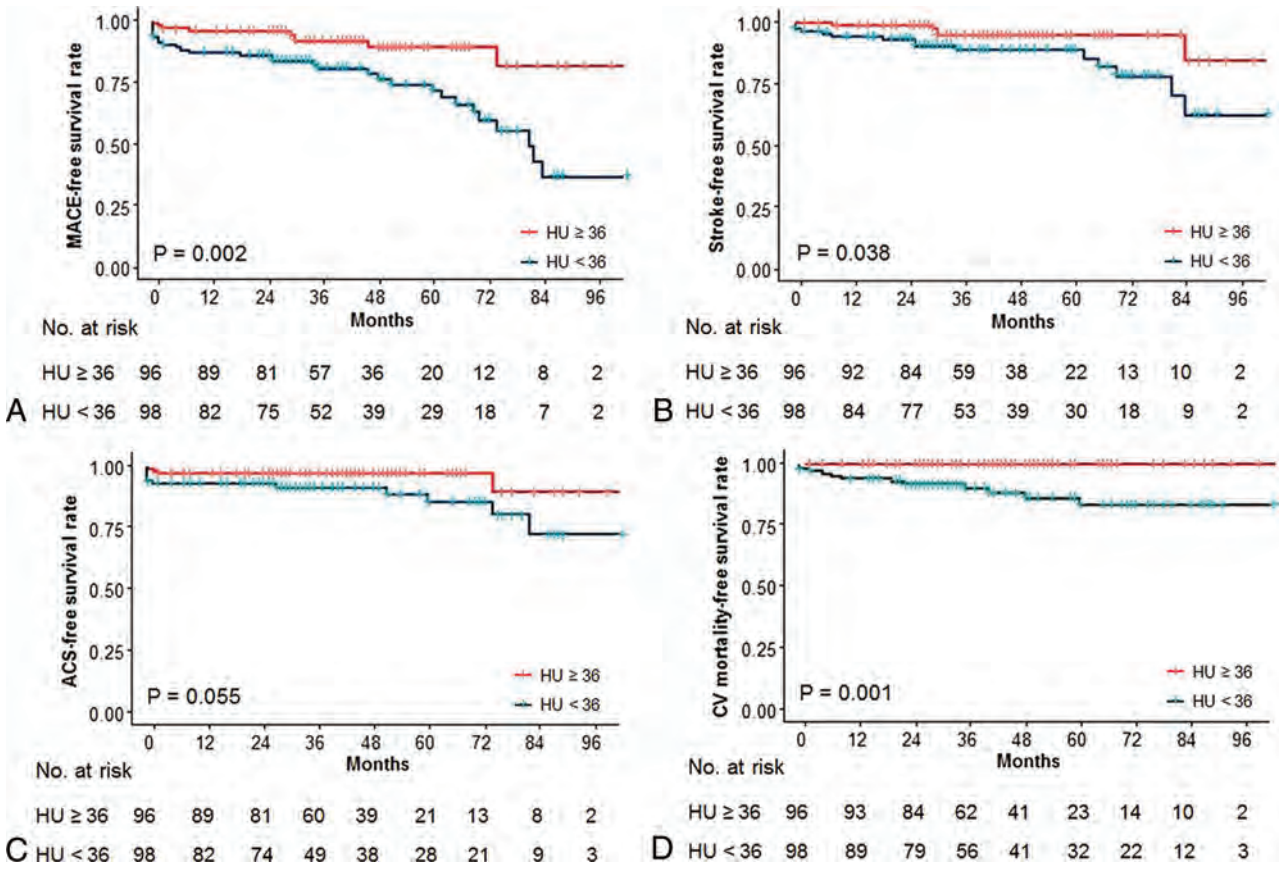

FIG 3. Kaplan-Meier survival analyses of the cumulative event-free rates based on the dichotomization of Hounsfield units at the median value of the cohort (36 HU). Cumulative event-free rates of MACE (*A*), stroke (*B*), ACS (*C*), and CV mortality (*D*), according to the carotid plaque density. CV indicates cardiovascular.

CTA,[10,27] few studies have independently focused on the CTA characteristics of different carotid plaques in association with future cardiovascular event risks.

In this study, we restricted our analysis to the 4 plaque characteristics commonly associated with ischemic complications.[29] Although spotty calcium detected via coronary CTA has been reported to be an important prognostic factor for ACS,[30] the association of spotty calcium in carotid CTA with MACEs has been rarely investigated.[31] Spotty calcium is likely to exist in lipid-rich plaques and be associated with inflammatory processes and vulnerability, unlike large calcifications in fibrocalcific plaques.[13,32] Hounsfield unit values are known to reflect plaque composition; lower Hounsfield unit values are associated with higher probabilities of unstable plaques with large lipid cores and intraplaque hemorrhage.[25,33] It is well accepted that the napkin-ring sign and higher calcium scores in coronary CTA are closely associated with MACEs.[29,33] Although the napkin-ring sign and calcium score in the carotid plaques were not associated with MACEs in our analysis, we found that plaque Hounsfield unit values and spotty calcium presence were independent predictors of future MACEs, and these could be surrogate markers of the atherosclerotic processes affecting different vascular beds.

The strength of this study was its design, which was suitable for investigating the association between carotid plaque composition and the risk of MACEs among asymptomatic subjects with CAS. Previous CT-based studies have been cross-sectional, comparing the composition of stable and unstable carotid plaques or symptomatic and asymptomatic plaques.[34] Carotid atherosclerosis is a complicated, dynamic process, which persists across time, even in cases of asymptomatic mild CAS. Through a remodeling process, carotid plaques may also stabilize, leading to a phenotype reversal from unstable to stable. Whereas the association between plaque composition and MACE risk has long been suspected, confirmation of this hypothesis requires reliable plaque assessments at baseline, followed by longitudinal assessments of clinical outcomes.[34] Cross-sectional studies cannot evaluate chronologic plaque changes; this issue may result in some differences in the assessments of plaque composition.

This study had important limitations that should be acknowledged. First, this was a retrospective analysis subject to selection bias. A number of subjects were excluded, and some clinical information was not available from the medical records. Calcified plaques (>130 HU), mild stenosis (<50%), and plaques with small volumes precluding interpretation were excluded from our analysis due to measuring difficulties. The presence of calcium artifacts is one of the main limitations of CTA because calcifications may obfuscate the correct quantification of the lipid core. Although the role of severe calcification in carotid plaque evaluation still needs to be clarified, several studies have postulated that a high degree of plaque calcification may be considered a

protective factor, especially when the tissue is located superficially.[27] Despite the controversy,[35,36] higher carotid calcium scores seem to be associated with higher MACE risk.[33] In our analysis, the mean calcium score was higher in the MACE group than in the non-MACE group, with a nonsignificant trend. However, higher carotid calcium scores were not associated with higher MACE risk.

Second, plaque Hounsfield unit density was measured via manual positioning of the ROIs. Although there was good agreement among observers in our analysis, manual ROI placement is time-consuming and may be subject to operator bias and beam-hardening artifacts from surrounding tissue. Previous studies have suggested various techniques for selecting ROIs to measure carotid plaque Hounsfield unit values.[24,37] Clinical feasibility and reproducibility are important for carotid plaque analyses. Manual selection of larger ROIs is difficult for irregularly shaped or circumferential carotid plaques,[38] which are more at risk of being affected by adjacent tissue densities, and manual selection is more operator-dependent. Although manual ROI positioning may be inferior to automatic or semiautomatic ROI measurement using plaque-analysis software,[27,34,39] it is advantageous over measurement using plaque-analysis software in terms of feasibility and widespread availability.[28] Third, we did not assess plaque volume as an independent predictor of MACEs. Fourth, the plaque Hounsfield unit density did not fully reflect the density of the entire plaque because we measured the Hounsfield unit values at minimally attenuated areas of the plaques at the most stenotic level. Finally, as with all observational studies, we cannot draw conclusions about causality, and our results should be considered as hypothesis-generating rather than definitive.

CONCLUSIONS

Despite all of these limitations and the debate regarding plaque interpretation by CTA, this pilot study provided evidence of an association between the state of carotid plaque composition, as evaluated by CTA, and the future risk of MACEs among subjects with asymptomatic CAS. The lower the carotid plaque Hounsfield unit density was, the higher was the probability that the artery was associated with the subsequent occurrence of a MACE; spotty calcium in the carotid plaque was an independent and significant predictor of greater subsequent MACE risk. The determination of plaque composition by CTA can provide valuable information for predicting the natural behavior of carotid plaques causing moderate to severe stenosis.

REFERENCES

1. Baber U, Mehran R, Sartori S, et al. **Prevalence, impact, and predictive value of detecting subclinical coronary and carotid atherosclerosis in asymptomatic adults: the BioImage study.** *J Am Coll Cardiol* 2015;65:1065–74 CrossRef Medline
2. Lahoz C, Mostaza JM. **Atherosclerosis as a systemic disease.** *Rev Esp Cardiol* 2007;60:184–95 CrossRef
3. Kwon H, Kim HK, Kwon SU, et al. **Risk of major adverse cardiovascular events in subjects with asymptomatic mild carotid artery stenosis.** *Sci Rep* 2018;8:4700 CrossRef Medline
4. Sutton-Tyrrell K, Wolfson SK, Thompson T, et al. **Measurement variability in duplex scan assessment of carotid atherosclerosis.** *Stroke* 1992;23:215–20 CrossRef Medline
5. Spence JD. **Cerebrovascular disease: Identifying high-risk patients from carotid plaque composition.** *Nat Rev Cardiol* 2010;7:426–28 CrossRef Medline
6. Saba L, Sanfilippo R, Sannia S, et al. **Association between carotid artery plaque volume, composition, and ulceration: a retrospective assessment with MDCT.** *AJR Am J Roentgenol* 2012;199:151–56 CrossRef Medline
7. Kwee RM, van Oostenbrugge RJ, Hofstra L, et al. **Identifying vulnerable carotid plaques by noninvasive imaging.** *Neurology* 2008;70:2401–09 CrossRef Medline
8. Christiansen MK, Jensen JM, Nørgaard BL, et al. **Coronary plaque burden and adverse plaque characteristics are increased in healthy relatives of patients with early onset coronary artery disease.** *JACC Cardiovasc Imaging* 2017;10:1128–35 CrossRef Medline
9. Brott TG, Halperin JL, Abbara S, et al; American Academy of Neurology and Society of Cardiovascular Computed Tomography. **2011 ASA/ACCF/AHA/AANN/AANS/ACR/ASNR/CNS/SAIP/SCAI/SIR/SNIS/SVM/SVS guideline on the management of patients with extracranial carotid and vertebral artery disease: executive summary.** *Stroke* 2011;42:e420–63 CrossRef Medline
10. Wintermark M, Jawadi SS, Rapp JH, et al. **High-resolution CT imaging of carotid artery atherosclerotic plaques.** *AJNR Am J Neuroradiol* 2008;29:875–82 CrossRef Medline
11. Mosleh W, Adib K, Natdanai P, et al. **High-risk carotid plaques identified by CT-angiogram can predict acute myocardial infarction.** *Int J Cardiovasc Imaging* 2017;33:561–68 CrossRef Medline
12. Otsuka K, Fukuda S, Tanaka A, et al. **Napkin-ring sign on coronary CT angiography for the prediction of acute coronary syndrome.** *JACC Cardiovasc Imaging* 2013;6:448–57 CrossRef Medline
13. Zhang F, Yang L, Gan L, et al. **Spotty calcium on cervicocerebral computed tomography angiography associates with increased risk of ischemic stroke.** *Stroke* 2019;50:859–66 CrossRef Medline
14. Agatston AS, Janowitz WR, Hildner FJ, et al. **Quantification of coronary artery calcium using ultrafast computed tomography.** *J Am Coll Cardiol* 1990;15:827–32 CrossRef Medline
15. Anderson JL, Adams CD, Antman EM, et al; American Heart Association Task Force on Practice Guidelines (Writing Committee to Revise the 2002 Guidelines for the Management of Patients With Unstable Angina/Non-ST-Elevation Myocardial Infarction); American College of Emergency Physicians; Society for Cardiovascular Angiography and Interventions; Society of Thoracic Surgeons; American Association of Cardiovascular and Pulmonary Rehabilitation; Society for Academic Emergency Medicine. **ACC/AHA 2007 guidelines for the management of patients with unstable angina/non-ST-elevation myocardial infarction: a report of the American College of Cardiology/American Heart Association Task Force on Practice Guidelines (Writing Committee to Revise the 2002 Guidelines for the Management of Patients With Unstable Angina/Non-ST-Elevation Myocardial Infarction) developed in collaboration with the American College of Emergency Physicians, the Society for Cardiovascular Angiography and Interventions, and the Society of Thoracic Surgeons endorsed by the American Association of Cardiovascular and Pulmonary Rehabilitation and the Society for Academic Emergency Medicine.** *J Am Coll Cardiol* 2007;50:e1–157 CrossRef Medline
16. Koo TK, Li MY. **A guideline of selecting and reporting intraclass correlation coefficients for reliability research.** *J Chiropr Med* 2016;15:155–63 CrossRef Medline
17. Kopczak A, Schindler A, Bayer-Karpinska A, et al. **Complicated carotid artery plaques as a cause of cryptogenic stroke.** *J Am Coll Cardiol* 2020;76:2212–22 CrossRef Medline
18. van Dijk AC, Truijman MT, Hussain B, et al. **Intraplaque hemorrhage and the plaque surface in carotid atherosclerosis: the Plaque At RISK Study (PARISK).** *AJNR Am J Neuroradiol* 2015;36:2127–33 CrossRef Medline
19. Steinvil A, Sadeh B, Bornstein NM, et al. **Impact of carotid atherosclerosis on the risk of adverse cardiac events in patients with and without coronary disease.** *Stroke* 2014;45:2311–17 CrossRef Medline

20. Lombardo A, Biasucci LM, Lanza GA, et al. **Inflammation as a possible link between coronary and carotid plaque instability.** *Circulation* 2004;109:3158–63 CrossRef Medline
21. Brunner G, Virani SS, Sun W, et al. **Associations between carotid artery plaque burden, plaque characteristics, and cardiovascular events: the ARIC Carotid Magnetic Resonance Imaging study.** *JAMA Cardiol* 2021;6:79–86 CrossRef Medline
22. Uchiyama S, Goto S, Matsumoto M, et al. **Cardiovascular event rates in patients with cerebrovascular disease and atherothrombosis at other vascular locations: results from 1-year outcomes in the Japanese REACH Registry.** *J Neurol Sci* 2009;287:45–51 CrossRef Medline
23. Libby P, Ridker PM, Hansson GK. **Progress and challenges in translating the biology of atherosclerosis.** *Nature* 2011;473:317–25 CrossRef Medline
24. Ajduk M, Pavic L, Bulimbasic S, et al. **Multidetector-row computed tomography in evaluation of atherosclerotic carotid plaques complicated with intraplaque hemorrhage.** *Ann Vasc Surg* 2009;23:186–93 CrossRef Medline
25. Nandalur KR, Baskurt E, Hagspiel KD, et al. **Calcified carotid atherosclerotic plaque is associated less with ischemic symptoms than is noncalcified plaque on MDCT.** *AJR Am J Roentgenol* 2005;184:295–98 CrossRef Medline
26. Singh N, Marko M, Ospel JM, et al. **The risk of stroke and TIA in nonstenotic carotid plaques: a systematic review and meta-analysis.** *AJNR Am J Neuroradiol* 2020;41:1453–59 CrossRef Medline
27. Veraldi GF, Nocini PF, Eccher A, et al. **Correlation between MDCTA and carotid plaque histological heterogeneity: a pilot study.** *Eur J Vasc Endovasc Surg* 2018;56:7–14 CrossRef Medline
28. Saba L, Yuan C, Hatsukami TS, et al; Vessel Wall Imaging Study Group of the American Society of Neuroradiology. **Carotid Artery Wall Imaging: Perspective and Guidelines from the ASNR Vessel Wall Imaging Study Group and Expert Consensus Recommendations of the American Society of Neuroradiology.** *AJNR Am J Neuroradiol* 2018;39:E9–31 CrossRef Medline
29. Michel JB, Martin-Ventura JL, Nicoletti A, et al. **Pathology of human plaque vulnerability: mechanisms and consequences of intraplaque hemorrhages.** *Atherosclerosis* 2014;234:311–19 CrossRef Medline
30. Puchner SB, Liu T, Mayrhofer T, et al. **High-risk plaque detected on coronary CT angiography predicts acute coronary syndromes independent of significant stenosis in acute chest pain: results from the ROMICAT-II trial.** *J Am Coll Cardiol* 2014;64:684–92 CrossRef Medline
31. Zheng C, Yan S, Fu F, et al. **Cervicocephalic spotty calcium for the prediction of coronary atherosclerosis in patients with acute ischemic stroke.** *Front Neurol* 2021;12:655156 CrossRef Medline
32. Halak S, Östling G, Edsfeldt A, et al. **Spotty carotid plaques are associated with inflammation and the occurrence of cerebrovascular symptoms.** *Cerebrovasc Dis Extra* 2018;8:16–25 CrossRef Medline
33. Gepner AD, Young R, Delaney JA, et al. **Comparison of carotid plaque score and coronary artery calcium score for predicting cardiovascular disease events: the multi-ethnic study of atherosclerosis.** *J Am Heart Assoc* 2017;6:e0051111179 CrossRef Medline
34. Chrencik MT, Khan AA, Luther L, et al. **Quantitative assessment of carotid plaque morphology (geometry and tissue composition) using computed tomography angiography.** *J Vasc Surg* 2019;70:858–68 CrossRef Medline
35. Yoon WJ, Crisostomo P, Halandras P, et al. **The use of the Agatston calcium score in predicting carotid plaque vulnerability.** *Ann Vasc Surg* 2019;54:22–26 CrossRef Medline
36. Katano H, Mase M, Nishikawa Y, et al. **Calcified carotid plaques show double symptomatic peaks according to agatston calcium score.** *J Stroke Cerebrovasc Dis* 2015;24:1341–50 CrossRef Medline
37. Haraguchi K, Houkin K, Koyanagi I, et al. **Evaluation of carotid plaque composition by computed tomography angiography and black blood magnetic resonance image.** *Interv Neuroradiol* 2008;14:39–43 CrossRef Medline
38. Eesa M, Hill MD, Al-Khathaami A, et al. **Role of CT angiographic plaque morphologic characteristics in addition to stenosis in predicting the symptomatic side in carotid artery disease.** *AJNR Am J Neuroradiol* 2010;31:1254–60 CrossRef Medline
39. Caetano Dos Santos FL, Kolasa M, Terada M, et al. **VASIM: an automated tool for the quantification of carotid atherosclerosis by computed tomography angiography.** *Int J Cardiovasc Imaging* 2019;35:1149–59 CrossRef Medline

Quantitative Analysis of the Olfactory System in COVID-19: An MR Imaging Study

E. Altunisik, A.H. Baykan, S. Sahin, E. Aydin, and S.M. Erturk

ABSTRACT

BACKGROUND AND PURPOSE: Anosmia or hyposmia, often accompanied by changes in taste, is recognized as a common symptom that can assist in the diagnosis of coronavirus disease 2019 (COVID-19). The pathogenesis of olfactory dysfunction in COVID-19 is not yet fully understood. MR imaging represents a useful anatomic imaging method for the evaluation of olfactory dysfunction associated with varying etiologies, including viral infection, trauma, and neurodegenerative processes. This case-control study was conducted to compare quantitative measurements of olfactory anatomic structures between patients diagnosed with COVID-19 associated with persistent olfactory dysfunction and healthy controls.

MATERIALS AND METHODS: This study has a retrospective design. Cranial MR imaging was performed on all participants in both the patient and control groups. The bilateral olfactory bulb volume, olfactory tract length, and olfactory sulcus depth were measured in all patients.

RESULTS: A total of 116 people aged 18–60 years, including 36 patients diagnosed with COVID-19 and 80 controls, were included in the study. All measured values were compared between the patient and control groups. The right, left, and total olfactory bulb volume values were significantly lower in the patient group than in the control group. The patient group also had significantly lower right and left olfactory sulcus depth and olfactory tract length values compared with those in the control group.

CONCLUSIONS: MR imaging findings can be used to demonstrate olfactory injury in patients with COVID-19. The olfactory pathway may represent an alternative route for virus entry into the central nervous system.

ABBREVIATIONS: COVID-19 = coronavirus disease 2019; CoV = human coronavirus; OB = olfactory bulb; OBV = olfactory bulb volume; OD = olfactory dysfunction; OSD = olfactory sulcus depth; OT = olfactory tract; OTL = olfactory tract length; SARS = Severe Acute Respiratory Syndrome

Coronavirus disease 2019 (COVID-19) was first reported in Wuhan, China, in December 2019. Although fever, cough, and shortness of breath were initially considered to be the predominant symptoms, other unusual symptoms, including smell and taste disorders, are receiving increasing attention.[1]

Growing evidence indicates that neurotropism is a common feature of human coronaviruses (CoVs),[2] and the virus has been detected in the CSF of patients with Severe Acute Respiratory Syndrome CoV (SARS-CoV) infections.[3] SARS-CoV-2 has also been suggested to have neuroinvasive potential (eg, in the brain stem), which might be partially responsible for respiratory failure among infected patients.[4] COVID-19 has been associated with a variety of CNS complications, including ischemic infarction, intracranial hemorrhage, acute hemorrhagic necrotizing encephalopathy, cerebral venous thrombosis, posterior reversible encephalopathy syndrome, and widespread leukoencephalopathy with microhemorrhage.[5,6] Angiotensin-converting enzyme 2 serves as a functional receptor for SARS-CoV-2, and its expression and distribution throughout the nervous system suggest that SARS-CoV-2 might be directly or indirectly responsible for neurologic symptoms. The olfactory pathway has also been

Received March 31, 2021; accepted after revision August 1.

From the Departments of Neurology (E. Altunisik) and Radiology (A.H.B.), Adiyaman University Faculty of Medicine, Adiyaman, Turkey; Department of Radiology (S.S.), Adiyaman Training and Research Hospital, Adiyaman, Turkey; Department of Radiology (E. Aydin), Baskent University Faculty of Medicine, Izmir, Turkey; and Department of Radiology (S.M.E.), Istanbul University Faculty of Medicine, Istanbul, Turkey.

The institution from which the work originated: Adiyaman University Faculty of Medicine, Yunus Emre Mahallesi 1164 Sokak No:13 02200 Merkez/Adıyaman/Turkey.

The following are the authors' contributions: data collection: A.H.B, E.A; study design: A.H.B, E.A, E.Ay; manuscript writing: E.A; statistical analysis: S.S; figures and illustration: A.H.B; review and final editing: A.H.B, E.A, S.M.E. All authors contributed to the elaboration, critical revision, and review of intellectual content. All authors read and approved the final manuscript.

Please address correspondence to Ali H. Baykan, MD, Adiyaman University Faculty of Medicine, Yunus Emre Mahallesi 1164 Sokak No:13 02200 Merkez/Adıyaman/Turkey; e-mail: drbaykan@yahoo.com; @DrbaykanHo

Indicates open access to non-subscribers at www.ajnr.org

http://dx.doi.org/10.3174/ajnr.A7278

suggested to serve as an alternative pathway for viral entry into the CNS.[7,8]

During COVID-19 infections, chemosensory symptoms, such as olfactory dysfunction (OD), may occur as a form of viral prodroma or may present concurrently with the development of other disease symptoms.[9] Anosmia or hyposmia, often accompanied by changes in taste, is now recognized as a common symptom that can assist in the diagnosis of COVID-19. However, the mechanism underlying these symptoms, which usually lasts for several weeks, has not yet been fully elucidated. Although the presence of OD in patients with COVID-19 was previously considered an unexpected symptom, the increasing number of patients with COVID-19 who present with OD has resulted in this symptom becoming a diagnostic criterion. Studies have reported taste and olfactory disorders at a rate of up to 88%, especially among mild and moderate cases.[10] In a study examining 114 patients with anosmia, 98% recovered olfactory function within 4 weeks.[11] Conversely, in another study of 1480 patients with COVID-19, OD was detected in 68% of the patients and was irreversible in 26% of those.[12]

The olfactory clefts are 2 narrow, vertical passages located in the upper part of the nasal cavity, forming an essential pathway for odor molecules in the air to reach the olfactory mucosa. Sensorial olfactory neurons arising from the olfactory mucosa pass through the cribriform lamina and form the olfactory bulb (OB), the terminal part.[13] The OB is an ovoid, long, flat neural structure connected to the brain by the olfactory tract (OT). The OB and OT are found in the olfactory sulcus on the lower face of the frontal lobe.[14] Projections arising from olfactory neural structures connect to the piriform cortex, amygdala, orbitofrontal cortex, thalamus, and insula.[15]

The standard measurements of the olfactory system with MR images were developed by Yousem et al[15] in 1998. The absence or hypoplasia of the OB and OT seen on MR imaging has been associated with OD.[16,17] Olfactory sulcus depth (OSD) is another parameter in the assessment of OD. Many diseases, including Parkinson, Behcet, and Alzheimer are associated with decreased OSD and reduction of the sense of smell.[18] Many later studies have shown MR imaging to be a reliable method for evaluating the olfactory system.[19,20] MR imaging–based evaluations of the olfactory structures are a useful anatomic imaging method for evaluating OD associated with a variety of causes, including viral infection, trauma, and neurodegenerative processes.[21] MR imaging can be used to discriminate among the various etiologies that can cause OD, such as sinonasal and neurodegenerative diseases, and can predict OD prognosis.[22] In adults, the OB can be easily identified by conventional MR imaging of the anterior cranial fossa, located above the cribriform plate and just below the olfactory sulcus.[17,23] The total OB volume (OBV) can be obtained by calculating the sum of the right and left OBVs.[24]

The aim of the current study was to determine whether structural damage to the olfactory anatomic pathways could be detected in patients with COVID-19 with persistent OD by measuring the OBV, OT length (OTL), and OSD using MR imaging.

MATERIALS AND METHODS

The study was conducted in accordance with the tenets of the Declaration of Helsinki after obtaining approval from the ethics committee of Adiyaman University Faculty of Medicine. Informed consent was not obtained because the study had a retrospective design. There are no publicly stored data sets associated with this article; data are available on request from the corresponding author.

This case-control study was conducted to perform quantitative measurements of olfactory anatomic structures in patients diagnosed with COVID-19 who present with persistent OD and to compare them with those measurements from control individuals. The patient group is composed of people 18–60 years of age who had a positive COVID-19 diagnosis confirmed by positive findings on a polymerase chain reaction test on a nasopharyngeal swab sample taken due to the presentation of initial COVID-19 symptoms and who presented to the neurology outpatient clinic of Adiyaman Education and Research Hospital, due to OD. The control group consisted of individuals who presented to the neurology outpatient clinic for different, nondegenerative reasons (tension headache, tinnitus, and so forth) who had no history of COVID-19 or OD symptoms and underwent a cranial MR imaging examination and were reported to have normal MR imaging findings. The MR imaging examination of the patients with COVID-19 was performed within 2–8 weeks after the initial diagnosis made by polymerase chain reaction. The following patients were excluded from the study: those with systemic and endocrine diseases, such as chronic renal failure, chronic liver disease, rheumatologic disease, thyroid dysfunction, hypertension, and diabetes; those with B_{12} deficiency; those with neurodegenerative diseases, such as Parkinson disease, multiple sclerosis, and Alzheimer disease; those with a history of head trauma; and pregnant women. In addition, patients with sinonasal diseases, such as allergic rhinitis and chronic sinusitis, were excluded (Fig 1).

MR Imaging Protocol

All MR imaging was performed on a Signa Explorer 1.5T MR imaging machine (GE Healthcare) with a 16-channel head coil. MR images were used for volumetric and morphometric measurements. Coronal FIESTA with phase cycling (FIESTA-C) 3D T2-/T1-weighted images were obtained using the following protocol: TR = 7.6 ms; TE = 2.7 ms; FOV = 170 × 170 mm; number of excitations = 4; thickness = 1.6 mm; gap = 0 mm; number of sections = 1024; matrix = 300 × 300 mm.

Image Analysis

Bilateral OBV, OTL, and OSD measurements were performed in all participants. The OB was observed as a hypointense, ovoid structure surrounded by hyperintense CSF on a coronal FIESTA-C series and sections obtained at a right angle to the cribriform plate (Figs 2 and 3). Volumetric measurements were obtained by manual segmentation based on the contour stack principle on a 3D workstation. OBV was calculated in cubic millimeters. The OTL measurement, recorded in millimeters, was performed on multiplanar reconstruction of 3D FIESTA-C sagittal images at the section where the entire nerve trace was best visualized (Fig 4). The OSD was measured on coronal FIESTA-C 3D images by drawing a line tangential to the lower boundaries of the gyrus rectus and medial orbital gyrus and measuring the deepest point between

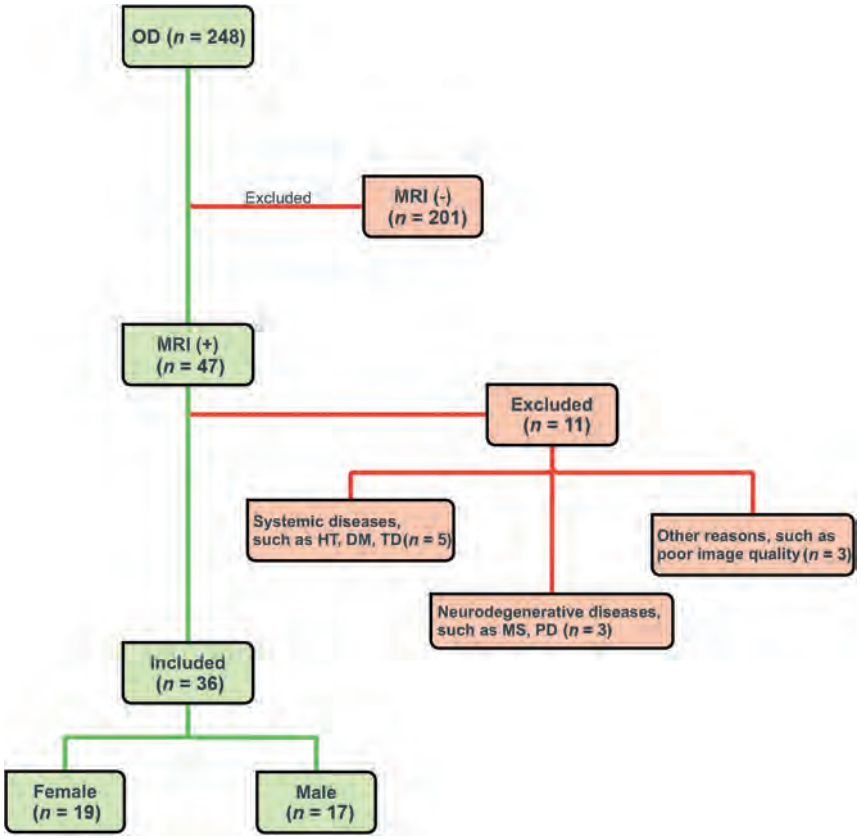

FIG 1. CONSORT flow diagram. HT indicates hypertension; DM, diabetes mellitus; TD, thyroid dysfunction; PD, Parkinson disease.

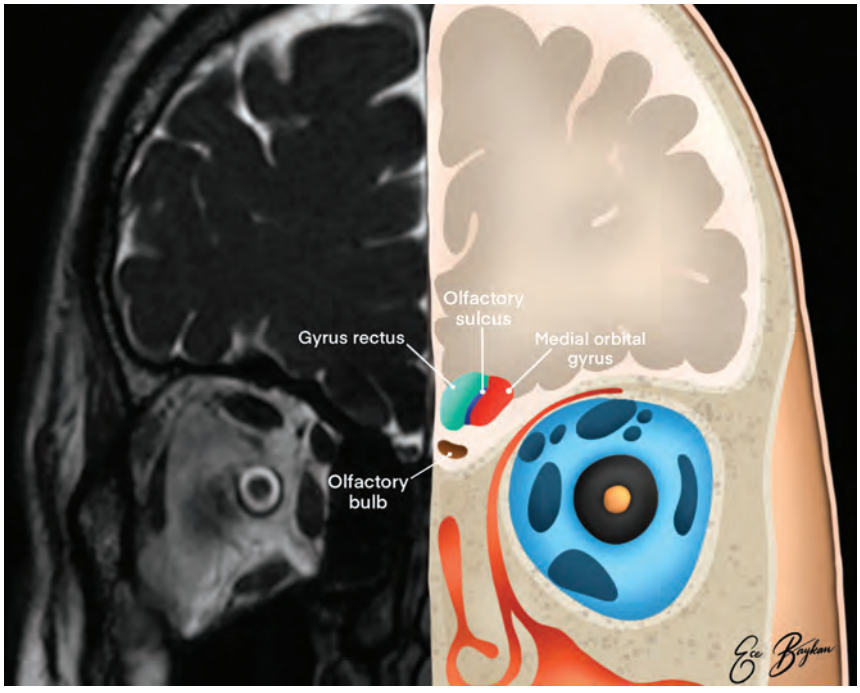

FIG 2. Illustration of the olfactory system on coronal plane MR imaging. The medial orbital gyrus (red area), gyrus rectus (green area), olfactory sulcus (blue area), and olfactory bulb (brown area) are shown.

these gyri and recorded in millimeters. All volumetric and length analyses were performed by 2 radiologists with at least 15 years of professional experience in head and neck radiology, and the measurements made by both radiologists were averaged.

Statistical Analysis

Statistical analyses were performed using SPSS, Version 22.0 (IBM). The compliance of all variables with a normal distribution was examined graphically using histograms and evaluated using the Shapiro-Wilk test. Descriptive statistics are presented as the mean (SD), median, and minimum–maximum values. Numeric variables were compared between groups using the independent t test because the data were found to be normally distributed. Categoric variables were compared using the Pearson χ^2 test. The Mann-Whitney U test was used when comparing skewed variables between groups. A P value $<$ .05 was considered significant. Interobserver agreement in OBV, OSD, and OTL measurements was evaluated using Bland-Altman graphics. The average difference and 95% limits of agreement (mean difference $\pm$ 1.96 SDs) are specified.

RESULTS

A total of 116 individuals 18–60 years of age, including 36 diagnosed with COVID-19 and 80 controls, were included in this study. The patient group included 19 (52.8%) women, and the control group included 44 (55%) women. The mean age of the patient group was 37.33 (SD, 7.38) years (range, 23–54 years) and that of the control group was 35.74 (SD, 8.38) years (range, 18–52 years). No significant difference was found between the mean ages of the patient and control groups ($P = .329$). The sociodemographic characteristics of the patient and control groups are summarized in Table 1.

In addition to typical COVID-19 symptoms and OD, 19 patients had persistent headaches, 6 had dizziness, and 8 experienced impaired taste. Sinonasal symptoms, such as nasal obstruction, were not detected in any of the patients included in the study.

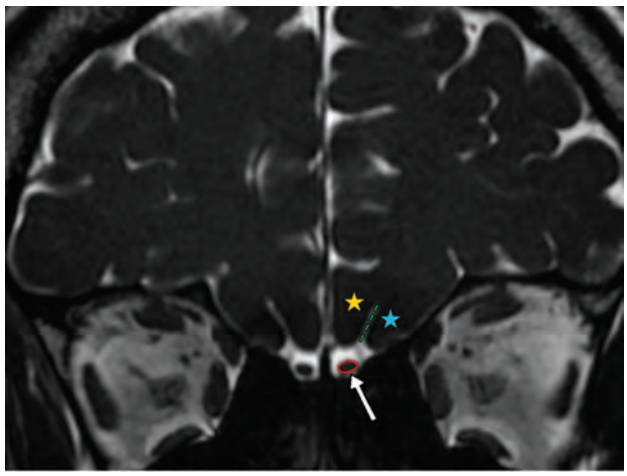

FIG 3. Coronal 3D-FIESTA-C MR image of a 41-year-old man showing the right and left olfactory bulbs as hypointense ovoid structures (*arrow*). The olfactory sulcus (*green dashed lines*) is seen as a hyperintense line between the medial orbital gyrus (*blue star*) and gyrus rectus (*yellow star*). Note the hyperintense CSF surrounding the OBs.

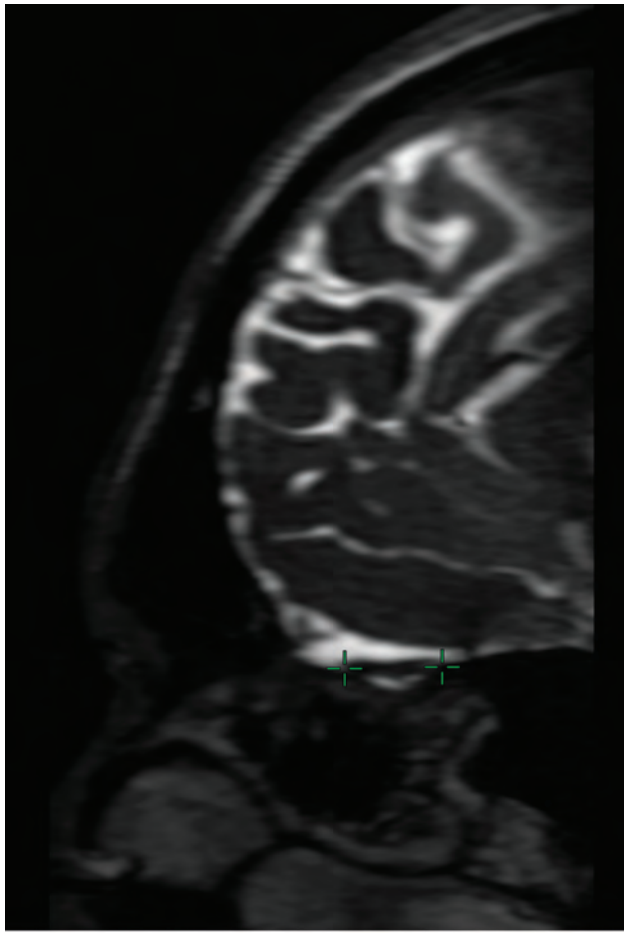

FIG 4. Sagittal multiplanar reconstruction of 3D-FIESTA-C MR imaging of a 27-year-old man showing the left olfactory tract (*crosshairs*).

Nine patients had sudden-onset and isolated OD, whereas 13 experienced OD followed by the onset of COVID-19-related symptoms. Fourteen patients developed OD during the course of the COVID-19 infection. The chest CT images of 2 patients revealed pulmonary involvement. The clinical characteristics of the patients are summarized in Table 2.

In 4 patients, the OBs were observed as bilateral points or lines in the coronal plane of MR images and were considered atrophic, with no changes observed for 1 patient on imaging at follow-up 3 months later (Fig 5). The measured values were

Table 1: Sex distribution and mean ages of the control and patient groups

	Control		Patient		*P*
Sex					
Male (No.) (%)	36	45	17	47.2	.824[a]
Female (No.) (%)	44	55	19	52.8	
Age (mean) (yr)	35.74 (SD, 8.38)		37.33 (SD, 7.38)		.329[b]

[a] χ^2 test.
[b] Mann-Whitney *U* test.

Table 2: Demographic and clinical features of patients

Features	No. (%)
Persistent headache	19 (53%)
Taste disturbance	8 (22%)
Vertigo/dizziness	6 (17%)
Pulmonary involvement	2 (6%)
Sinonasal symptoms	0 (0%)

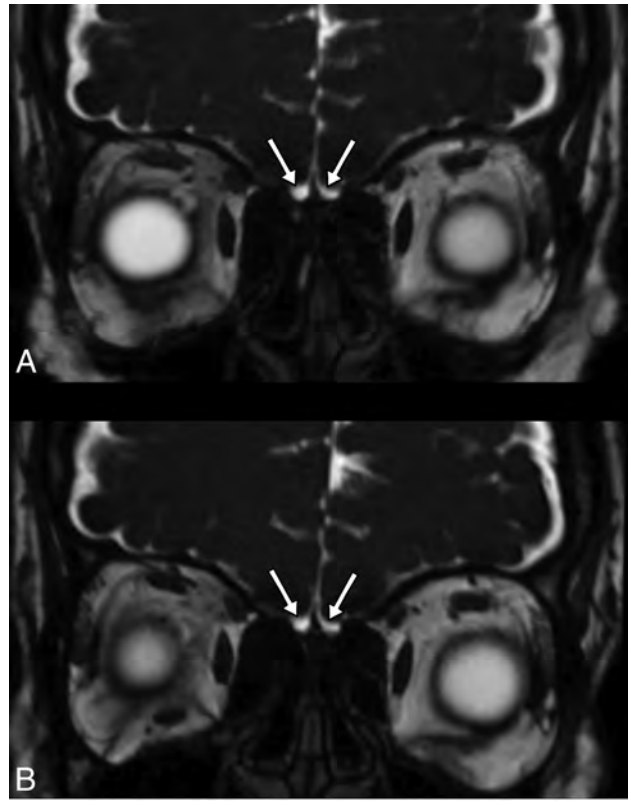

FIG 5. Coronal plane 3D-FIESTA-C MR images of a 33-year-old female patient with loss of smell who was proved to have COVID-19. The olfactory bulbs are seen as atrophic (*A*). The olfactory bulbs are still atrophic, though the loss of smell has improved, on MR image of the same patient 3 months later (*B*).

compared between the patient and control groups. The right, left, and total OBV values were significantly lower in the patient group (41.57 [SD, 16.96], 40.76 [SD, 15.93], and 82.34 [SD, 31.29] mm^3, respectively) compared with the control group (66.12 [SD, 16.86], 65.38 [SD, 18.80], and 131.50 [SD, 32.27] mm^3, respectively; $P < .001$, $P < .001$, and $P < .001$). The right and left OTL values were significantly lower in the patient group (11.08 [SD, 2.18] and 11.24 [SD, 2.57] mm, respectively) compared with the control group (12.85 [SD, 2.14] and 12.80 [SD, 2.60] mm, respectively; $P < .001$ and $P = .003$). The right and left OSD values were also significantly lower in the patient group (8.33 [SD, 1.65] and 8.64 [SD, 1.40] mm, respectively) compared with the control group (9.20 [SD, 1.64] and 9.29 [SD, 1.53] mm, respectively; $P = .01$ and $P = .033$; Table 3).

The key results are shown in Figs 6 and 7. In 7 cases (19.4%) in the patient group, focal intensity increased in the right OB in 4 patients, in the left OB in 2 patients, and in bilateral OBs in 1 patient (Fig 8). In the control group, focal intensity increased in the left OB in 1 individual. Normal and abnormal findings are shown side by side in Figs 9 and 10.

Table 3: Average, SD, and *P* values of OBV, OTL, and OSD measurements of patient and control groups

	Patient	Control	*P*[a]
R OBV (mm^3)	41.57 (SD, 16.96)	66.12 (SD, 16.86)	<.001
L OBV (mm^3)	40.76 (SD, 15.93)	65.38 (SD, 18.80)	<.001
T OBV (mm^3)	82.34 (SD, 31.29)	131.50 (SD, 32.27)	<.001
R OTL (mm)	11.08 (SD, 2.18)	12.85 (SD, 2.14)	<.001
L OTL (mm)	11.24 (SD, 2.57)	12.80 (SD, 2.60)	.003
R OSD (mm)	8.33 (SD, 1.65)	9.20 (SD, 1.64)	.01
L OSD (mm)	8.64 (SD, 1.40)	9.29 (SD, 1.53)	.033

Note:—R indicates right; L, left; T, total.
[a] Independent *t* test.

DISCUSSION

The pathogenesis of OD associated with COVID-19 is not yet fully understood, but mechanisms that involve damage to the olfactory neural structures have been emphasized. In this study, we evaluated a group of patients who presented with COVID-19-associated OD, which persisted despite improvements in the typical symptoms associated with COVID-19. The findings of the study provided evidence suggesting that the olfactory anatomic structures might be affected by this disease.

Some features distinguish OD observed in COVID-19 from other postviral forms of anosmia. Postviral anosmia that develops following upper respiratory tract infections is generally associated with mucosal obstructions and nasal congestion, and its pathogenesis is predominantly conduction-type OD that develops secondary to impaired airflow.[25] However, studies have not identified the significant coexistence of sinonasal symptoms with COVID-19 anosmia.[26,27] In most of our COVID-19 positive patients, no pathological evidence was identified to suggest inflammation in any sinonasal sinuses, such as mucosal obstruction or nasal obstruction.

Different mechanisms are likely to cause OD pathogenesis during the course of COVID-19 infection. Although angiotensin-converting enzyme 2 receptors, which are the target molecules for SARS-CoV-2, are expressed by non-neuronal support cells in the olfactory epithelium, they are not expressed in neural cells,[1] a feature that might explain the rapid recovery of olfactory function in many patients. However, CoVs have been reported to cause structural damage to olfactory neurons by directly invading olfactory sensory axons via the cribriform plate, and olfactory neuropathy has been detected in cases of SARS-CoV infections.[2] Therefore, the neuroinvasive potential of SARS-CoV-2 has been hypothesized.[1] The neurotrophic properties of SARS-CoV-2 may

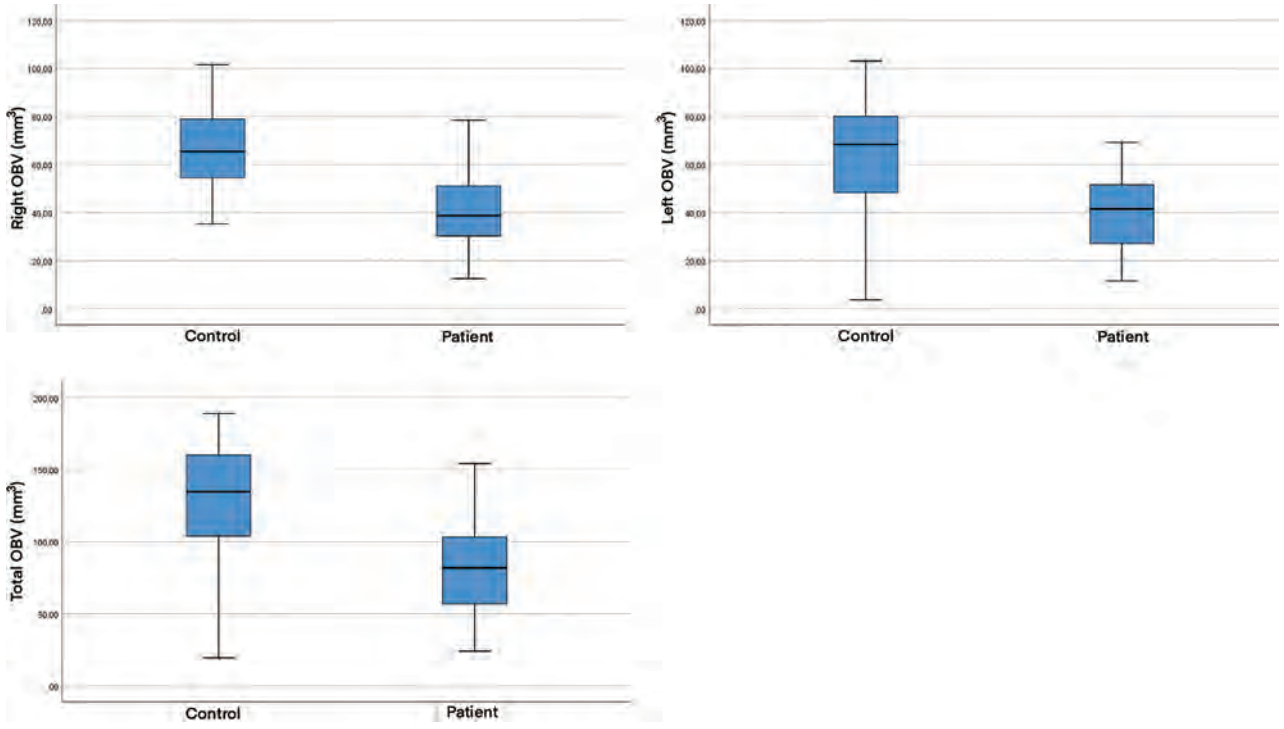

FIG 6. Boxplots of the right OBV, left OBV, and total OBV values in both patient and control groups.

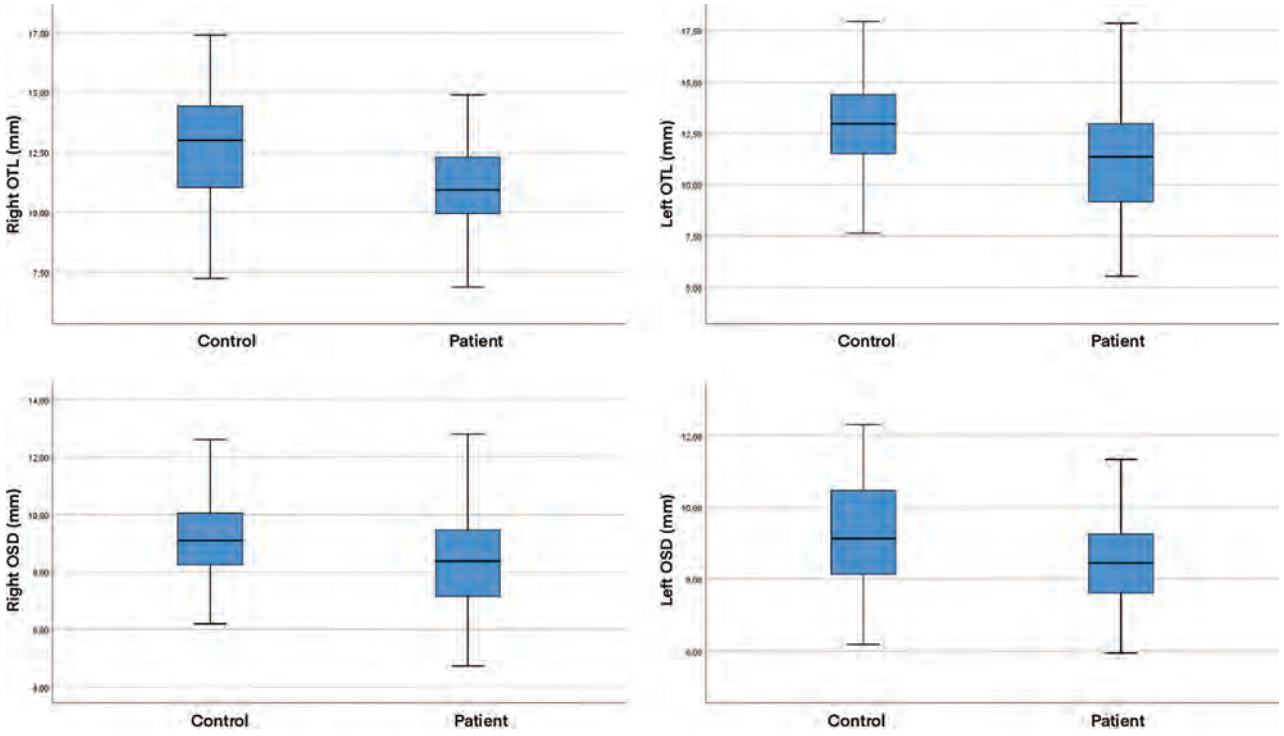

FIG 7. Boxplots of the right OTL, left OTL, right OSD, and left OSD values in both patient and control groups.

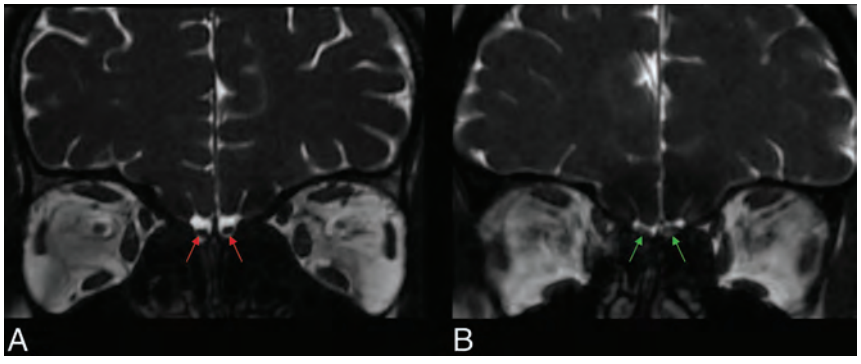

FIG 8. Coronal 3D FIESTA-C MR images of a 26-year-old male from control group (*A*) and a 25-year-old female patient with COVID-19 anosmia (*B*). Normal and increased signal intensity in bilateral olfactory bulbs (*red and green arrows*, respectively).

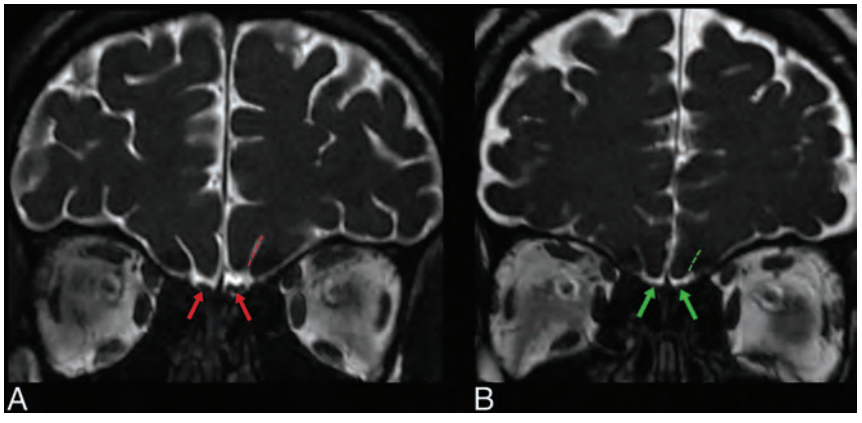

FIG 9. Coronal 3D-FIESTA-C MR images of a 28-year-old man from the control group (*A*) and a 36-year-old female patient (*B*). Note normal and abnormal olfactory bulbs (*red and green arrows*, respectively) and olfactory sulci (*red and green dashed lines*, respectively).

result in the destruction of sensory olfactory structures, and the retrograde viral invasion of olfactory pathways could explain the OD observed in COVID-19 infections to a certain extent. An example of olfactory neuroinvasion through a similar mechanism has been described for herpes simplex virus encephalitis.[28] However, no such pathologic evidence is currently available to support a neuroinvasive mechanism during COVID-19 infection. The permanence of anosmia in some cases of COVID-19 supports the idea of neuronal damage. The atrophic appearance of the OBs of 4 patients was detected on MR images, and no change was observed on follow-up images after 3 months in 1 patient who has experienced persistent anosmia, consistent with this hypothesis.

Imaging of the olfactory nerve is not routinely performed, though OD has been reported with high frequency in patients with COVID-19 and represents a neurologic disease marker. An MR imaging examination can be useful for the evaluation of patients with anosmia and hyposmia, allowing for the elaborative visualization of olfactory anatomic structures and the

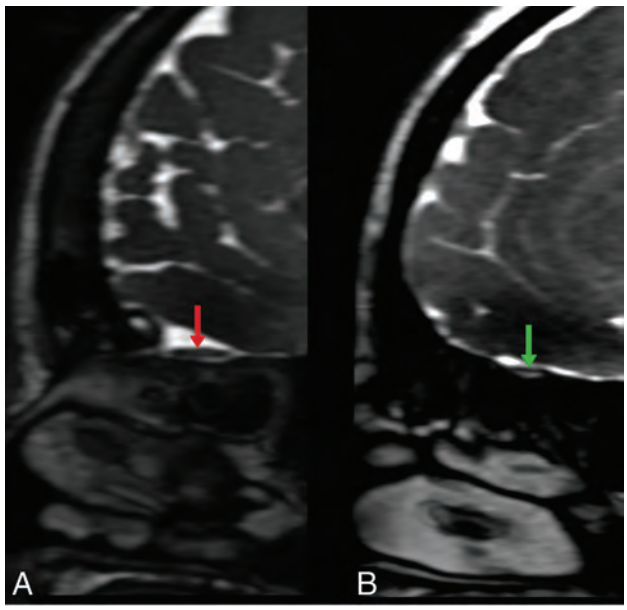

FIG 10. Sagittal multiplanar reconstruction of 3D-FIESTA-C MR images of a 42-year-old woman from the control group (*A*) and a 36-year-old female patient (*B*) showing normal and abnormal olfactory tracts (*red and green arrows*, respectively).

quantitative and qualitative measurement of these structures. The literature indicates that available imaging of the olfactory structures in COVID-19-associated OD has been primarily reported in the form of case reports, with limited studies on this subject. To our knowledge, our study is the first to perform quantitative olfactory measurements, such as OBV and OSD, in patients with COVID-19 and to compare them against those in a control group. Bilateral OB atrophy was previously detected in the MR imaging examination (on coronal T2-weighted fat-suppressed images with 3- mm section thickness) of a patient with COVID-19 who experienced anosmia.[29]

In another case report, the MR imaging examination (on coronal 3D constructive interference in steady-state T2-weighted images) of a patient with anosmia with COVID-19 revealed the bilateral edematous and hyperintense appearance of the OB, but the OB returned to normal during the follow-up examination performed after 4 weeks.[30] Tsivgoulis et al[31] compared the height of the OB in cases of COVID-19 associated with OD with that in a control group (on coronal T2-weighted turbo spin-echo images with 2-mm section thickness) and reported a significant reduction in the patient group. Li et al[32] showed (on coronal 3D T2-weighted turbo spin-echo images with 1-mm section thickness) a decrease in the right OBV and increased linear hyperintensities in the bilateral OBs of a patient with COVID-19 and anosmia. In a quantitative study of OB intensity (on coronal 3D-FLAIR sequence images with 2-mm section thickness) comparing patients with OD and normosmic COVID-19, the OB signal intensity in the OD group was significantly higher than that in the normosmic group.[33]

The results of our study are consistent with those of these previous studies. We found significant decreases in the values of all investigated MR imaging parameters (right OBV, left OBV, total OBV, right OTL, left OTL, right OSD, and left OSD) in the COVID-19 group compared with the control group. In addition, we found an increase in focal intensity in 7 patients in the patient group. We hypothesize that the presence of olfactory structural abnormalities detected on MR imaging in patients with COVID-19 may indicate olfactory neuropathy. In this respect, our study supports the idea that OD detected in patients with COVID-19 has a sensorineural origin, going beyond sinonasal involvement.

The presence of CNS complications, such as persistent headache and motor deficits, in patients with olfactory structural damage has led to the hypothesis that the virus uses the olfactory pathway as an entry route into the brain.[34] In preclinical experiments performed in transgenic mice, neuronal losses and the identification of viral expression in various brain regions have been demonstrated following the nasal administration of CoVs.[1] In a case report describing a patient with COVID-19, increased intensity was found in both the OB and the gyrus rectus. After 4 weeks, cortical hyperintensity completely disappeared on MR imaging, and OB hyperintensity decreased and became thinner.[35] The PET scan of a patient with COVID-19 with normal MR imaging findings revealed hypoactivity in the left orbitofrontal cortex.[36] In our study, we identified no structural abnormalities of the cranial structures in the MR imaging examinations of any patients with COVID-19. However, most patients described symptoms of persistent headache, impaired taste, and dizziness accompanying OD. The presence of CNS symptoms accompanying OD in these patients may indicate that the olfactory pathway serves as an alternative route for viral entry into the CNS. However, functional imaging, CSF, and cytologic examinations should be performed in larger patient groups to verify this hypothesis.

OD is likely a more common symptom of COVID-19 than has been reported. OD may exist in the background of disease symptomatology and may be overlooked. Patients may not be able to perceive unilateral anosmia because full unilateral anosmia can only be detected by a thorough physical examination. Therefore, OD should be considered as a potential symptom for the identification and isolation of infected patients to control the spread of the pandemic.

This study has certain limitations. The number of patients participating in the study was relatively small. In addition, the decision not to evaluate patients with severe pulmonary and systemic infections and long disease durations may create concerns related to possible patient selection bias. Another limitation is that patients' self-reported OD was accepted without performing objective smell-identification tests.

CONCLUSIONS

Clinicians should not overlook OD as a potential indicator for disease diagnosis, the determination of prognosis, pandemic control, and patient isolation. MR imaging can allow the diagnosis and prognosis prediction in patients with OD. MR imaging findings can be used to demonstrate olfactory injury in patients with COVID-19. We believe that studies comparing the initial and follow-up MR images performed in a larger number of patients are necessary to fully elucidate the mechanisms underlying SARS-Cov-2-induced OD. Future functional imaging and tractography studies will continue to shed light on the subject.

ACKNOWLEDGMENTS

The authors are grateful to Ece Baykan for her contribution to the design of the figures and illustrations and to MRI technician Kasim Tepe and Uğur Erol for their contributions to the creation of the MR imaging protocol.

Disclosures: Sukru Mehmet Erturk—*UNRELATED: Payment for Lectures Including Service on Speakers Bureaus:* Bayer AG, Siemens.* *Money paid to the institution.

REFERENCES

1. Brann DH, Tsukahara T, Weinreb C, et al. **Non-neuronal expression of SARS-CoV-2 entry genes in the olfactory system suggests mechanisms underlying COVID-19-associated anosmia.** *Sci Adv* 2020;6:eabc5801 CrossRef Medline
2. Li YC, Bai WZ, Hirano N, et al. **Coronavirus infection of rat dorsal root ganglia: ultrastructural characterization of viral replication, transfer and the early response of satellite cells.** *Virus Res* 2012;163:628–35 CrossRef Medline
3. Baig AM, Khaleeq A, Ali U, et al. **Evidence of the COVID-19 virus targeting the CNS: tissue distribution, host-virus interaction, and proposed neurotropic mechanisms.** *ACS Chem Neurosci* 2020;11:995–98 CrossRef Medline
4. Li YC, Bai WZ, Hashikawa T. **The neuroinvasive potential of SARS-CoV2 may play a role in the respiratory failure of COVID-19 patients.** *J Med Virol* 2020;92:552–55 CrossRef Medline
5. Aggarwal G, Lippi G, Henry BM. **Cerebrovascular disease is associated with an increased disease severity in patients with coronavirus disease 2019 (COVID-19): a pooled analysis of published literature.** *Int J Stroke* 2020;15:385–89 CrossRef Medline
6. Parauda SC, Gao V, Gewirtz AN, et al. **Posterior reversible encephalopathy syndrome in patients with COVID-19.** *J Neurol Sci* 2020;416:117019 CrossRef Medline
7. Mao L, Jin H, Wang M, et al. **Neurologic manifestations of hospitalized patients with coronavirus disease 2019 in Wuhan, China.** *JAMA Neurol* 2020;77:683–90 CrossRef Medline
8. Altunisik E, Sayiner HS, Aksoz S, et al. **Neurological symptoms in COVID-19 patients.** *Bratisl Lek Listy* 2021;122:39–44 CrossRef Medline
9. Sedaghat AR, Gengler I, Speth MM. **Olfactory dysfunction: a highly prevalent symptom of COVID-19 with public health significance.** *Otolaryngol Head Neck Surg* 2020;163:12–15 CrossRef Medline
10. Lechien JR, Chiesa-Estomba CM, De Siati DR, et al. **Olfactory and gustatory dysfunctions as a clinical presentation of mild-to-moderate forms of the coronavirus disease (COVID-19); a multicenter European study.** *Eur Arch Otorhinolaryngol* 2020;277:2251–61 CrossRef Medline
11. Klopfenstein T, Kadiane-Oussou NJ, Toko L, et al. **Features of anosmia in COVID-19.** *Med Mal Infect* 2020;50:436–39 CrossRef Medline
12. Wölfel R, Corman VM, Guggemos W, et al. **Virological assessment of hospitalized patients with COVID-2019.** *Nature* 2020;581:465–69 CrossRef Medline
13. Jafek BW, Murrow B, Michaels R, et al. **Biopsies of human olfactory epithelium.** *Chem Senses* 2002;27:623–28 CrossRef Medline
14. Cömert A, Kahiloğulları G, Cömert E, et al. **Bulbus Olfactorius, Tractus Olfactorius, Sulcus Olfactorius ve Trigonum Olfactorium Morfometrisi: Anatomik Çalışma.** *Ankara Üniversitesi Tıp Fakültesi Mecmuası* 2009;62:149–52
15. Yousem DM, Geckle RJ, Bilker WB, Doty RL. **Olfactory bulb and tract and temporal lobe volumes. Normative data across decades.** *Ann N Y Acad Sci* 1998;855:546–55 CrossRef Medline
16. Altunisik E, Baykan AH. **Comparison of the olfactory bulb volume and the olfactory tract length between patients diagnosed with essential tremor and healthy controls: findings in favor of neurodegeneration.** *Cureus* 2019;11:e5846 CrossRef Medline
17. Altunisik E, Baykan AH. **Decreased olfactory bulb volume in patients with restless legs syndrome.** *Anatolian Journal of Psychiatry* 2020;21:537–43
18. Cullu N, Yeniçeri IO, Guney B, et al. **Evaluation of olfactory bulbus volume and olfactory sulcus depth by 3 T MR.** *Surg Radiol Anat* 2020;42:1113–18 CrossRef Medline
19. Hummel T, Witt M, Reichmann H, et al. **Immunohistochemical, volumetric, and functional neuroimaging studies in patients with idiopathic Parkinson's disease.** *J Neurol Sci* 2010;289:119–22 CrossRef Medline
20. Sahin S, Baykan AH, Altunisik E, et al. **Quantitative analysis of healthy olfactory sulcus depth, olfactory tract length and olfactory bulb volume in the pediatric population: a magnetic resonance study.** *Folia Morphol (Warsz)* 2021;80:33–39 CrossRef Medline
21. Rombaux P, Duprez T, Hummel T. **Olfactory bulb volume in the clinical assessment of olfactory dysfunction.** *Rhinology* 2009;47:3–9 Medline
22. Duprez TP, Rombaux P. **Imaging the olfactory tract (cranial nerve 1).** *Eur J Radiol* 2010;74:288–98 CrossRef Medline
23. Schneider JF, Floemer F. **Maturation of the olfactory bulbs: MR imaging findings.** *AJNR Am J Neuroradiol* 2009;30:1149–52 CrossRef Medline
24. Chen S, Tan Hy, Wu Zh, et al. **Imaging of olfactory bulb and gray matter volumes in brain areas associated with olfactory function in patients with Parkinson's disease and multiple system atrophy.** *Eur J Radiol* 2014;83:564–70 CrossRef Medline
25. Welge-Lussen A, Wolfensberger M. **Olfactory disorders following upper respiratory tract infections.** *Adv Otorhinolaryngol* 2006;63:125–32 CrossRef Medline
26. Jalessi M, Barati M, Rohani M, et al. **Frequency and outcome of olfactory impairment and sinonasal involvement in hospitalized patients with COVID-19.** *Neurol Sci* 2020;41:2331–38 CrossRef Medline
27. Cooper KW, Brann DH, Farruggia MC, et al. **COVID-19 and the chemical senses: supporting players take center stage.** *Neuron* 2020;107:219–33 CrossRef Medline
28. Twomey JA, Barker CM, Robinson G, et al. **Olfactory mucosa in herpes simplex encephalitis.** *J Neurol Neurosurg Psychiatry* 1979;42:983–87 CrossRef Medline
29. Chiu A, Fischbein N, Wintermark M, et al. **COVID-19-induced anosmia associated with olfactory bulb atrophy.** *Neuroradiology* 2021;63:147–48 CrossRef Medline
30. Laurendon T, Radulesco T, Mugnier J, et al. **Bilateral transient olfactory bulb edema during COVID-19–related anosmia.** *Neurology* 2020;95:224–25 CrossRef Medline
31. Tsivgoulis G, Fragkou PC, Lachanis S, et al. **Olfactory bulb and mucosa abnormalities in persistent COVID-19 induced anosmia: a magnetic resonance imaging study.** *Eur J Neurol* 2021;1:6–8 CrossRef Medline
32. Li CW, Syue LS, Tsai YS, et al. **Anosmia and olfactory tract neuropathy in a case of COVID-19.** *J Microbiol Immun Infect* 2021;54:93–96 CrossRef Medline
33. Chetrit A, Lechien JR, Ammar A, et al. **Magnetic resonance imaging of COVID-19 anosmic patients reveals abnormalities of the olfactory bulb: preliminary prospective study.** *J Infect* 2020;81:816–46 CrossRef Medline
34. Aragão MF, Leal MC, Filho OC, et al. **Anosmia in COVID-19 associated with injury to the olfactory bulbs evident on MRI.** *AJNR Am J Neuroradiol* 2020;41:1703–06 CrossRef Medline
35. Politi LS, Salsano E, Grimaldi M. **Magnetic resonance imaging alteration of the brain in a patient with coronavirus disease 2019 (COVID-19) and anosmia.** *JAMA Neurol* 2020;77:1028–29 CrossRef Medline
36. Karimi-Galougahi M, Yousefi-Koma A, Bakhshayeshkaram M, et al. **^{18}FDG PET/CT scan reveals hypoactive orbitofrontal cortex in anosmia of COVID-19.** *Acad Radiol* 2020;27:1042–43 CrossRef Medline

Retrospective Review of Midpoint Vestibular Aqueduct Size in the 45° Oblique (Pöschl) Plane and Correlation with Hearing Loss in Patients with Enlarged Vestibular Aqueduct

K. Bouhadjer, K. Tissera, C.W. Farris, A.F Juliano, M.E. Cunnane, H.D. Curtin, L.A. Mankarious, and K.L. Reinshagen

ABSTRACT

BACKGROUND AND PURPOSE: Vestibular aqueduct measurements in the 45° oblique (Pöschl) plane provide a reliable depiction of the vestibular aqueduct; however, adoption among clinicians attempting to counsel patients has been limited due to the lack of correlation with audiologic measures. This study aimed to determine the correlation between midpoint vestibular aqueduct measurements in the Pöschl plane in patients with an enlarged vestibular aqueduct with repeat audiologic measures.

MATERIALS AND METHODS: Two radiologists independently measured the midpoint vestibular aqueduct diameter in the Pöschl plane reformatted from CT images in 54 pediatric patients (77 ears; mean age at first audiogram, 5 years) with an enlarged vestibular aqueduct. Four hundred nineteen audiograms were reviewed, with a median of 6 audiograms per patient (range, 3–17; mean time between first and last audiograms, 97.4 months). The correlation between midpoint vestibular aqueduct size and repeat audiologic measures (pure tone average, speech-reception threshold, and word recognition score) using a linear mixed-effects model was determined.

RESULTS: The mean midpoint vestibular aqueduct size was 1.78 mm (range, 0.81–3.46 mm). There was excellent interobserver reliability with intraclass correlation coefficients for the 2 readers measuring 0.92 ($P < .001$). Each millimeter increase in vestibular aqueduct size was associated with an increase of 10.5 dB ($P = .006$) in the pure tone average, an increase of 14.0 dB ($P = .002$) in the speech-reception threshold, and a decrease in the word recognition score by 10.5% ($P = .05$).

CONCLUSIONS: Midpoint vestibular aqueduct measurements in the Pöschl plane are highly reproducible and demonstrate a significant correlation with audiologic data in this longitudinal study with repeat measures. These data may be helpful for clinicians who are counseling patients with an enlarged vestibular aqueduct using measurements obtained in the Pöschl plane.

ABBREVIATIONS: EVA = enlarged vestibular aqueduct; IP-2 = incomplete partition-type 2; PTA = pure tone average; SRT = speech-reception threshold; WRS = word recognition score; VA = vestibular aqueduct

An enlarged vestibular aqueduct (EVA) is the most common radiologically detected finding in children undergoing imaging for sensorineural hearing loss.[1] Due to the sometimes progressive nature of the hearing loss, counseling of patients regarding their future hearing outcome is important, albeit challenging, due to the inconsistent pattern of hearing loss and overall unknown pathophysiology, in part because of the variable genetic background, association with cochlear malformations, and physical events that may predispose the patient to a sudden drop in hearing through trauma.[2-9]

Valvassori and Clemis,[10] in 1978, reported that the vestibular aqueduct could be considered enlarged when its width at the midpoint measured >1.5 mm on polytomography. Advances in multidetector CT resulted in further development of the Cincinnati criteria based on axial CT images, which considered the vestibular aqueduct enlarged when the midpoint or opercular widths or both surpass 0.9 and 1.9 mm, respectively.[11,12] To further elucidate the relationship between EVA size and auditory measures, Ascha et al[13] investigated the relationship between the

Received March 12, 2021; accepted after revision August 17.

From the Departments of Radiology (K.B., A.F.J., M.E.C., H.D.C., K.L.R.) and Otolaryngology (K.T., L.A.M.), Massachusetts Eye and Ear, Boston, Massachusetts; and Department of Radiology (C.W.F.), Massachusetts General Hospital, Boston, Massachusetts.

L.A. Mankarious and K.L. Reinshagen are co-senior authors.

This work was conducted with support from Harvard Catalyst/The Harvard Clinical and Translational Science Center (National Center for Advancing Translational Sciences, National Institutes of Health Award UL 1TR002541) and financial contributions from Harvard University and its affiliated academic healthcare centers.

The content is solely the responsibility of the authors and does not necessarily represent the official views of Harvard Catalyst, Harvard University and its affiliated academic healthcare centers, or the National Institutes of Health.

Please address correspondence to Katherine L. Reinshagen, MD, Department of Radiology, Massachusetts Eye and Ear, 243 Charles St, Boston, MA 02114; e-mail: katherine_reinshagen@meei.harvard.edu; @klreinshagen

Indicates open access to non-subscribers at www.ajnr.org

http://dx.doi.org/10.3174/ajnr.A7339

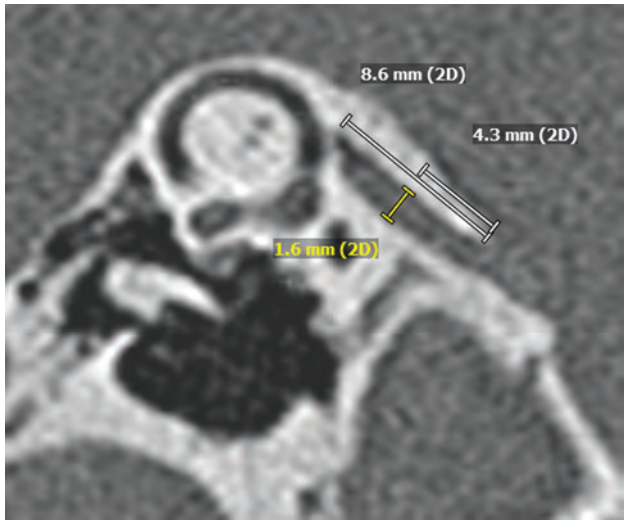

FIG 1. Measurement of the midpoint vestibular aqueduct size in the Pöschl plane. The length of the VA is determined, and the midpoint level is located. A measurement line perpendicular to the VA length is used to measure the midpoint VA size.

Cincinnati method of measurement for diagnosis of EVA and speech-related audiologic findings in a longitudinal retrospective study. They concluded that the degree of hearing loss as measured by the speech-reception threshold (SRT) and word recognition score (WRS) is likely influenced by the midpoint vestibular aqueduct (VA) width.

Due to the anatomic obliquity of the VA, the 45° oblique (Pöschl) plane has been proposed as a more reliable depiction of the VA in its entire length than the axial plane. It is thought to provide accurate and reliable measurements of VA size.[14] On the basis of normative data, a midpoint VA size of 0.71 mm is considered the 97.5th percentile for size, and at our institution, a measurement of 0.8 mm is considered borderline to slightly enlarged.[15] While the Cincinnati method of measurement has been correlated with audiologic findings, this has not yet been performed to a similar degree with the Pöschl plane midpoint VA measurement with repeat audiologic measures, limiting its adoption among clinicians attempting to counsel patients. This study aimed to determine to what extent EVAs measured in the Pöschl plane correlate with audiologic findings, namely pure tone average (PTA), WRS, and SRT, in a retrospective, longitudinal study.

MATERIALS AND METHODS

Study Population

This retrospective study received approval (IRB No: 2020P000295) through the Massachusetts Eye and Ear Institutional Review Board. The inclusion criteria were pediatric patients, 0–16 years of age, with either a unilateral or bilateral EVA determined by CT or MR imaging, either isolated or as part of a syndrome. These patients were identified through the Pediatric Hearing Loss Registry at Massachusetts Eye and Ear, a tool designed to keep track of patients with sensorineural hearing loss by etiology. One hundred four patients with EVA were located in the registry; 50 patients were excluded because they either had no available CT or <3 audiograms available. Fifty-four patients (77 ears) were included in the study.

Audiologic Data

Four hundred nineteen clinical audiograms from the 54 included patients were retrospectively reviewed from the electronic medical record. The measured values in the audiograms collected were PTA, SRT, and WRS. PTA is an average of hearing threshold levels typically at 500, 1000, 2000, 4000, and 8000 Hz and gives a quantitative description of the ear's hearing ability. SRT indicates the lowest sound intensity in decibels at which a listener can repeat 50% of presented 2-syllable words. WRS reflects the percentage of monosyllabic words a subject correctly repeats at a suprathreshold intensity of a 25- or 50-word list.[16] All patients included in the study had at least 3 audiograms. However, because values for SRT and WRS were not recorded as standard for all audiograms, occasionally fewer than 3 values of SRT and WRS were available for some patients. PTA values were available for 77 ears (54 patients), SRT values were available for 65 ears (48 patients), and WRS values were available for 67 ears (52 patients). Some audiograms used a score of "pass" for WRS. At our institution, this equates to a score in the range of 92% to 100%; thus, for these audiograms, a median score of 96% was used for quantitative evaluation.

Brookhauser et al[17] offered definitions for 4 types of hearing loss: stable, purely progressive, fluctuating progressive, and fluctuating nonprogressive hearing loss. We considered progressive hearing changes as present if the difference between initial and final PTA threshold was at least 10 dB. If the variability between each time point measure of PTA did not surpass 10 dB and the difference between first and last audiogram PTA did not surpass 10 dB, the hearing was classified as stable. If the PTA measurements had <10 dB of variability between measurements and the measurements between the initial and last audiogram were >10 dB, the hearing change was classified as purely progressive. If the PTA measurements did show a variability of at least 10 dB between time points and measurements returned to within 10 dB of the initial PTA, the hearing change was classified as fluctuating nonprogressive. If the PTA measurements did show a variability of at least 10 dB between time points and the measurements between the initial and last audiogram were >10 dB, the hearing change was classified as fluctuating progressive.

Radiologic Data

A retrospective review of multidetector CT of the temporal bone of the 54 patients (77 ears) was performed. Three CTs were performed at outside institutions. At our institution, multidetector CT (Discovery 750 HD; GE Healthcare) of the temporal bone was performed with 120 kV(peak), 165 mA, section thickness of 0.6 mm, and a 0.2-mm overlap. Overall, the mean section thickness was 0.6 mm (range, 0.5–0.8 mm), the mean x-ray current was 153 mA, and the mean voltage was 120 kVp. The Pöschl plane (mean section thickness, 0.6 mm; range, 0.5-0.8 mm) was created by using the thinnest available data in bone windows on all included ears using an Advantage Workstation VolumeShare 5 (GE Healthcare).

The Pöschl plane images (example in Fig 1) were independently reviewed by 2 blinded radiologists who determined the midpoint VA size using the technique outlined in Juliano et al.[15] The

mean midpoint VA size was determined and compared with the audiologic findings.

Statistical Analysis

To determine interobserver reliability between the 2 blinded readers, we calculated the intraclass correlation coefficient.[18] Because longitudinal repeat measurements were available for each patient, we chose a linear mixed-effects model to evaluate the relationship between the VA size and the 3 outcomes: PTA, SRT, and WRS. This allowed us to account for changes in hearing with time and to allow group measurements of all patients. The midpoint VA size, the age at the first audiogram, and the time since the first audiogram were chosen as the fixed effects, and the random effects included the intercepts for each patient and by-patient random slopes across time. The mixed-effects model was fit using the R statistical programming language, Version 4.0.4 (http://www.r-project.org/) software packages lmerTest and lme4. Further subgroup analysis and comparisons were performed using the Student *t* test.

P values ≤ .05 were considered statistically significant.

Table 1: Subgroup analysis of VA size by presence of inner ear anomaly

	EVA with IP-2	EVA without IP-2
No. (ears)	50	27
Mean (mm)	1.92	1.53
SD (mm)	0.58	0.48
P = .004		

Table 2: Subgroup analysis of VA size by presence of hearing fluctuation

	Fluctuating	Nonfluctuating
No. (ears)	30	47
Mean (mm)	1.94	1.68
SD (mm)	0.64	0.51
P = .04		

Table 3: Subgroup analysis of VA size by presence of hearing progression

	Progressive	Stable
No. (ears)	28	49
Mean (mm)	1.81	1.77
SD (mm)	0.5	0.62
P = .73		

Table 4: Subgroup analysis of VA size by hearing subtypes

	Progressive		Stable	
All patients	Fluctuating	Nonfluctuating	Fluctuating	Nonfluctuating
No. (ears)	13	15	17	32
Mean (mm)	1.88	1.75	1.98	1.65
SD (mm)	0.61	0.4	0.67	0.56
Subgroups				
IP-2				
No. (ears)	7	11	13	19
Mean (mm)	2.01	1.83	2.20	1.74
SD (mm)	0.62	0.36	0.60	0.62
Pendred				
No. (ears)	4	1	N/A	N/A
Mean (mm)	1.87	2.08	N/A	N/A
SD (mm)	0.35		N/A	N/A
Trauma				
No. (ears)	N/A	3	2	2
Mean (mm)	N/A	2.15	2.08	1.43
SD (mm)	N/A	0.34	0.29	0.53

Note:—N/A indicates not applicable.

RESULTS

Study Population

Fifty-four patients (25 males and 29 females) with a mean age at the first audiogram of 5 years met the inclusion criteria. Of the 54 patients, 25 patients had bilateral and the remaining 29 patients had unilateral EVAs. Due to missing audiogram data, 2 ears were excluded, resulting in a total of 77 ears included in this study. Thirty-four patients (50 ears) had radiographic evidence of an associated cochlear malformation, all incomplete partition-type 2 (IP-2) anomalies. One additional patient also showed radiologic findings of an IP-2 anomaly in the contralateral ear, which was not affected by the EVA and did not show a detectable anomaly of the inner ear on the side with the enlarged VA. Three patients (4 ears with EVA) had Pendred syndrome. Four patients (7 ears with an EVA) had a reported history of trauma.

Vestibular Aqueduct Size and Interobserver Reliability

The mean midpoint VA size of the 77 included ears was 1.78 ([SD. 0.57] mm; range, 0.81–3.46 mm). The intraclass correlation coefficient for these measurements between the 2 radiologists was 0.92 (95% CI, 0.84–0.95; $P < .001$), which indicated excellent interobserver reliability. Subgroup analysis of the mean (SD) of the VA size in ears/patients with and without IP-2 anomalies, Pendred syndrome, and trauma, with or without progressive hearing loss, is given in Tables 1–4.

Audiologic Findings

We reviewed 419 clinical audiograms from these 54 patients. A median of 6 audiograms per patient (range, 3–17) were available. The mean time between the first and last audiograms was 97.4 (SD, 50.9) months. Because of the necessary language development required to participate in SRT and WRS, these tests were not performed in patients younger than 13 months of age and 2.5 years of age, respectively, in our study population.

Five hundred ninety-three PTA measurements were obtained for 54 patients (77 ears). A linear mixed-effects model indicates that for each millimeter increase in VA size, there was an increase of 10.5 dB (95% CI, 3.1–17.9 dB; $P = .006$) in the PTA (Fig 2). For every additional year of age at the first audiogram, the PTA decreased by 2.1 dB (95% CI, −3.1 to −1.2 dB; $P < .001$). Twelve ears were classified as having fluctuating progressive hearing loss, 13 ears were classified as having fluctuating nonprogressive hearing loss, 16 ears were purely progressive,

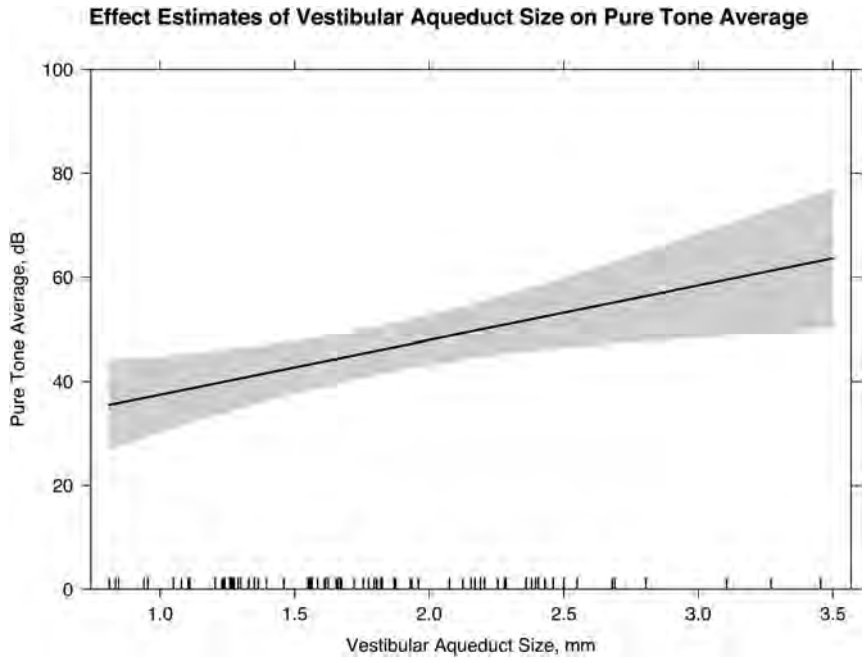

FIG 2. Linear mixed-effects model with the effect estimates of VA size on the PTA (slope of line; 95% confidence interval, *shaded gray*). For every millimeter increase in the midpoint VA size, there is a 10.5 dB increase in the PTA (95% CI, 3.1–17.9 dB; $P = .006$).

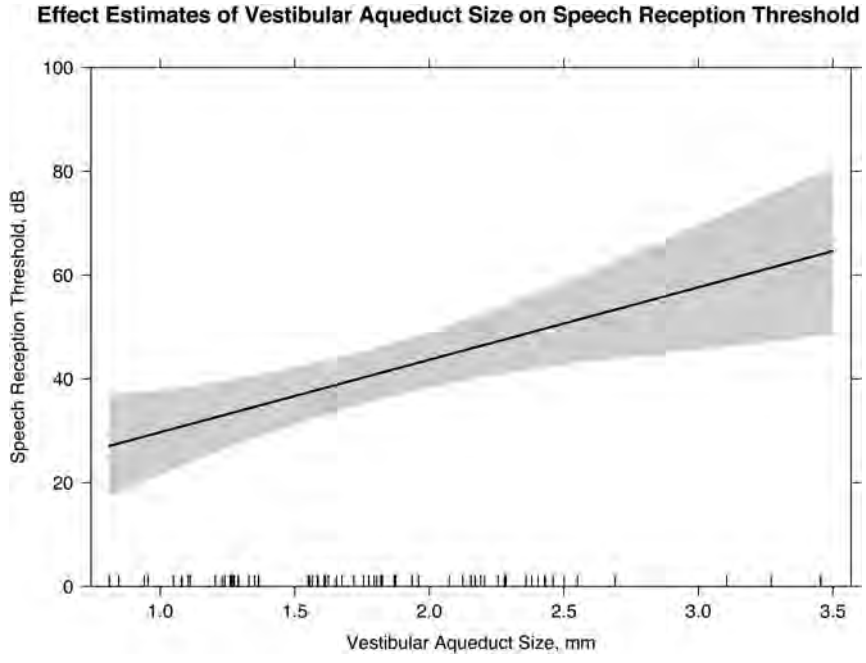

FIG 3. Linear mixed-effects model with the effect estimates of the VA size on the SRT (slope of line; 95% confidence interval, *shaded gray*). For every millimeter increase in midpoint VA size, there is an increase of 14.0 dB in the SRT (95% CI, 5.2–22.7 dB; $P = .002$).

and the remaining 36 ears were classified as having stable hearing. The VA size was significantly larger in patients with fluctuating hearing loss than in patients without fluctuating hearing loss (Tables 1–4, $P = .04$). There was no statistically significant difference in VA size in patients with progressive and nonprogressive or stable hearing loss (Tables 1–4, $P = .73$). Two of 4 patients (3 of 7 ears) with a reported history of trauma had progression of hearing loss. There was no statistically significant difference in VA size in ears with progression following trauma and ears without progression following trauma (Tables 1–4, $P = .51$).

One hundred fifty-nine SRT scores were obtained for 48 patients (65 ears). The linear mixed-effects model indicated that for each millimeter increase in VA size, there was an increase of 14.0 dB (95% CI, 5.2−22.7 dB; $P < .002$) in the SRT (Fig 3). For every additional year of age at the first audiogram, the SRT decreased by 1.8 dB (95% CI, −2.9 to −0.63 dB; $P = .002$).

Four hundred fifty-nine WRS values were obtained for 52 patients (67 ears). The linear mixed-effects model indicates a decrease of 10.5% (95% CI, −21%−0%; $P = .05$) in the WRS for each millimeter increase in VA size (Fig 4). For every additional year of age at the first audiogram, the WRS increased by 3.1% (95% CI, 1.6%−4.6%; $P < .001$).

DISCUSSION

EVA is the most common radiologically detected abnormality in patients undergoing evaluation for sensorineural hearing loss.[1] The hearing loss can be progressive in nature and can also be associated with a stepwise progression in hearing loss in association with head trauma.[2-4] Counseling of patients with EVA has, therefore, been of great importance to clinicians, though it has been challenging due to the inconsistent pattern of hearing loss, unknown pathophysiology, and mixed genetic backgrounds.[5-8] These challenges in prognostication have been highlighted in a recent meta-analysis that also emphasized the need for more robust low-bias data analysis in this complex population.[19]

Measurements of the VA were first conducted using polytomography, in which it was considered enlarged when the anterior-posterior diameter measured ≥1.5 mm at the midpoint.[10] Since the introduction of multidetector CT, the detection of EVA has continued to improve. The Cincinnati criteria suggested that VA size could be considered enlarged when the midpoint and opercular widths in the axial plane measured > 0.9 and 1.9 mm, respectively.[12] However, due to the inherent

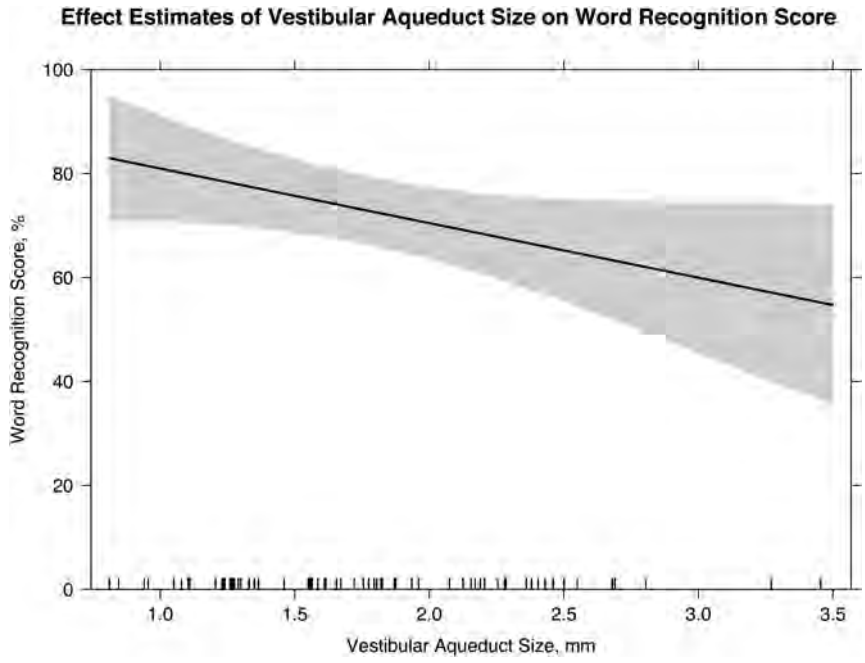

FIG 4. Linear mixed-effects model with the effect estimates of VA size on the WRS (slope of line; 95% confidence interval, *shaded gray*). For every millimeter increase in midpoint VA size, there is a 10.5% decrease in the WRS (95% CI, −21%–0%; $P = .05$).

obliquity of the VA relative to the axial plane, the 45° oblique (Pöschl) plane has also been proposed as an alternative plane for measurement. By means of normative values, 0.71 mm was found to be the 97.5th percentile for size, and it has been suggested that 0.8 mm at the midpoint in the Pöschl plane could be considered borderline to slightly enlarged.[15] The Pöschl plane has also been considered more reliable and reproducible than measurements obtained in the axial plane.[14] While the low-bias study performed by Ascha et al[13] correlated speech-related auditory measures, namely the SRT and WRS, with the size of the VA using the Cincinnati method of measurement in a retrospective study,[19] this correlation was not yet performed to a similar degree with the Pöschl plane measurements using repeat audiologic measures, thus, in part, limiting its value to clinicians who are attempting to counsel patients regarding their anticipated hearing outcomes.

In our study, we retrospectively reviewed a series of pediatric patients with EVA who underwent repeat audiograms to determine the correlation between the midpoint VA size in the Pöschl plane and PTA, WRS, and SRT in a longitudinal repeated-measures study. The intraclass correlation coefficient score between 2 independent, blinded radiologists was 0.92, indicating excellent interobserver reliability of the Pöschl plane midpoint measurement of VA size, consistent with findings in previous literature.[14] Because of the excellent interobserver reliability, the mean values of the midpoint VA size were thought to be representative.

We found a statistically significant correlation between the midpoint VA size and the degree of hearing loss as measured by PTA, SRT, and WRS. Each additional millimeter in midpoint VA size in the Pöschl plane resulted in an increase of 10.5 dB in PTA, an increase of 14.0 dB in SRT, and a decrease of 10.5% in the WRS in our longitudinal study. Our study supports prior studies by Antonelli et al[20] and Ascha et al,[13] which both found a correlation between VA size as measured in the axial plane and the SRT and speech-discrimination testing. Ascha et al reported a 17.5-dB increase in the SRT and a decrease of 21% in the WRS for every millimeter increase in the midpoint size of the VA by using the axial CT Cincinnati method of measurement.[13] In addition, for each additional year of age at the first audiogram, our patient cohort demonstrated an increase of 2.1 dB in the PTA, a decrease of 1.8 dB in the SRT, and an increase of 3.1% in the WRS. This finding is concordant with that of Ascha et al, who previously reported a decrease of 3.1 dB in the SRT and an increase of 1.6% in the WRS with each additional year of age at the first audiogram.

Other studies assessing the correlation between VA size and auditory measures have reported contradicting results. Zalzal et al[21] and Dahlen et al[22] found no correlation between VA size measured in the axial CT plane and hearing loss, with hearing loss categorized as stable or progressive, and degrees of severity such as profound, severe, moderate, and mild. This finding could possibly be explained, in part, by a limited number of patients (15 children in Zalzal et al and 11 patients in Dahlen et al), limited available audiometric data, and the possibility that the categorization of the hearing loss and the correlation performed on it might be less elucidative than measuring the performance of the ear as continuous values, the latter of which might better reflect the performance of the ear in progressive hearing loss.

Hwang et al[23] attempted a 2-fold investigation of VA size, testing the reliability of multiple types of VA measurements and correlating the VA measurements with PTA data. Hwang et al concluded that the Pöschl plane permits higher predictive accuracy for hearing loss than the conventional axial plane; however, they did not find a correlation with PTA. That study was limited in the number of audiograms available and did not assess repeat audiogram measures, SRTs, or WRSs; the latter 2 measures were subsequently used by Ascha et al[13] to address perceptual and cognitive-linguistic factors. In our study, repeat audiogram measures were used in a linear mixed-effects model to determine a hearing loss trend and represented our attempt to incorporate the sometimes-progressive nature of the disease.[24-26]

Most interesting, only 4 of the 54 patients (7/77 ears) in our study had a reported history of trauma. Two of the 4 patients (3/7 ears) had a progressive hearing loss, defined as an increase of the PTA of ≥10 dB between their first and last audiogram, in line with past studies that have reported varying incidences of hearing loss precipitated by trauma in patients with EVA ranging from 3% to 80%.[3,4,20,22,25,27-38] These data corroborate the variable link between traumatic events and progression of hearing loss in

patients with EVA. Although our subgroup of patients with trauma is relatively small, there was no statistically significant difference in the size of the VA in those with trauma and progressive hearing loss and those without progressive hearing loss. In our subgroup analysis of patient hearing trends, only those who were classified as having fluctuating hearing changes demonstrated a significantly larger VA size. Most interesting, all 3 patients with Pendred syndrome (5 included ears) had progressive hearing loss.

Our data are supportive of the prior study by Ascha et al[13] and may be helpful for clinicians who are counseling patients regarding their anticipated hearing loss outcomes using measurements obtained in the highly reproducible Pöschl plane.

Limitations

The results reported should be considered in light of some limitations. The effect estimates in the linear mixed-effect models are based on a retrospective observational study. Therefore, they are subject to biases that may have influenced our model estimates. Limited sample size and missing values in the obtained audiologic repeated measures in this study could play a role in the significance of the statistics. However, considering the retrospective nature of this study and this relatively rare condition, it is somewhat difficult to generate a large sample size at a single institution. Future studies could consider using multicenter data to increase the sample size.

A potential confounder could be the presence of a cochlear malformation, though the exact effect remains unknown because of the incompletely understood pathophysiology of the abnormality.[2] The EVA is often seen clinically in the setting of underlying cochlear malformations and might even be considered as a marker of a more extensive inner ear deformity.[39] However, the degree to which hearing loss is related to the underlying EVA or the underlying cochlear malformation is challenging to separate. Antonelli et al[20] demonstrated no significant correlation in the score or degree of cochlear modiolar deficiency and the severity of hearing loss in patients with EVA; however, EVA morphology and opercular size as measured in the axial plane did correlate with the severity of hearing loss. In an extensive review of human temporal bone specimens, Makary et al[40] also found patients with scala communis anomalies of the cochlea with normal hearing, suggesting the complicated nature of correlating cochlear anomalies with degree of hearing loss. Nevertheless, the role of the accompanying presence of a cochlear malformation on the overall hearing outcome of these patients remains unclear; thus, for our study and in keeping with the prior study by Ascha et al,[13] we included all patients with EVAs regardless of the presence of an associated cochlear malformation. Our subgroup analysis of the 50 ears in 34 patients with IP-2 anomalies demonstrated a significant difference in the size of the EVA between patients with IP-2 and those without a cochlear malformation. Thus, a conclusion from our patient population regarding the role of the IP-2 malformation versus the EVA size in the longitudinal audiometric measures was not possible. In addition, it is possible that subtle cochlear malformations may be underappreciated radiographically.

In our study, MR imaging may have been helpful to assess subtle cochlear malformations; however, only 5 patients included in this study had MR imaging studies.[41,42] More research would be helpful to understand the relationship and degree of hearing loss when faced with an EVA as the sole underlying radiographic pathology (as excluded with advances in MR imaging techniques) and in the setting of known genetic abnormalities. Furthermore, we recognize that by including only pediatric patients, there is potential for bias because an EVA can occasionally be below the clinical discovery threshold or cause symptoms at a later stage of life. Further study including adult patients may be helpful to account for these patients who present later in life.

In addition, because few patients in our study had a history of trauma, the data are limited in their applicability to patients with known traumatic events and an EVA, though the incidence of hearing loss in association with traumatic events is widely variable in the literature, ranging from 3% to 80%.[3,4,20,22,25,27-38] The relatively few patients with a history of trauma may reflect the counseling practices by our pediatric otolaryngologists. Similarly, because we had only 3 patients with a genetic diagnosis of Pendred syndrome, the data are also limited in their applicability to patients with genetic syndromes. Although it is interesting that all 3 patients (5 included ears) with Pendred syndrome demonstrated progressive hearing loss, further study or meta-analysis of the data with larger patient populations with genetic diagnoses would be helpful to assess a correlation among longitudinal audiologic outcomes in these patients.

CONCLUSIONS

Our longitudinal, repeated-measures study in patients with an EVA shows that midpoint VA measurements obtained in the Pöschl plane are highly reproducible and have a significant correlation with audiologic findings. For each millimeter increase in midpoint VA size in the Pöschl plane, there was an associated increase of 10.5 dB in PTA, an increase of 14.0 dB in SRT, and a decrease of 10.5% in WRS. These data may be helpful for clinicians who are counseling patients with EVAs regarding their hearing outcomes using measurements obtained in the highly reproducible Pöschl plane.

Disclosures: Mary E. Cunnane—*UNRELATED*: *Consultancy*: Akouos, *Comments*: I am retained as a consultant on volumetric measurements of tumors for which the company is developing a therapy. I have not yet done any work for them and have received no payment. Hugh D. Curtin—*RELATED*: *Royalties*: Elsevier royalties from previously published *Head and Neck Imaging*.

REFERENCES

1. Mafong DD, Shin EJ, Lalwani AK. **Use of laboratory evaluation and radiologic imaging in the diagnostic evaluation of children with sensorineural hearing loss.** *Laryngoscope* 2002;112:1–7 CrossRef Medline
2. Merchant SN. **Genetically determined and other developmental defects.** In: Merchant SN, Nadol JB, eds. *Schuknecht's Pathology of the Ear*. 3rd ed. People's Medical Publishing 2010; 275–77
3. Levenson MJ, Parisier SC, Jacobs M, et al. **The large vestibular aqueduct syndrome in children: a review of 12 cases and the description of a new clinical entity.** *Arch Otolaryngol Head Neck Surg* 1989;115:54–58 CrossRef Medline
4. Jackler RK, De La Cruz A. **The large vestibular aqueduct syndrome.** *Laryngoscope* 1989;99:1238–42; discussion 1242–43 CrossRef Medline
5. Pryor SP, Madeo AC, Reynolds JC, et al. **SLC26A4/PDS genotype-phenotype correlation in hearing loss with enlargement of the vestibular aqueduct (EVA): evidence that Pendred syndrome and**

non-syndromic EVA are distinct clinical and genetic entities. *J Med Genet* 2005;42:159–65 CrossRef Medline
6. Madden C, Halsted M, Meinzen-Derr J, et al. **The influence of mutations in the SLC26A4 gene on the temporal bone in a population with enlarged vestibular aqueduct.** *Arch Otolaryngol Head Neck Surg* 2007;133:162–68 CrossRef Medline
7. Birkenhäger R, Zimmer AJ, Maier W, et al. **Evidence of a novel gene for the LAV-syndrome** [in German]. *Laryngorhinootologie* 2007;86:102–06 CrossRef Medline
8. Zhao FF, Lan L, Wang DY, et al. **Correlation analysis of genotypes, auditory function, and vestibular size in Chinese children with enlarged vestibular aqueduct syndrome.** *Acta Otolaryngol* 2013;133:1242–49 CrossRef Medline
9. Griffith AJ, Arts A, Downs C, et al. **Familial large vestibular aqueduct syndrome.** *Laryngoscope* 1996;106:960–65 CrossRef Medline
10. Valvassori GE, Clemis JD. **The large vestibular aqueduct syndrome.** *Laryngoscope* 1978;88:723–28 CrossRef Medline
11. Boston M, Halsted M, Meinzen-Derr J, et al. **The large vestibular aqueduct: a new definition based on audiologic and computed tomography correlation.** *Otolaryngol Head Neck Surg* 2007;136:972–77 CrossRef Medline
12. Vijayasekaran S, Halsted MJ, Boston M, et al. **When is the vestibular aqueduct enlarged? A statistical analysis of the normative distribution of vestibular aqueduct size.** *AJNR Am J Neuroradiol* 2007 28:1133–38 CrossRef Medline
13. Ascha MS, Manzoor N, Gupta A, et al. **Vestibular aqueduct midpoint width and hearing loss in patients with an enlarged vestibular aqueduct.** *JAMA Otolaryngol Head Neck Surg* 2017;143:601–08 CrossRef Medline
14. Ozgen B, Cunnane ME, Caruso PA, et al. **Comparison of 45 degrees oblique reformats with axial reformats in CT evaluation of the vestibular aqueduct.** *AJNR Am J Neuroradiol* 2008;29:30–34 CrossRef Medline
15. Juliano AF, Ting EY, Mingkwansook V, et al. **Vestibular aqueduct measurements in the 45° oblique (Pöschl) plane.** *AJNR Am J Neuroradiol* 2016;37:1331–37 CrossRef Medline
16. Baiduc RR, Poling GL, Hong O, et al. **Clinical measures of auditory function: the cochlea and beyond.** *Dis Mon* 2013;59:147–56 CrossRef Medline
17. Brookhouser PE, Worthington DW, Kelly WJ. **Fluctuating and/or progressive sensorineural hearing loss in children.** *Laryngoscope* 1994;104:958–64 CrossRef Medline
18. Koo TK, Li MY. **A guideline of selecting and reporting intraclass correlation coefficients for reliability research.** *J Chiropr Med* 2016;15:155–63 CrossRef Medline
19. Saeed HS, Kenth J, Black G, et al. **Hearing loss in enlarged vestibular aqueduct: a prognostic factor systematic review of the literature.** *Otol Neurotol* 2021;42:99–107 CrossRef Medline
20. Antonelli PJ, Nall AV, Lemmerling MM, et al. **Hearing loss with cochlear modiolar defects and large vestibular aqueducts.** *Am J Otol* 1998;19:306–12 Medline
21. Zalzal GH, Tomaski SM, Vezina LG, et al. **Enlarged vestibular aqueduct and sensorineural hearing loss in childhood.** *Arch Otolaryngol Head Neck Surg* 1995;121:23–28 CrossRef Medline
22. Dahlen RT, Harnsberger HR, Gray SD, et al. **Overlapping thin-section fast spin-echo MR of the large vestibular aqueduct syndrome.** *AJNR Am J Neuroradiol* 1997;18:67–75 Medline
23. Hwang M, Marovich R, Shin SS, et al. **Optimizing CT for the evaluation of vestibular aqueduct enlargement: Inter-rater reproducibility and predictive value of reformatted CT measurements.** *J Otol* 2015;10:13–17 CrossRef Medline
24. Govaerts PJ, Casselman J, Daemers K, et al. **Audiological findings in large vestibular aqueduct syndrome.** *Int J Pediatr Otorhinolaryngol* 1999;51:157–64 CrossRef Medline
25. Gopen Q, Zhou G, Whittemore K, et al. **Enlarged vestibular aqueduct: review of controversial aspects.** *Laryngoscope* 2011;121:1971–78 CrossRef Medline
26. Lai CC, Shiao AS. **Chronological changes of hearing in pediatric patients with large vestibular aqueduct syndrome.** *Laryngoscope* 2004;114:832–38 CrossRef Medline
27. Arcand P, Desrosiers M, Dubé J, et al. **The large vestibular aqueduct syndrome and sensorineural hearing loss in the pediatric population.** *J Otolaryngol* 1991;20:247–50 Medline
28. Madden C, Halsted M, Benton C, et al. **Enlarged vestibular aqueduct syndrome in the pediatric population.** *Otol Neurotol* 2003;24:625–32 CrossRef Medline
29. Berrettini S, Forli F, Bogazzi F, et al. **Large vestibular aqueduct syndrome: audiological, radiological, clinical, and genetic features.** *Am J Otolaryngol* 2005;26:363–71 CrossRef Medline
30. Okumura T, Takahashi H, Honjo I, et al. **Sensorineural hearing loss in patients with large vestibular aqueduct.** *Laryngoscope* 1995;105:289–93; discussion 293–34 CrossRef Medline
31. Harker LA, Vanderheiden S, Veazey D, et al. **Multichannel cochlear implantation in children with large vestibular aqueduct syndrome.** *Ann Otol Rhinol Laryngol Suppl* 1999;177:39–43 CrossRef Medline
32. Lin CY, Lin SL, Kao CC, et al. **The remediation of hearing deterioration in children with large vestibular aqueduct syndrome.** *Auris Nasus Larynx* 2005;32:99–105 JunCrossRef Medline
33. Colvin IB, Beale T, Harrop-Griffiths K. **Long-term follow-up of hearing loss in children and young adults with enlarged vestibular aqueducts: relationship to radiologic findings and Pendred syndrome diagnosis.** *Laryngoscope* 2006;116:2027–36 CrossRef Medline
34. Steinbach S, Brockmeier SJ, Kiefer J. **The large vestibular aqueduct–case report and review of the literature.** *Acta Otolaryngol* 2006;126:788–95 CrossRef Medline
35. Grimmer JF, Hedlund G, Park A. **Steroid treatment of hearing loss in enlarged vestibular aqueduct anomaly.** *Int J Pediatr Otorhinolaryngol* 2008;72:1711–15 CrossRef Medline
36. Atkin JS, Grimmer JF, Hedlund G, et al. **Cochlear abnormalities associated with enlarged vestibular aqueduct anomaly.** *Int J Pediatr Otorhinolaryngol* 2009;73:1682–85 CrossRef Medline
37. Ma X, Yang Y, Xia M, et al. **Computed tomography findings in large vestibular aqueduct syndrome.** *Acta Otolaryngol* 2009;129:700–08 CrossRef Medline
38. Mamikoğlu B, Bentz B, Wiet RJ. **Large vestibular aqueduct syndrome presenting with mixed hearing loss and an intact mobile ossicular chain.** *Otorhinolaryngol Nova* 2000;10:204–06 CrossRef
39. Irving RM, Jackler RK. **Large vestibular aqueduct syndrome.** *Current Opinion in Otolaryngology & Head and Neck Surgery* 1997;5:267–71 CrossRef
40. Makary C, Shin J, Caruso P, et al. **A histological study of scala communis with radiological implications.** *Audiol Neurotol* 2010;15:383–93 CrossRef Medline
41. Reinshagen KL, Curtin HD, Quesnel AM, et al. **Measurement for detection of incomplete partition type II anomalies on MR imaging.** *AJNR Am J Neuroradiol* 2017;38:2003–07 CrossRef Medline
42. Hirai S, Cureoglu S, Schachern PA, et al. **Large vestibular aqueduct syndrome: a human temporal bone study.** *Laryngoscope* 2006;116:2007–11 CrossRef Medline

Prenatal Evaluation of Intracranial Hemorrhage on Fetal MRI: A Retrospective Review

K.N. Epstein, B.M. Kline-Fath, B. Zhang, C. Venkatesan, M. Habli, D. Dowd, and U.D. Nagaraj

ABSTRACT

BACKGROUND AND PURPOSE: The evaluation and characterization of germinal matrix hemorrhages have been predominantly described on postnatal head sonography in premature neonates. However, germinal matrix hemorrhages that are seen in premature neonates can be also seen in fetuses of the same postconceptual age and are now more frequently encountered in the era of fetal MR imaging. Our aim was to examine and describe the MR imaging findings of fetuses with intracranial hemorrhage.

MATERIALS AND METHODS: A retrospective review of diagnostic-quality fetal MRIs showing intracranial hemorrhage from January 2004 to May 2020 was performed. Images were reviewed by 2 radiologists, and imaging characteristics of fetal intracranial hemorrhages were documented. Corresponding postnatal imaging and clinical parameters were reviewed.

RESULTS: One hundred seventy-seven fetuses with a mean gestational age of 25.73 (SD, 5.01) weeks were included. Germinal matrix hemorrhage was identified in 60.5% (107/177) and nongerminal matrix hemorrhage in 39.5% (70/177) of patients. Significantly increased ventricular size correlated with higher germinal matrix hemorrhage grade ($P < .001$). Fetal growth restriction was present in 21.3% (20/94) of our population, and there was no significant correlation with germinal matrix grade or type of intracranial hemorrhage. An increased incidence of neonatal death with grade III germinal matrix hemorrhages ($P = .069$) compared with other grades was identified; 23.2% (16/69) of the neonates required ventriculoperitoneal shunts, with an increased incidence in the nongerminal matrix hemorrhage group ($P = .026$).

CONCLUSIONS: MR imaging has become a key tool in the diagnosis and characterization of intracranial hemorrhage in the fetus. Appropriate characterization is important for optimizing work-up, therapeutic approach, and prenatal counseling.

ABBREVIATIONS: GA = gestational age; GMH = germinal matrix hemorrhage; ICH = intracranial hemorrhage; SSFSE = single-shot fast spin-echo; US = sonography

Fetal MR imaging has become a valuable tool in the prenatal evaluation of the brain and has an important role in prenatal diagnosis and guiding prenatal/perinatal management and counseling.[1-3] MR imaging of the fetus has enabled the evaluation of parenchymal abnormalities that are not identified on sonography (US) and also confirms and elucidates the presence of intracranial hemorrhage (ICH).

Fetal ICH is rare, with an estimated incidence of 0.6–1/1000 cases.[4-6] The most common type of ICH in the fetus involves the germinal matrix, accounting for approximately two-thirds of cases, with the remainder involving non-germinal matrix hemorrhage locations.[7] Although the commonly used Burstein and Papile grading system was initially described on CT, the evaluation and characterization of germinal matrix hemorrhages (GMHs) have been predominantly described and classified on postnatal head US in premature neonates.[8,9] There is a 25%–40% reported incidence of GMH in premature neonates younger than 32 weeks' gestational age (GA) and those with a birth weight of <1500 grams.[10] However, GMHs that are seen in premature neonates can be also seen in fetuses of the same postconceptual age and are now more frequently encountered in the era of fetal MR imaging. GMH may result in considerable fetal and neonatal mortality and long-term neurologic morbidity in those neonates that survive, especially in the setting of grade III and IV GMHs.[11]

Our aim was to examine the MR imaging findings of fetuses with intracranial hemorrhage.

Received June 14, 2021; accepted after revision August 9.

From the Departments of Radiology and Medical Imaging (K.N.E., B.M.K.-F., U.D.N.), Neurology (C.V., D.D.), Maternal Fetal Medicine (M.H.), and Biostatistics (B.Z.), Cincinnati Children's Hospital Medical Center, Cincinnati, Ohio; University of Cincinnati College of Medicine (K.N.E., B.M.K.-F., B.Z., C.V., M.H., D.D., U.D.N.), Cincinnati, Ohio; and Department of Obstetrics and Gynecology (M.H.), Good Samaritan Hospital, Cincinnati, Ohio.

Please address correspondence to Katherine N. Epstein, MD, Department of Radiology and Medical Imaging, Cincinnati Children's Hospital Medical Center, 3333 Burnet Ave, Cincinnati, OH; e-mail: kepstein@salud.unm.edu; @KatieEpsteinMD

Indicates article with online supplemental data.

http://dx.doi.org/10.3174/ajnr.A7320

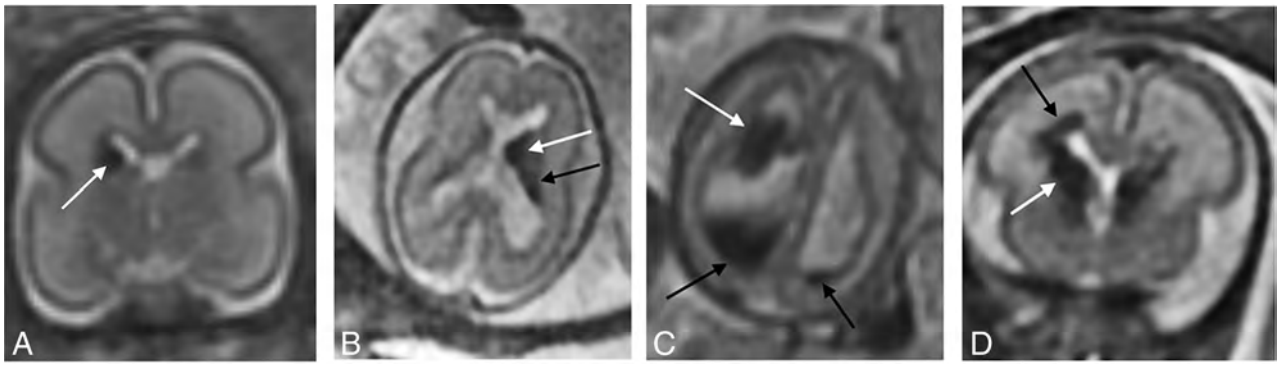

FIG 1. *A*, Grade I GMH in a 24 -weeks' GA fetus. Coronal T2 SSFSE of the brain demonstrates T2 hypointensity at the right caudothalamic groove (*white arrow*). *B*, Grade II GMH in a 24 weeks' GA fetus. Axial T2 SSFSE of the brain shows T2 hypointensity at the left caudothalamic groove (*white arrow*) extending posteriorly along the margin of the lateral ventricle (*black arrow*). *C*, Grade III GMH in a 20 weeks' GA fetus. Axial T2 SSFSE of the brain demonstrates globular T2 hypointensity near the right caudothalamic groove (*white arrow*) with layering T2 hypointensity/hemorrhage in the right greater than left posterior horns of the ventricles (*black arrows*). There is dilation of the bilateral ventricles, right greater than left, measuring up to 16 mm on the right. *D*, Grade IV GMH in a 26 weeks' GA fetus. Coronal T2 SSFSE of the brain shows T2 hypointensity at the right caudothalamic groove (*white arrow*), with T2 signal/hemorrhage extending into the periventricular white matter (*black arrow*). Grade II GMH is partially visualized on the left.

MATERIALS AND METHODS

Study Design

This study is a single-center retrospective chart review. The case list was compiled using Illuminate InSight software (Softek Illuminate) from January 2004 through May 2020 ($n = 219/6179$). Inclusion criteria were fetuses with diagnostic-quality fetal MR images demonstrating intracranial hemorrhage ($n = 177$), with 42 fetuses excluded. All studies were reviewed by a pediatric radiology fellow and pediatric neuroradiologist to confirm the imaging findings in the radiology report. Determination of diagnostic-quality imaging was made at the discretion of the neuroradiologist and fellow radiologist. All images were viewed in the PACS workstation. A chart review was performed to obtain relevant clinical data. This study was compliant with the Health Insurance Portability and Accountability Act and was approved by the institutional review board. The requirement for informed consent was waived.

Scanning Parameters

All fetuses included in our study were scanned prenatally on a 1.5T magnet at Cincinnati Children's Hospital Medical Center using an Ingenia 1.5T scanner (Philips Healthcare) or a 1.5T Signa HDxt (GE Healthcare) system. The routinely implemented fetal brain protocol included axial, sagittal, and coronal T2-single-shot fast spin-echo (SSFSE) and balanced fast-field echo/FIESTA images. A section thickness of 3-mm, no-gap, interleaved images at ≤24 weeks' GA, and 4-mm, no-gap, interleaved images at >24 weeks' GA were used. Axial T1, DWI, and EPI blood sequences of the fetal brain were also variably obtained, routinely implemented in July 2016. The TR and TE varied on each scanner and were changed at times of scanner upgrades to optimize image quality. At least 2 stacks of images in each plane were obtained to the radiologists' satisfaction. The smallest FOV possible was used.

Image Interpretation

Fetal brain MR images and postnatal neuroimaging were reviewed by a board-eligible pediatric radiology fellow (K.N.E.) and a board-certified radiologist (U.D.N.) with added qualifications in pediatric radiology and neuroradiology and >5 years of postfellowship attending experience in a large academic center.

Fetuses that were determined to have ICH on diagnostic-quality fetal MR imaging were recorded. Fetal ICH imaging characteristics that were documented included presence vs absence of associated T2-SSFSE, T1, DWI, and EPI signal. Hemorrhages were classified as GMH versus non-GMH, depending on location. The non-GMH group included fetuses with a layering intraventricular blood product with a normal appearance of the fetal germinal matrix (ie, in setting of Chiari II malformation), parenchymal hemorrhages in the cerebellum or cerebrum without clear intraventricular extension, and extra-axial hemorrhages. GMHs were subsequently graded by the Burstein and Papile Modified Grading System as follows: grade I, subependymal hemorrhage; grade II, intraventricular hemorrhage filling <50% of the ventricle a with ventricular size of ≤15 mm; grade III, intraventricular hemorrhage filling >50% of the ventricle with a ventricular size of ≥15 mm; and grade IV, intraparenchymal periventricular hemorrhage in the setting of grades I–III GMH (Fig 1).[8] The location of the hemorrhage was documented. Fetuses with subependymal cysts, believed to be the result of prior GMH, were also documented as grade zero (Fig 2). Cerebellar hemorrhages were reported separate from the GMH classification if there was not additional hemorrhage localized to the caudothalamic groove (Fig 3). Additional imaging parameter that was recorded included lateral ventricular size, by measuring the transverse atrial diameter on an axial or coronal image.[12] The presence or absence of a 2-versus-3 vessel umbilical cord, placental abnormality, and other fetal structural abnormalities was recorded.

The reports of fetal sonographic studies performed at Cincinnati Children's Hospital Medical Center or outside institutions were reviewed when available. The presence or absence of fetal growth restriction (estimated fetal weight less than the 10th percentile), large for gestational age (estimated fetal weight greater than the 90th percentile for GA), abnormal findings on fetal Doppler, and twin-twin transfusion syndrome was recorded.[13,14] For the purposes of this study, abnormal findings on fetal Doppler included the following:

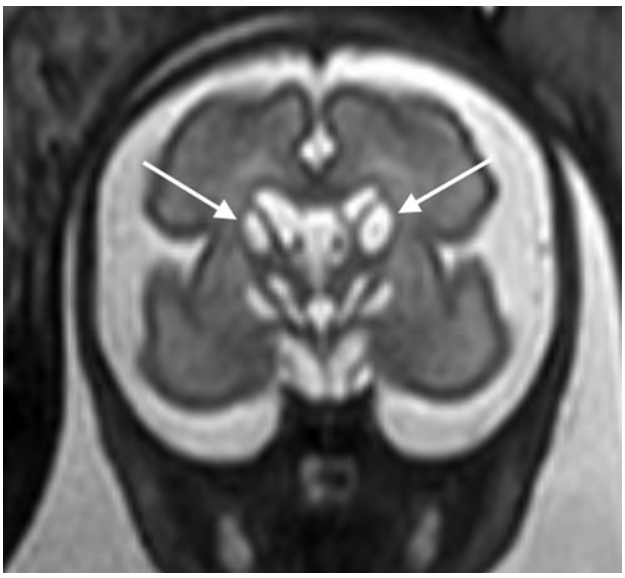

FIG 2. Grade 0 GMH in a 29 weeks' GA fetus. Coronal T2 SSFSE of the brain shows T2-hyperintense cystic lesions at the bilateral caudothalamic grooves (*white arrows*) and abnormal T2 hyperintense signal in the bilateral basal ganglia.

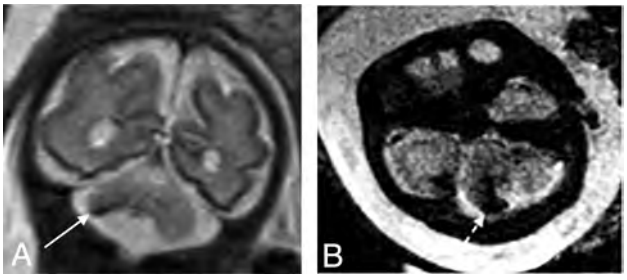

FIG 3. Coronal T2 SSFSE (*A*) and axial EPI (*B*) of the brain in a 31 weeks' GA fetus. Note T2 hypointensity at the margin of the inferior aspect of the deficient right cerebellar hemisphere (*arrow, A*) and an associated magnetic susceptibility signal at the right cerebellar hemisphere (*dashed arrow, B*) and vermis.

absent or reversal of diastolic flow in the umbilical artery; pulsatile umbilical vein; decreased, absent, or reversal of the a-wave in the ductus venosus; and/or elevated peak systolic velocity in the middle cerebral artery of >1.5 multiple of the mean.[14,15] Available postnatal neuroimaging was reviewed, including neonatal head US, brain MR imaging, and head CT. Imaging findings of ICH, neonatal brain parenchyma, and ventricular size were compared with the fetal MR imaging to assess whether there was interval worsening, stability, or improvement. Clinical parameters included the following: age of the mother, GA of the fetus at fetal MR imaging, sex of the fetus, singleton-versus-twin pregnancy, delivery outcome (death versus live birth), neonatal outcome (died versus alive after a live birth in the neonatal period), age at postnatal imaging, and the need for CSF diversion (shunting).

Statistical Analysis

Descriptive analyses were performed to demonstrate the distribution of the imaging findings. Continuous variables were presented as means (SDs), and categoric variables were presented as number (percentage). A 2-sample *t* test or 1-way ANOVA was used to detect the differences in continuous variables among different groups. The correlation among categoric variables was assessed by the χ^2 or Fisher exact test when appropriate. All analyses were performed using SAS, Version 9.4 (SAS Institute). A P value $< .05$ was considered statistically significant.

Table 1: Summary of cohort

Characteristics	Data ($n = 177$)
Sex	
Male	48.0% (85/177)
Female	40.1% (71/177)
Unknown	11.9% (21/177)
Singleton	70.1% (124/177)
Multiple gestation	29.9% (53/177)
Average GA at fetal MR imaging (wk)	25.73 (SD, 5.01)
GMH	60.5% (107/177)
Grade 0	12.1% (13/107)
Grade I	28.9% (31/107)
Grade II	28.0% (30/107)
Grade III	6.5% (7/107)
Grade IV	24.3% (26/107)
Non-GMH	39.5% (70/177)
Cerebellar hemorrhages	9% (16/177)
Fetal growth restriction	21.3% (20/94)
Other imaging abnormalities	79.1% (140/177)
Postnatal imaging	22.6% (40/177)
Head US (No.)	72.5% (29/40)
MR imaging (No.)	87.% (35/40)
CT (No.)	52.5% (21/40)
Average maternal age at fetal MR imaging (yr)	28.02 (SD, 6.02)

RESULTS

Description of Cohort

A total of 177 fetuses (85 males, 71 females, 21 unknown) met the criteria and were included in the analysis, with an incidence of 2.9% (177/6179) in our patient population. The average gestational age of 25.73 weeks (range, 16.57–37 weeks) at fetal MR imaging was characteristic of the cohort as a whole. Seventy-one percent (124/177) were singleton pregnancies, and 29.9% (53/177) were multiple gestation (50 twins and 3 triplets). The average maternal age at the time of fetal MR imaging was 28.02 (SD, 6.02) years. The most common clinical indications for fetal MR imaging included suspected brain anomaly (23.7%, 42/177), twin-twin transfusion syndrome (22.6%, 40/177), and ventriculomegaly (15.3%, 27/177). These and other descriptors of the cohort are summarized in Table 1.

Fetal MR Imaging Findings

The fetuses with ICH were broadly categorized into 2 groups: associated with the GMH and unassociated with the GMH (non-GMH). GMH was identified in 60.5% (107/177) of patients. The 107 GMHs were graded into 5 categories: grade 0 = 13, grade I = 31, grade II = 30, grade III = 7, grade IV = 26. Sixty-four percent (69/107) of GMHs were unilateral (35 right and 34 left), and 35.5% (38/107) were bilateral. However, 39.5% (70/177) of patients had non-GMH, and of those, 15.7% (11/70) had cerebellar hemorrhages. Isolated cerebellar hemorrhages were seen in

54.5% (6/11) of fetuses; the other 5 patients had additional hemorrhagic insults in the supratentorial brain. Other imaging abnormalities were seen in 79.1% (140/177) of fetuses: aqueductal stenosis ($n = 7$), Chiari II malformation ($n = 14$), twin-twin transfusion ($n = 34$), and extracranial congenital anomalies. T2 and EPI were positive for hemorrhage in 84.7% and 96.3% of all cases with positive findings, respectively (Table 2). However, T1 and DWI demonstrated 46% and 57.8% positivity, respectively. The mean ventricular size was 12.76 (SD, 7.54) mm, with 59.3% (105/177) of fetuses with ventriculomegaly (>10 mm). The mean ventricular size significantly correlated with GMH grade ($P \leq .001$) (Fig 4). There was no significant difference in mean ventricle size between GMH-versus-non-GMH groups (11.9 [SD, 6.4] mm versus 14.1 [SD, 8.8] mm, $P = .085$).

Prenatal Clinical Findings

There was no significant difference in fetal sex or maternal age between the GMH-versus-non-GMH groups ($P = .116$ and $P = .068$, respectively). The presence of fetal growth restriction and fetal Doppler abnormalities was reviewed for those fetuses that had undergone sonography at our institution or had available outside examinations for review. Fetal growth restriction was identified in 21.3% (20/94) of cases. There was no significant difference in the rate of fetal growth restriction between the GMH-versus-non-GMH groups or among the GMH grades. Fetal Doppler abnormalities were present in 43% (40/93) of fetuses with ICH, and 35% (14/40) of those were seen in the setting of twin-twin transfusion.

Table 2: Fetal MR imaging findings

ICH Imaging Characteristics	Data ($n = 177$)
T2 (+), $n = 177$	84.7% (150/177)
T1 (+), $n = 150$	46% (69/150)
DWI (+), $n = 135$	57.8% (78/135)
EPI (+), $n = 81$	96.3% (78/81)
Ventriculomegaly (>10 mm)	59.3% (105/177)
Ventricular size (mm)	12.76 (SD, 7.54)

Note:— + indicates positive imaging finding on fetal MR in those fetuses with ICH.

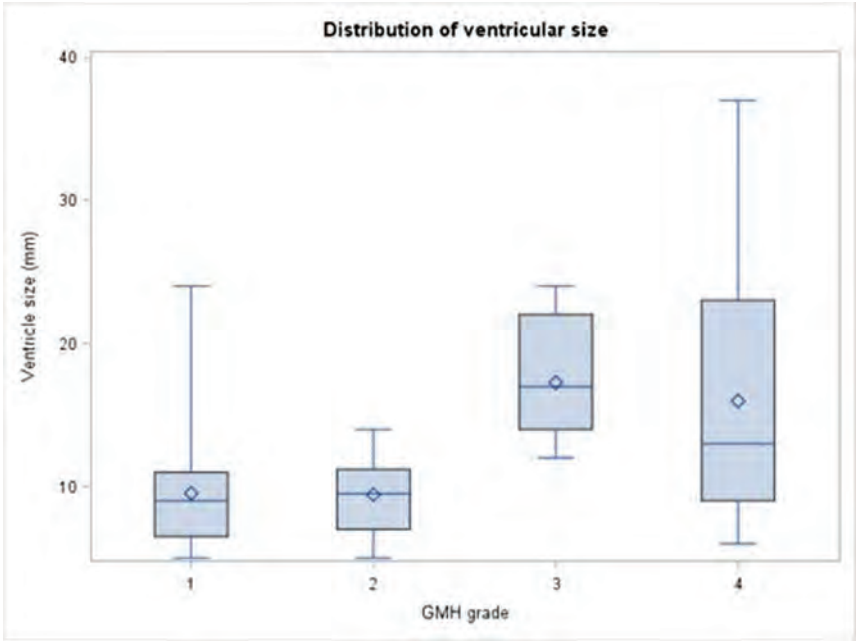

FIG 4. Linear regression model shows the ventricle size increased by 2.4 mm when the GMH grade increased by 1 ($P < .001$).

Postnatal Imaging Findings

A total of 40 neonates, 65% with GMH (26/40) and 35% with non-GMH (14/40), had postnatal imaging, including neonatal head US, brain MR imaging, and/or head CT examinations. Most neonates underwent >1 different imaging modality in the postnatal period. The postnatal imaging examinations overall demonstrated improvement of the prenatal ICH in most neonates, with overall decreased volume of hemorrhage (Fig 5 and Table 3). However, 3.4% (1/29) of head US, 11.4% (4/35) of brain MR imaging, and 4.8% (1/21) of head CT of neonates showed worsened findings of ICH. Postnatal head US and MR imaging showed a significant difference in brain parenchyma as correlated with GMH grade. Brain parenchymal findings were stable on head US and MR imaging, with a less severe GMH (grades 0–II) versus more severe GMH (grade III–IV); the latter demonstrated significant worsening of brain parenchymal findings, including cerebral or cerebellar white matter volume loss and/or injury and/or porencephalic cysts (Online Supplemental Data). However, the GMH grade did not significantly correlate with postnatal brain parenchymal findings on head CT. Evaluation of the brain parenchyma postnatally also showed no significant correlation between GMH-versus-non-GMH groups.

Postnatal Clinical Findings

There was a significant difference in neonatal outcome between GMH versus non-GMH ($P = .022$) when comparing those neonates who died within the first year of life with those who survived beyond the neonatal period after a live birth in the 48 fetuses who had available postnatal clinical data. Neonatal death occurred in 23% (9/40) of patients with GMH versus 50% (14/28) of those with non-GMH. However, there was not a significant difference in the delivery outcome ($P = .947$). There was also not a significant difference in the delivery or neonatal outcome among GMH grades ($P = .069$, $P = .253$). However, there was a higher incidence of death at delivery in those fetuses with grade III GMH at 57% (4/7) (grade 0 = 8%, grade I = 13%, grade II = 17%, and grade IV = 15%); 23.2% (16/69) of the neonates with available clinical data required a ventriculoperitoneal shunt. The χ^2 test revealed a statistically significant increased risk of shunt requirement in the non-GMH group compared with the GMH group ($P = .026$). Chiari II malformation was present in 40% (4/10) of the neonates

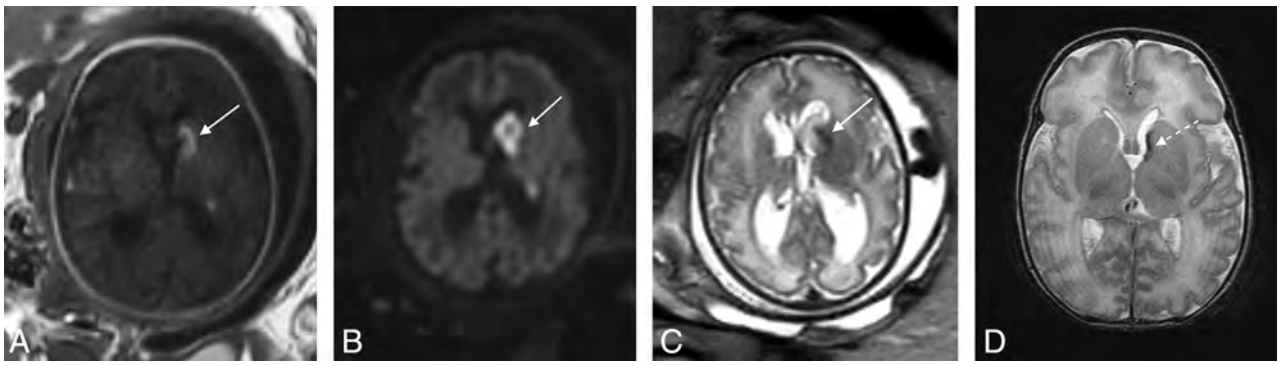

FIG 5. Left, grade IV GMH in a 35 weeks' GA fetus. Axial T1(*A*), DWI (*B*), and T2 SSFSE (*C*) images of the brain demonstrate blood products centered in the left caudothalamic groove, extending posteriorly along the left lateral ventricle with associated T1 hyperintensity, restricted diffusion, and T2 hypointensity (*arrows*). *D*, Postnatal axial T2 of the brain at day 6 of life shows decreased T2 hypointensity centered at the left caudothalamic groove (*dashed arrow, D*) compared with prenatal image (*C*), consistent with decreased volume of hemorrhage.

Table 3: Postnatal intracranial hemorrhage findings

Imaging Modality	Findings	Data
US	Same	27.6% (8/29)
	Better	69.0% (20/29)
	Worse	3.4% (1/29)
MR	Same	14.3% (5/35)
	Better	74.3% (26/35)
	Worse	11.4% (4/35)
CT	Same	0% (0/21)
	Better	95.2% (20/21)
	Worse	4.8% (1/21)

in the non-GMH group that required a ventriculoperitoneal shunt. In the GMH group, there was a significant correlation between the GMH grades and the need for shunt placement ($P = .029$). Of those neonates that required a shunt, the mean ventricle size was significantly larger than in those who did not need shunt placement (35.5 [SD, 17.2] mm versus 17.8 [SD, 15.8] mm, $P = .013$).

DISCUSSION

We examined and described imaging findings of ICH on fetal MR imaging and studied the pre- and postnatal clinical data and postnatal imaging findings in relation to the prenatal MR imaging. We made several observations: 60.5% (107/177) of fetal ICHs involved the germinal matrix and were presumed to be germinal matrix in origin. MRI sequences that were important in the identification of hemorrhage on prenatal imaging included T2 and EPI blood sequences because they were positive for hemorrhage in 84.7% (150/177) and 96.3% (78/81) of cases, respectively. There was a significant increase in the mean ventricular size as the GMH grade increased ($P \leq .001$). The neonates that had postnatal MR imaging demonstrated improved findings of ICH (74.3%, 26/35), though 51.4% (18/35) showed worsened brain parenchymal changes. Neonatal death was significantly increased in fetuses in the non-GMH compared with the GMH group ($P = .022$). However, within the GMH group, an increased incidence of neonatal death was seen in the grade III GMHs compared with the others ($P = .069$), though there was not a significant difference among the remaining grades.

Fetal ICH has been predominantly described and classified on US in the literature, with intraventricular hemorrhage the most common subtype of fetal ICH.[5,9,16,17] There are limited data of non-GMH forms of fetal ICH, including intraparenchymal hemorrhages in the cerebrum or cerebellum and subdural and subarachnoid hemorrhages. These data are further complicated by inconsistent descriptions in the literature because the true nature of parenchymal hemorrhages in the fetus and neonate is not always clear. Some report that the terms "periventricular hemorrhagic infarction" or "venous infarction" are preferred over grade IV intraventricular hemorrhage.[18] Previous studies of fetal ICH detected on US report an incidence of 0.5–0.9 of 1000 cases.[4,5] In a more recent study of fetal ICH detected on MR imaging, the incidence was higher and occurred in 1% of cases, a finding more comparable with those in our study in which fetal ICH occurred in 2.9% of our referral population.[19] The increased incidence may be the result of the increased sensitivity of MR imaging in the evaluation of ICH and/or the population of patients referred to our center.

Our results are similar to those in the study performed by Sanapo et al,[19] in which they discovered that ICH was confined to the GMH in 67% of fetuses versus a non-GMH location in the remainder (33%). Those hemorrhages that occurred in the cerebellum were classified in the non-GMH group in both studies. It is believed by some authors that cerebellar hemorrhages occur within the germinal matrix located in the subependymal layer of the roof of the fourth ventricle and in the subpial external granule cell layer.[20,21] Previously, most cerebellar hemorrhages were thought to be the result of significant birth-related trauma or associated with extensive supratentorial hemorrhage.[22,23] Given the uncertain classification of prenatal/neonatal cerebellar hemorrhages, we decided to classify those hemorrhages as non-GMH for this study.

The study of Sanapo et al[19] described ventriculomegaly in most of their cases (80%), compared with 59.3% in our study. The frequency of intrauterine fetal death was higher in the non-GMH-versus-GMH groups (58% versus 4%) in their study, and we, too, found a significant increase in neonatal death in the non-GMH group (50% versus 23%). The incidence of death in the GMH group was higher in our study, which is more comparable with the results of another study by Ghi et al,[17] in which the

authors observed a 16% incidence in death in fetuses with intraventricular hemorrhage. The etiology of the higher incidence of intrauterine fetal and neonatal death in the GMH group is unclear. However, the incidence in our study may be overestimated because a relatively large proportion of fetuses with less severe GMH (grades 0, I, and II) were lost to follow-up; therefore, the true incidence is likely much lower. Prior studies have demonstrated worse neurologic outcomes in the setting of grade III and IV GMHs.[5,17,19] Although we did not assess the long-term neurodevelopmental status of our patients, we found that more severe GMHs (grade III–IV) demonstrated worsened parenchymal findings in the postnatal setting, including cerebral or cerebellar white matter volume loss or porencephalic cysts, likely contributing to poorer neurologic outcomes.

Our study has several limitations, including the retrospective design of the study limiting its internal validity. Even though our fetal study population was relatively large, the postnatal follow-up imaging and clinical data were a much smaller sample size. Another limitation of our study was that the neurosonographic findings were not evaluated in detail. The study was also subject to some degree of selection bias because the imaging data were collected from a large tertiary care pediatric hospital, limiting the external validity of our findings. Also, the EPI blood sequence was not performed in all fetal MR imaging examinations in our study because it only became part of our routine protocol in 2016; therefore, some grade I GMHs and subtle non-GMHs could have been missed. The authors also acknowledge that the modified Burstein and Papile grading system used to classify GMHs in the fetus has its limitations because parenchymal hemorrhages and cerebellar hemorrhages may be of germinal matrix origin. However, in the absence of another widely published grading system in the fetus, we chose to use this classification system for this study. Finally, all of our examinations were performed on a 1.5T magnet, and it is plausible that use of a 3T magnet would have increased the sensitivity of the detection of ICH from increased signal-to-noise.[24]

CONCLUSIONS

Given that this is the largest single-center cohort of fetal ICH examined on MR imaging, we add several important findings to the existing literature. First, the EPI blood sequence is the most sensitive in the identification of fetal ICH, which, in conjunction with T2-SSFSE images, can allow optimizing classification and subsequent grading of GMHs in the fetus. Second, we reported a significant increase in neonatal death in the non-GMH-versus-GMH group and worsened brain parenchymal findings in more severe GMH grades (III–IV) on postnatal MR imaging. Last, we discovered a significant increased risk of shunt requirement in the non-GMH-versus-GMH group; and in those neonates that required a shunt, the mean ventricle size was significantly larger. All our findings demonstrate the importance of accurate classification of fetal ICH because it may have an impact on the therapeutic approach, prenatal/perinatal counseling, and neurologic outcomes.

Disclosure forms provided by the authors are available with the full text and PDF of this article at www.ajnr.org.

REFERENCES

1. Griffiths PD, Bradburn M, Campbell MJ, et al; MERIDIAN collaborative group. **Use of MRI in the diagnosis of fetal brain abnormalities in utero (MERIDIAN): a multicentre, prospective cohort study.** *Lancet* 2017;389:538–46 CrossRef Medline
2. Glenn OA, Barkovich AJ. **Magnetic resonance imaging of the fetal brain and spine: an increasingly important tool in prenatal diagnosis, Part 1.** *AJNR Am J Neuroradiol* 2006;27:1604–11 Medline
3. Glenn OA, Barkovich J. **Magnetic resonance imaging of the fetal brain and spine: an increasingly important tool in prenatal diagnosis, part 2.** *AJNR Am J Neuroradiol* 2006;27:1807–14 Medline
4. Vergani P, Strobelt N, Locatelli A, et al. **Clinical significance of fetal intracranial hemorrhage.** *Am J Obstet Gynecol* 1996;175:536–43 CrossRef Medline
5. Elchalal U, Yagel S, Gomori JM, et al. **Fetal intracranial hemorrhage (fetal stroke): does grade matter?** *Ultrasound Obstet Gynecol* 2005;26:233–43 CrossRef Medline
6. Cheung KW, Tan LN, Seto MT, et al. **Prenatal diagnosis, management, and outcome of fetal subdural haematoma: a case report and systematic review.** *Fetal Diagn Ther* 2019;46:285–95 CrossRef Medline
7. Kline-Fath BM. Supratentorial anomalies. In: Kline-Fath BM, Bulas DI, Lee W, eds. *Fundamental and Advanced Fetal Imaging Ultrasound and MRI*. 2nd ed. Wolters Kluwer; 2021:489–95
8. Burstein J, Papile La, Burstein R. **Hemorrhage and hydrocephalus in premature newborns: study with CT.** *AJR Am J Roentgenol* 1979;132:631–35 CrossRef Medline
9. Hintz SR, Slovis T, Bulas D, et all; NICHD Neonatal Research Network. **Interobserver reliability and accuracy of cranial ultrasound scanning interpretation in premature infants.** *J Pediatr* 2007;150:592–96 CrossRef Medline
10. Huang YF, Chen WC, Tseng JJ, et al. **Fetal intracranial hemorrhage (fetal stroke): report of four antenatally diagnosed cases and review of the literature.** *Taiwan J Obstet Gynecol* 2006;45:135–41 CrossRef Medline
11. Adiego B, Martínez-Ten P, Bermejo C, et al. **Fetal intracranial hemorrhage: prenatal diagnosis and postnatal outcomes.** *J Matern Neonatal Med* 2019;32:21–30 CrossRef Medline
12. Nagaraj UD, Kline-Fath BM. **Imaging diagnosis of ventriculomegaly: fetal, neonatal, and pediatric.** *Childs Nerv Syst* 2020;36:1669–79 CrossRef Medline
13. Gordijn SJ, Beune IM, Thilaganathan B, et al. **Consensus definition of fetal growth restriction: a Delphi procedure.** *Ultrasound Obstet Gynecol* 2016;48:333–39 CrossRef Medline
14. Quintero R, Morales W, Allen M, et al. **Staging of twin-twin transfusion syndrome.** *J Perinatol* 1999;19:550–55 CrossRef Medline
15. Mari G, Deter RL, Carpenter RL, et al. **Noninvasive diagnosis by Doppler ultrasonography of fetal anemia due to maternal red-cell alloimmunization: Collaborative Group for Doppler Assessment of the Blood Velocity in Anemic Fetuses.** *Obstet Gynecol Surv* 2000;55:341–42 CrossRef Medline
16. Abdelkader MA, Ramadan W, Gabr AA, et al. **Fetal intracranial hemorrhage: sonographic criteria and merits of prenatal diagnosis.** *J Matern Neonatal Med* 2017;30:2250–56 CrossRef Medline
17. Ghi T, Simonazzi G, Perolo A, et al. **Outcome of antenatally diagnosed intracranial hemorrhage: case series and review of the literature.** *Ultrasound Obstet Gynecol* 2003;22:121–30 CrossRef Medline
18. Brouwer AJ, Groenendaal F, Benders MJNL, et al. **Early and late complications of germinal matrix-intraventricular haemorrhage in the preterm infant: what is new?** *Neonatology* 2014;106:296–303 CrossRef Medline
19. Sanapo L, Whitehead MT, Bulas DI, et al. **Fetal intracranial hemorrhage: role of fetal MRI.** *Prenat Diagn* 2017;37:827–36 CrossRef Medline

20. Haines KM, Wang W, Pierson CR. **Cerebellar hemorrhagic injury in premature infants occurs during a vulnerable developmental period and is associated with wider neuropathology.** *Acta Neuropathol Commun* 2013;1:69 CrossRef Medline
21. Merrill JD, Piecuch RE, Fell SC, et al. **A new pattern of cerebellar hemorrhages in preterm infants.** *Pediatrics* 1998;102:e62 CrossRef Medline
22. Martin R, Roessmann U, Fanaroff A. **Massive intracerebellar hemorrhage in low-birth-weight infants.** *J Pediatr* 1976;89:290–93 CrossRef Medline
23. Grunnet ML, Shields DW. **Cerebellar hemorrhage in the premature infant.** *J Pediatr* 1976;88:605–08 CrossRef
24. Weisstanner C, Gruber GM, Brugger PC, et al. **Fetal MRI at 3T-ready for routine use?** *Br J Radiol* 2017;90:20160362 CrossRef Medline

Intracranial Hemorrhage on Prenatal MR Imaging

While intracranial hemorrhage (ICH) is a relatively common finding in preterm neonates, found in 40%–60% of those born before the gestational age of 32 weeks, it is considered rare in the prenatal period, with a reported incidence of no more than 0.1%,[1] particularly when estimated mostly on sonography (US) and in relatively small groups of patients. However, when MR imaging is used for prenatal diagnosis and larger cohorts of patients are reviewed, ICH (meant as all forms of bleeding, ie, germinal matrix hemorrhage [GMH] and all non-GMHs: intraventricular, intraparenchymal cerebral and cerebellar, subarachnoid, and subdural) occurs in 1% of pregnancies[2] or even in approximately 3% as shown in the article in this issue of the *American Journal of Neuroradiology* by Epstein et al,[3] who reviewed 6179 MR imaging scans and found 177 diagnostic-quality fetal MR images demonstrating intracranial hemorrhage. Taking into account one of the limitations of this study listed by the authors that T1, DWI, and EPI blood sequences were performed only in some of the MR imaging examinations since 2016 (the report includes MR imaging scans performed during 2004–2020) and that some subtle ICHs could have been missed, it becomes clear that, in fact, an even higher incidence of ICH in the prenatal period can be expected. This is in accordance with the results of 433 consecutive stillbirth postmortem examinations, in which there was intrauterine hemorrhagic brain injury in 4.6%.[4]

This is an important observation for the following reasons: 1) It confirms the importance of performing fetal MR imaging as an adjunct to prenatal US, enabling detection of the abnormalities that are not picked up on US, ICH being one of these; 2) in some cases, ICH might be the cause and not the result of preterm birth, or at least it precedes it; 3) it has severe medicolegal implications if the family sues the obstetricians and/or neonatologists for inadequate perinatal care; 4) in view of the expected posthemorrhagic hydrocephalus that carries an additional risk of adverse outcomes, follow-up imaging should be undertaken and ventriculoamniotic shunting is an option for the management in severe cases; and 5) the correct diagnosis should imply cesarean delivery to avoid additional hemorrhage or injury during vaginal delivery.

Although most fetuses from the above-mentioned study (60.5%) showed GMHs, there was also a significant group with non-GMH in the report of Epstein et al,[3] including cerebellar bleeding, which constituted 6.2% of the cohort (11/177) and is usually more difficult to visualize on US both in fetuses and in neonates. Cerebellar hemorrhages have been attributed in the literature to birth-related trauma so far, and this study shows that the insult may be prenatal. This finding, though not entirely new as the authors themselves state, may be significant in the attempt to explain the causes of autism spectrum disorder (ASD) and various additional behavioral disorders that have been found in extremely premature infants, >10 times more often than in term neonates (8% versus 0.6%); an increased risk of ASD has been found using the Screening Tool for Autism in Toddlers and Young Children (https://www.ocali.org/project/stat) in most cases of prematurity associated with cerebellar hemorrhage.[5]

Epstein et al[3] confirmed the results of a previous large study,[2] which showed statistically significantly poorer neurologic outcome of non-GMH than of GMH, including neonatal death and an increased necessity for ventricular shunting.

In utero shunting remains controversial. It was attempted in the 1980s and was abandoned due to lack of encouraging results. Currently, some active fetal therapy research groups are working on new devices, materials, and strategies to improve outcomes of these fetuses, and they encourage fetal MR imaging as providing more accurate information, allowing a more reliable diagnosis and exclusion of other anomalies.[6] Obviously, the procedure of shunting, curative by assumption, can cause complications, including secondary hemorrhages. In the records of my center, we have examples of ICH after shunting that was performed due to nonhemorrhagic hydrocephalus, eg, in congenital aqueductal stenosis.

Most interesting, there was a large representation of multiple pregnancies in the cohort examined by Epstein et al[3] (29.9%, 53/177), and in 34/53 cases, twin-twin transfusion syndrome (TTTS) was confirmed. It is not surprising because monochorionic twins are at high risk for adverse outcome due to complications related to placental vascular anastomoses, and these include both hemorrhagic and ischemic brain injury. Moreover, both kinds of brain damage are also observed in these patients with TTTS who are treated with fetoscopic laser surgery.[7]

Not surprising, it is crucial not only to diagnose ICH but also to rule it out because ICH belongs in the exclusion criteria for fetal surgery, open neural tube defect, and laser therapy for TTTS.[8] Consequently, a complete and reliable evaluation is necessary to qualify the fetus for various types of prenatal interventions. Fetal

MR imaging is usually one of the required procedures before deciding on the intrauterine treatment.

The already wide and still-growing spectrum of the capabilities of fetal MR imaging, including the use of 3T scanners, as well as the ever-expanding range of questions that have to be answered, including in cases of intracranial hemorrhage, means that we will certainly be dealing with more and more fetal observations using MR imaging.

REFERENCES

1. Kutuk MS, Yikilmaz A, Ozgun MT, et al. **Prenatal diagnosis and postnatal outcome of fetal intracranial hemorrhage.** *Childs Nerv Syst* 2014;30:411–48 CrossRef Medline
2. Sanapo L, Whitehead MT, Bulas DI, et al. **Fetal intracranial hemorrhage: role of fetal MRI.** *Prenat Diagn* 2017;37:827–36 CrossRef Medline
3. Epstein KN, Kline-Fath BM, Zhang B, et al. **Prenatal evaluation of intracranial hemorrhage on fetal MRI: a retrospective review.** *AJNR Am J Neuroradiol* 2021;42:2222–28 CrossRef Medline
4. Sims ME, Turkel SB, Halterman G, et al. **Brain injury and intrauterine death.** *Am J Obstet Gynecol* 1985;151:721–23 CrossRef Medline
5. Rutkowska M, Bekiesińska-Figatowska M, Kmita G, et al. **Neuroimaging results, short-term assessment of psychomotor development and the risk of autism spectrum disorder in extremely premature infants (≤28 GA): a prospective cohort study (preliminary report).** *Dev Period Med* 2018;22:39–48
6. Peiro JL, Fabbro MD. **Fetal therapy for congenital hydrocephalus: where we came from and where we are going.** *Childs Nerv Syst* 2020;36:1697–1712 CrossRef Medline
7. Bekiesinska-Figatowska M. MR imaging of multiple gestations. In: Masselli G, ed. *MRI of Fetal and Maternal Diseases in Pregnancy*. Springer-Verlag; 2016:231–44
8. Putbrese B, Kennedy A. **Findings and differential diagnosis of fetal intracranial haemorrhage and fetal ischaemic brain injury: what is the role of fetal MRI?** *Br J Radiol* 2017;90:20160253 CrossRef Medline

M. Bekiesinska-Figatowska
Department of Diagnostic Imaging
Institute of Mother and Child
Warsaw, Poland

http://dx.doi.org/10.3174/ajnr.A7319

Can MRI Differentiate between Infectious and Immune-Related Acute Cerebellitis? A Retrospective Imaging Study

G. Orman, S.F. Kralik, N.K. Desai, A. Meoded, H. Sangi-Haghpeykar, G. Jallo, E. Boltshauser, and T.A.G.M. Huisman

ABSTRACT

BACKGROUND AND PURPOSE: Acute cerebellitis is an acute neurologic condition attributable to a recent or concurrent infection or a recent vaccination or ingestion of medication, with MR imaging evidence of cerebellar edema. MR imaging can confirm an anatomic abnormality and may allow the radiologist to establish a differential diagnosis. The purpose of this research was to evaluate the MR imaging findings in children with acute cerebellitis due to infectious versus immune-related conditions, in particular whether MR imaging findings allow differentiation.

MATERIALS AND METHODS: Electronic medical records were reviewed between 2003 and 2020 in our quaternary children's hospital. Data included demographics and clinical records: presentation/symptoms, final diagnosis including acute cerebellitis and immune-related acute cerebellitis, length of stay, treatment, condition at discharge, and laboratory findings. Retrospective independent review of all brain MR imaging studies was performed.

RESULTS: Forty-three patients (male/female ratio, 28:15) were included in this study. Average age at presentation was 7.08 years (range, 0.05–17.52 years). Thirty-five children had infectious and 8 children had immune-related acute cerebellitis. Significant differences in neuroimaging were the following: 1) T2-FLAIR hyperintense signal in the brainstem (37.50% versus 2.85%, $P = .016$); 2) T2-FLAIR hyperintense signal in the supratentorial brain higher in the immune-related group (37.50% versus 0.00%, $P = .004$); and 3) downward herniation, higher in the infectious acute cerebellitis group (42.85% versus 0.00%, $P = .03$).

CONCLUSIONS: Acute cerebellitis is a rare condition, and MR imaging is helpful in the differential diagnosis. T2-FLAIR hyperintense signal in the brainstem and supratentorial brain may be indicative of immune-related acute cerebellitis, and downward herniation may be indicative of infectious acute cerebellitis.

ABBREVIATIONS: AC = acute cerebellitis; ACA = acute cerebellar ataxia; ADEM = acute disseminated encephalomyelitis; CE = contrast enhancement; IQR = interquartile range; WBC = white blood cells

Acute cerebellar ataxia (ACA) and acute cerebellitis (AC) are often used incorrectly and interchangeably in the literature.[1-3] Ataxia refers to an impaired ability to coordinate voluntary movements, impairing a person's ability to walk, talk, eat, and use fine motor skills in varying degrees.[2] ACA is a term used for a clinical constellation with a heterogeneous etiology. Not all children with ACA undergo imaging routinely; therefore, the exact percentage of AC in children with ACA is unknown.[4] The largest published series reported that AC occurred in 10% of children with ACA.[5]

Per definition, AC is an acute neurologic condition attributable to a recent or concurrent infective illness due to a virus or bacteria, a recent vaccination, or ingestion of medication, with MR imaging evidence of predominantly cerebellar edema.[1] The incidence of AC is uncertain because most of the existing literature is limited to single case reports or smaller case series.[1] Symptoms of AC are variable from classic symptoms of ACA to simple irritability, headache, photophobia, nuchal rigidity, or vomiting.[6,7] In addition, seizures, focal neurologic deficits, fever, and altered mental status are reported.[7] The most severe cases of AC may present with increased intracranial pressure due to severe cerebellar edema and resultant obstructive supratentorial hydrocephalus with serious morbidity and mortality. Diagnosis can be challenging in these cases. CSF examination is not always available in AC due to the

Received March 22, 2021; accepted after revision July 29.

From the Edward B. Singleton Department of Radiology (G.O., S.F.K., N.K.D., A.M., H.S.-H., T.A.G.M.H.), Texas Children's Hospital, Houston, Texas; Department of Obstetrics and Gynecology (H.S.-H.), Baylor College of Medicine, Houston, Texas; Institute for Brain Protection Sciences and Department of Neurosurgery (G.J.), Johns Hopkins All Children's, St. Petersburg, Florida; and Department of Pediatric Neurology (E.B.), University Children's Hospital Zürich, Zürich, Switzerland.

Please address correspondence to Gunes Orman, MD, Texas Children's Hospital, Edward B. Singleton Department of Radiology, 6701 Fannin St, Suite 470.12, Houston, TX 77030; e-mail: gxorman@texaschildrens.org

http://dx.doi.org/10.3174/ajnr.A7301

marked swelling and impending herniation, though pronounced pleocytosis and elevation of proteins may be present when testing is available.[7]

Neuroimaging plays an important role in the diagnostic work-up of children with AC. MR imaging can confirm anatomic abnormalities involving the cerebellum and allow the radiologist to establish a differential diagnosis.[7] Previous MR imaging studies in single patients showed varying imaging features in children with AC.[1] However, no definitive imaging feature was described, depending on the exact etiology. Differentiation is essential for selecting the correct treatment and predicting outcome. The purpose of this research was to evaluate the MR imaging findings in children with AC due to infectious (parainfectious, postinfectious) versus immune-related conditions, in particular whether the imaging findings allow differentiation between etiologies.

MATERIALS AND METHODS

Following institutional review board approval, a retrospective review of the MR imaging studies was performed among children (younger than 18 years of age) diagnosed with AC between 2003 and 2020 in our quaternary Texas Children's Hospital. A query search for MR imaging studies using the keywords "cerebellitis" and "ataxia" was performed in the PACS. Electronic medical records were reviewed for demographics (age, sex), clinical records (presentation/symptoms, final diagnosis including infectious AC and immune-related AC [acute disseminated encephalomyelitis, ADEM], hemolytic uremic syndrome, anti-*N*-methyl D-aspartate receptor encephalitis), length of stay, treatment, condition at discharge, and laboratory findings including white blood cells (WBC) in the complete blood count and CSF and glucose and protein levels in the CSF. Only the MRIs with a confirmed infectious AC or immune-related AC diagnosis were included in the study.

MR imaging studies of the brain were performed using standard departmental protocols on a 1.5T or 3T MR imaging scanner that included precontrast axial and sagittal T1-weighted turbo spin-echo, axial and/or coronal FLAIR, axial and coronal T2-weighted, axial gradient echo, axial DWI, and postcontrast axial and coronal T1-weighted turbo spin-echo imaging. Section thickness varied between 3 and 4 mm depending on the sequence.

A retrospective independent review of all brain MR imaging studies was performed by a board-certified pediatric neuroradiologist (S.F.K., with 9 years of experience) and a radiologist with pediatric neuroradiology research experience (G.O., with 8 years of experience). For all patients in whom there was a discordant MR imaging finding, the reviewers completed a secondary review to reach consensus. The consensus reading was used for final diagnosis.

MR imaging at initial presentation/diagnosis and follow-up MR imaging studies were evaluated for the following: 1) distribution of involvement of the cerebellum (unilateral, bilateral), brainstem, and/or supratentorial brain regions; 2) involvement of gray and/or white matter; 3) signs of compression and edema, effacement of fourth ventricle, effacement of the posterior fossa cisterns/subarachnoid spaces, downward or upward herniation, and supratentorial hydrocephalus; 4) contrast enhancement (CE); and 5) DWI characteristics, including vasogenic-versus-cytotoxic edema.

All statistical analysis was calculated using SAS/STAT software (https://www.sas.com/en_us/software/stat.html). All variables were assessed for normality. Comparisons between infectious versus immune-related AC groups for age at presentation were evaluated by unpaired *t* tests; complete blood count and CSF findings and length of stay were evaluated by the Wilcoxon signed rank test. Comparisons between infectious versus immune-related AC groups for MR imaging findings at presentation were evaluated by a 2-tailed Fisher exact test. Comparisons of MR imaging findings between presentation and follow-up studies for infectious versus immune-related AC groups were evaluated by the McNemar test. A P value $< .05$ was considered statistically significant.

RESULTS

A total of 2211 MR imaging and electronic medical records fulfilled the initial electronic search criteria for the study. Forty-three patients (male/female radio, 28:15) could be included in this study. There were 35 children with infectious (parainfectious and post-infectious) AC. The verified infectious agents were 2 HSV, 2 mycoplasma, 1 West Nile virus, 1 varicella virus, 1 enterovirus, 1 adenovirus, 1 influenza A virus. In 15 children no infectious agents were verified by testing, but they were diagnosed clinically during the acute infection and 11 children were post-infectious cases. Eight patients had immune-related AC (6 cases of ADEM, 1 hemolytic uremic syndrome, and 1 anti-*N*-methyl D-aspartate receptor encephalitis). A final diagnosis of an infectious AC agent was made by viral culture from the skin lesions in 2 patients with herpes simplex virus who had negative blood and CSF serology findings; by positive immunoglobulin M for 2 cases of mycoplasma; by polymerase chain reaction of the CSF and positive immunoglobulin M for 1 case of West Nile virus; by positive immunoglobulin M for 1 case of varicella virus; by polymerase chain reaction of blood in 1 case of enterovirus; by polymerase chain reaction of blood in 1 case of adenovirus; and by nasal swab in 1 case of influenza A virus. In addition, CSF culture and blood culture all had negative findings for these cases.

The average age at presentation was 7.08 years (range, 0.05–17.52 years); no statistically significant difference was found between infectious (mean, 7.19 [SD, 4.64] years) and immune-related AC (mean, 6.63 [SD, 5.60] years) groups ($P = .77$). Presenting symptoms in the infectious AC group were the following: 1) ataxia ($n = 17$), 2) altered mental status ($n = 7$), 3) headache ($n = 9$), and 4) seizure ($n = 2$). In the immune-related AC group, symptoms were the following: 1) ataxia ($n = 4$), 2) altered mental status ($n = 3$), and 3) seizure ($n = 1$). The median/interquartile range (IQR) for length of stay at our hospital was 8.0 days (5–13 days) days. No statistically significant difference was found between the infectious AC, 8 days (5–13 days), and immune-related AC, 7.5 days (5.5–19.5 days), groups ($P = .49$). Treatment with steroids was significantly higher in the immune-related AC, 100% ($n = 8$), than in the infectious AC group, 51.5% ($n = 17$) ($P = .01$). Twenty-one children were discharged after complete recovery; 20 patients were discharged after partial recovery, 12 of whom required occupational and/or physical therapy after their discharge. No significant difference was found between the infectious 27.3% ($n = 9$) and immune-related AC

Brain MR imaging findings at presentation between infectious ($n = 35$) and immune-related ($n = 8$) acute cerebellitis subgroups

T2/FLAIR Hyperintense Signal	Infectious (No.) (%)	Immune-Related (No.) (%)	*P* Value[a]
Unilateral cerebellar	4 (11.42)	2 (25.00)	.31
Bilateral cerebellar	27 (77.14)	4 (50.00)	.19
Brainstem	1 (2.85)	3 (37.50)	.016
Supratentorial brain	0 (0.00)	3 (37.50)	.004
Cerebellar white matter	10 (28.57)	1 (12.50)	.65
Cerebellar gray matter	25 (71.42)	5 (62.50)	.68
Associated findings			
Involvement of vermis	8 (22.85)	1 (12.50)	1.00
Effacement of fourth ventricle	12 (34.28)	1 (12.50)	.39
Effacement of posterior fossa subarachnoid spaces	11 (31.42)	0 (0.00)	.09
Downward herniation	15 (42.85)	0 (0.00)	.03
Upward herniation	10 (28.57)	0 (0.00)	.16
Supratentorial hydrocephalus	8 (22.85)	0 (0.00)	.31
Contrast enhancement			
Leptomeningeal	12 (34.28)	2 (28.57)	1.00
Cortical	7 (20.00)	1 (14.28)	1.00
Diffusion-weighted imaging			
Vasogenic edema	20 (58.82)	4 (50.00)	.71
Cytotoxic edema	6 (17.64)	1 (12.50)	1.00

[a] *P* is based on the Fisher exact test.

37.5% ($n = 3$) groups ($P = .67$). Two patients did not have any treatment or follow-up records available for review.

The median/IQR for CSF WBC (0–5/cu mm) was 22.5 (2–62)/cu mm; no statistically significant difference was found between the infectious (27 [2–62]/cu mm) and immune-related AC (8 [9–135]/cu m) groups ($P = .55$), despite both groups having elevated CSF WBC values. The median/IQR CSF glucose level (40–70 mg/dL) was 56.0 mg/dL (50.0–64.0 mg/dL). No statistically significant difference was found between the infectious (57 [50–64] mg/dL) and immune-related AC (52 [49–66] mg/dL) groups ($P = .99$). The median/IQR for CSF protein (15–45 mg/dL) was 29.5 mg/dL (18–59 mg/dL). No statistically significant difference was found between the infectious (27 [18–64] mg/dL]) and immune-related AC (35 [24–52] mg/dL) groups ($P = .77$). The median/IQR for blood WBC (5.0–14.5 10^3/UL) count was 10.72 10^3/UL (7.55–14.8310^3/UL). No statistically significant difference was found between the infectious (10.7 [7.8–14.2] 10^3/UL) and immune-related AC (12.2 [7.1–21.5] 10^3/UL) groups ($P = .55$). Urine tests for toxicology analysis were available for 15/43 (11/35 in infectious AC and 4/8 in immune-related AC) patients, which all had negative findings, 100% (15/15) in both groups.

All patients had brain MRIs (mean, 1.79; range, 0–8 days) following their initial presentation. The average age at first MR imaging was 7.09 years (range, 0.05–17.53 years). Only 19 (infectious AC = 15, immune-related AC = 4) patients had follow-up brain MRIs with a mean interval of 234.8 days (range, 3–1193 days) between the first and last MR imaging studies.

MR imaging findings at presentation for both the infectious and immune-related AC groups are summarized in the Table. Significant differences in imaging findings comparing both groups were the following: 1) The hyperintense signal percentage in the brainstem on T2-weighted and FLAIR sequences was higher in the immune-related AC group than in the infectious AC group (37.50% [$n = 3$] versus 2.85% [$n = 1$], $P = .016$); 2) the hyperintense signal percentage in the supratentorial brain (1 patient had subtle ill-defined T2 and FLAIR hyperintensity in the white matter adjacent to the trigone of the left lateral ventricle in the left parietal region; another patient had ill-defined T2 and FLAIR hyperintensity seen in the white matter of the right frontal lobe posteriorly, the left parietal region superiorly, and the left frontal lobe; and finally the last patient had extensive multifocal and confluent bilateral, slightly asymmetric, T2 and FLAIR hyperintensities involving the cerebral white matter of both cerebral hemispheres including subcortical white matter, deep white matter and periventricular white matter and the gray matter, including the bilateral basal ganglia and bilateral thalami, slightly greater on the right side than left) in T2-weighted and FLAIR sequences was higher in the immune-related AC group than in the infectious AC group 37.50% ($n = 3$) versus 0.00% ($n = 0$) ($P = .004$); and finally 3) the downward cerebellar herniation percentage was higher in the infectious AC group than in the immune-related AC group (42.85%, $n = 15$, versus 0.00% $n = 0$, $P = .03$) (Table). No statistically significant difference was found for CE or DWI characteristics when comparing the infectious and immune-related AC groups (Table).

Comparisons of MR imaging findings between presentation and follow-up were calculated. Only downward herniation was significantly decreased between presentation (47.37%, $n = 9$) and follow-up (10.53%, $n = 2$, $P = .016$), though a clear trend for a decrease in cerebellar white matter involvement (36.84%, $n = 7$, versus 10.53%, $n = 2$), supratentorial hydrocephalus (31.58%, $n = 6$, versus 5.26%, $n = 1$), and leptomeningeal CE (43.75%, $n = 7$ versus 12.50%, $n = 2$) was also observed ($P = .063$). Cerebellar atrophy on follow-up MRIs was found in 15.79% ($n = 3$) of patients.

Representative cases are demonstrated in Figs 1–6.

DISCUSSION

AC is one of the main causes of ACA in childhood. The etiologies of AC can be subclassified as primary infectious (para-/postinfectious) versus immune-related (reactive/autoimmune).[4,8] Certain MR imaging findings may be helpful to differentiate between infectious and immune-related AC. Our results show that T2-FLAIR hyperintense signal in the brainstem and/or supratentorial brain may be indicative of immune-related AC, and downward herniation may be indicative of infectious AC (Table).

Downward herniation was seen in almost half, and hydrocephalus, in almost one-quarter of our children with infectious AC. Yildirim et al[9] reported a higher incidence of cerebellar herniation; however, with a similar incidence of hydrocephalus in their AC cohorts, De Bruecker et al[10] reported hydrocephalus,

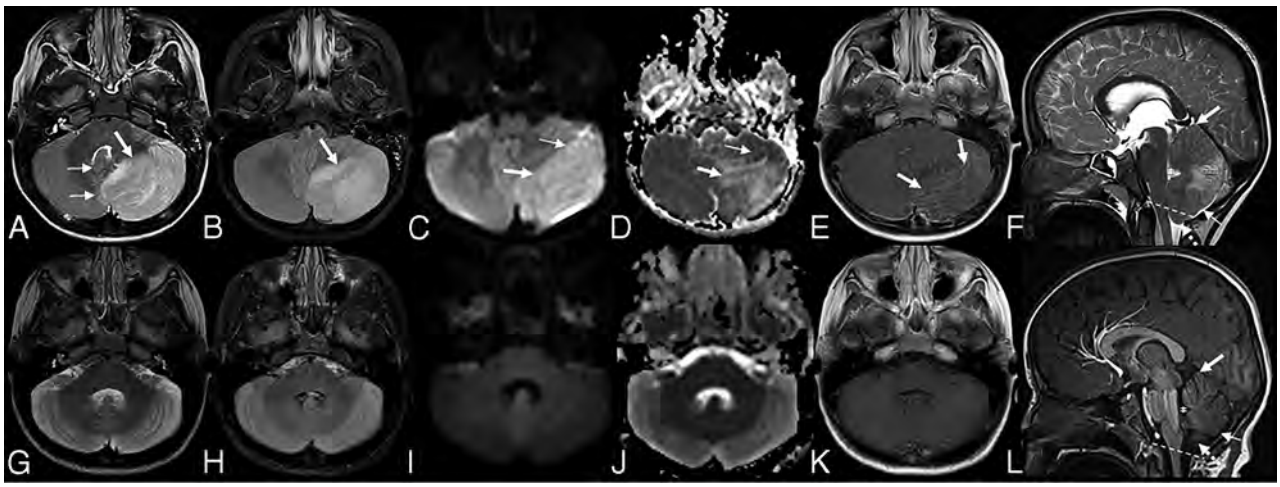

FIG 1. Unilateral cerebellitis in a 6-year-old boy who presented with ataxia with increased WBC on blood tests (infectious acute cerebellitis). Lumbar puncture was not performed. MR imaging acquired at presentation (*upper row*, *A–F)* shows unilateral left cerebellar gray matter and diffuse T2- and FLAIR hyperintensity (*A* and *B*, *thick arrow*), causing a shift of midline structures and displacement of the vermis (*A*, *thin arrows*). DWI (*C*) and an ADC map (*D*) show vasogenic (*C* and *D*, *thick arrows*) and cytotoxic edema (*C* and *D*, *thin arrows*). Leptomeningeal contrast enhancement is appreciated on postcontrast T1-weighted imaging (*E*, *thick arrows*). Sagittal T2-weighted imaging (*F*) shows the swollen cerebellum with upward (*F, thick arrow*) and downward (*F, dashed arrow*) herniation, supratentorial hydrocephalus, and effacement of the fourth ventricle (*F, asterisk*) and posterior subarachnoid spaces (*F, thin arrow*). Last follow-up MR imaging, which was acquired after 68 days, shows near-complete resolution of brain MR imaging findings (*lower row, G–L*) and atrophy. Note that sagittal T1-weighted imaging (*L*) shows the complete resolution of swollen cerebellum without any upward (*L, thick arrow*) and downward herniation (*L, dashed arrow*), no supratentorial hydrocephalus, and no effacement of the fourth ventricle (*L, asterisks*) and posterior subarachnoid spaces (*L, thin arrow*).

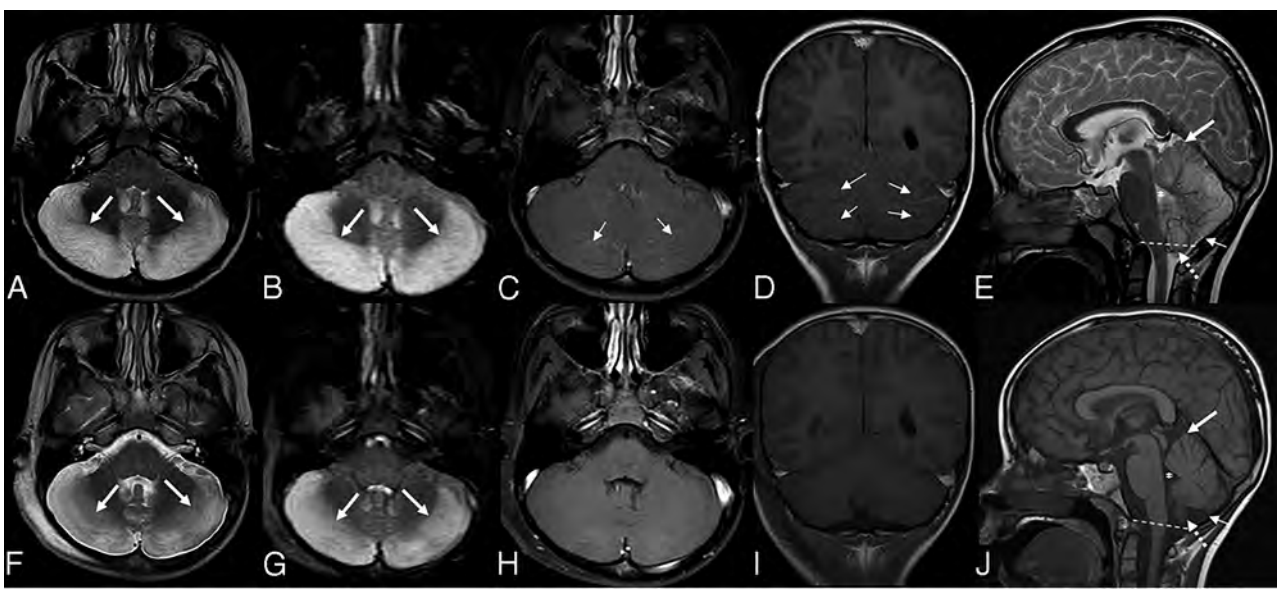

FIG 2. Bilateral cerebellitis in a 7-year-old boy who presented with ataxia and headache. He had a history of appendectomy 2 weeks before presentation (infectious acute cerebellitis). Blood tests at the time of imaging revealed WBC within normal limits. There were low total protein levels in the CSF, which was tapped 1 day before. The CSF culture had negative findings. A head CT (not shown) demonstrated diffuse swelling of the bilateral cerebellar hemispheres with crowding at the level of the foramen magnum with supratentorial hydrocephalus. Brain MR imaging acquired a day later (*upper row*, *A–E*) shows diffuse bilateral hyperintense signal on T2 (*A*, *thick arrows*) and FLAIR (*B*, *thick arrows*) sequences with corresponding leptomeningeal enhancement (*thin arrows*) on postcontrast axial (*C*) and coronal (*D*) T1-weighted imaging. Sagittal T2-weighted imaging (*E*) shows the swollen cerebellum with upward (*E*, *thick arrow*) and downward (*E*, *dashed arrow*) herniation, supratentorial hydrocephalus, and effacement of the fourth ventricle (*E*, *asterisk*) and posterior subarachnoid spaces (*E*, *thin arrow*). Follow-up MR imaging (*lower row*, *F–J*) acquired after 8 days shows improvement of hyperintense signal on axial T2 (*F*, *thick arrows*) and FLAIR (*G*, *thick arrows*) sequences. No contrast enhancement is seen on postcontrast axial (*H*) and coronal (*I*) T1-weighted imaging. Sagittal T1-weighted imaging (*J*) shows complete resolution of cerebellar edema, no upward (*J, thick arrow*) and downward (*J, dashed arrow*) herniation, no supratentorial hydrocephalus, and no effacement of the fourth ventricle (*J, asterisk*) and posterior subarachnoid spaces (*J, thin arrow*).

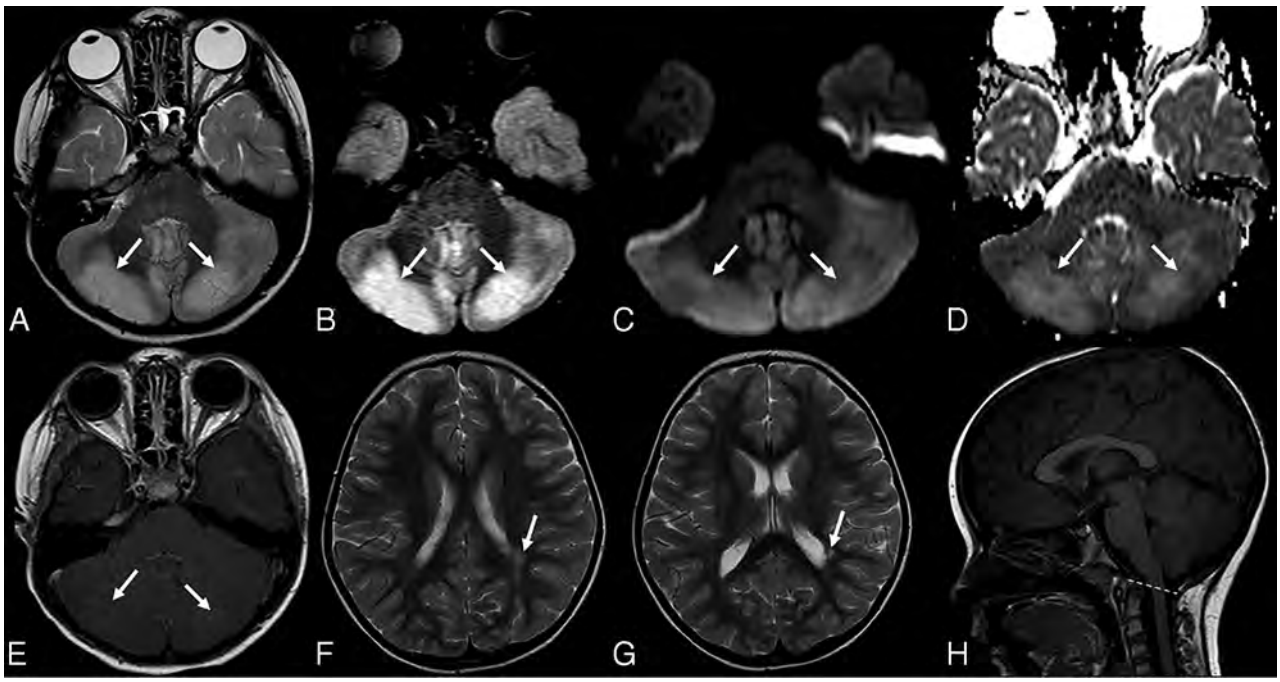

FIG 3. Acute disseminated encephalomyelitis in a 5-year-old girl who presented with ataxia and absent lower extremity reflexes (immune-mediated acute cerebellitis). Blood tests and CSF revealed an increased white blood cell count. CSF culture had negative findings. Brain MR imaging at presentation shows bilateral, diffuse, patchy hyperintense signal on axial T2 (*A*, *arrows*) and FLAIR (*B*, *arrows*) sequences. Corresponding vasogenic edema is seen on axial DWI (*C*, *arrows*) and ADC (*D*, *arrows*). Axial postcontrast T1-weighted imaging demonstrates bilateral, subtle leptomeningeal contrast enhancement (*E*, *arrows*). Consecutive supratentorial slices reveal subtle T2-hyperintense signal in the white matter of the adjacent trigone of the left lateral ventricle (*F* and *G*, *arrow*) without contrast enhancement or diffusion alteration (not shown). Sagittal T1-weighted imaging (*H*) shows no upward or downward herniation. Follow-up MR imaging was not available.

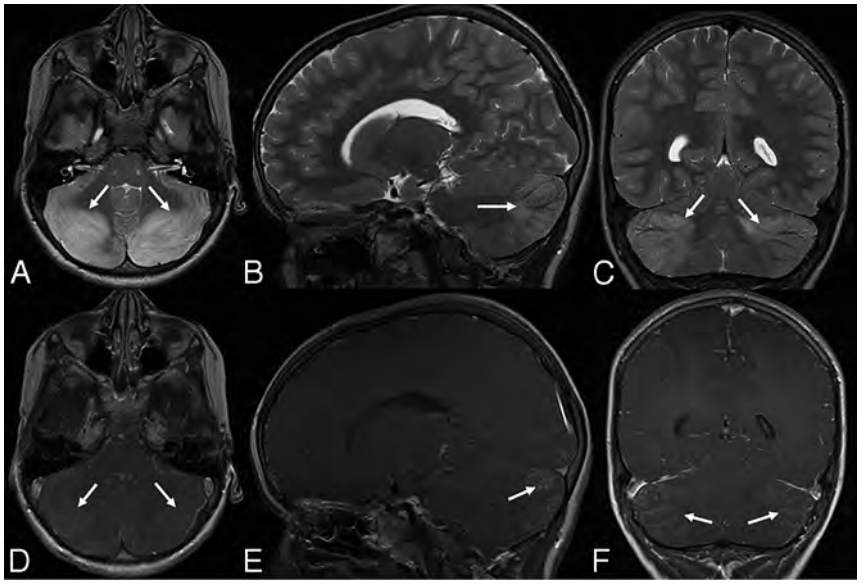

FIG 4. Bilateral cerebellitis in a 6.5-year-old boy (infectious acute cerebellitis) who had a history of gastroenteritis for 2–3 days. He developed marked and prolonged headache after a few days. Neurologic examination showed no cerebellar dysfunction. CSF examination was not performed. MR imaging shows bilateral, diffuse, T2 hyperintense signal and mild edema (*A–C*, *arrows*) in the cerebellar white and gray matter. Postcontrast imaging shows mild leptomeningeal contrast enhancement (*D–F*, *arrows*).

and Kornreich et al[11] reported tonsillar herniation and hydrocephalus. Bilateral cerebellar T2-FLAIR hyperintense signal was the most common finding in our infectious AC cases (Table). Yildirim et al, De Bruecker et al, and Kornreich et al reported similar MR imaging findings in their cases of AC. Unilateral involvement was less commonly observed in our patients. Involvement of 1 cerebellar hemisphere, also known as hemicerebellitis, is a rare variant of AC, and the mechanism for this preferential inflammation of 1 cerebellar hemisphere is unknown, though several hypotheses have been proposed, including impaired circulation or "subradiologic" involvement of the contralateral hemisphere.[1,12] On MR imaging, the differential diagnosis of hemicerebellitis should include a posterior fossa tumor and acute ischemia.

Leptomeningeal and cortical CE was seen in our infectious AC cohort.

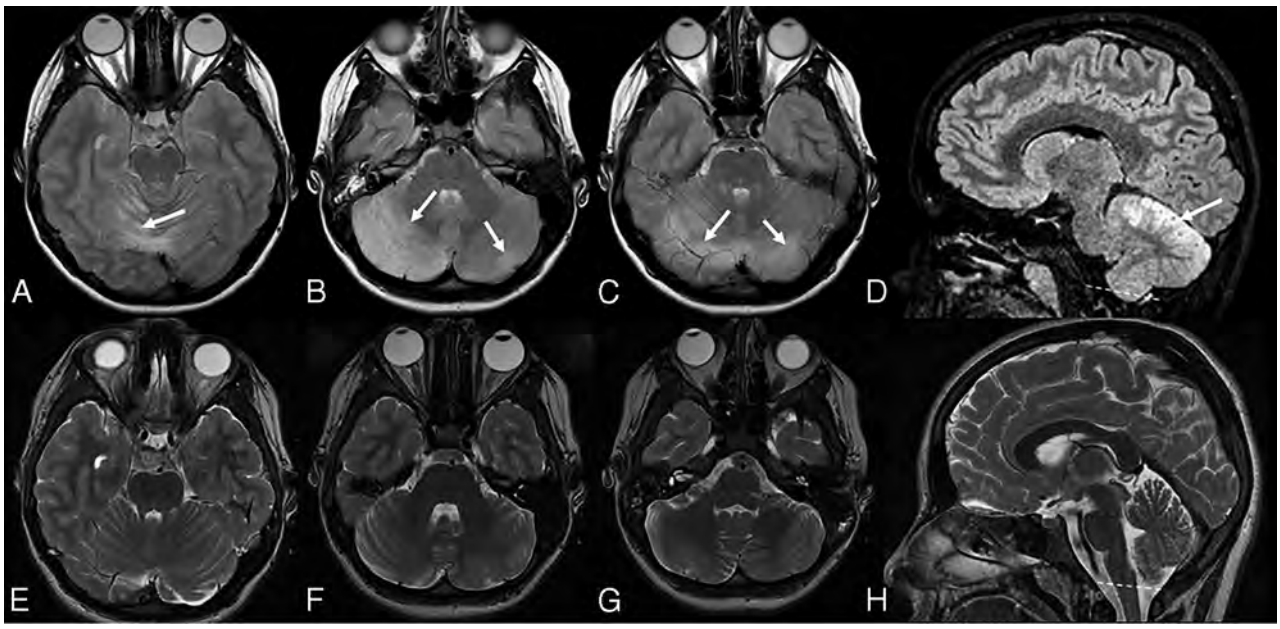

FIG 5. Bilateral cerebellitis in a 12.5-year-old girl (infectious acute cerebellitis). Initial presentation was nonspecific. The patient was tired with headache for a few days and spontaneously recovered. MR imaging at presentation (*upper row*) shows bilateral, diffuse, T2-hyperintense signal predominantly on the right side (*A–D*, *arrows*) and downward herniation (*D*, *dashed line*). A follow-up examination after 3 months shows no abnormal neurologic findings. Follow-up MR imaging after 3 months (*lower row*) shows complete resolution of previous MR imaging findings (*E–H*).

Yildirim et al[9] reported cortical and leptomeningeal CE, De Bruecker et al[10] reported pial CE, and Kornreich et al[11] reported CE in their patient groups. We did not find any statistically significant difference in CE patterns (leptomeningeal or cortical) between the infectious and immune-related AC groups (Table). However, leptomeningeal CE was a more frequent finding than cortical enhancement for both infectious and immune-related AC groups (Table). Pial enhancement has been reported previously.[10] The authors concluded that if a lumbar puncture was performed before the contrast-enhanced MR imaging, definite differentiation from leptomeningeal enhancement due to the lumbar puncture or to the AC itself was not possible. MR imaging was performed after lumbar puncture in 15 patients with infectious AC and in 4 patients with immune-related AC in our study. This finding will likely explain the higher percentage of leptomeningeal CE in both AC groups.

We did not find any statistically significant difference for DWI characteristics (vasogenic or cytotoxic edema) between infectious and immune-related AC groups (Table). Vasogenic edema was common in both infectious and immune-related AC groups. Schneider et al[13] found punctate areas of restricted diffusion in the cerebellum or cerebellar peduncles in patients presenting with acute and subacute onset of ataxia. We did not find any similar study to compare our DWI characteristics.

The differential diagnosis of infectious AC includes ADEM, Lhermitte-Duclos disease, diffusely infiltrating glioma or lymphoma, vasculitis, and drug-related causes.[10] We compared MRIs of our infectious AC group with MRIs of children diagnosed with immune-related conditions and found the following: 1) significantly higher T2-FLAIR hyperintense signal in the brainstem in the immune-related AC group; 2) significantly higher T2-FLAIR hyperintense signal in the supratentorial brain in the immune-related AC group; and 3) significantly higher degrees of downward cerebellar herniation in the infectious AC group. Takanashi et al[14] reported reversible splenial lesions (supratentorial hyperintense signal) in children with AC due to rotavirus infection. We did not find any other studies comparing infectious AC and immune-related AC groups. We suggest that our results may be helpful in the differential diagnosis of AC and may guide future studies.

Only 19 patients had follow-up brain MRIs, and cerebellar atrophy on follow-up brain MRIs was found in 15.79% of patients in our study. Hennes et al[15] reported cerebellar atrophy on follow-up MR imaging in 36.36% of their patient group. This difference could be explained by a limited number of available follow-up MR imaging studies in our patient cohort.

Strengths of this study include the large number of patients and relatively homogeneous ages of patients (children). Limitations of this study are the following: 1) Due to the retrospective nature of the study, infectious agents could not be verified in all patients; 2) a discrepancy in size between the 2 patient groups might have affected statistical analysis and results; 3) a limited number of follow-up MR imaging studies might have affected statistical analysis and results; 4) this was a single-center evaluation of patients; 5) being a quaternary center may cause referral/selection bias of patients; and 6) study cases for inclusion were initially identified on the basis of a search of radiology reports.

CONCLUSIONS

AC is a rare condition, and MR imaging is helpful in the differential diagnosis. T2-FLAIR hyperintense signal in the brainstem and supratentorial brain may be indicative of immune-related AC, and downward herniation may be indicative of infectious

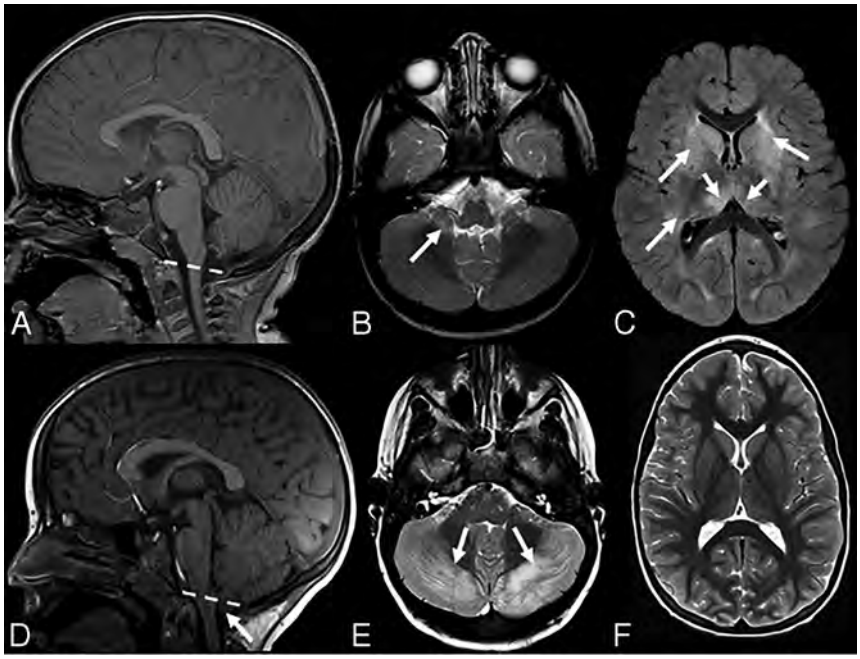

FIG 6. Upper row *A–C*, Acute disseminated encephalomyelitis in a 1-year 10-month-old boy (with immune-mediated acute cerebellitis) who presented with acute ataxia and fever with vomiting. A blood test revealed increased white blood cell count, and CSF revealed elevated WBC and normal protein and glucose levels. Blood culture and CSF culture had negative findings. Lower row *D–F*, Bilateral cerebellitis in a 5-year-old boy (with infectious acute cerebellitis) with a history dominated by intense headache, predominantly at night with some fluctuation. The patient had treatment of symptoms, but there was no clear improvement in headaches. MR imaging was performed about 2 weeks later. He had no cerebellar signs on examination. This figure aims to show the most predominant MR imaging findings for immune-mediated versus infectious acute cerebellitis. Note that there is no downward herniation in immune-mediated acute cerebellitis (*A*) versus cerebellar tonsil downward herniation in infectious acute cerebellitis (*D*, *arrow*). Axial T2 shows subtle hyperintense signal in right middle cerebellar peduncle in immune-mediated acute cerebellitis (*B*, *arrow*) versus bilateral diffuse T2-hyperintense signal with diffuse edema in infectious acute cerebellitis (*E*, *arrows*). Note that axial FLAIR shows extensive, multifocal, and confluent bilateral hyperintensity involving the cerebral white matter and the gray matter, including the bilateral basal ganglia extensively and bilateral thalami (*C*, *arrows*) in immune-mediated acute cerebellitis versus normal supratentorial brain axial T2 signal intensities in infectious acute cerebellitis (*F*).

AC. A decreased degree of downward herniation is the most significant MR imaging finding when comparing imaging at initial presentation and follow-up studies.

REFERENCES

1. Emelifeonwu JA, Shetty J, Kaliaperumal C, et al. **Acute cerebellitis in children: a variable clinical entity.** *J Child Neurol* 2018;33:675–84 CrossRef Medline
2. Baxter P. **Acute ataxia: epidemiology and differential diagnosis.** In: Boltshauser E, Schmahmann J, eds. *Cerebellar Disorders in Children.* Mac Keith Press; 2012:361–63
3. Tardieu M. **Acute inflammatory diseases of the cerebellum.** In: Boltshauser E, Schmahmann J, eds. *Cerebellar Disorders in Children.* Mac Keith Press; 2012;364–70
4. Poretti A, Benson JE, Huisman TA, et al. **Acute ataxia in children: approach to clinical presentation and role of additional investigations.** *Neuropediatrics* 2013;44:127–41 CrossRef Medline
5. Bozzola E, Bozzola M, Tozzi AE, et al. **Acute cerebellitis in varicella: a ten-year case series and systematic review of the literature.** *Ital J Pediatr* 2014;40:57 CrossRef Medline
6. Lancella L, Esposito S, Galli ML, et al. **Acute cerebellitis in children: an eleven-year retrospective multicentric study in Italy.** *Ital J Pediatr* 2017;43:54 CrossRef Medline
7. Desai J, Mitchell WG. **Acute cerebellar ataxia, acute cerebellitis, and opsoclonus-myoclonus syndrome.** *J Child Neurol* 2012;27:1482–88 CrossRef Medline
8. Rossi A, Martinetti C, Morana G, et al. **Neuroimaging of infectious and inflammatory diseases of the pediatric cerebellum and brainstem.** *Neuroimaging Clin N Am* 2016;26:471–87 CrossRef Medline
9. Yildirim M, Gocmen R, Konuskan B, et al. **Acute cerebellitis or postinfectious cerebellar ataxia? Clinical and imaging features in acute cerebellitis.** *J Child Neurol* 2020;35:380–88 CrossRef Medline
10. De Bruecker Y, Claus F, Demaerel P, et al. **MRI findings in acute cerebellitis.** *Eur Radiology* 2004;14:1478–83 CrossRef Medline
11. Kornreich L, Shkalim-Zemer V, Levinsky Y, et al. **Acute cerebellitis in children: a many-faceted disease.** *J Child Neurol* 2016;31:991–97 CrossRef Medline
12. Carceller Lechón F, Duat Rodríguez A, Sirvent Cerdá SI, et al. **Hemicerebellitis: report of three paediatric cases and review of the literature.** *Eur J Paediatr Neurol* 2014;18:273–81 CrossRef Medline
13. Schneider T, Thomalla G, Goebell E, et al. **Magnetic resonance imaging findings in patients presenting with (sub)acute cerebellar ataxia.** *Neuroradiology* 2015;57:551–59 CrossRef Medline
14. Takanashi J, Miyamoto T, Ando N, et al. **Clinical and radiological features of rotavirus cerebellitis.** *AJNR Am J Neuroradiol* 2010;31:1591–95 CrossRef Medline
15. Hennes E, Zotter S, Dorninger L, et al. **Long-term outcome of children with acute cerebellitis.** *Neuropediatrics* 2012;43:240–48 CrossRef Medline

Maternal Obesity during Pregnancy is Associated with Lower Cortical Thickness in the Neonate Brain

X. Na, N.E. Phelan, M.R. Tadros, Z. Wu, A. Andres, T.M. Badger, C.M. Glasier, R.R. Ramakrishnaiah, A.C. Rowell, L. Wang, G. Li, D.K. Williams, and X. Ou

ABSTRACT

BACKGROUND AND PURPOSE: Recent studies have suggested that maternal obesity during pregnancy is associated with differences in neurodevelopmental outcomes in children. In this study, we aimed to investigate the relationships between maternal obesity during pregnancy and neonatal brain cortical development.

MATERIALS AND METHODS: Forty-four healthy women (28 normal-weight, 16 obese) were prospectively recruited at <10 weeks' gestation, and their healthy full-term neonates (23 boys, 21 girls) underwent brain MR imaging. All pregnant women had their body composition (fat mass percentage) measured at ~12 weeks of pregnancy. All neonates were scanned at ~2 weeks of age during natural sleep without sedation, and their 3D T1-weighted images were postprocessed by the new iBEAT2.0 software. Brain MR imaging segmentation and cortical surface reconstruction and parcellation were completed using age-appropriate templates. Mean cortical thickness for 34 regions in each brain hemisphere defined by the UNC Neonatal Cortical Surface Atlas was measured, compared between groups, and correlated with maternal body fat mass percentage, controlled for neonate sex and race, postmenstrual age at MR imaging, maternal age at pregnancy, and the maternal intelligence quotient and education.

RESULTS: Neonates born to obese mothers showed significantly lower ($P \leq .05$, false discovery rate–corrected) cortical thickness in the left pars opercularis gyrus, left pars triangularis gyrus, and left rostral middle frontal gyrus. Mean cortical thickness in these frontal lobe regions negatively correlated ($R = -0.34$, $P = .04$; $R = -0.50$, $P = .001$; and $R = -0.42$, $P = .01$; respectively) with the maternal body fat mass percentage measured at early pregnancy.

CONCLUSIONS: Maternal obesity during pregnancy is associated with lower neonate brain cortical thickness in several frontal lobe regions important for language and executive functions.

ABBREVIATIONS: BMI = body mass index; FDR = false discovery rate; IQ = intelligence quotient

The most recent National Health and Nutrition Examination Survey reported that 39.7% of women in the United States 20–39 years of age are obese (body mass index [BMI], ≥30),[1] and the most recent national birth data showed that 54.7% of neonates in 2018 in the United States were born to overweight (BMI ≥25) or obese women.[2] Maternal obesity during pregnancy has become a prevalent health concern, not only for the pregnant women but also for their offspring,[3] including their neurodevelopment.[4,5] Recent studies have shown negative associations between maternal obesity and neurodevelopmental outcomes of children, including reduced infant cognitive development scores, increased risk of delayed mental development, lower cognitive performance, impaired executive function, lower full-scale intelligence quotient (IQ) and verbal IQ, higher attention-deficit/hyperactivity disorder symptom scores, increased risk for inattention and negative emotionality, and higher prevalence of autism.[4,6-18] These findings strongly suggest that maternal obesity during pregnancy can negatively influence an offspring's cognitive and neurodevelopmental outcomes. Nevertheless, little is known regarding the underlying mechanism of these associations.

Recent advances in early neuroimaging, particularly advanced and quantitative MR imaging, which can detect subtle changes in

Received May 20, 2021; accepted after revision August 9.

From the Department of Radiology (X.N., C.M.G., R.R.R., A.C.R., X.O.), College of Medicine (N.E.P., M.R.T.), and Departments of Pediatrics (A.A., T.M.B., C.M.G., R.R.R., X.O.) and Biostatistics (D.K.W.), University of Arkansas for Medical Sciences, Little Rock, Arkansas; Arkansas Children's Nutrition Center (X.N., A.A., T.M.B., X.O.), Little Rock, Arkansas; Arkansas Children's Research Institute (X.N., A.A., T.M.B., X.O.), Little Rock, Arkansas; and Department of Radiology (Z.W., L.W., G.L.), University of North Carolina at Chapel Hill, Chapel Hill, North Carolina.; and

This study was supported, in part, by the National Institutes of Health, R01HD099099, R01MH117943, R01MH116225, and US Department of Agriculture/Agricultural Research Service, 6026-51000-012-06-S.

Please address correspondence to Xiawei Ou, PhD, 1 Children's Way, Slot 105, Little Rock, Arkansas 72202; e-mail: ouxiawei@uams.edu

Indicates open access to non-subscribers at www.ajnr.org

http://dx.doi.org/10.3174/ajnr.A7316

Demographic information of the study participants

	Normal Weight ($n = 28$)	Obese ($n = 16$)	*P* Value
Maternal BMI (kg/m^2)	22.2 (SD, 1.9)	33.2 (SD, 1.5)	<.001
Maternal fat mass (%)	28.8 (SD, 4.2)	44.0 (SD, 3.9)	<.001
Maternal age at pregnancy (yr)	28.7 (SD, 2.9)	30.7 (SD, 5.0)	.19
Maternal IQ	107 (SD, 9.2)	106.6 (SD, 8.3)	.50
Gestational age (day)	275.1 (SD, 6.7)	274.7 (SD, 6.4)	.96
Neonate sex (boy/girl)	15/13	8/8	.83
Birth weight (kg)	3.5 (SD, 0.5)	3.6 (SD, 0.5)	.38
Birth length (cm)	50.6 (SD, 2.8)	50.5 (SD, 2.5)	.89
Head circumference (cm)	36.2 (SD, 1.1)	36.0 (SD, 0.8)	.25
Neonate age at MR imaging (day)	14.3 (SD, 1.6)	14.3 (SD, 1.7)	1
Postmenstrual age at MR imaging (day)	289.4 (SD, 6.4)	289 (SD, 6.3)	.93
Neonate race			
White/African American/American Indian/other)	22/2/1/3	10/5/1/0	.18
Mother's education			
No college/some college/graduate degree	3/17/8	0/9/7	.30
Father's education			
NA/no college/some college/graduate degree)	1/24/3/0	2/10/4/0	.20
Mother's income (US dollar)			
NA/ ≤ 20k/20–50k/>50k)	6/6/12/4	1/3/9/3	.57
Father's income (US dollar)			
NA/≤ 20k/20–50k/>50k)	1/0/14/13	3/0/6/7	.23

Note:—NA indicates not applicable.

the brain, provide a sensitive tool to detect the potential in utero effects of maternal obesity on the developing brain. These direct effects on early brain development, if observed, may link maternal obesity during pregnancy with adverse long-term neurodevelopmental outcomes in children and may shed light on the underlying mechanism. In fact, a few recent studies have reported significant changes in neonatal brain structural and functional development associated with maternal obesity. For example, neonates of obese, otherwise healthy, women showed lower brain white matter development measured by diffusion tensor imaging in widespread regions in the frontal and parietal lobes compared with neonates of healthy normal-weight women.[19] Weaker functional connectivity of the dorsal anterior cingulate cortex to the prefrontal networks in neonates born to obese-versus-normal-weight women was also observed in a study using independent component analysis of resting-state fMRI data,[20] and a further seed-based and graph theory of functional connectivity study indicated possible neonatal functional connectivity alterations in 4 functional domains implicated in adult obesity: sensory processing, reward processing, cognitive control, and motor control.[21] In addition, another study also observed that a higher maternal prepregnancy BMI was associated with greater local thalamic and lower frontothalamic functional connectivity in the neonatal brain.[22] Furthermore, studies have also shown that brain imaging features measured by early MR imaging are associated with long-term neurodevelopmental outcomes not only in neonates with medical conditions such as prematurity, congenital heart diseases, or hypoxic-ischemic encephalopathy[23-25] but also in neonates who are born full-term, healthy, and typically developing.[26] These findings suggest the importance of early neuroimaging in understanding the potential effects of maternal obesity during pregnancy on children's neurodevelopmental outcomes.

Brain cortical development starts in the first trimester of gestation and continues in the fetal and postnatal stages, with dynamic synapse formation in early life followed by gradual pruning throughout childhood. This process can be reflected by measurements of cortical thickness, which reaches a peak between 1 and 2 years of age[27] and starts to decrease thereafter.[28] Despite the obvious importance of brain cortical development in a child's brain function and cognitive outcomes, so far no published studies have evaluated whether maternal obesity during pregnancy would alter cortical development in the developing brain at early ages. In this study, we aimed to investigate relationships between maternal obesity and neonate brain cortical development. Our hypothesis was that maternal obesity during pregnancy would slow fetal cortical development and result in lower neonate cortical thickness in different brain regions. To test our hypothesis, we enrolled healthy normal-weight and obese pregnant women at first trimester, measured their BMI and body composition, performed brain MR imaging examination on their neonates, compared cortical thickness between the 2 groups of neonates, and evaluated its relationship with maternal body fat mass percentage measured at early pregnancy.

MATERIALS AND METHODS

Subjects

Healthy pregnant women of <10 weeks' gestation and their full-term healthy neonates were included in this study. All study procedures were approved by the University of Arkansas for Medical Sciences institutional review board, and all participants provided written informed consents. Inclusion criteria for the pregnant women were the following: prepregnancy BMI of 18.5–24.9 kg/m^2 [normal-weight group] or 30–35 kg/m^2 [obese group]), second parity, singleton pregnancy, 21 years of age or older, and conceived without assisted fertility treatments. Exclusion criteria for the pregnant women were the following: pre-existing medical conditions such as diabetes mellitus, seizure disorder, and serious psychiatric disorders; drug or alcohol abuse; sexually transmitted diseases; and medical complications during pregnancy such as gestational diabetes and pre-eclampsia. In addition, neonates born preterm (<37 weeks of gestation) or with medical conditions or medications known to influence growth and development or those unable to complete a brain MR imaging examination during natural sleep were also excluded.

All pregnant women had their body composition assessed using air displacement plethysmography (BOD POD; Cosmed) and BMI measured at ~12 weeks of pregnancy at Arkansas Children's Nutrition Center. Maternal IQ was also assessed using the Wechsler Abbreviated Scale of Intelligence (Pearson). After

delivery, birth weight and the length of the neonates were retrieved from the medical records, while head circumference was measured at ~2 weeks of age during the infant's study visit. Family socioeconomic status of the neonates including parental education and income was also obtained during the mother's pregnancy visits.

In total, 44 pregnant women (28 normal-weight, 16 obese) and their neonates completed the experimental procedures and were included in this study. Table summarizes the demographic information of the study participants.

MR Imaging Data Acquisition

At ~2 weeks of age, all neonates underwent an MR imaging examination of the brain during natural sleep without sedation at the Arkansas Children's Hospital, Department of Radiology. They were fed 15–30 minutes before the scan, swaddled in warm sheets, and bundled using a MedVac Infant Immobilizer (CFI Medical Solutions). No sedation was used. A pulse oximeter probe (InVivo) was placed on a foot to monitor oxygen saturation and heart rate, and Mini Muffs (Natus Medical) and a headset were placed over the ears to protect the neonates from the noise generated during the scan. The MR imaging examinations were performed on a 1.5T Achieva MR imaging scanner (Philips Healthcare) with a 60-cm bore size, 33-mT/m gradient amplitude, and 100-mT/m/ms maximum slew rate. We used a pediatric 8-channel sensitivity encoding head coil and a neonatal brain MR imaging protocol, which included sagittal 3D turbo field echo T1-weighted imaging reconstructed to 3 planes, axial T2-weighted, axial diffusion-weighted, and axial susceptibility-weighted imaging sequences. This conventional neonatal MR imaging protocol was used for the neuroradiologists to screen subjects for incidental findings, while the 3D T1-weighted images with TR =7.1 ms, TE = 3.2 ms, flip angle = 8°, and resolution = 1 × 1 × 1 mm were used for subsequent cortical brain morphometry analysis, particularly measurements of cortical thickness. Imaging quality control was performed on the scanner by experienced MR imaging technicians. Scans were repeated if considerable motion artifacts were present, and those neonates who woke up during the scan without a valid 3D T1 dataset were excluded from this study.

MR Imaging Data Analysis

All MR images were exported to the local PACS system from the scanner and were reviewed by one of our neuroradiologists. No incidental findings needing medical attention were noted. All of the 3D T1-weighted images were also exported to local workstations for further cortical analysis. Specifically, DICOM images were converted to NIfTI format and were postprocessed by the new iBEAT V2.0 software (Developing Brain Computing Lab and Baby Brain Mapping Lab). iBEAT V2.0 is a toolbox using advanced approaches including deep learning for processing pediatric brain T1- and T2-weighted MR images. It is an upgrade from the previous iBEAT software and has demonstrated superior capability and accuracy in infant structural MR imaging data postprocessing. For neonatal MR imaging, 3D T1-weighted images are adequate for the automated postprocessing because of the considerable contrast between different tissues. For this study, 3D T1-weighted MR images were corrected for inhomogeneity before skull stripping,[29] followed by tissue segmentation to gray matter, white matter, and CSF. Left/right hemisphere separation and topology correction were then performed.[30,31] Cortical surfaces including inner cortical and outer cortical surfaces were reconstructed. Cortical parcellation was performed on the basis of the infant developmental parcellation maps.[27,32] The UNC Neonatal Cortical Surface Atlas,[32,33] which parcellates the brain cortex in each hemisphere into 34 different regions, was used to calculate the mean cortical thickness for each cortical region for each neonate. Cortical thickness was defined as the closest distance from the white surface to the pial surface at each vertex of each surface.

Statistics

For the comparison of demographic parameters between the normal-weight and obese groups, Wilcoxon rank sum tests were performed to determine whether there were significant group differences (P values $\leq$ .05) for numeric parameters, while χ^2 tests were used for categoric parameters. To compare the cortical thickness between neonates born to normal-weight or obese mothers, we performed ANOVA with covariates of neonate sex and race, postmenstrual age at MR imaging, maternal age at pregnancy, as well as IQ and education for each cortical region defined by the UNC Neonatal Cortical Surface Atlas. Sex and postmenstrual age were controlled as potential confounders because infant brain differences associated with sex and gestational/postmenstrual age have been reported.[34,35] Effects of maternal age and IQ were also controlled because of potential effects on the offspring's brain development or neurodevelopmental outcomes.[36] For family socioeconomic status, due to missing data in the father's education and parental income for several subjects, only maternal education was added as a covariate in the analysis. The cortical thickness was not normalized to total brain volume because the literature suggested that normalizing did not improve the discriminant and predictive performance of cortical thickness measures.[37] False discovery rate (FDR) correction was used for multiple-comparison correction associated with the 68 brain cortical regions evaluated in total, and regions with FDR-corrected P values $\leq$.05 were regarded as significant regarding cortical thickness. In addition, to investigate whether there is a linear relationship between maternal body composition and neonate brain development, we evaluated correlations between maternal fat mass percentage measured at ~12 weeks of gestation and neonate brain cortical thickness at ~2 weeks of postnatal age for those regions identified by ANOVA using the Spearman rank partial-correlation test. Partial correlation coefficients (R values) and significance levels (P values) were calculated, and those correlations with P values $\leq$ .05 after controlling of neonate sex and race, postmenstrual age at MR imaging, maternal age at pregnancy, and IQ and education were regarded as significant. All statistics analyses were done in Matlab software, Version R2018b (MathWorks).

RESULTS

The normal-weight and obese pregnant women differed significantly in mean BMI measured at ~12 weeks of pregnancy (22.2 [SD, 1.9] versus 33.2 [SD, 1.5], $P < .001$), as well as in body fat

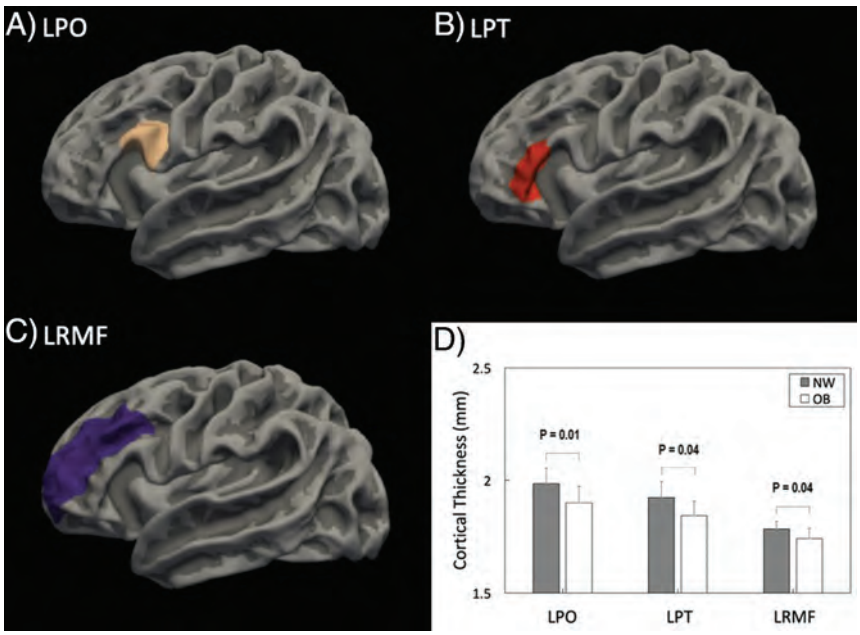

FIG 1. The anatomic locations for the 3 brain cortical regions that showed significant differences (FDR-corrected $P \leq .05$) in mean cortical thickness between neonates born to normal-weight-versus-obese women: the left pars opercularis (LPO) gyrus (*A*), the left pars triangularis (LPT) gyrus (*B*), and the left rostral middle frontal (LFMF) gyrus (*C*). The comparison of mean cortical thickness for these 3 regions in these groups of neonates is illustrated in *D*.

percentage (28.8% [SD, 4.2%] versus 44.0% [SD, 3.9%], $P < .001$). Other maternal/family measures such as maternal age at pregnancy and IQ as well as family socioeconomic status were not different (Table). For the neonates, there were no group differences in sex, race, birth weight/height, head circumference, gestational age at birth, or postmenstrual age at MR imaging (Table).

For comparison of cortical thickness at ~2 weeks' postnatal age for the neonates, the ANOVA analysis (with effects of neonate sex and race, postmenstrual age at MR imaging, maternal age at pregnancy, and IQ- and education-controlled) showed that there were 3 regions with significant differences (FDR-corrected, $P \leq .05$) between neonates born to normal-weight versus obese women in the 68 cortical regions defined by the UNC Neonatal Cortical Surface Atlas. Specifically, the mean cortical thickness in the left pars opercularis gyrus was higher in neonates born to normal-weight-versus-obese women (1.99 [SD, 0.07] mm versus 1.90 [SD, 0.07] mm; FDR-corrected, $P = .01$); the mean cortical thickness in the left pars triangularis gyrus was also higher in neonates born to normal-weight-versus-obese women (1.92 [SD, 0.07] mm versus 1.84 [SD, 0.06] mm; FDR-corrected, $P = .04$); and the mean cortical thickness in the left rostral middle frontal gyrus was also higher in neonates born to normal-weight-versus-obese women (1.78 [SD, 0.03] mm versus 1.74 [SD, 0.04] mm; FDR-corrected, $P = .04$). The anatomic location of these 3 cortical regions as well as the comparison of mean cortical thickness in these 3 regions are illustrated in Fig 1. No other regions showed differences in cortical thickness between the 2 neonate groups.

For the 3 cortical regions identified using the ANOVA analysis, the Spearman rank partial correlation test was used to evaluate whether there is a linear relationship the between mother's body composition (particularly body fat mass percentage) and the neonatal brain development (particularly cortical thickness). Similarly, neonate sex and race and postmenstrual age at MR imaging, as well as maternal age at pregnancy and IQ and education were controlled in the partial correlation analysis. There were significant negative correlations ($P < .05$) between maternal fat mass percentage and neonate brain cortical thickness in all of these 3 regions (Fig 2). Specifically, neonate brain regional mean cortical thickness measured at ~2 weeks' postnatal age negatively correlated with maternal body fat mass percentage measured at ~12 weeks of pregnancy in the left pars opercularis gyrus ($R = -0.34$, $P = .04$), the left pars triangularis gyrus ($R = -0.50$, $P = .001$), and the left rostral middle frontal gyrus ($R = -0.42$, $P = .01$).

DISCUSSION

Our study indicated significant relationships between the mother's BMI status and body composition at early pregnancy and the neonate's brain cortical development at ~2 weeks of age. The more obese the pregnant women were during early pregnancy, the lower the cortical thickness was in several brain regions in their neonates. All pregnant women included in this study were healthy, without medical conditions or medication use during pregnancy that may affect fetal brain development, and all neonates were also healthy, born full-term, without any birth defects or medical conditions that may impact their brain development. Our results suggest that there may be a negative impact of maternal obesity during pregnancy on the offspring's brain development because cortical thickness increases during infancy in normal development and it appears that maternal obesity may have slowed or impaired cortical development at 2 weeks' postnatal age.

The brain regions showing the potential impact of maternal obesity on cortical development are all in the frontal lobe, indicating that frontal lobe brain regions may be most vulnerable to potential disturbances in fetal programming due to maternal obesity. This finding is consistent with previous findings that microstructure integrity evaluated by DTI was lower in widespread frontal white matter regions in neonates born to obese-versus-normal-weight mothers[19] and that functional connectivity from the dorsal anterior cingulate cortex to the prefrontal network measured by resting-state fMRI was lower in neonates born to obese-versus-normal-weight mothers.[20] This is also consistent with another functional connectivity study of infants born to adolescents or young adult women that demonstrated that higher maternal BMI was associated with lower frontothalamic connectivity in the infant brain.[23] While the underlying and potential neurobiologic processes for the vulnerability of frontal lobe

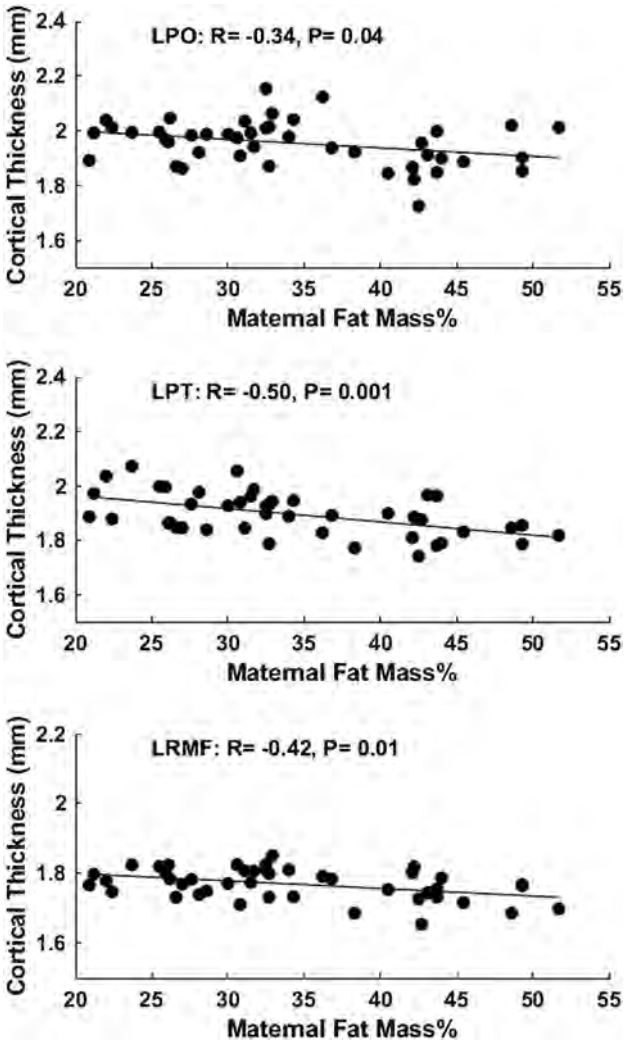

FIG 2. Partial correlation analysis showed significant negative correlations ($P < .05$) between maternal body fat mass percentage measured at ~12 weeks of pregnancy and neonate brain mean cortical thickness measured at ~2 weeks' postnatal age in the left pars opercularis (LPO) gyrus, left pars triangularis (LPT) gyrus, and left rostral middle frontal (LRMF) gyrus.

development to maternal obesity are unclear, numerous studies have indicated that the rapid infant frontal brain development is sensitive to early environmental experiences,[38] including exposures to different adverse prenatal environmental factors.[39,40]

For the 3 specific frontal lobe regions that showed decreased cortical thickness associated with maternal obesity, the left pars opercularis gyrus and the left pars triangularis gyrus form the middle and posterior parts of the left inferior frontal gyrus and are commonly regarded as the Broca area, which is important for expressive language function such as speech production. The left rostral middle frontal gyrus largely overlaps with the dorsolateral prefrontal cortex and is critical for executive function such as emotion regulation and working memory. Thinner cortices in these language- and executive function–related brain regions in early life may have important functional implications because recent studies have shown that maternal obesity is associated with lower composite language scores[14] or a different language developmental trajectory,[41] as well as lower cognitive flexibility[42] or poorer executive functioning in areas of attention, inhibition control, and working memory[43] in children.

Most interesting, frontal brain structural and functional changes have also been observed in children, associated with childhood obesity. For example, in recent analyses of National Institutes of Health Adolescent Brain and Cognitive Development Study data, increased BMI in 9- to 11-year-old children significantly correlated with reduced cortical thickness in the frontal lobe and lower performance in several tasks involving executive functions,[44] and reduced thickness in a number of frontal cortical regions partially accounted for reductions in executive function.[45] Many fMRI studies have also demonstrated differences in brain activation involving the frontal lobe during task performance between normal-weight and overweight/obese children/adolescents.[46-50] Given that maternal obesity may predispose offspring to a higher risk of childhood obesity, the similarities of changes in the developing brain associated with maternal obesity and childhood obesity may suggest potential consequential effects, eg, maternal obesity may possibly program persistent changes in certain regions of the developing brain, which, in turn, may cause behavior issues in childhood (such as deficiency in inhibitory control toward food) and further increase the risk of developing childhood obesity. While this is a speculation that cannot be validated by the data in our current study alone (eg, whether there are persistent changes in the brain associated with maternal obesity that will require follow-up imaging studies), our results certainly can contribute to the growing field striving to understand more about obesity-brain relationships.

Our study design was prospective and longitudinal, and we recruited pregnant women in early pregnancy, measured their body composition, followed up their pregnancy, and evaluated their infants' brain development using MR imaging. Nevertheless, 1 limitation of our findings is that we only have complete MR imaging data for the cohort at neonatal age. Follow-up MR imaging and neurodevelopmental assessments at later ages will be necessary to determine whether brain changes associated with maternal obesity in neonates persist into later childhood and impact long-term neurodevelopmental outcomes. Another limitation is the relatively small sample size of this study. A larger-scale study may allow us to control for more potential confounders and may identify more brain regions and imaging features in the developing brain associated with maternal obesity. Last, family socioeconomic status may also be a confounding factor for infant brain development.

In our statistical analysis, we controlled for the mother's education, for which we have data for all subjects ($n = 44$). For other socioeconomic parameters for which we have missing data including the mother's income ($n = 37$) and the father's education ($n = 41$) and income ($n = 40$), we compared the available data, and there were no group differences (Table). In addition, the significant group differences as well as significant correlations between maternal body fat mass percentage and neonate cortical thickness in the 3 regions we report still hold (all P values in Figs 1*D* and 2 are still $< .05$ except for one) if we add parental incomes and the father's education as additional covariates in the data analysis (despite the missing data and the relatively large number of covariates compared with the sample size in the statistical model).

CONCLUSIONS

Neonates born to obese women showed lower cortical thickness measured by MR imaging at ~2 weeks of age in several frontal brain regions important for language and executive function. The mother's body fat mass percentage measured in early pregnancy negatively correlated with the neonate's brain cortical thickness in these regions. Our results indicate that there may be a negative impact of maternal obesity during pregnancy on the offspring's cortical brain development.

Disclosure forms provided by the authors are available with the full text and PDF of this article at www.ajnr.org.

REFERENCES

1. Hales CM, Carroll MD, Fryar CD, et al. **Prevalence of obesity and severe obesity among adults: United States, 2017-2018.** *NCHS Data Brief* 2020:1–8 Medline
2. Martin JA, Hamilton BE, Osterman MJ, et al. **Births: final data for 2018.** *Natl Vital Stat Rep* 2019;68:1–47 Medline
3. Santangeli L, Sattar N, Huda SS. **Impact of maternal obesity on perinatal and childhood outcomes.** *Best Pract Res Clin Obstet Gynaecol* 2015;29:438–48 CrossRef Medline
4. Edlow AG. **Maternal obesity and neurodevelopmental and psychiatric disorders in offspring.** *Prenat Diagn* 2017;37:95–110 CrossRef Medline
5. Kong L, Chen X, Gissler M, et al. **Relationship of prenatal maternal obesity and diabetes to offspring neurodevelopmental and psychiatric disorders: a narrative review.** *Int J Obes (Lond)* 2020;44:1981–2000 CrossRef Medline
6. Casas M, Chatzi L, Carsin AE, et al. **Maternal pre-pregnancy overweight and obesity, and child neuropsychological development: two Southern European birth cohort studies.** *Int J Epidemiol* 2013;42:506–17 CrossRef Medline
7. Hinkle SN, Schieve LA, Stein AD, et al. **Associations between maternal prepregnancy body mass index and child neurodevelopment at 2 years of age.** *Int J Obes (Lond)* 2012;36:1312–19 CrossRef Medline
8. Basatemur E, Gardiner J, Williams C, et al. **Maternal prepregnancy BMI and child cognition: a longitudinal cohort study.** *Pediatrics* 2013;131:56–63 CrossRef Medline
9. Buss C, Entringer S, Davis EP, et al. **Impaired executive function mediates the association between maternal pre-pregnancy body mass index and child ADHD symptoms.** *PLoS One* 2012;7:e37758 CrossRef Medline
10. Huang LS, Yu XD, Keim S, et al. **Maternal prepregnancy obesity and child neurodevelopment in the Collaborative Perinatal Project.** *Int J Epidemiol* 2014;43:783–92 CrossRef Medline
11. Rodriguez A, Miettunen J, Henriksen TB, et al. **Maternal adiposity prior to pregnancy is associated with ADHD symptoms in offspring: evidence from three prospective pregnancy cohorts.** *Int J Obes (Lond)* 2008;32:550–57 CrossRef Medline
12. Rodriguez A. **Maternal pre-pregnancy obesity and risk for inattention and negative emotionality in children.** *J Child Psychol Psychiatry* 2010;51:134–43 CrossRef Medline
13. Krakowiak P, Walker CK, Bremer AA, et al. **Maternal metabolic conditions and risk for autism and other neurodevelopmental disorders.** *Pediatrics* 2012;129:E1121–28 CrossRef
14. Reynolds LC, Inder TE, Neil JJ, et al. **Maternal obesity and increased risk for autism and developmental delay among very preterm infants.** *J Perinatol* 2014;34:688–92 CrossRef Medline
15. Jo H, Schieve LA, Sharma AJ, et al. **Maternal prepregnancy body mass index and child psychosocial development at 6 years of age.** *Pediatrics* 2015;135:e1198–209 CrossRef Medline
16. Girchenko P, Tuovinen S, Lahti-Pulkkinen M, et al. **Maternal early pregnancy obesity and related pregnancy and pre-pregnancy disorders: associations with child developmental milestones in the prospective PREDO Study.** *Int J Obes (Lond)* 2018;42:995–1007 CrossRef Medline
17. Casas M, Forns J, Martinez D, et al. **Maternal pre-pregnancy obesity and neuropsychological development in pre-school children: a prospective cohort study.** *Pediatr Res* 2017;82:596–606 CrossRef Medline
18. Contu L, Hawkes CA. **A review of the impact of maternal obesity on the cognitive function and mental health of the offspring.** *Int J Mol Sci* 2017;18:1093 CrossRef Medline
19. Ou X, Thakali KM, Shankar K, et al. **Maternal adiposity negatively influences infant brain white matter development.** *Obesity* 2015;23:1047–54 CrossRef Medline
20. Li X, Andres A, Shankar K, et al. **Differences in brain functional connectivity at resting state in neonates born to healthy obese or normal-weight mothers.** *Int J Obes (Lond)* 2016;40:1931–34 CrossRef Medline
21. Salzwedel AP, Gao W, Andres A, et al. **Maternal adiposity influences neonatal brain functional connectivity.** *Front Hum Neurosci* 2018;12:514 CrossRef Medline
22. Spann MN, Scheinost D, Feng T, et al. **Association of maternal prepregnancy body mass index with fetal growth and neonatal thalamic brain connectivity among adolescent and young women.** *JAMA Netw Open* 2020;3:e2024661 CrossRef Medline
23. Perlman JM. **White matter injury in the preterm infant: an important determination of abnormal neurodevelopment outcome.** *Early Hum Dev* 1998;53:99–120 CrossRef Medline
24. Peyvandi S, Chau V, Guo T, et al. **Neonatal brain injury and timing of neurodevelopmental assessment in patients with congenital heart disease.** *J Am Coll Cardiol* 2018;71:1986–96 CrossRef Medline
25. Weeke LC, Groenendaal F, Mudigonda K, et al. **A novel magnetic resonance imaging score predicts neurodevelopmental outcome after perinatal asphyxia and therapeutic hypothermia.** *J Pediatr* 2018;192:33–40.e2 CrossRef
26. Feng K, Rowell AC, Andres A, et al. **Diffusion tensor MRI of white matter of healthy full-term newborns: relationship to neurodevelopmental outcomes.** *Radiology* 2019;292:179–87 CrossRef Medline
27. Wang F, Lian C, Wu Z, et al. **Developmental topography of cortical thickness during infancy.** *Proc Natl Acad Sci U S A* 2019;116:15855–60 CrossRef Medline
28. Fjell AM, Grydeland H, Krogsrud SK, et al. **Development and aging of cortical thickness correspond to genetic organization patterns.** *Proc Natl Acad Sci U S A* 2015;112:15462–67 CrossRef Medline
29. Wang L, Li G, Shi F, et al. **Volume-based analysis of 6-month-old infant brain MRI for autism biomarker identification and early diagnosis.** *Med Image Comput Comput Assist Interv* 2018;11072:411–19 CrossRef Medline
30. Li G, Nie J, Wang L, et al. **Measuring the dynamic longitudinal cortex development in infants by reconstruction of temporally consistent cortical surfaces.** *Neuroimage* 2014;90:266–79 CrossRef Medline
31. Li G, Wang L, Yap PT, et al. **Computational neuroanatomy of baby brains: a review.** *Neuroimage* 2019;185:906–25 CrossRef Medline
32. Li G, Wang L, Shi F, et al. **Construction of 4D high-definition cortical surface atlases of infants: methods and applications.** *Med Image Anal* 2015;25:22–36 CrossRef Medline
33. Wu Z, Li G, Meng Y, et al. **4D infant cortical surface atlas construction using spherical patch-based sparse representation.** *Med Image Comput Comput Assist Interv* 2017;10433:57–65 CrossRef Medline
34. Ou X, Glasier CM, Ramakrishnaiah RH, et al. **Gestational age at birth and brain white matter development in term-born infants and children.** *AJNR Am J Neuroradiol* 2017;38:2373–79 CrossRef Medline
35. Lehtola SJ, Tuulari JJ, Karlsson L, et al. **Associations of age and sex with brain volumes and asymmetry in 2-5-week-old infants.** *Brain Struct Funct* 2019;224:501–13 CrossRef Medline
36. Veldkamp SA, Zondervan-Zwijnenburg MA, van Bergen E, et al. **Parental age in relation to offspring's neurodevelopment.** *J Clin Child Adolesc Psychol* 20201–13 CrossRef Medline

37. Westman E, Aguilar C, Muehlboeck JS, et al. **Regional magnetic resonance imaging measures for multivariate analysis in Alzheimer's disease and mild cognitive impairment.** *Brain Topogr* 2013;26:9–23 CrossRef Medline
38. Hodel AS. **Rapid infant prefrontal cortex development and sensitivity to early environmental experience.** *Dev Rev* 2018;48:113–44 CrossRef Medline
39. Posner J, Cha J, Roy AK, et al. **Alterations in amygdala–prefrontal circuits in infants exposed to prenatal maternal depression.** *Transl Psychiatry* 2016;6:e935 CrossRef Medline
40. Humphreys KL, Camacho MC, Roth MC, et al. **Prenatal stress exposure and multimodal assessment of amygdala–medial prefrontal cortex connectivity in infants.** *Dev Cogn Neurosci* 2020;46:100877 CrossRef Medline
41. Torres-Espinola FJ, Berglund SK, García-Valdés LM, et al; PREOBE team. **Maternal obesity, overweight and gestational diabetes affect the offspring neurodevelopment at 6 and 18 months of age: a follow up from the PREOBE cohort.** *PLoS One* 2015;10:e0133010 CrossRef Medline
42. Menting MD, van de Beek C, de Rooij SR, et al. **The association between pre-pregnancy overweight/obesity and offspring's behavioral problems and executive functioning.** *Early Hum Dev* 2018;122:32–41 CrossRef Medline
43. Mina TH, Lahti M, Drake AJ, et al. **Prenatal exposure to maternal very severe obesity is associated with impaired neurodevelopment and executive functioning in children.** *Pediatr Res* 2017;82:47–54 CrossRef Medline
44. Laurent JS, Watts R, Adise S, et al. **Associations among body mass index, cortical thickness, and executive function in children.** *JAMA Pediatr* 2020;174:170–77 CrossRef Medline
45. Ronan L, Alexander-Bloch A, Fletcher PC. **Childhood obesity, cortical structure, and executive function in healthy children.** *Cereb Cortex* 2020;30:2519–28 CrossRef Medline
46. Batterink L, Yokum S, Stice E. **Body mass correlates inversely with inhibitory control in response to food among adolescent girls: An fMRI study.** *Neuroimage* 2010;52:1696–703 CrossRef Medline
47. Bruce AS, Holsen LM, Chambers RJ, et al. **Obese children show hyperactivation to food pictures in brain networks linked to motivation, reward and cognitive control.** *Int J Obes (Lond)* 2010;34:1494–500 CrossRef Medline
48. Bruce AS, Lepping RJ, Bruce JM, et al. **Brain responses to food logos in obese and healthy weight children.** *J Pediatr* 2013;162:759–764.e2 CrossRef Medline
49. Davids S, Lauffer H, Thoms K, et al. **Increased dorsolateral prefrontal cortex activation in obese children during observation of food stimuli.** *Int J Obes (Lond)* 2010;34:94–104 CrossRef Medline
50. van Meer F, van der Laan LN, Eiben G, et al; I.Family Consortium. **Development and body mass inversely affect children's brain activation in dorsolateral prefrontal cortex during food choice.** *Neuroimage* 2019;201:116016 CrossRef Medline

Anatomic Neuroimaging Characteristics of Posterior Fossa Type A Ependymoma Subgroups

N.D. Sabin, S.N. Hwang, P. Klimo Jr, N. Chambwe, R.G. Tatevossian, T. Patni, Y. Li, F.A. Boop, E. Anderson, A. Gajjar, T.E. Merchant, and D.W. Ellison

ABSTRACT

BACKGROUND AND PURPOSE: Posterior fossa type A (PFA) ependymomas have 2 molecular subgroups (PFA-1 and PFA-2) and 9 subtypes. Gene expression profiling suggests that PFA-1 and PFA-2 tumors have distinct developmental origins at different rostrocaudal levels of the brainstem. We, therefore, tested the hypothesis that PFA-1 and PFA-2 ependymomas have different anatomic MR imaging characteristics at presentation.

MATERIALS AND METHODS: Two neuroradiologists reviewed the preoperative MR imaging examinations of 122 patients with PFA ependymomas and identified several anatomic characteristics, including extension through the fourth ventricular foramina and encasement of major arteries and tumor type (midfloor, roof, or lateral). Deoxyribonucleic acid methylation profiling assigned ependymomas to PFA-1 or PFA-2. Information on PFA subtype from an earlier study was also available for a subset of tumors. Associations between imaging variables and subgroup or subtype were evaluated.

RESULTS: No anatomic imaging variable was significantly associated with the PFA subgroup, but 5 PFA-2c subtype ependymomas in the cohort had a more circumscribed appearance and showed less tendency to extend through the fourth ventricular foramina or encase blood vessels, compared with other PFA subtypes.

CONCLUSIONS: PFA-1 and PFA-2 ependymomas did not have different anatomic MR imaging characteristics, and these results do not support the hypothesis that they have distinct anatomic origins. PFA-2c ependymomas appear to have a more anatomically circumscribed MR imaging appearance than the other PFA subtypes; however, this needs to be confirmed in a larger study.

ABBREVIATIONS: PF = posterior fossa; PFA = posterior fossa type A, PF-EPN-A; PFB = posterior fossa type B, PF-EPN-B

Ependymomas account for >5% of pediatric CNS tumors and approximately 50% of brain tumors in children younger than 5 years of age.[1,2] Approximately 90% of pediatric ependymomas are intracranial, and about 70% occur in the posterior fossa.[3] Posterior fossa (PF) ependymomas are usually centered in the fourth ventricle or cerebellopontine angle cistern, often extend through the foramina of Luschka and/or the foramen of Magendie, and tend to encase cranial nerves and vascular structures, making it difficult to achieve a gross total surgical resection, the most important prognostic factor for prolonged survival.[4,5]

Developments in molecular characterization and genetic profiling of pediatric brain tumors have led to improvements in risk stratification and associated treatment modification for these neoplasms.[6-8] For example, these methods now divide medulloblastoma into 4 molecular groups and 12 subgroups, which may be used for prediction of outcomes and stratification of treatment.[6,8] Deoxyribonucleic acid methylation profiling has been used to divide PF ependymomas into 3 molecular groups, posterior fossa type A/PF-ependymoma (EPN)-A (PFA), posterior fossa type B/PF-EPN-B (PFB), and posterior fossa subependymoma/PF-subependymoma.[9-11] PF-subependymoma tumors are rare adult subependymomas, and approximately 90% of PF ependymomas are from the PFA group.[10] PFA ependymomas primarily occur in infants and young children (median age at presentation, 3 years), and PFB ependymomas are mostly seen in adolescents and young adults, with a median age at presentation of 30 years. The PFA

Received February 18, 2021; accepted after revision August 9.

From the Departments of Diagnostic Imaging (N.D.S., S.N.H., E.A.), Pathology (N.C., R.G.T., D.W.E.), Oncology (A.G.), Biostatistics (T.P., Y.L.), Radiation Oncology (T.E.M.), and Surgery (P.K., F.A.B.), St. Jude Children's Research Hospital, Memphis, Tennessee; and Semmes Murphey (P.K., F.A.B.), Memphis, Tennessee.

This work was supported, in part, by the National Cancer Institute through a Cancer Center Support Core Support Grant (CA21765) and by the American Lebanese Syrian Associated Charities.

Please address correspondence to Noah D. Sabin, MD, JD, Department of Diagnostic Imaging, St. Jude Children's Research Hospital, 262 Danny Thomas Place, MS-220, Memphis, TN 38105; e-mail: noah.sabin@stjude.org

Indicates open access to non-subscribers at www.ajnr.org

http://dx.doi.org/10.3174/ajnr.A7322

group is divided into 2 subgroups, PFA-1 and PFA-2.[9] PFA-1 tumors express specific *Homeobox* family genes, which are upregulated in the caudal brainstem and upper spinal cord during CNS development, while genes located more rostrally in the developing brainstem at the midbrain-hindbrain junction (eg, *EN2*, *CNPY1*) are expressed in PFA-2 ependymomas.[9] These distinct gene expression profiles suggest that PFA-1 and PFA-2 tumors originate from different brainstem locations. DNA methylation profiling has also revealed 9 subtypes of PFA ependymomas, 6 in the PFA-1 subgroup (1a through 1f) and 3 in the PFA-2 subgroup (2a through 2c).[9] The PFA subgroups and subtypes are associated with different genetic and clinical variables, including different prognoses and patterns of relapse.[9]

The concept that imaging findings may be associated with molecularly distinct pediatric CNS tumors is supported by evidence that different molecular groups of medulloblastoma arise from different anatomic locations and that these differences are visible on MR imaging.[12-15] In a recent study that extended this idea to the posterior fossa ependymoma groups, Yonezawa et al[16] found that in 16 patients with posterior fossa ependymomas (9 PFAs and 7 PFBs), PFB tumors enhanced to a greater extent than PFA lesions. In that investigation, however, no significant difference was detected between PFA and PFB tumors in their tendency to extend beyond the fourth ventricle. Imaging analyses of posterior fossa ependymomas and evaluations of operative findings and techniques related to their resection have identified anatomic characteristics of the tumor that impact resectability and survival. These include location, relationship to blood vessels and cranial nerves, and extension of the tumor into adjacent anatomic regions.[4,17-19]

An evaluation of a small group of PFA ependymomas performed as part of a larger study of the molecular characteristics of those tumors found some differences in the anatomic locations of the PFA subgroups.[9] We wanted to expand on that small combined imaging and surgical analysis by examining the differences in the anatomic characteristics seen solely on imaging between the 2 subgroups of PFA ependymomas in a larger group of patients. Our primary aim in this study was to evaluate potential differences in the anatomic characteristics of PFA-1 and PFA-2 ependymomas seen on MR imaging and determine whether those differences support different anatomic origins of the tumor subgroups. As an exploratory objective, we investigated potential different anatomic characteristics of the PFA subtypes as seen on MR imaging, with particular attention paid to the PFA-2c subtype, which is the subtype with the best prognosis.[9]

MATERIALS AND METHODS

The study was approved by our institutional review board. One hundred twenty-two patients with PF ependymoma treated at or who presented for consultation to the St. Jude Children's Research Hospital between 1996 and 2017 with evaluable preoperative MR imaging examinations and tumor specimens available for DNA methylation profiling were identified. The preoperative examinations were performed at outside institutions and varied with respect to pulse sequences obtained and imaging technique. Suitable studies were those that provided anatomic definition that allowed distinction of tumor from adjacent anatomic structures, including fourth ventricle foramina and major arteries. T1WI was available for all subjects; T2WI, for 120 subjects, and FLAIR images, for 106 subjects. One hundred nineteen subjects had postcontrast T1-weighted images. Two radiologists, each with Certificates of Added Qualification in neuroradiology and >10 years' practice experience and who were blinded to each other's evaluations, reviewed the preoperative MRIs and determined for each case whether the tumor extended below the foramen magnum, involved the foramina of Luschka, or encased the basilar artery and/or vertebral arteries. Tumors that extended below a line drawn from the tip of the clivus to the opisthion were considered to extend below the foramen magnum. Any tumor that extended beyond the margin of the fourth ventricle into one or both foramina of Luschka was characterized as involving those structures, and a tumor that appeared to extend around at least 50% of the circumference of the basilar and/or vertebral artery was classified as encasing those vessels.

The radiologists categorized the ependymomas as midfloor type, lateral type, or roof type using criteria described by U-King-Im et al.[18] According to these criteria, midfloor tumors are those that generally displace the brainstem anteriorly, the entire brainstem is seen in its entirety in 1 sagittal image, and the obex is filled with tumor (Fig 1*A, -B*). Lateral tumors are centered in the lateral recess of the fourth ventricle or cerebellopontine angle cistern, usually do not involve the obex, and generally displace the brainstem laterally (Fig 1*C, -D*). For our evaluation, lesions that appeared inseparable from the roof of the fourth ventricle with a complete or partial gap between the tumor and floor were classified as roof-type tumors, though no criteria for this type of posterior fossa ependymoma were provided by U-King-Im et al (Fig 1*E, -F*). The radiologists also evaluated the tumors for imaging evidence of necrosis, defined by the presence of centrally located nonenhancing areas within the lesions and ring enhancement. Finally, the radiologists determined whether hydrocephalus was present on the preoperative examination. Discrepancies between the radiologists' conclusions were resolved by consensus between the 2 reviewers.

Genomic DNA was extracted from 23 frozen tumor specimens following standard procedures for proteinase K (ThermoFisher Scientific) digestion, phenol:chloroform:isoamyl alcohol extraction and ethanol precipitation,[20] and from 99 formalin-fixed and paraffin-embedded tissue specimens using the Maxwell RSC DNA formalin-fixed and paraffin-embedded kit (AS1450; Promega). DNA samples were quantified using Picogreen (Invitrogen). Genome-wide DNA methylation profiles were generated from Infinium HumanMethylation450 (450K) or MethylationEPIC BeadChip arrays (Illumina), following the manufacturer's instructions.

Ninety-nine of 122 tumors were included in our prior study and assigned to the PFA-1 or PFA-2 subgroup.[9] In the present study, we first confirmed that all 122 tumors were assigned to the PFA subgroup using the Molecular Neuropathology brain tumor classifier (v11b4) (www.molecularneuropathology.org).[21] Next, we classified 23 new samples as PFA-1 or PFA-2 by consensus clustering of the study cohort using the exact same parameterization as in our prior study.[9] Prior subgroup designation was

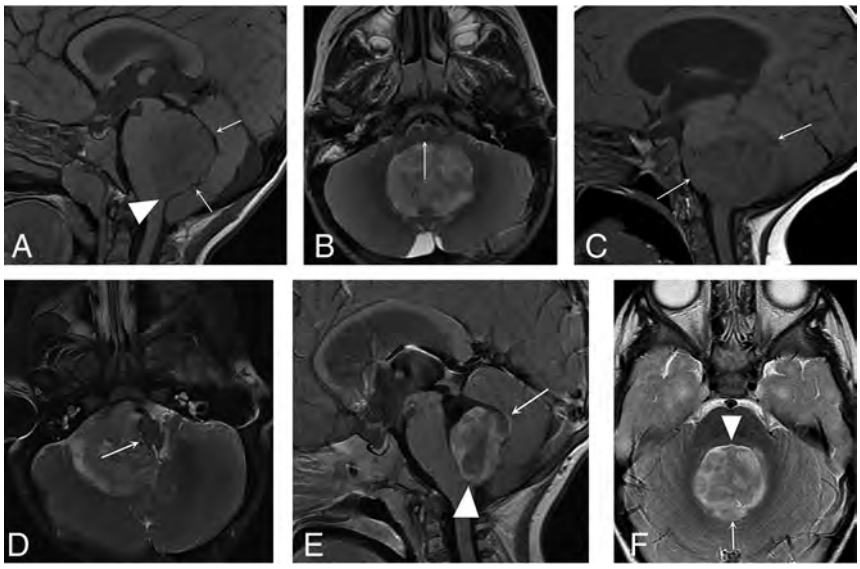

FIG 1. PFA ependymoma types based on location. Sagittal T1- (*A*) and axial T2-weighted images (*B*): Midfloor-type posterior fossa ependymomas fill the obex (*arrowhead*), and a gap may be seen between the roof of the fourth ventricle and the tumor (*arrows*, *A*). The brainstem is displaced anteriorly (*arrow*, *B*), and in the sagittal plane, it is seen in its entirety in a single sagittal image. Sagittal T1- (*C*) and axial T2-weighted images (*D*): Lateral-type posterior fossa ependymomas are centered in the lateral recess of the fourth ventricle or cerebellopontine angle (*arrows*, *C*) and displace the brainstem laterally (*arrow*, *D*). The brainstem usually cannot be seen in a single sagittal image. Postgadolinium sagittal T1- (*E*) and axial T2-weighted images (*F*): Roof-type posterior fossa ependymomas appear closely associated with the roof of the fourth ventricle (*arrows*, *E* and *F*) and do not fill the obex (*arrowhead*, *E*). A gap is usually seen between the tumor and the floor of the fourth ventricle (*arrowhead*, *F*).

Table 1: Association of imaging variables with PFA ependymoma subgroups

	Yes (%)	No (%)
Extends below foramen magnum, $P = .18$		
PFA-1	67 (89.3)	8 (10.7)
PFA-2	37 (78.7)	10 (21.3)
Total	104 (85.2)	18 (14.8)
Involves foramina of Luschka, $P = .55$		
PFA-1	61 (81.3)	14 (18.7)
PFA-2	41 (87.2)	6 (12.8)
Total	102 (83.6)	20 (16.4)
Encases blood vessels, $P = .73$		
PFA-1	33 (44.0)	42 (56.0)
PFA-2	23 (48.9)	24 (51.1)
Total	56 (45.9)	66 (54.1)
Necrosis ($P = .03$)[a]		
PFA-1	59 (80.8)	14 (19.2)
PFA-2	28 (60.9)	18 (39.1)
Total	87 (73.1)	32 (26.9)
Hydrocephalus, $P = .36$		
PFA-1	65 (86.7)	10 (13.3)
PFA-2	44 (93.6)	3 (6.4)
Total	109 (89.3)	13 (10.7)

[a] Data for this variable were available for 119 subjects because 3 patients did not have preoperative postcontrast images available.

Table 2: Anatomic type on imaging ($P = .24$)

	Lateral (%)	Midfloor (%)	Roof (%)
PFA-1	33 (44.0)	32 (42.7)	10 (13.3)
PFA-2	14 (29.8)	23 (48.9)	10 (21.3)
Total	47 (38.5)	55 (45.1)	20 (16.4)

consistent with the k = 2 clustering solution. New samples were labeled according to the subgroup label of their assigned consensus cluster in this joint analysis. All computational analyses were performed in R statistical and computing software (Version 3.6; http://www.r-project.org). Methylation array processing was performed for 122 samples as described previously,[9] with the additional step of using the combineArrays function to obtain a virtual array of the subset of probes common across the 450K and EPIC array platforms. Normalization and filtering steps were unchanged. Data on PFA subtypes from our prior study were available for 98 of 122 PFA ependymomas in the present study.[9]

Associations between imaging variables and PFA subgroup variables were investigated using the χ^2 test because the expected cell counts were >5 in all contingency tables. Given the small number of tumors in some of the PFA subtypes, descriptive statistics such as frequency tables were provided to explore the relationships of the imaging characteristics of the tumors with the subtypes. All the analyses were performed in R software (Version 3.6.2).

RESULTS

The 122 subjects ranged in age from 5.3 months to 13.5 years (mean, 2.76 [SD, 2.26] years; median, 2.15 years), and most were male (71 [58.2%]). Of 122 PFA ependymomas, 75 (61%) were classified as PFA-1, and 47 (39%), as PFA-2. There was no significant difference in the mean age (PFA-1, 2.9 years; PFA-2, 2.6 years; $P = .50$, 2-sample t test) or sex distribution (PFA-1, 31 female, 44 male; PFA-2, 20 female, 27 male; $P = 1.00$; χ^2 test) between the PFA subgroups. PFA subtypes were distributed among 98 tumors for which data were available as follows: PFA-1a, 13; PFA-1b, 16; PFA-1c, 4; PFA-1d, 9; PFA-1e, 14; PFA-1f, 4; PFA-2a, 24; PFA-2b, 9; PFA-2c, 5.

None of the imaging variables were associated with the 2 PFA subgroups except for necrosis (Tables 1 and 2). Review of contingency tables showed a larger proportion of tumors of the PFA-2c subtype not extending below the foramen magnum, not involving the foramina of Luschka, and not encasing vessels compared with the other PFA-2 subtypes or all other subtypes taken together (Tables 3 and 4). A greater proportion of PFA-2c ependymomas were of the midfloor type than the other PFA-2 subtypes or all other subtypes taken together. On the basis of these findings, a flag variable that incorporated the variables of "no" for extension below the foramen magnum and "no" for encasement of vessels and midfloor-type was used, and a frequency table showed that a much greater proportion of the PFA-2c ependymomas had the

Table 3: Imaging characteristics of PFA-2c ependymomas compared with other PFA-2 subtypes and all other PFA subtypes[a]

	Yes	No
Extends below foramen magnum		
PFA-2c	0 (0%)	5 (100%)
PFA-2a and PFA-2b	29 (87.9%)	4 (12.1%)
All other PFA tumors	96 (88.9%)	12 (11.1%)
Encases blood vessels		
PFA-2c	0 (0%)	5 (100%)
PFA-2a and PFA-2b	17 (51.5%)	16 (48.5%)
All other PFA tumors	50 (46.3%)	58 (53.7%)
Involves foramina of Luschka		
PFA-2c	2 (40%)	3 (60%)
PFA-2a and PFA-2b	31 (93.9%)	2 (6.1%)
All other PFA tumors	92 (85.2%)	16 (14.8%)

[a] Ninety-eight subjects had subtype data available. "All other PFA tumors" includes the PFA-1 subgroup and the PFA-2a and 2b subtypes. The 15 subjects with PFA-1 subgroup ependymomas that could not be subtyped were included in the category of All other PFA tumors. The 8 patients with PFA-2 tumors that could not be subtyped were not included in this analysis.

Table 4: Imaging type of PFA-2c ependymomas compared with other PFA-2 subtypes and all other PFA subtypes[a]

	Lateral	Midfloor	Roof
PFA-2c	0 (0%)	5 (100%)	0 (0%)
PFA-2a and PFA-2b	10 (30.3%)	14 (42.4%)	9 (27.3%)
All other PFA tumors	43 (39.8%)	46 (42.6%)	19 (17.6%)

[a] Ninety-eight subjects had subtype data available. "All other PFA tumors" includes the PFA-1 subgroup and the PFA-2a and 2b subtypes. The 15 subjects with PFA-1 subgroup ependymomas that could not be subtyped were included in the category of All other PFA tumors. The 8 patients with PFA-2 tumors that could not be subtyped were not included in this analysis.

Table 5: PFA-2c ependymomas compared with other PFA-2 ependymoma subtypes and all other PFA subtypes with respect to flag variable 1[a]

Flag Variable 1[b]	Yes	No
PFA-2c	5 (100%)	0 (0%)
PFA-2a and PFA-2b	3 (9%)	30 (91%)
All other PFA tumors	6 (5.6%)	102 (94.4%)

[a] Ninety-eight subjects had subtype data available. "All other PFA tumors" includes the PFA-1 subgroup and the PFA-2a and 2b subtypes. The 15 subjects with PFA-1 subgroup ependymomas that could not be subtyped were included in the category of All other PFA tumors. The 9 patients with PFA-2 tumors that could not be subtyped were not included in this analysis.
[b] The flag variable incorporates the following 3 variables: "no" for extension below the foramen magnum, "no" for encases blood vessels, and "midfloor-type" tumor.

features of the flag variable than other PFA-2 subtypes or all the other subtypes as a whole (Table 5).

DISCUSSION

Previous investigations of PF ependymomas have revealed associations between tumor location and operative or disease outcomes.[4,5,17,18,22,23] For example, Ikezaki et al,[17] U-King-Im et al,[18] and Nagib and O'Fallon[22] noted lower survival rates and greater difficulty in obtaining a gross total resection for laterally located tumors (those involving the lateral recess of the fourth ventricle and cerebellopontine angle). Sanford et al[5] pointed out that cerebellopontine angle ependymomas in children arising from the foramen of Luschka and the lateral aspect of the medulla tend to encase cranial nerves and blood vessels and are difficult to resect completely, leading to lower survival rates. Sabin et al[4] determined that pediatric PF ependymomas could be divided into 2 distinct anatomic groups based on the location of their centroids and that the groups were associated with differences in progression-free survival and central-versus-lateral tumor location. The results of these studies with respect to clinical outcomes of posterior fossa ependymomas contributed to our hypothesis that the anatomic characteristics of a pediatric PFA ependymoma might also help predict its subgroup. In fact, though no survival difference was shown among the subgroups, an imaging and operative analysis of 40 tumors described in the article by Pajtler et al[9] outlining the PFA ependymoma subgroups and subtypes found that the PFA-1 lesions were more likely to be located laterally than the PFA-2 subgroup and that the origin of PFA-2 tumors was more frequently from the roof of the fourth ventricle than the origin of PFA-1 ependymomas, suggesting that the subgroups arise from cells at different brainstem levels. These prior investigations suggested that an imaging evaluation of a larger group of PFA ependymomas would result in identification of distinct anatomic markers for the PFA subgroups.

In this investigation, however, traditional anatomic characteristics seen on imaging could not be used to separate PFA tumors into their subgroups, and the findings do not provide support for the hypothesis that the PFA-1 and PFA-2 subgroups arise in different locations. The association of necrosis with subgroups is of uncertain significance. If different sites of origin for the PFA subgroups lead to different vascular supplies for the PFA-1 and PFA-2 tumors, this difference could, theoretically, cause the PFA-1 subgroup to have more tenuous neovascularization with a greater tendency to thrombosis and necrosis. Our results, however, suggest that gross anatomic characteristics of PFA ependymomas visible on MR imaging at presentation are not indicative of where PFA-1 and PFA-2 tumors arise. This outcome may reflect loss of visibility on MR imaging of key anatomic distinctions related to the PFA subgroups by the time a tumor has grown large enough to cause symptoms. Given their ability to capture more subtle differences between imaging characteristics of tumors, machine learning techniques and radiomics may be beneficial in future efforts to use imaging to classify PFA ependymomas by subgroup and determine their anatomic origins. These imaging approaches have recently been used with MR imaging to predict the subgroups of medulloblastomas.[24,25]

Examination of the imaging characteristics of tumors among the PFA subtypes, while limited by the small number of subjects in some of the subtypes, revealed that a larger proportion of PFA-2c ependymomas did not involve fourth ventricle foramina and/or did not demonstrate vascular encasement compared with other subtypes. A greater proportion of PFA-2c tumors also showed a group of imaging characteristics contained in a flag variable than the other PFA subtypes. These variables (no extension below the foramen magnum, no encasement of vessels, and midfloor-type) suggest that the PFA-2c lesions tend to be more anatomically circumscribed than PFA ependymomas of other subtypes. PFA-2c tumors had the best survival profile of all the PFA subtypes in our earlier study,[9] and this could be related to a greater proportion of that subtype having imaging characteristics, contained in the flag variable, associated with greater resectability and better outcomes.[4,5,18,19,22,23] Although additional study of larger numbers of PFA-2c subtype ependymomas is needed

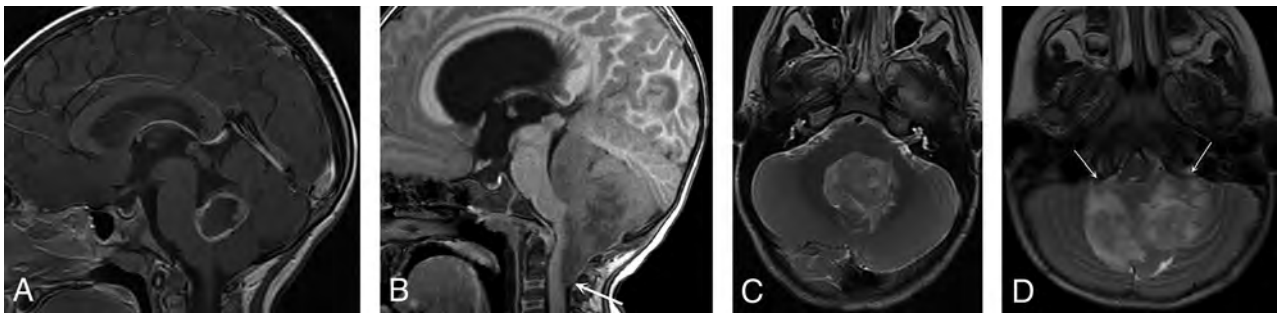

FIG 2. PFA-2c ependymoma versus another subtype. Postgadolinium sagittal T1- (*A*) and axial T2-weighted (*C*) MR images of a PFA-2c subtype ependymoma and sagittal T1- (*B*) and axial T2-weighted (*D*) MR images of another PFA ependymoma subtype (1b) show that the PFA-2c ependymoma has a more circumscribed appearance in that it does not wrap around the brainstem or extend below the foramen magnum in distinction from the PFA-1b subtype (*arrow*, *B*). The PFA-2c ependymoma in this case did not extend through the foramina of Luschka, unlike the PFA-1b tumor (*arrows*, *D*), or encase the basilar or vertebral arteries. This more circumscribed appearance was seen in the 5 PFA-2c tumors in our study, though evaluation of a larger number of this subtype is needed to confirm this appearance as a characteristic of PFA-2c ependymomas.

before any firm conclusions can be made, the subtype appears to have a distinct appearance that may be associated with its better outcome compared with the other PFA subtypes (Fig 2). If accurate imaging prediction of the PFA-2c subtype can be achieved, it would provide a noninvasive method to aid in clinical decision-making and determining prognosis.

Limitations of this investigation include the heterogeneity of the preoperative MR imaging examinations, which were performed at different institutions and with inconsistent imaging techniques. This might have limited consistent evaluation of the tumors, including determination of anatomic areas of involvement. The studies were only included, however, if they provided adequate visualization of the posterior fossa structures of interest, and all determinations of tumor characteristics were made by 2 neuroradiologists, with any differences resolved by consensus. Another limitation was the difficulty in distinguishing midfloor-type tumors from roof-type tumors because both types are centered in the fourth ventricle and it was sometimes difficult to determine whether a gap between the tumor and roof or floor of the fourth ventricle was present. Thus, some tumors may have been misclassified as midfloor or roof type. This limitation may have been lessened by the use of consensus between the neuroradiologists for difficult cases.

CONCLUSIONS

Pediatric PFA ependymomas cannot be separated into their subgroups on the basis of traditional MR imaging characteristics, and these imaging characteristics, by themselves, do not provide support for different sites of origin. Evaluation of limited numbers of PFA ependymoma subtypes suggests that the PFA-2c subtype may have distinctive imaging characteristics; however, this possibility needs to be confirmed using a suitable statistical method with a larger number of PFA subtypes.

ACKNOWLEDGMENTS

The authors thank Dr Zoltan Patay for his review of the manuscript and Ms Mary Baltimore for her assistance in its preparation.

Disclosures: Noah D. Sabin—*RELATED: Grant:* National Cancer Institute, *Comments:* Cancer Center Support Core Support Grant (CA21765).* Amar Gajjar—*UNRELATED: Consultancy:* Genentech/Roche. *Money paid to the institution.

REFERENCES

1. Ostrom QT, Patil N, Cioffi G, et al. **CBTRUS Statistical Report: Primary Brain and Other Central Nervous System Tumors Diagnosed in the United States in 2013-2017.** *Neuro Oncol* 2020;22:iv1–96 CrossRef Medline
2. Zhang C, Ostrom QT, Semmes EC, et al; Glioma International Case-Control Study (GICC). **Genetic predisposition to longer telomere length and risk of childhood, adolescent and adult-onset ependymoma.** *Acta Neuropathol Commun* 2020;8:173 CrossRef Medline
3. Vaidya K, Smee R, Williams JR. **Prognostic factors and treatment options for paediatric ependymomas.** *J Clin Neurosci* 2012;19:1228–35 CrossRef Medline
4. Sabin ND, Merchant TE, Li X, et al. **Quantitative imaging analysis of posterior fossa ependymoma location in children.** *Childs Nerv Syst* 2016;32:1441–47 CrossRef Medline
5. Sanford RA, Merchant TE, Zwienenberg-Lee M, et al. **Advances in surgical techniques for resection of childhood cerebellopontine angle ependymomas are key to survival.** *Childs Nerv Syst* 2009;25:1229–40 CrossRef Medline
6. Gajjar A, Robinson GW, Smith KS, et al. **Outcomes by clinical and molecular features in children with medulloblastoma treated with risk-adapted therapy: results of an International Phase III Trial (SJMB03).** *J Clin Oncol* 2021;39:822–35 CrossRef Medline
7. Juraschka K, Taylor MD. **Medulloblastoma in the age of molecular subgroups: a review.** *J Neurosurg Pediatr* 2019;24:353–63 CrossRef Medline
8. Malbari F, Lindsay H. **Genetics of common pediatric brain tumors.** *Pediatr Neurol* 2020;104:3–12 CrossRef Medline
9. Pajtler KW, Wen J, Sill M, et al. **Molecular heterogeneity and CXorf67 alterations in posterior fossa group A (PFA) ependymomas.** *Acta Neuropathol* 2018;136:211–26 CrossRef Medline
10. Pajtler KW, Witt H, Sill M, et al. **Molecular classification of ependymal tumors across all CNS compartments, histopathological grades, and age groups.** *Cancer Cell* 2015;27:728–43 CrossRef Medline
11. Louis DN, Perry A, Wesseling P, et al. **The 2021 WHO Classification of Tumors of the Central Nervous System: a summary.** *Neuro Oncol* 2021;23:1231–51 CrossRef Medline
12. Gibson P, Tong Y, Robinson G, et al. **Subtypes of medulloblastoma have distinct developmental origins.** *Nature* 2010;468:1095–99 CrossRef Medline
13. Ly KI, Wen PY, Huang RY. **Imaging of central nervous system tumors based on the 2016 World Health Organization Classification.** *Neurol Clin* 2020;38:95–113 CrossRef Medline
14. Patay Z, DeSain LA, Hwang SN, et al. **MR imaging characteristics of wingless-type-subgroup pediatric medulloblastoma.** *AJNR Am J Neuroradiol* 2015;36:2386–93 CrossRef Medline

15. Perreault S, Ramaswamy V, Achrol AS, et al. **MRI surrogates for molecular subgroups of medulloblastoma.** *AJNR Am J Neuroradiol* 2014;35:1263–69 CrossRef Medline
16. Yonezawa U, Karlowee V, Amatya VJ, et al. **Radiology profile as a potential instrument to differentiate between posterior fossa ependymoma (PF-EPN) group A and B.** *World Neurosurg* 2020;140: e320–27 CrossRef Medline
17. Ikezaki K, Matsushima T, Inoue T, et al. **Correlation of microanatomical localization with postoperative survival in posterior fossa ependymomas.** *Neurosurgery* 1993;32:38–44 CrossRef Medline
18. U-King-Im JM, Taylor MD, Raybaud C. **Posterior fossa ependymomas: new radiological classification with surgical correlation.** *Childs Nerv Syst* 2010;26:1765–72 CrossRef Medline
19. Ma SC, Li CD, Agazzi S, et al. **Clinical characteristics and prognostic factors of treatment in pediatric posterior cranial fossa ependymoma.** *Pediatr Neurosurg* 2019;54:98–107 CrossRef Medline
20. Pearson H, Stirling D. **DNA extraction from tissue.** *Methods Mol Biol* 2003;226:33–4 CrossRef Medline
21. Capper D, Jones DTW, Sill M, et al. **DNA methylation-based classification of central nervous system tumours.** *Nature* 2018;555:469–74 CrossRef Medline
22. Nagib MG, O'Fallon MT. **Posterior fossa lateral ependymoma in childhood.** *Pediatr Neurosurg* 1996;24:299–305 CrossRef Medline
23. Witt H, Mack SC, Ryzhova M, et al. **Delineation of two clinically and molecularly distinct subgroups of posterior fossa ependymoma.** *Cancer Cell* 2011;20:143–57 CrossRef Medline
24. Iv M, Zhou M, Shpanskaya K, et al. **MR imaging-based radiomic signatures of distinct molecular subgroups of medulloblastoma.** *AJNR Am J Neuroradiol* 2019;40:154–61 CrossRef Medline
25. Yan J, Liu L, Wang W, et al. **Radiomic features from multi-parameter MRI combined with clinical parameters predict molecular subgroups in patients with medulloblastoma.** *Front Oncol* 2020;10:558162 CrossRef Medline

A Closer Investigation of the Synchronous Bilateral Pattern of MRI Lesions in Acute Necrotizing Encephalopathy Type 1

A. Horváthy-Szőcs, Z. Liptai, S. Dobner, G. Rudas, and P. Barsi

ABSTRACT

SUMMARY: We observed a lesion pattern in a series of 4 cases of *RANBP2*-mutation–linked acute necrotizing encephalopathy, which appears to be specific for this condition. The setting of synchronous bilateral mammillary, amygdaloid, and lateral geniculate lesions, along with claustro-parahippocampal lesions, can serve as a diagnostic tool in this condition. We add several further details to the MR imaging features of the typical brain lesions encountered in this disease.

ABBREVIATIONS: ANE1 = acute necrotizing encephalopathy type 1; RANBP2 = RAN binding protein 2

As a subgroup of the more heterogeneous entity named acute necrotizing encephalopathy of childhood,[1] acute necrotizing encephalopathy type 1 (ANE1) is an underrecognized, infection-induced condition with autosomal dominant inheritance of several pathogenic mutations of the gene *RANBP2*, showing incomplete penetrance.[2-4] This condition is also named autosomal dominant acute necrotizing encephalopathy or, less commonly, infection-induced/triggered acute encephalopathy type 3. The gene encodes RAN binding protein 2 (RANBP2), a nuclear pore protein with many intracellular functions.[5] Its dysfunction causes alterations in intracellular metabolism, mitochondrial distribution, nucleocytoplasmatic trafficking,[5] and cytokine overproduction.[6] On the basis of current scientific data, it is not clear how the pathophysiologic alterations predispose to attacks[5] or why certain brain areas are specifically targeted.

MR imaging manifestations of encephalopathy and myelopathy are described in the literature.[3,5,7-9]

MATERIALS AND METHODS

We registered 4 pediatric cases of *RANBP2*-mutation–linked acute necrotizing encephalopathy. Patient 1 is male and was 4 months old at the time of the first of his 2 attacks. Patient 2 is male and was 6 years old at his first and single attack. Patient 3 is female and was 10 months old at the first of 3 attacks. Patient 4 is female, and was 4 years old at the first attack, and had 2 attacks. Patients 1 and 2 are related (half-siblings). All our patients were treated in the intensive care unit during all their attacks. Clinical follow-up was 6–18 years: Patient 1 has mild cerebral palsy, well-controlled epilepsy, and only minor school problems. Patient 2 has no neurocognitive sequelae and maintains excellent grades at school. Patients 3 and 4 have minor motor coordination issues and moderate mental retardation based on neurocognitive testing.

We used 3T Achieva and 3T Ingenia (Philips Healthcare) scanners for our work. We performed our standard head imaging protocol during the attacks (axial DWI/ADC, T2, FLAIR, SWI, 3D TOF-MRA, non-enhanced, and contrast-enhanced 3D T1 sequences), and an additional 3D FLAIR sequence for assessing small necrotic lesions in the chronic phase.

RESULTS

In the acute phase, restricted diffusion according to DWI and ADC map images, increased signal intensity on T2, FLAIR, and moderately decreased signal intensity on T1 were, in each case, seen in the bilateral mammillary, amygdaloid, and lateral geniculate bodies (patients 1, 2 and 4; Fig 1). Swelling of the mammillary bodies was also visible.

In the chronic phase, necrosis isointense with CSF was evident in each case in the amygdalae, lateral geniculate bodies, and bilateral claustro-parahippocampal regions (Fig 1). Additionally, atrophy of the mammillary bodies was also detected (3D FLAIR, Fig 1).

Moreover, typical thalamic and/or brainstem (pontine, bulbar) lesions were observed.

Received May 17, 2021; accepted after revision August 3.

From the Department of Neuroradiology (A.H.-S., G.R., P.B.), Medical Imaging Centre, and Second Department of Pediatrics (Z.L., S.D.), Semmelweis University, Budapest, Hungary; and Department of Pediatric Infectology (Z.L., S.D.), St. Laszlo Hospital, Budapest, Hungary.

Paper previously presented, in part, at: Annual Congress of the Hungarian Society of Neuroradiology, November 8–10, 2018, Eger, Hungary.

Please address correspondence to Anna Horváthy-Szőcs, MD, Semmelweis University Medical Imaging Centre, Department of Neuroradiology, Ûllői út 78a, 1082, Budapest, Hungary; e-mail: annaszocs@gmail.com

http://dx.doi.org/10.3174/ajnr.A7305

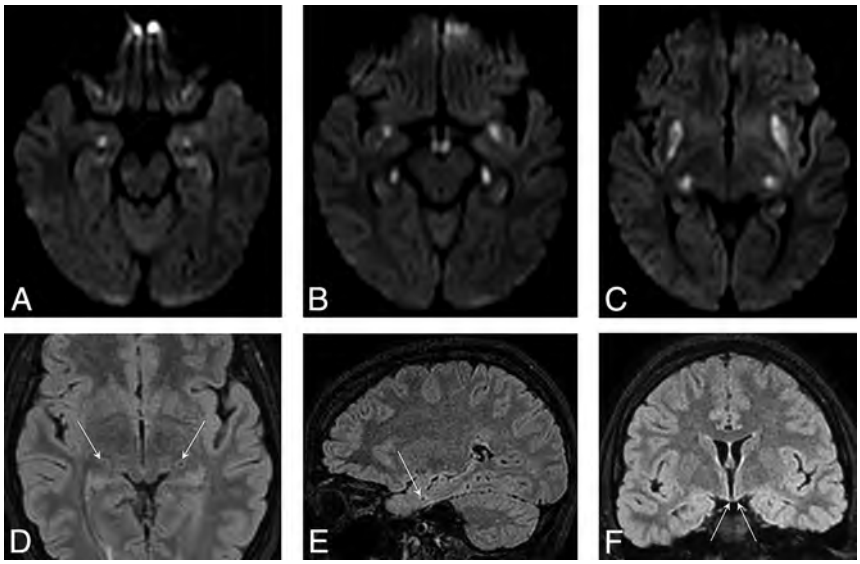

FIG 1. Axial DWI shows symmetric diffusion restriction in the amygdalae (*A*), at the anterior aspect of parahippocampal gyri, in the mammillary bodies (*B*), in the lateral geniculate bodies (*B* and *C*) and claustra (*C*). The 3D FLAIR images show the necrotic, lacunar lesions of specifically targeted, tiny structures, the lateral geniculate bodies (*D*), amygdala (*E*), and the necrotic atrophy of mammillary bodies (*F*).

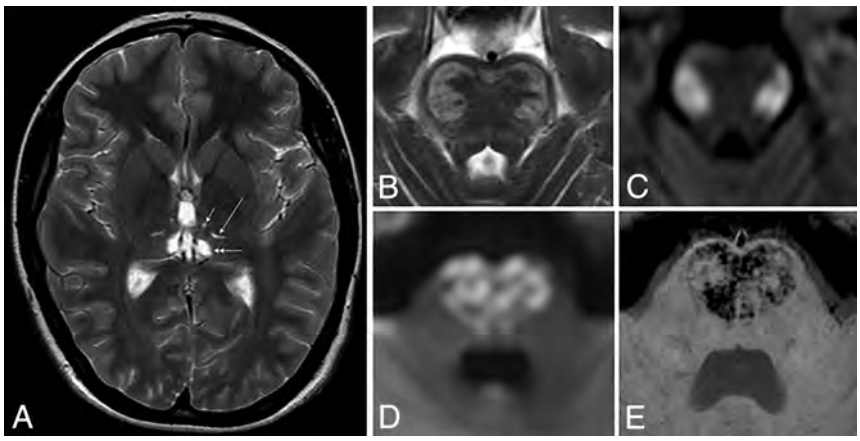

FIG 2. Axial T2WI shows chronic thalamic lesions, identified by necrosis in the ventromedial (*short arrow*), dorsolateral (*long arrow*), and dorsomedial (*double arrow*) nuclei (*A*). The axial T2WI (*B*) and DWI (*C*) show typical lateral pontine manifestations with diffusion restriction and T2-hyperintensity during the acute phase. The axial DWI (*D*) and SWI (*E*) show medial pontine manifestations with diffusion restriction and petechial hemorrhage (heart-shaped lesion).

We found that the thalamic lesions were localized in the ventromedial and/or dorsomedial and/or dorsolateral (also named ventral posterior) nuclei. This was clearly demonstrated in the chronic, postnecrotic stage (Fig 2). In the acute phase, the perifocal edema may be more widespread (involving the whole thalamus or even the surrounding regions like the internal capsule).

We found that the core of the pontine lesions in 3 of our patients arose at the lateral and, in 1 patient (during a different attack), at the central parts of the pontine base (Fig 2). One patient did not present pontine lesions. When the bilateral central parts were involved, they had a heart-shaped appearance on transverse sections (Fig 2).

Finally, we observed that typical bulbar lesions were located symmetrically in the regions of the vestibular nuclei.

DISCUSSION

To our best knowledge, we are the first to describe bilateral symmetric lesions of the lateral geniculate bodies in acute necrotizing encephalopathy type 1.

Bilateral lesions of these structures are demonstrated by MR imaging exclusively in the setting of another condition in literature.[10] In this case of pancreatitis and microangiopathy, the rest of the associated lesions typically found in ANE1 were absent.

The lateral geniculate body is an anatomic part of the thalamus (located inferolateral to the thalamic pulvinar). Therefore, we emphasize that the typical thalamic lesions considered to be most common in the radiologic setting of this disease[11] are located in other parts of the thalami, as described in the Results section.

Many authors refer to bilateral temporomedial involvement, but our current investigation shows that it is more precisely located at the most anterior, subcortical aspect of the parahippocampal gyri (Fig 1). These lesions were confluent with those in the claustrum (hence the above term "claustro-parahippocampal") during the acute phase but became isolated lacunar necrotic lesions in the chronic stage.

The lesions were exceptional in targeting a specific area of white matter, while being similar in appearance to the other bilateral lesions targeting gray matter.

We clarified that the symmetric lesions previously described in the temporal medial regions are actually situated at the most anterior subcortical aspect of the parahippocampal gyri and are unique in involving the white matter. Attention must be paid to differentiate them from the amygdaloid lesions because the proximity of the 2 small structures can lead to misinterpretation, appearing confusingly in figure captions of otherwise excellent articles.[3]

The "heart appearance" of the pontine lesions on MR imaging was previously described in a case of bilateral medial pontine

infarction.[12] We present ours as a variation of this radiologic sign in type 1 acute necrotizing encephalopathy.

CONCLUSIONS

On the basis of the analysis of the MR imaging studies of 4 patients, we describe several observations that can improve the diagnostic accuracy in ANE1 and may help the understanding of the pathomechanisms of this disease. The pattern of a synchronous appearance of bilateral amygdaloid, mammillary, lateral geniculate, and claustro-parahippocampal lesions appears to be constant and is potentially highly specific for this disease. This pattern, in combination with the features of thalamic and brainstem lesions described in detail, might play a role in further development of the neuroradiologic diagnostics or prognostic scoring. To estimate the specificity and sensitivity rates, further investigation on a broader patient group is needed.

Disclosure forms provided by the authors are available with the full text and PDF of this article at www.ajnr.org.

REFERENCES

1. Wong AM, Simon EM, Zimmerman RA, et al. **Acute necrotizing encephalopathy of childhood: correlation of MR findings and clinical outcome.** *AJNR Am J Neuroradiol* 2006;27:1919–23 Medline
2. Neilson DE, Eiben RM, Waniewski S, et al. **Autosomal dominant acute necrotizing encephalopathy.** *Neurology* 2003;61:226–30 CrossRef Medline
3. Neilson DE, Adams MD, Orr CM, et al. **Infection-triggered familial or recurrent cases of acute necrotizing encephalopathy caused by mutations in a component of the nuclear pore, RANBP2.** *Am J Hum Genet* 2009;84:44–51 CrossRef Medline
4. Neilson DE. **The interplay of infection and genetics in acute necrotizing encephalopathy.** *Curr Opin Pediatr* 2010;22:751–57 CrossRef Medline
5. Levine JM, Ahsan N, Ho E, et al. **Genetic acute necrotizing encephalopathy associated with RANBP2: clinical and therapeutic implications in pediatrics.** *Mult Scler Relat Disord* 2020;43:102194 CrossRef Medline
6. Shen Q, Wang YE, Truong M, et al. **RanBP2/Nup358 enhances miRNA activity by sumoylating Argonautes.** *PLoS Genet* 2021;17: e1009378 CrossRef Medline
7. Wu X, Wu W, Pan W, et al. **Acute necrotizing encephalopathy: an underrecognized clinicoradiologic disorder.** *Mediators Inflamm* 2015;2015:792578 CrossRef Medline
8. Denier C, Balu L, Husson B, et al. **Familial acute necrotizing encephalopathy due to mutation in the RANBP2 gene.** *J Neurol Sci* 2014;345:236–38 CrossRef Medline
9. Wolf K, Schmitt-Mechelke T, Kollias S, et al. **Acute necrotizing encephalopathy (ANE1): rare autosomal-dominant disorder presenting as acute transverse myelitis.** *J Neurol* 2013;260:1545–53 CrossRef Medline
10. Mudumbai RC, Bhandari A. **Bilateral isolated lateral geniculate body lesions in a patient with pancreatitis and microangiopathy.** *J Neuroophthalmol* 2007;27:169– 75 CrossRef Medline
11. Singh RR, Sedani S, Lim M, et al. **RANBP2 mutation and acute necrotizing encephalopathy: 2 cases and a literature review of the expanding clinico-radiological phenotype.** *Eur J Paediatr Neurol* 2015;19:106–13 CrossRef Medline
12. Ishizawa K, Ninomiya M, Nakazato Y, et al. **"Heart appearance" infarction of the pons: a case report.** *Case Rep Radiol* 2012;2012:690903 CrossRef Medline

Accuracy and Clinical Utility of Reports from Outside Hospitals for CT of the Cervical Spine in Blunt Trauma

K. Rao, J.M. Engelbart, J. Yanik, J. Hall, S. Swenson, B. Policeni, J. Maley, C. Galet, T. Granchi, and D.A. Skeete

ABSTRACT

BACKGROUND AND PURPOSE: Multidetector CT is the workhorse for detecting blunt cervical spine injury. There is no standard of care for re-interpretation of radiology images for patients with blunt trauma transferred to a higher level of care. The clinical impact of discrepancies of cervical spine CT reads remains unclear. We evaluated the discordance between primary (from referring hospitals) and secondary radiology interpretations (from a receiving level I tertiary trauma center) of cervical spine CT scans in patients with blunt trauma and assessed the clinical implications of missed cervical spine fractures.

MATERIALS AND METHODS: Medical records of patients with blunt trauma transferred to our institution between 2008 and 2015 were reviewed. Primary and secondary interpretations were compared and categorized as concordant and discordant. Two senior neuroradiologists adjudicated discordant reports. The benefit of re-interpretation was determined. For discordant cases, outcomes at discharge, injury severity pattern, treatment, and arrival in a cervical collar were assessed.

RESULTS: Six hundred fifty patients were included; 608 (94%) presented with concordant reports: 401 (61.7%) with fractures and 207 (31.8%) with no fractures. There were 42 (6.5%) discordant reports; 18 (2.8%) were cervical spine injuries undetected on the primary interpretation. Following adjudication, the secondary interpretation improved the sensitivity (99.3% versus 95.7%) and specificity (99.1% versus 91.7%) in detecting cervical spine fractures compared with the primary interpretation alone ($P < .001$).

CONCLUSIONS: There was an overall 6.5% discordance rate between primary and secondary interpretations of cervical spine CT scans. The secondary interpretation of the cervical spine CT increased the sensitivity and specificity of detecting cervical spine fractures in patients with blunt trauma transferred to higher-level care.

ABBREVIATIONS: CSI = cervical spine injury; ICD = International Classification of Diseases

Radiology studies are a frequent component of patient transfer between hospital emergency departments, especially with the increasing use of CT in the emergency department setting.[1-5] Patients experiencing trauma are often transferred to higher levels of care on the basis of findings from screening imaging studies. The consequences of a missed traumatic injury can be serious, yet the clinical implications are scarcely discussed in the current blunt cervical spine trauma literature. According to the American College of Surgeons, level I and II trauma centers are required to have systems in place to view radiographic imaging from referring hospitals.[6,7] Unfortunately, the absence of a standard of care in reviewing referring hospitals' studies has led to important interinstitutional variability in handling these examinations, especially given differences in image-acquisition techniques, lack of previous comparison examinations, and variability in reimbursement.[8-11]

A recent survey of radiologists and emergency providers at a large academic medical center revealed that while sharing images and reports from referring hospitals is highly valued, concerns regarding image quality and accurate interpretation remain.[12] Although the lack of confidence may be related to academic bias, the literature offers support for secondary interpretations. A meta-analysis of discrepancy rates among primary and secondary interpretations across trauma and nontrauma imaging data showed an overall discrepancy rate of 32.2%, including a 20.4% discrepancy rate for major findings; the overall discrepancy rate for trauma studies was 19.7%.[13] One possible reason may be that community hospitals encounter less frequent major trauma, and

Received March 31, 2021; accepted after revision August 18.

From the Departments of Radiology (K.R., B.P., J.M.), Surgery (J.M.E., C.G., T.G., D.A.S.), Acute Care Surgery Division, and Orthopedics and Rehabilitation (J.Y., J.H., S.S.), University of Iowa, Iowa City, Iowa.

Dr Granchi's current address is Envision Healthcare, Webster, Texas.

Please address correspondence to Dionne Skeete, MD, Department of Surgery, Division of Acute Care Surgery, University of Iowa, 200 Hawkins Dr, Iowa City, IA 52242; e-mail: dionne-skeete@uiowa.edu; @JMEngelbart

Indicates article with online supplemental data.

http://dx.doi.org/10.3174/ajnr.A7337

variation in radiologists rotating through an emergency call pool may contribute to a higher miss rate than subspecialty-trained fellowship radiologists at a level I trauma academic center.[14,15] To the authors' knowledge, only 1 study has investigated the clinical impact of discrepancy in cervical spine CT interpretations.[16] In their study, Khalilzadeh et al[16] included only adult patients. In this population, they concluded that secondary reads improved diagnosis and benefited patient care.

The primary aim of this study was to evaluate the discordance between radiology interpretations from referring hospitals and secondary interpretations of cervical spine CT for patients with concern for cervical spine injury (CSI) transferred to our institution, a level I tertiary trauma center. A secondary aim was to evaluate the clinical implications of the discordant reports. We hypothesized that a secondary interpretation of referring hospitals' cervical spine CTs would increase the detection of CSI, potentially impacting treatment and time to cervical spine clearance for patients experiencing trauma transferred to a higher level of care.

MATERIALS AND METHODS

Study Design and Data Collection

This retrospective study was approved by the University of Iowa institutional review board (IRB No. 201712728). Medical records of patients transferred to our institution, an academic level I trauma and tertiary care center, following blunt trauma injury between July 2008 and September 2015 were reviewed. Per our institutional protocol, all patients experiencing trauma accepted for transfer who have accompanying radiology images that are complete are requested to have a secondary interpretation of transferred radiology images. Inclusion criteria for data analysis were the availability of cervical spine CT images from the referring hospital with an external radiology report (primary interpretation) at the time of transfer and an available internal radiology interpretation (secondary interpretation) of the external images performed at admission. Patients were excluded if the referring hospital's cervical spine images and reports were not available for review or if a secondary read was not performed at our institution. Patients were referred from 25+ surrounding regional/private nonacademic community hospitals in the United States, within a 200-mile radius of our institution. This study follows the Strengthening the Reporting of Observational Studies in Epidemiology (STROBE) reporting guidelines for cohort studies.[17,18]

A thorough chart review was performed to compare the primary with the secondary interpretations of the same CT images of the cervical spine. Images were received as trauma protocol scans of the cervical spine, with available axial, sagittal, and coronal multiplanar reformations with soft-tissue and bone windows. These were transferred electronically from the referring hospital or via a CD and were uploaded to our institution's PACS and interpreted by fellowship-trained neuroradiology or musculoskeletal radiology faculty. For the patients who met the inclusion criteria, the following variables were collected from electronic medical records: patients' demographics (age and sex) and principal and secondary diagnoses with the respective International Classification of Diseases-10 (ICD-10) codes.

For all included patients, primary interpretations were compared against the secondary interpretations and categorized into concordant or discordant groups. Discordant cases were then adjudicated by 2 senior board-certified neuroradiologists (B.P. and J.M., both with 15+ years of practice). Both adjudicators reviewed the external CT images and the primary and secondary radiology reports to adjudicate the presence of CSI. The adjudicators were blinded to the radiologists who interpreted the primary and secondary reports and the facility at which the imaging and interpretation took place. Adjudicators had access to MR imaging performed at our institution in 17/42 patients to classify discordant reports more accurately. STIR sequences were part of the protocol for MR imaging performed at our institution.

For patients with discordant reports, we collected the following additional clinical information: neurologic symptoms at presentation, outcome at discharge (alive versus deceased), CSI stability pattern, operative-versus-nonoperative treatment, treatment with a cervical collar, and patient arriving in a cervical spine collar at the time of transfer. The authors defined the following injuries as unstable CSI patterns: atlanto-occipital dislocation, anterior atlantoaxial dislocation, Jefferson (C1 burst) fracture, C2 dens fracture, hangman fracture, flexion teardrop fracture, extension teardrop fracture, bilateral facet dislocation, anterior subluxation, multilevel fracture, and fracture dislocation.[19]

Sample Size Calculation

A statistically adequate sample size was estimated using the Cohen κ statistic based on Khalilzadeh et al,[16] who showed that 31% of patients presented with cervical spine injury on the initial interpretation. With an SD of 0.2, a minimum of 633 subjects would be required to observe a 92% agreement between the primary radiology interpretation and the secondary interpretation performed at our center.

Statistical Analysis

Statistical analysis was performed using SPSS 25 (IBM). Descriptive statistics were obtained from demographic and outcomes data. Variables were expressed as descriptive statistics including number, percentage, mean, and SD. Interrater reliability was established with the Cohen κ statistic.

RESULTS

Study Population

A sample of 1251 patients who experienced blunt traumatic injury and were transferred from a referring hospital with a "store and interpret" order of the cervical spine were identified from July 1, 2008, to September 31, 2015. Of these patients, 601 patients (48%) did not have external images or a primary interpretation available and/or did not have a secondary interpretation of the available external images. These patients were excluded from the study. External images and primary interpretations as well as secondary interpretations were available for the 650 patients who were included in this study. As we reached the sample size determination, further data collection was stopped. Of the 650 patients who met the inclusion criteria, 374 (57%) were male. Ages ranged from 7 to 90 years (mean, 55 [SD, 23] years). Twenty of 650 patients were younger than 18 years of age (age

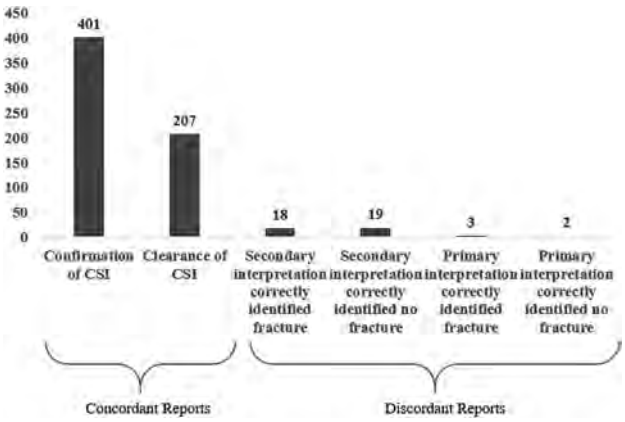

FIG 1. Report comparison of primary and secondary interpretations.

range, 7–17 years). The most frequent ICD codes for admission were closed fractures of the second cervical vertebra (11.4%) followed by closed fractures of the thoracic vertebrae without mention of spinal cord injury (6.5%) and closed fractures of the lumbar vertebrae without mention of spinal cord injury (5.6%).

Concordant Interpretations

Of the 650 patients, 608 (94%) had a concordant interpretation when comparing the primary interpretation with the secondary interpretation. Four hundred one patients (62%) had CSI identified on both the primary and secondary interpretations and were classified as having concordant reports with CSI (Fig 1). The most common CSIs identified by ICD codes were closed fractures of the second cervical vertebra (11.4%), seventh cervical vertebra (5.2%), and first cervical vertebra (4.8%). Two hundred seven patients (32%) did not have a CSI on both the primary and secondary interpretations and were classified as having concordant reports without CSI.

Discordant Interpretations

There was a disagreement between the primary and secondary interpretations in 42 patients (6.5%), with only 1 discordant case involving a patient younger than 18 years of age. Adjudication of the discordant reports by 2 senior neuroradiologists determined that the primary interpretation correctly identified fractures in 3 of 42 reports (7.1%) and correctly identified no fractures in 2 reports (4.8%), with the secondary interpretation being incorrect. Adjudication of the discordant reports also determined that the secondary interpretation identified fractures in 18 of 42 reports (42.9%) that were missed on the primary interpretation and identified no fractures in 19 reports (45.2%) that were initially diagnosed in the primary interpretation. The results of adjudication revealed that 88.1% of the discordant reports matched the secondary interpretation; however, the secondary interpretation did not match the adjudication for 11.9% of discordant reports.

Compared with the primary interpretation alone, the secondary interpretation improved the sensitivity from 95.7% to 99.3% and specificity from 91.7% to 99.1% for detecting cervical spine fractures. Positive predictive values (95.5%–99.5%) and negative predictive values (92.1%–98.7%) improved with the addition of a secondary interpretation compared with only a primary interpretation, a statistically significant improvement ($P < .001$) (Table 1). Interrater reliability analysis resulted in a κ statistic of 0.8581.

Table 1: Adjudication of the discordant results[a]

	Presence of CSI	
Primary interpretation identified CSI	Yes	No
Yes	404	19
No	18	209
Secondary interpretation identified CSI		
Yes	419	2
No	3	226

[a] Sensitivity and specificity of primary (95.7% and 91.7%, respectively) and secondary interpretations (99.3% and 99.1%, respectively) were compared after adjudication.

Use of MR Imaging

MR imaging was performed within 24–48 hours of admission as ordered by the clinical team when indicated to further evaluate injury. Within the discordant group, a secondary interpretation was reported in all except 1 case before MR imaging was performed during hospitalization. There were 17 cases in the discordant group in which MR imaging was available to adjudicators to classify reports more accurately. From those 17 cases, there were 2 instances in which the MR imaging proved the primary interpretation, positive for CSI, to be correct, which was missed on the secondary interpretation. There were 6 instances in which the MR imaging confirmed a positive CSI on the secondary interpretation that was missed on the primary interpretation. There were 6 instances in which MR imaging excluded injury, confirming the negative finding on the secondary interpretation when the primary interpretation reported a CSI. There was 1 case in which the MR imaging excluded injury, confirming the negative findings on the primary interpretation when the secondary interpretation reported an injury. Finally, there were 2 cases in which the MR imaging interpretation did not comment on a fracture when the primary interpretation reported no injury and a secondary interpretation reported CSI.

We further evaluated the discordant groups because management of these patients was most likely to be impacted. The most frequent CSIs identified on the primary interpretation with no consensus on the secondary interpretation were facet fractures (32%, $n = 6$), vertebral body fractures (26%, $n = 5$), and lamina fractures (21%, $n = 4$) (Table 2). An example of a discordant falsely identified fracture is shown in Fig 2. The most frequent injuries undetected in the primary interpretation but detected in the secondary interpretation were fractures of the seventh cervical vertebra (transverse process, facet fractures: 50%, $n = 9$) and C2 injuries (lateral mass, dens, odontoid fractures: 28%, $n = 5$) (Table 2). In this population, 2 missed cervical spine injuries were classified as unstable (multilevel fractures at C2 and C5, and a C3 teardrop fracture) (Table 2). An example of a discordant missed injury on the primary interpretation, an unstable pattern teardrop fracture, is shown in Fig 3.

Clinical Implications

The subgroup of interest with respect to clinical outcomes was the discordant group in which secondary interpretation identified

Table 2: Discordant primary interpretations with false-positives and false-negatives by frequencies of adjudicated injury types[a]

Discordant Reports	No.	%
Discordant falsely identified fractures	19/650	3
Discordant falsely identified fractures by type		
Facet	6/19	32
Vertebral body	5/19	26
Lamina	4/19	21
Transverse process	2/19	11
Spinous process	1/19	5
Subluxation	1/19	5
C1 arch	1/19	5
Discordant fractures missed on primary interpretation	18/650	2.8
Discordant missed fractures by type		
C7 (transverse process, facet, or endplate)	9/18	50
C2 (dens, odontoid, pedicle, transverse foramen, lateral mass)	5/18	28
C4 (spinous process, vertebral body, foramina)	4/18	22
Occipital condyle	2/18	11
C5 (transverse process, foramina)	2/18	11
Teardrop	1/18	5.5
C1 arch	1/18	5.5

[a] Data presented in this table are those of patients with discordant results postadjudication. Note that some cases had multiple cervical spinal fractures.

FIG 2. Example of a falsely diagnosed fracture on primary interpretation. The referring hospital falsely identified a chip fracture of the right inferior articular facet of C5 (CT images, *A* and *C*). MR imaging was performed to assess right upper extremity weakness and did not show any evidence of fracture or ligamentous injury. Axial T1 (*B*) and sagittal STIR (*D*).

an injury not identified in the primary interpretation, 2 of which were adjudicated as no fracture present and 18 with fracture present (Online Supplemental Data). Two of the 18 patients had an unstable CSI pattern at the secondary interpretation; 1 of those 2 patients required an operation. The unstable patterns not appreciated on the primary interpretation included multilevel C2 and C5 fractures and a C3 teardrop fracture (Fig 3). Both patients with the missed unstable injury pattern (teardrop fracture and C2 and C5 fractures) had a clinical diagnosis of central cord syndrome based on physical examination. Two patients, both found to have stable injury patterns on the secondary interpretation and subsequently managed with cervical immobilization, arrived from referring hospitals without a cervical collar. The remaining 16 of 18 patients with missed CSIs on the primary interpretation were treated with cervical immobilization. There was 1 mortality in this group, but it was unrelated to the cervical spine pathology.

DISCUSSION

Access to accurate radiographic interpretations is paramount for providers.[12] In the case of transferred patients, treating providers may be biased to radiographic interpretations from their own facility.[12] The decision to obtain secondary interpretations of imaging performed from referring hospitals should be considered on the basis of current literature evidence and local assessments of discordance rates, considering time, resources, and the cost of overreads or missed injuries. Sung et al[20] identified a 12% discordance rate for outside trauma imaging requested for secondary interpretation at higher level of care centers; their scans were inclusive of abdomen/pelvis, brain, chest, and other body region studies. More recently, Robinson et al[21] showed an 8.5% rate of discrepancy between referring hospitals' primary interpretations and internal secondary interpretations in the emergency department for imaging of transfer patients with and without trauma. Because surgical subspecialists, including spine specialists, are not always available in our catchment area, a large number of patients are transferred for management of injuries identified on imaging. Our center performs secondary interpretations as ordered by the treating providers. The purpose of this study was to examine the discrepancy rates specifically in cervical spine imaging. Our goals were the following: 1) add to the relatively sparse body of literature available for institutions considering secondary interpretation of trauma imaging, 2) identify patterns in the missed and falsely diagnosed cervical spine fractures, 3) evaluate the clinical implications of a missed CSI, and 4) assess whether the practice of secondary interpretations of transferred imaging should continue.

We found a 6.5% rate of discordance in cervical spine CT interpretations in our study. This is similar to findings of Khalilzadeh et al,[16] who found an 8% discordance rate between referring hospital CT cervical spine reports and internal secondary interpretations in patients experiencing trauma transferred to a higher level of care. This is the only additional study in the literature to look specifically at discordance rates in cervical spine imaging in patients experiencing trauma. The sample size of our study is double that of Khalilzadeh et al. While there are studies that cite average generalized diagnostic error rates, this study focused specifically on the subset of cervical spine CT imaging in patients experiencing trauma, comparing concordance and discordance between radiology

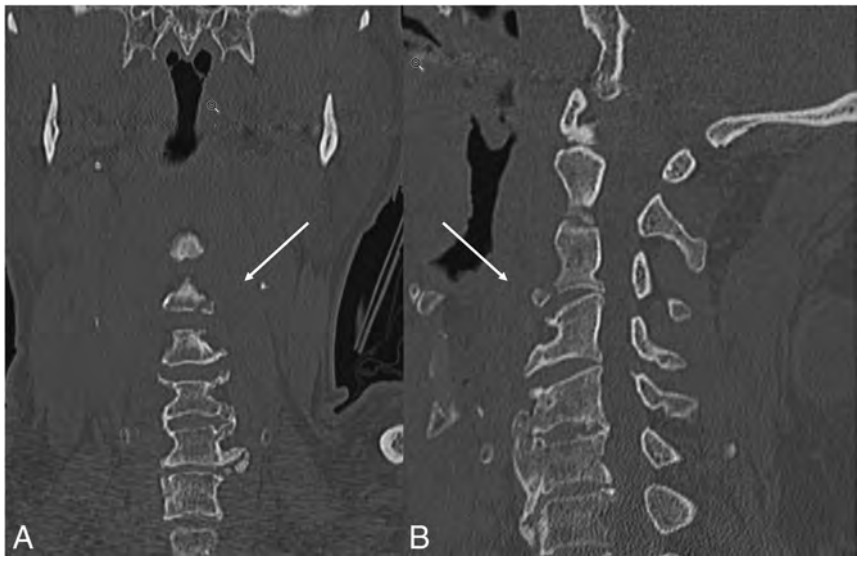

FIG 3. Example of a missed, unstable pattern fracture on the primary interpretation from the referring hospital, which was identified as a C3 teardrop fracture seen in both the coronal (*left*) and sagittal (*right*) reformations on the secondary interpretation (*arrows*). The patient presented with upper extremity weakness and was treated nonoperatively with a cervical collar.

providers covering rural community hospitals and radiologists at an academic level I trauma center to determine whether there is utility in requesting a secondary interpretation on patient transfer. This study adds to the literature because it presents the largest cohort studied to date. It is the first to include pediatric patients and to report the clinical implications of a missed CSI, including management of injury, operative repair, complications pertaining to CSI, and investigation of further advanced imaging. The methodology of this study including the adjudication process is also a strength compared with current literature.

For all 42 discordant cases, all primary reads were from community-based radiologists. Although the authors are not privy to the training background of the primary radiologists, we hypothesize that the discordance rate and missed CSI on primary interpretation is explained by the variability of general radiologists rotating through emergency calls (as opposed to dedicated emergency-trained radiologists), with comparatively less frequent trauma exposure in smaller community hospitals. The most frequently missed radiologic findings in this study population were transverse process fractures and dens fractures, a pattern consistent with the prior study.[16] We observed a relatively higher frequency of missed C7 fractures in this population, for which there is not a strong explanation. External cervical spine CTs were performed with a trauma protocol and imaged through T2–T3 vertebral bodies on the sagittal view, providing for complete examinations. Satisfaction of search may explain missed C7 injuries because this region of the cervical spine often falls at the end of the search pattern. The most frequent overcalled findings were facet fractures and lamina fractures. In addition, the miss rate of CSI can be influenced by image quality, the presence of multilevel degenerative disease, existing spine instrumentation/hardware, and normal variants (accessary ossicles, limbus vertebrae, unfused apophysis), which add to the challenge of interpreting trauma CT scans of the cervical spine and can confound acute findings. Further studies of the incidence of discordance and analysis of commonly missed radiographic findings can provide a foundation for education and improvement for radiologists.

The clinical implications of missing cervical spine injuries should be an important factor in the decision to perform secondary interpretations of imaging in transferred patients. In this study population, 2 of 18 patients with missed fractures on primary interpretations had an unstable fracture pattern. Another 2 of 20 were transferred to a higher level of care without cervical immobilization. Two patients of 18 presented with neurologic symptoms. Although an overall small percentage of patients fell into this group, the authors favored the secondary interpretation because of the improved sensitivity and specificity of detecting cervical spine fractures following secondary interpretation. The authors recognize that very few discrepancies led to surgical interventions or were unstable fractures affecting morbidity or mortality. The 6.5% discrepancy rate may, in part, reflect an underlying 3%–5% diagnostic error rate reported in the literature.[22] However, this percentage is a general estimate that includes multiple imaging modalities, whereas our study evaluates a specific imaging format (cervical spine CT) in a specific population (patients with blunt trauma) between community hospitals in rural areas that see trauma less frequently and a level I trauma academic center. The decision to recommend a secondary interpretation as a standard of practice will depend on locoregional error rates, imaging technique, and acuity of the injury, among other factors such as reimbursement. Previous studies supporting secondary interpretations of imaging performed in transferred patients have found decreased rates of subsequent imaging use and improved patient diagnosis and care.[16,23] Arguments against secondary interpretation would be a lack of standardized protocols in liability and reimbursement for external interpretations, added time and resource use, and clinical delay of clearing negative findings on cervical spine examinations for patients experiencing trauma.

This study has some limitations. First, this is a retrospective study that introduces a risk of selection bias and incomplete data capture from poor documentation or missing data. From the 1251 patients retrospectively identified, 48% did not have external radiology imaging or a primary interpretation on transfer to our institution. For some transfers, cervical spine imaging was not performed at the referring hospital, depending on the type of traumatic injury. Subsequently, transfer patients in whom cervical spine imaging was performed on the basis of clinical suspicion or mechanism of injury resulted in a higher rate of CSI detection (61.7%) compared with the literature. This is likely because this study specifically looked at patients transferred for concern for spine injury in the setting of blunt trauma.[24-26] Although our study included pediatric patients,

only 20 of the 650 included cases were pediatric cases, and only 1 discordant case involved a child, limiting our impact to comment on discordant rates in pediatric populations.

The study did not address additional fractures that were missed in the cervical spine, and discordance was based on whether a cervical spine injury was called. The smaller sample size of discordant reports also limited our ability to perform a more robust statistical analysis pertaining to clinical outcomes. Future studies comparing outcomes between the discordant and concordant patient groups are warranted. The authors also acknowledge that the imaging quality, windowing, and motion of the external hospital CT scanner were factors beyond the scope and control of this study and may have impacted image interpretation. Finally, our demographic analysis did not include identification of the mechanism of injury, which could affect the odds of having CSI.

CONCLUSIONS

In this review of 650 cervical spine CT studies on patients transferred from community hospitals to a level I trauma center, there was a 6.5% discordance rate between the primary and secondary interpretations of the CT scans of the cervical spine, with 3% of patients presenting with a CSI not appreciated on the primary interpretation. This discordance impacted both the nonoperative and surgical management of patients in this study. The secondary interpretation significantly improved the sensitivity and specificity for the detection of cervical spine fractures in patients transferred to higher-level care. While re-interpreting external CT scans of patients with blunt trauma poses challenges with respect to time, resource allocation, medicolegal liability, and compensation, secondary interpretations of external cervical spine CTs present improved detection of injuries resulting in a benefit in terms of care and safety for patients with blunt trauma transferred to a higher level of care. On the basis of the findings of this study and the existing literature, the authors suggest that secondary interpretation of CT scans for patients with blunt trauma transferred to a higher level of care should become a standard practice nationally, but they recognize that the decision to do so is additionally influenced by the baseline locoregional diagnostic error rate and policies in reimbursement.

ACKNOWLEDGMENTS

The authors would like to acknowledge Tzu Chuan Yen for her contribution in chart review.

Disclosures: Jacklyn Engelbart—*UNRELATED*: *Grants/Grants Pending*: National Institutes of Health, *Comments*: I am a research resident with my salary funded by the National Institutes of Health T32 Surgical Oncology Research Grant at my institution. This project was completed outside of the scope of that research and funding.* *Money paid to the institution.

REFERENCES

1. Selvarajan SK, Levin DC, Parker L. **The increasing use of emergency department imaging in the United States: is it appropriate?** *AJR Am J Roentgenol* 2019;213:W180–84 CrossRef Medline
2. Rui PK. **National Hospital Ambulatory Medical Care Survey: 2017 Emergency Department Summary Tables.** 2017. https://www.cdc.gov/nchs/data/nhamcs/web_tables/2017_ed_web_tables-508.pdf. Accessed March 1, 2021
3. Kocher KE, Meurer WJ, Fazel R, et al. **National trends in use of computed tomography in the emergency department.** *Ann Emerg Med* 2011;58:452–62 CrossRef Medline
4. Broder J, Warshauer DM. **Increasing utilization of computed tomography in the adult emergency department, 2000-2005.** *Emerg Radiol* 2006;13:25–30 CrossRef Medline
5. Bellolio MF, Heien HC, Sangaralingham LR, et al. **Increased computed tomography utilization in the emergency department and its association with hospital admission.** *West J Emerg Med* 2017;18:835–45 CrossRef Medline
6. American College of Surgeons, Committee on Trauma. *Resources for Optimal Care of the Injured Patient*. 6th ed. America College of Surgeons, Committee on Trauma; 2014
7. American College of Surgeons. ACS BEST PRACTICE GUIDELINES IN IMAGING. https://www.facs.org/-/media/files/quality-programs/trauma/tqip/imaging_guidelines.ashx. 2018. Accessed March 1, 2021
8. Swenson DW, Ellermeier A, Dibble EH, et al. **Review of outside studies by radiology residents: national survey of chief residents.** *Emerg Radiol* 2014;21:479–84 CrossRef Medline
9. Robinson JD, McNeeley MF. **Transfer patient imaging: a survey of members of the American Society of Emergency Radiology.** *Emerg Radiol* 2012;19:447–54 CrossRef Medline
10. Lu MT, Hallett TR, Hemingway J, et al. **Secondary interpretation of CT examinations: frequency and payment in the Medicare fee-for-service population.** *J Am Coll Radiol* 2016;13:1096–1101 CrossRef Medline
11. Lu MT, Tellis WM, Fidelman N, et al. **Reducing the rate of repeat imaging: import of outside images to PACS.** *AJR Am J Roentgenol* 2012;198:628–34 CrossRef Medline
12. Rosenkrantz AB, Smith SW, Recht MP, et al. **Perceptions of radiologists and emergency medicine providers regarding the quality, value, and challenges of outside image sharing in the emergency department setting.** *AJR Am J Roentgenol* 2020;214:843–52 CrossRef Medline
13. Rosenkrantz AB, Duszak R Jr, Babb JS, et al. **Discrepancy rates and clinical impact of imaging secondary interpretations: a systematic review and meta-analysis.** *J Am Coll Radiol* 2018;15:1222–31 CrossRef Medline
14. Lyon M, Sturgis L, Lendermon D, et al. **Rural ED transfers due to lack of radiology services.** *Am J Emerg Med* 2015;33:1630–34 CrossRef Medline
15. Saketkhoo DD, Bhargavan M, Sunshine JH, et al. **Emergency department image interpretation services at private community hospitals.** *Radiology* 2004;231:190–97 CrossRef Medline
16. Khalilzadeh O, Rahimian M, Batchu V, et al. **Effectiveness of second-opinion radiology consultations to reassess the cervical spine CT scans: a study on trauma patients referred to a tertiary-care hospital.** *Diagn Interv Radiol* 2015;21:423–27 CrossRef
17. Vandenbroucke JP, von Elm E, Altman DG, et al; STROBE Initiative. **Strengthening the Reporting of Observational Studies in Epidemiology (STROBE): explanation and elaboration.** *Epidemiology* 2007;18:805–35 CrossRef Medline
18. von Elm E, Altman DG, Egger M, et al;. STROBE Initiative. **The Strengthening the Reporting of Observational Studies in Epidemiology (STROBE) statement: guidelines for reporting observational studies.** *Epidemiology* 2007;18:800–04 CrossRef Medline
19. Adams J, Lin M, Mahadevan SV. **Spine trauma and spinal cord injury.** In: Adams JC, Baron J, DeBlieur PM, et al. *Emergency Medicine: Clinical Essentials*. Elsevier Saunders, 2013
20. Sung JC, Sodickson A, Ledbetter S. **Outside CT imaging among emergency department transfer patients.** *J Am Coll Radiol* 2009;6:626–32 CrossRef Medline
21. Robinson JD, Linnau KF, Hippe DS, et al. **Accuracy of outside radiologists' reports of computed tomography exams of emergently transferred patients.** *Emerg Radiol* 2018;25:169–73 CrossRef Medline
22. Itri JN, Tappouni RR, McEachern RO, et al. **Fundamentals of diagnostic error in imaging.** *Radiographics* 2018;38:1845–65 CrossRef Medline

23. Sodickson A, Opraseuth J, Ledbetter S. **Outside imaging in emergency department transfer patients: CD import reduces rates of subsequent imaging utilization.** *Radiology* 2011;260:408–13 CrossRef Medline
24. Dreizin D, Letzing M, Sliker CW, et al. **Multidetector CT of blunt cervical spine trauma in adults.** *Radiographics* 2014;34:1842–65 CrossRef Medline
25. Goldberg W, Mueller C, Panacek E, et al; NEXUS Group. **Distribution and patterns of blunt traumatic cervical spine injury.** *Ann Emerg Med* 2001;38:17–21 CrossRef Medline
26. Hasler RM, Exadaktylos AK, Bouamra O, et al. **Epidemiology and predictors of cervical spine injury in adult major trauma patients: a multicenter cohort study.** *J Trauma Acute Care Surg* 2012;72:975–81 CrossRef Medline

Vessel Wall Imaging: A Powerful Diagnostic Tool but Not a Substitute for Biopsies

We read with interest the letter from Drs Corrêa and Hygino da Cruz, Jr, describing their patient with Varicella zoster virus vasculitis.[1] We agree that a biopsy is not always necessary for diagnosing vascular inflammation with the use of high-resolution 3D vessel wall MR imaging (VWMRI) in the appropriate clinical context. However, we caution readers who might then believe that brain biopsy can be replaced with VWMRI.

Determining the underlying etiology of a patient's intravascular inflammation is essential to determining prognostication and treatment. In the case presented by Drs Corrêa and Hygino da Cruz, Jr, Varicella zoster virus infection was diagnosed by polymerase chain reaction performed on CSF, suggesting that VWMRI was not needed in this case. In the many cases in which serum, CSF, and other work-ups are nondiagnostic for an underlying etiology, we suggest that biopsy remains instrumental in tailoring therapy. Notably, our data indicate that VWMRI can be used to identify inflamed intracranial vessels but is otherwise unable to distinguish among primary, infectious, and/or any etiology leading to perivascular inflammation.[2]

Thus, VWMRI should be paired with diagnostic tools that can confirm an etiology, namely VWMRI-directed intracranial biopsy, after which VWMRI could be useful for tracking treatment response. Thus, we disagree with the assertions of Drs Corrêa and Hygino da Cruz, Jr, that might encourage readers to turn to current VWMRI to avoid invasive procedures such as brain biopsy.

http://dx.doi.org/10.3174/ajnr.A7277

REFERENCES

1. Corrêa DG, Hygino da Cruz LC Jr. **High-resolution vessel wall MR imaging as an alternative to brain biopsy.** *AJNR Am J Neuroradiol* 2019;40:E17–18 CrossRef Medline
2. Zeiler SR, Qiao Y, Pardo CA, et al. **Vessel wall MRI for targeting biopsies of intracranial vasculitis.** *AJNR Am J Neuroradiol* 2018;39:2034–36 CrossRef Medline

S.R. Zeiler
Department of Neurology
Johns Hopkins University
Baltimore, Maryland

B.A. Wasserman
Department of Diagnostic Radiology & Nuclear Medicine
University of Maryland School of Medicine and The Russell H. Morgan
Department of Radiology and Radiological Sciences
Johns Hopkins University
Baltimore, Maryland

Usefulness of a Radial-Specific Neurointerventional Guiding Sheath

It is with much consideration that we have read the article "Distal Transradial Access for Diagnostic Cerebral Angiography and Neurointervention: Systematic Review and Meta-Analysis," by Hoffman et al.[1] We completely agree with the authors' conclusion that early experience with distal transradial access (dTRA) suggests that it is a safe and effective alternative to proximal transradial access (pTRA) and femoral access for performing diagnostic cerebral angiography and interventions. Meanwhile, the authors reported, in the "Future Directions" section, that the development of catheters specifically designed for transradial neurointervention may improve the efficacy of the approach.[1] Transradial access, including pTRA and dTRA, can be technically challenging for a certain population of patients with an unfavorable acute takeoff of the target common carotid artery (CCA), such as those with right CCA lesions with steep angulation to the right subclavian artery, or left CCA lesions of nonbovine origin. In such cases, a conventional straight-shaped guiding system can prolapse into the aortic arch or can cause catheter kinking, resulting in device entrapment/fracture.

We previously reported that first-line transradial access with a 6F preshaped Simmons guiding sheath (0.088-inch inner diameter, 6F Axcelguide STIFF-J, 90 cm; Medikit) provides a high procedural success rate without catheter kinking or system instability for all aortic arch types and target CCAs.[2-4] The 6F Simmons guiding sheath is a radial-specific neurointerventional sheathless guiding catheter whose distal end comprises a kink-resistant Simmons curve specially designed for CCA cannulation. The 6F Simmons guiding sheath is introduced into the target CCA by using the "push-in" or "pull-back" cannulation techniques based on the access side, aortic arch type, and target CCA. The push-in technique is a procedure to coaxially advance a 6F Simmons guiding sheath using a push-in maneuver, while the pull-back technique is a procedure to coaxially deliver a 6F Simmons guiding sheath using a pull-back maneuver after the reformation of the natural reversed curve (Simmons curve) within the ascending aorta.[2-4] Transradial carotid cannulation with the pull-back technique is technically simple and is unique to this radial-specific neurointerventional guiding sheath. We believe that dTRA with the radial-specific 6F Simmons guiding sheath will be a useful option in anterior circulation interventions.

Finally, we would like to congratulate the authors for their interesting review, which improves the transradial neurointerventional approach.

REFERENCES

1. Hoffman H, Jalal MS, Masoud HE, et al. **Distal transradial access for diagnostic cerebral angiography and neurointervention: systematic review and meta-analysis.** *AJNR Am J Neuroradiol* 2021;42:888–95 CrossRef Medline
2. Hanaoka Y, Koyama JI, Ogiwara T, et al. **Usefulness of a novel technique to make up for a deficiency in transradial neurointervention with a 6Fr Simmonds guiding sheath: original experience with the subclavian artery anchoring technique.** *World Neurosurg* 2019;131:e362–70 CrossRef Medline
3. Hanaoka Y, Koyama JI, Yamazaki D, et al. **Transradial approach as the primary vascular access with a 6-Fr Simmons guiding sheath for anterior circulation interventions: a single-center case series of 130 consecutive patients.** *World Neurosurg* 2020;138:e597–606 CrossRef Medline
4. Hanaoka Y, Koyama JI, Ogiwara T, et al. **Feasibility and safety of radial-first approach with a radial-specific neurointerventional guiding sheath for intracranial aneurysm coiling in the anterior circulation.** *World Neurosurg* 2020;142:e297–306 CrossRef Medline

J.-I. Koyama
Neuroendovascular Therapy Center
Shinshu University Hospital
Matsumoto, Japan

Y. Hanaoka
Department of Neurosurgery
Shinshu University School of Medicine
Matsumoto, Japan

T. Ogiwara
T. Horiuchi
Department of Neurosurgery
Shinshu University School of Medicine
Matsumoto, Japan

http://dx.doi.org/10.3174/ajnr.A7226